Geological and mineralogical investigation of Rotliegend gas reservoirs in the Netherlands and their potential for CO_2 storage

Dissertation

zur Erlangung des akademischen Grades
doctor rerum naturalium
(Dr. rer. nat)

vorgelegt dem Rat der Chemisch-Geowissenschaftlichen Fakultät der Friedrich-Schiller-Universität Jena

von Dipl.-Geow. Svenja Waldmann

geboren am 20.04.1982 in Göttingen

1. Gutacher: Prof. Dr. Reinhard Gaupp,
   Institut für Geowissenschaften, Universität Jena

2. Gutacher: Dr. Étienne Brosse,
   Geology – Geochemistry - Geophysics, IFP Énergies nouvelles, Frankreich

Tag der öffentlichen Verteidigung: 16.12.2011

Content

Acknowledgement

This thesis would not have been possible without the initiation by Prof. Reinhard Gaupp and Dr. Dieter Pudlo from Jena University. I am deeply thankful for the support of Prof. Reinhard Gaupp during all the time.

I am grateful to the company Nederlandse Aardolie Maatschappij B.V. (NAM) and its partners Energie Beheer Nederland (EBN) and ExxonMobil Production Netherlands (EMPN) who funded this project. My special thanks go to Dr. Kees van Ojik and Dr. Alice Post for their support.

I would like to thank my colleagues from Shell Global Solutions International B.V. in Rijswijk, Netherlands where I performed the geochemical and reactive transport modelling. Thanks are given to Dr. Claus Otto who initiated my sojourn time in Rijswijk. In particular I am thankful for the intensive and interesting discussion with Dr. Andreas Busch. Thanks are also given to Dr. Lingli Wei, Dr. Jeroen Snippe and Dr. Chris Pentland who supported me during reactive transport modelling performance. Dr. Suzanne Hangx and Dr. Emilia Liteanu are thanked for their friendliness and support and special thanks go to Suzanne for writing a computer program for surface area calculation of feldspar. Thanks are further given to Dr. Anthony Park from Sienna Geodynamics & Consulting for his discussion about the geochemical modelling results.

I am grateful to have had the opportunity to perform several analyses at other institutions where I received a lot of help and supporting discussions. Pieter Bertier from University Aachen performed the batch-experiments wherefore I am thankful. My thanks are given to Dr. Ulrich Gernert and François Gilbert from the Central Institution for Electronic Microscopy of the Technical University Berlin with whom I worked at the electron microprobe and secondary electron microscope. I am thankful for the support by Dr. Volker Karius from University Göttingen where I performed X-Ray diffraction analyses. Also for the BET-analysis which were performed by Dr. Katja Heister from the Technical University Munich. Thanks are also given to Dr. Rainer Dohrmann and Dr. Stephan Kaufhold for the infrared spectroscopy analyses of kaolinite, further discussions of the results and calculation of the illite/smectite content in altered detrital grains.

At University Jena many thanks go to Dr. Ulrich Bläß and Dr. Robert Schöner for their introduction in the electron microprobe analysis. Sigried Bergmann and Frank Linde carried out the sample preparation for thin section microscopy and X-Ray diffraction analysis. My thanks go to them. Thanks are also given to Dr. Dirk Merten and colleagues for sample preparation and measurements of total digestions and fluids. Thanks are given to Daniel Beyer who performed pore space image analyses on samples from well Aw05. I am indebted to many colleagues from the Geology Group to support me. Especially Ulrike Hilse and Jens Köster are thanked for their patience and help.

I want to thank my friends Johanna and Claus, Thomas, Thomas, Tina, and Kathrin. Special thanks are given to Enrico who helped me a lot especially during the final phase and who prepared the spatial mineral images for me. Finally I owe my deepest gratitude to my parents Birgit and Uwe who supported me all the time wherefore I am deeply thankful.

List of abbreviations

ADB	Anglo-Dutch-Basin
anhy	anhydrite
ank	ankerite
APCRC	Australian Petroleum Cooperative Research Centre
bar	barite
BET	surface area determination after Brunauer et al. (1938)
Bit	bitumen
BSE	Backscatter Electron
Cc	calcite
CCS	Carbon Capture and Storage
CEB	Central European Basin
cut	cutan
dol	dolomite
EDX	Energy Disperse System
EGR	Enhanced Gas Recovery
EOR	Enhanced Oil Recovery
FeOx	Fe-oxide
gal	galena
GFZ	Deutsches GeoForschungs-Zentrum
GZG	Geowissenschaftliches Zentrum Göttingen
ha	halite
hem	hematite
hel-chl	helminth-chlorite
HR-SEM	High Resolution Electron Microscopy
IC	tangential illite
ICP-MS	Inductively Coupled Plasma Mass Spectroscopy
ICP-OES	Inductively Coupled Plasma Optical Emission Spectroscopy
IGV	intergranular volume
ill/smec	illitisation/smectite formation of grains
IM	meshwork illite
IPCC	International Panel on Climate Change
kaol	kaolinite
Kfsp	K-feldspar
Lc	replacement of grain by carbonates (e.g. dolomite)
Lm	metamorphic grain
L_{QFG}	quartz-feldspar-mica grain
Ls	sedimentary grain
Lv_{fel}	felsic volcanic grain
Lv_{maf}	mafic volcanic grain
Ma	million years
musc	muscovite
NAM	Nederlandse Aardolie Maatschappij B.V.
NASCENT	Natural Analogues for the storage of CO_2 in Geological Environment
NGB	North German Basin
PEEK	Polyether Ether Ketone
PHREEQCi	Software for geochemical modelling
plag	plagioclase
Por_{inter}	intergranular porosity
Por_{intra}	intragranular porosity; mainly in feldspar or volcanic grains
ppm	parts per million
PT	Polish Trough
PTFE	polytetrafluorethen
Qc	chert grain: micro- to cryptocrystalline quartz
Qz	quartz
Qz_{au}	authigenic quartz
Qz_m	monocrystalline quartz grains
Qz_p	polycrystalline quartz grains
SD	Standard Deviation
SE	Secondary Electron
SEM	Scanning Electron Microscopy
sid	siderite
Smec	smectite
SPB	Southern Permian Basin
SSA	Specific Surface Area
Ti-Fe	titan-iron bearing mineral
UK	United Kingdom
UNFCC	United Nations Framework Convention on Climate Change
WDS	Wavelengths Dispersive Spectrometers
XRD	X-ray Diffraction Analysis
ZELMI	Zentraleinrichtung für Elektronenmikroskopie
*ill	illitisation of grains
*ill/smec	illitisation/smectite formation of grains
*kaol	kaolinitisation of grains
µQz	microcrystalline quartz

Abstract

Underground storage of CO_2 is receiving growing attention by the industry as an option to reduce CO_2 emissions. Rotliegend sediments of Permian age exhibit under certain conditions good reservoir quality and therefore may offer a suitable candidate for underground storage. The current study aims at analysing Rotliegend reservoir rocks in terms of mineralogical features, diagenetic mineral types, the determination of the availability of minerals within the rock and mineral (reactive) surface areas which are exposed to open pores and the integration of these results in CO_2-water-rock simulations. Target areas are Rotliegend sandstones from the northeast Netherlands which were deposited within the North German Basin and were buried to about 2000-3000 m depth. Core data and material from three reservoirs which are located proximal and distal to the basin margin and are covering different environmental settings were selected.

Eodiagenetic and early mesodiagenetic processes are comparable between the different locations within the sedimentary basin and include the formation of clay cutan (mainly illite), Fe-oxide, syntaxial quartz overgrowth, dolomite, anhydrite and barite. Evidence was found for an early precipitation of Mg-rich chlorite and the transformation into grain rimming kaolinite during further burial under the supply of CO_2 into the formation water. Mesodiagenetic mineral reactions are influenced by changing fluid conditions and the migration of liquid hydrocarbons from underlying Carboniferous source rocks into the sandstones. This causes the bleaching of red beds located near the basin margin by the dissolution of inherited Fe-oxides, the reduction of iron and the incorporation in Fe-rich carbonates. Further to the basin centre eodiagenetic Fe-oxides have been preserved down to maximum burial depth. Many sandstones are affected by leaching processes of unstable grains (mainly K-feldspar) and the formation of intragranular porosity, kaolinite and illite. A more intense dissolution grade of K-feldspar grains occurs in samples located further to the basin centre. Mesodiagenetic kaolinite appears with a vermicular habitus in all samples, but may be arranged as elongated single crystals forming dense pore-filling cements and/or sheaf-like structures in samples distal to the basin margin. Locally fibrous to meshwork illite and late stage pore-filling quartz and/or carbonate precipitated in the remaining pore space.

The spatial mineral arrangement was analysed by petrographic investigations and image analysis on thin sections. The volumetric composition of the samples is dominated by the mineralogy of detrital grains like quartz and K-feldspar. Authigenic minerals, especially clay minerals are volumetrically rare but exposed due to their small crystal size (nm- to µm-scale) a large specific surface area in comparison to the detrital grains. The effective mineralogy is defined as the percentage amount of minerals which are exposed to open pores and is a function of the presence of grain covering minerals and pore-filling cements. Approximately 30 % of the detrital grains are frequently covered by cements which block the grain surface areas accessible for potential water-rock interactions. These minerals are Fe-oxide, clay cutan, kaolinite, quartz, carbonate (dolomite, ankerite and siderite), sulphate (anhydrite and barite) and galena. In general samples near the basin margin are less cemented than distal deposits. Hence the size, distribution and accessibility of detrital and authigenic minerals regulate the availability of chemical species for water-rock interactions in the pore space.

The results of the volumetric mineralogy (VOL) and the effective mineralogy data (EFF) were integrated in geochemical simulations of CO_2-water-rock interactions. For kinetic modelling no initial equilibrium between the fluid and the reservoir rock was assumed. The lower pH at the beginning of the simulation is caused by the influx of CO_2 and results in the short-term dissolution of carbonates. The main difference between the VOL and EFF mineralogy data are long-term carbonate and related silica reactions. Due to the dissolution of K-feldspar and kaolinite and the release of K^+, Al^{3+} and silica into the solution Mg-smectite precipitates. The Mg^{2+} required for the precipitation is procured by the dissolution of dolomite. For the VOL data Mg-smectite starts to dissolve after 10000 years. Instead illite is formed at the expense of Mg-smectite, K-feldspar and kaolinite. In comparison, Mg-smectite stays in equilibrium with the solution for the EFF data. This is caused by a higher amount of hematite in the initial mineral assemblage and the released Fe^{2+} which is consumed by siderite. This reaction lowers the bicarbonate content in the solution which results in the consequent dissolution of dolomite and ankerite and the supply of Mg^{2+} for Mg-smectite precipitation. Reactive transport modelling coupled with geochemical modelling for a 2-dimensional CO_2 flow indicate only minor carbonate and hematite reactions within the first 150 years.

The investigations indicate that the consideration of the effective mineralogy in comparison to the bulk rock composition which is traditionally used in geochemical models results in different short-term and long-term carbonate, sulphate and silica reaction during CO_2 storage. This study may help to understand the behaviour of water-rock interactions (under the supply of CO_2) in sedimentary basin systems.

Zusammenfassung

Untertagespeicherung von CO_2 wird von der Industrie als Möglichkeit gesehen CO_2 Emissionen zu reduzieren. Rotliegend Sedimente permischen Alters besitzen unter bestimmten Bedingungen gute Eigenschaften zur Lagerung von CO_2. Das Ziel der vorliegenden Arbeit ist die Analyse von Rotliegend Gesteinen im Hinblick auf ihre mineralogische Zusammensetzung, diagenetische Mineraltypen und Mineraloberflächen exponiert zum offenen Porenraum und die Integration der gewonnen Daten in CO_2-Fluid-Gesteins Simulationen. Untersuchungsobjekte sind Rotliegend Sandsteine im Nordosten der Niederlande, die im Bereich des Norddeutschen Beckens abgelagert wurden und bis zu einer maximalen Tiefe von ungefähr 2000-3000 m versenkt wurden. Kernmaterial und Daten von drei verschiedenen Lagerstätten wurden ausgewählt. Diese befinden sich proximal und distal zum Beckenrand und umfassen verschiede sedimentologische Ablagerungstypen.

Eodiagenetische und frühe mesodiagenetische Prozesse sind vergleichbar für Proben, die sich in unterschiedlicher Position im Sedimentbecken befinden und umfassen Tonkutane (vor allem Illite), Fe-Oxide, Quarz, Dolomit, Anhydrit und Baryt. Kornrandständige Kaolinite weisen auf eine frühe Präzipitation von Mg-reichen Chloriten und die Umwandlung in Kaolinit während der weiteren Versenkung unter dem Eintritt von CO_2 ins Formationswasser hin. Mesodiagenetische Mineralreaktionen sind vor allem durch sich verändernde Fluidzusammensetzungen und die Migration von flüssigen Kohlenwasserstoffen gekennzeichnet. Dies führt, nahe des Beckenrandes, zu einer Bleichung von rot gefärbten Sandsteinen bedingt durch die Lösung von Fe-Oxiden. Viele Sandsteine unterlagen einer, zum Teil, intensiven Lösung von detritischen Körnern (vor allem K-Feldspat) und der Bildung von intragranularer Porosität, Illit und Kaolinit. Intensivere Kornlösung tritt in Sandsteinen distal vom Beckenrand auf. Mesodiagenetischer Kaolinit liegt bevorzugt mit einem vermicularen Habitus vor und wurde in allen Proben nachgewiesen. In einigen Sandsteinen tritt Kaolinit in Form länglicher Kristalle auf, die dichte, porenfüllende Zemente bilden oder eine garbenförmige Struktur aufweisen. Vereinzelt wurde fibröser bis maschenförmiger Illit und später porenfüllender Quarz und/oder Karbonat nachgewiesen.

Die räumliche Verteilung von Mineralen wurde mit Hilfe von petrographischen und bildanalytischen Methoden untersucht. Die volumetrische Zusammensetzung der Sandsteine wird von detrtischen Körnern, wie Quarz und K-Feldspat, dominiert. Authigene Minerale, vor allem Tonminerale sind volumetrisch nicht bedeutend, zeigen aber auf Grund ihrer geringen Mineralgröße (nm- bis µm-Skala) eine große spezifische Oberfläche im Vergleich zum Detritus. Die effektive Mineralogie definiert sich über den prozentualen Anteil der Mineralphasen und wird vor allem durch den Gehalt an kornüberziehenden und porenfüllenden Zementen gesteuert. Ungefähr 30 % der detritischen Körner sind von authigenen Mineralen überzogen und stehen nicht für potentielle Mineral-Fluid-Reaktionen zur Verfügung. Diese Minerale sind Fe-Oxide, Tonkutane, Kaolinit, Quarz, Karbonate (Dolomit, Ankerit, Siderit), Sulphate (Anhydrit, Baryt) und Bleiglanz. Im Allgemeinen sind Sandsteine in der Nähe des Beckenrandes geringer zementiert als distale Ablagerungen. Demzufolge steuert die Verteilung und Erreichbarkeit von detritischen und authigenen Mineralen die Verfügbarkeit von Reaktionspartnern für mögliche Fluid-Gesteins-Reaktionen im Porenraum.

Die Ergebnisse der volumetrischen Mineralogie (VOL) und der effektiven Mineralogie (EFF, Minerale exponiert zum Porenraum) wurden in CO_2-Fluid-Gesteins Simulationen integriert. Für kinetische Modellierungen wurde kein initiales Gleichgewicht zwischen Fluid und Gestein angenommen. Zu Beginn der Simulation sinkt der pH auf Grund von zugeführten CO_2 und führt zur partiellen Lösung von Karbonaten. Die Hauptunterschiede zwischen den VOL und EFF Datensätzen liegt in den späten Silikat- und Karbonatreaktionen. Mg-Smektit bildet sich auf Kosten von K-Feldspat, Kaolinit und Dolomit/Ankerit. Für den VOL Datensatz geht Mg-Smektit nach ungefähr 10000 Jahren wieder in Lösung, wohingegen ein Gleichgewichtszustand zwischen Fluid und Mg-Smektit für den EFF Datensatz vorliegt. Dies wird durch einen höheren initialen Fe-Oxide Anteil bedingt, der während der Auflösung Eisen für die Sideritbildung bereitstellt. Die Fällung von Siderit verringert den verfügbaren Hydrogencarbonatanteil in der Lösung und Dolomit und Ankerit werden gelöst und Magnesium für die Mg-Smektit Präzipitation bereitgestellt. Modellierungen von reaktivem Flusstransport für ein 2-dimensionales CO_2 Flusssystem gekoppelt mit geochemischen Modellierungen zeigen geringe Karbonat und Hämatit Mineralreaktionen für die ersten 150 Jahre.

Die Untersuchungen zeigen, dass die Betrachtung der effektiven Mineralogie im Vergleich zur klassischen Verwendung der volumetrischen Gesteinsanalyse in geochemischen Modellen zu unterschiedlichen Ergebnissen führen kann. Die Ergebnisse der Studie können dabei helfen das Verhalten von Fluid-Mineral-Reaktionen (unter dem Einfluss von CO_2) in Sedimentbecken besser zu verstehen.

1 Introduction

1.1 Study objective

Underground carbon capture and storage (CCS) in geological formations is receiving growing attention by industry, research institutions and politics as an option to reduce CO_2 emissions. A variety of demo and/or pilot projects are therefore conducted for a better understanding of the conditions for underground storage in various geological settings (IPCC, 2005). Permian Rotliegend sediments are important reservoir rocks worldwide and hold a significant proportion of the northwest European hydrocarbon reserves. The deposits in the North German Basin have been explored by the petroleum industry for many decades. Many of the gas and oil fields have produced or are still producing. This may offer suitable candidates for underground storage of CO_2 as these fields exhibit good reservoir quality, are volumetrically large structures, and are geographically close to the most important industrial CO_2 sources (IPCC, 2005).

Physical and geochemical trapping mechanisms of CO_2 in depleted gas reservoirs are mainly controlled by the reservoir and seal structure (e.g. Gunter et al., 2004; IPCC, 2005; Friedmann, 2006; UCE, 2006), the temperature and pressure conditions (Root et al., 2004), the composition, permeability and porosity of reservoir rocks and the character of fluids/gas in the pore space (e.g. Gunter et al. 1993; Hitchon, 1996; Kharaka et al., 2005; IPCC, 2005). Hence for each potential gas reservoir suitable for CO_2 storage detailed investigations of these parameters are indispensible because of the heterogeneity of geological formations.

Much effort was put into research of Rotliegend clastic sediments in the North German Basin, especially on sedimentary facies, stratigraphy and environmental deposits (e.g. Plein, 1978; Gast, 1998; Lokhorst, 1998; Gaupp et al., 2000; Gaupp and Okkerman, 2011). However, different parts of the basin system show contrasting diagenetic evolutions and different detrital compositions. Since these differences may have a great input on potential CO_2-fluid-rock interactions a detailed study of mineral types, spatial distribution and diagenetic evolution of the sediments are indispensible. Furthermore, the mineral surface areas which stay in contact to the open pore system (effective mineralogy) need to be defined. Commonly geochemical CO_2 modelling is conducted with volumetric mineral assemblages and standard values of specific mineral surface areas. However, the accuracy of predictions of chemical mineral reactions under the influence of CO_2 may increase with considering the effective mineralogy instead of the volumetric composition.

In cooperation with NAM (Nederlandse Aardolie Maatschappij B.V.) the current study aims to characterise Rotliegend reservoir rocks in terms of mineralogical features and particular diagenetic mineral types. Against the background of CO_2 injection and storage the rock reactivity will be evaluated. For a better understanding of potential fluid-rock interactions the intention of the project is to document:

(1) the present composition of high permeable sandstone horizons where detrital grains and authigenic minerals may act as potential reaction partners (chapter 4);
(2) the determination of mineral surface areas exposed to the open pore system (chapter 5);
(3) and the prediction of these potential effects by coupled fluid flow – geochemical modelling (chapter 6 and 7).

1.2 Study area

For CO_2 injection three potential gas fields will be studied (▶ figure 1.1). The main focus will be on the alluvial fan dominated gas reservoir "A" south of the Groningen field in the north of the Netherlands. The sediments are mainly attributed to the Upper Slochteren Formation with sandstones and conglomerates. The field is located at a depth of 2900-3100 m. Four wells were chosen (compare chapter 2.1) and from these 25 samples were analysed in detail. The reservoir "B" consists mainly of dry and damp sandflat deposits which are locally intercalated with shaley wet sandflats of the interdune pond environment. The field is located in the southeast of the province Friesland. Three wells with twelve samples were selected. The third field is the playa lake deposits dominated gas reservoir "C". The sequences consist largely of aeolian dunes, aeolian (dry) sandflat, sandy sabkha (damp) sandflat and muddy sabkha (wet) sandflat deposits. The field is located north of Leeuwarden near the coastline to the Waddenzee. Four wells with eleven samples were chosen for analyses. An extensive data set in addition to the core material was released by NAM. The reservoir and well names have been decoded to comply with the requirements of confidentially for industry data.

Figure 1.1: Approximate locations of the gas-bearing fields A, B and C in the northeast Netherlands which are investigated in this study. The reservoir names have been decoded due to confidentially for industry data.

1.3 Carbon capture and storage of CO_2 – a brief overview

During the last years the discussion about climate change related to human activity became more and more important. Many experts believe that the increasing atmospheric temperature is directly connected to the emission of greenhouse gases, especially anthropogenic CO_2. After the IPCC report (2005) atmospheric CO_2 is responsible for ~64 % of the so called "greenhouse effect" and has been increasing since the start of the Industrial Revolution in the late 18th century (Crowley, 2000). In August 2011 the atmospheric CO_2 concentration yields ~390 ppm and was measured by the Mauna Loa Observatory (Tans and Keeling, 2011). In contrast the CO_2 concentration in ice core levels of the year 1832 yields 284 ppm, (Etheridge et al., 1998) which is ~30 % below the present situation. The implication of the greenhouses gases on climate change was purpose for many political and scientific meetings. The importance for CO_2 reduction was e.g. initialised by the International Panel on Climate Change (IPCC) in 1995 and 2005 and the United Nations Framework Convention on Climate Change (UNFCC) in 1997. Amongst other

factors the decisions lead in the Kyoto Protocol from December 1997 which aims at a reduction of greenhouse gas emissions. The protocol includes the recommendations of the improvement of energy efficiency, substituting energy generators with high CO_2 emission against others with minor CO_2 emission (e.g. natural gas for coal) and the use of renewable energy and nuclear power (Gale, 2004).

Carbon capture and storage

A potential technology for reduction of CO_2 emissions is carbon capture and storage (CCS). The underground storage of CO_2 is considered to be carried out in large geological structures which should be located close to the most important industrial CO_2 emitters. These structures are depleted oil and gas reservoirs, deep saline aquifers and deep unminable coal seams (IPCC, 2005). Especially depleted oil and gas reservoirs held some attractive features for the industrial operator. Small exploration costs and a well known reservoir structure which is proven to be an oil or gas trap over millions of years are the main characteristics (IEAGHG, 2001). However for the injection of CO_2 into geological formations, several physical and chemical aspects have to be considered: The rate of dissolved CO_2 into the formation water, the chemical reaction with diverse minerals from the host rock, the flow behaviour and migration rate of CO_2 within the reservoir, as well as the seal integrity. These aspects are mainly controlled by the reservoir and seal structure, (e.g. Gunter et al., 2004; IPCC, 2005; Friedmann, 2006; UCE, 2006), the stratigraphy and distribution of architectural elements (e.g. facies type), the mineralogical composition, the presence and type of faults and/or fractures, the temperature and pressure conditions within the storage area and the chemistry and hydrodynamic behaviour of in situ formation fluids (e.g. Gunter et al. 1993; Hitchon, 1996; Root et al., 2004; Kharaka et al., 2005; IPCC, 2005). Furthermore enhanced oil recovery (EOR) and enhanced gas recovery (EGR) have already been applied, especially in the United States (IEAGHG, 2001). This technology has the potential for an increasing oil/gas production in nearly depleted oil/gas reservoirs. For EOR injected CO_2 will dissolve with the crude oil which leads to swelling and reducing of the viscosity. The combination of these processes will initiate a higher flow of crude oil to the production wells (IEAGHG, 2001). The mechanisms which control EGR are gas displacement and reservoir pressurisation while CO_2 is moving through the pore system (Oldenburg et al., 2001).

CO_2 trapping in geological formations

For underground storage the CO_2 has to be compressed to high pressure to achieve a density which is close to water at the supercritical point (~400 to 700 kg/m^3; ▶ figure 1.2) (Rochelle et al., 2004). Changes in temperature and pressure within the reservoir have a non-linear influence on the CO_2 density under supercritical pressure conditions (ICCP, 2005). The relation between depth and CO_2 density is plotted in ▶ figure 1.2 for different geothermal gradients (20, 30 and 50°C per 1000 m depth) (Peng and Robinson, 1976).

Supercritical CO_2 is less viscous than water and the migration is mainly controlled by the mobility difference between CO_2 and the formation fluid (Celia et al., 2005; Nordbotten et al., 2005). In comparison to natural gas supercritical CO_2 is more viscous and the horizontal migration front will be relatively stable (IPCC, 2005). However CO_2 is denser than natural gas and will migrate downwards within a gas reservoir (vertical migration) due to buoyancy forces (Oldenburg et al., 2001) (▶ figure 1.3).

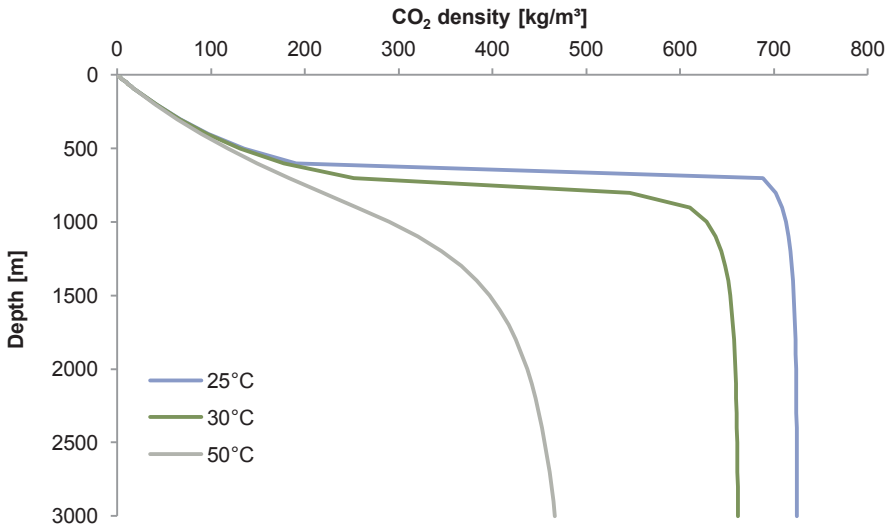

Figure 1.2: The CO_2 density in geological structures depends on depth and temperature, expressed as geothermal gradients for 25, 30 and 50°C. Equations for calculations which are used in this diagram are adapted from Peng and Robinson (1976).

Four main CO_2 storage mechanisms lead to a trapping of CO_2 within the reservoir (IPCC, 2005) (▶ figure 1.4): (1) Structural and stratigraphic trapping, (2) residual CO_2 trapping, (3) solubility trapping and (4) mineral trapping. Structural trapping occurs below low permeable seals like shales or salt beds located on top of the reservoir (IPCC, 2005) and folded or fractured rocks may function as structural traps (Salvi et al., 2000). During the migration of CO_2 towards the reservoir top, parts of the CO_2 will be trapped in the brines within the pores of the hostrock (e.g. Obdam et al., 2003; Kumar et al., 2005) (residual CO_2 trapping). The amount of CO_2 which could be trapped in the pore system depends on the intergranular pore geometry and is inversely correlated with the residual gas saturation (Holtz and Bryant, 2005).

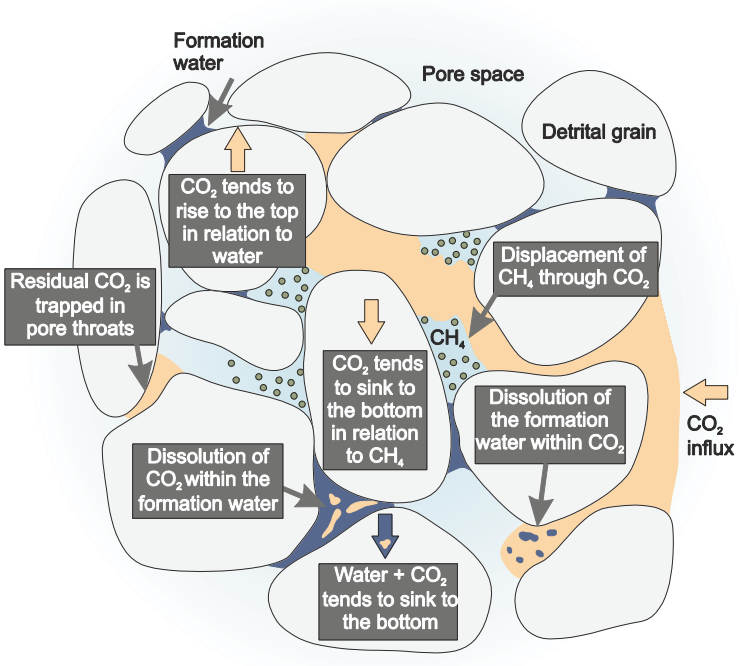

Figure 1.3: Behaviour of supercritical CO_2 (light orange) and CH_4 (green) in not water saturated porous sandstones (e.g. Enick and Klara, 2001; Bachu et al., 1994; McPherson and Cole, 2000; Doughty et al., 2001; Oldenburg et al., 2001; Bachu and Adams, 2003; Ennis-King et al., 2003; IPCC, 2005).

As CO_2 migrates through the reservoir rock parts will slowly dissolve within the formation water with an average saturation of 30-60% (e.g. McPherson and Cole, 2000; Doughty et al., 2001; Ennis-King et al., 2003; IPCC, 2005) (solubility CO_2 trapping). The CO_2-rich water is slightly denser (~1 %) than the formation water (Enick and Klara, 2001; Bachu and Adams, 2003) and tends to sink to the bottom in comparison to the residual fluid (Bachu et al., 1994). The amount of dissolved CO_2 in water depends on temperature and salinity and range between 1.5 and 6.0 wt.-% (Pruess, 2006) (▶ figure 1.5). The dissolution of CO_2 into the formation water lowers the pH due to increasing proton content (▶ equation 1.1) and produces a weak acid (IPCC, 2005).

$$CO_{2\,(g)} + H_2O \leftrightarrow H_2CO_{3\,(aq)} \leftrightarrow {HCO_3}^-_{(aq)} + H^+ \leftrightarrow {CO_3}^{2-} + 2H^+ \quad (1.1)$$

The dissociation of CO_2 is strongly pH dependent: At low pH the dominant species is H_2CO_3, at intermediate pH bicarbonate (HCO_3^-) is formed which may further dissociate to CO_3^{2-} with increasing pH (Kharaka et al., 2005). In terms of concentration $CO_{2(aq)}$ will dominate H_2CO_3 in the conditions of CO_2 storage. The CO_2-rich fluid may further react with the surrounding rock (IPCC, 2005) and may cause the precipitation of authigenic minerals (mineral CO_2 trapping). Besides pH the precipitation of e.g. carbonate depends on the availability of minerals which may dissolve under changed physicochemical conditions and the released cations (e.g. Ca, Mg and Fe) (Gunter, 2005) (e.g. ▶ equation 1.2). If the pH value is buffered, large amounts of dissolved CO_2 can be trapped in aquifers. Several detrital and authigenic minerals may act as reactants for CO_2. The main reactive minerals are feldspar, rock fragments and clay minerals (▶ equations 1.2, 1.3 and 1.4). After Haszeldine et al. (2005) feldspars are chemically most reactive on timescales between 10 to 400 years. Especially for plagioclase several reactions are assumed under the influence of CO_2 resulting in the precipitation of e.g. kaolinite, calcite and quartz (Gunter et al., 1997) (▶ equations 1.2 to 1.5).

$$\underset{\text{PLAGIOCLASE}}{CaAl_2Si_2O_8} + 2H_2O + CO_2 \rightarrow \underset{\text{KAOLINITE}}{Al_2Si_2O_5(OH)_4} + \underset{\text{CALCITE}}{CaCO_3} \quad (1.2)$$

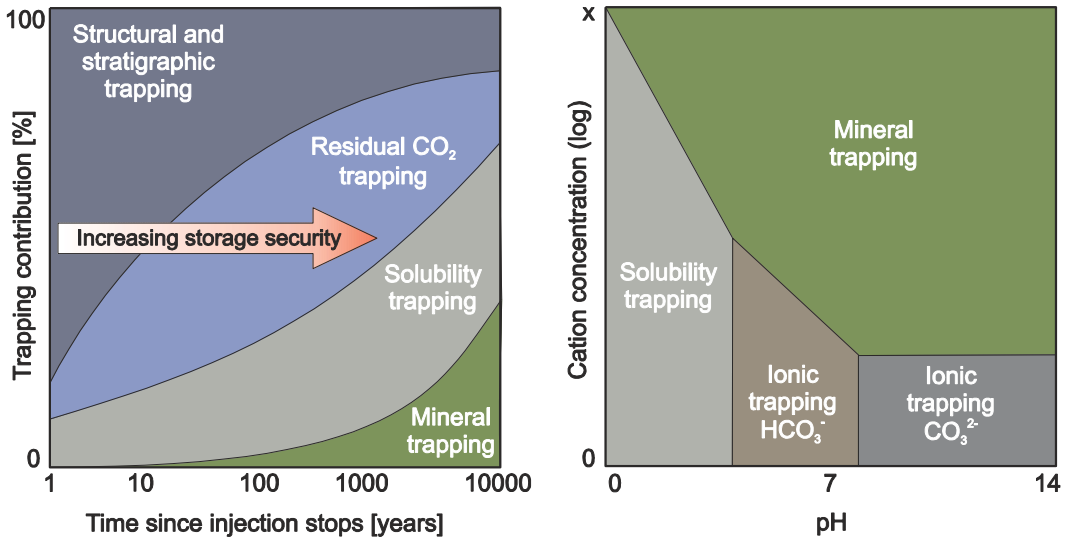

Figure 1.4: Left – At the beginning of CO_2 storage structural/stratigraphic and residual trapping are the most important trapping contributions. With increasing time solubility and mineral trapping becomes more important. The change of trapping mechanisms results in an increasing storage security (UCE, 2006). Right – Trapping mechanisms in variation with pH and cation concentrations (Gunter, 2005).

$$Ca_4[Al_8Si_{16}O_{48}] + 16H_2O + 4CO_2 \rightarrow 4Al_2Si_2O_5(OH)_4 + 4CaCO_3 + 8SiO_2 + 8H_2O \quad (1.3)$$
PLAGIOCLASE — KAOLINITE — CALCITE — QUARTZ

$$2CaNaAl_3Si_5O_{16} + 7H_2O + 4CO_2 \rightarrow 3Al_2Si_2O_5(OH)_4 + 2CaCO_3 + 4SiO_2 + 2NaAlCO_3(OH)_{2(aq)} \quad (1.4)$$
PLAGIOCLASE — KAOLINITE — CALCITE — QUARTZ — DAWSONITE

Gunter et al. (1997) described the formation of Na-smectite instead of kaolinite for the previous equation 1.4. Furthermore Na-bearing feldspars may react with CO_2 forming kaolinite and quartz (Watson et al., 2003) (▶ equation 1.5). Therefore the CO_2 is trapped in calcite or sodium-bicarbonate, respectively.

$$2NaAlSi_3O_8 + 3H_2O + 2CO_2 \rightarrow Al_2Si_2O_5(OH)_4 + SiO_2 + 2NaAlCO_3(OH)_{2(aq)} \quad (1.5)$$
ALBITE — KAOLINITE — QUARTZ — DAWSONITE

A further possibility of CO_2 trapping is the storage as ionic species in the formation water. The dissociation of CO_2 (▶ equation 1.1) is strongly pH depended and forms with available cations ionic species like $NaHCO_3^+$, $CaHCO_3^+$, $MgHCO_3^+$ (Gunter, 2005; Kharaka et al., 2005) under intermediate to high pH values (▶ figure 1.4).

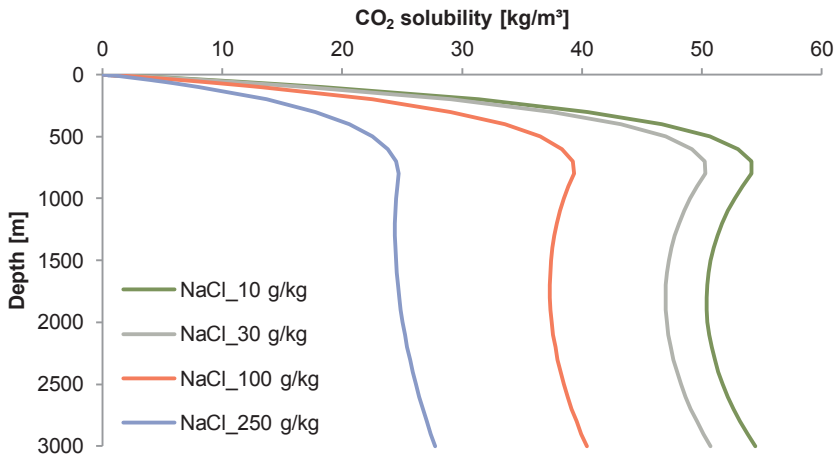

Figure 1.5: CO_2 solubility in saline water (10 – 250 g/kg NaCl) for a geothermal gradient of 30°C per 1000 km depth (Duan and Sun, 2003).

Analogue systems

The understanding of the migration and reaction of CO_2 with the surrounding material (e.g. sandstone) on a long timescale (≥10.000 years) is indispensible for secure underground storage (IPCC, 2005). Analogue systems are studied to improve the behaviour of CO_2 in geological formations. Therefore (1) laboratory experiments and engineered storage involve short timescales of months to tens of years and (2) natural analogues may show the development of the diagenesis under CO_2 influence for ten to hundred thousands of years. Many laboratory studies were run in a short time scale. Under high temperatures (>150°C) the reaction rates of water-rock interactions will increase to several orders of magnitude faster than for natural systems. Hence the mineral reactions observed in experiments which are used in geochemical modelling software do not fit well with the reactions during CO_2 storage. Another, and possible

more serious reason, is that thermodynamic constants and consequently domains of mineral stability strongly change with temperature.

To investigate the CO_2 influence on natural systems several studies were carried out. Natural CO_2 can be derived from deep seated sources like contact and regional metamorphism, magma degassing, organic maturation under e.g. the influence of bacterial processes and atmospheric CO_2 which is dissolved in groundwater (Baines and Worden, 2004). One of the most intense studied natural analogues is the Otway Basin in southeast Australia, investigated by a research group of the Australian Petroleum Cooperative Research Centre (APCRC). For example, in Europe the project NASCENT (Natural Analogues for the Storage of CO_2 in Geological Environment) and in the USA the program NACS (Natural Analogues for Geologic CO_2 Sequestration) investigate natural CO_2 reservoirs. For more detailed descriptions about diagenetic processes which may be related to CO_2 influences in this study please regard to section 4.5.3.

2 Methodology

2.1 Sampling methods

Three locations within the North German Basin were chosen for analyses: samples from the producing gas reservoirs “field A”, “field B” and “field C”, which are located in the northern Netherlands, contain mainly sandstones which are attributed to the Upper Slochteren Formation.

Rotliegend samples from the northern Netherlands have been taken in the core magazine in Assen from the company Nederlandse Aardolie Maatschappij B.V. (NAM). In total eleven wells of the three producing gas fields were chosen. For field A 25 samples were taken from wells Aw02, Aw03, Aw04 and Aw05. Altogether twelve samples were selected from wells of field B: Bw01, Bw02 and Bw03. Eleven samples are attributed to the wells Cw01, Cw02, Cw03 and Cw04 from field C.

Samples from the northern area of field A, from field B and field C are nearly homogeneous fine to medium grained sandstones. The sediments from the southern area of field A are alluvial fan and sheetflood dominated deposits with coarse grained sandstones and conglomerates. The potential pathways of injected CO_2 are high permeable sandstones of the Upper Slochteren Formation. According to previous porosity and permeability measurements from NAM sandstones with different permeabilities were chosen according to defined permeability classes, respectively for each well. For field A and field B the classes low (<500 mD), medium (500-1000 mD) and high (>1000 mD) were defined. For field C the mean permeability yields ~200 mD. Hence the classes are: low (<50 mD), medium (50-100 mD) and high (>100 mD). Muddy siltstones and mudstones of the sabkha environment are not sampled. Furthermore additional thin sections of the wells Aw05, Aw01, Bw01, Cw01 and Cw04 were provided by NAM.

2.2 Optical microscopy

The optical microscopy study focuses on the detrital and authigenic mineralogy, porosity and texture of 82 thin sections. 25 thin sections were prepared from sandstone samples and analysed in detail with additional methods. Additionally 382 thin sections were provided by NAM and from these 53 thin sections were selected for a more detailed study. All samples were emanated from Permian sandstones of the Upper Slochteren Formation. The pores were impregnated with bluedyed epoxy resin. The thin sections were polished (for e.g. electron microprobe analysis) or covered with glass after impregnating half of the sample with Alziran Red-S for calcite determination. No other samples from e.g. adjacent mudstones were prepared. A ZEISS Axioplan 2 microscope was used to analyse the thin sections under plane and cross polarised light. Images were taken with a Hitachi HV-C20 digital colour camera.

Quantification of 74 thin sections was accomplished by point counting of 300 points per thin section with an automatic point counter (PRIOR Model G). For inhomogeneous samples (grain size or sorting) medium to coarse grained layers were preferred in comparison to finer grained units. Authigenic clay minerals with platy or hairy crystal structure (e.g. kaolinite) show partly a significant amount of microporosity between the crystals. Because of the small pore and mineral sizes (<5 µm) it is difficult to distinguish between pore and crystal. This often leads to an overestimation of point counting data. Analyses of kaolinite by scanning electron microscopy (SEM) assumed an average internal microporosity of ~20 % for kaolinite with a booklet like

habitus. After point counting 20 % of the kaolinite content was subtracted and added to the intergranular or intragranular porosity, respectively. No estimation was made for tangential clay mineral cutans on grain surface areas.

Certain diagenetic evaluations were conducted by semi-quantitatively classifications: (1) feldspar dissolution/alteration is difficult to evaluate by point counting. Hence a standardised chart was chosen (▶ figure 2.1). (2) Thick bitumen aggregates within the pore space were point counted. However solid bitumen impregnations on e.g. clay minerals and (3) illitisation and kaolinitisation of detrital grains (e.g. feldspar and volcanic rock fragments) were classified on a four class scale (0 = none; 1 = poor; 2 = medium; 3 = strong).

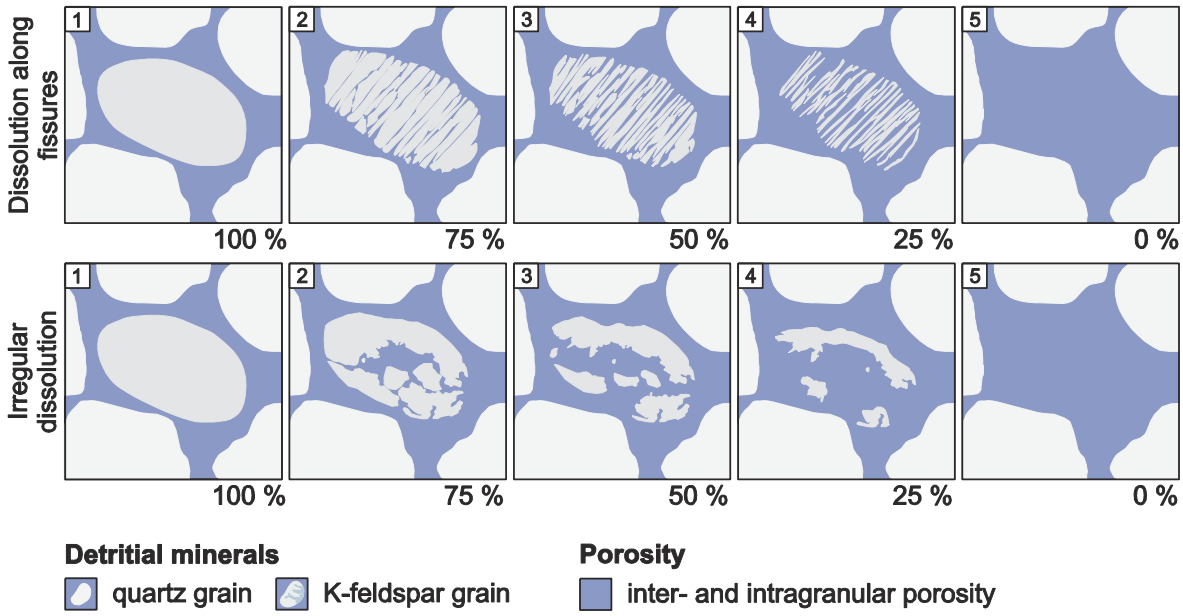

Figure 2.1: Semi-quantitative estimation chart for the dissolution grade of detrital feldspar grains in sandstones. Feldspar dissolution takes place either along fissures or without any preferred orientation. Image 1 represents an undissolved grain and 2 to 4 different grain dissolution grades (25 to 75 %). Total dissolution leads to an "oversized pore", imaged in number 5.

Minor inaccuracies are present for authigenic grain coatings which consist of varying amounts of clay minerals (e.g. illite) and Fe-oxide or show solid bitumen impregnations. Furthermore inter- and intragranular porosity is differentiated during point counting. Sometimes a differentiation between pore and oversized pore (totally dissolved detrital grain) is difficult. Hence the result of the intergranular porosity may be higher (~2 %) as the original value. Standardised charts were used for the characterisation of grain sorting (Longiaru, 1987), roundness (Tucker, 1991) and grain contacts (Pettijohn et al., 1987).

2.3 Electron microprobe analysis (EMS)

Quantitative analyses on polished thin sections were realised at the "Zentraleinrichtung für Elektronenmikroskopie" (ZELMI) at the Technical University Berlin with a machine of the company Cameca which is equipped with four wavelengths dispersive spectrometers (WDS system). For matrix correction the method PAP (after Pouchou and Pichoire, 1991) was used.

The samples were measured with an acceleration voltage of 15 kV, a beam current of 15 nA and a beam diameter of 12-15 µm. Clay minerals (e.g. kaolinite and illite) were analysed with a focused beam with 1µm in diameter. In ▶ table 2.1 the standard minerals for quantitative analysis and the spectrometer crystals are listed.

Table 2.1: Standard minerals and spectrometer crystals for quantitative electron microprobe analysis.

element	crystal	standard	element	crystal	standard
Na	TAP	albite	Ca	PET	wollastonite
Mg	TAP	olivine	Ti	PET	metallic Ti
Al	TAP	corundum	Mn	LIF	metallic Mn
Si	TAP	wollastonite	Fe	LIF	metallic Fe
K	PET	orthoclase			

Semi-quantitative chemical analyses with energy disperse system (EDX) and backscatter electron images (BSE) from detrital and authigenic minerals were prepared in Jena with a Cameca SX50. In total eight samples from the northern Netherlands were analysed. The thin sections were coated with carbon to avoid charging during measurement.

2.4 High resolution scanning electron microscopy (HR-SEM)

High resolution SEM (sub-µm scale) was used to characterise the morphology and surface structure of detrital grains and authigenic minerals. Therefore a Hitachi S-4000 at the "Zentraleinrichtung für Elektronenmikroskopie" (ZELMI) at the Technical University Berlin was used. Scanning electron microscopy was combined with an energy disperse system for semi-quantitative chemical analysis. Measurements were realised with an acceleration voltage of 20 nA. For near surface analyses of thin minerals (e.g. clay minerals) a lower voltage of 8-10 nA was used. Digital images of backscattered and secondary electron were recorded. Broken rock chips were fixed with conductive silver on the sample carrier and coated with carbon. In total seven samples from field A, B and C were analysed.

2.5 X-ray diffraction analysis (XRD)

For a detailed clay mineral study X-ray diffraction analysis was added to microscopic studies for a few selected samples. 23 samples were chosen from field A (generally low clay content: three samples), field B (six samples) and field C (five samples). In a hydraulic press clean samples were carefully crushed to grain sizes of <2 mm. The material was filled with deionised water in a 2 l beaker and stirred slowly in a mixer for two hours. After centrifugation and decanting the suspension the procedure of washing was repeated for all samples from field C until the water appeared almost clear and no more flocculation was present. No Na-pyrophosphate solution (20 g/l $Na_4P_2O_7*10H_2O$) was added to the samples. In an Atterberg-cylinder the fraction <6 µm was separated by gravity setting. The fraction was chosen because prior thin section analysis evidenced kaolinite crystals with diameters between 2-40 µm. The concentrated suspension was directly spread on a porous ceramic disk. Therefore a vacuum generated by a (water) pump was used to prepare oriented samples. The samples were analysed at the "Geowissenschaftliches Zentrum Göttingen" (GZG) at the University Göttingen with a Philips X'Pert machine (Ni-filtered

Cu-Kα radiation at 40 kV and 30 mA). The step range for air-dried, glycol-solvated and tempered measurements were marginally different: air-dried samples were measured between 2° and 65° 2θ, glycol-solvated samples from 4° to 19° 2θ and heated samples (at ~500°C for one hour) in a range between 4° and 26° 2θ, all in 0.02° 2θ step size, respectively. For evaluation the software program *MacDiff* (Petschick, 2002) was used in combination with literature for clay mineral analysis (e.g. Brindley and Brown, 1980).

2.6 (Local) infrared spectroscopy (IR-S)

(Local) infrared-spectroscopy was used to specify the crystalline character of authigenic kaolinite minerals of (1) the <2 µm fraction and (2) of thin sections. The measurements were realised at the "Bundesanstalt für Geowissenschaften und Rohstoffe" (BGR) Hannover with an IR-spectrometer Nexus of the company Thermo Nicolet which is coupled with an IR-microscope, type Continuum. For sample preparation of the <2 µm fraction please regard to the method description for X-ray diffraction (XRD). However the samples Bw01-02 and Cw04-03 were freeze-dried to avoid the damage of the kaolinite crystals. The materials were mixed up with water-free KBr (150 mg per 1 mg substance), pressed to a tablet and were measured under normal and air-dried conditions. The relative adsorption spectres were detected between wavelengths of 4000 cm^{-1} to 400 cm^{-1}. Additionally, local IR-spectroscopy was applied on a thin section to prove the classical method results. Therefore two mappings with 10 µm resolution (2200 measure points) were prepared. The results of both methods were compared to several mineral standards (e.g. quartz, feldspar, carbonates, sulphates and most notably clay minerals) available at the BGR Hannover.

2.7 Inductively coupled plasma mass spectroscopy (ICP-MS) and inductively coupled plasma optical emission spectroscopy (ICP-OES)

Total digestions from selected samples were analysed with an ICP-OES system from type Spectroflame of the company Spectro (Kleve, Germany) and an ICP-MS from type XSeries II of the company Thermo Fischer Scientific (Bremen, Germany). Main, minor and trace elements were measured (▶ table 2.2).

Table 2.2: Elements analysed with ICP-OES and ICP-MS for total digestions.

ICP-OES	Ca, Mg, Fe, K, Na, P, Sr, B
ICP-MS	Al, Ba, Mn, Ni, Ti, Zn, Li, Sc, V, Cr, Co, Cu, As, Y, Cd, Cs, La, Ce, Pr, Nd, Sm, Eu, Gd, Tb, Dy, Ho, Er, Tm, Yb, Lu, Th, Pb, U

The samples were powdered with a centrifugation ball mill (agate grinding jar, type S100 of the company Retsch) to finer than 63 µm and dried for a minimum of 24 hours at 75°C. The amount of 100 to 150 mg with 0.1 mg accuracy of each sample was solubilised with a pressure digestion system of the company PicoTrace. The sandstones were treated with 3 ml 40% HF and 3 ml 70% $HClO_4$ to get all compounds in solution. After the closed vessels stood overnight they were tightened and heated up to 180° within four hours. The temperature was maintained for twelve hours before cooling it down. Again the temperature was increased to 180°C in a period of four

hours for twelve hours heating time using a special evaporation hood. Then 2 ml 65% HNO_3, 0.6 ml 30 % HCl and 7 ml of pure water was added to the residual sample material. The mixture was dissolved by heating at 150°C for ten hours. Finally the sample was mixed with 25 ml pure water and measured with an ICP-OES and -MS system.

2.8 Specific surface area analysis (BET-analysis)

The determination of the specific surface area [m^2/g] was realised by low pressure N_2 adsorption based on the method by Brunauer, Emmett and Teller (1938). The BET-isotherm describes the adsorption of gases in monomolecular layers on solid surfaces. The equation of the surface area is given by ▶ equation 2.1:

$$n^s = \frac{n_m^s C p}{(p_0 - p)[1 + (C-1)\frac{p}{p_0}]} \tag{2.1}$$

with n^s is the quantity of gas adsorbed at an equilibrium pressure p; p_0 = vapour pressure of the adsorbate; n_m^s = value of n^s at a monolayer coverage and C = a constant related to the heat of condensation (ΔH_c) and the heat of adsorption into the first layer (ΔH_1). A linearized form of the previous is used for plotting the results (▶ equation 2.2):

$$\frac{p}{n^s(p_0 - p)} = \frac{(C-1)p}{n_m^s C p_0} + \frac{1}{n_m^s C} \tag{2.2}$$

Nitrogen is commonly used as adsorbent for determining mesoporous to microporous (<2 nm) structures (e.g. sandstones). The gas has a high affinity to mineral surface areas but is not bounded to organic material. Furthermore a nitrogen molecule has a diameter of 0.38 nm and is too large to interpenetrate the interlayers of non-swelling clay minerals like illite. However during the experiments small amounts of nitrogen may enter the interlayers (Aylmore et al., 1970). On the other hands swelling smectite can be penetrated by nitrogen.

The measurements were realised at the Technical University Munich (department for soil sciences). Therefore a Quantachrome Autosorb 1 was used. All samples have been evacuated at 40°C over night. Samples from field C needed more than 15 hours evacuation time. Nitrogen was introduced in eleven pressure steps (p/p_0 = 0.05-0.3) at a temperature of 77.35 K (boiling temperature of nitrogen).

2.9 Image analysis

Type and amount of minerals (detrital grains and authigenic phases) which stay in direct contact to an open pore system have a large influence on chemical reactions during CO_2 storage processes. Hence image analysis on thin sections was performed to define the mineral type, frequency and distribution within sandstones from field A and B in a 2-dimensional system. Therefore two analysis types were used. The first type (1) gives evidence for the intergranular pore system and the second type (2) is used for porosity determination within detrital grains or authigenic minerals (e.g. carbonate) and for the determination of the mineralogical grain composition.

Mineral tracing

The software JMicroVision 1.2.7 in combination with a pen tablet (Bamboo Fun) of the company Wacom is used for surface area determination on thin section images (▶ figure 2.2). Therefore 25 to 30 images which represent a mean mineral (detrital and authigenic) composition and distribution within a sample were selected. Lines were drawn along each mineral phase to derive percentage information about mineral surface areas. Resolution is 0.70 µm, but realistic for a straight or curved line is ~5 µm. Hence the roughness in nm-scale of detrital grains and authigenic minerals is not investigated in this method. The lines were assigned to several mineral classes (e.g. quartz, feldspar, clay cutan). Detrital grains with or without surrounding authigenic minerals (e.g. clay cutan, Fe-oxide, bitumen and kaolinite) are assumed to have a plane surface area and a mean chemical composition. Especially for grains consisting of diverse mineral types (e.g. a felsic volcanic rock fragments which is mainly composed of quartz and feldspar) a line represents a mean percentage of quartz and feldspar, respectively. Intragranular porosity is not considered. Further information of intra-porosity and detailed mineral composition gives another image analysis method (2nd type) which is based on grey scale thresholds. Agglomeration of different minerals, esp. for grain covering Fe-oxide, clay cutan and/or bitumen are difficult to separate in thin section images. Clay cutans were counted as single mineral phases where no Fe-oxide and/or bitumen are present. Especially Fe-oxide and bitumen are overestimated in thin section images and during image analysis.

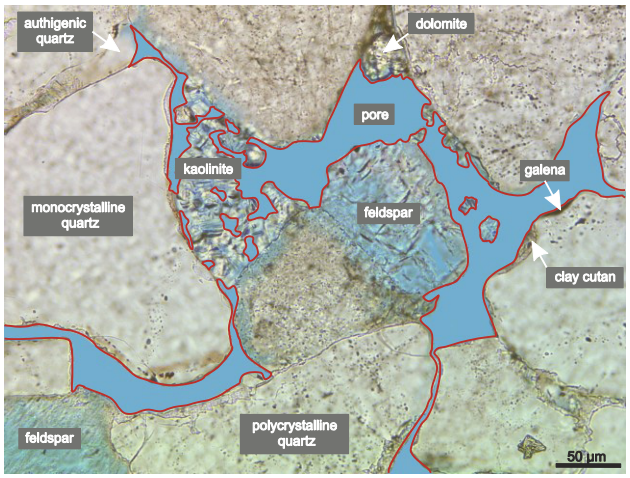

Figure 2.2: Surface area determination by mineral tracing in thin section images. Each section (red line) is assigned to an authigenic or detrital mineral phase which is exposed to the open pore system (blue colour).

Therefore the achieved results should be handled carefully. Varying amounts and thicknesses of clay cutans and thin layers of meshwork illite are present in Rotliegend sandstones and are visible with HR-SEM only. Where kaolinite appears as single crystals around detrital grains with a minimum length of ~30 µm they were traced. For smaller crystals perpendicular to grain surface areas a straight/curved line was drawn. Further theoretical calculations for the kaolinite size and distributions are investigated for these areas. Vermicular kaolinite was traced along the boundary between crystal and pore space. Porosity between each kaolinite crystal was not investigated and will also find consideration in theoretical calculations. Furthermore a third kaolinite group is represented by a sheaf-like arrangement of pseudo-hexagonal plates. Where they appear in open pores they were treated just like vermicular kaolinite. However especially in samples from field C the pore space is often filled with single crystals and sheaf-like arrangements and it is not possible to draw lines around those. For authigenic quartz the surface area is assumed to be plane and no further information is assigned. With this method

sulphate/sulphide and dolomite are considered to be identical in composition, respectively. Note that an operator-effect is to consider for this method. Furthermore focusing effects of mineral phases in thin section images are present.

Grey scale threshold

Image analysis was used for the determination of (1) the detrital grain composition, (2) the intragranular and intramineral porosity and (3) for estimation of dolomite generations based on different grey intensities (due to varying Fe and/or Mn-contents) from backscatter electron images (BSE). For BSE image acquisition an electron microprobe machine Cameca SX50 at the University Jena (EMS) was used. In scanning electron microscopy the amount of backscattering is proportional to the mean atomic number. Different grey intensities (from black to white) allow a relative identification of minerals. The EDX-system was used for single-point analysis to identify mineral species.

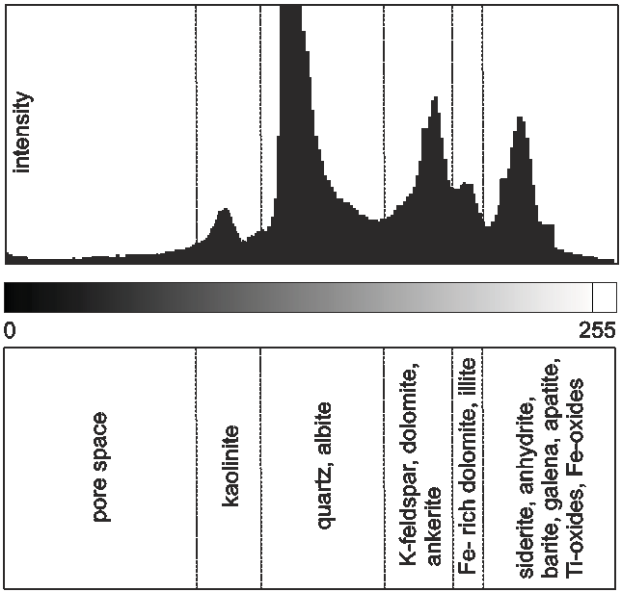

Figure 2.3: Example for a pixel intensity histogram of grey scale thresholds of backscatter electron images (BSE). The histogram is used for image analysis to define mineralogical composition and pore content in detrital grains and authigenic minerals. Sample: Aw02-03.

For analysis the software JMicroVision 1.2.7 of the company Wacom was used. The resolution of 0.37 µm equates to 1 pixel. Field of interests are defined by drawing a 2-dimensional area around the detrital grain or authigenic mineral. Grey scale thresholds are generated for the image and assigned to present pores and mineral phases, respectively (▶ figure 2.3). Pore space appears normally black, but may be dark grey in small pores within detrital grains. Kaolinite and quartz can be identified in all samples. According to their composition (light grey to white coloured dolomites contain more Fe and/or Mn than dark grey cements) dolomites may be separated in three categories: grey, light grey and white. K-feldspar has nearly the same grey threshold as early mesodiagenetic dolomite cement and it is not possible to separate this generation from other dolomites when K-feldspar is present. Furthermore in some volcanic rock fragments green coloured illite/smectite minerals precipitated as an alteration product during burial diagenesis. In BSE images they appear as middle grey phases. Minerals with high atomic numbers have light grey to white colours and cannot be separated during image analysis. Therefore following minerals are affected: siderite, anhydrite, barite, galena, Ti-oxides and Fe-oxides. At mineral rims a different orientation to the detector may lead to another grey intensity

and should be considered for interpretation. Furthermore different measurements on thin section may cause changed grey scale thresholds. For the field of interest and for each mineral and pore the area and perimeter was calculated.

2.10 Geochemical and reactive transport modelling

CO_2-water-rock interactions were simulated with the software code PHREEQCi (Parkhurst and Appelo, 1999) with a zero dimensional kinetic reaction model (short and long term model) for a CO_2 saturated fluid. The computer program is able to simulate chemical reactions in equilibrium with an aqueous solution with reacting mineral and gas phases (Parkhurst and Appelo, 1999). The simulations were run for an equilibrium model and are further interconnected with kinetic parameters to simulate water-rock interactions under the supply of CO_2. The results from the PHREEQCi model are connected with the in-house Shell software MoReS for 2-dimensional reactive transport modelling.

For a more detailed description of the models (input data and further parameter) please regard to chapter 6 (geochemical modelling of CO_2-water-rock interaction) and chapter 7 (reactive transport modelling with coupled geochemical information).

3 Geological setting

3.1 Tectonic and structural evolution of the Central European Basin

The Central European Basin (CEB) extends from England to Poland and is bordered by the Variscan Mountains (including e.g. the Rhenish Massif and the London-Brabant Massif) in the south and by the Sorgenfrei-Tornquist/Tornquist-Thesseire Zone in the north. This fault zone separates the Precambrian East European crust from the Palaeozoic crust of Central Europe (Berthelsen, 1992). The basin is subdivided in several sub-basins, where the two largest are the Northern and Southern Permian Basin which are separated by the Mid-North-Sea High and the Ringkøbing-Fyn High. Furthermore the Southern Permian Basin (SPB) is subdivided from west to east in the Anglo-Dutch Basin (ADB), the North German Basin (NGB) and the Polish Trough (PT) (▶ figure 3.1). The available study focuses on the Rotliegend sediments of the western part of the North German Basin. The NE onshore and the northern offshore areas of the Netherlands belong also to the NGB as well as north Germany and western Poland. An overview on the tectonic and structural history and the geology of the SPB is e.g. given by Ziegler (1990) and Glennie (1998). More detailed information about structural, geochemical and geological evolutions for the NGB are given by Baldschuhn et al. (1996, 2001).

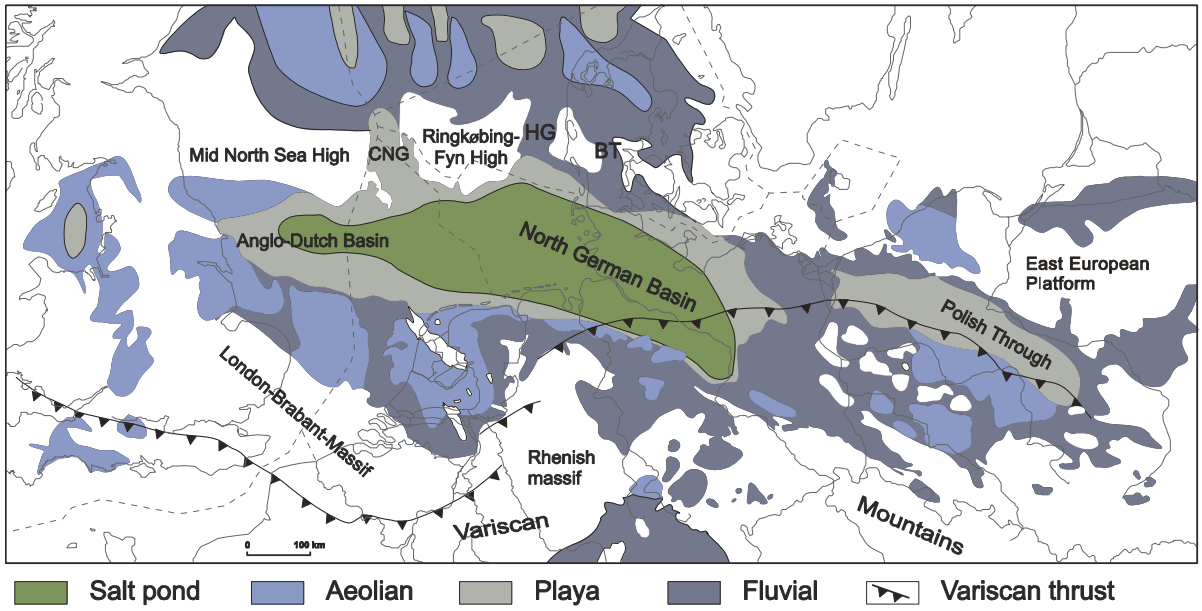

Figure 3.1: Present-day distribution map of Upper Rotliegend sediments attributed to late Middle to early Late Permian in the Southern Permian Basin. HG = Horn Graben; BT = Bramble Through; CNG = Central North Sea Graben. Modified from Geluk (2005).

The basement units of the NGB beneath the sedimentary basin fill are from north to south the Baltic Shield, the Caledonides and the Variscan fold and thrust belt. The Baltic Shield is composed of undeformed Cambro-Silurian sediments and crystalline rocks. Between earliest Silurian and Late Ordovician the collision of East Avalonia with Baltica results in the Caledonian Orogeny and is documented by seismic lines of thrusting (e.g. Tanner and Meissner, 1996; Abramovitz et al., 1998; Krawczyk et al., 2002). The passive margin of Baltica which was overthrusted by Avalonia is located between the Elbe-Odra Line (EOL) and the Thor suture (TS)

(▶ figure 3.2). This zone is indicated by high velocities (6.8-7.0 km/s), high densities (no further specification in literature) (Bayer et al., 2002; Aichroth et al., 1992; Yegorova et al., 2007) and by a regional thinning of the lithosphere from the Baltic Shield towards the Elbe-Odra Line (Gregersen et al., 2002 and 2005; Shomali et al., 2006).

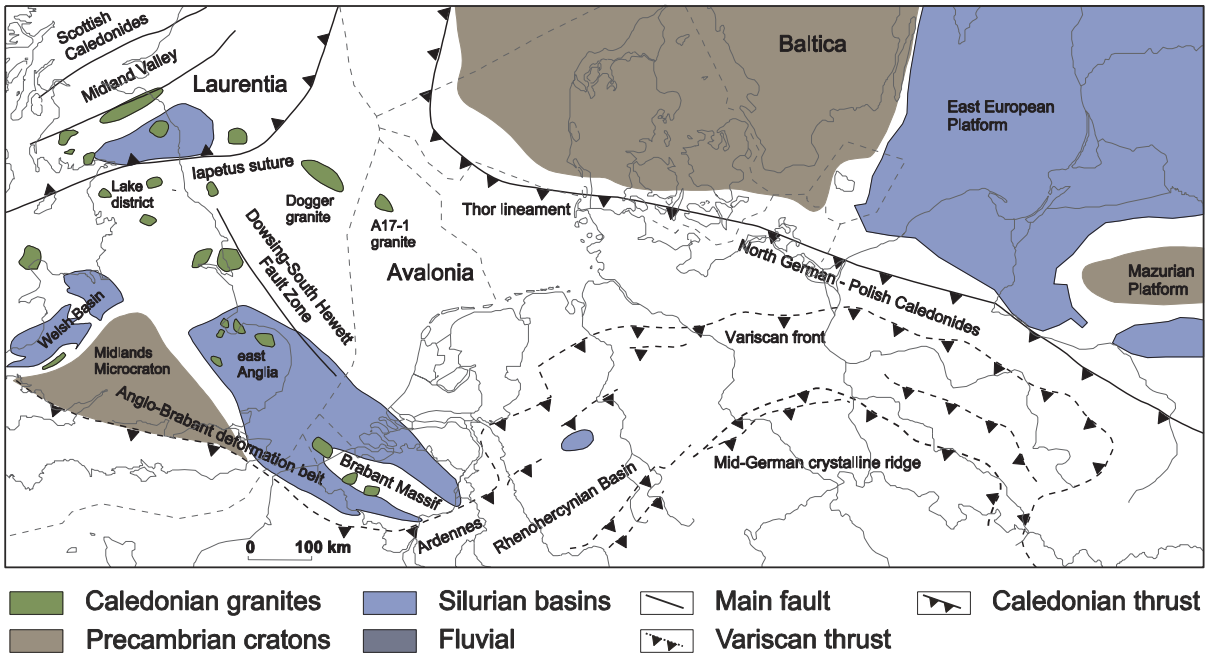

Figure 3.2: Structural overview of NW Europe with the main Caledonian and Variscan structures. Modified from Geluk et al. (2007).

During Early to Middle Carboniferous the collision of Gondwana and Gondwana-terranes with the southern border of East Avalonia and the closure of the Rheic Ocean results in the Variscan Orogeny (Ziegler, 1990; Scotese and McKerrow, 1990; Vai, 2003) (▶ figures 3.2 and 3.4). In parts the Rheic suture is well imaged by seismic reflection data as a crustal shear zone (Pharaoh, 1999). In the course of the collision a foreland basin with northward migrating basin axis and a general NW-SE strike was formed in the north of the rising Variscan orogen during Late Carboniferous to Early Permian. This phase was marked by an active wrench fault along the Elbe fault system, dextral transition and horizontal movement which are considering the distribution of the initial deposits (Bachmann and Grosse, 1989; Scheck and Bayer, 1999). Igneous activity (mainly rhyolites and andesites) and active faulting appeared during this period (e.g. Gast, 1988; Plein, 1990; Ziegler, 1990; Dadlez et al., 1995; Bachmann and Hoffmann, 1997; Bayer et al., 1999; Abramovitz and Thybo, 1999). After Brink (2005) the subsidence of the Southern Permian Basin is related to metamorphism of the lower crust (30 % of the total subsidence rate), resulting in increasing rock density and subsequent decrease in rock volume, and to the sedimentary load (70 %) (e.g. Ziegler, 1990; Scheck and Bayer, 1999; van Wees et al., 2000).

Initiated by rifting related to the Mesozoic break-up of Pangea e.g. in the North and Central Atlantic domain and in the Mediterranean (Ziegler, 1990) several pulses of extensional tectonics entail in the formation of sub-basins or grabens in the SPB. These areas are mostly linked to intense subsidence, like e.g. in the area surrounding the Ringkøbing-Fyn High, in the Glückstadt Graben, the Horn Graben and the Rheinsberg Trough (e.g. Ziegler, 1990; Clausen and Pederson,

1999; Baldschuhn et al., 2001; Evans et al., 2003; Maystrenko et al., 2006) (▶ figure 3.3). With an average NE-SW striking orientation these graben systems did not follow the general trend of the SPB which is more or less NW-SE. After Best et al. (1983) the structures are due to pre-existing faults which were active during Permian and Late Paleozoic time. Furthermore the ensuing evolution of the SPB after the Triassic is mainly influenced by mobilized evaporitic deposits (e.g. Trusheim, 1957; Jaritz, 1973; Brink, 1984; Scheck et al., 2003; Mohr et al., 2005). From the Early Triassic onwards subsidence slowed down in the ADB and the PT whereas the NGB continued to subside rapidly (van Wees et al., 2000; Geluk, 2005).

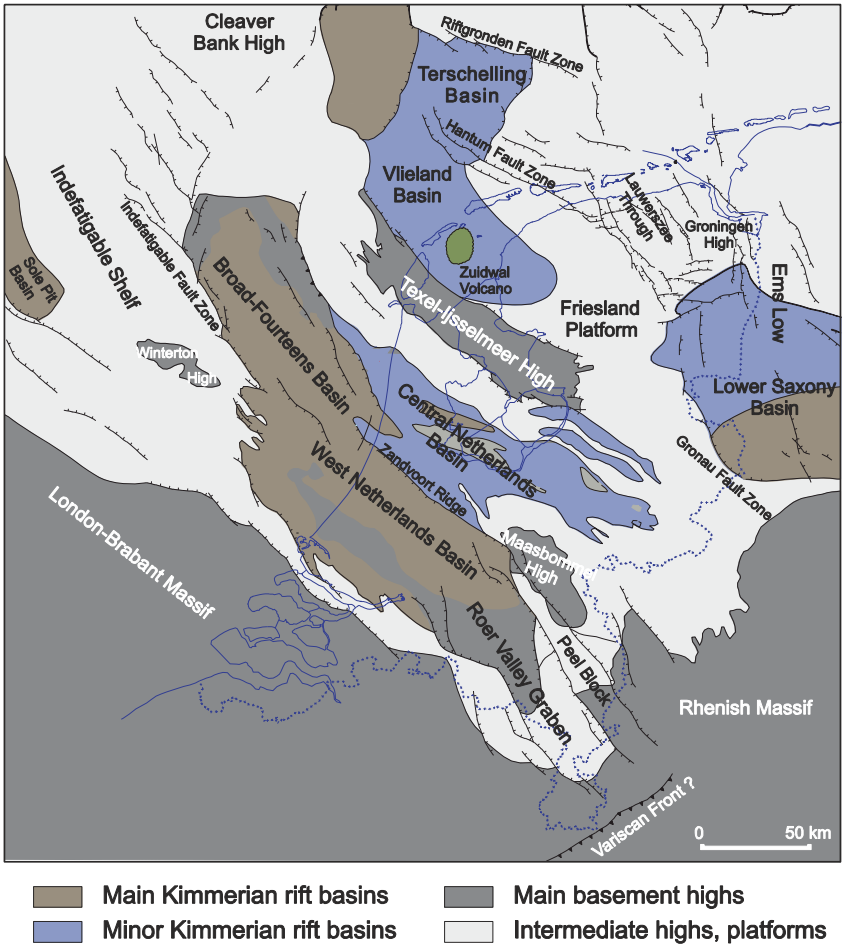

Figure 3.3: Map of the structural elements of the Netherlands with Mid and Late Kimmerian (Jurassic and Early Cretaceous) basins, highs and platforms. Modified from de Jager (2007).

During the Rhaetian and Early Jurassic a marine transgression was followed by shale and sandstone sedimentation. In this time organic-rich shales were deposited and form important hydrocarbon source rocks for Meso- and Cenozoic reservoir rocks (Bentz, 1958). During the Middle Jurassic continued extension leads to continental break-up of Pangea and opening of the Central Atlantic Ocean. This phase was followed by a rifting of the area of the Norwegian and Greenland seas in the Late Jurassic to Early Cretaceous (Ziegler, 1990). Rifting in several areas of the SPB yields to e.g. the formation of the Lower Saxony Basin, the Central Graben, the West Netherlands Basin and the Central Netherlands Basin (e.g. van Wijhe, 1987; Betz et al., 1987; Jordan and Kockel, 1991; Oakman and Partington, 1998; Nielsen, 2002; Möller and Rasmussen,

2003; Duin et al., 2006) (▶ figure 3.3). Simultaneously the adjacent platforms were uplifted and eroded. During Late Cretaceous and Early Paleogene times the collision of Africa-Arabia and Eurasia induced compressional stresses on the continents. During the changing tectonic regime, some basins (e.g. the Lower Saxony Basin) underwent a tectonic inversion and were uplifted (Ziegler, 1990; Gemmer et al., 2003; Kley and Voigt, 2008). Compressional deformations led to the formation of deep reaching faults and flexures which are due to significant erosion of the southern margin of the SPB and along the Tornquist Zone. Furthermore the Late Cretaceous was characterised by regional thermal subsidence and rising sea level (Ziegler, 1990). During Late Cretaceous to Early Tertiary an inversion of the basin was forced by the movement along previous tensional faults. This results in uplift, folding and erosion (Kley and Voigt, 2008). The impact of the uplift on Rotliegend sedimentation is a lowering temperature, formation of fracture systems and the enter of meteoric water and deep basinal Carboniferous and/or Zechstein brines (Gaupp and Okkerman, 2011).

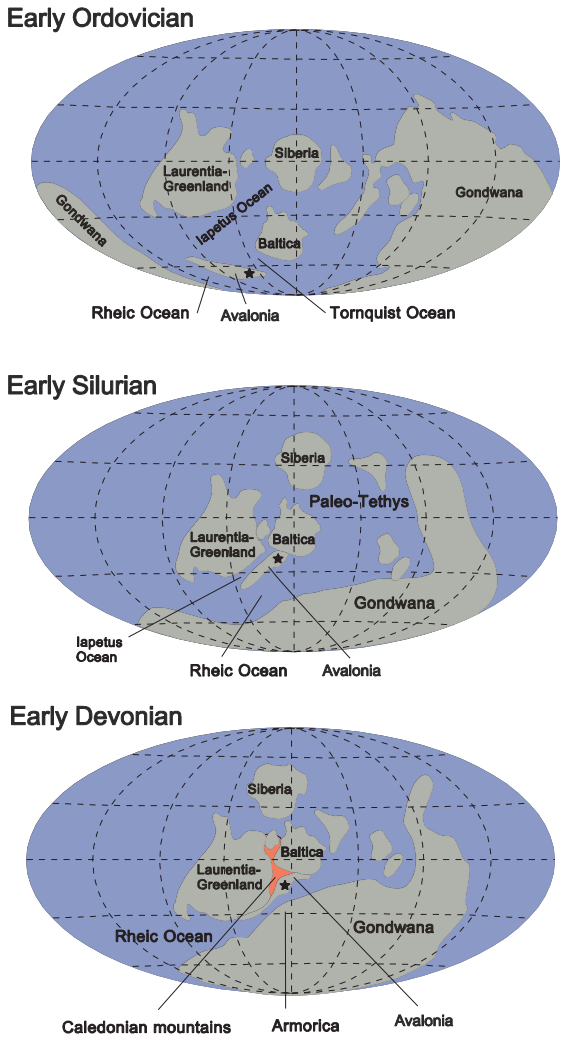

Figure 3.4: Reconstruction of the paleo-tectonic northward drift of Avalonia and its collision with Baltica and Laurentia during Early Ordovician to Early Devonian. The star indicates the paleo-position of the Netherlands. Modified from Scotese and McKerrow (1990).

During the Paleogene the formation of depocentres is evident within the North Sea. Throughout this time a subsequent subsidence in the North Sea and adjacent onshore areas in the Netherlands and NW Germany is observed (Sclater and Christie, 1980; Ziegler, 1990; Hall and White, 1994; Nielsen, 2002; Scheck-Wenderoth and Lamarche, 2005). In Pleistocene times the area was repeatedly covered by an ice shield.

3.2 Rotliegend sedimentology

The depositional system of the Rotliegend Basin was influenced by several variables, e.g. the availability of sediments, climate, the connection to the ocean and tectonic subsidence. The tectonic and structural evolution of the basin was discussed previously. The sediments of the Rotliegend Basin were deposited under arid to semi-arid climate conditions in intracontinental basins on the super-continent Pangea. The depositional thicknesses increase from less than 50 m in the south of the Southern Permian Basin to almost 2000 m in the north (e.g. in the Glückstadt Graben). But the present thicknesses were often influenced by salt movement. The

sediments were buried between 3000 to 6000 m depth. The Permian is divided into three lithostratigraphic groups: The Lower Rotliegend (volcanic and clastic rocks and limited geographic distribution), the Upper Rotliegend (fine to coarse grained clastic sediments and evaporites) and the Zechstein Group (mainly marine evaporites and carbonates) (e.g. Lokhorst, 1998).

Table 3.1: Stratigraphic chart of the Rotliegend in the Netherlands (modified from Lokhorst, 1998). The numerical ages are according to Menning (1995). Fm = Formation.

age [Ma]	Group		Fm	Member (south)	Member (north)
258	Rotliegend	Upper Rotliegend	Silverpit and Slochteren	Ten Boer Upper Slochteren Ameland	Upper Silverpit Claystone Silverpit Evaporate Lower Silverpit Claystone
260					
262				Lower Slochteren	
264					
266					
296		Lower Rotliegend			

The stratigraphic classification (▶ table 3.1) is mainly based on lithostratigraphy, but also chemostratigraphy, magnetostratigraphy and sequence stratigraphy were applied, biostratigraphic tools were successful only locally (e.g. George and Berry, 1993; Yang and Baumfalk, 1994; Menning, 1995; Plein, 1995; Glennie, 1998; ICS, 2003). Radiometric dating of the Lower Rotliegend Group in Germany yield an Early Permian age (Plein, 1995; Stemmerik et al., 2000) in comparison to a Middle Permian age in the Netherlands (Sissingh, 2004; Geluk, 2005).

3.2.1 Lower Rotliegend

The Lower Rotliegend Group is known as the Altmark Group in Germany (Plein, 1995) and as the Karl Formation in the Netherlands, Denmark and the United Kingdom (Johnson et al., 1994). Volcanic rocks of the Lower Rotliegend are widespread in Germany and Poland but only in minor amounts in the Netherlands (Ems Low, Dutch Central Graben and Horn Graben) (Lokhorst, 1998; Evans et al., 2003). The maximal thickness is reached in NE Germany (~2500 m) whereas in the onshore Netherlands a maximal thickness of 80 m is to notice in the Ems Low (Plein, 1995; Geluk, 2005). The volcanic rocks consist of rhyolithes, andesites and minor amounts of basalts and appear as lava flows and ignimbrites with partly intercalated tuffs and volcanoclastics (Marx et al., 1995; Plein, 1995; Benek et al., 1996). In the eastern part of Germany three subsequent stages of volcanism are identified: a lower andesitic rhyolithe, further ignimbritic rhyolithes and finally alkaline basalts. Minor amounts of claystones and subordinate contents of sandstones are interbedded in the volcanic material (Schneider and Gebhardt, 1993; Gaitzsch et al., 1995). The Rotliegend volcanics show considerable variations in their relative stratigraphy and absolute ages (Lokhorst, 1998). This reflects the presence of several volcanic activities in different times. On the basis of radiometric age dating (289-291 Ma) and lithological composition of the basalt the Lower Rotliegend in Germany is classified as the Early Permian (Plein, 1995). K/Ar ages of 290 Ma (Sissingh, 2004) in the western part of the Netherlands fall within the age range of the north German volcanics. The volcanic rocks of the eastern part of the Netherlands (Ems Low) show a much younger age (K/Ar dating: 258 ±6 Ma) of the volcanic pulse (NITG, 2000) and may be placed in the Middle to Late Permian. After Breitkreuz and Kennedy (1999) U/Pb dating of magmatic zircons from NE Germany indicates a short volcanic activity at the boundary between Carboniferous and Permian. Prior to the deposition of Upper Rotliegend sediments the upper part of the volcanic material was mostly eroded (Bachmann and Hoffmann, 1997).

3.2.2 Upper Rotliegend

Thick continental, red-coloured siliciclastica and minor amounts of evaporites were deposited in the Central European Basin under semi-arid to arid climate conditions (Glennie, 1972 and 1983). A general distribution of four facies types dominates the succession of sediments: (1) ephemeral fluvial systems (wadis) are located at the basin margin and consist mainly of sandstones, siltstones and conglomerates. The sediments form irregular interlocking with (2) aeolian depositions. (3) Playa lake and mudflats were deposited in the deepest parts of the basin and include (4) saline lake environments (▶ figure 3.5). In dry periods halite and other evaporites were deposited in the basin centre, whereas during more humid climate conditions the lake expanded and silt and clay were deposited in more marginal areas. During Rotliegend sedimentation the playas merged into one large continuous hypersaline playa lake and covered the complete North German Basin (Gralla, 1988; Gast, 1991; Plein, 1993). The main sediment input was carried out from the southern basin margin in the northward dipping basin (Plein, 1978; Gast, 1988). An additional significant input applied also from the eastern part of the basin margin (Gast et al., 1998; Rieke, 2001). The principle subdivision of the Upper Rotliegend in Germany is considered applicable to the Southern Permian Basin (Plein, 1995). Three subgroups have been accounted as the Müritz, Havel and Elbe subgroup (▶ table 3.1). Only the youngest stage of sediment deposition has taken place in the Netherlands. The fine grained evaporitic Silverpit Formation in the northern half of the Netherlands and the sandy Slochteren Formation in the south may form the lateral equivalent of the German Elbe subgroup (Glennie 1998; Geluk,

2005). The Müritz subgroup (Early Permian) describes the oldest sediments of the Upper Rotliegend and was deposited in local fault-bounded basins in the North German Basin and in the Polish Trough. Minor depositions were linked to movements along the Tornquist Zone. The central part of Germany was connected along NNE-SSW orientated faults with southward located intracontinental basins, like the Hessian Depression, the Saale-Nahe Basin and the Kraichgau Through. The succession comprises mainly volcanic breccias, fluvial sandstones and playa deposits. The maximum thickness reaches 600 m (Plein, 1993; Hoffmann et al., 1997).

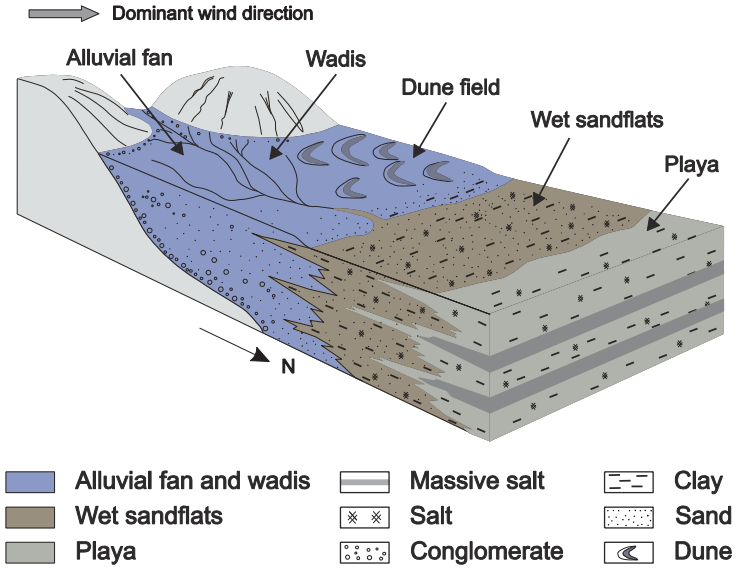

Figure 3.5: Depositional facies of the Upper Rotliegend Group in the Netherlands which show the transition from the sandy Slochteren Formation at the basin margin into the Silverpit Formation located in the basin centre. Modified from Geluk (2005).

The sedimentation of the Havel subgroup is assumed during Middle Permian time in the North German Basin and the Polish Trough. The subgroup comprises the Parchim and Mirow Formation. The main sediment input occurs from the southward located Variscan Mountains. N-S trending horst and graben structures at the south of the basin margin influenced strongly the sedimentation rate (Gast, 1988). Minor amounts of sediments were supplied from the Ringkøbing-Fyn High and the Fennoscandian hinterland (Plein, 1978). The base of the Havel subgroup sediments consist of thick conglomerates which were deposited as alluvial fans (mainly depris flow and sheet flood). In the upper part of the succession fluvial plains and aeolian dunes are dominant. Fluvial sandstones at the southern basin margin are the result of ephemeral stream environments (Glennie, 1972). The aeolian sediments were deposited in graben structures and in vicinities of paleo-morphological highs (Drong et al., 1982; Gast, 1988; Rieke, 2001). The paleo wind direction occurred from NE-E towards SW-W (Glennie, 1972; Katzung, 1975; Nairn and Smithwick, 1976). Interbedded basalts indicate partial tectonic movements (Hoffmann et al., 1997). Sedimentation gradually expanded from the grabens over a larger area and is leading to a westward movement of the NGB, in comparison to the Müritz subgroup (Gast, 1988). The maximum thickness reaches over 1100 m in the NGB.

The Elbe subgroup is divided in the Slochteren/Silverpit Formation in the Netherlands (▶ table 3.1). The Slochteren Formation comprises mainly sandstones and conglomerates of fluvial and aeolian origin whereas the Silverpit Formation is composed of claystones, siltstones and evaporites (Geluk, 2005). Their transition occurs in a relatively narrow zone in the north of the Netherlands and form interfingers between the two formations. Several claystone tongues of the Silverpit Formation reach far to the south into the sandy bodies of the Slochteren Formation.

The Silverpit Formation is subdivided into the Lower Silverpit Claystone, the Silverpit Evaporite Member and the Upper Silverpit Claystone. In the area where the two formations interfinger the Slochteren Formation can be subdivided in the main sandstone members Lower and Upper Slochteren, which are separated by the clay- and siltstones of the Ameland Member (Geluk, 2005) (▶ figure 3.6). During deposition of the Elbe subgroup subsidence, probably related to thermal contraction of the lithosphere, continued at the beginning of the Dethlingen and Silverpit Formation. The sedimentation area gradually expanded mainly west- and southward, but also across the Tornquist Fault Zone onto the East European Platform. The greatest expansion of the Rotliegend Basin was reached with the deposition of the Hannover Formation (Plein, 1993 and 1995). Two minor extensional pulses led to differential subsidence rates in the eastern and northern Netherlands (RGD, 1991; Plein, 1993; NITG, 1998). Fluvial sediments were deposited in large terminal fans and ephemeral stream systems mainly at the southern basin margin and are partly reworked by wind action (Plein, 1978; Gaupp et al., 2000; Rieke, 2001).

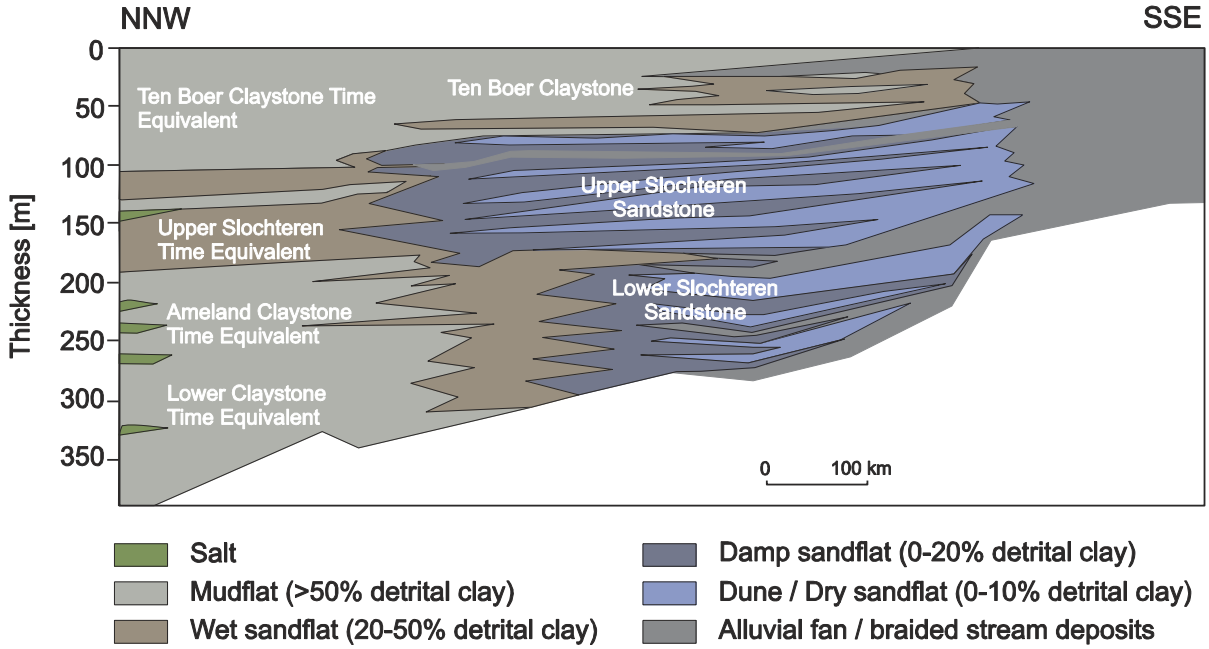

Figure 3.6: Stratigraphical distribution of the Upper Rotliegend in the Netherlands from NNW to SSE showing the intercalation between sand (e.g. Slochteren Formation) and shale (e.g. Silverpit Formation) deposits. Modified from Reijers and Koster (1993).

Furthermore aeolian and shoreface/shoreline sandstones were deposited and form irregular interlocking patterns with fluvial sediments. In the basin centre cyclic sedimentation of pelites, evaporites (rock salt and subordinate anhydrite) and evaporitic mudstones/sandstones are common in a perennial saline lake. Mud- and sandflats were periodically flooded during water level fluctuation (Gralla, 1988; Gast, 1991; Gaupp et al., 2000) which is arising from climate changes and episodic marine incursion and cause to a migration of facies boundaries (Gast, 1991; Schneider and Gebhardt, 1993; Gaupp et al., 2000; Legler et al., 2005). The Elbe subgroup sediments reach a maximum thickness of 1500 m in the North German Basin, 800 m in the Polish Trough and 300 m in the Anglo-Dutch Basin. A subdivision of Upper Rotliegend lithofacies (e.g. aeolian, fluvial and sabkha) was developed by George and Berry (1993) for the UK and Dutch sector of the southern North Sea. The description of different facies types, which are

deposited in the study area (northern Netherlands), are supplemented (1) by lithological interpretations of wells from the reservoirs A and C, prepared by PanTerra Geoconsultants B.V. and (2) by facies definitions after Reijers et al. (1993). Aeolian sediments are formed during periods with high sand supply related to dry climate conditions. All sediments show varying amounts of bleached horizons, layers or clay fragments with gray and/or green colours in comparison to the red and red-brown sandstone and mudstone units.

3.3 Potential Carboniferous source rocks

In the Late Carboniferous the deposition areas were located at and near the equator. There, material from tropical forests and swamps were deposited on a large paralic plain with low relief. The main sediment supply occurred from the southern Variscan Mountains and minor amounts from the northward existing Caledonides.

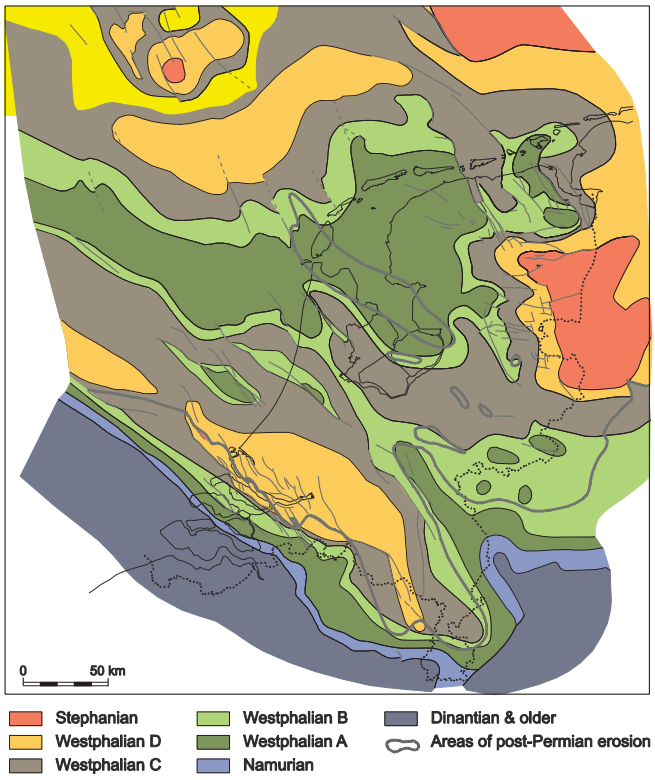

Figure 3.7: Subcrop map of the Base Permian Unconformity with Carboniferous deposits in the Netherlands. In areas of post-Permian erosion or where no deposition has taken place the top Carboniferous under younger unconformities is shown. Modified from van Buggenum and de Hartog Jager (2007).

After Franke (1995) the facies changed from dominantly marine to paralic, limnicfluvial and finally continental during Carboniferous. Thick Namurian sediments (e.g. basinal clays, organic-rich shales and turbidites) and igneous intrusions were deposited in the Rhenoherzynian Zone. During the Westphalian the Variscan deformation front migrated northward and the earlier Namurian sediments were deformed. The Westphalian is characterised by a high sedimentation rate and a decrease of the inter-central lake size, were shallow-water, swamp dominated and fluvial sedimentation took place. During the Westphalian A and B continuing subsidence of the basin took place in the Netherlands. In NW Germany inversion-related uplift was predominant and occurred from the Westphalian C onward. In most areas the transition from coal-bearing facies types to continental red beds took place in the Westphalian C-D (Hedemann and

Teichmüller, 1971). The present day distribution of Carboniferous deposits is shown in ▶ figure 3.7.

3.4 Sedimentology and stratigraphy of the reservoir and horizons investigated

Rotliegend clastic sediments of the reservoirs A, B and C were deposited in the North German Basin. Coarse grained sediments and conglomerates which were deposited as alluvial fans and braided river sequences are developed northward into finer grained sandstones and mudstones of fluvial or aeolian units (▶ figure 3.5). Correlations of the available succession based on gamma-ray log and lithology indicate sediments of the Upper Slochteren and Ten Boer Claystone Member which are part of the Slochteren Formation (Elbe Subgroup) (▶ table 3.1). Based on investigations of core images and gamma ray logs the following well descriptions are compiled for the wells Aw02, Aw03, Aw04, Aw05, Bw01, Bw02, Bw03, Cw02, Cw03 and Cw04 and are listed in appendix A1-09 (field A), A1-10 (field B) and A1-11 (field C). From these wells samples were taken for petrographic and geochemical investigations (compare chapter 4).

Due to confidentiality to the company NAM no map of the reservoir structures and wells and no further information about the field locations are shown in this thesis.

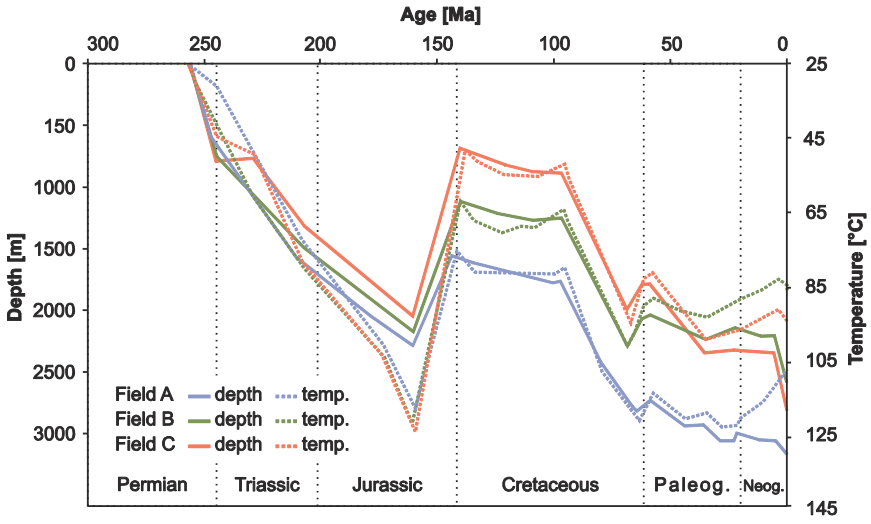

Figure 3.8: Burial history and related temperatures for the northeast Netherlands during Permian and Quaternary time for the areas of field A, B and C. Data were provided by NAM and calculated with an Shell in-house software

3.4.1 Field A

Reservoir structure

Field A is located at the southern margin of the South Permian Basin. The reservoir extends from the rim of an intra-basinal paleohigh to the giant gas field Groningen in the north. This paleohigh was probably originated during Variscan time (van Wijhe et al., 1980) and retained this level during Mesozoic (Stäuble and Milius, 1970). The gas accumulation is contained in an elongated horst block (E-W: ~15 km and N-S: ~5 km in distance), whereby the traps are a combination of fault-dip closures. To the northwest the high is bounded by the Lauwerszee Trough and to the east by the Ems Graben in Germany (▶ figure 3.3). Two main boundary faults border the reservoir in the south and north. The Field A is dip-closed to the west and fault-closed to the flank of the Groningen field. The horst block is sloped southward. In the eastern part the structure of the reservoir is seismically intangible because of the overlaying Veendam salt wall.

Different pressure observations in the Veendam area in comparison to the western part of the reservoir indicate that the gas in this block follows the Groningen pressure decline (van Sande et al., 2001). The reservoir is cut by several north-south orientated faults. They are mapped at base Zechstein and were vertical extrapolated to the top of the Rotliegend deposits. Within the reservoir the distance between several faults are <10 m which cannot be observed on the 3D seismic surveys (Veenhof, 1996). Three major fault systems can be distinguished: (1) Extensional N-S faults are located at the boundary of the reservoir and are offset by E-W trending faults. They may represent reactivated Carboniferous lineations (Veenhof, 1996). (2) E-W faults show an oblique slip with largely normal component. Under the Saale Unconformity a dip change indicates a reactivation of a pre-Saalian structural lineament at the northern boundary fault. WNW-ESE Riedel-type faults are often associated to the E-W fault system. (3) NW-SE faults of extensional nature trending towards Groningen. After Stäuble and Milius (1970) they are interpreted to be post-Permian age (probably Late Kimmerian). It is difficult to specify the sealing capacity of the faults in coherence to the mentioned fault types. The thicknesses of the N-S faults inhibit the sealing of these structures. The top of the reservoir and the north is sealing against Zechstein salt (Post, 2010, person. comm.).

An aquifer is active in the western part of the reservoir. There, a connection via the Slochteren Formation is open to the neighbouring Vries field. The aquifer is bounded by the southern boundary fault of Field A. Furthermore an aquifer is present at the south of the field. Over the years a gradual increase in water saturation is to observe. The original (at year 1975) gas-water contact was located at 3074 m depth. Today the contact lay at an average depth of about 3060 m (van Sande et al., 2001) or in some regions at shallower depth (van Ojik, 2011, person. comm.).

Sedimentology and stratigraphy of the reservoir

The basin evolution during early Permian initiated Rotliegend sedimentation over Carboniferous deposits. The Rotliegend Group is represented by the Upper Slochteren Member (mainly sandstones and conglomerates) which is overlain by the Ten Boer Claystone Member. The top Rotliegend is masked by a mudstone unit which forms the base of the Zechstein deposits (▶ table 3.1). The total thickness reaches from 80 m in the SE to 320 m in the NW (van Sande et al., 2001).

Carboniferous sequences were deposited in the area with thicknesses of at least 2500 m. They consist mainly of sediments which are attributed to Namurian to Westphalian B, C and D (van Wijhe and Bless, 1974; van Ojik, 2011, person. comm.) (▶ figure 3.7). The depositions of the Early Westphalian B are mainly influenced by fluvial sedimentation. During the late Westphalian B and Early Westphalian C swamp dominated fluvial systems are common in the eastern Netherlands. In the Groningen area sandstones of the Tubbergen Formation form a reservoir underlying the Rotliegend horizons. A climate change from tropical to arid (Westphalian D) combined with uplift of the Variscan front lead to the deposition of floodplain-dominated sediments with silty claystones and intercalated sandstones (van Buggenum and den Hartog Jager, 2007). The deposits are separated from Rotliegend sediments by the Saale Unconformity. The gas reservoir consists of Upper Rotliegend sediments of Guadalupian age (van Wijhe et al., 1980; van Ojik, 2011, person. comm.). Lower Rotliegend deposits are absent. Under semi-arid to arid climate conditions continental red-coloured siliciclastica were deposited in the area. A fining-upward trend can be recognised from the basis to the top of the reservoir: (1) conglomerates and coarse grained sandstones of an alluvial fan to braided river system, (2)

fluvial deposits of stratified and non-stratified fine to medium grained sandstones, (3) aeolian dune deposits of well cross-bedded sandstones and (4) muddy siltstones, sandstones and mudstones of a lacustrine environment (Veenhof, 1996). The conglomerate and sandstone deposits (1-3) are attributed to the Upper Slochteren Formation and the fine grained siliciclastica (4) form the Ten Boer Claystone Member. The Ameland Claystone Member and the Lower Slochteren Formation are absent in field A. The Upper Slochteren Formation has been subdivided into six genetic units (Nicholls et al., 1987; Veenhof, 1996). The subdivision was based on core evaluation and log correlations of wells from field A and the Groningen field. Information about thicknesses of sediment horizons are derived from investigations of core images and gamma ray logs from different wells which were provided by NAM for this study.

Unit (1) are basal conglomerates. The unit consists of conglomerates and pebbly sandstones. At the southern basin margin conglomerates were deposited in alluvial fan environments (e.g. well Aw05). Whereas further north laterally equivalent braided river sequences were present (Veenhof, 1996) (e.g. wells Aw01 to Aw04). The thickness yields between 30 and 40 m. For well Aw05 the sediments show a mean porosity of ~12 % (maximum: 25.5 %) and a mean horizontal permeability of ~260 mD (maximum: 9900 mD) (appendix C3).

Unit (2) consists of pebbly sandstones. The facies was deposited in braided river and alluvial fan environments with a close association to the conglomerate facies. Coarse to fine grained sandstones form the main part of the unit. Furthermore some conglomerates and shale layers are intercalated. The shale layers are interpreted as fluvial braid plain sediments (Veenhof, 1996).

Unit (3) enfolded aeolian and fluvial fine to medium grained sandstones which form the best reservoir conditions for field A. The sediments consist of homogeneous, horizontal-bedded, cross-bedded and adhesion ripple lamination sequences. Commonly they are moderately poorly or well-sorted. Shale layers and conglomerates are intercalated. Burial diagenesis expressed in precipitation and dissolution processes of minerals play a major role for reservoir quality. In combination with depositional facies differences (e.g. aeolian and fluvial environments) porosity and permeability values may be influenced (Veenhof, 1996). The thickness of the main sandstone unit ranges between 20 and 50 m.

Unit (4) is characterised by a thin layer (thickness <5 m) of conglomerates (Veenhof, 1996) which indicates a high energetic braided-stream environment. Possibly storm-induced sheet floods are present. In comparison to the other units no clay beds are intercalated. A mudstone bed directly underlays the conglomerates and could represent a partial barrier for vertical directed gas and water flow (Veenhof, 1996).

Unit (5) is the most prolific reservoir after unit three. It contains fine to medium grained sandstones with intercalated clay layers, pebbles and conglomerates (Veenhof, 1996). The sediment sequences are a result of changing environmental conditions: fluvial, aeolian and lacustrine. The thickness increases gradually from south (10 m) to the north (24 m).

Unit (6) represents the Ten Boer Claystone Member which was deposited at the southern basin margin and consists of shale layers with intercalations of sandstones and siltstones. A clear trend from coarse to fine grained clastics to the basin centre has been recognised (Veenhof, 1996). The lower sequences contain reservoir quality sands which stay in contact with the Upper Slochteren sandstone units. The thickness of the Ten Boer Claystone Member increases gradually from east to west. The depth of top Rotliegend is located between 2900 and 3060 m depth (Structural map, Top Rotliegend, Internal report NAM, 1979). From east to west the

thicknesses of gas charged Rotliegend Slochteren units decrease from 81 m in well Aw10 to 154 m in well Aw11 and 132 m in well Aw12.

During the hole Permian a marine transgression leads in the ending of Rotliegend sedimentation processes. Evaporites and carbonates of the Zechstein which were deposited in the South Permian Basin, covered also the area of field A and form a seal for the gas reservoir. The Zechstein comprises five cycles (Glennie et al., 1990). In the eastern part of field A salt of the Veendam salt wall penetrated into Tertiary sediments (Post, 2010, person. comm.).

The sediments were first buried to 2100 m depth in Jurassic and further uplifted in Cretaceous time to 1500 m depth. The maximum burial depth was achieved in Paleogene/Neogene with 3000 m depth and temperature of maximum 122°C (▶ figure 3.8). The burial history has been generated in-house through Shell proprietary software. This software combines available data such as (reconstructed) thickness grids of (time) layers, heat flow, temperature measurements, distribution of insulators such as salt, maturity data, bathymetry reconstructions, etc. (van Ojik, 2011, person. comm.)

3.4.2 Field B

Reservoir structure

The field B is located within the Friesland platform between the Texel Ijsselmeer High in the southwest and the Hantum fault zone in the northeast (Paterson, 1996). Two main boundary faults limit the reservoir to the NW and SE. The field consists of four elongated N-S orientated fault blocks. The two largest blocks are block one (N-S: 5000 m, E-W: 3500 m) and two (N-S: 6500 m, E-W: 2500 m). They are separated by a NW-SE orientated fault zone with a significant high magnitude (20-60 m). An unresolved fault separates block three (N-S: 1500 m, E-W: 2000 m) and two. Block four seems to have no connection to the main reservoir area and is not penetrated by producing wells. A pod with sediments of Triassic age is located between block three and four (Grecula, 2002). Furthermore a number of smaller faults exist inside of the large field compartments. The traps are a combination of fault-dip closures. The structural dip is between 1° and 3°. The spill point is probably in the structurally complicated southern part of the field, where field B may be spilling towards Ureterp in the southeast (Pröpper, 1987). Zechstein deposits above the Rotliegend sediments are a good top seal (Post, 2010, person. comm.). A bottom seal does not exist because the underlying sandstone of the Limburg Group has reservoir quality. An aquifer is active in the NW part of the reservoir with distances between 10 to 21.5 km lengths. There, a connection via the Slochteren Sandstone is open to neighbouring Noord Friesland area. The gas-water contact lay at an average depth of about 2670 m depth (Post, 2010, person. comm.).

Sedimentology and stratigraphy of the reservoir

The Rotliegend is represented by the Upper Slochteren Member (mainly sandstones and siltstones) and the Ten Boer Claystone Member. The top of the Rotliegend sediments are covered by Zechstein clay deposits. The total thickness reaches ~150 m across the total field B (Nicholls et al., 1987).

Carboniferous sequences were deposited in the area. The sediments are attributed to the Westphalian A (van Buggenum and den Hartog Jager, 2007). This period is indicated by a high

water level and depositions of deltaic origin. The Westphalian A sequences were deposited in coarsening upward cycles. Each cycle started during a brief lacustrine transgression or a marine incursion and is followed by a deltaic progradation. In the upper part of the depositions channel sandstones and coal seams are intercalated. The channel sandstones have reservoir character. During the Westphalian B-D the water level continually decreased (Langenaeker, 2000; van Buggenum and den Hartog Jager, 2007).

The Rotliegend deposits of the gas reservoir consist of Upper Rotliegend sediments which are dominated by a lower desert plain environment (Nicholls et al., 1987; Pröpper, 1987). There, dry and damp sandflats existed. Locally they are intercalated with wet sandflats of the interdune pond environment. Sheetfloods from the basin margin in the southeast and Lauwerszee Trough rarely extended. The continental, mainly red-coloured siliciclastica were deposited under semi-arid to arid climate conditions. The sediments can be subdivided in three main units: (1) predominantly non reservoir-rocks of the Ten Boer Claystone Member, which were deposited in a playa environment. Sand stringers with 1-3 m thickness and probably aeolian in origin are intercalated within the claystone. The thickness varies northward from 47 to 54 m across the field. Unit (2) consist of aeolian sandstones (Upper Slochteren Formation) of at least 86 m thickness. A claystone horizon (typically 1-2 m thick) at the top of the sandstone sequences extends through all wells from field B. (3) The lower part of the Upper Slochteren sandstones show more frequent claystone and siltstone intercalations. Only the structurally highest wells are located above the gas-water contact (e.g. well Bw02, Bw03, Bw04 and Bw05). Lower Rotliegend deposits are absent. The depth of top Rotliegend is located between 2391 m (well Bw03) and 2457 m (Bw06) depth (Pröpper, 1987).

3.4.3 Field C

Reservoir structure

The field C is located in the South Permian Basin within the Friesland platform (Al-Hasani, 2004). The reservoir extends from the Hantum fault zone in the north about ~6000 m to the south and is there bordered by another large fault zone. To the east the reservoir is bounded by NW-SE orientated faults and to the west by the Lauwerszee Trough. Furthermore the field is cut by several NW-SE orientated faults (Al-Hasani, 2004). The “Main field” is orientated in NW-SE (4000 m length) and NE-SW (1500 m length) direction. Zechstein deposits above the Rotliegend sediments are a good top seal. The underlying Carboniferous sediments (sandstones of the Westphalian A) have reservoir quality. Over the field a significant varying (minimum: 2612 m and maximum: 2630 m depth) gas-water contact is recognised (Laksana, 2000). Reliable pressure measurements are absent to define a free-water-level (average depth for the whole reservoir: 2638 m) (Laksana, 2000).

Sedimentology and stratigraphy of the reservoir

The Rotliegend sedimentation is represented by the Upper Slochteren Member (mainly sandstones and siltstones) and by the Ameland and Ten Boer Claystone Member (Al-Hasani, 2004). In comparison to the southward lying reservoirs the field C is dominated by dry, damp and wet sandflats. The top Rotliegend is masked by a mudstone unit which forms the base of Zechstein deposits (le Guen, 2001). The total thickness of the Upper Slochteren Member reaches between 92 and 114 m across the “Main field”. The mean reservoir thickness is about 25 m.

Carboniferous sequences were deposited with thicknesses varying between 500 to 1500 m. They consist of sediments which are attributed to Namurian to Westphalian A (van Ojik, 2011, person. comm.). The sediments were deposited in a deltaic shallow-water environment prograding from the northern and southern basin margin into the lake (Langenaeker, 2000; van Buggenum and den Hartog Jager, 2007). Lower Rotliegend deposits are absent.

Under semi-arid to arid climate conditions Upper Rotliegend sediments were deposited in a lower desert plain environment. They consist of wet and damp sandflats with intercalated mudflats, dry sandflats and aeolian dune sediment. In comparison to the southward located reservoirs A and B sheetflood depositions appear only subordinated. The sediments of the Upper Slochteren Formation can be subdivided in five main units (Al-Hasani, 2004): (1) fine grained sandstones are depositions of the damp and dry sandflat sub-environment. Aeolian dune sediments are intercalated with a maximum thickness of 1.2 m. The massive sediments have good reservoir qualities. Unit (2) is a four meter thick shale layer with minor silty sandstone intercalations (decimeter-thickness) of the pond and mudflat sub-environment. The silty sandstones are interpreted as sheetflood deposits. The unit has non-reservoir character with a local vertical seal potential. Unit (3) is between seven and twelve meter thick and with fine grained sandstones similar to unit 1. Unit (4) consist of 30 m thick sediments from the damp and dry sandflat sub-environment with intercalated fine grained sandstones (aeolian dunes). In many places the sandstones are marked by a strong anhydrite cementation. The reservoir is interpreted as low permeable (mean 3.5 mD) to tight. Some minor sandstone horizons have permeabilities between 20 and 200 mD. With 40 to 50 m thickness unit (5) represent a good reservoir interval with similar sub-environment types as unit 1. The top of the unit is locally affected by anhydrite cementation. The depth of top Rotliegend is located between 2554 m and 2590 m.

4 Controlling factors on reservoir quality

4.1 Detrital mineralogy

Samples from field A, B and C have been taken from different horizons from the Upper Slochteren Formation (appendix C1). There will be no differentiation between stratigraphic ages and positions within the reservoirs. Only minor differences on the mineralogical inventory between the facies types are available: Coarse grained sandstones (e.g. alluvial fan sediments) contain more rock fragments (e.g. polycrystalline quartz) compared to finer grained alluvial or aeolian sediments. Fine to medium grained sediments which were deposited in dry, wet or damp sandflats contain more quartzitic material than coarser grained sandstones (appendix C2).

The analyses of the sandstones showed that they are dominated by mono- and polycrystalline quartz (32-78 vol.-%), feldspar (2-15 vol.-%) and rock fragments (1-39 vol.-%) (appendix C2). Monocrystalline quartz is normally clear and show undulatory extinction. Partly they show fluid inclusions. Polycrystalline quartz consists dominantly of uniformly sized grains with straight or sutured contacts. Some grains show elongated crystals or a crystal-mosaic (appendix A2-01F). Subordinate contents of detrital quartz (monocrystalline quartz or chalcedony) with inclusions of vermicular, dark green coloured clay minerals ("helminth-chlorite", compare Tröger, 1967) are present in some samples from field A (appendix A2-01H). Chemical analyses of the "helminth-chlorites" yield 10 wt.-% Fe, 6.1 wt.-% K and 2.5 wt.-% Mg (appendix C4-01). Calculated as chlorite on the basis of 28 oxygen the silica content is with $Si_{9.6}$ too high (originally should be Si_8) for a pure chlorite structure. Especially the high iron and potassium contents may indicate an illitic structure within the clay minerals. Detrital feldspar grains are represented by K-feldspar (3-13 vol.-%), albite (<1 vol.-%) and Ca-plagioclase (<1 vol.-%) (appendix C2). Furthermore K-feldspar is a common constituent in felsic igneous rock fragments and quartz-feldspar-mica aggregates which may be volcanic or metamorphic in origin (appendix A2-01E). The abundant detrital rock fragments are felsic volcanic grains which are represented by dominantly quartz-feldspar textures (Lv_{fel}) and quartz-feldspar-mica grains (L_{QFM}) (appendix A2-01G and A2-02H). Minor constituents are basaltic grains with a porphyric texture and inclusions of apatite and partly hornblende. Sedimentary lithoclasts are less common and are build up by sandstones, siltstones and shales (appendix A2-01E). Minor amounts (<1-6 vol.-%) of fine to coarse grained cherts are present in many samples. Carbonate grains are uncommon. Intraformational mud flakes may partly be interpreted as "pseudomatrix", but are present as subordinate phenomena in few samples (<1 vol.-%). Sandstones deposited as damp and wet sandflats show commonly higher amounts of pseudomatrix. Furthermore metamorphic rock fragments are dominantly represented by slates, phyllites and quartz-mica-schists. Quarzites are less abundant.

Subordinate contents of illite as an alteration product of rock fragments (Lv_{fel} and L_{QFG}) and feldspar are present in samples from field A (very poor illitisation grade) and field B (poor to medium illitisation grade) (appendix C2). Note that only minor amounts (proven for well Aw03 and Cw04) of authigenic radial or meshwork illite is present in the intergranular pore space (appendix A3-01C and A3-02D). In samples from field C (well Cw03 and Cw04) the illitisation is a more common feature (poor to medium illitisation grade) (appendix C2). In almost every sample significant amounts (with different percentage) of a dense, green coloured clay mineral are present in igneous rock fragments (which consist dominantly of feldspar, quartz, apatite and Fe-oxide) (appendix A2-02C, D and G). The total K-feldspar content may be reduced during albitisation processes by (1) direct substitution of sodium against potassium or (2) via

carbonate or sulphates precipitation (compare section 4.2.5), dissolution and/or replacement by dolomite, calcite, anhydrite, barite and quartz. Furthermore the precipitation of kaolinite with a booklet-like shape within K-feldspar grains or detrital rock fragments is a common feature (appendix A2-02E). In nearly all cases the detrital grain is completely dissolved and kaolinite is arranged as aggregates in the intragranular pore space. Especially sandstones from well Bw02 are dominated by kaolinite which have their origin in altered feldspar grains. Dissolution of detrital feldspar grains and feldspar within volcanic rock fragments (appendix A2-01G and A2-02A) is a common feature in all samples. Different dissolution stages of (i) no dissolution, (ii) partial dissolution and (iii) complete dissolution with the formation of "oversized pores" are to mention. In samples (e.g. Cw04-01 and Bw01-02) where Fe-oxide coatings and/or illite cutans are present around detrital grains the mineral phases remained after grain dissolution (appendix A2-02A). Accessory minerals are opaque Fe- and/or Ti-oxides, zircon, tourmaline, white mica, biotite and subordinate contents of detrital chlorite. White mica and biotite are absent in samples deposited as alluvial and aeolian sediments.

According to McBride (1963) the sandstones can be classified as sublitharenites and (lithic) subarkoses (▶ figure 4.1). The mean composition can be expressed as $Q_{76}F_{12}L_{12}$ for field A, $Q_{81}F_{8}L_{11}$ for field B and $Q_{77}F_{9}L_{14}$ for field C.

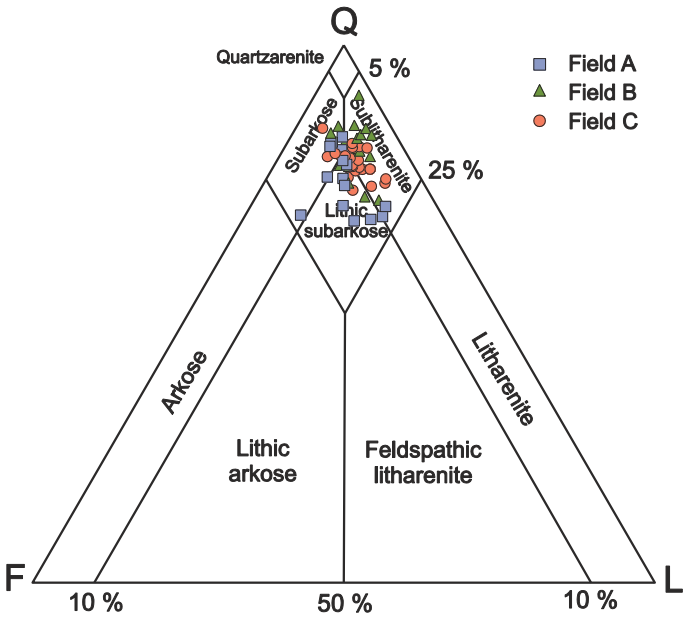

Figure 4.1: Classification of Rotliegend sandstones for field A, B and C after McBride (1963). The Rotliegend sandstones which are investigated in this study are dominated by subarkoses, sublitharenites and lithic subarkoses. Q= Quartz, F= Feldspar and L= Lithoclasts. Data are derived from point counting analysis.

Provenance analysis

According to the plate tectonic provenance interpretation by Dickinson (1985), all samples suggest a recycled orogenic provenance with quartzose and/or transitional source (▶ figure 4.2). Conglomerates and coarse grained sandstones were deposited at the south basin margin (compare section 3.4). The type, size, shape and abundance of detrital grains (polycrystalline quartz and volcanic rock fragments with acid to intermediate composition) indicate a nearby source in the Variscan Mountains at the south of the basin system. In the Netherlands only minor amounts of Lower Rotliegend volcanics are deposited in the South Permian Basin (Lokhorst, 1998; Evans et al., 2003). Non-igneous clasts may indicate a mixed hinterland of (micro)-granite or metamorphic origin. "Helminth-chlorite" may have been generated from low-grade metamorphic rocks (Frank et al., 1992). Elongated mud flakes which are often orientated to

bedding are intrabasinal re-depositions and may have their origin from mud deposits. Fe- and/or Ti-oxides may have been generated from near-surface incrustations.

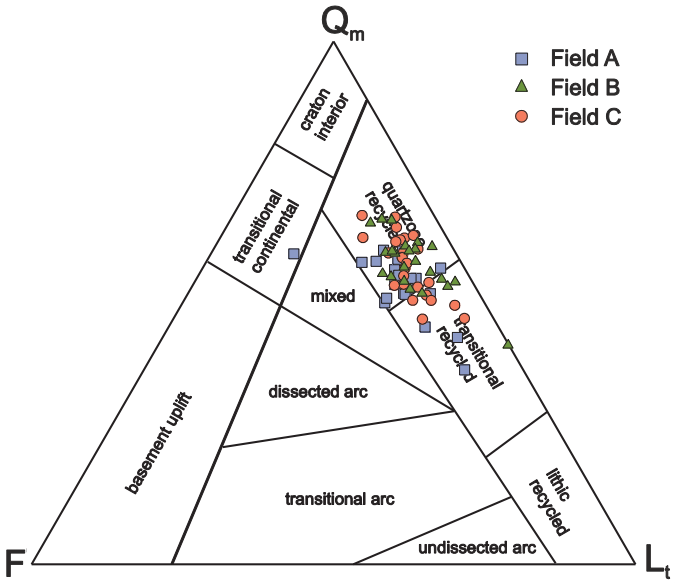

Figure 4.2: After the plate tectonic provenance interpretation from Dickinson (1985) the Rotliegend sandstones which are investigated in this study (from field A, B and C) have their origin mainly in quartzose and/or transitional recycled orogenic. Q_m = Monocrystalline Quartz, F = Feldspar and L_t = Lithoclasts. The data are derived from point counting analysis.

4.2 Authigenic mineralogy

The most abundant authigenic minerals in Rotliegend sandstones from the gas-bearing reservoirs A, B and C are Fe-oxide, dolomite, quartz and kaolinite. In general, sandstones from field A are less cemented than samples from fields B and C (▶ figure 4.3). High cement volumes are caused by blocky dolomite or anhydrite cement (appendix A2-04B and D). The mineralogical inventory is similar for all three fields, but some significant differences are present. Hence each authigenic mineral will be discussed separately in comparison between the fields in the following sections.

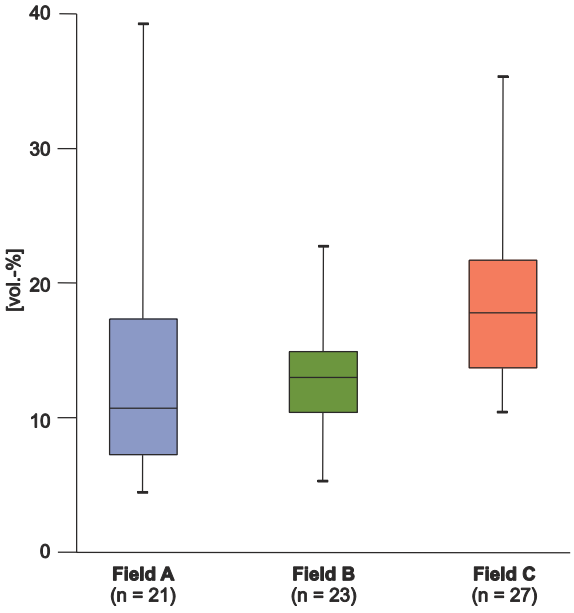

Figure 4.3: Box-Whisker-Plot of all authigenic minerals [vol.-%] (Fe-oxide, illite cutan, quartz, carbonate, sulphate, galena and kaolinite) derived from point counting data in Rotliegend sandstones from fields A, B and C. The mean cement content is increasing from field A in the southern area of the South Permian Basin to the basin centre (field B and C), whereas the highest contents are found in carbonate cemented sandstones from field A.

The definition of eodiagenesis and mesodiagenesis are given by Berner (1980): Eodiagenesis is defined to include all processes that occur at or near the surface of the sediments. The water chemistry is mainly influenced by the depositional environment. The eodiagenetic domain may extend only a few hundred meters in low permeable sediments, but over thousand meters in coarse grained porous sandstones. Mesodiagenesis involves all processes which occur during burial once the sediment has passed the influence of meteoric waters. The boundaries between diagenesis and low-grade metamorphism are not sharp and are mainly influenced by the sediment properties.

4.2.1 Carbonate

The abundant carbonate minerals are early mesodiagenetic and late stage dolomite/ankerite (with varying amounts of iron and manganese) cements. Siderite is present as late mesodiagenetic cement growing commonly around earlier generations (▶ figure 4.6), and calcite is ancillary cement. In ▶ figure 4.4 the total amount for all carbonate is sketched.

Dolomite, ankerite and siderite

Eodiagenetic dolomite which is reported by Gaupp et al. (1993) is volumetrically rare in Rotliegend sediments and has not been proven in samples from the Upper Slochteren Formation investigated in this study.

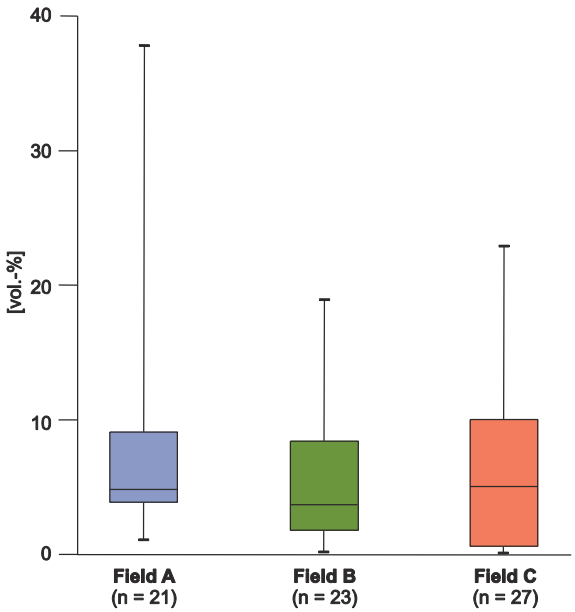

Figure 4.4: Box-Whisker-Plot of authigenic early and late mesodiagenetic carbonate minerals [vol.-%] derived from point counting data in Rotliegend sandstones from fields A, B and C. Note that dolomite, Fe-rich dolomite and siderite are summarised and calcite is a subordinate phase which is only visible with secondary electron microscopy. The mean value for the three fields is comparable. Dolomite is the only carbonate phase in samples from field B and C whereas ankerite and siderite appear in samples from field A, too.

Investigations of thin sections showed that two mesodiagenetic generations of dolomite can be mentioned. They show different chemical compositions and may be separated in two sub-generations, respectively (▶ figure 4.5). The first generation (1a) is common in all samples and appears as small (10-20 µm in diameter) rhombohedral crystal (▶ figure 4.6). A sub-generation of dolomite cement (1b) precipitated most commonly around earlier generations and appears as rhombohedral crystal with straight boundaries or form partly blocky cements in the intergranular pore space (▶ figure 4.6). These dolomites (1a and 1b) grow commonly in open

pores after the main compaction phase and authigenic quartz but before kaolinite. Sometimes they may have grown corrosively against quartz or feldspar grains (appendix A2-04E and F). Dolomitisation of detrital grains (feldspar, volcanic rock fragments and pelitic grains) or clay matrix is a common process in samples from field A and field B, where the remaining grain is dissolved during further burial (appendix A2-02F). Some crystal boundaries show dissolution voids on their surface. Electron microprobe analysis yields varying amounts of $(Fe,Mn)CO_3$ (0.45 to 82.4 mol%) (▶ figure 4.7) (appendix C4-02). According to Deer et al. (1992) the term ankerite is commonly used for carbonates with >20 mol% $FeCO_3$ and a higher Fe than Mn content. Therefore these carbonates are called Fe-rich dolomites or ankerite, respectively to their Fe and Mn content. Late mesodiagenetic carbonates precipitated after bitumen impregnation and the second kaolinite generation (only present in samples from field A). In backscatter electron images these dolomites are indicated by different grey colour intensities (the lighter the more Fe and Mn are present) (▶ figure 4.6). The older dolomite cement (2a) show a lower $CaCO_3$ and a higher $MgCO_3$ content compared to early mesodiagenetic ankerites (▶ figure 4.5).

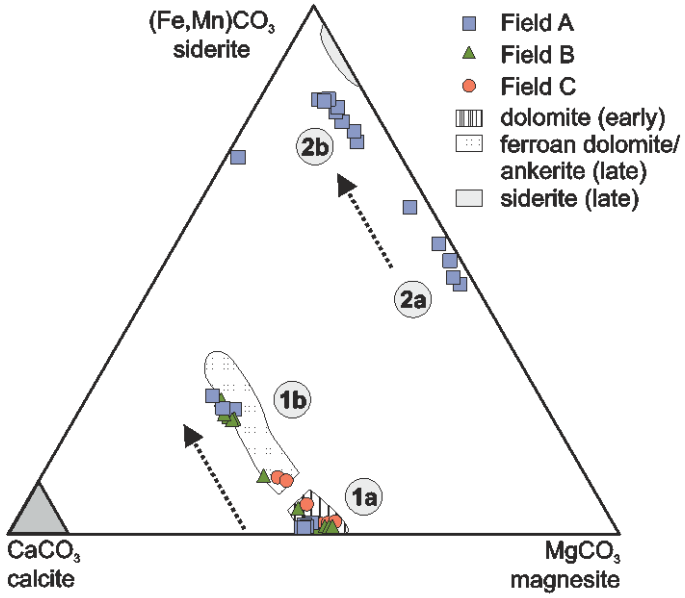

Figure 4.5: Ternary diagram (modified from Platt (1991) and Gaupp et al. (1993)) for mesodiagenetic dolomite, ankerite and siderite cements [mol%] in samples from field A, B and C. For all samples one generation (1a and 1b) with an increasing Fe and/or Mn content are to note. Furthermore a second generation is present in samples from field A. These carbonates are characterised by (2a) a decreasing Ca and increasing Mg and Fe and/or Mn content and (2b) are further developed to higher Mn and Fe contents with nearly siderite composition.

With further burial diagenesis these carbonates are developed to (2b) a higher $FeCO_3$ and $MnCO_3$ content with respect to $MgCO_3$. The latest generation yields at most 82.4 mol% $(Fe,Mn)CO_3$, and is therefore classified as siderites (▶ figure 4.7). Late siderite generations precipitated around earlier dolomite and ankerite. In comparison to the first generation pore-filling blocky cements are present. Sharp crystals boundaries are partly accomplished, only. Irregular contacts between the two sub-generations are common (▶ figure 4.6). Conspicuous differences on crystal size and distribution within the samples from field A compared to field B and C are found: For field B and C early and late mesodiagenetic authigenic dolomite/ankerite (generation 1 and 2) appears to be small (20-60 µm) rhombohedral crystals which are unequally distributed within the intergranular pore space (appendix A2-04). In comparison, field A is dominated by an aggregation of several dolomite crystals which form blocky cements. These blocky cements dominantly contain late mesodiagenetic Fe- and Mn-rich carbonates (third generation), but earlier small (5-10 µm) rhombohedral dolomites are present (▶ figure 4.6). These pore-filling cements often replace detrital grains (e.g. K-feldspar) and generate a large

intergranular volume of ~40 % (appendix A2-04D). Note that a differentiation between inter- and intragranular porosity is difficult and that the true intergranular volume will be smaller than the identified one. In all samples from field A authigenic dolomite crystals are often surrounded by thin dark coloured solid bitumen (?) and/or Fe-oxide (?) rims (appendix A2-04F).

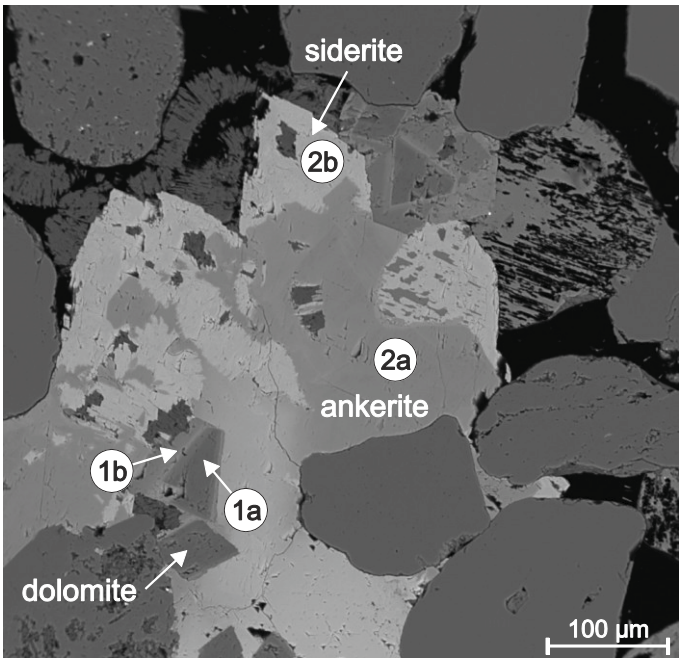

Figure 4.6: Backscatter electron image of mesodiagenetic carbonate with rhombohedral early mesodiagenetic dolomite crystals (1a and 1b) surrounded by later generations of ankerite (2a) and siderite (2b). Sample: Aw02-03. The different carbonate types are further explained in figure 4.5 and within the text.

These coatings are (1) located between the first and second dolomite generation within the cement, (2) between detrital grains and dolomite, where they often appear thicker than (3) on the crystal surface area in contact to open pore space. The dolomite crystals show a maximum of four (clear) cement generations (after different grey intensities of backscatter electron images).

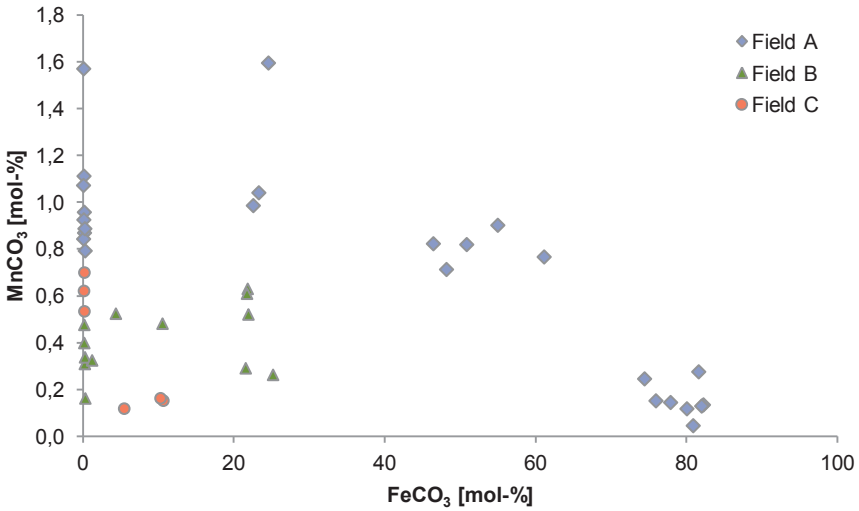

Figure 4.7: $FeCO_3$ [mol%] vs. $MnCO_3$ [mol%] content for early and late mesodiagenetic dolomite cements. Earlier dolomites (core) show minor amounts of Fe than later generations (rim). Note the different amounts of Mn within the oldest generation for the fields, respectively.

Note that low variations of element concentrations may not be visible in backscatter electron images or are not detectable by electron microprobe analysis (EMP). Thin light grey coloured areas within the dolomite crystals indicate manganese enrichment. From core to rim an overall decreasing Mn (from 12.3 to 0.05 % $MnCO_3$) and an increasing Fe (from 0.05 to 82.2 % $FeCO_3$) content is to note. Fe-rich dolomite was also detected by X-ray diffraction analysis. Strontium, barium and other elements (e.g. Zn, Cd, Co, Ni, Pb) which attendant in dolomites are below the detection limit of the EMP. The total carbonate content (mean ~7.0 vol.-%) of all three fields shows no significant difference (appendix C2).

Calcite

Authigenic calcite is often reported in Rotliegend sandstones (e.g. Gaupp et al., 1993) where it typically grows in open pores or replaces detrital feldspar and volcanic rock fragments. However calcite is volumetrically rare (<1.0 vol.-%) in the samples investigated in this study. There is no evidence for an early eodiagenetic calcite generation which has been reported from other Rotliegend deposits (Gaupp et al., 1993). Calcite precipitated as small aggregates (≤1 µm) after kaolinite and the latest ankerite/siderite generation (appendix A3-02H). There is no evidence if calcite precipitated contemporaneous or subsequent to albitisation. The calcite cement has a xenomorphic crystal structure. The chemical composition of calcite is not detectable with electron microprobe analysis.

Interpretation

Early calcite and dolomite cements, which are likely eodiagenetic in origin, could occupy large intergranular volume (IGV). They are not proven for sandstones investigated in this study but some aspects indicate their presences during eodiagenesis. Permian sandstones of the South German Basin (SGB) have a mean IGV of ~40 vol.-% (Houseknecht, 1987) which is preserved by eodiagenetic cements (compare section 4.5.1). The sandstones investigated in this study have an IGV between 15 and 40 vol.-% (mean 25 vol.-%) (appendix C2), which indicate in combination with point, length and rare concave/convex grain-grain contacts (appendix C2), an early diagenetic grain structure stabilisation. This process may have taken place over the first 1000-2000 m depth, where the main mechanical compaction is expected (Füchtbauer, 1979). Several authors describe the presence of early carbonate cements in Rotliegend sandstones for the SGB which precipitated from meteoric-type pore waters in an evaporitic basin system (Walker et al., 1978; Bjørlykke, 1983; Burley, 1984; Platt, 1994; Morad et al., 2000; Schöner, 2006). The gas field A is located near the basin margin where commonly carbonates are the first precipitates (Strong and Milodowski, 1987; Garcia et al., 1998). From the basin margin to the basin centre the presence of carbonates decreases whereby sulphates and further halite become the most abundant cements (Drong, 1979; Platt, 1994). However the precipitation of early cements in sandstones located distal to the basin margin (field B and C) may be influenced by different evaporation rates and therefore by the precipitation of carbonate and/or sulphate and/or halite.

Certainly, most carbonates (calcite, dolomite, ankerite and siderite) were formed during burial and mechanical compaction during mesodiagenesis. The first generation is indicated by mainly dolomitic composition and sharp crystal boundaries, followed by Fe-rich dolomite and ankerite which precipitated around earlier cements. In combination with varying Mn and Fe contents within the crystals (from core to rim) a fluctuation of the water composition during burial may be a possible explanation. On the other hand kaolinite, which precipitated after dolomite, is

enclosed by ankerite in some samples. This may indicate a second dolomite generation which is late mesodiagenetic in origin. Furthermore the latest ankerite cement show dissolution voids on the surface, caused by changing chemical fluid properties (e.g. pH, water saturation).

A possible source for carbonates may be a redistribution of dissolved early calcite which precipitated during further burial (Saigal and Bjørlykke, 1987; Bjørlykke et al., 1989) and/or the alteration and dissolution of volcanic rock fragments (Boles and Ramseyer, 1987). Furthermore later carbonate generations may be due to the dissolution and redistribution of earlier cements (Platt, 1991 and 1994). The formation of Fe- and Mn-rich carbonates is related to reducing fluids, carrying ferrous iron which may have been generated in underlying Carboniferous sediments. Based on isotopic analysis, Platt (1994) suggests an influx of Zechstein fluids into Rotliegend sandstones in the vicinity to faults.

4.2.2 Sulphate/sulphide

Minor amounts of anhydrite are present in samples from field A and B with up to 2.3 vol.-% and 5.3 vol.-%, respectively. Field C is characterised by higher anhydrite contents with a maximum of 23 vol.-% and a mean percentage of 2.3 vol.-% .-% (▶ figure 4.8). Barite and galena are present with <1 vol.%.

Anhydrite typically occurs as pore-filling blocky cement (appendix A2-04A, B and C). There are two diagenetic generation paths for sulphates, where the first precipitated before kaolinite, contemporaneous with dolomite (Fe-poor) and after the first quartz generation (appendix A2-04C). Partly these anhydrites enclose early diagenetic rhombohedral dolomite crystals in the intergranular pore space (appendix A2-04A). The second anhydrite cement precipitated after kaolinite intragranular in partly intensively dissolved feldspar grains (appendix A2-04C). Furthermore in samples from field A (well Aw05) anhydrite is present in the vicinity of bitumen (appendix A2-05A). Late stage anhydrite dissolution of early diagenetic cement is found in samples from field A and B. Semi-quantitative electron microprobe analysis of anhydrite indicates almost pure $CaSO_4$. An earlier generation, which has been reported by other authors (e.g. Gaupp et al., 1993) is not proven.

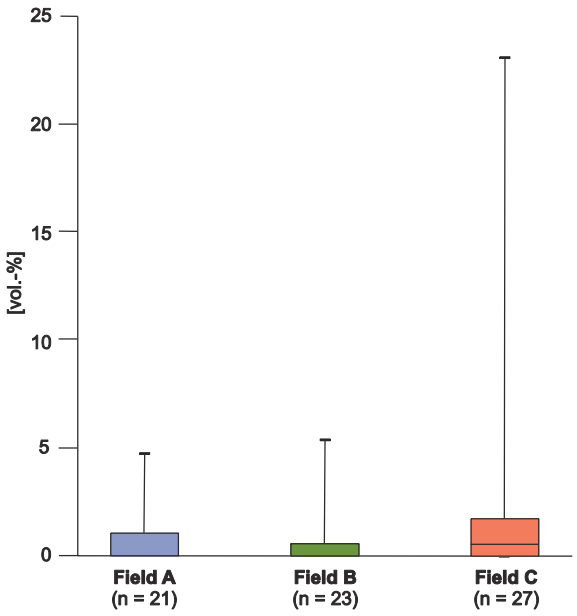

Figure 4.8: Box-Whisker-Plot for early and late mesodiagenetic anhydrite cement [vol.-%] derived from point counting data. Note that both anhydrite generations are summarised, and barite as well as galena (PbS) is not sketched. The total anhydrite content in all samples is relatively low. Only one sample from field C contains >20 vol.-% of anhydrite.

Early mesodiagenetic barite precipitated after meshwork illite, contemporaneous to the first anhydrite generation and before kaolinite in the intergranular pore space (appendix A3-02C). There seems to be a second generation, related to late mesodiagenetic anhydrite which precipitated intragranular in (partly) dissolved K-feldspar grains and/or volcanic rock fragments and between bitumen impregnated vermicular kaolinite (appendix A2-04C).

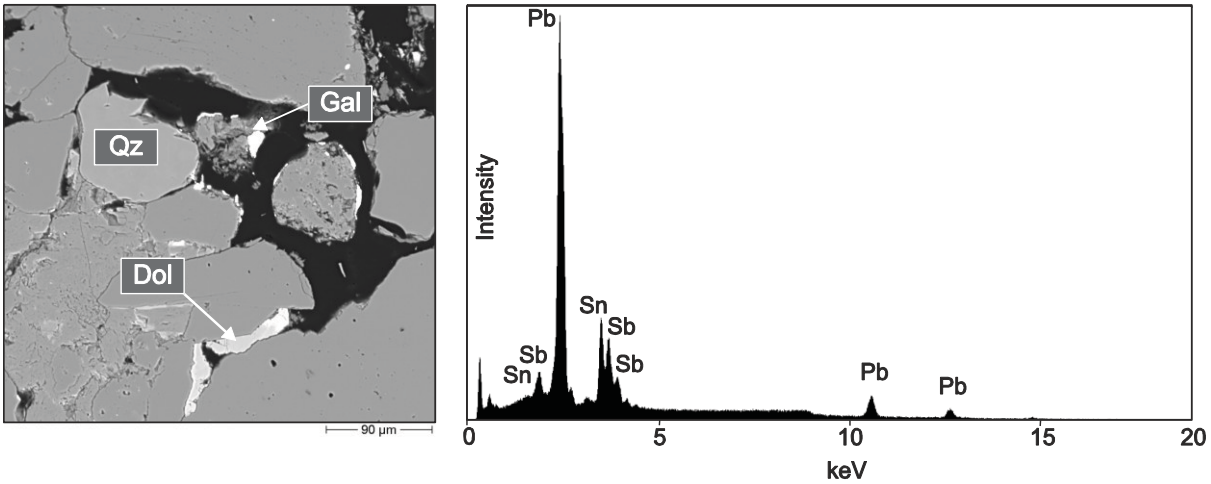

Figure 4.9: Left: Backscatter electron image with authigenic dolomite and galena. Right: XRD spectra from galena. The mineral consists in addition to sulphur and lead (Pb) of antimony (Sb) and tin (Sn).

Barite commonly appears as lath cement (appendix A3-02C). Furthermore in samples from field A authigenic galena (PbS) precipitated intergranular around detrital grains, syntaxial quartz cement and intragranular in (partly) dissolved K-feldspar grains and volcanic rock fragments. The sulphides are developed as irregular aggregates (appendix A2-04G). Semi-quantitative analysis on thin sections derived from an energy dispersive X-ray spectroscopy, yield minor amounts Sb and Sn (▶ figure 4.9).

Interpretation

Eodiagenetic and early mesodiagenetic sulphate cements are widespread in many reservoir sandstones. In coastal sabkha settings anhydrite and barite are common (Morad et al., 2000). The sulphate for anhydrite precipitation could have been derived by dissolution of early gypsum cements and re-precipitation within the sandstones (Holliday, 1970). Or anhydrite may be formed due to the dehydration of gypsum and conversion into anhydrite during burial (Glennie et al., 1978; Dixon et al., 1989). After Gaupp et al. (1993) early anhydrite and gypsum cements are common in Rotliegend sandstones in the North German Basin. The precipitation of barite may be related to the release of barium from dissolution/albitisation of K-feldspar grains and volcanic rock fragments. Late anhydrite and barite precipitation may be linked to the infiltration of Zechstein brines (Pye and Krinsley, 1986; Bath et al., 1987; Glennie and Provan, 1990). Platt (1994) suggests only a minor influence of Zechstein fluids in most parts of Rotliegend sediments. Furthermore dissolved sulphate may be derived from dissolved earlier anhydrite and/or gypsum generations. Gaupp (2005) suggests late mesodiagenetic anhydrite dissolution in sandstones which are attributed to Rotliegend sediments located near the city Hannover.

The transport of sulphides (S^{2-}) in fluids is only possible under reducing conditions. In neutral and (weak) acid fluids sulphur exists predominantly as SO_4^{2-} anion. In acid fluids with pH <4 sulphuric acid is not completely dissolved and residual HSO_4^- anions may be present. Dissolved sulphate can be reduced by hydrocarbon compounds producing H_2S, HCO_3^- and solid bitumen (Machel et al. 1995). However sulphate is reduced either by bacterial sulphate reduction, which is related to temperatures below 80°C, or by thermochemical sulphate reduction which seems to require temperatures between 100 and ≥140°C (Machel, 2001). After Machel (2001) bacterial and thermochemical sulphate reductions are represented by various organic compounds and dissolved sulphate as reactants and H_2S, CO_2, carbonates, elemental sulphur and metal sulphide as products and/or by-products.

In aqueous environments with pH below 6 lead is generally present as $Pb^{2+}_{(aq)}$, but it may also form complexes with organic anions, chloride and hydroxide and poorly soluble or insoluble compounds with sulphide, sulphate, hydroxyl carbonate and phosphate anions. If $Pb^{2+}_{(aq)}$ is present a hydrogen-sulphide will probably be formed and may decompose to lead(II)-sulphide (galena) (▶ equation 4.1) (Mortimer, 2001).

$$Pb^{2+}{}_{(aq)} + 2HS^{-}{}_{(aq)} \leftrightarrow Pb(SH_2)_{(s)} \leftrightarrow PbS_{(s)} + H_2S_{(aq)} \quad (4.1)$$

The source for galena is unclear for the samples investigated in this study. Either galena precipitated in association with hydrocarbons in gas or oil reservoirs under high temperature and pressure during production of natural gas. The mineral phase becomes supersaturated when the brine is released to the surface by artificial wells during extraction, because of the lower solubility of solids and gas under decreasing temperature and pressure (Hartog and Jonkers, 2001). Or galena is a natural product which precipitated during late mesodiagenesis under reservoir conditions and is not linked to drilling. Hartog and Jonkers (2001) propose the source for lead from dissolved Rotliegend feldspars and Fe-oxides which have a Late Carboniferous signature and/or by influx of Zechstein brines into Rotliegend gas reservoirs with a younger isotopic lead signature. Furthermore the amount of lead in sedimentary rocks may be controlled by the presence of carbonate (e.g. McNeil and Mohr, 1993; McNeil and Little, 1999), mica and clay minerals. The precipitation of galena may be associated to a hydrothermal environment and a co-precipitation with dolomite, Fe-rich dolomite, barite, sphalerite and calcite (Schrijver et al., 1996; Ledesert et al., 1999).

4.2.3 Quartz

Authigenic quartz could partly occlude the pore space or is nearly absent (<1 to 12 vol.-%). Sandstones from field A and C are influenced by a (partly) intense quartz cementation. For field B only minor amounts (mean <1 vol.-%) are present (▶ figure 4.10). Subordinate contents (<1 vol.-%) of eodiagenetic quartz appears as syntaxial overgrowth on detrital grain surface areas with the same crystallographic orientation (Waugh, 1970), partly after Fe-oxide precipitation (appendix A2-03E and A2-04C). In some cases thin quartz overgrowths are difficult to distinct between eodiagenetic and early mesodiagenetic quartz overgrowth. Two mesodiagenetic events of quartz cementation can be mentioned: The most frequent quartz cement is an early generation which is located as syntaxial overgrowth on detrital grains with partly intercalated Fe-oxide and/or clay cutan (appendix A2-03E). It precipitated after the main compaction phase and before dolomite, anhydrite and kaolinite. According to sharp crystal edges and almost perfect crystal habit they may have been grown into the open pore space. Pore-filling quartz

cements often show bitumen coatings on the surface area. Secondary electron microscopy (SEM) investigations indicate microcrystalline and macrocrystalline quartz growing on detrital grain surface areas (appendix A3-02A), but a chronological order is not to assign. A second generation is volumetrically rare in all samples (<5 vol.-%) and precipitated before the latest generation of dolomite and sulphate and after the main dissolution of K-feldspar and volcanic rock fragments. This cement type appears in form of small idiomorph crystals in the inter- and intragranular pore space (appendix A3-01H).

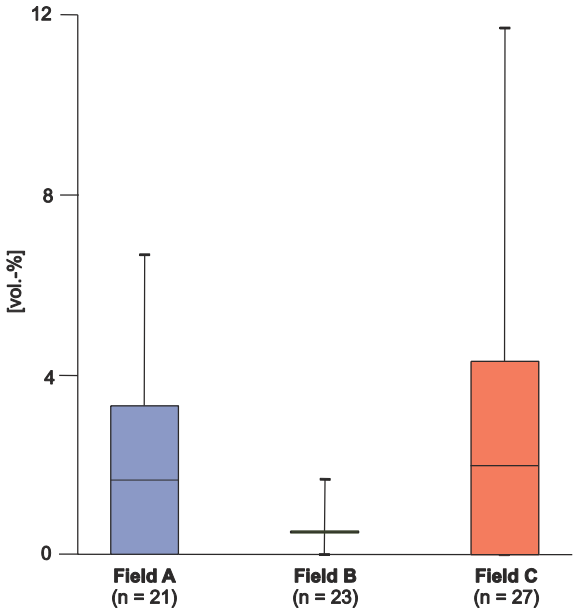

Figure 4.10: Box-Whisker-Plot of eodiagenetic and early and late mesodiagenetic quartz cements [vol.-%] derived from point counting data of thin sections. Samples from field A and C are partly dominated by an intensive quartz cementation in form of blocky pore-filling cements. Otherwise quartz is often lacking in sandstones from field B.

Interpretation

Platt (1994) pointed out that early syntaxial quartz overgrowths are common in Rotliegend sabkha facies with semi-arid and arid environments where they occur together with authigenic sulphates. These early cements may precipitate from meteoric waters during lower burial depth (Bjørlykke and Egeberg, 1993; Hartmann et al., 2000) and temperatures between 25 and 60°C (Pagel, 1975; Burley et al., 1989; Walderhaug, 1990). After Worden and Morad (2000) the main precipitation rate of quartz cements occur during burial depths deeper than 2500 m and temperatures between 90 and 130°C. Possible sources for mesodiagenetic pore-filling quartz cements are dissolution of feldspar, clay mineral transformation (e.g. illitisation of smectite) and solution at grain-grain contacts between quartz at deeper burial depth (e.g. Leder and Park, 1986; Abercrombie et al., 1994; Worden and Morad, 2000). Compaction waters from adjacent shales, which are partly intercalated within the sandstones (compare section 3.4), may have transported dissolved $H_4SiO_{4(aq)}$ released from clay transformation and/or dissolution processes into Rotliegend sandstones. Intergranular pressure solution is influenced by the sort of grain-contacts, temperature, pressure ratio between the grains and the lithological pressure rates, as well as the presence of mica or clay minerals around the grains (Hartmann et al., 2000; Worden and Morad, 2000). According to James et al. (1986) and Porter and James (1986) is grain-grain solution mainly present in fine to medium grained sandstones, as they are reported from the study area (compare section 4.4). A clear discrimination between early and late mesodiagenetic quartz cement is often difficult if meshwork illite is absent (Schöner, 2006). Microcrystalline quartz (diameter <5µm) seems to be related to a continuous silica oversaturation and the

precipitation of several small crystals instead of a larger one (Parks, 1984; Williams et al., 1985). Williams et al. (1985) suggests temperatures below 80°C and a slow crystal growing. Furthermore McBride (1989) points out that microcrystalline quartz is often formed under near surface conditions.

4.2.4 Fe-oxide/-hydroxide

Thin section petrography and X-ray diffraction analyses indicate that Fe-oxide is present in several samples from field A, B and C. However no Box-Whisker-Plot is shown because Fe-oxides are difficult to detect in thin section images and are often overestimated (compare section 2.2).

Fe-oxide occurs as µm-thick (<1.0 to 20 µm) coatings around detrital grain surface areas and are typically thicker in embayments (appendix A2-03F). These coatings consist of varying amounts of Fe-oxide, clay mineral (esp. illite) and minor Ti-oxide (appendix C4-01). After petrographic considerations Fe-hydroxide is absent in all samples. Especially in unbleached samples from field B and C grains are often covered completely, but show typically no rounding by abrasion (appendix A2-03D and F). Hence an early origin prior to the mechanical compaction could be assumed. The abundance of Fe-oxide ranges between <1.0 to 17 vol.-%. But it is problematic to separate Fe-oxide, clay mineral and solid bitumen during point counting and the volumetric results are considered to be an overestimation. In some areas Fe-oxide appears as small aggregates. Partly Fe-oxide is located between dolomite crystals and may indicate a remobilisation of iron during diagenesis. This evidence is supported by Fe-oxide which is located on syntaxial quartz cements. The sandstones containing no or only minor amounts of Fe-oxide have a (brownish) grey to white colour. It is to note that a decreasing Fe-oxide content is associated to increasing bitumen content.

Interpretation

Fe-oxide cutans may be inherited from weathering processes under near-surface condition (Gaupp, 1996). They are early diagenetic in origin and were formed in uncompacted or poorly compacted sediments. Fe-oxide and -hydroxide precipitation is characteristic for semi-arid depositions (e.g. Walker, 1967; van Houten, 1968; Folk, 1976). Internal sources of iron are volcanic rock fragments, ilmenite and magnetite. Under oxidic surface conditions the alteration of the grains is nearly complete. In addition to in situ alteration and release of iron an external source could be assumed. Under reduced conditions large amounts of iron may have been transported from adjacent iron-rich areas. Under various reducing conditions Fe-oxide and Fe-hydroxide could precipitate during fluctuation of the water and transform into hematite during further burial of the sediments (Chukhrov, 1973; Walker, 1976).

The presence of solid bitumen in samples from field A (esp. well Aw05) may indicate a removal of iron by the movement of hydrocarbons through the rock. This relationship was documented by several authors (e.g. Levandowski et al., 1973; Segal et al., 1985; Surdam et al., 1993; Chan et al., 2000). Iron in sediments is immobile as Fe^{3+} under normal pore fluid conditions and must be reduced to Fe^{2+} for transport (Drever, 1997). After Moulton (1922) red beds could be bleached under surface temperatures and under the presence by hydrogen sulphide. Shebl and Surdam (1996) suggest a colour change of aeolian sandstones from red to light pink, dark grey, grey and white during pyrolysis experiments of water-rock-hydrocarbon mixtures. Organic acids, methane and hydrogen sulphide are also capable of causing iron reduction and a colour change

in sediments (Chan et al., 2000). Haszeldine et al. (2005) suggests that H_2S commonly associated with CO_2 has reduced the iron in the Colorado Springs. But the process of sandstone and shale bleaching is yet not well understood.

Early diagenetic pore-filling cements like quartz, carbonates or sulphates are not present in the sandstones. It is not clear, if such cements limit the precipitation of Fe-oxide and -hydroxide in sandstones where no hematite is present.

4.2.5 Feldspar

K-feldspar overgrowths are absent in all samples, whereas authigenic albite is common. According to Gaupp et al. (1993) feldspar overgrowths on K-feldspar and volcanic rock fragments and small euhedral albite crystals are volumetrically not important (<1 vol.-%) in Rotliegend sandstones.

For all samples (a partial intense) albitisation of detrital K-feldspar and plagioclase is to observe. Electron microprobe analyses of detrital K-feldspar and authigenic albite revealed that the phases are nearly pure end-members (appendix C4-01). Dissolution voids appear either as intragranular porosity or are filled with dolomite or sulphate (anhydrite and barite) cements (appendix A2-04C and E). These cements often embedded authigenic albite. Albitised grains show (1) blocky euhedral albite crystals whose nucleation starts simultaneously at several sites and (2) albitisation along microfractures, or (3) within dolomite, anhydrite or barite. The crystal texture is related to their genesis: in combination with dolomite, anhydrite or barite albite appears with sharp edges and corners. In case where substitution of potassium with sodium has taken place they show irregular boundaries between K-feldspar and authigenic albite.

Interpretation

Albitisation of feldspar is common in deeper buried sediments. The phenomenon is recognised by several authors for K-feldspar (e.g. Walker, 1984; Morad, 1986; Saigal et al., 1988; Aagaard et al., 1990) and plagioclase (e.g. Land and Milliken, 1981; Boles, 1982; Morad et al., 1990; Ben Baccar et al., 1993). Albitisation of detrital feldspar is a wide-spread and important process which can significantly change the original compositions of sandstones.

The conversation from K-feldspar to albite (albitisation process) may take place directly by ion exchange (Walker, 1984; Saigal et al., 1988) or it may involve prior replacement of the K-feldspar by calcite, dolomite or anhydrite (Walker, 1984). Furthermore there are minor amounts (<1 vol.-%) of replacement in barite cements. In total the second process is negligible in sandstones from the northern Netherlands. Albitisation is associated with feldspar dissolution during mesodiagenesis. The main reaction of albitisation of K-feldspar can be summarised as a replacement reaction from sodium against potassium (Saigal et al., 1988) and can be expressed as the following ▶ equation 4.2:

$$\underset{\text{K-FELDSPAR}}{KAlSi_3O_8} + Na^+ \rightarrow \underset{\text{ALBITE}}{NaAlSi_3O_8} + K^+ \qquad (4.2)$$

With increasing burial and temperature the potassium to sodium ratio appears to be rather constant. For albitisation of K-feldspar a temperature between 65 and 120°C is assumed (Bjørlykke et al., 1986; Saigal and Bjørlykke, 1987). Ben Baccar et al. (1993) suggest a temperature between 120 to 150°C. At higher temperatures (>90°C) the formation waters are

normally supersaturated with respect to albite. This leads to an aqueous solution close to the K-feldspar/albite equilibrium (Saigal et al., 1988) (▶ figure 4.11).

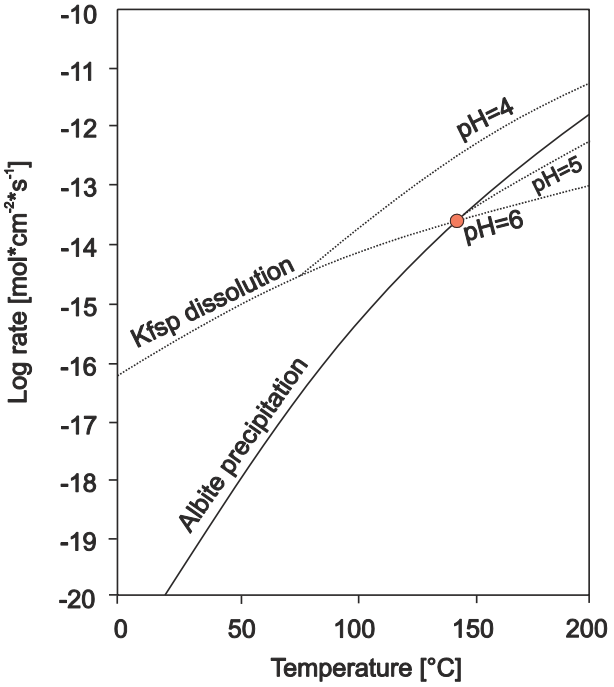

Figure 4.11: Dissolution rate of K-feldspar and precipitation of albite as a function of temperature for reservoir conditions. Below 145°C (orange circle) the K-feldspar dissolution is faster than the albite precipitation for a pH between 5 and 6. Below pH 5 the dissolution rate of K-feldspar is still faster for higher temperatures. Modified from Aagaard et al. (1990).

Aagaard et al. (1990) suggested that formation waters from Upper Jurassic rocks from offshore Norway are charged with respect to sodium which cannot account for calculated albitised K-feldspar. By dissolving K-feldspar potassium is released in the pore water which will be supersaturated with respect to albite. Consequently albite may precipitate. In a closed system the potassium to sodium activity ratio is more sensitive to the amount of potassium, which is released by K-feldspar dissolution, than to sodium. For the albitisation of K-feldspar the sodium concentration in the pore water is less important, if the potassium concentration can be kept low. Hence a removal from potassium from the aqueous phase is to require.

Five mechanisms appear to be a sink for released potassium: (1) Fluids with potassium and sodium activity ratios near the equilibrium may precipitate K-feldspar overgrowth on detrital grains and/or (2) authigenic illite could precipitate. (3) Potassium may be absorbed by tangential smectite or illite/smectite (I/S) cutan (4) or for the transformation of kaolinite into illite (Saigal et al., 1988). (5) Potassium is removed by fluid flow or potentially in adjacent shales by diffusive and advective mass transport e.g. for the transformation of smectite to illite (e.g. Boles and Franks, 1979; Boles, 1982). This reaction begins at a burial temperature of approximately 65°C (e.g. Perry and Hower, 1970; Hower et al., 1976). Illitisation of smectite could also be a source of sodium. Furthermore the amount of dissolved potassium and silica depends on the dissolution rate of K-feldspar. The slower the K-feldspar dissolves the more potassium and silica could be required (Thyne, 2001). In general, albitisation of K-feldspar is a slow process which depends especially on the removal of potassium and/or the supply of sodium. At lower temperatures (<90°C) albitisation often produce intragranular porosity as the growth of albite is too slow to keep up with the K-feldspar dissolution and removal of potassium. With increasing temperature larger albite crystals will precipitate. But below 145°C the dissolution of K-feldspar is always faster as the albite precipitation (Saigal et al., 1988; Aagaard

et al., 1990) (▶ figure 4.11). In hydrocarbon bearing sandstones the albitisation process may be stopped by the emplacement of hydrocarbon (Saigal et al., 1988).

4.2.6 Kaolinite

Kaolinite minerals have been observed for the fields A, B and C in all samples (▶ figure 4.12). The occurrence and crystal shape of kaolinite is slightly different in comparison to other Rotliegend sandstones reported by e.g. Gaupp et al. (1993) and Platt (1994), where kaolinite typically appears as vermicular structure with a booklet-like shape. In addition to vermicular kaolinite single crystals and a sheaf-like arrangement of several kaolinite plates are present in samples from the Upper Slochteren Formation onshore the Netherlands (▶ figure 4.13).

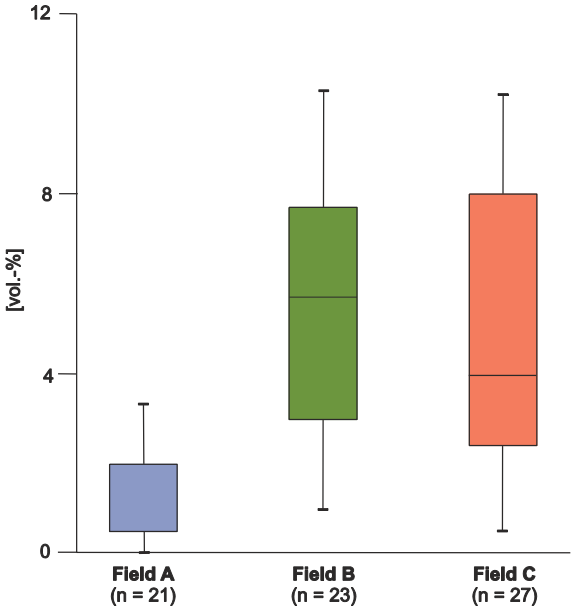

Figure 4.12: Box-Whisker-Plot of early and late mesodiagenetic kaolinite [vol.-%] derived from point counting data. Note that different kaolinite types (e.g. "booklets", single and sheaf-like kaolinite) are summarised. Kaolinite "booklets" are common in all samples, whereas in sandstone which are attributed to field B and C grain rimming, pore-filling single kaolinite and kaolinite with a sheaf-like habitus are present. Especially in field B and C kaolinite is the dominant clay mineral and makes up to > 10 vol.-%. For further explanation please regard to the text.

Especially elongated single kaolinite crystals with a mean diameter of circa 10-20 µm length are untypical for Rotliegend sediments. The habitus reminds on halloysite crystals which are common in soil sediments. But XRD-analysis of the <6 µm fraction indicates kaolinite and the absence of halloysite and Al-rich chlorites like sudoite and/or tosudite (appendix B1). These results are confirmed by IR-spectroscopy (<2 µm fraction) and space-resolved IR-spectroscopy on thin sections for two samples, respectively.

For IR-spectroscopy the absorption spectrum of the samples (from 4000 cm^{-1} to 400 cm^{-1}) contains many characteristic bands (▶ figure 4.14) which are reported in literature. They can be divided in hydroxyl stretching bands in the high frequency region and in skeletal bands in the low frequency region. The first one is characterised by two intense peaks at 3695 cm^{-1} and 3620 cm^{-1}, and two weaker intensities at 3669 cm^{-1} and 3652 cm^{-1}. The band on 3620 cm^{-1} is attributed to the stretching of inner hydroxyl and the others are attributed to stretching of the inner-surface hydroxyl groups (e.g. Frost et al., 1993; Balan et al., 2001). The next four bands (1112 cm^{-1}, 1103 cm^{-1}, 1032 cm^{-1} and 1008 cm^{-1}) are the most intense Si-O stretching modes and can be observed in most of silica minerals (Farmer, 1974). The bands at 935 cm^{-1} and 912 cm^{-1} are attributed to hydroxyl vibration modes.

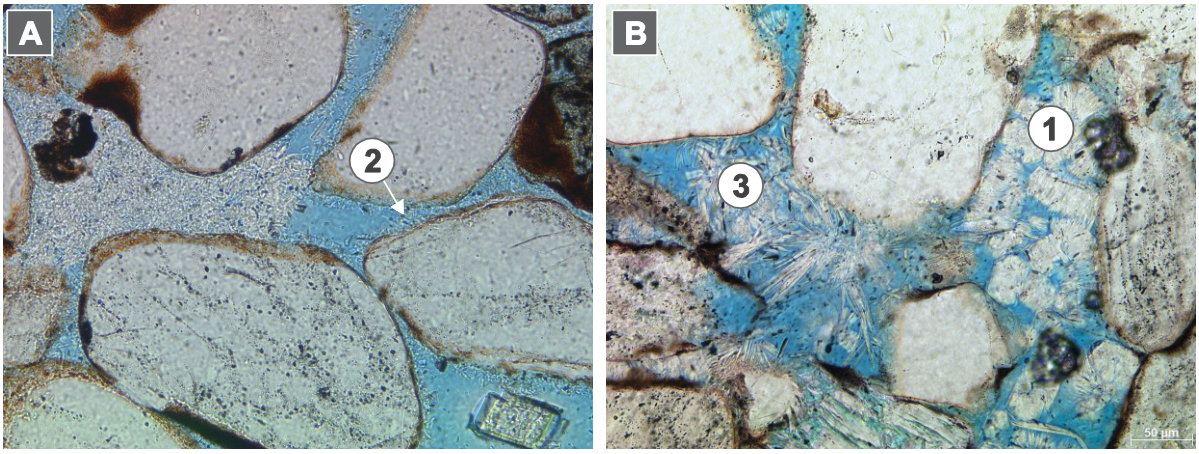

Figure 4.13: Kaolinite types as they occur in sandstone samples from the Upper Slochteren Formation of the northeast Netherlands. (1): kaolinite "booklets"; (2): grain rimming kaolinite and (3): sheaf-like, elongated kaolinite. For further explanation please regard to the text.

As the frequency decreases the assignment of characteristic bands becomes more difficult which is in this case due to the presence of other silica minerals like e.g. feldspar, mica and quartz. The band 537 cm^{-1} has been attributed to different vibrations as deformation or stretching (Frost et al., 1993; Johansson et al., 1998). The bands 468 cm^{-1} and 430 cm^{-1} can be traced to modes of the SiO_4 tetrahedra (Frost et al., 1993). Adsorbed water which is present in kaolinite is reflected by a strong broadened OH stretching band present at around 3435 cm^{-1} and a weaker OH bending band at around 1630 cm^{-1} (van der Marel and Beutelspacher, 1976). Furthermore spectroscopic analysis suggests a very well crystalline kaolinite structure, but no dickite (Kaufhold, 2010, person. comm.).

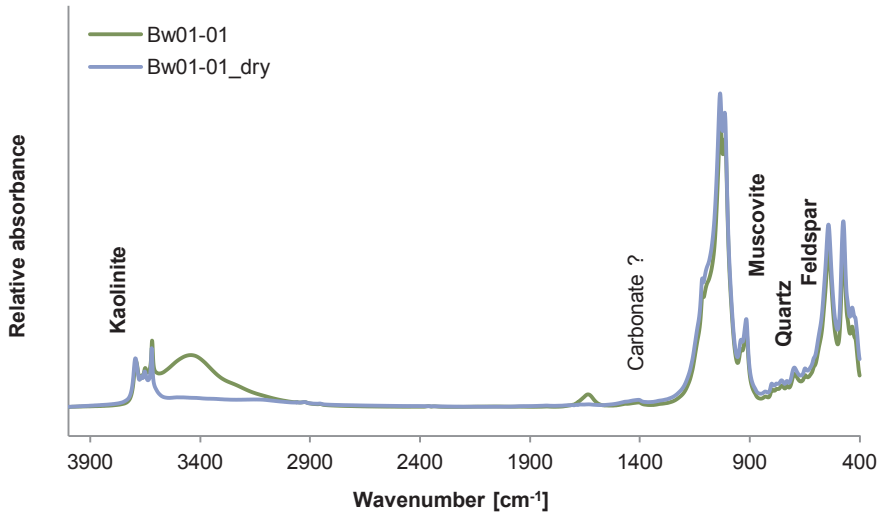

Figure 4.14: Absorption spectra for IR-spectroscopy for sample Bw01-01 for the wet and dry <2 µm fraction, respectively. The strong abundance at higher wavenumbers indicate the presence of a well crystalline kaolinite.

Based on petrographic investigations of thin sections and secondary electron microscopic images three kaolinite types are defined. The different kaolinite types (single, vermicular and

sheaf-like) are described in the following section. Comparisons between samples from the three gas-fields are considered.

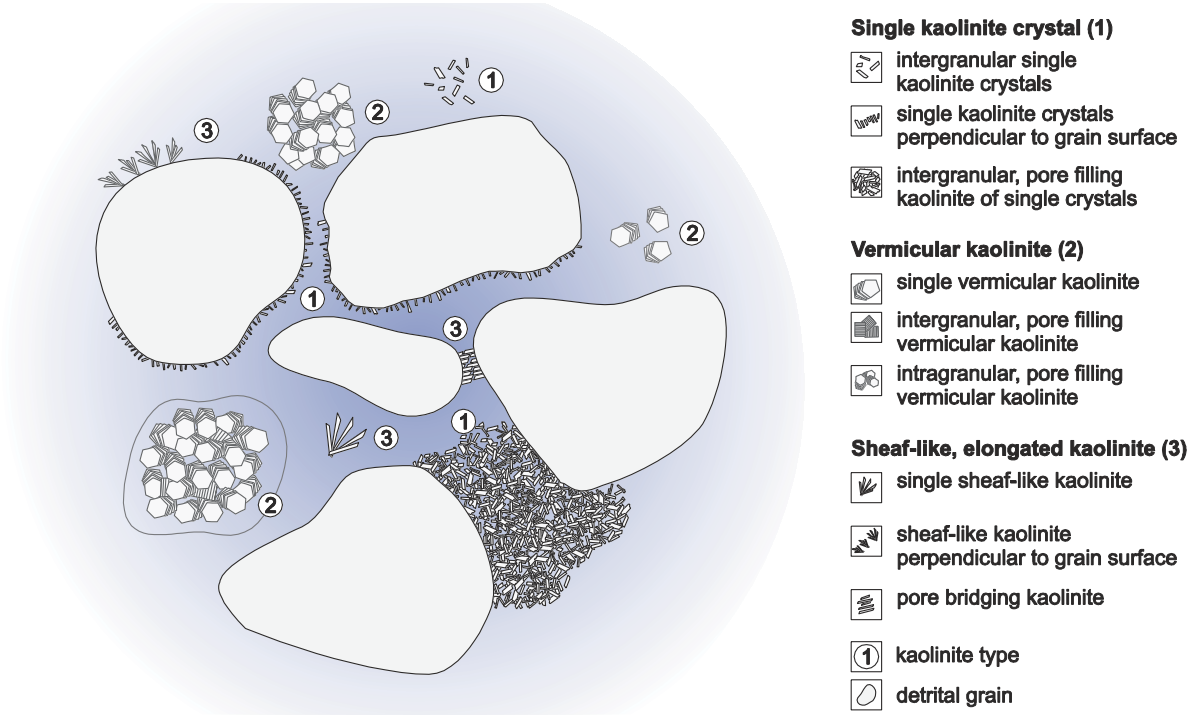

Figure 4.15: Sketch of different kaolinite types (1, 2 and 3) derived from petrographic investigations. Type 1 is a typical vermicular kaolinite which is present in all Rotliegend samples investigated in this study and appears in the inter- and intragranular pore space. The most abundant kaolinite in samples from field B are (grain rimming) single crystals (type 2). And in samples from field C type 3 is most frequent. Note that transition forms between the stated kaolinite types are present (esp. between type 1 and 3). For further explanation please regard to the text.

The first type (1) are single kaolinite crystals which are (a) arranged as grain rimming kaolinite, orientated perpendicular to the grain surface area or (b) appear as single plates in open pores (▶ figure 4.15; appendix A2-02D and A2-03E and F). In some samples these single crystals are arranged as a closer packing and are forming pore-filling cements (appendix A2-03F). Radial kaolinite (type 1a) precipitated on Fe-oxide coatings and clay cutans in early mesodiagenesis (▶ figure 4.22). The crystals are between ~5 and ~15 µm long and only a few micrometers (<2 µm) thick. In thin section images they are arranged nearly parallel to each other, forming a dense sword-like structure. This seems to be due to cutting effects in a 2-dimensional orientation, because in secondary electron microscopy images chaotic structures without any preferred crystal orientation on detrital grain surface areas are to observe (appendix A3-01B and C). Type 1b is characterised by single kaolinite or by an accumulation of a few crystals. These kaolinites are present within the intergranular pore space, but as well as type 1a not in (partial) dissolved feldspar grains or volcanic rock fragments (appendix A2-03C). In comparison to samples from field B are grain rimming kaolinites from samples attributed to field C partly twice the length. Investigations of secondary electron microscopy indicates an aggregation of two or more crystals forming elongated kaolinite which is orientated perpendicular to the grain surface area (appendix A3-01E and F), partly pore-bridging (appendix A2-03D and A3-01G). However kaolinite appears not between grain contacts. Hence the precipitation occurred after deposition and the main sediment compaction.

(2) Kaolinite appears as pseudo-hexagonal crystals forming typical booklet-like aggregates (appendix A2-03G and H). They are present as (a) single booklets, (b) intergranular pore-filling cements and (c) as an alteration product of detrital feldspar grains and/or volcanic rock fragments (appendix A2-02E). Two generations of vermicular kaolinite (type 2a and 2b) are to mention which are early and late mesodiagenetic in origin. The first generation precipitated after the first dolomite and anhydrite generation and after meshwork illite, but before hydrocarbon migration. The second generation precipitated after hydrocarbon migration but contemporaneous to feldspar dissolution. In thin section images the first vermicular kaolinite generation shows a brownish colour which may indicate bitumen impregnation (appendix A2-05C). Adjacent white kaolinite light grey coloured kaolinite is present in the intergranular pore space (appendix A2-05F). Hence type 2c (intragranular kaolinite) may have been precipitated after hydrocarbon migration. There is no petrographic evidence, if the alteration of detrital grains to kaolinite took place pre, post or contemporaneous to the intergranular kaolinite formation. Furthermore samples from field B suggest a precipitation of radial kaolinite before vermicular kaolinite. Note that vermicular kaolinite in samples from field B cannot be attributed to one of the two generations reported for samples from field A, because only minor amounts of bitumen are present. The size of one kaolinite booklet ranges between 10 to 60 µm widths and a variable length. Furthermore in samples from well Aw05 the first kaolinite generation (with bitumen impregnation) is commonly longer (≤50 µm) than the second generation (≤10 µm) (appendix A2-05F). Thin section and secondary electron microscope images indicate a parallel aggregation between two to five single booklets to an expanded kaolinite (appendix A2-02G). Several booklets without any preferred orientation to each other form pore-filling cements which are commonly located in embayments between detrital grains.

Furthermore kaolinite may form aggregates which have (3) an elongated sheaf-like arrangement. These sheaf-like kaolinite is (a) on the one hand orientated perpendicular to grain surface areas or (b) appear intergranular as single sheafs (appendix A2-03B, C and G). Secondary electron microscope analysis shows that such sheaf-like kaolinite is formed by several pseudo-hexagonal crystals which stand in direct contact in one point and are widened otherwise (appendix A3-03H). Transitions between widened kaolinite "booklets" and sheaf-like arrangements are present.

Table 4.1: Semi-quantitative analyses (increasing content from absent [-] to rare [o], present [+], common [++] and very common [+++]) of different kaolinite types (single, vermicular and sheaf-like habitus). For explanation please regard to the text.

	single kaolinite	**vermicular kaolinite**	**sheaf-like kaolinite**
field A	-	++	-
field B	+++	+	o
field C	+	+	+++

Samples from field A are dominated by two generations (pre and post hydrocarbon migration) of vermicular kaolinite which precipitated as single booklets or pore-filling cements. Minor amounts of altered feldspar grains to kaolinite are present. Single and sheaf-like kaolinite is absent. In comparison, all defined kaolinite types are present in samples from field B and C, but with a different frequency, respectively (▶ table 4.1). Especially samples from field B are

dominated by grain rimming and single kaolinite, which may form dense pore-filling cements. Minor amounts of inter- and intragranular kaolinite booklets and ancillary amounts of sheaf-like kaolinite are present. In contrast, samples from field C are dominated by a partly extensive precipitation of sheaf-like kaolinite perpendicular to the grain surface area or as single aggregates. For field B and C transitions between type 1 (vermicular kaolinite) and type 3 (sheaf-like kaolinite) are common and different types (1, 2 and/or 3) may be located in direct neighbourhood in thin section scale. A partial alteration of kaolinite during diagenesis is to note which is visible in form of irregular crystal boundaries (appendix A3-01F).

Interpretation

The properties of kaolinite minerals are investigated by exploration companies in conjunction with authigenic mineral precipitation in sedimentary deposits (e.g. Gaupp et al., 1993; Platt, 1994) and by e.g. paper and ceramic industry (e.g. Weiss and Russow, 1963; Lahav, 1990; Singh and Mackinnon, 1996; Friedrich et al., 2005). The precipitation of kaolinite directly from pore fluids depends on acidic condition, a positive Eh and a relatively low salinity (Curtis and Spears, 1971). This is given (1) by the introduction of meteoric freshwater into the Rotliegend sandstones (Hancock and Taylor, 1978) and (2) by the influx of acidic or CO_2-rich fluids which may arise by bacterial processes in organic-rich sediments adjacent to the sandstones (Curtis, 1983; Surdam et al., 1984). The first process is likely in eodiagenetic and shallow burial depth with contact to meteoric water. After Giles and Marshall (1986) meteoric fluids are not likely in depths greater than 2000 m. During the Late Jurassic/Early Cretaceous basin inversion meteoric waters may have been entered in Rotliegend sandstones and facilitate the precipitation of authigenic kaolinite (Ziegler et al., 1994). An early diagenetic kaolinite formation is implausible because they are buried to over 2000-3000 m depth and kaolinite precipitates post compaction in the free pore space and/or replaces K-feldspar grains and volcanic rock fragments. The second process rather occurs in deeper buried sediments where the fluid received acidic fluids from interbedded organic-rich mudstones or coals for kaolinite precipitation (e.g. Lanson et al., 1996; van Keer et al., 1998). After Curtis (1983) kaolinite requires the presence of aluminium. Aluminium may have been provided from dissolution of alumosilicates, albitisation of feldspar or derived over external pore-fluids. An external source for aluminium-rich fluids may be the presence of Al-complexes which are linked to organic molecules derived from underlying coal-bearing Carboniferous rocks (Gaupp et al., 1993; Platt, 1993). Due to their acidity they are able to dissolve more feldspar and become further enriched in protons when they entered the Rotliegend sediments. Migration of acidic fluids and precipitation of kaolinite at the expense of K-feldspar has been demonstrated by Ehrenberg (1991) in sandstones from the Garn Formation (Norwegian shelf). Close to the contact of Rotliegend sediments and Carboniferous Coal Measures Formation Gaupp et al. (1993) and Platt (1993) recognised a zone with major kaolinite or dickite and strong feldspar dissolution. Further away from such contacts illite will be the dominant authigenic phase. The illitisation of kaolinite takes place only in systems with an oversaturation in respect to illite. Because of this kinetic barrier kaolinite could exist in sandstones with deep burial depths. Kaolinite could also be formed as a by-product from albitisation of plagioclase at temperature over 100°C (Boles, 1982). There is no petrographic evidence that plagioclase dissolution and precipitation is associated with kaolinite formation. With greater burial depth kaolinite will transform over an interstage of well crystallised kaolinite to dickite as a result of the invasion of acidic fluids with an organic origin and increasing temperature (Clauer et al., 1999; Lanson et al., 2002). Dickite is often associated to

feldspar dissolution, authigenic fibrous illite, iron-rich chlorite and bitumen impregnation (Deutrich, 1993). However IR-spectroscopic investigations indicate the absence of dickite in this study. Kaolinite could appear in combination with dolomite as a result of the chemical equilibrium between chlorite/calcite and kaolinite/dolomite which is influenced by the CO_2 concentration and temperature (compare section 4.5.3) (Hutcheon, 1980 and 1989).

Properties of kaolinite

The properties of kaolinite minerals and their behaviour in aqueous solution are briefly discussed in the following section. The surface charge on kaolinite crystals is ascribed to two conditions: (1) the isomorphous substitution of Si^{4+} by Al^{3+} in the tetrahedral sheets which lead to a negative charge and (2) the pH dependant protonation/deprotonation of silanol and aluminol groups located at the particle edges (Jasmund and Lagaly, 1993). Zhou and Gunther (1992) and Ma and Eggleton (1999) pointed out that the cation exchange capacity of kaolinite is due to the ionisation of edges and basal charges and that the reaction at the particle edges seems to be more reactive than the basal octahedral surface areas. After Brady et al. (1996) no basal plane participation is required to explain the total surface charge of kaolinite. Hence kaolinite is able to adsorb different inorganic and organic molecule species. The adsorption of inorganic molecules was studied by several authors (e.g. Lagaly, 2001; Tarasevich and Klimova, 2001; Osmanlioglu, 2002) e.g. in conjunction with immobilisation of toxic wastes. Furthermore detailed studies are dealing with the reactivity between kaolinite and organic polymers (e.g. Lagaly, 1999; LeBaron et al., 1999; Gardolinski et al, 2000).

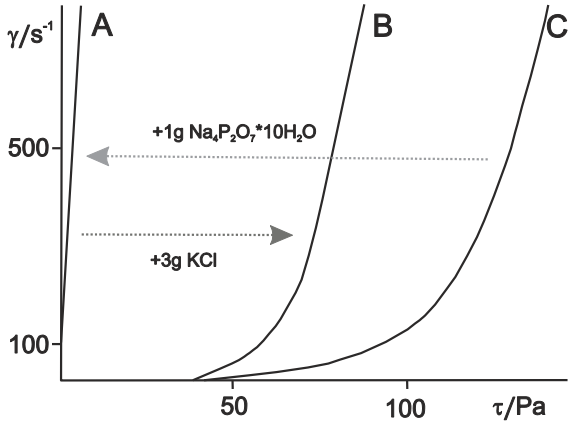

Figure 4.16: Liquefaction of kaolinite by addition of diphosphate (curve C to A) and re-solidification by addition of potassium chloride (curve A to B). Modified from Jasmund and Lagaly (1993).

The rheological properties of aqueous kaolinite dispersion are influenced by the properties of the kaolinite mineral (particle size, crystal defects at the surface area, etc.), the presence of accessory minerals, the solid content of the dispersion, pH value and the type (esp. Na^+ and Ca^{2+}) and concentration of ions (Jasmund and Lagaly, 1993). Under acidic conditions the bonding of single kaolinite layers to each other is possible (1) over hydroxyl groups at the edges of kaolinite crystals building a tri-dimensional framework ("cardhouse structure") and (2) over hydroxyl groups which are located on the interlayer basal surface area, pointing to the interlayer space. They are responsible for the cohesion between kaolinite layers by bonding the hydrogen bond with the oxygen atoms. Both types may interact with other ions and/or molecules. Several ions and molecules (inorganic and organic species) influence the properties of bonding effect of kaolinite layers. If sodium ions are present, kaolinite dispersions can stay in fluid at a relatively

high solid content while no or only minor contacts are build between the layers. Otherwise the formation of framework structures becomes more attractive by the addition of potassium chloride or calcium chloride. On the other hand, the liquefaction of kaolinite dispersions is evoked by the addition of e.g. sodium diphosphate (Jasmund and Lagaly, 1993) (▶ figure 4.16). Furthermore the presence of Fe-oxide influences the behaviour of kaolinite dispersions. At pH 3 Fe-oxide is positively charged and adsorbed on the kaolinite mineral surface areas where they neutralise the particles so that no framework can be formed. With increasing pH and the addition of e.g. NaOH negative charges are build at the edges and contacts between the particles. The contacts disappear again when Fe-oxide is re-charged. By adding acid, Fe-oxide is able to bridge the negative kaolinite particles in a rigid framework, so the yield point increases to a maximum. Otherwise high positive charge of Fe-oxide leads to a breakdown of the kaolinite-Fe-oxide contacts (Jasmund and Lagaly, 1993).

As mentioned earlier, hydroxyl groups at the interlayer surface area cause the bonding of single kaolinite layers. By grouping of parallel orientated layers vermicular kaolinite is formed. During further diagenesis the ideal booklet structures are widened based on the interaction with other ions and/or molecules (▶ figure 4.17). This process is called exfoliation and is reported in detail in literature from industrial application like e.g. ceramic and paper industry (e.g. Weiss and Russow, 1963; Lahav, 1990; Singh and Mackinnon, 1996; Friedrich et al., 2005). There, exfoliation and further delamination of vermicular kaolinite aggregates is indispensible. Exfoliation is defined as the breakdown of large aggregates in smaller particles and delamination describes the separation of individual monolayers of these particles (Jasmund and Lagaly, 1993). Especially exfoliation influences the rheological properties of dispersions (Jasmund and Lagaly, 1993), whereas true delamination of kaolinite in stable monolayers was not yet achieved (Lahav, 1990). Chemical exfoliation is based on the intercalation of molecules such as urea, ammonium acetate (Weiss and Russow, 1963), potassium acetate (Singh and Mackinnon, 1996) or polar organic molecules like e.g. dimethylsulfoxide (Friedrich, 2002).

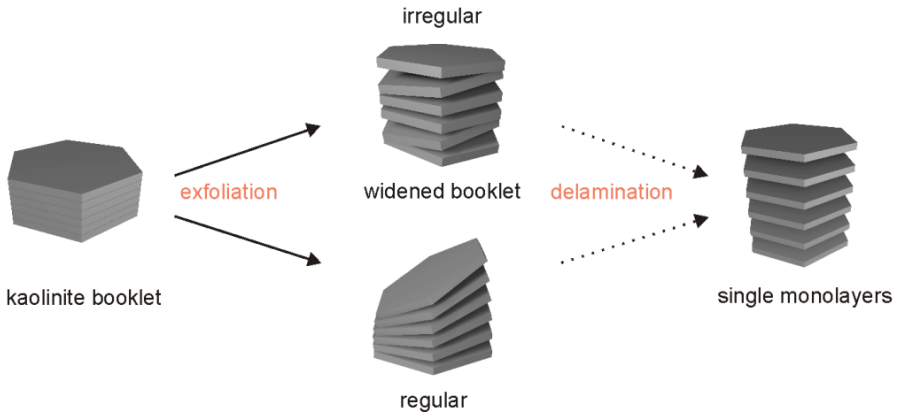

Figure 4.17: Exfoliation describes the widening of kaolinite "booklets" by the intercalation of ions and/or molecules between the layers and delamination stands for the separation of single monolayers due to further intercalation grade (Jasmund and Lagaly, 1993). In subject to where the ions and/or molecules penetrate towards the centre "widened booklets" or "fan shape structures" are formed. Note that true delamination has yet not been achieved in industrial experiments (Lahav, 1990).

Origin of sheaf-like and grain rimming kaolinite

The intercalation reaction described above starts at the edges of the kaolinite plates and penetrates towards the centre where the molecules act as wedges between the kaolinite plates and cause the layers to be elastically deformed (Jasmund and Lagaly, 1993). The basal spacing of the kaolinite can be up to 50 % greater than the original 7.1 Å phase. With increasing intercalation grade of molecules on kaolinite monolayers the booklets will be widened and fan-shape structures are formed. Exfoliation of kaolinite booklets seems to be a common process in Rotliegend sediments. Transitions between nearly parallel orientated booklets to a sheaf-like arrangement of kaolinite layers may indicate different exfoliation stages. Otherwise sheaf-like aggregates which are located on detrital grain surface areas may have been precipitated directly from pore fluid or by exfoliation of primary thin (<20 µm) kaolinite booklets. There is no petrographic evidence on how these structures are formed. True delamination of kaolinite booklets is not yet achieved by using chemical treatment in industrial experiments as it is described above. It seems implausible that single kaolinite crystals located on detrital grain surface areas are formed by exfoliation and further delamination of primary kaolinite booklets. After all, secondary electron microscope investigations indicate that single kaolinite crystals are not parallel orientated but show a chaotic arrangement. For their origin two mechanisms will be discussed: (1) direct precipitation from pore fluid and (2) the transformation form precursor grain rimming chlorites.

(1) Single kaolinite crystals may have been precipitated directly from pore fluids. Therefore as discussed above, the hydroxyl groups on the interlayer surface areas need to be blocked by ions and/or molecules to inhibit the bonding of two individual kaolinite layers. The source of inorganic and organic ions and molecules which cause a widening of the kaolinite booklets may be acidic or CO_2-rich pore fluids derived from adjacent or underlying Carboniferous sediments which may generate organic molecules. In samples from field A solid bitumen impregnation on authigenic minerals (e.g. kaolinite) indicate hydrocarbon migration during mesodiagenesis. (2) Grain rimming chlorites may have been precipitated directly from alkaline playa groundwater with a high cation (e.g. Mg and Al) concentration (Wright, 1992). The chlorites appear as small platy crystals (10-20 µm diameters) and are commonly arranged in a honeycomb fabric (Platt, 1993). In a CO_2 analogue study in the Otway Basin in Australia (Ladbroke Grove field) Watson et al. (2003 and 2004) reported the direct replacement of precursor grain rimming chlorites by kaolinite under the presence of CO_2 and increasing temperature (▶ equation 4.3). This mineral reaction is reported in detail by Hutcheon et al. (1980) and Hutcheon (1989). Based on natural gas analysis from field A 0.68 mol% CO_2 are present today (appendix C8).

$$\underset{\text{CHLORITE}}{(Fe,Mg)_5Al_2Si_3O_{10}(OH)_8} + \underset{\text{CALCITE}}{5CaCO_3} + 5CO_2 \rightarrow \underset{\text{DOLOMITE}}{5Ca(Fe,Mg)(CO_3)_2} + \underset{\text{KAOLINITE}}{Al_2Si_2O_5(OH)_4} + \underset{\text{QUARTZ}}{SiO_2} + 2H_2O \quad (4.3)$$

The cogenetic habit of kaolinite and quartz (▶ equation 4.3) is attributed to the influence of CO_2 on diagenesis (Watson et al., 2003). Note that kaolinite and quartz may be formed by albitisation of feldspar according to the following ▶ equation 4.4:

$$\underset{\text{ALBITE}}{2NaAlSi_3O_8} + 3H_2O + 2CO_2 \rightarrow \underset{\text{KAOLINITE}}{Al_2Si_2O_5(OH)_4} + \underset{\text{QUARTZ}}{SiO_2} + \underset{\text{DAWSONITE}}{2NaAlCO_3(OH)_{2(aq)}} \quad (4.4)$$

The alteration of plagioclase to kaolinite and quartz under the influence of CO_2 is insignificant for samples from the Upper Slochteren Formation because of the low detrital plagioclase content (<1 vol.-%). Hence grain rimming kaolinite may have been originated from precursor chlorite

under the influence of CO_2. For a more detailed discussion please regard to the section 4.5.3. In adjacent areas in the northeast Netherlands early diagenetic grain rimming Mg-rich chlorites occur in sandstones from the Upper Slochteren Formation. They are reported in close association with the presence of evaporites or in sandstone shale intercalations (Gaupp et al., 1993).

4.2.7 Illite

After Gaupp (1996) two main types of authigenic illite are typical for Rotliegend sandstones: (1) Early diagenetic tangential illite cutans which cover detrital grain surface areas. This type is often associated with alluvial fans and ephemeral stream deposits (Gaupp et al., 1993). (2) Illite meshworks with platy or fibrous habitus precipitated during burial diagenesis. This type includes also radial illite which precipitated perpendicular to grain surface areas. Illite occurs in samples from field A, B and C as tangential illite cutans on grain surface areas (appendix A3-02G) and as fibrous/meshwork illites (appendix A3-02C and D). The cutans range from sub-µm thin layers up to several µm thicknesses (<1 to 20 µm). The thickest areas are located in embayments and are associated to an early (prior or contemporaneous to deposition) dissolution of the detrital grains (appendix A2-05G). Clay rims also occur between grain contacts. Where tangential illite appears it is often associated with Fe-oxide and form thin red rims.

Table 4.2: Theoretical calculation of clay mineral compositions (data from EMS investigations) which are present as alteration products in igneous rock fragments. The calculations are based on the theoretical assumption that the minerals consist of 90 % illite, 5 % Na-smectite and 5 % Ca-smectite.

oxide	ox.-%	90 % illite	5 % Na-smectite	5 % Ca-smectite	sum I/S	difference
Na_2O	0.19	-	4.00	-	0.20	-0.01
MgO	2.65	3.00	-	-	2.70	-0.05
Al_2O_3	19.9	17.0	30.0	30.0	18.3	1.57
SiO_2	48.3	54.0	66.0	66.0	55.2	-6.95
K_2O	7.05	7.50	-		6.75	0.30
CaO	0.50	-	-	4.00	0.20	0.30
TiO_2	0.07	-	-	-	0.00	0.07
MnO	0.02	-	-	-	0.00	0.02
Fe_2O_3	6.37	2.00	-	-	1.80	4.57
						-0.18

The chemical composition analysed by electron microprobe yield in addition to aluminium and potassium 4.41 wt.-% Fe, 1.02 wt.-% Mg, 0.81 wt.-% Ca and 0.10 wt.-% Ti (appendix C4-01). This suggests that the clay rims are no pure illite but mixed layers from illite and chlorite and/or smectite. XRD analyses suggest the presence of authigenic smectite (appendix B1).

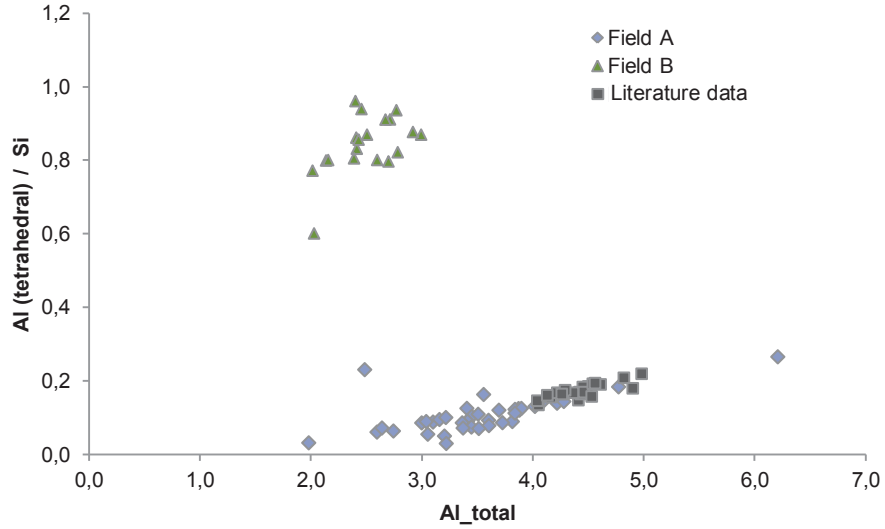

Figure 4.18: Chemical analysis of intragranular green coloured illite/smectite (90 % illite and 10 % Na/Ca-smectite) in felsic igneous rock fragments from field A and B. The tetrahedral to silica ratio is fitting with illite data from Deutrich (1993) and Pudlo (2009, unpublished). Otherwise the illite/smectite from Field B show higher amounts of tetrahedral aluminium than silica. The calculations are based on 22 oxygens.

Meshwork illites with a fibrous habitus are rare and only visible with secondary electron microscopy (SEM). Hence they are proven for the following samples which were investigated by SEM: samples from well Aw03, Bw01, Cw02, Cw03 and Cw04 (appendix A3-02C and D). Illite precipitated in early mesodiagenesis after the main compaction event prior to kaolinite, dolomite and sulphates as grain covering mineral. XRD analyses indicate the presence of illite, but note that these results involve illite cutans and meshwork illites (appendix B1). However in all samples kaolinite is the dominant authigenic mineral and appears with different crystal habitus (compare section 4.2.6). As mentioned in section 4.1 about detrital mineralogy, the alteration of felsic igneous rock fragments is a common process. There, feldspar is (partly) dissolved and green coloured illites are formed during diagenesis. Chemical analysis and the calculation of an illite/smectite structure indicate an illite content of 90 % and 10 % of Ca/Na smectite (▶ table 4.2). Calculated on the basis of 22 oxygens the tetrahedral aluminium content per silica atom is higher for illite/smectite from field B than for field A. No data is available for field C. Figure 4.17 shows that illite data from Deutrich (1993) and Pudlo (2009, unpublished) agree with the calculations for samples from field A. Otherwise illite/smectite from field B have much higher tetrahedral aluminium to silica ratios.

Interpretation

Several mechanisms are discussed in literature for the origin of clay cutans. (1) They may be formed prior deposition of the grains (Wilson, 1992). (2) Clay cutans could be interpreted as a result of alteration of unstable lithic grains during early diagenesis (Glennie et al., 1978) and (3) they could have their origin in an early diagenetic infiltration of water containing suspended clay particles (Walker et al., 1978; Matlack et al., 1989) or (4) occur as a result of bioturbation (Molenaar, 1986). (5) They could be formed by adhesion of clay at wet or damp surfaces (Wilson, 1992; Gaupp, 1996). After Wilson (1992) clay infiltration is a possible process in

ephemeral fluvial environments of semi-arid continental basins. They are present between grain-grain contacts, thicker in depressions and partly removed by abrasion during transport.

After Wilson and Pittman (1977) all detrital clay minerals have irregular outlines and vary widely in size. Clay cutans contain different clay types with varying crystallinities. During diagenesis clay cutans may convert to minerals with a higher crystallinity (Wilson, 1992). Tangential illite cutans may transform from smectite or illite/smectite mixed layer. They are typically for arid and semi-arid environments (Worden and Morad, 2003). Mg-rich smectite can also be formed in coastal sabkha environments under evaporitic conditions. With burial and heating dioctahedral smectite could transform into illite or chlorite. The transformation into illite requires a supply of potassium (K^+) and a loss of silica ($SiO_{2(aq)}$) at the expense of aluminium (Al^{3+}). After Weaver (1958) the conversion does not take place by simple cation process like the substitution of potassium. But also an increase of the negative layer charge of the tetrahedral and/or octahedral layers by substitution of aluminium for silica, iron (Fe^{2+}) and magnesium (Mg^{2+}) (Hower et al., 1976) is an important factor. Otherwise missing potassium increases the stability of smectite and an inhibition of the transformation process (McKinley et al., 2003). Illitisation of smectite is possibly linked to feldspar dissolution during burial diagenesis. Diagenetic illite is formed at temperatures <90°C. Further smectite can transform into chlorite when magnesium, iron and aluminium are supplied. With larger depth, mixed layer chlorite/smectite (C/S) will be formed to higher crystallinity in conjunction with a decrease in magnesium and an increase in iron and aluminium.

After Deutrich (1993) and Gaupp et al. (1993) an internal redistribution of potassium released from K-feldspar could suffice for the precipitation of authigenic illite. Furthermore tangential smectite and/or illite may receive the free potassium. Other authors propose an external source for potassium (Goodchild and Whitaker, 1986; Gluyas and Leonard, 1995). But in contrast previous studies also suggest that feldspar dissolution in sandstones is the major potassium source for the illitisation of illite/smectite (I/S) mixed-layer minerals in nearby shales (e.g.; Milliken et al., 1994; Lynch et al., 1997; Barclay and Worden, 2000; Thyne, 2001; Wilkinson et al., 2003). Authigenic illite may precipitate at temperatures of 130-150°C at intermediate burial depth with K-feldspar as source of potassium (Bjørlykke, 1984). Bjørkum and Gjelsvik (1988) argue that illitisation of kaolinite can take place at temperatures of ≤50°C. Its formation depends on the silica activity and the presence of K-feldspar. In a closed-system simulation Sanjuan et al. (2003) show that the optimum illite formation in sandstones is obtained when the molar K-feldspar/kaolinite ratio is lower or equal to 1. Other variables like temperature (between 100 and 150°C), pCO_2 and aqueous acetate concentrations have no main control on the precipitation of illite. Darby et al. (1997) suggested illite growth in Jurassic sandstones in the Central Graben (North Sea) between temperatures of 47-63°C. The authors assumed that temperature is not the most important factor controlling illite precipitation. But it may be triggered by hydrogeological controls. Wilkinson and Haszeldine (2002) found that the growth of fibrous illite is limited by the kinetics of nucleation and not by thermodynamic or kinetic controls. But the fundamental process of illite precipitation is yet not well understood. The authors suggest that illite growth in sandstones is an episodic event which depends on high degrees of porefluid supersaturation, high pore fluid flow velocities, high temperatures or a catalyst. Furthermore a rapid illite growth results in fibrous crystals.

Furthermore illite growth is related to high fluid rates (Darby et al., 1997), to hot fluids which may migrate during tectonically active periods into the sediments (Gaupp et al., 1993; Zwingmann et al., 1999; Liewig and Clauer, 2000) or to acidic fluids originated from

carboniferous strata (Gaupp et al., 1993). In addition illite may grow during oil charging (Liewig et al., 1987; Glasmann et al., 1989; Hamilton et al., 1992; Clauer et al., 1999; Barclay and Worden, 2000). The absences of authigenic fibrous or platy illite suggest a discharge of potassium from the sandstone. This phenomenon is observed by several authors in reservoir volumes with extensive illitisation where individual layers of shale-sand intercalations stand out with only minor or lacking illite growth. The movement of pore-water is controlled by fluid migration within a reservoir and between different sedimentary horizons (Thyne, 2001). Sandstone-shale couplets can be treated as open systems with ion exchange from sand to shale and vice versa. Wilson and Stanton (1994) suggest that the movement of pore-water between sand and shale is driven by compaction, organic maturation or clay dehydration. Or it is a combination of all these processes. After Thyne (2001) dissolved potassium and silica could diffuse into the shale lowering the total amount of authigenic illite and quartz in the sandstone. The amount on dissolved potassium and silica depends on the dissolution rate. The slower K-feldspar dissolves the more potassium and silica will be required.

Green coloured illite is reported by Hay et al. (1991) as an authigenic mineral which contains 18.3 ox.-% Fe_2O_3 and is likely formed by the reactions of detrital materials with descending brines. After Clifford et al. (1999) the green colour in illite is due to high Cr_2O_3 (up to 2.3 ox.-%) and low K_2O (7.1 to 7.6 ox.-%) contents which indicate a 1M illite structure with ≤ 10 % smectite and a formation temperature between 175 and 200°C. This maintains the calculation for a 90 % illite and 10 % Ca/Na-smectite structures as discussed above. However temperatures above 120°C are not established for the study area (▶ figure 3.8).

4.2.8 Halite

Euhedral NaCl-crystals are located in open pores as late diagenetic phases. Thin section and HR-SEM analyses show that halite is a minor phase in the rocks investigated by Beyer (2010) for samples from well Aw05.

Interpretation

Halite could be formed during (late) burial diagenesis or during core desiccation. It is not clear which process is responsible for the forming of halite in these samples. After Putnis and Mauthe (2001) halite crystals could precipitate in permeable rocks which are located to an adjacent salt dome. Halite may also precipitate from formation waters during drilling.

4.3 Organic inventory

Solid bitumen was proven especially in coarse grained sandstones from well Aw05 in the southern area of field A. Further traces are present in sandstones of the northern area and from field B (appendix A2-05A, B and C). For field C no solid bitumen was proven in thin sections, but core images indicate black coloured impregnations parallel to the stratification which may be interpreted as solid bitumen (appendix A1-03). In pore spaces bitumen appears on the one hand as thin brown coloured phases covering detrital grain surface areas and where kaolinite is present, the first generation of vermicular kaolinite. In samples from field A a second generation of kaolinite is bitumen free and precipitated after hydrocarbon migration and the formation of solid bitumen. On the other hand bitumen appears as thick dark brown to black coatings and

smaller aggregates, sometimes with shrinkage cracks (appendix A2-05A). In all cases no bitumen was found in the intragranular pore space (e.g. partly dissolved K-feldspar). Hence the main dissolution of feldspar and feldspar bearing volcanic rock fragments has taken place after hydrocarbon migration. Solid bitumen following directly after meshwork illite precipitation is reported for many Rotliegend sandstones (e.g. Gaupp et al., 1993; Schöner and Gaupp, 2005) but could not be proven because of lacking illites. Only thin meshwork illite layers could be detected with secondary electron microscopy. Note that no further authigenic minerals have been precipitated on surface areas which are covered with bitumen. An intense bitumen impregnation correlates with grey coloured sandstone horizons.

Interpretation

Solid bitumen indicates the presence of former liquid hydrocarbons migration through permeable sandstones (Parnell, 1994; Littke et al., 1996). Source for hydrocarbons in the northern Netherlands are Carboniferous deposits underlying Rotliegend reservoir rocks. The expulsion took place mainly during Late Triassic and Early Jurassic and in some areas also in Late Jurassic time (e.g. de Jager et al., 1996). The main hydrocarbon generating sequences are the Namurian A and Westphalian A and B which resided in the gas generation window. The gas presence in the region may indicate a conversion of oil to gas in reservoir rocks with residual solid bitumen in some areas. This assumption is maintained by a vitrinite reflectance of 0.80 to 0.99 for well Aw04 and Aw10, respectively (van Ojik, 2010, person. comm.). But this process is unlikely to occur at temperatures below 160°C (Horsfield et al., 1992; Schenk et al., 1997). Basin modelling results in a maximum temperature of ~120°C in Late Jurassic which is too low for thermal cracking (▶ figure 3.8). Also the generation of solid bitumen by biodegradation of liquid hydrocarbons (e.g. Machel, 2001; Larter et al., 2003) is unrealistic since the Rotliegend sandstones were buried to ~2000 m depth in Late Jurassic. There is no evidence for the formation of solid bitumen by the reaction of organic compounds with minerals or water reported by Shebl and Surdam (1996). However the most significant formation may be the asphaltene precipitation from oil due to gas influx (Ehrenberg et al., 1995). The source rocks for field B and C are deposits attributed to the Westphalian A and for field A Westphalian B and C, minor D underlie the Rotliegend sandstones (van Buggenum and den Hartog Jager, 2007). The gas charging into the Rotliegend reservoirs influence the mineralogical reactions between fluid and rock (Gaupp, 2008). The diagenetic reactions will slow down due to the absence of a fluid phase which may transport solutes. Hence the reactions will take place only with the bound water.

4.4 Rock texture

The rock texture describes the structure of sediments: sorting, grain size distribution, type and frequency of grain-grain contacts and the roundness and sphericity of single grains. These factors depend on the depositional system, the plaeo-climate and paleo-topography and the burial history of the sediment.

The grain sizes of samples investigated in this study range between 71.0 and 978 µm with a mean value of 256 µm for fluvial and aeolian deposits (▶ figure 4.19). The southern basin margin is dominated by coarser grained sandstones and conglomerates which are attributed to sheetfloods, braided river and alluvial fan environments. Further to the north fine to medium grained fluvial, aeolian and sandflat deposits are more frequent (compare section 3.2.2). This

trend is reflected in the mean grain size for the southern and northern area of field A, field B and C (▶ table 4.3). Commonly unimodale normal grain size distribution occurs in samples from fluvial and aeolian environments independently from the distance to the basin margin (▶ figure 4.20).

Table 4.3: Mean grain size [µm] of samples from field A, B and C. The number of analysed samples is n.

	mean [µm]	**n**
field A (south)	318	35
field A (north)	210	19
field B	239	22
field C	218	28

The contour plot (▶ figure 4.21) shows the sorting and main roundness for each sample according to the mean grain size after the depositional environment classified after fluvial, aeolian and dry sandflat deposits. Only a few samples (n = 5) were analysed for a damp and wet sandflat environment which cannot be plotted in contour plots but are listed in ▶ table 4.4. For fluvial deposits a wide range in sorting (between 0.35 and 2.0) is to note. However the smaller the grain sizes the better is the sorting for angular to rounded grains. In comparison deposits from dune sediments are very well to moderate sorted with subangular to rounded grains. The mean grain sizes range between 150 and 300 µm. Deposits from dry sandflats are characterised by a well grain roundness (subrounded to rounded) and sorting between well and moderate. The mean grain size ranges between 150 and 250 µm.

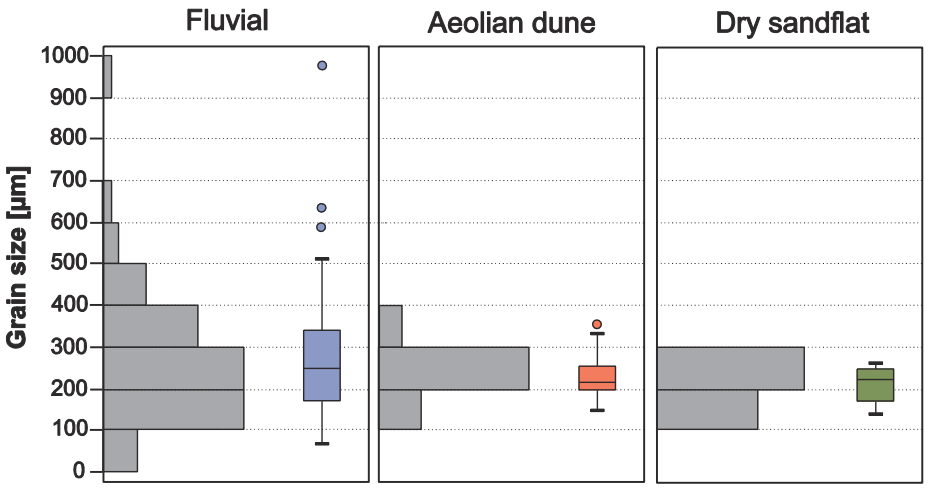

Figure 4.19: Distribution diagram and Box-Whisker-Plot of grain sizes from sandstones attributed to fluvial (n=56), aeolian dune (n=20) and dry sandflat (n=10) deposits. For each sample 100 grains were measured using optical microscopy.

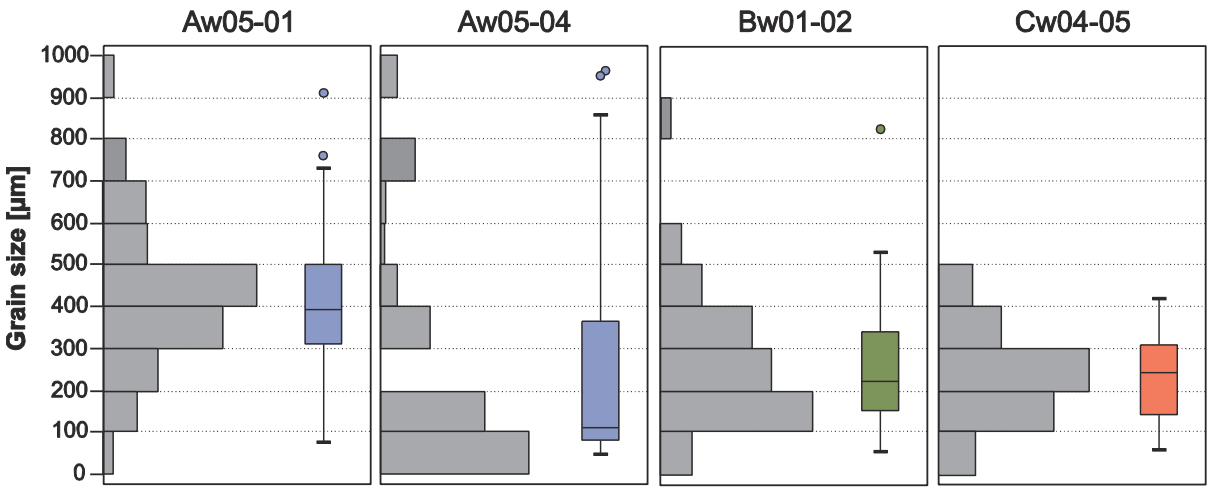

Figure 4.20: Distribution diagram and Box-Whisker-Plot for grain size [µm] of four samples from field A, B and C, respectively. Sample Aw05-1 and Aw05-04 are fluvial deposits, sample Bw01-02 was deposited as dune sediment and sample Cw04-05 is attributed to a dry sandflat environment. For each sample 100 grains were measured.

Deposits from wet and damp sandflats are moderately to poorly sorted sediments with angular to subrounded detrital grains. Grain contacts derived from thin sections give not the true value as they are present in a 3-dimensional sandstone system. But they may give evidence how dense the sandstone is packed. Well sorted aeolian dune, dry sandflat and fluvial sediments are less dense packed (mainly point- and length-contacts) than poorly sorted damp and wet sandflat and fluvial deposits which are dominated by point-, length- and concave/convex grain contacts (appendix C2). Sutured grain contacts are absent in all samples. Samples from the mudflat environment are not considered for thin section analysis. But the investigation of core images indicate poorly sorted fine grained sediments with intercalated mudflakes.

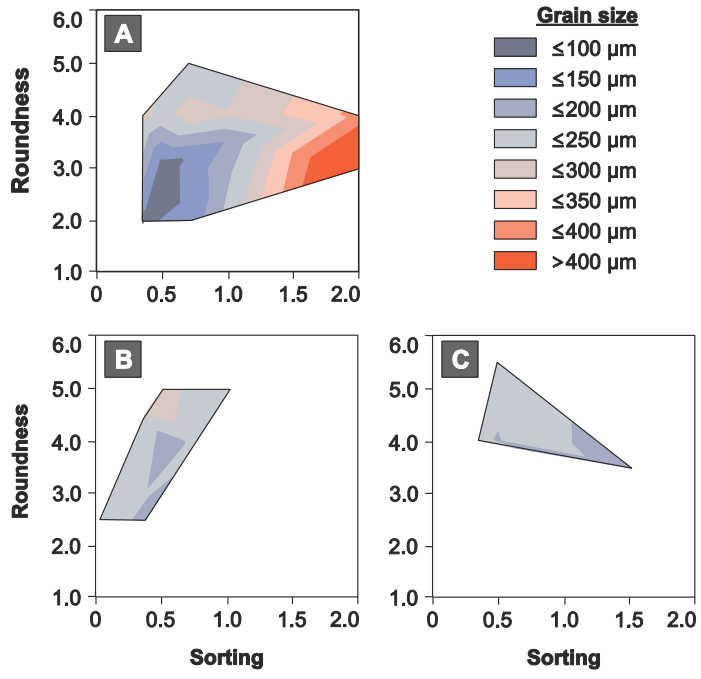

Figure 4.21: Contour diagram for sandstone roundness and sorting after grain size for samples from field A (n=21), B (n=23) and C (n=27), respectively. Especially for field A sandstones with smaller grain sizes show a higher roundness and a better sorting than coarse grained sandstones.

Table 4.4: Rock texture data for wet and damp sandflat environments from different wells (field B and C). The sorting is derived after Longiaru (1987) with 1.0 represents a moderate and 0.71 a well/moderate sorted sandstone. The roundness is classified after Tucker (1991) in angular (2), subangular (3), subrounded (4) and rounded (5) grains. Based on the classification of grain contacts (Pettijohn et al., 1987) the numbers stand for different grain-grain contact types: floating grains (0), point contacts (1), long contacts (2), concavo/convex contacts (3) and sutured grains (5). The value is a semi-quantitatively approximation derived from thin section images. The sphericity is defined after Pettijohn et al. (1987). The grain size is given in µm.

well	depth [m]	sorting	roundness	sphericity	gr cont	gr size [µm]	facies
Cw04	2710.90	1.00	2-4	low	1>2>0	218	damp sf
Cw03	2984.00	1.00	2-5	low	2>1>3	163	wet sf
Cw04	2740.30	0.71	2-4	high	2>3>1	146	wet sf
Bw01	2568.70	0.71	2-4	low	1>3>2	102	wet sf
Bw01	2574.90	1.00	2-4	low	2>3>1	195	wet sf

4.5 Summary and discussion of diagenetic processes

This chapter will give an overall summary and discussion of diagenetic reactions with the main focus to changing fluid compositions (e.g. salinity, type of cations) and conditions (e.g. pH, temperature) during diagenesis. In ▶ figure 4.22 the diagenetic evolution of mineral reactions and processes is shown for sandstones from field A, B and C.

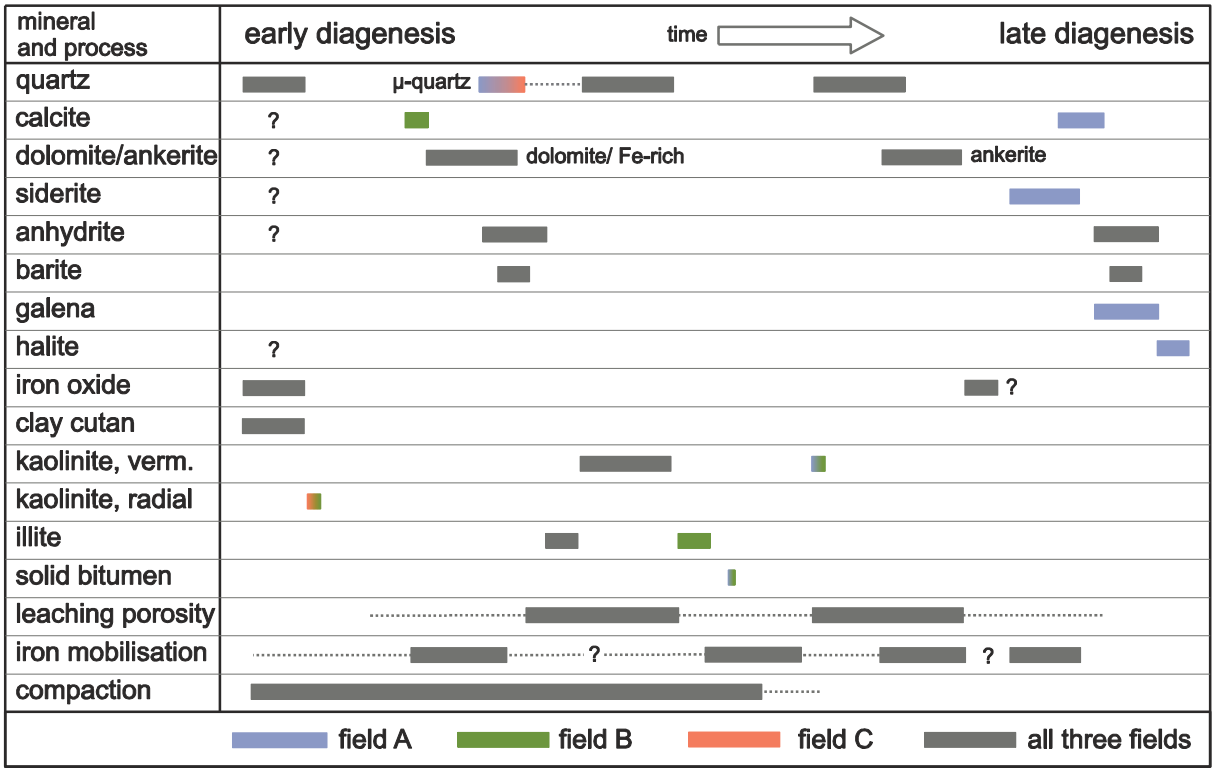

Figure 4.22: Diagenetic sequence of Rotliegend sandstones from the Upper Slochteren Formation, northern Netherlands. Note that not all mineral and processes are present within each sample. For further explanation please regard to the text.

In ▶ figure 4.23 diagenetic processes which occur in the same time interval are summarised to different stages (A to D) with related species released and/or consumed by mineral dissolution and/or precipitation. Furthermore where species are necessary for mineral precipitation but could not derive from an internal source an influx of further formation water carrying the dissolved solutes is assumed. Assumed compaction grade, permeability, porosity, intergranular volume and salinity are listed in ▶ table 4.5 for each stage, respectively. Estimation of the intergranular volume, porosity and permeability are based on the distribution, amount and type of authigenic minerals and may show a high variability due to e.g. different environmental deposits, position within the stratigraphy, distance to adjacent shales and mudstones, pore space distribution and detrital inventory. Stage A represents the condition after deposition of the sediment, the infiltration of clay (forming clay cutans around detrital grains) and the precipitation of Fe-oxide, quartz, carbonate and sulphate at eodiagenetic time. Dissolution of early grain stabilising cements like carbonate and sulphate and K-bearing minerals caused redistribution of elements and the precipitation of carbonate, sulphate, kaolinite and quartz (compare section 4.2) in stage B.

Table 4.5: Estimation of compaction grade, intergranular volume and permeability behaviour of Rotliegend sediments during diagenesis divided in stage A to D (▶ figure 4.23) for samples investigated in this study. The salinity is based on data from Tesmer et al. (2007) (▶ figure 4.27).

Stage A	• low compaction grade • low porosity • high intergranular volume: ~40 vol.-% • medium permeability due to lacking clay content and blocky pore-filling cements • low salinity
Stage B	• increasing compaction grade • high porosity • low intergranular volume: 30-40 vol.-% (?) • low permeability due to grain rimming chlorite(?)/kaolinite in samples from field B and C • high permeability in samples from field A • medium salinity
Stage C	• increasing compaction grade • medium porosity • lower intergranular volume: 25-30 vol.-% (?) • lower permeability due to grain rimming kaolinite, kaolinite “booklets” and meshwork/fibrous illite • medium salinity
Stage D	• medium porosity • lower intergranular volume: 25 vol.-% • lower permeability due to grain rimming kaolinite, kaolinite “booklets” and meshwork/fibrous illite • high salinity

Especially for grain rimming kaolinite an external source of aluminium and silica is assumed because only minor amounts of K-feldspar are dissolved. Another possibility is the transformation of precursor grain rimming chlorite to kaolinite under the influence of CO_2 (compare section 4.5.3). Stage C is characterised by an intensive precipitation of kaolinite "booklets", illite and quartz caused by K-feldspar dissolution and by the precipitation of Fe-bearing carbonates (esp. ankerite) due to the release of Fe from eodiagenetic Fe-oxides. For the latest stage D an influx of species which are necessary for carbonate, sulphate and galena precipitation is assumed because no evidence is found for dissolution processes of minerals which are related to stage C. A further stage would describe the possible mineral compositions over (geological) time during CO_2 storage which is investigated by geochemical coupled with reactive transport modelling (chapter 7 and 8).

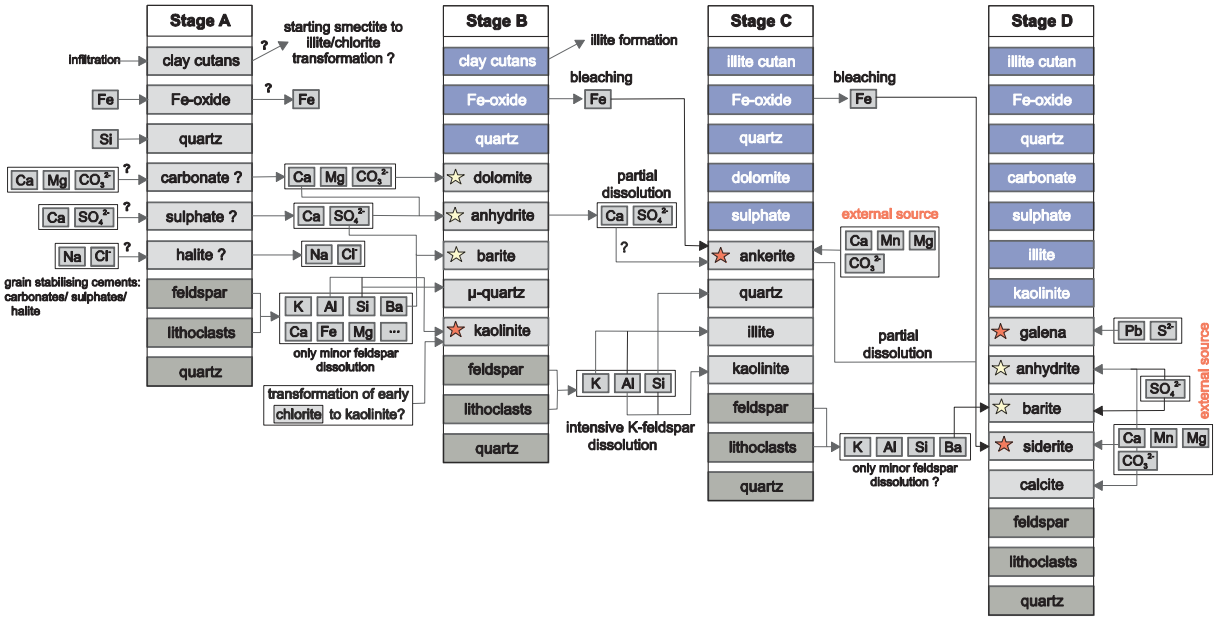

Figure 4.23: Diagenetic sequence of Rotliegend sandstones divided in stage A to D for diagenetic processes (e.g. dissolution and precipitation of minerals) which are related to similar time periods. Dark grey coloured boxes stand for detrital grains (quartz, feldspar and lithoclast), light grey boxes represent new precipitates at each stage, respectively which are inherited for the next stage (blue boxes). Inherited minerals are summarised to mineral groups (e.g. dolomite and ankerite to carbonates). Species which are not linked to specific previous mineral dissolution are assumed to be derived from additional formation waters entering the sandstone (marked as yellow stars for minor supply and as orange stars for an obvious input). All minerals and processes are a summarised description of all samples (field A, B and C) investigated in this study.

4.5.1 Eodiagenesis

The diagenetic alteration of Rotliegend sediments is mainly influenced by facies and detrital composition of the reservoir rock (e.g. Glennie et al., 1978; Drong, 1979). External factors are climatic conditions (e.g. the availability of water and temperature), the type of fluid which is circulating through the rock, as well as the composition and physicochemical attributes (e.g. temperature and pH value). Furthermore the biological activity of bacteria, fungi and algae will influence the diagenetic evolution under near surface conditions. Rotliegend deposits of the northeast Netherlands are composed of sediments which are attributed to a fluvial, aeolian or

playa environment. The sediments consist of varying amounts of detrital quartz, feldspar and rock fragments (mainly volcanic lithoclasts). Towards the basin centre the silt and clay content increase. The climate during Upper Rotliegend is considered to be an arid and semi-arid desert climate with changing temperature conditions on the sediment surfaces (Gast, 1991; Howell and Mountnay, 1997). The fluids which entered the Rotliegend sediments had a highly variable composition and were mixtures of different sources: atmospheric water, meteoric surface water run-off, brackish-saline ground water, brackish to highly saline playa lake water and deeper water derived from underlying Carboniferous rocks (Platt, 1993; Ziegler, 2006; Gaupp and Okkerman, 2011). The movement of surface water (atmospheric and meteoric run-off water) is mainly downward into the sediment, transporting solutes and fines. However a vertical upward movement of water is due to evaporation processes followed by changing salinities of the fluid (Gaupp and Okkerman, 2011). Based on these processes early cements are infiltrated (clay particles forming cutans tangential to detrital grains) or precipitated (e.g. carbonates, sulphates, halite, metal-oxides) from pore fluids. The diagenetic evolution started during and/or immediately after deposition of the sediments (Walker et al., 1978). The type of cement depends on the position within the sedimentary basin: At the proximal basin margin calcite precipitated due to less salinity of the groundwater. Further to the basin centre the system developed from calcite to dolomite over anhydrite/gypsum and subsequently to halite in more distal positions (Drong, 1979; Platt, 1994). These cements often appear as blocky, pore-filling cements or as nodules, partly linked to sediment laminae. Furthermore stable isotope analysis indicates precipitation of early diagenetic quartz overgrowth at low temperatures (20-60°C) from meteoric water (Sullivan et al., 1994; Amthor and Okkerman, 1998). Eodiagenetic cements have stabilised the grain framework and may have dissolved during further burial. These cements could not be proven by petrographical investigations in samples from the northeast Netherlands (this study), but should have been existed due to primary point and length contacts between detrital grains. Metal-oxides may have been precipitated in desiccation cycles during changing wetting and drying of the sediment.

4.5.2 Mesodiagenesis and telodiagenesis

An initial burial phase to ~2000 m occurred in the northeast Netherlands from Lower Permian to Jurassic, followed by an inversion and uplift to ~1500 m in Late Jurassic to Early Cretaceous, with a locally minor uplift in Late Cretaceous. A second period of subsidence occurred after the inversion to the present depth in ~2500-3000 m (▶ figure 3.8). The main diagenetic reactions including dissolution of detrital grains and/or cements and the precipitation of authigenic minerals occurred during the first burial phase under a maximum temperature of ~120°C. The system was dominated by Zechstein brines and fluids derived from underlying Carboniferous deposits along fault zones and fractures. The salinity is highly variable (Gaupp et al., 2008) and seems to be mainly influenced by the overlying Zechstein Group and Upper Triassic Group by dissolution of evaporites which were transported by diffusion and density driven flow (e.g. Leveille et al., 1997). The uplift and removal of Jurassic and Triassic sequences may have moved the sediments close to the surface where diagenetic reactions were influenced by partly meteoric oxidising fluids (Ziegler, 2006). Fluid influx from Carboniferous sequences and Zechstein salts is likely. Hence a mixture of fluids, with different salinities and acidities can be expected (e.g. Lee et al., 1989). Further burial had a smaller effect on the digenetic reactions and with this on the reservoir quality (Gaupp and Okkerman, 2011).

Fluid composition and influences on mineral reactions

Mineral reactions are influenced by several physicochemical parameters like temperature, fluid composition, pH/Eh value and oxidising or reducing fluid conditions. Researches on natural analogues showed that mineral reactions are mainly influenced by changing pH conditions which are caused by different processes and are not attributed to the presence of CO_2 only. Mineral reactions are influenced by the presence of organic acids (e.g. Kharaka et al., 1986; Muchez et al., 1992; McCollom and Seewald, 2003), hydrocarbons (e.g. Burley, 1984; Kilgore and Elmore, 1989; Surdam et al., 1989; Surdam et al., 1993; Lee and Bethke, 1994; Chan et al., 2000; Garden et al., 2001; Parry et al., 2004), CO_2 bearing fluids carrying H_2S and/or SO_4 (e.g. Haszeldine et al., 2005; Palandri and Kharaka, 2005), bacterial processes (Machel et al., 1995; Worden and Smalley, 1996; Machel, 2001) and the presence of microorganisms (e.g. Kashefi and Lovley, 2003; Kashefi et al., 2004).

There are general sources for reactive agents influencing acidity of a fluid and may cause mineral precipitation and dissolution of detrital grains and cements. Major dissolution events of minerals in reservoir rocks are interpreted to be dominantly linked to liquid hydrocarbons, organic acids and the presence of CO_2, H_2S and/or SO_4 (e.g. Curtis, 1983; Surdam et al., 1984). Oxidising agents are hydrocarbons, Fe-oxides, sulphates and the formation water itself (e.g. Seewald, 2001 and 2003). However there seems to be several sources of reducing agents within the reservoir rocks and mineral reactions are eventually due to more than one specific agent.

Sandstones of the Upper Slochteren Formation are lying on top of Carboniferous sediments which may have released hydrocarbons, organic acids, acids, CO_2 and sulphur species like H_2S and SO_4 during burial. The present rock composition is, among other parameter (e.g. detrital mineralogy) characterised by the (end)-products of mineral reactions. Hence the development of mineral dissolution and/or (re)-precipitation during diagenesis will give a hint for the possible influence of changing fluid conditions (e.g. acidity, temperature). The most known indication for reducing conditions is the removal of Fe-oxide in sediments which leads to a bleaching from (light) red coloured to grey sandstones and green coloured mudstones and the formation of Fe-rich authigenic minerals (compare section 4.2). Furthermore (intense) K-feldspar dissolution and the alteration of volcanic rock fragments are attributed to changing fluid conditions. The released ions may be bonded in other authigenic minerals (e.g. kaolinite and illite).

Bleaching of sediments and redistribution of Fe

Fe-oxides are removed in many reservoir rocks, especially in samples from field A, where all sandstones show a grey colour (e.g. appendix A1-01). Residual Fe-oxides between early diagenetic quartz cements and detrital grains were protected from reducing pore fluids. Where quartz is missing it is difficult to decide if Fe-oxides were removed or never present. However samples from field B and C show bleached sandstone and shale horizons, but red to light red coloured sandstones with varying amounts of Fe-oxides are still present. The bleaching occurred dominantly in high permeable sandstones, but also lower permeable sandstone and shale horizons are affected (e.g. appendix A1-01).

Fe^{3+} is immobile under normal pore fluid conditions and needs to be reduced to Fe^{2+} to be transported in solution (Drever, 1997). Based on the previous listing of organic and inorganic agents it is relatively difficult to determine the processes that leads to a (partly) intense bleaching of red beds and the removal of iron. Leaching processes are most likely in sediments which stand in direct contact to Carboniferous Coal Measures (Platt, 1991; Deutrich, 1993;

Gaupp et al., 1993), where the major influx of liquid hydrocarbon, organic and inorganic acids occurs. Solid bitumen could be proven in many samples from field A, and minor from field B and C. From intercalated shale horizons of a damp or wet sandflat and interpond environment distal to the basin margin acidic compaction waters will be released during burial.

Liquid hydrocarbons may be generated from underlying Carboniferous source rocks during burial and further migration into the Rotliegend sediments (Schöner and Gaupp, 2005). Oil-rock-water experiments at 200-360°C for redox reaction simulation were carried out by Shebl and Surdam (1996). The authors showed that Fe-oxides were reduced (for example to pyrite) and hydrocarbons were oxidised to CO_2 and organic acids according to the following equation (▶ 4.5, Surdam et al., 1993).

$$0.15\ C_9H_{20} + 0.5Fe_2O_3 \rightarrow 0.675CH_3COOH + FeS_2 + 0.15H_2O \quad (4.5)$$

Chan et al. (2000) presented another possible reaction based on the presence of CH_2O instead of hydrocarbons (▶ equation 4.6).

$$CH_2O + 2Fe_2O_3 + 8H^+ \rightarrow CO_2 + 5H_2O + 4Fe^{2+} \quad (4.6)$$

Substantial amounts of CO_2 and organic acids could be released during decarboxylation and/or oxidation reactions in sedimentary environments (Seewald, 2001; McCollom and Seewald, 2003; Seewald, 2003). Organic acids and anions like acetic acid and acetate are abundant in oil field brines. They may cause the reduction of ferric iron and the release of CO_2 during oxidation (Carothers and Kharaka, 1978; Kharaka et al., 1986; Muchez et al., 1992; McCollom and Seewald, 2003) (▶ equation 4.7).

$$CH_3COOH + 5H_2O \rightarrow 2CO_2 + 4H^+ \quad (4.7)$$

Furthermore magnetite is formed according to ▶ equation 4.8. Note that magnetite is absent in all samples, according to the present study and that the stability field for solid magnetite is relatively small and requires high pH (>10) and a negative Eh (<-0.4) (Takeno, 2005).

$$3Fe_2O_3 + H_2 \rightarrow 2Fe_3O_4 + 4H_2O \quad (4.8)$$

The interaction of CO_2 bearing fluids carrying SO_2 and/or H_2S with Fe-oxides will cause mineral reduction and the release of iron within the formation water. The reaction of SO_2 with the formation water leads to a decreasing pH and release of protons by further dissociation of H_2S and H_2SO_4 to S^{2-} and SO_4^{2-} (Getahun et al., 1996; Symonds et al., 2001).

$$4SO_{2(g)} + 4H_2O_{(l)} \rightarrow H_2S_{(aq)} + 3H_2SO_{4(aq)} \quad (4.9)$$

After Palandri and Kharaka (2005) hematite can be reduced by H_2S, CO_2 and SO_2 according to ▶ equations 4.10 and 4.11.

$$4Fe_2O_3 + 15H_2S + H_2SO_4 \rightarrow 8FeS_2 + 16H_2O \quad (4.10)$$

The removal of hematite under relatively low pH is shown by Metcalfe et al. (1994) for the reaction with H_2S.

$$4Fe_2O_3 + H_2S + 14H^+ \rightarrow 8Fe^{2+} + {SO_4}^{2-} + 8H_2O \quad (4.11)$$

CO_2-rich groundwater causes bleaching of red beds as well (Schumacher, 1996; Allis et al., 2001). Soluble iron may (1) further be removed from the system which is considered over high permeable horizons and/or fractures, (2) precipitates as Fe-oxide aggregates in open pores under changing oxygen/reducing fluid conditions or (3) may be bonded in other authigenic minerals, like e.g. Fe-carbonates, leucoxene and/or Fe-rich chlorites and illites.

Chemical analysis of sandstone samples show varying amounts of iron (2559 to 16175 µg/g) (appendix C5). The high amount is linked to a bleached, Fe-oxide poor sample (Aw02-03). This may indicate no or only minor removal of iron from the system but redistribution and bonding in other authigenic minerals. In samples from field A Fe-oxide aggregates are present in the intergranular pore space and may have been precipitated in the late mesodiagenesis under changing oxidising and reducing fluid conditions. The most common cements are Fe-rich dolomites, ankerites and siderites in samples from field A which are associated to bleached horizons. But also minor amounts of Fe-rich dolomites (and ankerite) are present in red and grey coloured sandstones from fields B and C. After Crossey et al. (1986) the formation of Fe-carbonates is due to the presence of carboxyl acids and a related temperature of 80-120°C (Giordano and Kharaka, 1994) in deep (>2500 m) environments. Furthermore the formation of siderite depends on a high Fe^{2+}/Ca^{2+} ratio (>0.4) under reducing fluid conditions (Füchtbauer et al., 1988) and a low CO_2 partial pressure of at least 10^{-6} atm (Curtis, 1967). Sulphur ions like HS^- and H_2S need to be absent to precipitate siderite instead of pyrite. Where siderite precipitates the pH decreases and produces additional protons which are released into the fluid (▶ equation 4.12).

$$H_2CO_3 + Fe^{2+} \rightarrow FeCO_3 + 2H^+ \quad (4.12)$$

Siderite may precipitate as the result of the reaction from hematite with CO_2 and SO_2 according to the following overall ▶ equation 4.13 after Palandri and Kharaka (2005).

$$4Fe_2O_3 + 2CO_2 + SO_2 + H_2O \rightarrow 2FeCO_3 + H_2SO_4 \quad (4.13)$$

Fe-rich chlorites as well as pyrite and magnetite are absent as direct precipitates from pore fluid in all samples. Exclusively Fe-rich illite/smectite minerals appear as alteration products in volcanic rock fragments where the source of required cations and anions is found within the detrital grain (compare section 4.2). The release of protons during clay transformation of e.g. smectite to illite may lead to increasing water acidity and may be derived from compacted shales during burial (Bjørlykke, 1983). Released ferric iron may cause oxidation of hydrocarbons (Surdam and Crossey, 1985). Based on mass balance calculations Giles and Marshal (1986) pointed out that organic acids, acids or CO_2 which were generated especially in shales by clay transformation processes will be neutralised already in the source rock.

Relatively high N_2 concentrations in Permian gas fields of the Netherlands may have been derived from organic material of underlying Carboniferous coals (Krooss et al., 2005). However, especially the eastern area of the Netherlands is underlain by Namurian shales with relatively low contents of organic material. In consequence a second source of nitrogen is feasible for clastic sedimentary rocks. Various studies indicate the presence of ammonium ions (NH_4^+) which can be bonded inorganically in feldspar, illite and smectite, substituting monovalent cations such as potassium and sodium (Krooss et al., 2005). The oxidation of ammonium to N_2 trough bacterial processes in the subsurface may drive the redox transfer from Fe^{3+} to Fe^{2+} (e.g. Broholm et al., 2000; Clément et al., 2005) and a consequent bleaching of the sediments.

Feldspar dissolution

Dissolution processes of detrital grains (e.g. K-feldspar, plagioclase, volcanic lithoclasts) are a common feature during burial in many reservoir rocks (e.g. Bjørlykke, 1984; Surdam et al., 1984; Giles, 1986; Shebl and Surdam, 1996). The dissolution grade of grains is variable and range from (1) partly etched surface areas over (2) an intense dissolution with residual grain skeletons to (3) total dissolved grains forming oversized pores. Partly, detrital grains are replaced by illite, Fe-rich illite/smectite, kaolinite or dolomite cements. However in samples from field B an intense dissolution of detrital K-feldspar appeared during burial but without affecting the presence of Fe-oxide coatings around the grains. This relation may give an indication of a specific fluid pH and Eh dependence during K-feldspar dissolution: The comparison of stability fields (Eh vs. pH) for Fe-O-H and Al-O-H as well as literature data about feldspar dissolution experiments (e.g. Blake and Walter, 1996 and 1999) indicate a strong pH and Eh dependence in combination with the fluid composition (▶ figure 4.24). In order to dissolve K-feldspar without affecting the Fe-oxide coatings relative low pH (<5) and high positive Eh (>0.3) are required. At these conditions K-feldspar grains will be dissolved to K^+, $AlOH^{2+}$ or Al^{3+} and $H_4SiO_{4(aq)}$.

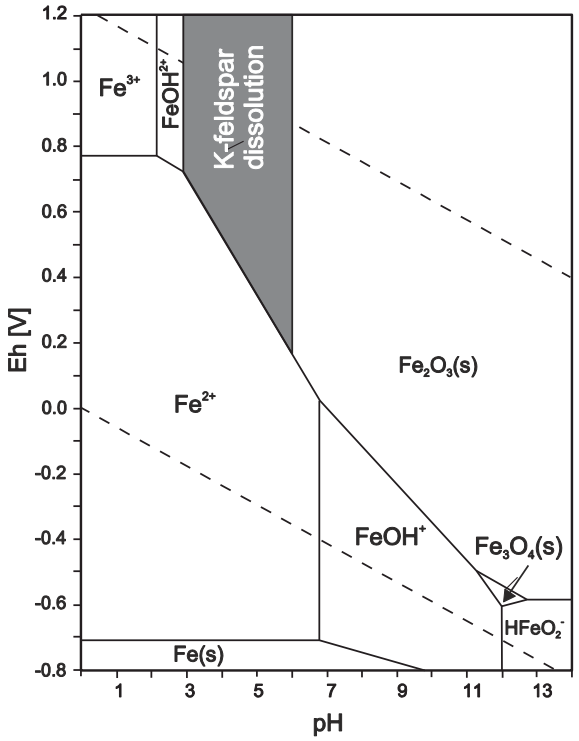

Figure 4.24: Stability field (Eh vs. pH) for Fe-O-H for 25°C which was calculated with the software FACTSAGE after Takeno (2005). The field where K-feldspar dissolution takes place, but solid hematite (Fe_2O_3) is stable is marked in grey colour.

It is impossible to quantify the total surface areas of partly dissolved grains by using petrographic methods (e.g. thin section microscopy, SEM, EMS). But after Wilkinson and Haszeldine (1996) grain dissolution is always underestimated in petrographic observations. Feldspar dissolution is largest at or close to contacts between the Carboniferous Coal Measures and Rotliegend deposits, where acidic fluids can enter the sediments (Platt, 1991; Deutrich, 1993; Gaupp et al., 1993). Watson et al. (2003) pointed out that the dissolution of detrital sodium-rich plagioclase grains (▶ equation 4.4) is directly related to the presence of CO_2 in the Ladbroke Grove field in the Australian Otway Basin. Furthermore calcium-rich plagioclase and K-feldspar remain relatively unaffected (▶ equation 4.14).

$$2CaNaAl_3Si_2O_{16} + 7H_2O + 4CO_2 \rightarrow 2CaCO_3 + 3Al_2Si_2O_5(OH)_4 + 4SiO_2 + 2NaAlCO_3(OH)_2 \quad (4.14)$$

PLAGIOCLASE — CALCITE — KAOLINITE — QUARTZ — DAWSONITE

Based on considerations of Gunter et al. (1997) the alteration of albite is linked to the formation of a Na-rich smectite and quartz. Furthermore calcium-rich plagioclase and K-feldspar remain relatively unaffected (Watson et al., 2003). However Gunter et al. (1997) pointed out that the alteration of anorthite under the influence of CO_2 yield in the precipitation of calcite and kaolinite (▶ equation 4.15).

$$\underset{\text{PLAGIOCLASE}}{CaAl_2Si_2O_8} + H_2O + CO_2 \rightarrow \underset{\text{KAOLINITE}}{4Al_2Si_2O_5(OH)_4} + \underset{\text{CALCITE}}{CaCO_3} \quad (4.15)$$

Mineral precipitation

Mesodiagenetic kaolinite and meshwork illite

Illite is uncommon in all samples and appears as thin meshwork and/or fibrous illite in sandstones from the Upper Slochteren Formation, only. The dominant clay mineral in all samples is kaolinite (compare section 4.2).

As mentioned in the previous section, the formation of grain rimming kaolinite is unclear and untypical for Rotliegend sandstones in the northeast Netherlands. There, Mg-rich pore-lining radial chlorites are reported by several authors (e.g. Gaupp et al., 1993; Ziegler, 2006). If kaolinite is formed by replacement of precursor chlorite the fluid system during the time of precipitation may indicate alkaline conditions which were expelled from intercalated Rotliegend shales (Gaupp et al., 1993). Another hypothesis is the direct precipitation of grain rimming kaolinite from low saline acidic water (Curtis and Spears, 1971). Petrographic evidence indicates no major K-feldspar dissolution and release of aluminium and silica at time of burial. Hence for kaolinite formation significant amounts of aluminium must have been transported by e.g. organic ligands within the aqueous phase at low or high pH (Curtis, 1983). Platt (1991) pointed out that aluminium and silica required for kaolinite formation within the German Rotliegend needs to be transported by Al-rich fluids and could not be released by feldspar dissolution which can be confirmed for this study. For a more detailed description of (1) a possible correlation between the precipitation of early diagenetic chlorite and the following transformation to kaolinite during further burial or (2) a direct precipitation at shallow burial please regard to section 4.2.6 and 4.5.3.

Mesodiagenetic leaching of detrital feldspar is associated with the formation of diagenetic illite and kaolinite. Bitumen impregnation reported by different authors (e.g. Gaupp et al., 1993; Schöner and Gaupp, 2005) for Rotliegend sediments could not be proven for this study, because illite is visible in SEM images only. The process of illite precipitation is not well understood yet (Schöner, 2006). Several authors suggest the presence of acidic/CO_2-bearing fluids during the early stage of oil migration (e.g. Barclay and Worden, 2000). Gaupp et al. (1993) and Platt (1993) recognised a zone of intense kaolinite formation and minor illitisation near tectonic contacts of the Rotliegend against Carboniferous Coal Measures. Further away from such contacts illite becomes the dominant clay mineral whereas kaolinite is absent. Lanson et al. (1996) agrees with the distribution of illite and kaolinite for the Dutch offshore and the precipitation of kaolinite according to the influx of acidic fluids from underlying Carboniferous sediments. During Late Jurassic/Early Cretaceous meteoric waters may have entered the Rotliegend and caused the dissolution of detrital feldspar and precipitation of lower temperature kaolinite and quartz (Ziegler et al., 1994).

Pore-filling cements

Shallow burial pore-filling cements like quartz, calcite, dolomite, anhydrite and barite precipitated in a partial compacted grain framework near the surface. Therefore an influx of silica, Ca, Mg, Ba, SO_4^{2-} and CO_3^{2-} needed to occur. It is possible that they are re-precipitations from dissolved eodiagenetic carbonates and sulphates. The late diagenetic precipitation of anhydrite, barite and galena is due to the presence of sulphur species and changing fluid compositions. The anions required for these cements may be derived from dissolved earlier cements or detrital grains or from clay transformation (e.g. smectite to illite) in adjacent mudstones (Boles and Franks, 1979). After Platt (1994) may the influx of late Zechstein brines caused the precipitation of late carbonate and sulphate cements at the southern margin of the Southern Permian Basin.

4.5.3 Evidence of CO_2-bearing fluids during diagenesis

Advices for the influence of CO_2 on precipitation and/or dissolution of authigenic minerals and changes in the detrital inventory are noticed in several geological settings. They are studied as natural analogues for CO_2 storage (compare section 1.3). Fluid-rock interactions are influenced by several components/species and processes lowering the pH in a fluid. The following components/species may be involved: organic acids (e.g. short- and long-chain acids (e.g. McCollom and Seewald, 2003)), hydrocarbons, bacterial processes (e.g. bacterial sulphate reduction (e.g. Machel (2001)), CO_2, H_2S, SO_4^{2-}, and microorganisms. Since a fluid is a complex assemblage of different components/species and a variability of potential reactive minerals within a rock it is often difficult to assign single fluid-mineral reactions to one component/species which may trigger the reaction (e.g. decreasing pH with increasing CO_2 content). However some mineral reactions are due to (1) an increasing H^+ content and (2) the presence of HCO_3^- as dissociation products of H_2CO_3 and may be assigned to the presence of CO_2 during diagenesis and/or CO_2 storage processes.

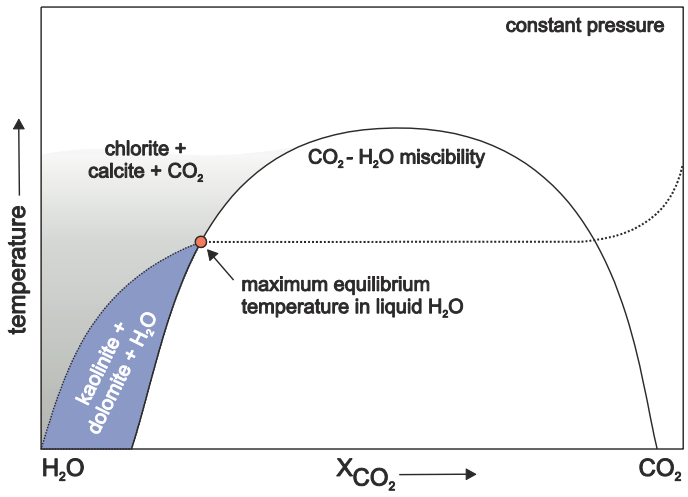

Figure 4.25: With increasing CO_2 content in the vapour phase kaolinite and dolomite are formed at the expense of chlorite and calcite. The reaction stays stable with increasing CO_2 content at higher temperatures. Once the CO_2-H_2O miscibility curve (solid) is reached carbon dioxide vapour is produced and chlorite and calcite will precipitate. The reactions are reversible. Modified from Hutcheon (1983).

The illitisation of K-feldspar and albite requires the presence of H^+ within the fluid (▶ equation 4.16 and ▶ equation 4.17). The protons may be released by the dissociation of H_2CO_3 (▶ equation 1.1). Both initial feldspar minerals are proven by petrographic analyses of the samples investigated in this study and the alteration of detrital grains to green coloured illite/smectite

are the result of changing fluid composition during diagenesis (compare section 4.2.7). The illitisation is initially driven by an increasing amount of potassium and is controlled by the presence of albite which provides the aluminium (▶ equation 4.16) (Bertier et al., 2009).

$$\underset{\text{K-FELDSPAR}}{KAlSi_3O_8} + \underset{\text{ALBITE}}{2NaAlSi_3O_8} + H^+ \rightarrow \underset{\text{ILLITE}}{KAl_3Si_3O_{10}(OH)_2} + \underset{\text{QUARTZ}}{6SiO_2} + 2Na^+ \quad (4.16)$$

The reaction continues until all albite is consumed or the mineral stays in equilibrium with the surrounding fluid. K-feldspar may further react with H^+ to illite and quartz and may release significant amounts of potassium in the solution (▶ equation 4.17) (McAulay et al., 1993; Platt, 1993).

$$\underset{\text{K-FELDSPAR}}{3KAlSi_3O_8} + 2H^+ \rightarrow \underset{\text{ILLITE}}{KAl_3Si_3O_{10}(OH)_2} + \underset{\text{QUARTZ}}{6SiO_2} + 2K^+ \quad (4.17)$$

K-feldspar dissolution yields in a decreasing aluminium concentration in the fluid followed by undersaturation of kaolinite. Hence kaolinite is consumed in the illitisation process. This reaction is not agreed for the samples investigated since the kaolinite is a pure clay mineral (compare section 4.2.6). However the precipitation of kaolinite at the expense of K-feldspar is a common process in all samples investigated during early diagenesis (▶ figure 4.22). Also this reaction requires the presence of protons (▶ equation 4.18) (Land and Milliken, 1981).

$$\underset{\text{K-FELDSPAR}}{2KAlSi_3O_8} + H_2O + 2H^+ \rightarrow \underset{\text{KAOLINITE}}{Al_2Si_2O_5(OH)_4} + \underset{\text{QUARTZ}}{4SiO_2} + 2K^+ \quad (4.18)$$

Based on geochemical modelling of diagenetic reactions for the Montmiral field (Southeast Basin, France) Gaus et al. (2004) and Pauwels et al. (2007) propose the direct reaction of K-feldspar with CO_2 to kaolinite/illite, quartz and dolomite/calcite. The reaction is given for kaolinite in (▶ equation 4.19).

$$\underset{\text{K-FELDSPAR}}{2KAlSi_3O_8} + 2CO_2 + 3H_2O + Ca^{2+} + Mg^{2+} \rightarrow \underset{\text{KAOLINITE}}{Al_2Si_2O_5(OH)_4} + \underset{\text{QUARTZ}}{4SiO_2} + \underset{\text{DOLOMITE}}{CaMg(CO_3)_2} + 2K^+ + H^+ \quad (4.19)$$

This reaction is confirmed by Higgs et al. (2007) for the Kapuni Group (Taranaki Basin, New Zealand). The authors suggest no precipitation of carbonate under the supply of calcium and magnesium but the presence of bicarbonate (▶ equation 4.20).

$$\underset{\text{K-FELDSPAR}}{2KAlSi_3O_8} + 2CO_2 + 11H_2O \rightarrow \underset{\text{KAOLINITE}}{Al_2Si_2O_5(OH)_4} + 4H_4SiO_4 + 2K^+ + 2HCO_3^- \quad (4.20)$$

Furthermore both reactions (▶ equation 4.7 and ▶ equation 4.8) are applicable for albite and anorthite instead of K-feldspar (Gaus et al., 2004; Higgs et al., 2007). The dissolution of Fe-oxide requires reducing fluid conditions and the reduction of Fe^{3+} to Fe^{2+} which results in a consumption of protons and release of water (compare section 4.7.2, ▶ equation 6.5). As discussed in (compare section 4.7.2) bleaching of sediments may be controlled by the presence of e.g. CO_2, S-species, CH_2O and/or hydrocarbons. Hence it is not possible to assign this process only to the presence of CO_2.

Especially in samples from field A significant amounts of ankerite and siderite are present which indicate reducing fluid conditions and the mobility of Fe^{2+} within the fluid. However in nearly all samples dolomite is the dominant carbonate. After Curtis (1978) results the reaction of HCO_3^- and cations like calcium, magnesium and iron (M^{2+} in ▶ equation 4.21) in the precipitation of

carbonates (calcite, dolomite, ankerite and siderite) under the release of protons. This reaction may consume the HCO_3^- provided by the dissociation of H_2CO_3.

$$HCO_3^- + M^{2+} \rightarrow MCO_3 + H^+ \quad (4.21)$$

In section 4.2.6 the possible formation of kaolinite as a direct replacement reaction of precursor grain rimming chlorite under the influence of CO_2 is briefly discussed. The reaction (▶ equation 4.3) is reversible and depends on the presence of CO_2 and changing temperature. The formation of dolomite and kaolinite from chlorite and calcite is pushed forward with rising CO_2 concentration whereas the reaction is forced back by increasing temperature (▶ figure 4.25). According to the iron content within the chlorite ankerite and siderite may precipitate instead of a pure Ca-Mg dolomite (Hutcheon, 1989).

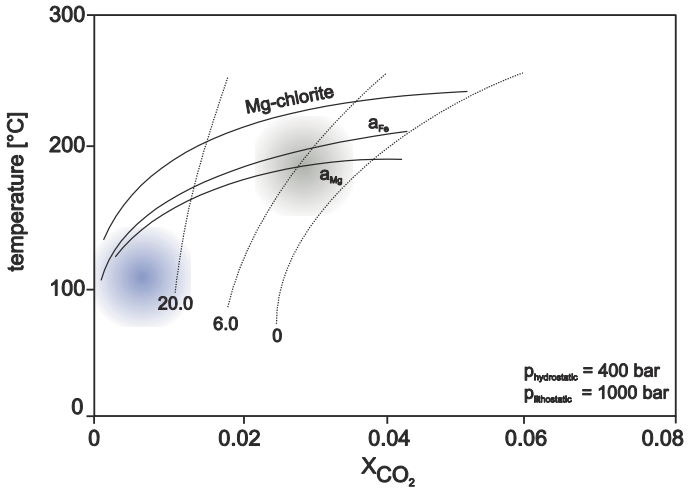

Figure 4.26: After Hutcheon (1989) influences the activity of magnesium within chlorite the formation temperature. The reaction for a pure Mg-chlorite (clinochlore) intersects the solubility curve for CO_2 (20, 6 and 0 wt.-% NaCl-H_2O liquid, respectively) at much higher temperatures than Mg-Fe-chlorite (a_{Fe} and a_{Mg}). In this study a temperature between 100 and 120 °C and a salinity of 25.5 wt.-% (blue circle) is to observe, today. The brown circle may represent the formation conditions of chlorite during eodiagenesis.

After Hutcheon et al. (1980) and Hutcheon (1983) is the maximum temperature for the formation of chlorite from kaolinite + dolomite for the Kootenay Formation 180°C at a burial depth of 5-6 km and a total pressure (lithostatic and hydrostatic pressure) of 1300-1600 bar. For the Ventura area at the east coast of Canada Hutcheon (1989) proposed a maximum temperature of 170°C. No temperature range is given for the chlorite transformation to kaolinite within the Pretty Hill Formation of the Otway Basin which was analysed by Watson et al. (2003 and 2004). The reaction temperature (▶ equation 4.3) depends on several parameters: Hutcheon (1989) pointed out that the activity of magnesium within chlorite influences the formation temperature. The reaction for a pure Mg-chlorite (clinochlore) intersects the solubility surface at much higher temperatures as Mg-Fe-chlorite (▶ figure 4.26). However the salinity influences the solubility of CO_2 within a saline fluid. The higher the salinity the lower is the CO_2 solubility and the lower is the formation temperature at a given pressure (▶ figure 4.25) (Hutcheon, 1983).

Rotliegend fluids from the northeast Netherlands contain ~25.5 wt.-% NaCl today. However brines from the North German Basin were analysed by Hoth et al. (2005) and Tesmer et al. (2007) of Late to Early Permian and Late Triassic to Early Tertiary age. The results indicate two groups of samples (▶ figure 4.27): The first group show a correlation of increasing depth (up to ~2300 m) and total dissolved solids (TDS) (up to ~270 g/l). And the second group is characterised by an increase of TDS up to ~300 g/l with varying depth. Based on these results a salinity of approximately 50-75 g/l TDS at depth >500 m may be assumed for Rotliegend fluids

present during eodiagenesis. Based on the relation between the CO_2 content within a fluid and the formation temperature of chlorite at a given salinity which is proposed by Hutcheon (1989), this approximation may indicate that chlorite precipitated at higher temperatures than they are assumed for Rotliegend sediments in the study area. However Hillier (1994) described grain rimming Mg- and Fe-rich chlorites of different age. A Fe-rich chlorite from the Intra Dunlin Sand Formation (Early Jurassic) and the Tofte Formation offshore Norway have a similar habitus like the kaolinite described in this study. The formation temperature for this chlorite is assumed to be ~120°C and ~155°C, respectively (Hillier, 1994). In contrast the Mg-rich chlorite from Rotliegend precipitated at higher temperatures (Gaupp et al., 1993; Hillier, 1994). But the habitus is with a more box-work-like arrangement different to Fe-rich chlorite (Hillier, 1994). On the other hand as temperature increases the CO_2 produced by the reaction of kaolinite + dolomite to chlorite + calcite is added to the vapour phase and yields in an increase of the mole fraction which requires higher temperatures for the reaction (▶ equation 4.2). The reaction will follow the curve in ▶ figure 4.24 until the miscibility curve of CO_2-H_2O is reached and no CO_2 is longer dissolved in the fluid. From burial history (▶ figure 3.8) of the sediments investigated in this study a maximum temperature of 120°C is to observe. But the formation temperature of chlorite and the following transformation to kaolinite would have taken place at much lower burial depth (< 1500 m) and temperature (80-100°C) according to petrographic investigations (compare chapter 4.2). The precipitation of an early diagenetic Mg-(Fe)-rich grain rimming chlorite may be followed by an increasing CO_2 content within the formation water. This influx pushes the reaction (▶ equation 4.2) in the stability field of kaolinite and dolomite (▶ figure 4.25) under the consumption of CO_2 and the release of H_2O. Watson et al. (2003) and May (2005) pointed out that the reaction of chlorite with CO_2 might be more reactive than the reaction with K-feldspar. But intense feldspar dissolution may be an advice for the presence of CO_2-bearing fluids (Kaszuba et al., 2003; Watson et al., 2003), too. Furthermore the reaction (▶ equation 4.2) results in a cogenetic precipitation of kaolinite and quartz (appendix A3-01H) as it is observed in the samples investigated in this study.

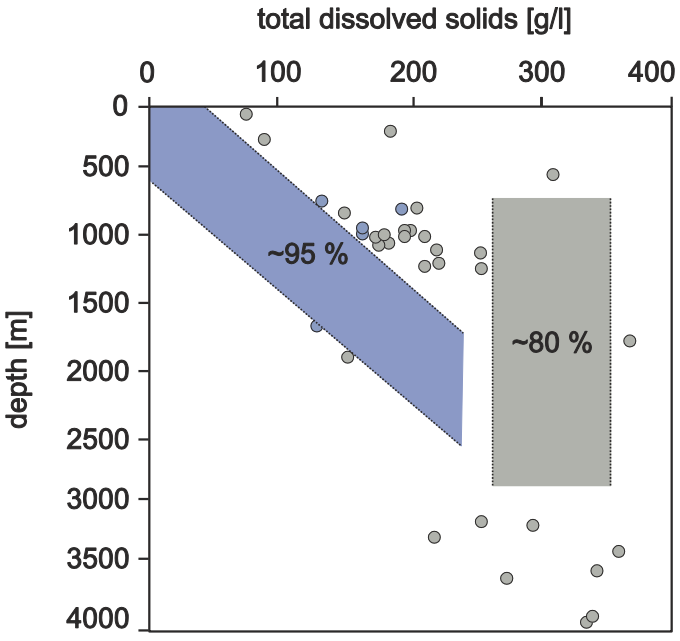

Figure 4.27: Total dissolved solids (TDS) in brines from the North German Basin of Late to Early Permian and Late Triassic to Early Tertiary age (Hoth et al., 2005; Tesmer et al., 2007). The first group show a correlation of increasing depth (up to ~2300 m) and TDS (up to ~270 g/l). Around 95 % of all samples plot within the blue box. The grey box includes ~80 % and represents a second group which is characterised by an increase of TDS up to ~300 g/l with varying depth.

The CO_2 required for the mineral reactions may have been generated from (1) the fermentation

and (2) bacterial oxidation of organic components in intercalated organic rich shale layers at shallow burial depth (Baines and Worden, 2004). (3) By decarboxylation of kerogen processes from underlying petroleum source rocks (e.g. ▶ equation 4.11) (Kharaka et al., 1985; Seewald, 2001; McCollom and Seewald, 2003), (4) as a result of precursor dissolved carbonates (Cathles et al., 1986; Baines and Worden, 2004) and (5) by bacterial sulphate reduction of hydrocarbons (Machel, 2001). A CO_2 source from the deep crust or mantle and from volcanoes seems to be insignificant for this study area due to the absence of very deep fractures and volcanic activity. However grain rimming kaolinite was formed at shallow burial depth in eodiagenesis before hydrocarbon migration (▶ figure 4.22). But precursor organic components released from underlying Carboniferous source rocks may have been migrated through the rock at this time (Gaupp, 2011, person. comm.). Based on natural gas analysis from field A 0.68 mol% CO_2 are present today (appendix C8). The mineral reactions under a possible influence of CO_2 which are described above are summarised in ▶ figure 4.28 in relation to the diagenetic evolution of the sandstones.

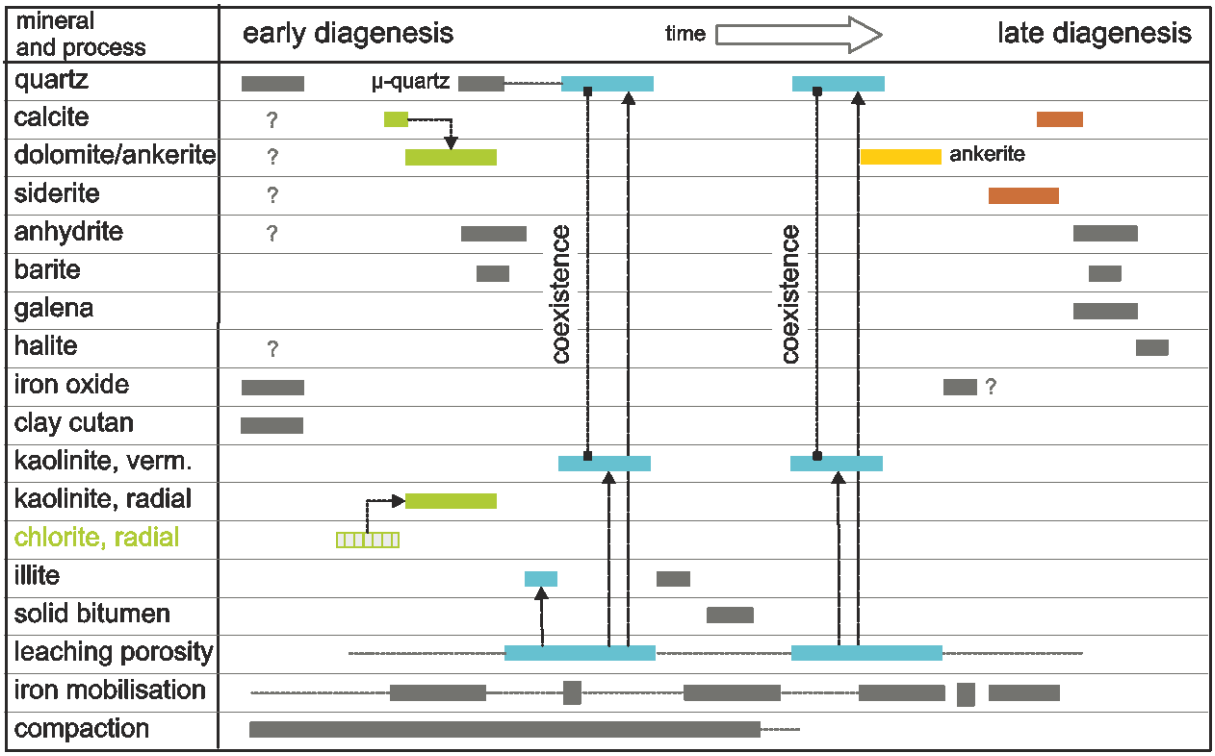

Figure 4.28: Diagenetic sequence of Rotliegend sandstones from the Upper Slochteren Formation, northern Netherlands and related possible mineral reactions under the influence of CO_2 during burial. The green coloured lines represent the transformation of chlorite/calcite to kaolinite/dolomite after Hutcheon (1980 and 1983). The blue lines stand for the correlation between K-feldspar leaching and the formation of illite and kaolinite and the related precipitation of quartz (e.g. Kaszuba et al., 2003; Watson et al., 2003). Furthermore, the precipitation of dolomite, ankerite and siderite are related to the presence of CO_2, too (e.g. Curtis, 1978). The dissolution of plagioclase may release required calcium for dolomite/ankerite precipitation. For further explanation please regard to the text.

5 Spatial mineral arrangement in porous sandstones

The fluid-rock interactions during CO_2 storage are controlled by different properties of the sandstone-fluid-CO_2 system. To estimate chemical reactions within a natural system the knowledge about the (1) total porosity (inter- and intragranular) and permeability, (2) pore geometry, size and distribution, (3) pore space connectivity, (4) distribution and accessibility of detrital and authigenic minerals, (5) mineral surface areas in exposure to open pores and (6) the chemical composition of each mineral within the sandstone is indispensable. Additionally the knowledge about the (7) fluid composition, (8) reservoir temperature, (9) water saturation of the sandstone and (10) the disequilibrium stage of the fluid in regard to the rock are important characters. For point seven to ten please regard to chapter 6.

For geochemical modelling all these parameters need to be simplified in regard to ideal mineral composition and geometry. Therefore a theoretical model of spatial sandstone reconstruction is used and specific mineral surface areas are calculated for each mineral phase present in the samples investigated.

5.1 Characterisation of porous sandstones

5.1.1 Porosity, intergranular volume and permeability

Porosity (inter- and intragranular) and horizontal permeability data derived from measurements of coarse to fine grained sandstones and siltstones were provided by NAM for field A, B and C and are listed in (▶ table 5.1) and (▶ table 5.2). The median porosity yields between 12.9 % and 17.6 %. Even 90 % of all data are equal or smaller than 18.8 % (field A), 22.6 % (field B) and 23.0 % (field C). In comparison porosities derived from point counting show slightly lower values between 1.00 % and 27.2 % (▶ table 5.3).

Table 5.1: Porosity values [%] for field A, B and C provided by NAM. The minimum, maximum and data equal or lower than a certain percentage (10, 25, median [50], 75 and 90 %), as well as the number n of data are listed.

	min	10 %	25 %	median	75 %	90 %	max	n
field A	0.80	6.96	9.50	12.9	15.9	18.8	27.4	1492
field B	0.50	12.1	15.1	17.6	20.0	22.6	31.1	1228
field C	2.00	8.30	11.9	15.1	19.8	23.0	30.0	854

This phenomenon appears especially in samples from field B and C which are dominated by grain rimming clay minerals (esp. kaolinite and illite) (compare section 4.2). It has been differentiated between intergranular (between detrital grains) and intragranular (within partly dissolved grains) porosity during point counting. Note that the assignment of oversized pores to one of the pore types is difficult. The results which are listed in ▶ table 5.3 show a median intragranular porosity for field A of 1.00 %, for field B of 3.70 % and for field C of 2.70 %. The higher values for field B and C are linked to a more intense dissolution of detrital K-feldspar and feldspar bearing volcanic rock fragments (compare section 4.1 and 4.2).

Table 5.2: Horizontal permeability [mD] values for all data from different wells for field A, B and C provided by NAM. The minimum, maximum and data equal or lower a percentage value (10, 25, median [50], 75 and 90 %), as well as the number n of data are listed.

	min	10 %	25 %	median	75 %	90 %	max	n
field A	0.01	1.30	7.20	39.0	179	490	9900	1278
field B	0	0.73	2.40	8.90	27.0	79.0	3300	1061
field C	0	0.12	0.24	0.60	2.05	6.51	206	673

Two dissolution phases are recognised for Rotliegend sediments: (1) prior or contemporaneous to kaolinite (and illite) precipitation with a subsequent hydrocarbon impregnation and (2) bitumen and kaolinite/illite free intragranular pores suggest a later dissolution stage of detrital grains (compare section 4.6.2). The intragranular porosity may again be destroyed during burial by late diagenetic mineral precipitation (e.g. clay minerals, quartz, carbonates and sulphates) or may still be open (e.g. appendix A2-02A and A2-03C). Furthermore mesodiagenetic minerals, like carbonates and sulphates (compare section 4.2.1 and 4.2.2) show dissolution patterns on the surface, visible as irregular boundaries or embayments.

Table 5.3: Intergranular (inter), intragranular (intra) and total porosity values [%] for field A, B and C derived from point counting of thin sections. The minimum, maximum and data equal or lower than a certain percentage value (10, 25, median [50], 75 and 90 %), as well as the number n of data are listed.

	field	min	10 %	25 %	median	75 %	90 %	max	n
inter	field A	1.00	4.40	6.65	11.7	17.0	22.3	26.7	21
inter	field B	0.50	3.08	4.00	6.70	10.4	12.6	15.0	27
inter	field C	5.40	6.10	8.00	10.3	14.7	18.0	22.2	23
intra	field A	0	0.10	0.50	1.00	1.50	2.56	3.30	21
intra	field B	0	0.50	2.30	3.70	4.30	4.90	6.00	27
intra	field C	0	0.50	1.30	2.70	3.70	4.72	6.70	23
total	field A	1.50	4.80	8.50	13.0	17.8	23.6	27.2	21
total	field B	1.00	5.52	8.00	10.3	13.0	16.2	19.0	27
total	field C	5.70	6.82	10.3	14.8	17.4	20.9	27.2	23

The intergranular volume reflects the compaction grade of the sandstone after burial. In combination with the present cementation grade evidence can be given if the porosity is dominantly destroyed by compaction and/or cementation (Houseknecht, 1987; Ehrenberg, 1989). The median intergranular pore volume range between 24.0 and 24.6 % and shows no significant difference between the three fields (▶ table 5.3). Only two samples have a higher intergranular volume and cement content greater than 35 vol.-% due to an intense anhydrite (Cw04-2728.3) and carbonate (Aw01-2924.52) cementation (appendix C2). Note that corrosion from carbonates against detrital grains (e.g. quartz) adulterate the true intergranular volume (appendix A2-04E). The minimum intergranular volume yields 15.6 vol.-% (▶ table 5.4). As shown in ▶ figure 5.1 for 89 % of the samples (n = 71) the destruction of the pore space is dominated rather by compaction than by cementation and only a few samples have a cement content greater than 20 vol.-%. No evidence is found for a correlation between the intergranular

volume and cement content to the depositional environment, sediment sorting, grain roundness or grain size.

Table 5.4: Intergranular volume data [vol.-%] for field A, B and C derived from point counting of thin sections. The minimum, maximum and data equal or lower a percentage value (10, 25, median [50], 75 and 90 %), as well as the number n of data are listed.

	min	10 %	25 %	median	75 %	90 %	max	n
field A	16.7	19.3	22.3	24.0	25.0	31.5	40.3	21
field B	15.7	20.8	22.6	24.6	26.7	33.0	35.4	27
field C	15.6	17.9	21.6	24.6	27.0	29.9	30.7	23

The median horizontal permeability decreases from 39.0 mD (field A) to 8.90 mD (field B) down to 0.60 mD (field C) (▶ table 5.3, ▶ figure 5.2) from the basin margin in the southwest to the basin centre located in the northeast. This development is caused by an intense cementation of samples from field B and C which is mainly because of grain rimming clay minerals like kaolinite and illite (e.g. appendix A2-03D). Field A has a median clay mineral content of 1.80 vol.-% in comparison to 7.30 vol.-% (field B) and 7.50 vol.-% (field C) (▶ table 5.5) based on point counting data. Note that the clay mineral content is difficult to determine in thin section images due to the relatively small crystal size (nm- to µm-scale).

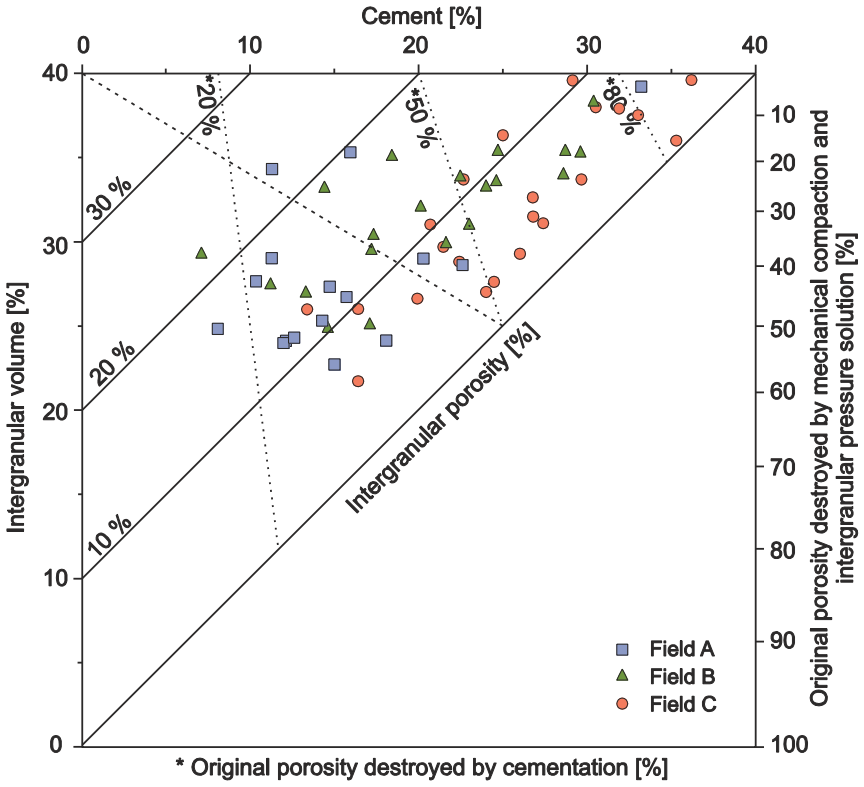

Figure 5.1: Effect of compaction and cementation on porosity of well sorted sandstones with an initial porosity of 40 % for Rotliegend samples from field A, B and C. Modified from Houseknecht (1987) and Ehrenberg (1989).

Table 5.5: Clay mineral content [vol.-%] in samples from field A, B and C based on point counting data of thin sections: The minimum, maximum and data equal or lower a percentage value (10, 25, median [50], 75 and 90 %), as well as the number n of data are listed.

	min	10 %	25 %	median	75 %	90 %	max	n
field A	0.50	0.60	1.15	1.80	3.60	5.16	5.50	21
field B	2.00	2.70	5.30	7.30	10.2	12.2	14.8	27
field C	1.00	2.28	4.40	7.50	9.80	11.2	12.8	23

The minimum permeability is found in fine grained sand- to siltstones (appendix C3) and the maximum permeability of 9900 mD is attributed to a ~20 cm thick well sorted sandstone horizon of well Aw05 in ~3253 m depth. The relatively high permeability (90 % are lower or equal to 490 mD, ▶ table 5.2) in samples from field A is due to large, well connected pores which are less cemented (< 10 vol.-%) (appendix A2-05D). On the other hand the lower permeability of median 8.90 mD for field B and 0.60 for field C (▶ table 5.2) is caused by a partly intense cementation of the sediments during burial with especially clay minerals (e.g. appendix A2-03D and F).

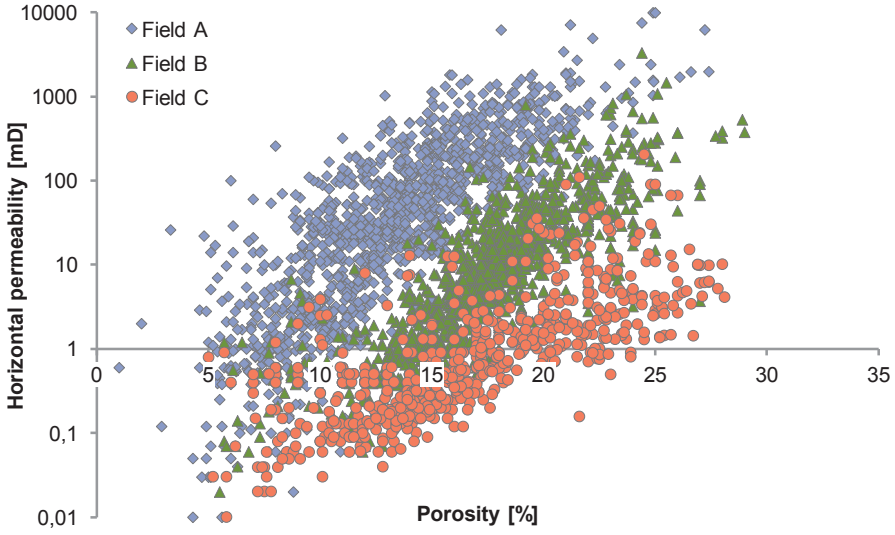

Figure 5.2: Permeability and porosity values for samples (n=3589) from the Upper Slochteren Formation northeast Netherlands separated for the fields A, B and C. Field A is located near the basin margin of the South Permian Basin and show higher permeability values than sandstones from Field B and C which are deposited further to the basin centre. The porosity ranges between <5 and ~30 %.

Interpretation

Grain rearrangement is the first process taking place after deposition of the sediment. Several authors have described this process as a repacking of grains into a closer-fitting system (Pryor, 1973; Atkins and McBride, 1992) under near-surface conditions. For a random close packing of equal spheres Scott and Kilgour (1969) defined a porosity of 36.3 vol.-% and for a random loose packing the porosity was limited to 40 vol.-% (Scott, 1960). Natural sands analysed by Beard and Weyl (1973) yield 39 vol.-% for well-sorted sands and 42 vol.-% for extremely well-sorted sands. However Pryor (1973) analysed recent sands from different dune and beach locations

and measured porosities between 39 vol.-% and 56 vol.-%, with an average of 42 vol.-%. After Houseknecht (1987) the initial porosity of a fine to medium grained, well sorted sandstone is commonly assumed to be ~40 vol.-%. This approximation is confirmed for Permian sandstones of the South German Basin by intergranular volumes of about ~40 vol.-% which are preserved by eodiagenetic cements (Gaupp et al., 1993) and can be confirmed for the samples investigated in this study. During burial diagenesis initial porosity may be (1) destroyed by precipitation of authigenic minerals and/or compaction or (2) may increase as a result of dissolution processes of detrital grains and/or cements during further burial. Deep buried sandstones (>2000 m depth) with high porosities (>15 vol.-%) and intergranular volume (>15 vol.-%) suggest an early grain stabilisation with eodiagenetic near-surface cements, like e.g. carbonates, sulphates or halite which inhibit the compaction of the sandstone. No evidence of these early cements is found in Rotliegend sediments from the Upper Slochteren formation today, which indicate intense dissolution during diagenesis. Gaupp (2005) suggested that calcite and anhydrite are affected by late dissolution caused by hydrocarbon migration into Rotliegend sediments located near Hannover. After Gaupp et al. (1993) feldspar corrosion is most distinct close to faults which displace Rotliegend sediments against Carboniferous Coal Measures and may explain the two dissolution phases. Furthermore the discrepancy between measured and point counted porosity may be due to fractures and microporosity between e.g. clay minerals which can be underestimated investigating thin sections.

Several studies were dealing with the importance of permeability in sandstones during many decades, especially for oil and gas exploration. Detailed studies of network models have shown that permeability is sensitive to pore sizes and their distribution within the sandstone and to the connectivity properties of the pore network (Constantinides and Payatakes, 1989; Bryant et al., 1993; Ioannidis and Chatzis, 1993; Latief et al., 2010). In addition permeability is mainly influenced by the presence of authigenic minerals (especially clay minerals like illite and kaolinite, e.g. Hutcheon, 1983). This may explain the significant differences between fields A, B and C.

5.1.2 Pore geometry and accessibility of minerals

For CO_2 storage the present distribution and accessibility of minerals is for preferential interest in comparison to the diagenetic evolution and will be described in the following section.

Pore description of a sandstone body and the determination of spatial distribution of minerals assume on the one hand description of the natural conditions and have to be simplified for implementation in theoretical models. Therefore different pore types and the accessibility of minerals exposed to open pore system need to be defined. According to previous pore space studies (e.g. Dullien, 1979; Brower and Morrow, 1985; Thompson et al., 1987; Bernabe, 1991; Al-Kharusi and Blunt, 2007; Nabawy et al., 2009; Amirtharaj et al., 2011) and thin section analyses of the samples investigated in this study four main categories of pore space are defined and are sketched in ▶ figure 5.3: (1) intergranular round to slightly elongated pores between three or more grains, (2) connective pores which are situated between two or more grains showing a long elongated shape and may be described as throats, (3) low connected small pores between three or more grains which have no portion to total connectivity and (4) intragranular pores with a different grade of connectivity to the intergranular pore system. 3-dimensional studies on synthetic rock analogues (e.g. hot-pressed calcite) suggest the possible existence of a further connective pore type, which can be described as tubular conduit (Bernabe et al., 1982;

Drory and Glaeser, 1985; Olgaard and Fitz Gerald, 1988). This pore type is difficult to visualize in 2-dimensional pore space images and could not be proven in the investigation of thin section images in this study.

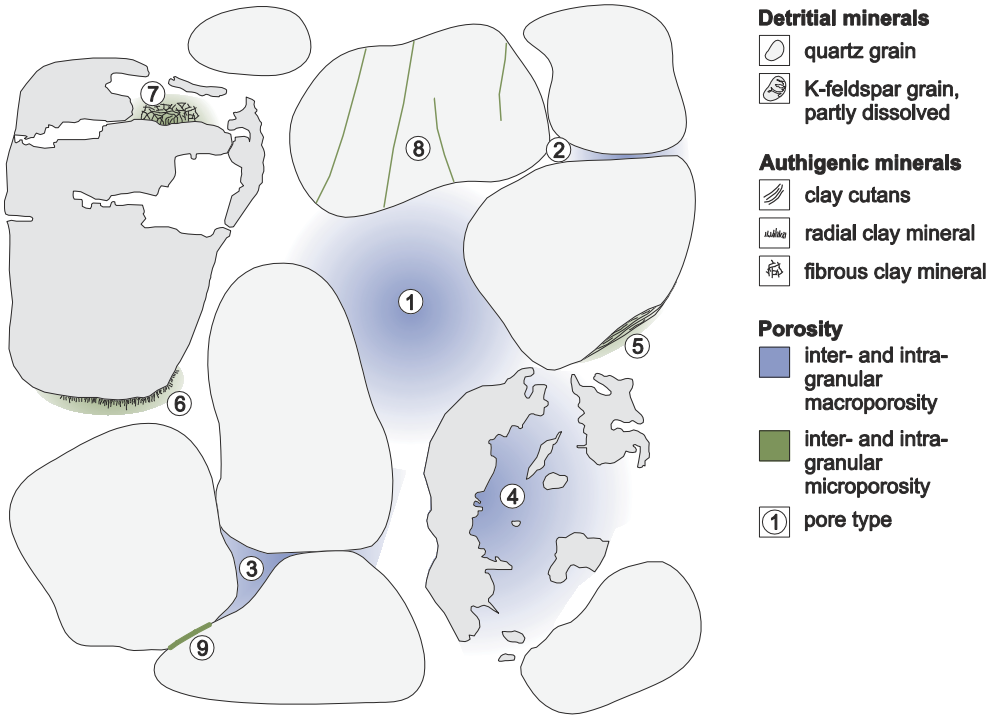

Figure 5.3: Definition of inter- and intragranular pore types for Rotliegend sandstones. Macroporosity is characterised by (1) round to slightly elongated pores between three or more grains (in parts representing oversized pores), (2) small elongated pore channels/throats between two grains, (3) pores which show none (or low) connectivity in 2D-scale and (4) intragranular macroporosity in e.g. (partly) dissolved K-feldspar grains or volcanic rock fragments. Microporosity is illustrated by using the example of authigenic illite: intercrystalline microporosity between (5) layered illite crystals (cutans) and (6) radial illite (e.g. radial rims or meshwork). (7) Represents intragranular microporosity between e.g. intragrain meshwork illite. Furthermore, microporosity is present in (8) small cracks within a detrital grain and (9) between direct contacts of two or more grains.

The different macro-pore spaces described above are only applicable for non-cemented porous sandstones with a uniform grain size. But Rotliegend sediments are highly influenced by diagenesis and mineral (re)-precipitation and dissolution processes as well as compaction during burial (compare section 4.2). According to these processes the pore shape, size and connectivity is changing over time. And with this the accessibility of minerals in contact to the open pore space and passing fluids and/or hydrocarbons. Macroporosity is most present between detrital grains, grain and cement and negligible amounts between authigenic cements like carbonates, sulphates or quartz. In subject to the clay mineral content and type within the inter- and intragranular pore space the amount of microporosity between the mineral crystals is an important parameter for the total porosity in clay rich sandstones. Wilson and Pittman (1977) defined two types of microporosity (with no specification of pore size): (1) pore lining clay minerals (e.g. illite cutan) which are located on grain surfaces and (2) intergranular pore-filling clay minerals (e.g. meshwork illite, chlorite and kaolinite). Furthermore the present study

indicates minor amounts of connected intragranular pores with authigenic clay minerals. Microprosity occurs between grain-grain contacts, grain-cement contacts, authigenic clay minerals and rarely between blocky cement crystals and within fractures of detrital grains.

As shown in section 4.1 there are only minor differences in the detrital inventory between the environments of fluvial and aeolian sandstone deposits. One important difference is the more intense feldspar dissolution in samples from field C which are located further in direction to the basin centre. Hence the distribution and accessibility of authigenic minerals regulate the availability of chemical species for water-rock interactions within the pore space. By using mineral tracing image analysis on thin section images (compare section 2.10) percentage information about detrital and authigenic minerals exposed to open pore are derived. Based on these investigations and thin section microscopy simplified mineral-pore systems which represent a typical distribution and accessibility of minerals for high permeable (> 10 mD) sandstone horizons can be classified.

Minerals in contact to open pores are defined as “effective mineralogy”. Approximately between 5.15 % (Aw04-02) and 65.2 % (Bw02-02) of the grain surface area is covered by authigenic minerals (▶ figure 5.4). These minerals are clay cutans, Fe-oxide, kaolinite, quartz, carbonate and sulphate. It is assumed that the same surface area of blocky carbonate and sulphate cements which are exposed to the pore system stay in contact to a detrital grain. Quartz minerals grow perpendicular to the grain surface area as syntaxial overgrowths and are calculated entirely as “grain covering minerals”. The mean covered grain surface area is lower for samples from field A (22.8 %) than for field B (41.5 %). This difference is caused by different authigenic minerals covering the grains. Many sandstones from field B are characterised by an intense cementation with Fe-oxides. As discussed in section 4.2.4 Fe-oxides are often overestimated in thin section analysis, but in this study a clear differentiation between (light) red to brown coloured sandstones from field B in comparison to bleached grey to very light red sandstones from field A is noted (appendix A1).

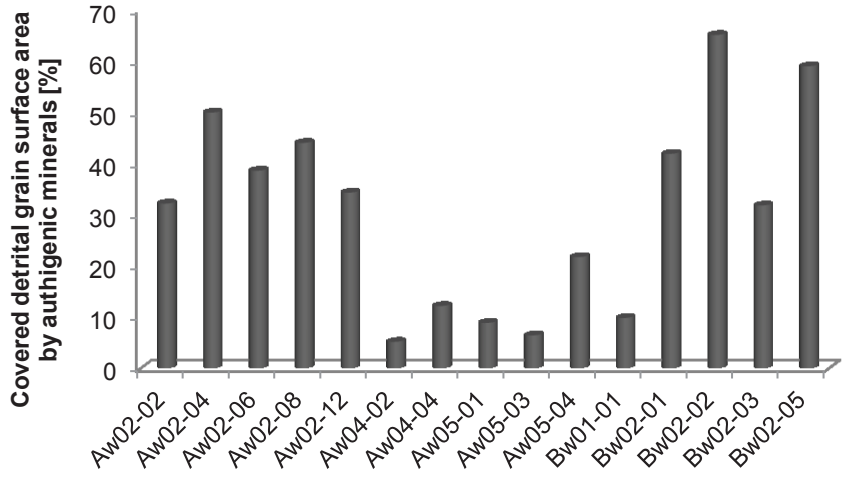

Figure 5.4: Percentage amount of detrital grains (e.g. quartz, K-feldspar) which are covered by authigenic minerals for samples investigated by pore lining image analysis (detection of the effective mineralogy).

The Fe-oxide content that covers detrital grains is with 14.7 % (field B) ~10 times higher than in samples from field A with 1.51 %. A second mineral covering grain surface areas in samples from field B is a grain rimming kaolinite (compare section 4.2.6) with a mean percentage value of 14.2 % (n = 5). The minimum yields 0.31 % (sample Bw02-05) and the maximum 47.5 % (sample Bw02-02). On the other hand samples from field A are dominated by clay cutans as grain covering minerals. The mean value yields 15.6 % for field A in comparison to 0.41 % from field B. Based on petrographic investigations lacking grain covering minerals (Fe-oxide, clay cutans, kaolinite and quartz) in samples from field A yield in a relatively high amount (52.9 %) of detrital surface areas in direct contact to the pore space (appendix A2-04F, G and H) in comparison to field B (19.8 %). Further secondary electron microscopy investigations indicate thin clay cutans intercalated with minor amounts of Fe-oxide on the grain surface areas which are not visible in thin section images (appendix A3-02G). For blocky cements like carbonates and sulphates no difference in the total amount covering detrital grains between the two fields was found. However in sample Aw05-04 anhydrite surrounds early diagenetic dolomite crystals (▶ figure 5.5). Especially for samples from the southern area of field A (well Aw05) partial intense bitumen impregnation of detrital and authigenic minerals is characteristic (appendix A2-05A, B and C). In sample Aw05-03 more than 73.0 % of authigenic and detrital minerals are impregnated by bitumen with a mean value of 18.5 % for all samples from field A (▶ figure 5.6).

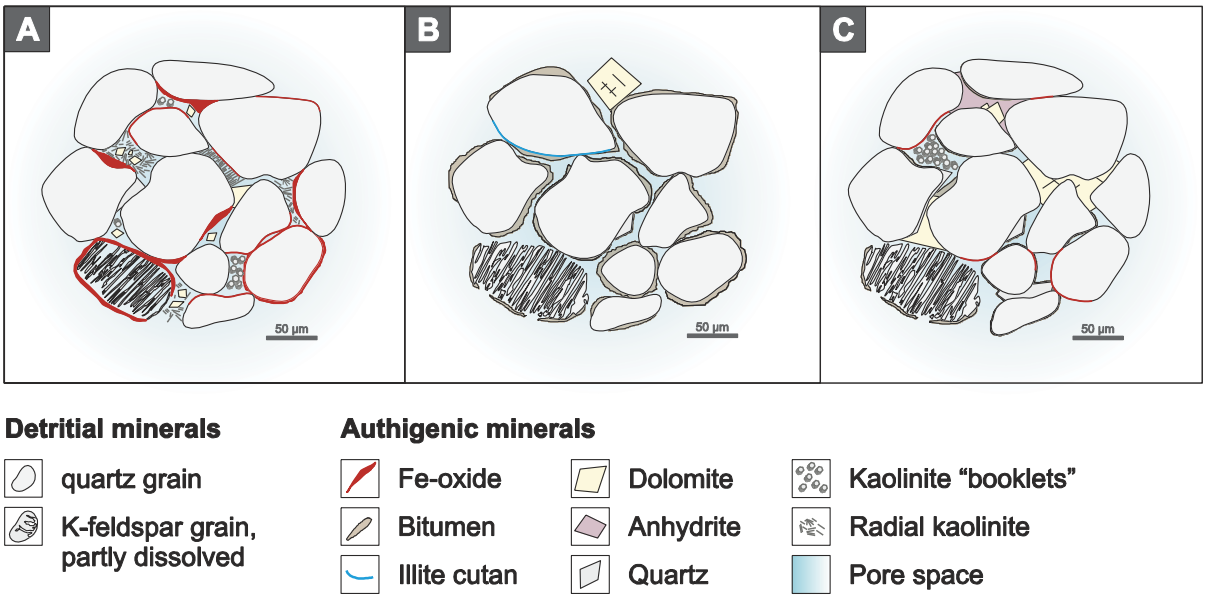

Figure 5.5: Mineral accessibility and distribution within three typical sandstone samples from field A and C. **A**: Sample Cw02-01 is characterised by partly thick Fe-oxide coatings and an intense cementation with radial and "booklet"-like kaolinite and small disperse distributed dolomite crystals. **B**: At the southern basin margin bitumen impregnation of detrital grains and authigenic minerals is common (sample Aw05-03). Dolomite precipitated after hydrocarbon migration. **C**: In the northern part of field A dolomite and a later anhydrite cement is common. Syntaxial quartz overgrowths are partly covered by bitumen. Kaolinite and illite cutans are the dominant clay minerals.

In comparison <1 % of all minerals are covered by bitumen in field B. In samples from field A early diagenetic dolomite is surrounded by ankerite/siderite (▶ figure 5.5). For this reason a direct contact between dolomite and a potential fluid/gas is uncommon since it would react with

the ankerite/siderite first. However in samples from field B and C ankerite and siderite is absent and the main carbonate reaction partner is dolomite. Where kaolinite "booklets" are present they are partly surrounded by barite or carbonate (▶ figure 4.6).

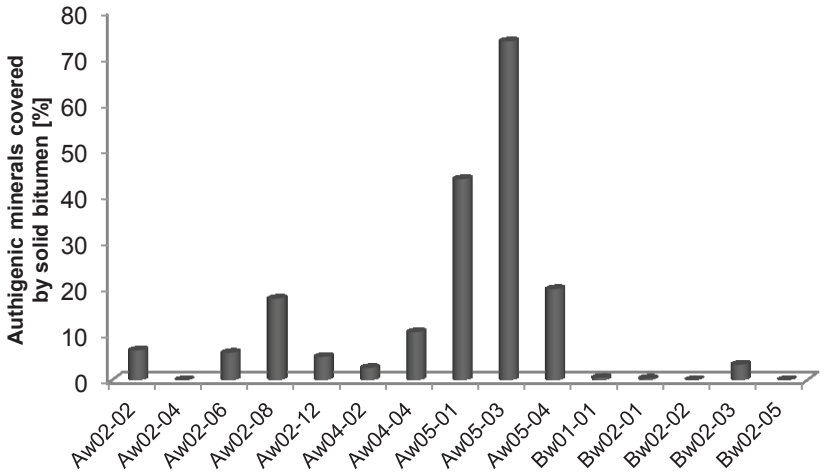

Figure 5.6: Authigenic mineral content (e.g. kaolinite, quartz) which are covered by solid bitumen for samples investigated by pore lining image analysis (detection of the effective mineralogy).

As mentioned earlier the pore shape depends on the distribution and shape of authigenic minerals. It is assumed that well connected pores are more frequent in samples with elongated large pores in comparison to intense cemented sandstones with small round pores (▶ figure 5.7).

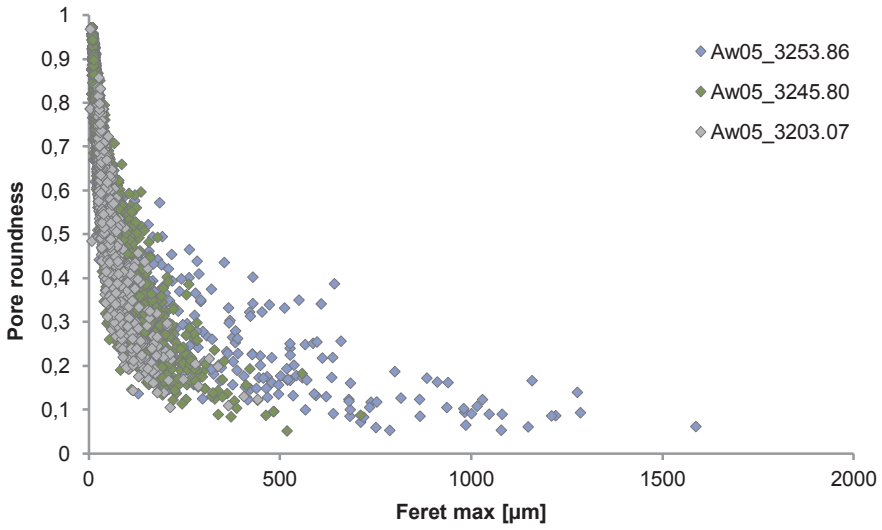

Figure 5.7: Example for the correlation between the pore size, expressed as $feret_{max}$, and the roundness (0-1) of pores. The porosity of sample Aw05-(3253.86 m) yield 25 %, Aw05-(3245.80 m) is 21 % and Aw05-(3203.07 m) is 11 %.

Therefore 2-dimensional pore space analysis (macroporosity) on thin sections was performed for high permeable sandstones (> 100 mD) from well Aw05 which is located at the southern basin margin of field A. A geometrical description of pores is the "feret maximum" which is defined as the largest distance of two tangents parallel to each other located at the pore side and the pore roundness. The pore roundness is the ratio between area and perimeter of a pore with one being equal to a circle. The example in ▶ figure 5.7 shows the dependency of the feret maximum and roundness for different sandstone porosities. For small pores (< 100 µm) negligible differences of the roundness are noted for samples with different porosities of 3.70 %, 12.0 % and 16.3 %, respectively. For larger pores (> 100 µm) the roundness becomes much more variable and decreases from 0.7 to 0.07 whereas the feret maximum increases up to 1580 µm length for sample Aw05_3253.86 with a total porosity of 16.3 % (▶ figure 5.7). In comparison the feret maximum increases only up to 440 µm length for the less porous (3.70 %) sample Aw05_3203.07. These differences may be due to the amount of authigenic minerals. Sample Aw05_3203.07 is characterised by a relatively high amount of carbonates (10.7 vol.-%) in comparison to 4.30 vol.-% (Aw05_3245.80) and 2.70 vol.-% (Aw05_3253.86) (▶ table 5.6).

Table 5.6: Authigenic mineral content [vol.-%] and porosity [%] for three samples from well Aw05 based on point counting investigations of thin sections.

sample	quartz	clay cutan	anhydrite	carbonate	kaolinite	porosity
Aw05_3203.07	3.00	1.30	0	10.7	1.00	3.70
Aw05_3245.80	1.70	3.70	0	4.30	3.30	12.0
Aw05_3253.86	3.70	1.00	1.00	2.70	3.30	16.3

Interpretation

For natural porous media, like e.g. sandstones the pore space constitution is mainly influenced by the initial sandstone composition (e.g. grain size and shape), the grade of sediment compaction as a result of burial and by the presence of authigenic minerals. These parameters directly determine the pore geometry, size and distribution within the sandstone and therewith the connectivity and tortuosity. Dissolution processes of detrital and authigenic minerals during further burial diagenesis will supply additional inter- and intragranular pore space. The sum of these processes influence the accessibility of minerals within the sandstone body. Hence late diagenetic precipitates (▶ figure 4.22) like siderite, quartz and anhydrite are present in the residual pore space and stay in contact to open pores. In comparison early cements may be dissolved during burial diagenesis or are blocked by later cements. Hence a detailed study of the processes taking place during diagenesis is indispensible for estimation of fluid-rock interactions over time.

5.1.3 Discussion of the distribution of pore types and the accessibility of minerals

Interconnected pores represent the *effective porosity*, whereas the sum of closed pores is called *ineffective porosity* (Smith et al., 2003). Generally, the pores are well connected and ineffective porosity is negligible in sandstones. This is especially the case for loose packed sandstones with low grades of compaction and low authigenic mineral contents. For sandstones with e.g. an early diagenetic blocky cement of carbonate or sulphate the amount of ineffective pores will increase.

In Rotliegend sandstones grain coating clay cutans, Fe-oxides and -hydroxides are a common feature (e.g. Gaupp et al., 1993). These thin layers (maximum thickness of ~15 µm, this study) may act as diffusive pathways between compacted detrital grains. Based on this assumption a more detailed consideration of ineffective pores is recommended. If the transport of dissolved components within the fluid is possible through such micropores there will be no ineffective pores on a long time scale. Between grain-grain contacts an adsorbed water film may be present where solutes can be transported in the pore fluid by diffusion (Rutter, 1976; Spiers and Brzesowsky, 1993; Renard and Ortoleva, 1997). But the thickness of the water film depends on the lithostatic and hydrostatic pressure as well as on the water saturation within the sandstone body (Renard and Ortoleva, 1997). For field A the top Rotliegend is located between 2850 m and 3100 m depth (Praagman and Snijder, 1988) under a hydrostatic pressure of 285 bar to 310 bar before gas production. Using the mean rock density of 2.65 g/cm^3 (for quartz) the lithostatic pressure ranges between 755 bar and 821 bar. For field A the reservoir pressure developed from 320 bar to 10 bar during gas production (Post, 2010, person. comm.), which results in an effective pressure (P_{lith}-P_{hydro}) between 745 bar and 811 bar today. The water film thickness Δ is a constant ($5.0*10^{-08}$) divided by the effective pressure (Renard and Ortoleva, 1997) and yield between 0.62 Å and 0.67 Å for the given example (▶ figure 5.8). But the size of a CO_2 molecule is with 3.23 Å over four times larger than the thickness of the water film between two grains. Based on these results the water film could not function as a diffusion pathway for molecules or other species. But even if the water film would be thick enough at some places the diffusion coefficient would be relatively low. For a water film in quartzite aggregates the grain boundary diffusion coefficient (D) of ^{18}O is $2.52*10^{-09}$ m^2/sec at 100°C (Fukuda et al., 2009). Hence chemical reactions can only be expected in the attached water present in larger pores between detrital grains.

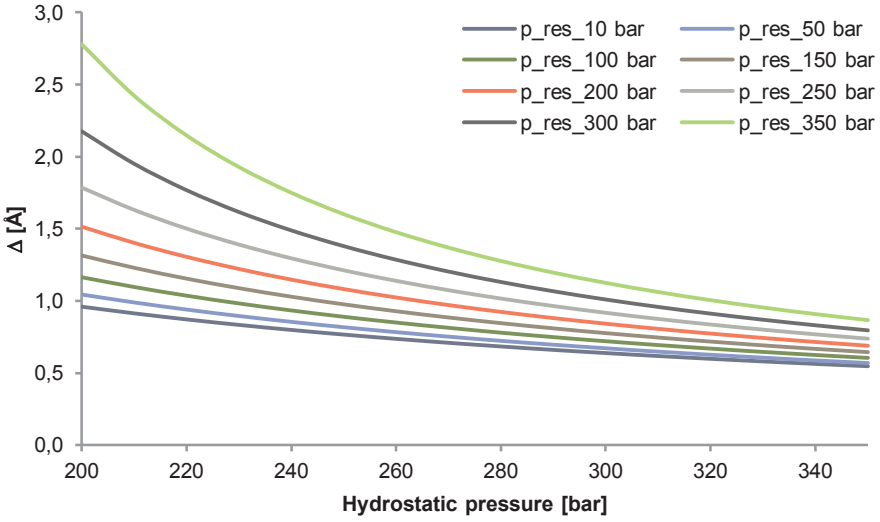

Figure 5.8: Water film thickness [Å] between grain-grain contacts for different hydrostatic pressure (200 to 350 bar) and reservoir pressure (10 to 350 bar). Calculations adapted from Renard and Ortoleva (1997).

The accessibility of minerals exposed to open pores was further studied by Peters (2009) for the Viking sandstones (Alberta sedimentary basin, Canada). The author demonstrated the accessibility of minerals in sedimentary rocks by an imaging study of backscatter electron

images with a processing algorithm which was integrated within MATLAB (The Mathworks Inc.) However the images were analysed by Peters (2009) due to different grey intensities. Hence several minerals need to be summarised to four groups because of their similar grey intensity in backscatter electron images. Only quartz and the pore space could be assigned to one defined grey scale. The total quartz content of ~73 vol.-% decreases to ~17 % which stays in contact to open pores. This result is in a good agreement with this study and performance of effective mineralogy determination.

Furthermore mineral precipitation and/or dissolution rates are directly correlated to the pore size distribution in porous sandstones (Putnis et al., 1995). The results are based on observations in sandstones without any authigenic clay minerals. With decreasing pore size the ratio of the surface area to volume will increase (Emmanuel et al., 2010) if the pores are not cemented during diagenesis. Hence the effective solubility of minerals is directly controlled by the dimension of the voids due to interfacial energy effects on the nm-scale which will lead to a more rapid mineral dissolution. On the other hand the supersaturation in a fluid required for mineral precipitation is higher for small pore sizes (Putnis and Mauthe, 2001).

5.2 Theoretical sandstone reconstruction for geochemical modelling

According to geochemical modelling Gaus et al. (2008) summarised the results of five research groups who worked on a simulations for a Norwegian saline aquifer CO_2 storage project (Sleipner project). The authors pointed out that on the one hand the difference between the results are related to different software codes and on the other hand by differences in the mineralogical assemblage and defined mineral surface areas of each mineral phase. The rate law in geochemical simulations is directly related to the reaction rate of a mineral and to the surface area in contact to the aqueous phase. Therefore, Gaus et al. (2008) conducted that the reactivity and distribution of specific mineral surface areas is an important factor for chemical reactions. The total surface area of a rock can be measured by e.g. low-pressure nitrogen adsorption using the BET analysis. But the assignment to different mineral phases within the rock is difficult and requires a detailed petrographic work. Even then, it is difficult to estimate the true mineral surface area. Hence theoretical models are always an approximation to the real mineral surface area.

This simplification of a relative complex and heterogeneous sandstone system is a common procedure in spatial sandstone reconstruction models where all grains are assumed to be equal spheres. The reconstruction and behaviour of granular assemblages are studied in several disciplines, like physics, material sciences, powder technology, geotechnique, geosciences and soil sciences. There, two theoretical approaches are pursuing: (1) process-based numerical simulation of object-based particle packing (e.g. compaction), also known as discrete element model and (2) a static reconstruction of (realistic) porous media. The second model type is mainly focused on acquiring a realistic end-product, where the boundary conditions can be used for fluid flow simulation, electric conductivity and mechanical strength of granular assemblages. In geosciences the second model is the most important one to describe burial related processes, like e.g. compaction and cementation (e.g. Scott, 1960; Bernal and Mason, 1960; Scott and Kilgour, 1969; Finney, 1970; Bradley, 1980; Roberts and Schwaartz, 1985; Bryant and Pallat, 1996; Bakke and Øren, 1997; Uri et al., 2004; Latief et al., 2010). Several processes influence the composition and packing of sediments during deposition and further burial diagenesis. The main variables are given by Giles (1996): the mineralogy of detrital grains, initial rock texture,

sedimentation rate, vertical effective stress, type of pore fluid, temperature, time, maximum burial depth and cementation processes. All these parameter have a directly (e.g. compaction) or indirectly (e.g. among other parameters the temperature is controlling precipitation and/or dissolution of detrital and authigenic minerals) influence on the total sandstone porosity (Giles, 1996). A 3-dimensional sandstone model which contains all processes, and is time depended, does not exist. Hence theoretical models include only a few parameters. Standards analysis for random packing were set by Scott (1960), Bernal and Mason (1960), Scott and Kilgour (1969) and Finney (1970). Bradley (1980) designed a simple theoretical model based on regular equal spheres where the porosity was reduced by coating the spheres with additional material. The model was used to approximate the relationship between porosity and permeability, conductivity and formation factors. Based on these first assumptions Roberts and Schwartz (1985) developed the theory to analyse the electric conductivity for ordered and disordered equal spheres. The disordered packing simulation is based on the so called "Bernal distribution" (after Bernal, 1960) which describes the coordinates of the particle centres for a dense random packing. Some reconstruction models are build for sedimentation processes: e.g. simple sedimentation simulation was performed by Visscher and Bolsterli (1972). Schwartz and Banavar (1989) investigated the transport properties of granular packing and Coelho et al. (1997) used a model with sequential deposition of non-spherical particles. In contrast Pilotti (2000) simulated the interaction of falling with already settled grains. The grain shape could be adapted after the sedimentation process was finished. In laboratory Finney (1970) constructed a random packing of equal spheres. This theory was used in further studies by Bryant et al. (1993) and Bryant and Pallat (1996) to generate a network of pores, throats and spheres for modelling diagenetic processes. Based on numerical simulation of the main sandstone forming processes (sedimentation, compaction and diagenesis) Bakke and Øren (1997) performed fluid flow simulation on a theoretical model. The authors compared simulated thin sections with results derived from sandstone analysis and aligned the data among each other until statistical properties (e.g. petrographical and geometrical) are the same. The data are generated for a 3D model with the same properties as simulated for thin sections. The results of capillary pressure and relative permeability were compared with experimental data and show a good agreement. Other experiments are dealing with soft grains which have the ability to deform during a compaction experiment (Uri et al., 2004). Latief et al. (2010) reconstructed a 3D model of the Fontainebleau sandstone based on investigations of crystallite properties and diagenetic parameters from 2D images. The authors showed that a continuum geometrical modelling approach for quantitative microstructure statistic is in a good agreement to experimental µ-CT images.

For geochemical modelling (compare chapter 6) using the software code PHREEQCi (Parkhurst and Appelo, 1999) the specific surface area of each mineral phase is required. To get an overview how the specific surface area changes according to e.g. different mineral sizes a theoretical model is created based on the assumption that all grains are equal spheres and that all authigenic minerals are equal distributed within the sandstone. The results are compared to petrographic investigations of Rotliegend samples from field A which will be included in the geochemical model for the effective and volumetric mineralogy. Based on the consideration of different mineral morphologies (e.g. platy kaolinite, detrital grains) correction factors for mineral lengths (CF_{length}) along a defined straight line can be calculated. This information is useful for the determination of effective mineralogy in thin sections because they reflect the difference of a straight line to a more realistic surface area.

5.2.1 Definition of mineral surface areas

The characterisation of surface areas is described by mathematical terms and is always a theoretical model. These models are based on calculations of ideal cubes or spheres which build up the theoretical volume. In real samples, like e.g. sandstones, claystones or loose powders the real surface area value is influenced by irregularities of particle size and shape, as well as porosity. Furthermore roughness and other imperfections may influence the total surface area, which will be larger than the corresponding mathematical model.

Different theoretical assumptions are described in literature for surface area calculation (Lüttge and Arvidson, 2008): (1) geometric surface area, (2) total or BET surface area, (3) specific surface area and (4) the reactive surface area. Geometric surface areas (A_{geom}) of authigenic and detrital minerals are described by an ideal geometrical body, expressed as a sphere, cube or rhombohedra. These models do not consider any influence on grain surface roughness or topography. Such irregularities on mineral surface areas are summarised to yield a total surface area (A_{total}) characterisation. Therefore Helgeson et al. (1984) introduced the surface roughness term λ (▶ equation 5.1).

$$\lambda = \frac{A_{total}}{A_{geom}} \tag{5.1}$$

After Lüttge and Arvidson (2008) the total surface area with several small pits or pores is not necessarily larger than a plane mineral surface area with only one or two large pits. For nearly all methods (e.g. AFM – atomic force microscopy, VSI – vertical scanning interferometry) surface roughness estimation is always problematical and highly defective. The only sensible measurement for the total surface area determination is the so called BET-method after Brunauer et al. (1938). The far-from-equilibrium dissolution rate of a mineral phase is assumed to be proportional to the reactive surface area (Lasaga, 1981; Aagaard and Helgeson, 1982; Oelkers, 2001). But it is generally not possible to measure the reactive surface area for each mineral phase individually within a volume specific rock sample. Hence BET-analysis is often used to quantify mineral dissolution rates for geochemical models, but always underestimate the true mineral surface area.

5.2.2 Theoretical calculations of specific mineral surface areas

For specific mineral surface area calculation a theoretical model is created based on different simplifications of a heterogeneous sandstone system. Spatial sandstone reconstructions include only a few parameters and are based on the assumption that all grains are spheres of equal size (e.g. Bakke and Øren, 1997). This assumption is not comparable to the sandstones investigated in this study. The grains are well to partly (sub)-rounded and very well to very poorly sorted fluvial and aeolian deposits (appendix C2). However for specific surface area calculations a spatial sandstone reconstruction is more applicable. For the model used in the following calculations it is assumed that grain contacts between the spheres are absent. Based on thin section analysis mainly point and length-length grain contacts are present (appendix C2) and can be neglected. Furthermore investigations of backscatter electron images indicate that thin (<10 µm in diameter) pathways between detrital grains (without clay cutans and/or other authigenic minerals on their grain surface areas) are open and not cemented during diagenesis (appendix A2-05E). In ▶ figure 5.9 the transformation of 2-dimensional information (e.g. grain size, mineral distribution) from thin sections into a 3-dimensional system is sketched.

Figure 5.9: Sketch for the transferability of 2-dimensional information (e.g. grain size) into a spherical sandstone model with authigenic minerals covering the grain surface areas.

Detrital grains

The most abundant detrital grains are quartz and K-feldspar. Rock fragments are presented by felsic volcanic grains which consist of quartz-feldspar (Lv_{fel}) and quartz-feldspar-mica (L_{QFM}) textures (appendix C2). From image analysis of backscatter electron images percentage information of the quartz and K-feldspar content within volcanic rock fragments are gathered (▶ figure 5.10).

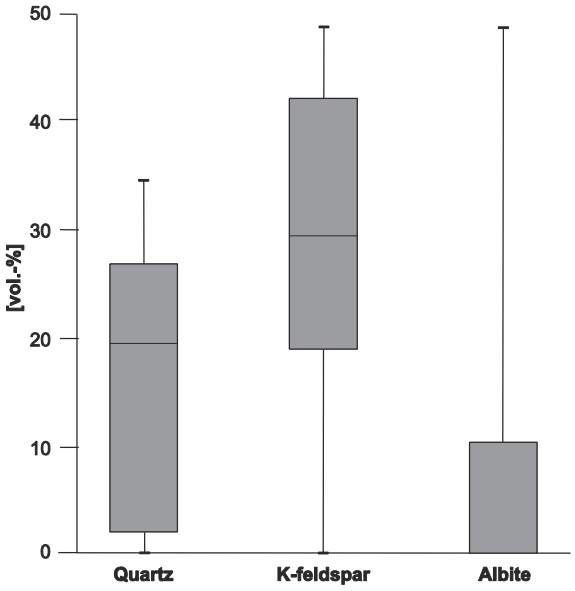

Figure 5.10: Box-Whisker-Plot of the main composition of volcanic rock fragments for quartz, K-feldspar and albite derived from image analysis of backscatter electron images (n=22). Negligible amounts of e.g. apatite and mica are not considered.

The results show that the grains consist of varying amounts of quartz, K-feldspar and albite. Since the total albitisation of K-feldspar is negligible it is assumed that volcanic rock fragments consist of ~50 % quartz and ~50 % K-feldspar. These amounts are added to the quartz and K-feldspar content, respectively. Minor amounts of minerals like apatite and mica are assumed to be negligible. Less common and disregarded in the model are basaltic grains with a pohphyric texture, sedimentary lithoclasts, carbonate clasts, metamorphic rock fragments, intraformational mud flakes and plagioclases (compare section 4.1). Monocrystalline quartz, polycrystalline quartz and chert are summarised to quartz. The amount of authigenic quartz is relatively low (mean <2 vol.-% for all samples (appendix C2)) and is added to the detrital content.

According to secondary image analysis detrital **quartz** grains show only minor dissolution voids on the surface areas which are less than a few nanometer deep (appendix A3-01A). Therefore quartz is assumed to have a plane surface area and a spherical shape. The specific surface areas of spheres are calculated based on a mean grain diameter for each sample (▶ table 5.7) after ▶ equation 5.2.

Table 5.7: Grain diameter [ø] of samples investigated in pore lining image analysis and related surface area [A], volume [V] and specific surface area calculation [SSA].

sample	ø [µm]	A [m^2]	V [m^3]	SSA [m^2/g]
Aw02-01	178	9.95E-08	2.95E-12	1.28E-02
Aw02-02	174	9.54E-08	2.77E-12	1.31E-02
Aw02-04	192	1.16E-07	3.72E-12	1.19E-02
Aw02-06	194	1.18E-07	3.81E-12	1.18E-02
Aw02-08	320	3.22E-07	1.72E-11	7.13E-03
Aw02-12	225	1.59E-07	5.96E-12	1.01E-02
Aw02-08	320	3.22E-07	1.72E-11	7.13E-03
Aw04-02	117	4.32E-08	8.43E-13	1.95E-02
Aw04-04	249	1.95E-07	8.09E-12	9.16E-03
Aw05-01	422	5.59E-07	3.93E-11	5.41E-03
Aw05-03	263	2.17E-07	9.51E-12	8.68E-03
Aw05-07	250	1.96E-07	8.18E-12	9.13E-03
Bw01-01	195	1.19E-07	3.88E-12	1.17E-02
Bw02-01	171	9.19E-08	2.62E-12	1.33E-02
Bw02-02	108	3.66E-08	6.60E-13	2.11E-02
Bw02-03	153	7.35E-08	1.88E-12	1.49E-02
Bw02-05	230	1.66E-07	6.37E-12	9.92E-03

$$SSA_{quartz} = \left(\frac{1}{(V_{sphere} * \delta_{quartz})}\right) * A_{sphere} \quad (5.2)$$

For different grain sizes (100 to 500 µm in 10 µm steps) the specific surface areas are calculated and range between 2.3*10^{-02} and 4.6*10^{-03} m^2/g. The relation is expressed by the equation y = 2.3*x^{-01} (▶ figure 5.11) for R^2 = 1. The specific surface area calculations for quartz grains investigated in this study result in a minimum value of 5.4*10^{-03} m^2/g for a grain diameter of 117 µm and a maximum value of 2.0*10^{-02} m^2/g for a grain diameter of 422 µm (▶ figure 5.11). No correction factor (CF_{length}) is defined for quartz grains because they are assumed to have a plane surface area.

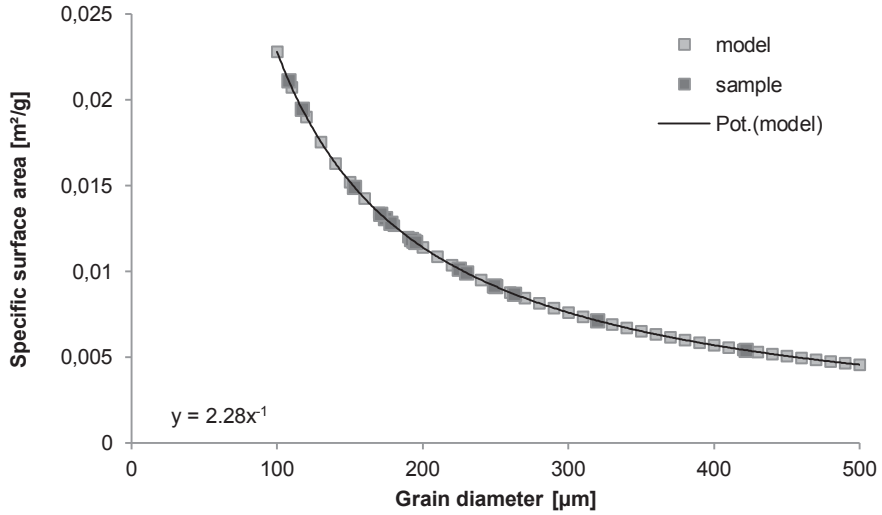

Figure 5.11: Grain diameter [µm] versus the specific surface area [m^2/g] for different diameters of detrital quartz grains from field A (n = 11).

For **K-feldspar** grains the assumptions as they are made for quartz are not applicable in all cases. Some grains show only shallow dissolution voids which are negligible for the model, but around 20 % of the K-feldspar grains are replaced by authigenic minerals like dolomite, ankerite, siderite, anhydrite or barite or show a (partly) intense illitisation or kaolinitisation (compare section 4.2.5).

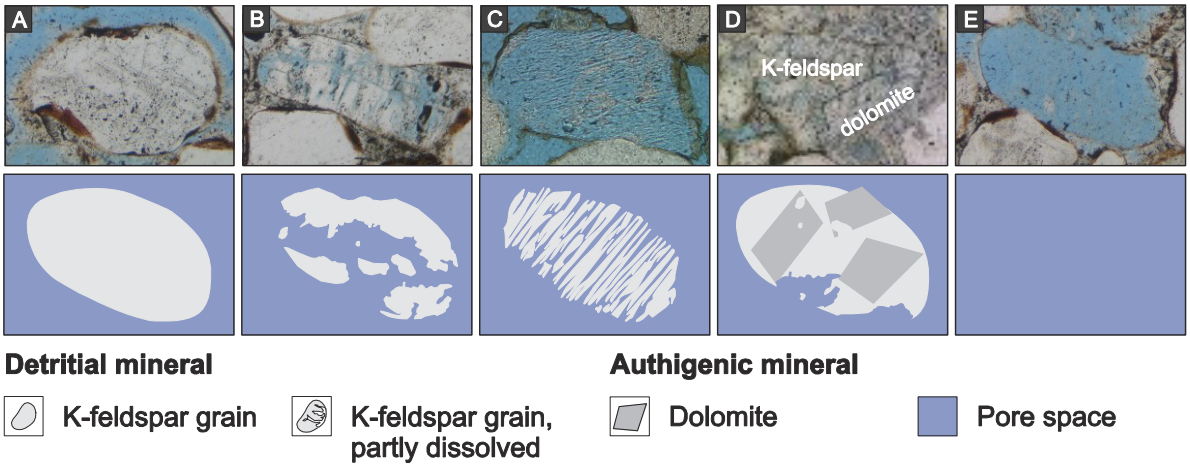

Figure 5.12: Feldspar dissolution types in Rotliegend sandstones. A: undissolved detrital K-feldspar grain; B: irregular dissolution; C: partial dissolution along fissures; D: replacement by e.g. carbonate or sulphate; E: complete dissolution and formation of an oversized pore.

These K-feldspar grains are handled as undissolved equal spheres with a plane surface area. Otherwise deep dissolution voids are present either along fissures or appear as irregular structures without any preferred orientation (▶ figure 5.12). In both cases the surface area increases in comparison to an undissolved grain. The estimation of surface areas in thin sections and in secondary electron images of partial dissolved feldspar grains is difficult. Therefore a

theoretical model is created for specific surface area calculations based on equal spherical grains and different dissolution grades along fissures (▶ figure 5.13).

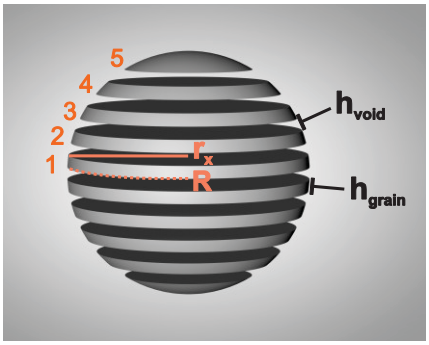

Figure 5.13: Sketch of a partly dissolved detrital K-feldspar grain along fissures and separation in equal grain slices (h_{grain}) with voids (h_{void}) in between. Radius R is the radius of the sphere at the bottom of the grain slice 1. And r_x represents the top of slice 1 and simultaneously the bottom of the void between slice 1 and 2.

A K-feldspar sphere with a mean arbitrary diameter is assumed to dissolve along fissures with regular arranged pairs of the residual K-feldspar grain and the void in between. The number [n] of grain-void pairs is calculated over ▶ equation 5.3 with a radius R of the sphere and h as the thickness of the residual grain (h_{grain}) and the void (h_{void}) in between, respectively. The number of slices is rounded, so partial slices are missing in the final calculation.

$$n = \left(\frac{R}{(h_{grain}+h_{void})}\right) * 2 \tag{5.3}$$

Equations for the description of spherical segments are used starting with r_x is equal to R where r_x is the bottom radius of the first grain-void pair and r_{x+1} the top of the grain segment expressed by ▶ equation 5.4 (▶ figure 5.13).

$$r_{x+1} = \sqrt{{r_x}^2 - {h_{grain}}^2 - \sqrt{R^2 - {r_x}^2} * 2 * h_{grain}} \tag{5.4}$$

Using the result of r_{x+1} the radius r_{x+n} with n > 1 of further grain segments can be calculated until the top of the last grain-void pair is reached. For each grain segment the surface area A (▶ equation 5.5) and the volume V (▶ equation 5.6) are calculated and summarised.

$$A = \pi \left(2 * R * h_{grain} + {r_x}^2 + {r_{x+n}}^2\right) \tag{5.5}$$

$$V = \frac{\pi * h_{grain}}{6}\left(3 * {r_x}^2 + 3 * {r_{x+1}}^2 + {h_{grain}}^2\right) \tag{5.6}$$

A mean grain diameter of 100, 200 and 250 µm and thicknesses for h_{grain} and h_{void} between 0.1 µm and 30 µm was chosen as input data based on petrographical results. For a diameter of 250 µm the results are plotted in ▶ figure 5.14. In total 3878 variations of the thicknesses of h_{grain} and h_{void} are calculated and result in $R^2 = 0.98$ with $y = 78.0*x - 0.60$. The specific surface area is highly variable for the number of grain-void pairs smaller than 20, resulting in 0.001 m^2/g to 0.8 m^2/g surface area of one sphere. An undissolved sphere has a specific surface area of $9.4*10^{-03}$ m^2/g (▶ figure 5.14) and is ~16 times smaller than the mean surface area calculated for K-feldspar grains dissolved along fissures for samples investigated in this study. Therefore secondary electron microscopy images are analysed referring to the thickness of residual feldspar grains and voids in between (appendix A3-02E). The specific surface area for grains with thicknesses for h_{grain} and h_{void} between 1 µm and 10 µm for a regular void-grain distribution

(h_{grain} = h_{void}) ranges between 0.09 to 0.40 m^2/g and a mean value of 0.15 m^2/g (▶ table 5.15). Based on thin section analysis it is assumed that ~50 % of the K-feldspar grains are partly dissolved, either along fissures or without any preferred orientation. The residual amount of ~50 % is assumed to be undissolved and the specific surface area is calculated for a sphere. No calculations are performed for an irregular K-feldspar dissolution because of the mathematical difficulties for irregular structures. The definition of a correction factor for pore lining image analysis is difficult because of the high variability of K-feldspar dissolution grades. On the one hand an undissolved grain has a correction factor of 1 whereas an intense dissolved grain has a CF_{length} >1.

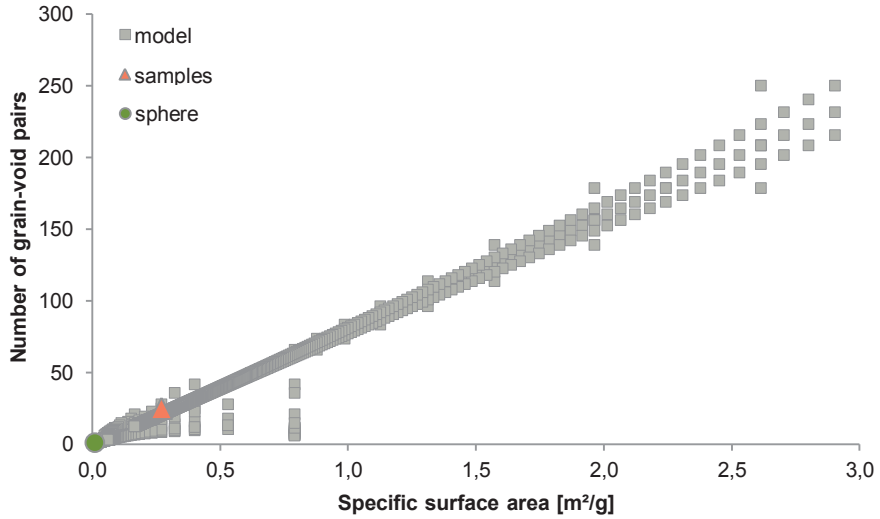

Figure 5.14: Diagram for theoretical calculated specific surface areas [m^2/g] of K-feldspar grains (diameter is 250 µm) dissolved along fissures in comparison to an undissolved sphere (green circle) and samples (orange rectangle) investigated in this study.

Grain covering authigenic minerals (illite cutan and Fe-oxide)

Detrital grains are frequently (or completely) covered by authigenic minerals like clay cutans (mainly illite), Fe-oxides, grain rimming kaolinite and/or meshwork illites (appendix C2). Minerals like carbonates, sulphates, quartz and vermicular kaolinite precipitates in the free pore space but stay in contact to neighbouring grain surface areas. In some cases these minerals may enclose the detrital grain and optionally other authigenic minerals (compare section 5.1.2).

Illite coatings and Fe-oxides are forming a dense cluster of tangential orientated minerals parallel to the grain surface area and are inherited from eodiagenesis (appendix A3-02G). Thin (nm-scale) fibrous illite crystals are growing perpendicular from the illite coating into the pore space and are smaller than 1 µm in size. Hence for a specific surface area calculation it is assumed that all illite is tangentially oriented and that these small illite crystals are negligible (CF_{length}=1). The coatings range between 1 µm to 15 µm thickness. For calculating the specific surface area of each mineral a mean thickness of 10 µm is assumed and has been calculated for a spherical shape (▶ figure 5.15). For a theoretical model for different grain sizes (100 to 500 µm) the specific surface areas range between $2.6*10^{-2}$ and $3.6*10^{-2}$ m^2/g (▶ figure 5.11).

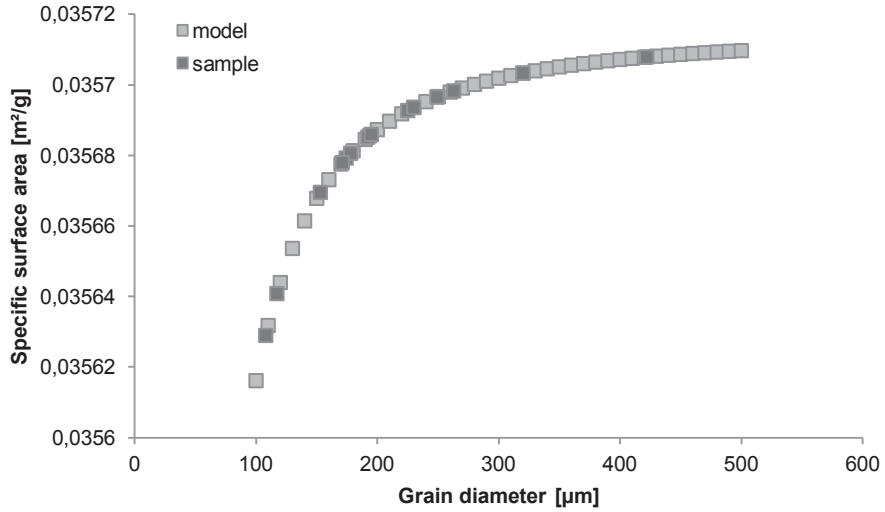

Figure 5.15: Grain diameter [µm] for different diameters of detrital grains versus the specific surface area [m^2/g] for illite coatings with a thickness of 10 µm calculated for a spherical shape.

For the samples investigated in this study the specific surface areas yield $3.56*10^{-2}$ to $3.57*10^{-2}$ m^2/g. Fe-oxide microcrystal are spatially distributed and are situated in-between the illite layers. The single aggregates are smaller than 2 µm in diameter (appendix A3-02G). Note that Fe-oxides are always overestimated in thin section analysis due to the intense red-brown colour of the mineral. The specific surface area for an assumed discoid shape ranges between 3.13 and 31.2 m^2/g (▶ table 5.16). Due to the spatial distribution of Fe-oxides within clay cutans the correction factor (CF_{length}) is 0.4.

Kaolinite

The shape, distribution and origin of authigenic kaolinite are discussed in section 4.2.6. For specific surface area calculations two main types are selected: (1) grain rimming and (2) vermicular kaolinite. Sheaf-like kaolinite is disregarded for theoretical surface area calculations because they are special cases of grain rimming kaolinite. Kaolinite is formed by the linkage of $(Si_4O_{10})^{4-}$ with SiO_4 tetrahedra in a hexagonal array. Ending oxygens and additional $(OH)^-$ ions form the base of a gibbsite-type layer with $(OH)_6$-Al_4-$(OH)_2O_4$. This arrangement forms a hexagonal structure in [001]-direction with a structural formula of $Al_4Si_4O_{10}(OH)_8$ (Deer et al., 1992). For kaolinite surface area calculation the framework has to be idealised based on the following assumptions: an ideal hexagonal structure with a parallel orientation, the same thickness at each location of the kaolinite crystal, no tilting and no rotation for kaolinite "booklets". For grain rimming kaolinite an ideal structure and the same thickness and size for each calculation step is necessary. The specific surface area of kaolinite depends on the crystal size and thickness. Based on secondary electron microscopy investigations different crystal sizes are measured for a theoretical model which represents a realistic data set for Rotliegend samples from the northeast Netherlands. ▶ Figure 5.16 shows an idealized kaolinite "booklet" with geometrical parameters for specific surface area calculations.

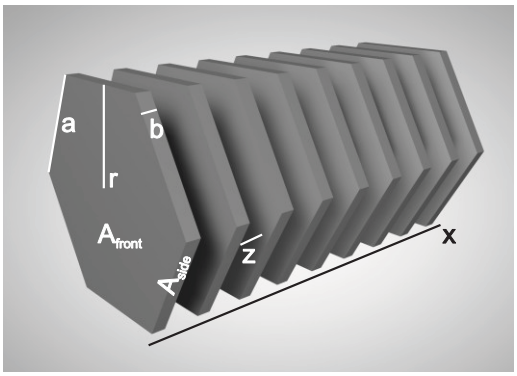

Figure 5.16: Sketch of idealized hexagonal kaolinite crystals which are arranged as a "booklets". A_{front} is the surface area in [001]-direction and A_{side} in x-direction. The radius *r* is the distance between centre and line a. The thickness is marked as *b* and length *x* is the sum of all kaolinite crystals in one "booklet" with equal distance *z* in between.

The total surface area of one kaolinite is the sum of the surface areas in [001]-direction (A_{front}) and the surface areas in x-direction (A_{side}) which can be calculated using ▶ equations 5.7 to 5.9:

$$A_{front} = \frac{c}{2} * r^2 * sin\frac{360°}{c} \tag{5.7}$$

$$A_{side} = b * \frac{A_{front}}{3r} \tag{5.8}$$

$$A_{one\ kaolinite} = 2 * A_{front} + 5 * A_{side} \tag{5.9}$$

Where *c* is the number of polygon sides *a*, *r* the distance between centre and line *a* and *b* is the thickness of one kaolinite.

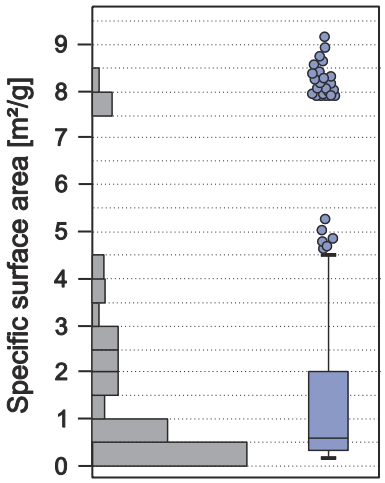

Figure 5.17: Box-Whisker-Plot for specific surface area [m^2/g] distribution for kaolinite. The crystal size is derived from investigation of secondary electron images. The kaolinite thickness range between 0.1 and 5.0 µm and the radius between 0.5 and 15 µm. Based on these results several (n=2190) combination of kaolinite thicknesses and sizes were combined and the specific surface area were calculated.

The specific surface area depends on the ratio between the radius *r* and the thickness *b*. The smaller the thickness of a kaolinite crystal the smaller is the volume in comparison to the surface area. A kaolinite thickness between 0.1 µm and 5.0 µm and a radius between 0.5 µm and 15 µm is assumed. In total 2190 calculations were performed by varying the ratio between the thickness and crystal size. The distribution of the calculated specific surface areas are plotted as a Box-Whisker-Plot in ▶ figure 5.17 and shows that over 90 % of all data are smaller or equal to 3.99 m^2/g. For the theoretical model a mean specific surface area of 1.58 m^2/g was calculated (▶ table 5.9).

Table 5.8: Specific surface area [m^2/g, SSA] for kaolinite based on theoretical calculations for different thicknesses between 0.1 and 5.0 µm and different radii between 0.5 and 15 µm: The minimum, maximum and data equal or lower a percentage value (10, 25, median [50], 75 and 90 %), as well as the number n of data and the mean value are listed.

	min	10 %	25 %	median	75 %	90 %	max	n	mean
SSA	0.20	0.26	0.34	0.61	2.02	3.99	9.11	2190	1.58

The total surface area (A_{total}) of certain grain rimming kaolinite on a defined area (e.g. 100 μm^2) is equal for parallel and disordered arraignment, but different for a total kaolinite length (L_{total}) along a defined length of a straight line (▶ figure 5.18), since the number of the kaolinite crystals is the same for both scenarios. Based on this assumption the total kaolinite length calculations will be conducted for a parallel arraignment with a defined distance between each kaolinite crystal. The total kaolinite length is defined over the maximum diameter perpendicular to the basis which is located parallel to the grain surface area multiplied by the number n of kaolinite on an estimated length.

$$L_{total\_ordered} = (4 * r + b) * n_{kaolinite} \tag{5.10}$$

Note that the thickness b and distance z between the kaolinite is always the same at each calculation for n kaolinite.

$$n_{kaolinite/void} = \frac{x}{(b+z)} \tag{5.11}$$

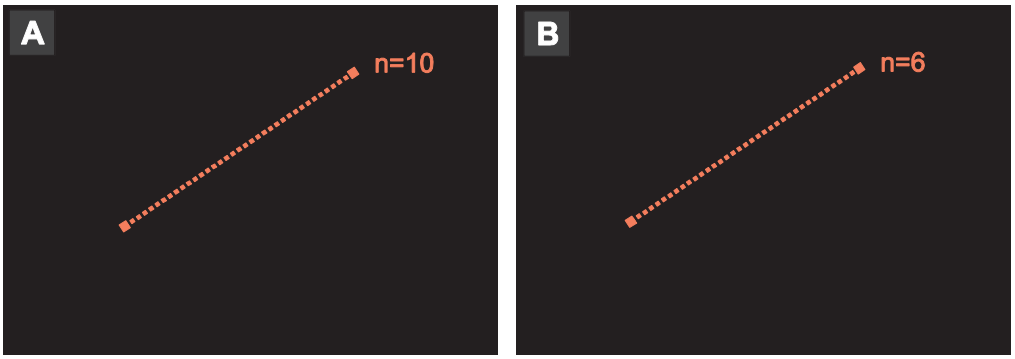

Figure 5.18: Sketch for kaolinite plate distribution on a grain surface area in a regular (A) and irregular (B) arrangement. On a defined line length (orange line) different numbers (10 for a regular arrangement and 6 for an irregular arrangement) of plates are counted.

As mentioned earlier the total length (L_{total}) of kaolinite will be different (smaller, equal or larger) for a disordered arraignment as it is typical for natural sandstones. Therefore the thickness b and the number of kaolinite crystals on an estimated length L can be measured using secondary electron microscope imaging, since the void (z) in between the kaolinite is the length minus the sum of the thicknesses b. A correction factor is calculated for an estimated length of 100 µm (CF_{length}) for an ordered arrangement (▶ table 5.9). The relation between the distance z (0.5 µm to 5.0 µm) and the correction factor CF_{length} is expressed by a logarithmic equation for y = 8.20 * $e^{-0.14x}$ and a regression of R^2 = 0.97 (▶ figure 5.19).

Table 5.9: Correction factors for the length (CF_{length}) and area (CF_{area}) for theoretical approaches of ordered kaolinite arrangements with different thicknesses *z* (0.5 – 5.0) between the crystals.

z [µm]	CF_{length}
0.5	21.0
1.0	14.4
2.0	9.37
5.0	4.86

Natural sandstones and comparison to theoretical approaches – The specific surface area calculations for a single kaolinite are applicable for grain rimming single kaolinite which occur in samples from field B (appendix A3-01C) because these samples are characterised by isolated equally ordered kaolinite which are not in contact to adjacent crystals growing perpendicular on the grain surface area.

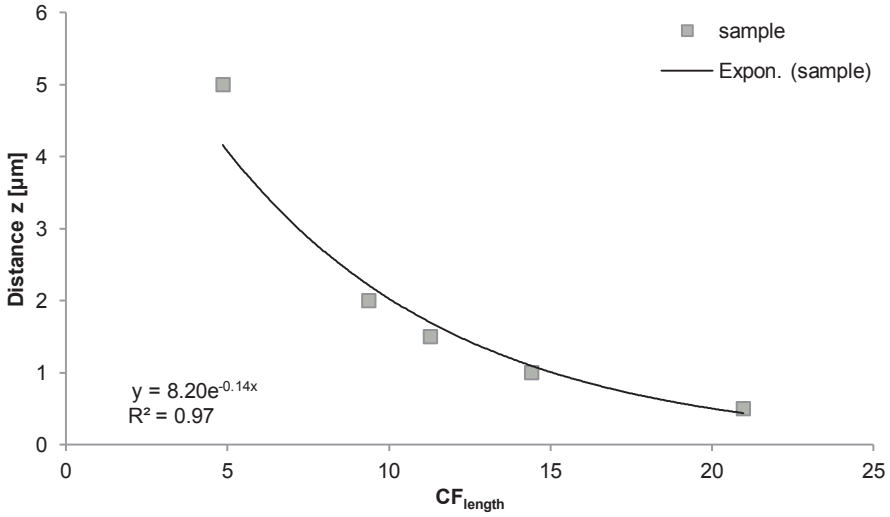

Figure 5.19: The relation of the distance *z* between kaolinite plates within a "booklet"-like structure to the correction factor for a defined length (CF_{length}) is expressed as an exponential function.

Note that large areas of kaolinite are partly covered by fibrous/meshwork illites (appendix A3-01C). However intense cementation of dense grain rimming kaolinite is characteristic for samples from field C (appendix A3-01B). Some of the kaolinite is tilted and/or growing together forming a dense structure of kaolinite with different thicknesses and shapes. However secondary electron images show that the difference between the crystal structure and an idiomorph kaolinite structure is negligible for theoretical calculations. A further problem is the overlapping of kaolinite crystals and the decreasing surface area. In summary the determination of the kaolinite crystal and corresponding surface areas exposed to open pores is difficult and is only an approximation to the real surface area. For both fields the same theoretical approaches are assumed and the specific surface areas of natural sandstones are comparable to the theoretical model.

Table 5.10: Mean, minimal and maximal radius (*r*), thickness (*b*) and side length (*a*) for one kaolinite crystal. Information derived from investigations of secondary electron images from samples of field B and C. The total surface area (A_{total}), the volume (V_{total}) and the specific surface area [m^2/g, SSA] are calculated based on the different kaolinite crystal sizes. n is the number of measured lengths.

	mean	min	max	n
r [m]	5.36E-06	7.44E-07	1.38E-05	110
b [m]	7.09E-07	9.56E-08	2.78E-06	202
a [m]	4.64E-06	6.44E-07	1.20E-05	109
A_{total} [m^2]	1.65E-10	3.18E-12	1.16E-09	-
V_{total} [m^3]	5.29E-17	1.38E-19	1.37E-15	-
SSA [m^2/g]	1.22	9.05	0.33	85

The correction factor for the length is different for samples from field B in comparison to field C. The results are listed in ▶ table 5.11. The information about size and distribution on grain surface areas are derived from secondary electron microscope studies. For an estimated length of 100 µm the number of kaolinite situated along this line is counted (▶ figure 5.18) for samples from field B and C. Admittedly it is assumed that all kaolinite is growing perpendicular to the detrital grain and that all kaolinite has a mean surface area of 1.65E^{-10} m^2 (▶ table 5.10). Based on these assumptions the correction factor for the length (CF_{length}) is 2.61 (well Bw01) for kaolinite from field B and CF_{length} = 9.62 for field C (well Bw03 and Bw04) (▶ table 5.11). No grain rimming kaolinite is present in samples from field A.

Table 5.11: Mean, minimum and maximum values of the specific surface area (SSA) and the correction factor (CF_{length}) for grain rimming kaolinite from field B and C.

	mean	min	max	n
CF_{length} (field B)	2.61	0.36	6.84	51
CF_{length} (field C)	9.62	1.34	25.2	34

Vermicular kaolinite consists of the linkage of several single kaolinite crystals forming a "booklet"-like structure (▶ figure 5.20). The geometric description and calculation of one kaolinite within this structure is the same as for single and grain rimming kaolinite (▶ table 5.10). The assumption that all kaolinite remains in direct contact to each other is an oversimplification for the samples investigated. Analysis of thin sections and secondary electron images indicate voids between the plates. These voids are irregularly distributed and show varying thicknesses in µm-scale (appendix A3-01B). Based on this observation five different scenarios are calculated: (1) the total surface area (A_{total}) is defined over the number of kaolinite plates and their thickness *b* without any space between them (▶ equation 5.12), (2) 25% of the surface area in [001]-direction stays in direct contact to an adjacent kaolinite (▶ equation 5.13), (3) for 50% (▶ equation 5.14) and (4) for 75% (▶ equation 5.15). (5) None of the kaolinite has contact points among themselves (▶ equation 5.16). This scenario is described for grain rimming kaolinite with an ordered parallel arraignment (▶ figure 5.18).

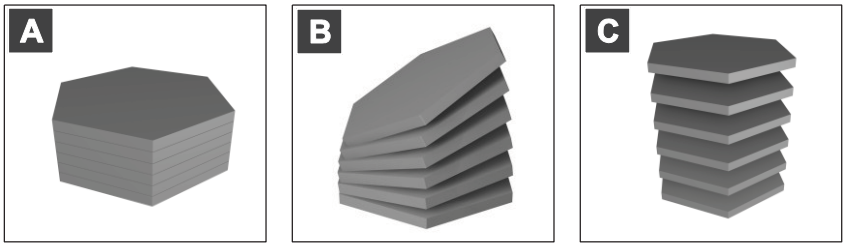

Figure 5.20: Sketch for different arrangements of kaolinite plates within a "booklet"-like structure. A: Closed structure without any in-between space; B: Partly widened kaolinite structure; C: no contacts between the plates.

$$A_{total\,(closed)} = 2 * A_{front} + 5 * A_{side} * n_{kaolinite} \quad (5.12)$$

$$A_{total\,(25\%\,widened)} = 2 * A_{front} + 5 * A_{side} * n_{kaolinite} + \frac{1}{2} * A_{front} * (n_{kaolinite} - 2) + \frac{1}{2} * A_{front} \quad (5.13)$$

$$A_{total\,(50\%\ widened)} = 2 * A_{front} + 5 * A_{side} * n_{kaolinite} + A_{front} * (n_{kaolinite} - 2) + A_{front} \quad (5.14)$$

$$A_{total\,(75\%\,widened)} = 2 * A_{front} + 5 * A_{side} * n_{kaolinite} + \frac{3}{2} * A_{front} * (n_{kaolinite} - 2) + \frac{3}{2} * A_{front} \quad (5.15)$$

$$A_{total\,(100\%\,widened)} = (2 * A_{front} + 5 * A_{side}) * n_{kaolinite} \quad (5.16)$$

The accumulation of several kaolinite "booklets" is a common feature in all samples investigated (appendix A3-01A). There single "booklets" which consist of a number of plates lay one on top of each other. The contact area between the kaolinite reduces the total surface area of a kaolinite "booklet" which stays in contact to the open pore system. Assuming that a fluid may pass through the aggregations by diffusion they may be included in surface area calculation. The volume for the different kaolinite "booklet" calculation (0 to 100 % widening) is always the same, but the surface area changes. Hence the specific surface area is lower for a scenario with 0% widening in comparison to single kaolinite (100 % widening) (▶ table 5.12).

Table 5.12: Specific surface area [m^2/g] calculation for theoretical models of kaolinite "booklets" with a different widening between the single plates from 0 % to 100 %.

	min	10%	25%	median	75%	90%	max	mean	n
0 %	0.05	0.06	0.06	0.09	0.17	0.35	1.31	0.16	2044
25 %	0.09	0.12	0.16	0.29	0.72	1.19	3.29	0.54	2044
50 %	0.13	0.17	0.22	0.44	1.14	2.08	5.23	0.91	2044
75 %	0.16	0.21	0.29	0.53	1.58	3.04	7.17	1.28	2044
100 %	0.20	0.26	0.35	0.63	2.05	4.01	9.11	1.65	2044

$$L_{total\,(closed)} = 4 * r + b * n_{kaolinite} \quad (5.17)$$

$$L_{total\,(25\%\,open)} = 4 * r + b * n_{kaolinite} + r * (n_{kaolinite} - 2) + r \quad (5.18)$$

$$L_{total\,(50\%\,open)} = 4 * r + b * n_{kaolinite} + 2 * r * (n_{kaolinite} - 2) + 2 * r \quad (5.19)$$

$$L_{total\,(75\%\,open)} = 4 * r + b * n_{kaolinite} + 3 * r * (n_{kaolinite} - 2) + 3 * r \quad (5.20)$$

$$L_{tota\ (100\%\ open)} = (4 * r + b) * n_{kaolinite} \quad (5.21)$$

The total length (L_{total}) can be calculated over the radius r and the thickness b of a kaolinite crystal after the same definition described for the total surface area (A_{total}) calculation. For the theoretical approach the mean correction factor for pore lining image analysis ranges between 1.31 and 21.0 due to different widening of kaolinite "booklets" and the distance z between the kaolinite crystals (▶ table 5.13).

Table 5.13: Mean correction factor (CF_{length}) for kaolinite "booklets" due to the distance z [µm] of 0 (for closed structures) and 0.5 µm between the kaolinite.

	CF_{length} (mean)	**z [µm]**	**n**
0 %	1.31	0	2044
25 %	5.98	0.5	2044
50 %	11.0	0.5	2044
75 %	16.0	0.5	2044
100 %	21.0	0.5	2044

For natural samples from field A, B and C the specific surface area and the correction factor (CF_{length}) is calculated based on secondary electron microscope investigations. The minimum specific surface area yields 0.19 m^2/g and the maximum is 4.98 m^2/g for an approximated kaolinite widening of 50 % (▶ table 5.16).

Meshwork illite

In some samples (e.g. well Bw01, Cw02, Cw03 and Aw03 (appendix A3-02C and D) illite is present (< 1 vol.-%) as a thin grain coating mineral which is visible with electron microscopy only. Meshwork illite consists of illite crystals orientated perpendicular to the grain surface area, forming a "honeycomb"-structure. Each comp is surrounded by thin (nm- to µm-scale) illite crystals with height h and a border line l which span up an area inside the comp (A_{basis}). This field may be characterised as a rectangle, defined over the area A_{basis}, length l, height h and width d (▶ figure 5.21). The area of the side can be calculated over ▶ equation 5.22 and the volume over ▶ equation 5.23.

$$A_{side} = l * h * 2 + l * d \quad (5.22)$$

$$V_{side} = l * h * d \quad (5.23)$$

The length of line l, the width d and the area was measured by using image analysis (software: JMicroVision). The height h is assumed to be 5 µm in average and the thickness of each illite is 10 nm (appendix A3-01C). Based on these results the mean surface area of one comp is 38.5 $µm^2$ and the mean illite volume is 17.5 $µm^3$ per grain (n = 117) in average.

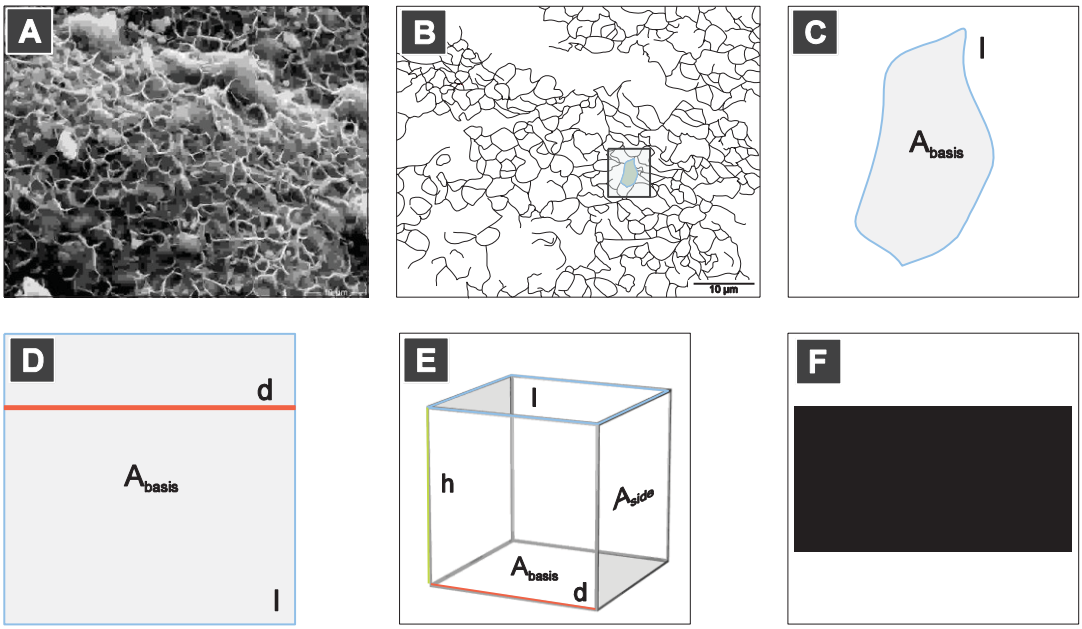

Figure 5.21: (A) Backscatter electron image of meshwork illite coating on detrital grain surface. (B) Sketch of image A. Marked is a single field surrounded by illite crystals. (C) This field is characterised by an area A_{basis} and a border line *l*. The rectangle in image (D) includes the same geometrical information (A_{basis} and l) as in image B with the diameter *d*. The cube in image (E) is the 3-dimensional illustration of the rectangle and (F) a string a cubes.

This results in a specific surface area for meshwork illites of 7.21 m^2/g. The crystal thickness has a major influence on the specific surface area which reflects the relation between the surface area *A* and the volume *V* considering the mineral density, whereas the height and length have only negligible effects. In ▶ figure 5.22 the relation between the illite thickness and the resulting specific surface area is shown and is expressed by the equation $y = 0.80*x^{-0.97}$ with $R^2 = 0.99$. For 0.01 µm to 2.0 µm thickness the specific surface area ranges between 0.43 m^2/g to 71.5 m^2/g. Investigations of authigenic illite with electron microscopy showed that the thickness of single crystals is highly variable and changes between nm to µm due to the illite type. Meshwork illites are typically thicker (10 nm to 100 nm, (appendix A3-02D) in comparison to fibrous illites (< 10 nm, (John, 2010)) which may be due to the spatial arrangement of illite parallel to each other forming a dense structure. A correction factor for meshwork illite is calculated due to electron microscope investigations. The illite length of one field is calculated using ▶ equation 5.24 and the total illite length along a defined line length using ▶ equation 5.25. Based on these equations the correction factor CF_{length} is 4.2 (▶ table 5.16).

$$L_{one\ field} = 2 * h + d \tag{5.24}$$

$$L_{total} = (n_{illite\ crystals} * 2 * h + d) + 2 * h \tag{5.25}$$

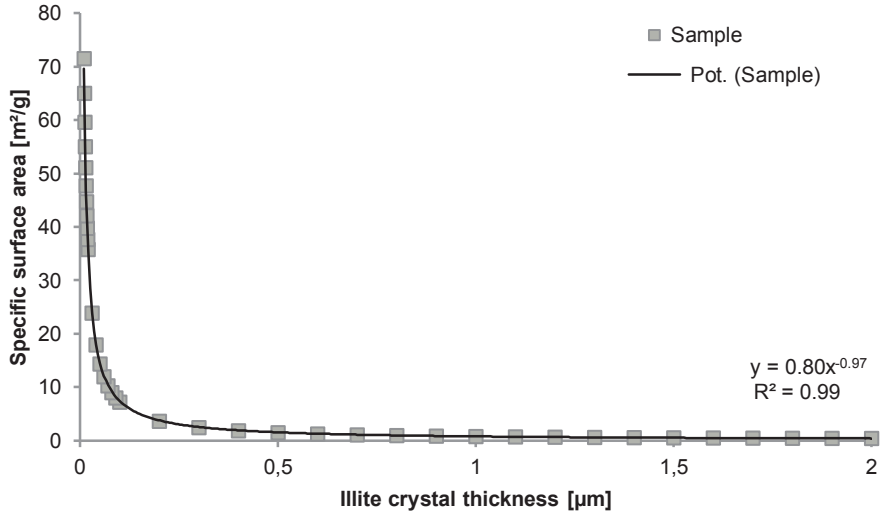

Figure 5.22: The relation between illite crystal thickness [µm] and specific surface area [m^2/g] is expressed by a power function.

Carbonate

Based on scanning electron microscope investigations carbonates (dolomite, ankerite, siderite and calcite) have an almost cubic shape (appendix A3-01D) in comparison to an idiomorph crystal with a trigonal-rhombohedral habitus. The surface area appears (1) as relatively smooth planes, (2) with pattern of growth present as small steps in nm- to µm-scale (appendix A3-02D) or (3) as regular orientated smaller crystals (nm-scale) on the carbonate surface area (appendix A3-03G). Nanometer deep dissolution voids/edge pits are visible in secondary electron microscope images (appendix A2-03D), but appear larger (5-20% internal porosity) in backscatter electron images (▶ figure 4.6). The difference may be due to cutting effects in the thin section plane. Carbonate is often situated between two or more grains or in contact with a grain along a corner (appendix A2-04E and H). For geochemical modelling the shape and distribution of carbonates has to be simplified. Therefore it is assumed that all carbonate minerals have a cubic shape and one of the six side walls stays in contact to a surface area of a detrital grain. For case one the calculation is relatively simple based on a mean edge length which is assumed to be 40 µm in average for this study. The calculations of the surface area for case two is much more difficult. But since the total amount of carbonates in all samples (<5 vol.-%, (appendix C2)) and the number of irregular surface areas (case two and three) is relatively low, it seems reasonable to assume a cubic shape for all carbonates. The chemical composition is highly variable and is primarily due to different amounts of Ca, Mg, Fe and Mn (compare section 4.2). Three carbonate members are defined and used for geochemical modelling: dolomite, ankerite and siderite. For dolomite and siderite the same stoichiometric information is used in the database for PHREEQCi. There, dolomite is defined as a pure Ca-Mg-carbonate with 50% $CaCO_3$ and 50% $MgCO_3$ and siderite as a pure Fe- carbonate. In the database the term ankerite is defined as $(Ca,Mg)_{0.3}Fe_{0.7}(CO_3)_2$ but is described by Deer et al. (1992) as a carbonate with >20 mol% $FeCO_3$. Further chemical differences, especially in the manganese content are not considered in the model. Based on image analysis of backscatter electron images a mean carbonate composition of 1/3 dolomite, ankerite and siderite, respectively is defined. The amount of calcite is negligible and is not considered in the geochemical model.

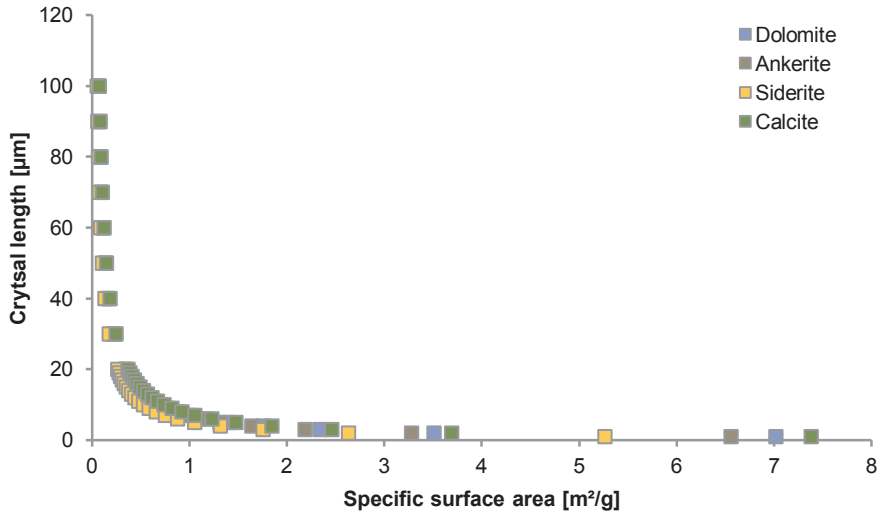

Figure 5.23: Specific surface area [m^2/g] in relation to the crystal length [µm] for carbonates.

The relation between the specific surface area and the crystal length is shown in ▶ figure 5.23. The smaller the edge length the larger is the resulting specific surface area. In ▶ table 5.16 the mean, minimum and maximum values are given for the different carbonate minerals for a crystal length between 1 and 100 µm.

Table 5.14: Specific surface area [m^2/g, SSA] for theoretical calculations of carbonate minerals with a cubic shape and an edge length of 40 µm.

mineral	SSA [m^2/g]
dolomite	0.18
ankerite	0.16
siderite	0.13

Following secondary electron microscopy the edge length of the carbonate crystals ranges between 25 and 45 µm. Note that Fe-rich carbonate phases are always growing around earlier dolomite generations. Hence the assumptions are an oversimplification for the geochemical model. Furthermore small (<1 µm) calcite crystals are proven in one sample by secondary electron microscopy (appendix A3-02H). For calculating the specific surface area of all carbonates a mean edge length of 40 µm was chosen which results in the specific surface areas listed in ▶ table 5.14. Based on the assumption that carbonates have a relatively plane surface area with only minor amounts of dissolution voids no correction factor (CF_{length}) is calculated.

Sulphate/sulphide

For the sulphates anhydrite and barite a prismatic mineral shape is assumed (appendix A3-02C) with a long edge length (a) of 1 µm to 100 µm. The short side length (c) is assumed to be half the length b which is in turn the half of length a. For galena a cubic shape is assumed as it is described for carbonate minerals. In ▶ figure 5.24 the specific surface area in conjunction with

the side length (*a*) is plotted and the minimum, maximum and mean values are listed in ▶ table 5.16.

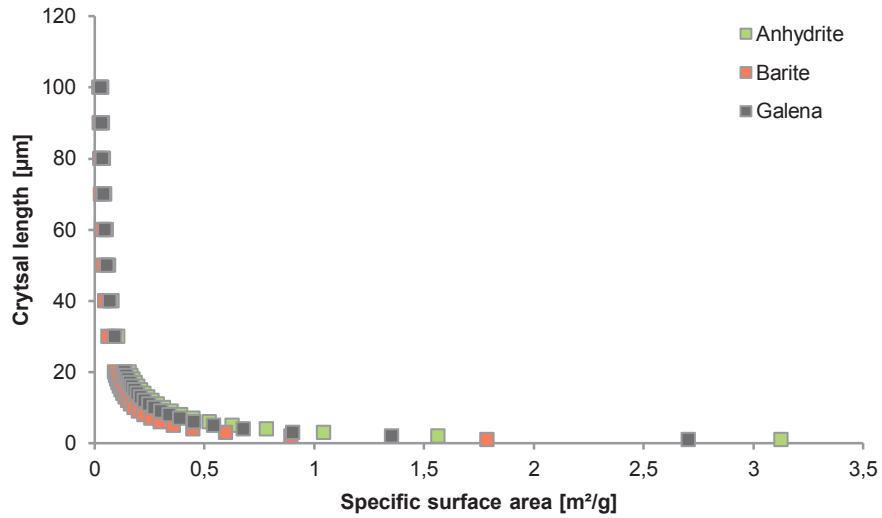

Figure 5.24: Specific surface area [m^2/g] in relation to the crystal length [µm] for sulphates. For Rotliegend sandstones investigated in this study the mean crystal length a (for a prismatic shape) ranges between 1 and 60 µm. Length *b* is the half of length *a* and *c* the half of length *b*, respectively.

Based on thin section analysis and secondary electron microscopy the mean edge length (*a*) is assumed to be 60 µm for anhydrite, 30 µm for barite and 10 µm for galena. Therefore specific surface areas are calculated and summarised in ▶ table 5.14. Based on the assumption that sulphates and sulphides have a relatively smooth surface area with only minor amounts of dissolution voids no correction factor (CF_{length}) is calculated.

Table 5.15: Specific surface area [m^2/g, SSA] calculation for sulphate (anhydrite and barite) with a prismatic shape and for galena with a cubic shape. The edge lengths *a*-*c* are listed in µm.

mineral	a [µm]	b [µm]	c [µm]	SSA [m^2/g]
anhydrite	60	30	15	$5.21*10^{-02}$
barite	30	15	7.5	$5.95*10^{-02}$
galena	10	10	10	0.27

5.2.3 Comparison between the specific surface areas of the volumetric and effective mineralogy data with whole rock BET-analysis

The total surface area of the sandstones was measured by using the BET-analysis (compare section 2.8) and range between 0.2 and 1.9 m^2/g for samples from field A. As discussed in the previous section the considerations of the volumetric and effective mineralogy results in different percentage amounts of mineral phases within one sample, since the volumetric mineralogy favours the detrital grain composition (e.g. quartz, K-feldspar and rock fragments) and the effective mineralogy reflects the amount of minerals which stay in contact to open pores and which may act as reaction partners in water-rock-(CO_2) interaction. For each mineral phase a specific surface area was calculated for the samples investigated in this study (compare section

5.2.2). However the specific surface area of each mineral was calculated based on the assumption that the mineral has a similar shape and size, independently to the spatial distribution within the reservoir and the position within the stratigraphy. For each sample of field A which was investigated by image analysis for the determination of the effective mineralogy the total specific surface area was calculated and compared to the volumetric mineralogy and whole rock BET-analysis (▶ figure 5.25). The results show that for the volumetric mineralogy data the total specific surface area ranges between 0.03 and 0.08 m^2/g (mean is 0.05 m^2/g), which is in average 3.9 % of the whole rock BET surface area. In comparison, the total specific surface area for the effective mineralogy ranges between 0.16 and 0.53 m^2/g (mean is 0.37 m^2/g) which makes up around 28 % of the whole rock BET surface area. For nearly all samples the BET surface area is larger than the total surface area calculated for the effective and volumetric mineralogy data. Only for sample Aw05-01 the calculated specific surface area (for the volumetric and effective data) is larger than the whole rock value.

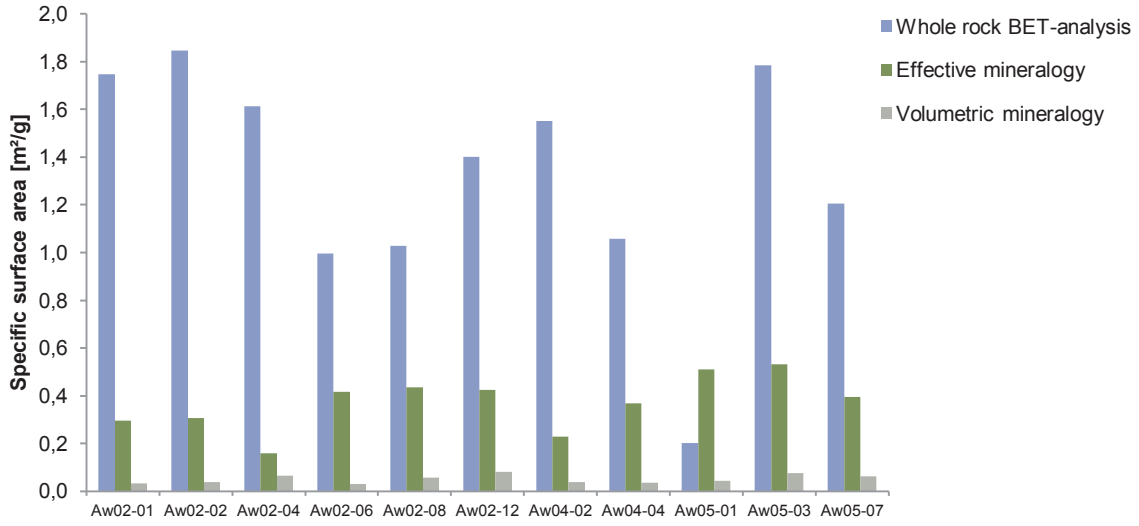

Figure 5.25: Total specific surface area [m^2/g] for samples from field A after BET-analysis and for theoretical calculations of the volumetric and effective mineralogy data. The theoretical values include the percentage amounts of minerals and specific surface area calculation for each mineral phase.

Interpretation

The comparison between measured BET surface areas and the calculations for the volumetric and effective mineralogy data shows that the total specific surface area of minerals which stay in contact to open pores are closer to the real specific surface area than the volumetric considerations. However the theoretical calculations are an approximation, only. In natural sandstones the total amount of specific surface areas of minerals is highly variable and depends on the amount of dissolution voids and/or edge pidges on the surface area and the accessibility within the sandstone. Petrographic investigation of sandstones in this study showed, that different dissolution stages of e.g. K-feldspar (undissolved and partial dissolution) is varying for each sample. Furthermore the total amount of authigenic quartz content which has a relatively plane surface are in comparison to irregular surface areas of detrital quartz grain influences the total specific surface area of a sandstone. These differences between the true value and the theoretical approaches are reflected in the results for sample Aw05-01. This sample is an

exception in comparison to all other samples investigated in this study: First, the permeability is with 9900 mD extremely high which is due to a very low authigenic mineral content. Especially clay minerals, like illite and smectite are lacking. Some kaolinite "booklets" are present. The approaches in the specific mineral surface area as they are calculated and applied for the samples from field A are not applicable for this sample, because less K-feldspar is (partly) dissolved and authigenic kaolinite "booklets" are larger in size in comparison to samples from the northern area of field A. These results show how important a specific calculation of the specific surface area of each mineral phase within one sample is to reach a realistic value.

5.2.4 Transferability of 2D information in a 3D system

After Oosthuyzen (1980) specific 2-dimensional (2D) observations in thin sections are representative for a 3-dimensional (3D) model. These include areal and volumetric information, but no information about the size, shape and orientation of pores and pore throats. Moreover it is difficult to define between a larger pore and a pore throat in a 2D thin section. Grain contacts in thin sections are classified after Pettijohn et al. (1987) in floating grains, point-, length-, concave/convex-contacts and sutured grains. A floating grain has no contact points in a 2D scale but may have e.g. a point-contact outside the thin section plane. On the other hand a grain contact could be the only one between the neighbouring grains. After Bernal and Mason (1960) and Aste et al. (2005) equal spheres have between six and seven contacts per sphere in a 3-dimensional random packing. The basic assumptions for all studies dealing with the transferability from 2D information in a 3D system are that the structure of the sandstone is homogeneous and anisotropic and that the 2D images cover a larger area to avoid microscopic variability (Beard, 1973). Reed (1996) analysed homogeneous isotropic marine sands in terms of pore geometry for 2D and 3D considerations. The author points out that there was a high similarity between different investigations. For a given resolution, pore body and pore throat sizes are similar in a 2D and 3D system. Furthermore 2-D images do not capture the tortuous nature of pore throats which are reconstructed in a 3-D model because they are underestimated in a 2D system. Geometric analysis of 2D pore images is limited by the objective identification of individual pores or pore throats. A 3D pore system appears in a 2D section as a collection of disconnected or partly connected voids. But it may show a good connectivity in a natural 3D system (Doyen, 1988).

5.2.5 Summary and discussion of specific mineral surface areas

Table 5.16 summarises all specific surface areas and correction factors for the minerals discussed in the previous section 5.2. The theoretical approaches for specific mineral surface areas used in this study are based on thin section and secondary electron microscopy investigations. The determinations of mineral surface areas always depends on the measurement type which is used and range in a macroscopic to microscopic scale for this study (▶ figure 5.26). But the real surface area of minerals may be larger than those calculated. Furthermore different measurement types (e.g. BET, EGME) result in different specific surface areas for the same mineral. This is shown by Macht et al. (2010) for illite: The authors measured surface areas of illite using the BET, AFM and liquid ethylene glycol monomethyl ether (EGME) method. The specific surface areas for BET yields 46 m^2/g and for AFM 64 m^2/g (▶ table 5.17). These values are six and nine times larger than calculated for the meshwork illites in Rotliegend

samples, respectively. On the other hand EGME penetrates into the interlayer space of the clay minerals due to its polarity in compared to the non-polar gas nitrogen (Macht et al., 2010). This explains the higher specific surface area for illite of 112 m^2/g and it may indicate that the clay interlayer will not be affected by the presence of CO_2 during underground storage, since CO_2 is non-polar (Macht et al., 2010).

Table 5.16: Summary of specific surface areas [m^2/g, SSA] (minimum, mean and maximum value) for different minerals assuming simplified crystal shapes in the Rotliegend sandstones from the Upper Slochteren Formation. Furthermore the correction factor for an assumed length according to pore lining image analysis is listed.

mineral	shape	SSA_min	SSA_max	SSA_mean	CF_{length}
		[m^2/g]	[m^2/g]	[m^2/g]	
quartz	sphere	$5.4*10^{-03}$	$2.0*10^{-02}$	$1.2*10^{-02}$	1
K-feldspar	sphere $_{undissolved}$	$5.4*10^{-03}$	$2.0*10^{-02}$	$1.2*10^{-02}$	1
K-feldspar	sphere $_{partly\ dissolved}$	0.09	0.40	0.15	>1
illite (IC)	sphere	$3.563*10^{-02}$	$3.571*10^{-02}$	$3.568*10^{-02}$	1
illite (IM)	prismatic	0.43	71.5	7.21	4.20
kaolinite (GR)_field B	hexagonal	0.33	9.05	1.22	2.61
kaolinite (GR)_field C	hexagonal	0.33	9.05	1.22	9.62
kaolinite (booklets)	hexagonal	0.19	4.98	0.67	11.0
dolomite	cubic	$7.0*10^{-02}$	7.02	0.94	1
ankerite	cubic	$6.6*10^{-02}$	6.56	0.88	1
siderite	cubic	$5.3*10^{-02}$	5.26	0.70	1
anhydrite	prismatic	$3.1*10^{-02}$	3.13	0.42	1
barite	prismatic	$1.8*10^{-02}$	1.79	0.24	1
galena	cubic	$2.7*10^{-02}$	2.70	0.36	1

However, Giesting et al. (submitted) showed that these interlayers are penetrated by CO_2. Specific surface area measurements using the BET method for different clays were conducted by Dogan et al. (2006). The authors showed that specific mineral surface areas of montmorillonite (standard clay from The Clay Mineral Society: SAz-1 and SWy-2) vary between 65.2 and 22.7 m^2/g. For a synthetic mica-montmorillonite (SYn-1) 118 m^2/g are measured and for a palygorskite (PFI-1) the specific surface area yield 173 m^2/g. Hence it is obvious that N_2 (or CO_2) which is used for experiments can penetrate clay interlayer. But under reservoir conditions and a mean water saturation of 25% it can be assumed that there is only a thin water layer present between the single clay layers and minor chemical reactions between the mineral and the fluid ($+CO_2$) may occur. Hence a plane surface area for illite coatings is reasonable for the model. The thickness of illite crystals used for the model is in a good agreement with other studies. Dudek and Srodoń (2003) showed that illite-smectite interstratifications of different shale samples are 2 nm thick, whereas discrete illite seems to be thicker (>2 nm). Illite thicknesses from pelitic samples with different metamorphic grades (diagenesis to high anchizone) were measured by Brime and Eberl (2002) and range between 3.9 and 17.8 nm (average is 7.1 nm for n = 25). Dogan et al. (2006) measured the specific surface area of two different kaolinite provided from the Clay Mineral Society using BET-analysis. The well ordered KGA-1b kaolinite has a lower specific surface area (13.1 m^2/g) in comparison to the poorly ordered KGa-2 kaolinite with 21.7 m^2/g (▶ table 5.18).

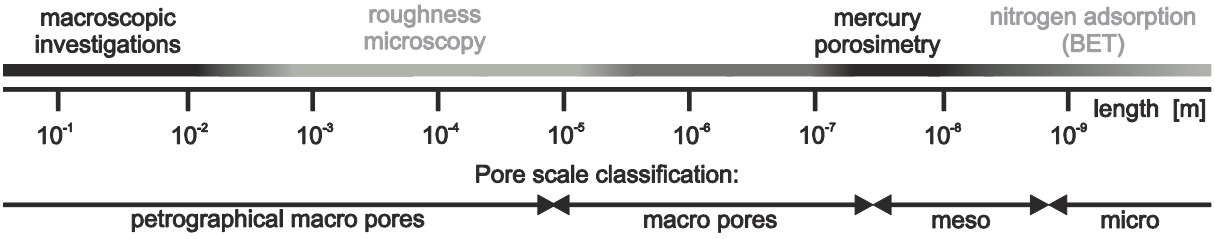

Figure 5.26: Surface area quantification methods and their spatial resolution. Modified from Fischer and Gaupp (2005).

The calculated surface area for this study range between 0.33 and 9.05 m^2/g for well ordered kaolinite (▶ table 5.16) which is (partly) in good agreement with the results from Dogan et al. (2006). The theoretical calculations for this study are based on measured crystal sizes in secondary electron images. For the BET-analysis from the Clay Mineral Society no information about the crystal size and thickness is given. Hence a comparison of the specific surface area is not fully applicable.

Table 5.17: Specific surface areas [m^2/g] of illite and kaolinite measured with BET (Brunau et al., 1938), AFM (Atomic Force Microscopy) and EGME (Ethylene Glycol Monomethyl Ether).

mineral	BET (N_2)	BET (CO_2)	AFM	EGME	author(s)
illite	46	-	64	112	Macht et al. (2010)
Na-illite (Fithian)	105	72.4	-	-	Aylmore et al. (1970)
Na-illite (Willaloka)	195	162	-	-	Aylmore et al. (1970)
Cs-illite (Willaloka)	184	159	-	-	Aylmore et al. (1970)
kaolinite (well ordered, KGA-1b)	13.1	-	-	-	Dogan et al. (2006)
kaolinite (poorly ordered, KGa-2)	21.7	-	-	-	Dogan et al. (2006)

For dolomite the BET surface area was calculated between 0.18 and 0.70 m^2/g. This is in a good agreement with other authors: Karaca et al. (2006) measured a dolomite surface area of 0.14 m^2/g in conjunction to the adsorptive removal of phosphate from aqueous solutions by raw and calcinated dolomite. For the replacement of calcite by dolomite Baker and Kastner (1981) measured a BET surface area of 0.51 m^2/g for calcite used as starting material for experiments. A dolomite surface area of 0.6 m^2/g was measured by Johnson et al. (2005) for heterogeneous uptake of gaseous nitric acid on dolomite and calcite. No literature data is available for ankerite and siderite. But based on the similar crystal structure and their similar behaviour during mineral dissolution may the specific surface areas of dolomite comparable to other carbonate minerals. The specific surface area of anhydrite ranges between 0.42 and 3.13 m^2/g and is in a good agreement with measurements by Bildstein et al. (2001) and Brantley and Mellott (2000) who propose a specific surface area between 0.07 and 0.50 m^2/g. Brantley and Mellott (2000) measured several BET-surface areas for primary minerals. The studies result in specific surface areas for feldspar grains (albite, oligoclase, labradorite, bytownite and anorthite) between 0.03 and 1.79 m^2/g (▶ figure 5.27).

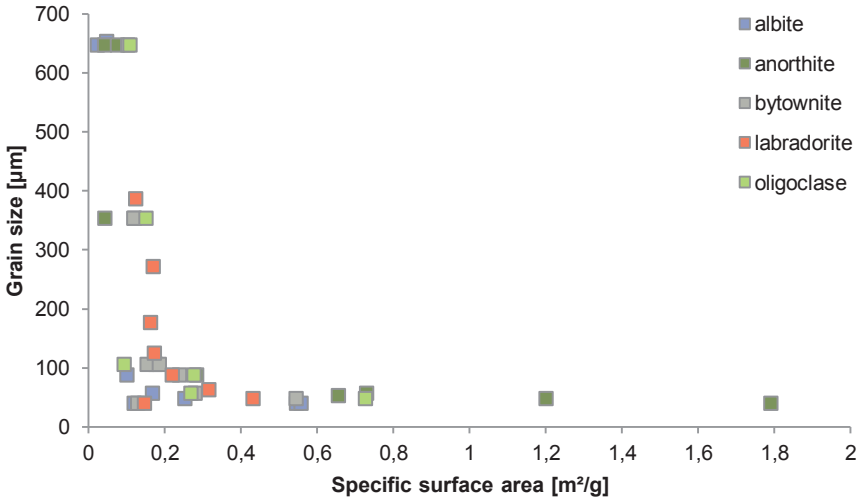

Figure 5.27: Specific surface areas [m^2/g] for different feldspar and grain size measured using BET (Kr and N_2) analysis. Data are adapted from Brantley and Mellott (2000).

According to a lower grain size the specific surface area increases. Other studies listed in the publication by Brantley and Mellott (2000) agree with these results. However the theoretical SSA calculations are with a mean value of 0.15 m^2/g (▶ table 5.16) similar to natural feldspar grains. For geochemical modelling specific surface areas of minerals are used which show significant differences to results derived from this study and measurement of minerals by other authors as described above. In ▶ table 5.18 the specific surface area of selected minerals by Gherardi et al. (2007) and Xu et al. (2010) are listed.

Table 5.18: Specific surface areas [m^2/g] of selected minerals are commonly used for geochemical modelling adapted from literature.

mineral	Xu et al. (2010)	Gherardi et al. (2007)
illite	0.015	0.015
kaolinite	0.015	$2.3*10^{-03}$
chlorite	0.015	$2.0*10^{-03}$
smectite	0.015	0.015
hematite	$9.8*10^{-04}$	$1.3*10^{-03}$
carbonate	$9.8*10^{-04}$	$1.0*10^{-03}$
sulphate	$9.8*10^{-04}$	$1.0*10^{-03}$
quartz	$9.8*10^{-04}$	$1.0*10^{-03}$
K-feldspar	$9.8*10^{-04}$	$1.0*10^{-03}$

6 Geochemical modelling of CO_2-water-rock interaction

Water-rock interactions in reservoir sandstones under the influence of CO_2 are generally complex processes which act on different time and spatial scales (e.g. Gaus et al., 2008). Software supported geochemical modelling is a powerful tool to subdivide this complex system into chemical reactions. (1) The reaction between CO_2, rock and the formation water within the reservoir is most relevant for any short time period (up to 25 years) during the injection phase and mainly affect the near distance of the injection well(s) (IPCC, 2005; Ketzer et al., 2009). Mineral precipitation and/or dissolution are important processes as it may change reservoir permeability and porosity and may immobilise CO_2 as carbonates (Soong et al., 2004; Giammar et al., 2005; Zerai et al., 2006). (2) On the other hand long term integrity modelling studies (>1000 years) provide an overview about the chemical reactions for e.g. the whole reservoir and cap rock (Gaus et al., 2008). (3) A third kind of modelling studies are long term considerations of the wells, since well leakage is identified as a potential risk during CO_2 storage (IPCC, 2005). But this topic is not considered in the present study. In this study CO_2-water-rock interactions were simulated using the software code PHREEQCi (Parkhurst and Appelo, 1999) with a zero dimensional kinetic reaction model (short and long term model) for a CO_2 saturated fluid. The computer program is able to simulate chemical reactions in equilibrium with an aqueous solution with reacting mineral and gas phases (Parkhurst and Appelo, 1999). Most important, kinetic reactions can be interconnected with the equilibrium reactants. The interaction between free CO_2 gas and the rock is not considered because of the less reactivity in comparison to CO_2 dissolved in brines (Holloway et al., 1996). For a two dimensional reactive transport model the in-house Shell software MoReS is used to simulate the behaviour of CO_2 within the reservoir structure (long term model) (compare chapter 7). Kinetic data and rate laws for geochemical modelling used in PHREEQCi are summarised by e.g. Palandri & Kharaka (2004) and Gaus et al. (2008). In ▶ figure 6.1 the different modelling steps with PHREEQCi and MoReS are listed.

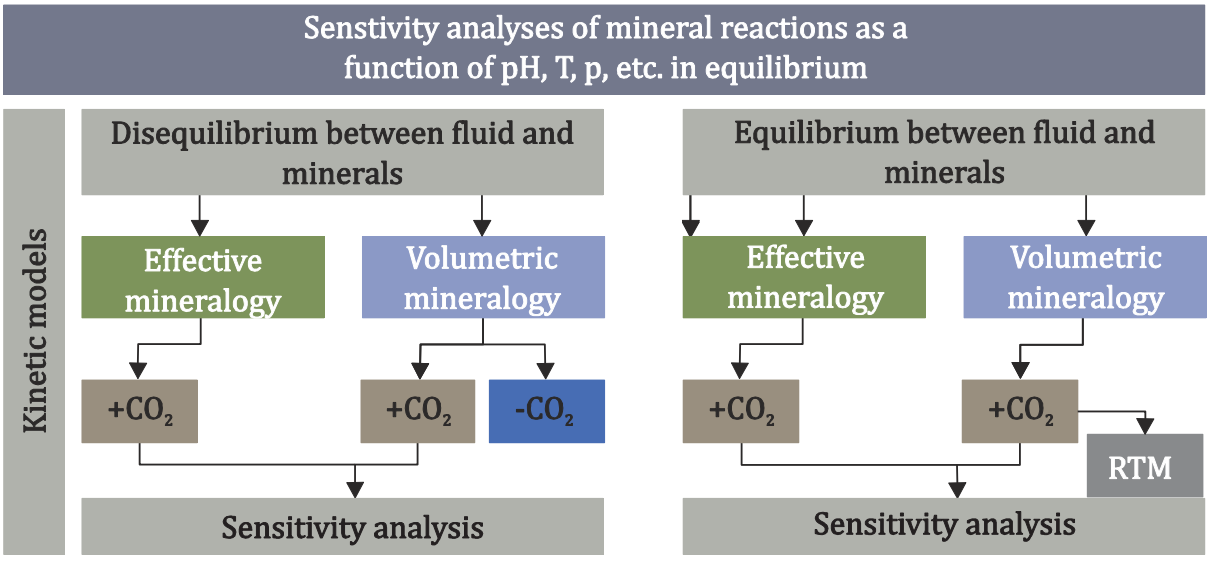

Figure 6.1: Flow diagram for geochemical modelling (PHREEQCi) and reactive transport modelling (RTM; MoReS) for a dutch Rotliegend reservoir (field A).

For PHREEQCi simulations different input data need to be defined: The database which is used for the model, the initial aqueous and gas phase and the mineral assemblage (solid phase) (compare section 6.1). Based on these input data an equilibrium model (compare section 6.2) is simulated and these results are integrated in kinetic models (compare section 6.3). The kinetic test scenarios include the simulation of an aqueous phase (fluid) with a primary mineral assemblage (volumetric and effective mineralogy, respectively). It is assumed that the fluid is oversaturated with respect to some primary minerals (▶ table 6.5) and is called "disequilibrium model" in the following section. The test scenarios are modelled under the supply of CO_2 to demonstrate the mineral reactivity during CO_2 storage. For both test scenarios different sensitivity analysis are run and the results are compared among each other (compare section 6.4). Therefore the test scenarios are modelled without the supply of CO_2, no mineral oversaturation with respect to the fluid (initial equilibrium between aqueous and solid phase), lower initial salinity, different temperatures and pressures, different water-rock ratios and various changes in the initial primary mineral assemblage.

6.1 Input data

6.1.1 Database

For aqueous solutions PHREEQCi uses ion-associations and Debye Hückel expressions (Parkhurst and Appelo, 1999). This model can be used at low ionic strength but may break down at higher ionic strengths. By Truesdell and Jones (1974) the Debye Hückel expressions were extended by an ionic-strength term and are fitted with the major ions using chloride mean-salt activity-coefficient data and then may be reliable at higher ionic strengths. For very high ionic strength brine solutions, as they are typically present in the Rotliegend formation waters from the northeast Netherlands (▶ table 6.1), a specific interaction approach to thermodynamic properties should be used (e.g. Pitzer, 1979; Harvie and Weare, 1980; Harvie et al., 1984; Plummer et al., 1988). This approach is not incorporated in PHREEQCi. The Debye Hückel model predicts a continuous decrease of activity coefficients with increasing ionic strength. However, this approach is incorrect because activity coefficients start increasing at higher ionic strength as a result of charge and radius of the species and is much more pronounced for multivalent species. For high fluid salinities the Debye Hückel model will predict lower activity coefficients than the real ones (e.g. calculated by the Pitzer model), so certain phases will be undersaturated, while in reality they should be saturated. This effect is especially conspicuous for highly charged species, such as Al^{3+} or silica. In summary all silica minerals (e.g. K-feldspar, kaolinite) which may react with the fluid during CO_2 storage may be undersaturated within the model but may precipitate in reality. On the other hand the Pitzer model is a semi-empirical method which is much more suitable for high ionic strength solutions. In this model some of the parameters used in the activity coefficient calculations are actually determined from real solutions. The available database still lacks some parameter for important species (e.g. Al, Si, Fe) which are important for silica reactions (e.g. Bartels et al., 2005). Because of these lacking parameters the Pitzer model cannot be used for the model in this study.

6.1.2 Aqueous phase

According to this study detailed analyses were performed for mineral determination and composition (compare chapter 4) and the distribution of minerals in contact to open pores and the evaluation of the effective mineralogy (compare chapter 5). Different fluid compositions

were provided by NAM and are summarised in ▶ table 6.1 (NL, Aw01, Aw13 and Aw14). The brine composition "NL" agrees well with other data sets from the North Sea Formation Waters Atlas (Warren and Smalley, 1994) for Upper Slochteren sandstones from the Rotliegend (▶ table 6.1, NSFWA). Considering different water compositions available for the study area (▶ table 6.1) the water is under- and/or oversaturated with respect to the primary minerals within the sandstone. For example the total calcium content ranges between 50 and 27000 mg/l. This difference may influence the precipitation of carbonate minerals like calcite and dolomite: An oversaturation may be reached sooner for a higher calcium concentration within the fluid.

However, a major input on modelling results is driven by the relative high salinity of the water. For this model the Debye Hückel equation is used which gives incorrect activity coefficients for high ionic strength as it is discussed in section 6.1.1.

Table 6.1: Mean fluid composition for Rotliegend sandstones from the northeast Netherlands provided by NAM (NL), three formation water analyses from field A (wells Aw01, Aw13 and Aw14; Internal report NAM SPC/3 489/87) and an average composition from the North Sea Formation Waters Atlas (Warren and Smalley, 1994) for Rotliegend (Upper Slochteren) Reservoirs (NSFWA). The species concentrations are given in mg/l. TDS stands for Total Dissolved Solids.

species	NSFWA [mg/l]	NL [mg/l]	Aw01 [mg/l]	Aw13 [mg/l]	Aw14 [mg/l]
Na^+	65323	80933	1600	56000	1530
K^+	2300	2233	600	2000	700
NH^{4+}	-	160	-	-	-
Ca^{2+}	17331	22097	50	15000	27000
Mg^{2+}	3188	2343	120000	2800	104000
Sr^{2+}	850	625	-	390	-
Ba^{2+}	41	19	-	10	-
Pb^{2+}	-	28	-	-	-
Zn^{2+}	-	125	-	-	-
total Fe	202	323	750	1300	1250
Cl^-	141394	173648	345000	137000	360000
SO_4^{2-}	961	203	-	260	-
HCO_3^-	226	1400	-	-	-
SiO_2	21	-	-	-	-
TDS	231816	284137	468000	214760	494480
pH	5.0	4.2	4.6	4.1	3.9
density [g/ml]	-	1.19	1.34	-	1.36
T [°C]	88	-	-	-	-
p [bar]	275	-	-	-	-

The brine can be classified as a NaCl solution with additional K^+, Ca^{2+} and Mg^{2+} (and other cations) having a high ionic strength. The total dissolved solids (TDS) yield 284 g/l. The pH was balanced on neutrality and reconciled with Scalechem V2.2 to pH = 4.2. For the simulation the pH was set to 7.0 and the pe (redox potential) to 4.0 as initial values. Sensitivity analyses (compare section 6.3.2) showed that the initial pH (7.0 versus 4.2) is not affecting the simulation. According to further kinetic studies Al^{3+} and H_4SiO_4 were added to the initial solution with $1.0*10^{-03}$ mol/kgw, (mol per kg water) respectively, because PHREEQCi requires some initial silica and aluminium species in the fluid to find a solution for silica precipitation. Due to the high amount of species the density is with 1.19 g/ml higher than for pure water. The

temperature used is 100°C. These data are used for the test scenario where rock and fluid are in disequilibrium (compare section 6.3.1). For determination of a fluid which stays in equilibrium with the chosen mineral assemblage the initial fluid was equilibrated with a concentration of 1 mol/kgw for each mineral phase in a simple equilibrium batch model in PHREEQCi. The final fluid composition is listed in ▶ table 6.2. It is still basically a NaCl solution with additional K^+, Ca^{2+} and Mg^{2+} (and others) and a high ionic strength. The pH is with 4.96 higher than for the disequilibrium model (pH=4.2). The pe results in -1.7. The density yields 1.19 g/ml and the temperature is fixed to 100°C. However the fluid was changed to another initial composition, but the amount of each mineral is adapted from the disequilibrium model (▶ table 6.3).

Table 6.2: Fluid composition of the disequilibrated fluid [mol/kgw] as it is used for PHREEQCi and the fluid composition after equilibrating the intital fluid with the primary minerals using a simple PHREEQCi batch model.

species	disequil. [mol/kgw]	equil. [mol/kgw]
Na^+	0.06	3.89
K^+	0.01	0.13
NH^{4+}	0.61	0.01
Ca^{2+}	0.11	0.46
Mg^{2+}	8E-04	0.17
Sr^{2+}	2E-04	8E-03
Ba^{2+}	1E-04	5E-05
Pb^{2+}	2E-03	9E-10
Zn^{2+}	0.01	2E-03
total Fe	4E-08	0.05
Al^{3+}	5.41	6E-08
Cl^-	2E-03	5.41
SO_4^{2-}	0.03	0.02
HCO_3^-	2E-08	8E-03
SiO_2	0.06	9E-04
pH	7.0	4.97
pe	+4.0	-1.7
T [°C]	100	100
density [g/ml]	1.19	1.19
Pressure [bar]	100	100

6.1.3 Gas phase

The gas phase used in the model is pure CO_2 without any other gases like CH_4 or H_2S and a fixed pressure of 100 bar (101.33 atm). The initial reservoir pressure for field A is 320 bar, but is lowered to 10 bar after gas production (Post, 2010, person. comm.). Hence sensitivity analyses were run for 10, 50 and 300 bar, respectively. The results show differences for lower pressures, only (compare section 6.3.2). It is assumed that the partial pressure of CO_2 is the same as the hydrostatic pressure in the reservoir based on the equation when the injection did not lead to a significant overpressure.

6.1.4 Solid phase

For equilibrium and kinetic modelling the definition of primary (initial mineral assemblage) and secondary minerals (new formed minerals) are required. The unit used in PHREEQCi for primary minerals is the molality with moles of solids per kilogram water [mol/kgw]. During mineral precipitation and/or dissolution processes additional water can be produced or consumed based on mineral reactions. This increase/decrease in water content is not considered by the software, but can be comprehended by summarising the total molality of an aqueous species and comparing it to the total number of moles in the system. The reference to one kilogram water involve the water saturation of the sandstone and with this the water/rock ratio. Additionally for kinetic calculation the surface area in m^2 per kg water for each mineral phase is considered in PHREEQCi. (1) The volume percentages of each mineral are obtained from point counting analysis on thin sections and (2) the effective mineralogy (mineral surface areas in contact to open pores) is based on image analysis.

Figure 6.3: For primary minerals the rate constants *k*, Arrhenius activation energy *Ea* [J/mol] are listed for acidic (a), intermediate (n) and basic (b) conditions and the reaction order *n* relative to H^+ are listed for acidic and basic conditions. The data were adapted from Palandri and Kharaka, 2005. For each mineral phase an acidic pH [< pH (a)], a neutral pH [> pH (a)] and a basic pH [> pH (n)] was defined. For the volumetric (VOL) and effective (EFF) mineralogy data the mineral amount *m0* [mol/kgw], the mineral surface area per kilogram water *Am*, the specific mineral surface area *SSA* [m^2/g] and the mass *m* [kg] and are listed. For galena the kinetic parameter of pyrite and for siderite of ankerite were used. For the reaction order *n* of anhydrite data from barite were used. Note that not all rate constants and Arrhenius activation energy data are available for the mineral assemblage. Hence the lacking information were adapted from available information of acidic/neutral/basic values for the mineral, respectively and are marked in blue colour.

	anhy	ank	barite	dol	galena	hem	kaol	Kfsp	musc	Qz	sid
k25 (a)	6.5E-04	6.5E-04	1.3E-07	6.5E-04	3.0E-08	4.1E-10	4.9E-12	2.5E-11	1.4E-12	1.0E-14	6.5E-04
k25 (n)	6.5E-04	3.0E-08	1.3E-08	3.0E-08	2.8E-05	2.5E-15	6.6E-14	3.9E-13	2.8E-14	1.0E-14	3.0E-08
k25 (b)	6.5E-04	7.8E-06	1.3E-08	7.8E-06	2.8E-05	2.5E-15	8.9E-18	6.3E-22	2.8E-15	5.1E-17	7.8E-06
Ea (a)	14300	36100	30800	36100	56900	66200	65900	57100	22000	87600	36100
Ea (n)	14300	52200	30800	52200	56900	66200	22200	38000	22000	87600	52200
Ea (b)	14300	34800	30800	34800	56900	66200	17900	94100	22000	1.1E+08	34800
n (a)	0.22	0.50	0.22	0.50	0.50	0.42	0.77	0.50	0.37	0.00	0.50
n (b)	0.22	0.50	0.22	0.50	0.50	0.42	-0.47	-0.82	-0.22	-0.50	0.50
pH (a)	6,00	5,00	6,00	6,00	6,00	6,00	6,00	6,00	6,00	6,00	6,00
pH (n)	8,00	14,00	8,00	8,00	8,00	8,00	8,00	8,00	8,00	8,00	8,00

VOL	anhy	ank	barite	dol	galena	hem	kaol	Kfsp	musc	Qz	sid
m0	0.28	0.54	0.22	0.53	0.36	0.49	0.63	2.40	0.13	61.6	1.12
Am	0.08	0.78	0.18	0.78	1.18	0.06	8.80	2.31	0.07	67.1	0.78
SSA [m^2/g]	8.3E-04	2.9E-03	1.4E-03	3.1E-03	5.4E-03	2,9E-04	2.2E-02	1.4E-03	5.5E-04	7.2E-03	2.4E-03
m [kg]	0.10	0.26	0.13	0.25	0.22	0.20	0.41	1.69	0.13	9.35	0.33

EFF	anhy	ank	barite	dol	galena	hem	kaol	Kfsp	musc	Qz	sid
m0	0.23	0.28	1E-04	0.27	3E-03	1.,23	11.2	1.52	0.37	21.0	0.58
Am	4E-04	4E-03	3E-10	4E-03	4E-07	3,1E-03	90,3	1E-01	5E-03	5.80	4E-03
SSA [m^2/g]	6.9E-04	1.5E-03	7.1E-07	1.6E-03	3.8E-05	7,9E-04	3.8E-01	8.6E-04	1.5E-03	2.4E-03	1.2E-03
m [kg]	6E-04	3E-03	4E-07	2E-03	9E-06	4E-03	2E-01	2E-01	3E-03	2.40	3E-03

For a more detailed description and the calculation of (specific) mineral surface areas, please regard to chapter 5. An average water saturation of 25 % and 15 % porosity was assumed for sandstones for field A which results in a percentage rock-water ratio of 22.7 and a density ratio for rock (2.27 g/cm^3)/fluid (1.19 g/ml) of 2.28. A CO_2 saturation index (SI) of 1.9 was set for the test scenario. The mineral rate constants, the amount of each mineral phase per kilogram water and the specific surface areas are listed in ▶ table 6.3.

Secondary minerals may precipitate and (re)-dissolve during simulation and are linked to equilibrium, only. For kinetic calculations no secondary minerals are defined because it would affect the computation time drastically. That means that PHREEQCi calculates the precipitation of secondary minerals as an instantaneous event without considering kinetic precipitation rates. Hence the minerals which are listed as secondary minerals are the result of the oversaturation with respect to the fluid composition. Therefore kinetic mineral reactions are only controlled by the dissolution of primary minerals and not precipitation rates and further dissolution of secondary minerals. Furthermore no information is available for specific surface areas of new formed minerals. Hence for the kinetic simulation the results from equilibrium are combined with the kinetic driven dissolution and precipitation of primary minerals (Bertier, 2011, person. comment). According to diagenetic natural analogous the composition and crystal structure of illite which is formed on expense of K-feldspar and kaolinite is highly similar to that of muscovite and contains no further contaminations (Meunier et al., 2004). For the simulation in this study the kinetic data for muscovite are used.

6.2 Equilibrium modelling

For modelling equilibrium conditions the volumetric mineralogy data were considered.

Table 6.4: Results of the equilibrium modelling for primary and secondary minerals (Initial = 0) and the pH and pe. SI is the Saturation Index, IAP is the Ion Activity Product and KT is the equilibrium constant at a given temperature. The mineral molality is given in mol/kgw for the initial and final stage. Δ is the difference between the initial and final stage.

	SI	**log IAP**	**log KT**	**initial stage**	**final stage**	**Δ**
				mol/kgw	**mol/kgw**	**mol/kgw**
anhydrite	0	-5.35	-5.35	0.28	0.35	0.06
ankerite	0	-0.81	-0.81	0.54	1.12	0.59
barite	0	-9.48	-9.48	0.22	0.22	$1*10^{-04}$
dolomite	-0	0.13	0.13	0.53	0.44	-0.09
galena	-0	-12.1	-12.1	0.36	0.24	-0.12
hematite	-1.43	-6.02	-4.59	0.49	0	-0.49
K-Feldspar	-0	-1.78	-1.78	2.40	0.04	-2.36
kaolinite	-1.13	-0.10	1.02	0.63	0	-0.63
muscovite	0	-45.4	-45.4	0.13	1.33	1.21
quartz	0	-3.06	-3.06	61.6	66.3	4.73
siderite	0	-1.48	-1.48	1.12	1.68	0.56
CO_2(g)	1.90	-6.45	-8.35	10.0	8.00	-2.00
pH	-	-	-	7.00	4.54	-2.46
pe	-	-	-	4.00	-0.17	-4.17

The minerals which are listed in table 6.3 are primary and secondary minerals. No further secondary minerals precipitated as result of the input of CO_2 into the solution and a decreasing pH (from 7.00 to 4.42) and pe (from 4.00 to 0.56).

The minerals hematite and kaolinite dissolve completely and dolomite, galena and K-feldspar show residual amounts. Note that 98.5% of the K-feldspar is dissolved. The species which are released during dissolution processes are redistributed and bonded in the minerals anhydrite, ankerite, muscovite, quartz and siderite. Changes in the barite content are negligible. Furthermore, saturation indexes (SI) larger zero are reached for celestite ($SrSO_4$) and strontianite ($SrCO_3$). But it is assumed that Sr, which is present in the initial solution (▶ table 6.2), precipitates not as discrete minerals, but is bonded in authigenic dolomite and anhydrite. The saturation index is zero for all minerals which precipitate, but negative for those which dissolve. The negative saturation index (-0) suggests that dolomite, galena and K-feldspar are close to being in equilibrium. Furthermore 2.00 mol/kgw CO_2 are consumed at the given pressure of 100 bar and temperature of 100°C. Furthermore the initial fluid composition which is provided by NAM is oversaturated with respect to carbonate, sulphate, Fe-bearing and clay minerals as they are listed in ▶ table 6.5. This initial oversaturation is important according to the short-term reactions taking place during CO_2 storage as it is modelled with PHREEQCi.

Table 6.5: Saturation index (SI) of selected minerals which are oversaturated in the initial fluid provided by NAM which is used for geochemical modelling.

mineral	**SI**
anhydrite	0.28
aragonite	2.67
calcite	2.77
chlorite (14Å)	4.37
dolomite	5.03
goethite	10.4
hematite	23.3
K-Jarosite	4.02
strontianite	1.24

Interpretation

The equilibrium model only provides results for the initial and finial fluid composition and the mineral content before and after the addition of CO_2. It is not possible to interpret the results accordingly to the interaction of species among each other. Hence the interpretation given below shows the release and consumption of species, only. While dolomite and galena (partly) dissolves the species Ca^{2+}, Mg^{2+}, Pb^{2+} CO_3^{2-} and HS^- are provided into the solution. Due to a decreasing pH by adding CO_2 into the solution and the presence of a sulphur species hematite is completely dissolved. The mentioned cations are then bonded in the mineral ankerite [$(Ca,Mg)_{0.3}Fe_{0.7}(CO_3)_2$]. Galena is dissolved while the released sulphur, together with Ca^{2+} is consumed by additional anhydrite. By the (total) dissolution of K-feldspar and kaolinite the amount of K^+, Al^{3+} and silica increases significantly. The more stable silica phases are muscovite and quartz. Furthermore iron is bonded in siderite.

6.3 Kinetic modelling

For the kinetic modelling some results are adapted from the previous equilibrium simulation: (1) the list of primary minerals and (2) the initial aqueous solution and gas phase. The volumetric and effective mineralogy data are modelled under the supply of CO_2. For both models sensitivity analyses are performed (section 6.3.2). The simulation time is 100.000 years. The choose of secondary minerals like muscovite and Mg-smectite is based on activity diagrams, mineral saturation indexes and the presence of these clay minerals in natural analogue systems (e.g. Bjørlykke and Aagaard, 1992). However the program suggests the precipitation of Al-rich minerals like diaspore (AlOOH) which seems to be an unlikely mineral in deep buried (> 2000 m depth) sediments and is not considered in the models. All other minerals which precipitate during the simulation are identical with the primary mineral assemblage (e.g. quartz, dolomite).

6.3.1 Results

In the following section the results of the geochemical model for the volumetric data set will be described and compared to the effective mineralogy.

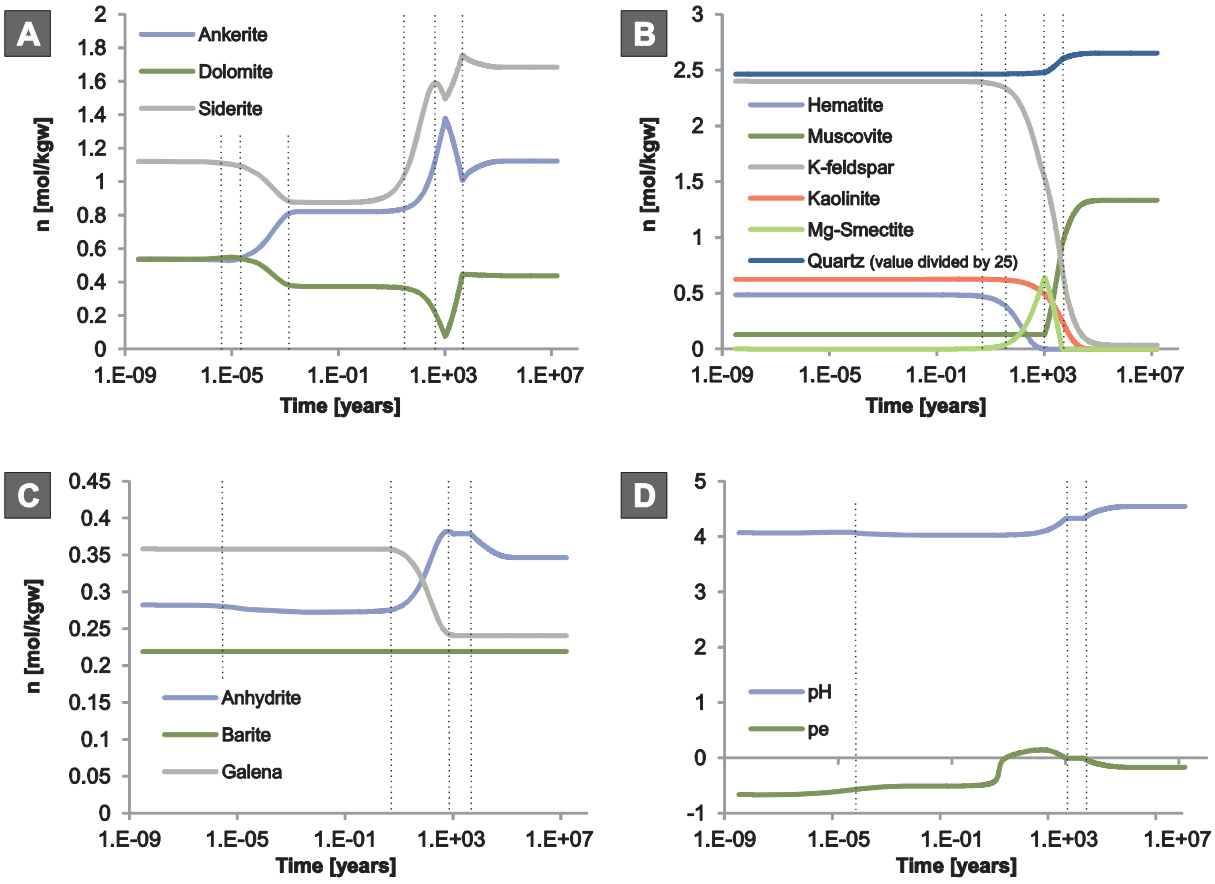

Figure 6.2: PHREEQCi modelling for volumetric mineralogy data.

Within the first seconds minor increasing dolomite and decreasing ankerite for the ***volumetric mineralogy*** data is observed (▶ figure 6.2A). Simultaneously anhydrite (▶ figure 6.2C) dissolves which results in an increasing Ca^{2+} concentration and an oversaturation of dolomite.

Due to insufficient availability of Mg^{2+} for dolomite precipitation, ankerite is undersaturated and releases further Mg^{2+}, Ca^{2+} and Fe^{2+} into the solution because dolomite is kinetically more stable than ankerite (▶ figure 6.2A). This reaction and the carbonate dissolution and precipitation which occur within the first minutes during simulation are due to the low pH (4.07) (▶ figure 6.2D) which is in turn caused by the input of CO_2 into the fluid and the related dissociation of HCO_3^- (▶ equation 1.1). During this time dolomite and siderite starts to dissolve (▶ equation 6.1) and release HCO_3^- and the elements Mg^{2+}, Ca^{2+} and Fe^{2+} into the solution (appendix B3-01G).

$$MCO_3 + H^+ \rightarrow HCO_3^- + M^{2+} \tag{6.1}$$

In turn ankerite precipitates and consumes the released metals from siderite and dolomite. After 33 min (▶ figure 6.2A) a further equilibrium stage for the carbonates is reached which continuous until 42 days for siderite, 526 days for dolomite and 617 days for ankerite (figure 6.2A). A slightly decreasing HCO_3^- content indicates that more bicarbonate is provided by dolomite and siderite as it is consumed by ankerite (appendix B3-01G). After this period dolomite dissolves in conjunction with the precipitation of ankerite and siderite. The Fe^{2+} which is consumed in siderite and ankerite is procured by hematite dissolution (▶ figure 6.2B). Contemporaneously the pH rises due to the release of protons during illitisation of K-feldspar and kaolinite which results in the production of HCO_3^- (appendix B3-01G). After ~5.000 years siderite becomes undersaturated and releases Fe^{2+} into the solution which is consumed by ankerite which becomes undersaturated itself after ~10.000 years. At this point ankerite dissolves and dolomite and siderite precipitate. A further equilibrium is reached after 94.600 years. After 3.5 years galena is undersaturated, starts to dissolve and releases 1.18 mol into the solution following ▶ equation 6.2.

$$PbS + H^+ \rightarrow HS^- + Pb^{2+} \tag{6.2}$$

Simultaneously anhydrite starts to precipitate and consumes SO_4^{2-} anions. However as shown in appendix B3-01H the concentration of SO_4^{2-} increases which may indicate oxidation of HS^- which is released from galena. This process disturbs the S(-II)/S(+VI) ratio which cause an increasing pe (▶ figure 6.2D). Due to ▶ equation 6.2 the pH should decrease based on the consumption of protons, but as shown in ▶ figure 6.2D the pH increases. This may be due to the illitisation process mentioned in the previous section. The earliest silica reaction (long term reaction) starts with the dissolution of K-feldspar and the release of K^+, Al^{3+} and silica into the solution which is initially consumed by Mg-smectite (▶ figure 6.2C). The Mg^{2+} required for the precipitation is procured by the dissolution of dolomite (▶ figure 6.2A). After 10.000 years Mg-smectite starts to dissolve. Instead illite (muscovite in the model) is formed until equilibrium is reached after ~53.000 years. A few years after the start of K-feldspar dissolution kaolinite becomes undersaturated and releases additional aluminium and silica for Mg-smectite formation and illitisation of both minerals is a common process. The illitisation of K-feldspar requires the presence of proton (▶ equation 4.17) which results in an increasing pH and in turn in the additional dissociation of $CO_{2(aq)}$ (▶ equation 1.1) and the precipitation of carbonates (▶ figure 6.2A). In comparison the illitisation of kaolinite is controlled by the amount of dissolved K-feldspar (▶ equation 6.3) (Worden and Morad, 2003).

$$\underset{\text{KAOLINITE}}{Al_2Si_2O_5(OH)_4} + \underset{\text{K-FELDSPAR}}{KAlSi_3O_8} \rightarrow \underset{\text{ILLITE}}{KAl_3Si_3O_{10}(OH)_2} + \underset{\text{QUARTZ}}{SiO_2} + H_2O \tag{6.3}$$

Both reactions result in the precipitation of quartz which is reflected in increasing quartz content during simulation time (▶ figure 6.2D). Furthermore K^+ content increases due to K-

feldspar dissolution after ▶equation 4.17. Note that the illitisation of kaolinite produces negligible amounts of water which disturbs the reference unit of one kilogram water for the model. Simultaneous to the precipitation of carbonates and the lower Fe^{2+} content in the solution, hematite dissolves under the consumption of protons (which are partly released by carbonate precipitation) and the production of water according to ▶ equation 6.4.

$$Fe_2O_3 + 6H^+ \rightarrow 2Fe^{3+} + 3H_2O \quad (6.4)$$

The Fe^{3+} is further reduced to Fe^{2+}. This reaction may be due to the release of HS^- by galena dissolution (▶ equation 6.2) and the oxidation to SO_4^{2-} (▶ equation 6.5) which would explain the increasing content SO_4^{2-} contemporaneously to the mineral reactions.

$$8Fe^{3+} + HS^- + 4H_2O \rightarrow 8Fe^{2+} + {SO_4}^{2-} + 9H^+ \quad (6.5)$$

However the reaction of hematite starts earlier than the dissolution of galena and simultaneous to ankerite and siderite precipitation. Hence another reducing agent seems to be present before HS^- is released from galena.

For the ***effective mineralogy*** data differences have been observed for short and long term reactions in comparison to the volumetric mineralogy. The pattern of carbonate reactions are the same as described for the volumetric data set, but the reactions start a few hours later (▶ figure 6.3A). The main difference is present for the long term reactions. Dolomite and siderite dissolve consequently until a minimum is reached after ~335 years. Due to the release of Ca^{2+}, Mg^{2+}, Fe^{2+} and HCO_3^- ankerite precipitates.

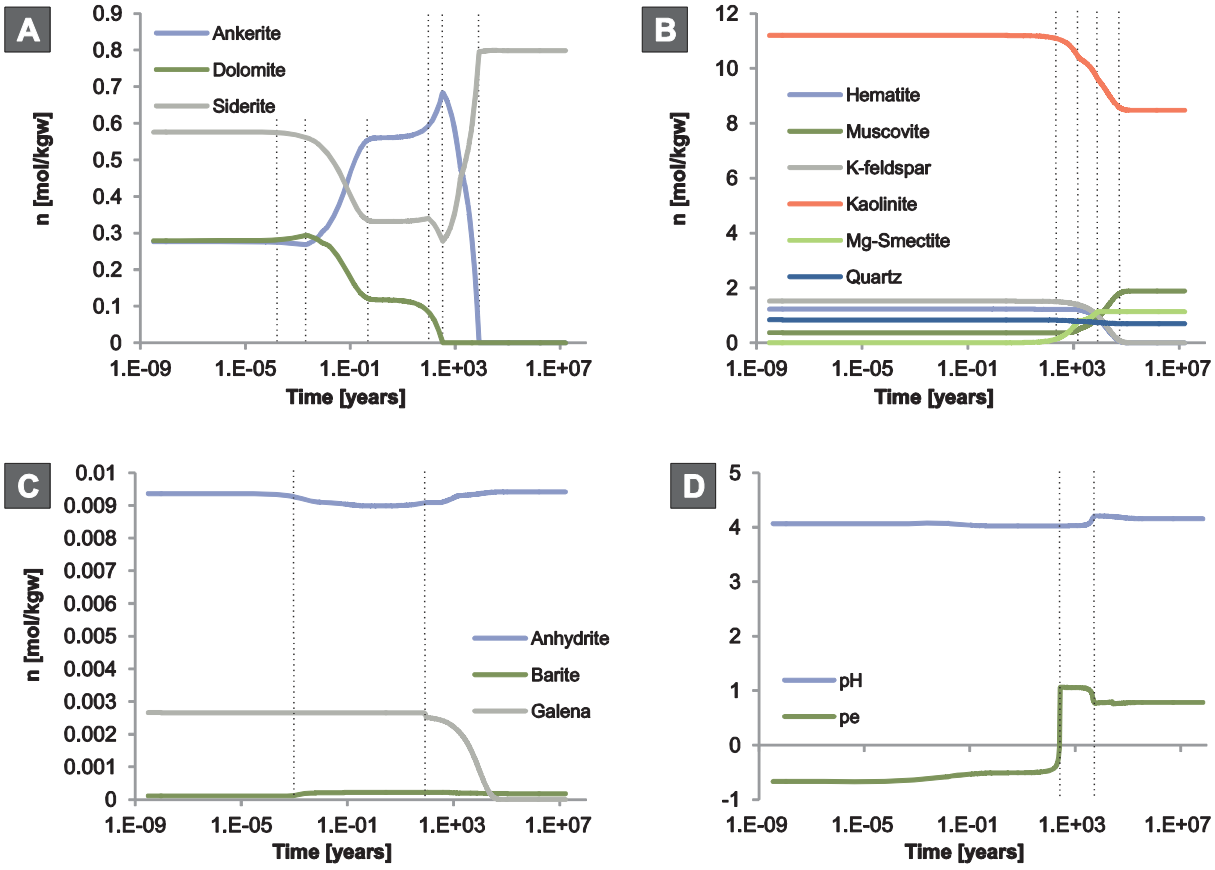

Figure 6.3: PHREEQCi modelling for effective mineralogy data.

During this period the HCO_3^- (appendix B3-02G) content is constant which indicates that all bicarbonate which is released from dolomite and siderite is consumed by ankerite. After ~335 years dolomite is completely dissolved. The released Mg^{2+} is consumed by Mg-smectite which stays in equilibrium with the solution. In comparison to the volumetric data set, Mg-smectite is completely dissolved after a short period and dolomite precipitates again (▶ figure 6.2A). Furthermore siderite precipitates as a result of ankerite dissolution and the supply of iron from hematite dissolution (▶ figure 6.3A). At the end of the simulation siderite is the only remaining carbonate phase. Simultaneous to ankerite and dolomite dissolution and siderite precipitation the bicarbonate content increases (appendix B3-02G). At the same time galena starts to dissolve (▶ figure 6.3B), the redox potential increases from -0.2 to +1.1 (▶ figure 6.3D) which is caused by the oxidation of HS^- to SO_4^{2-} (▶ equation 6.5). The release of HS^- influences the dissolution process of hematite which is completely dissolved after ~10.000 years. The released Fe^{3+} is reduced to Fe^{2+} and consumed in a first step by ankerite and after this by siderite. These reactions are caused by the amount of dissolved dolomite which is in turn controlled by the precipitation of Mg-smectite. An increasing Fe^{3+} content and a slightly decreasing or constant Fe^{2+} content (appendix B3-02F) indicates that not the total amount of released iron from hematite is reduced and consumed by Fe-rich carbonates. In comparison to the volumetric data more initial hematite is present which starts to dissolve ~1000 years later. The changes of the anhydrite and barite contents are negligible. The illitisation of K-feldspar is expressed by ▶ equation 4.17, 4.18 and 6.3.

But as shown in ▶ figure 6.3B quartz starts to dissolve after ~1000 years which is caused by the lower initial quartz content in comparison to kaolinite (▶ table 6.2) and the requirement of silica for clay precipitation. The smaller initial K-feldspar content (1.52 mol) releases less K^+ into the solution which is consumed by illite compared to the volumetric data (K-feldspar: 2.40 mol). However the final amount of illite is higher for the effective mineralogy data (▶ figure 6.3B) (Δ=0.56 mol). This indicates that the precipitation of Mg-smectite (▶ equation 6.6) is connected to the dissolution of kaolinite and dolomite which releases the species required for the reaction.

$$Kaolinite + Mg^{2+} \rightarrow Mg\_smectite \tag{6.6}$$

Note that the formula for Mg-smectite in the database ($Mg_{0.405}[(Si_{3.97}Al_{1.77})O_{11.48}](H_2O)_{0.52}H_{0.96}$) is difficult to assign to a direct stochiometric transformation of kaolinite as it is listed in the database ($Al_2Si_2O_5(OH)_4+6H^+$).

6.3.2 Sensitivity analysis

A (geochemical) model has to be tested according to the uncertainty of the output data and the possible appropriation to the input data (Saltelli et al., 2008). A sensitivity analysis of the water-rock-CO_2 interactions and the related input data of the test scenarios will be described in the following section. Therefore the input data are changed according to reasonable dimensions which are based on previous rock and fluid analysis.

Model runs without CO_2

To test how the fluid would react with the rock without the addition of CO_2 the simulation was run for both, the volumetric mineralogy and effective mineralogy data, respectively.

For the ***volumetric mineralogy*** the reaction starts with a pH of 5.19 (appendix B3-03E) which is slightly higher than under the supply of CO_2 (pH=4.07). The short term carbonate reactions show the same pattern as with CO_2, but the reactions start a few minutes later (appendix B3-03A). However, the late carbonate reactions are influenced by the precipitation of Mg-smectite and the associated removal of Mg^{2+} from the solution (▶ equation 6.6). Because of the lower protons content, less K-feldspar dissolves (▶ equation 4.17) and less illite is formed (appendix B3-03C). However, kaolinite dissolves completely and/or is transformed to Mg-smectite. The lower final amount of siderite is caused by a lacking Fe^{2+} content which is in turn influences by the precipitation of hematite. Based on the lower proton content galena stays in equilibrium until no HS^- is brought into solution (▶ equation 6.2) which is turn potentially needed for hematite reduction (▶ equation 6.5). Hence no hematite dissolves and ankerite becomes unsaturated and releases cations into the solution which are consumed by siderite. Dolomite dissolves completely caused by Mg-smectite precipitation. Anhydrite is undersaturated and starts to dissolve after ~10 years.

The simulation for the ***effective mineralogy*** shows similar results. The initial pH decreases from 5.19 to 4.09. The only difference to the test scenario are the slowed down short term carbonate reactions which start a few minutes later, which influence in turn the long term reactions (appendix B3-04A).

Only minor differences are observed for fluid-rock interaction between the sandstone and the chosen fluid composition without the addition of CO_2.

Effect of initial equilibrium between rock and fluid

For both data sets (volumetric and effective) the simulation was run with an initial equilibrium between rock and fluid to test the scenario of an undisturbed rock-fluid system under reservoir conditions. Therefore an equilibrium model was run for the rock and fluid composition as used for kinetic modelling. The composition is listed in ▶ table 6.2.

For the ***volumetric mineralogy*** the simulation starts at a pH of 3.4 which is lower than for the test scenario. A fast increase of the pH within the first seconds appears and ends at pH 4.03 (appendix B3-05E) which will further increase after ~10 years due to carbonate precipitation (▶ equation 6.1). However in the first ~10 years no short term reactions appear (appendix B3-05A, B, C and D). The late term carbonate reactions show the same pattern in comparison to the test scenario. However at the final equilibrium stage less siderite (Δ=-0.26) and dolomite (Δ=-0.15) precipitate (appendix B3-05A). Therefore the ankerite content increases (Δ=+0.31). The sulphate/sulphide and silica reactions show no differences, except of a residual amount of K-feldspar (0.12 mol) which is not dissolved at the final stage (appendix B3-05C).

The ***effective mineralogy*** data show similar results in regard to the precipitation/dissolution behaviour of the minerals. The initial pH increases from 3.39 to 4.03 within the first seconds. Ankerite and siderite start to precipitate after ~10 years. A few years later siderite partly dissolves which seems to be caused by no further hematite dissolution and lacking Fe^{2+} content which is further linked to galena dissolution (appendix B3-06A, B and C). Consequently ankerite dissolves and siderite precipitates due to the release of Fe^{2+} (▶ equation 6.1). Consequently anhydrite precipitates caused by the release of Ca^{2+} from dolomite and ankerite and SO_4^{2-} as an oxidation product of HS^-. The same pattern is present for all silica reactions.

The lacking short term carbonate reactions may be caused by the equilibrium between rock and fluid and/or low pH at the beginning of the simulation. Only minor effects are to note for all long term reactions. Hence an initial equilibrium between rock and fluid may influence all reactions within the first ~10 years.

Effect of initial fluid composition

For the initial fluid composition a lower salinity scenario was tested for the volumetric and effective mineralogy in conjunction with other fluid analyses provided by NAM. The initial fluid composition was assumed to have less salinity which still has a Cl^-/Na^+ mass-ratio of ~2.15, but with total lower amounts of 20000 mg/l Na^+ and 43000 mg/l Cl^-. The analyses from well Aw13 and from the North Sea Formation Water Atlas (Warren and Smalley, 1994) are similar to the "Northern Netherlands" fluid which was chosen for the test scenario. The information from well Aw01 and Aw14 are not sufficient for a model due to the absence of sulphur (e.g. SO_4^{2-}) and carbon species (e.g. HCO_3^-) (▶ table 6.1).

Lower Cl^- and Na^+ contents only have negligible effects on the ***volumetric mineralogy*** data. The precipitation of dolomite and dissolution of ankerite which take place within the first seconds (appendix B3-07A) are absent in this simulation. This may be due to a lower ionic strength. Caused by minor amounts of Cl^- which occur as compound with Ca^{2+} and Mg^{2+} forming $CaCl_2$, $CaCl^+$ and $MgCl^+$ more dissociated amounts of Ca^{2+} and Mg^{2+} in the solution are available (▶ table 6.7). However the pH is not affected for a lower salinity. Hence dolomite and ankerite are in equilibrium with the fluid and no precipitation/dissolution of the carbonates appears within the first seconds. No other effects on mineral reactions have been observed.

Also for the ***effective mineralogy*** no difference in comparison to the test scenarios are to note (appendix B3-08).

Table 6.7: Species concentration [mol/l] at step 1 for the test scenario for the volumetric mineralogy in comparison to a changed Na^+ and Cl^- content as sensitivity analysis.

species	high salinity	low salinity
	[mol/l]	[mol/l]
Na^+	2.52	0.71
Cl^-	3.62	0.96
NaCl	1.36	$7.9*10^{-02}$
Ca^{2+}	0.38	0.45
Mg^{2+}	$4.6*10^{-02}$	$6.5*10^{-02}$
$CaCl_2$	0.13	$8.3*10^{-02}$
$CaCl^+$	$8.7*10^{-02}$	$2.7*10^{-02}$
$MgCl^+$	$5.7*10^{-02}$	$2.0*10^{-02}$

Effect of temperature

The influence of lower temperatures was tested for 20°C and 50°C because the CO_2 which is injected in the sandstone has a lower temperature than the reservoir. The results are listed for ***volumetric mineralogy*** data in appendix B3-09 (20°C) and B3-10 (50°C) and for the ***effective mineralogy*** data in appendix B3-11 (20°C) and B3-12 (50°C).

Lower temperature increases the density of CO_2 in an aqueous phase (▶ figure 1.2) (Peng and Robinson, 1976; UCE, 2006). The relation is not linear and is further related to the hydrostatic pressure (UCE, 2006). The increasing CO_2 solubility is reflected in increasing aqueous bicarbonate content after ▶ equation 1.1 at lower temperature (for volumetric mineralogy data: appendix B3-09G and -10G and for effective mineralogy data: appendix B3-11G and -12G). The higher CO_2 solubility results in an increasing amount of protons and therewith in a decreasing pH as it is shown in appendix B3-09E and -10E and appendix B3-11E and -12E. The lower pH and higher bicarbonate content cause the carbonate minerals to react faster due to a higher under- or oversaturation of dolomite, ankerite and siderite. For the long term carbonate reactions the lower Fe^{2+} activity which is caused by limited hematite dissolution counteracts the reaction rates for Fe-bearing carbonates. The higher carbonate reaction rates at lower temperatures force the pH to decrease due to carbonate dissolution (appendix B3-09A and -10A) and (appendix B3-11A and -12A). The changing pH influences silica to react later than in the test scenario, since the K-feldspar dissolution is linked to the presence of protons (▶ equation 4.17). This initial silica reaction causes the formation of illite and the dissolution of kaolinite to appear later (appendix B3-09C and -10C and appendix B3-11C and -12C). The lacking dolomite undersaturation which procures Mg^{2+} for Mg-smectite precipitation in the test scenario forces kaolinite to be oversaturated due to the higher amount of aluminium and silica in the solution. This results in a short event of kaolinite precipitation after ~4000 years (appendix B3-10C). Furthermore the reaction of galena is controlled by the presence of protons after ▶ equation 6.2 and is slowed down due to lacking protons available in the solution. This reaction causes hematite to start to dissolve later than in the test scenario and therewith affecting the availability of Fe^{2+} for siderite and/or ankerite precipitation. As shown, the effects of lower temperatures are similar to the volumetric and effective mineralogy data.

Effect of pressure

The effect on CO_2 pressure was tested at 10, 50 and 300 bar, respectively. Results are listed for the ***volumetric mineralogy*** data in appendix B3-13 (10 bar), B3-14 (50 bar) and B3-15 (300 bar) and for the ***effective mineralogy*** data in appendix B3-16 (10 bar), B3-17 (50 bar) and B3-18 (300 bar). As mentioned in the previous section the solubility of gaseous CO_2 into water depends on temperature and pressure. The Henry's Law constant (▶ equation 6.7) indicates that the solubility is also a function of the fugacity of CO_2 and indirectly of the CO_2 pressure. The lower the CO_2 pressure the lower is the CO_2 solubility causing a higher pH.

$$K_{sp} = \frac{a_{CO_2}(aq)}{f_{CO_2}(g)} = K_h \tag{6.7}$$

Henry's Law constant (K_h) is equal to the solubility product (K_{sp}) which in turn is the ratio of the activity of the aqueous CO_2 (a) and the fugacity of the gaseous CO_2 (f). The different pressures used for the simulation were added as equilibrium phases with different saturation indexes (▶ table 6.8).

With decreasing CO_2 pressure the short term carbonate reactions slow down due to fewer protons content in the solution. No major differences are to note for the long term carbonate reactions until the pressure reaches 10 bar (appendix B3-13A) for the ***volumetric mineralogy*** data. At this pressure the amount of protons for K-feldspar dissolution is relatively low resulting in minor dissolution and precipitation of illite (▶ equation 4.17). However kaolinite still dissolves and release aluminium and silica into the solution. Based on this reaction Mg-smectite

precipitates consequently. This reaction yields in an undersaturation of dolomite and a complete dissolution. The release of Ca^{2+}, Mg^{2+} and bicarbonate is partly consumed by ankerite and under the supply of Fe^{2+} by siderite. The excess of aluminium and silica from kaolinite dissolution and released potassium results in a short event of K-feldspar precipitation (appendix B3-13C). However a few years later K-feldspar will further consequently dissolve until ~55 % of K-feldspar is dissolved and/or transformed to illite. Furthermore the effect of less protons influence the dissolution of galena (▶ equation 6.2) and therewith the reduction of hematite (▶ equation 6.5). Increasing CO_2 pressure (300 bar) has negligible influences on mineral reactions.

Table 6.8: Saturation index (SI) according to CO_2 pressure [bar].

pressure	SI
10	1.00
50	1.70
100	1.90
300	2.48

For the ***effective mineralogy*** similar effect with decreasing CO_2 pressure are to note. In comparison to the volumetric data set Mg-smectite precipitates in the test scenario. Hence all mineral reactions show the same pattern but starts a few days or years later, respectively. However with increasing pressure no change in the mineral assemblage during simulation should appear. With increasing pressure less CO_2 is dissolved within the fluid and pH rises. Due to this reaction minor amount of kaolinite and K-feldspar dissolve followed by minor Mg-smectite formation (▶ table 6.9) which causes in turn minor Mg^{2+} bonding in the mineral phase. The additional amount of Mg^{2+} causes ankerite to dissolve more slowly. At the end of the simulation residual ankerite (0.28 mol) is present in the rock.

Table 6.9: Difference between initial and final mineral content [mol/kgw] for silica minerals at 100 bar and 300 bar for volumetric and effective mineralogy data. Negative values mean dissolution and positive values mineral precipitation. Note that muscovite is used for illite in the simulation.

	volumetric mineralogy		effective mineralogy	
mineral	50 bar	300 bar	50 bar	300 bar
kaolinite	-0.27	-0.25	-2.75	-2.50
K-feldspar	-1.52	-1.52	-1.52	-1.52
muscovite	1.52	1.50	1.54	1.50
Mg-smectite	1.08	0.87	1.14	9.25

Effect of water-rock-ratio

The water-rock-ratio was simulated for 5 %, 50 %, 75 % and complete water saturation according to different water saturation stages within the reservoir (appendix A4-04). The results are listed for ***volumetric mineralogy*** data in appendix B3-19 (5%), B3-20 (50%), B3-21 (75%) and B3-22 (100%) and for the ***effective mineralogy*** data in appendix B3-23 (5%), B3-24 (50%), B3-25 (75%) and B3-26 (100%).

The water-rock ratio is directly related to the rock content per kilogram water with an estimated porosity of 15 %. The higher the water saturation the more rock material may potentially react. Based on this estimation the reaction rate of short term carbonate reactions increases for water saturation >25 % and starts after the first seconds (appendix B3-20A, -21A and -22A) for the ***volumetric mineralogy***. In comparison to the test scenario dolomite dissolves completely. This reaction is faster the higher the water saturation and releases Ca^{2+}, Mg^{2+} and bicarbonate into the solution. Immediately ankerite, siderite and Mg-smectite precipitate (appendix B3-20C, -21C and -22C). When increasing the water/rock ratio the reaction rates for all silica reactions increase. A water saturation of 5 % has major impact on mineral reactions. The pattern of dolomite and ankerite is the same in comparison to the test scenario (appendix B3-19A), but the rates are much lower. The main difference of the carbonate reactions is the consequent precipitation of siderite after ~10 years which is linked to the release of iron from hematite dissolution and further reduction to Fe^{2+} (▶ equation 6.4). With less water content the saturation and dissolution kinetics increase faster and the equilibrium stage between the fluid and a mineral is reached sooner. Hence K-feldspar dissolves slower and reaches the equilibrium after ~10.000 years until ~34 % is dissolved, only (appendix B3-19C). Linked to this reaction less illite is formed (▶ equation 4.17).

For the ***effective mineralogy*** data K-feldspar dissolves completely, but kaolinite is the dominant silica phase which partly dissolves (Δ=22 %). The influence of less water availability is the same for the effective mineralogy in comparison to the volumetric data.

Effects of changing carbonate content

According to thin section analyses different carbonate contents are noted for the sandstones investigated in this study. The total amount ranges between 0 and 38 vol.-% with an average of 7.2 vol.-% (appendix C2). Samples from field A are dominated by blocky dolomite, ankerite and siderite whereas samples from field B and C contain dolomite and Fe-rich dolomite only (compare section 4.2.1). Hence the addition of 30 % dolomite, ankerite and siderite, respectively and the removal of ankerite and siderite as primary minerals were tested.

The simulation of the ***volumetric mineralogy*** shows that the addition of 30 % carbonates (10 % dolomite, ankerite and siderite, respectively) results in lower reaction rates because more material is available which reacts with the same volume of fluid. Hence the reaction rates are slower for all carbonate minerals but the pattern is still the same as in the test scenario (appendix B3-27A). All other reactions are not affected by the supply of carbonate to the system. For the effective mineralogy data the supply of dolomite, ankerite and siderite has the same influence on the mineral reactions than for the volumetric data. The removal of ankerite and siderite as initial mineral phases results in a lacking of short term carbonate reactions (appendix B3-29A). This is due to an equilibrium stage between the fluid and dolomite. Simultaneous to the reaction of kaolinite under the supply of magnesium Mg-smectite is formed and dolomite becomes undersaturated and releases also Ca^{2+} and bicarbonate into the solution which is immediately consumed by ankerite and siderite precipitation. By the consumption of protons the pH increases (appendix B3-29E) due to illitisation of K-feldspar. Due to the precipitation of illite Mg-smectite dissolves and the released species are consumed by illite, dolomite and ankerite.

For the ***effective mineralogy*** data the removal of ankerite and siderite results in a consequent dissolution of dolomite due to Mg-smectite transformation of kaolinite (▶ equation 6.6). Only

negligible amounts of ankerite and no siderite precipitate. The pH is relatively constant at 4.06 until ~10.000 when dolomite starts to dissolve under the consumption of protons (appendix B3-30E). Further effects which rise the pH is the dissolution of hematite (appendix B3-30C) and the illitisation of K-feldspar (▶ equation 4.17). All iron released from hematite is consumed by ankerite which is in turn controlled by the presence of the aqueous Ca^{2+} content and causes the Fe^{2+} acitivity to decrease.

Effect of removing hematite

The removal of hematite in the ***volumetric mineralogy*** data point out the relation between hematite dissolution under the consumption of protons (▶ equation 6.4) and reduction of Fe^{3+} to Fe^{2+} by HS^- (▶ equation 6.5) which in turn is released by galena dissolution (▶ equation 6.2). Because hematite is absent no Fe^{3+} is produced which forces galena to become undersaturated due to the reaction with HS^- and the oxidation to SO_4^{2-}. This relation is further expresses in anhydrite dissolution which is controlled by the presence of aqueous Ca^{2+} and the minor SO_4^{2-} which again increases in the residual solution because no other sulphate (e.g. barite) precipitates (appendix B3-31B). Furthermore the pH increases due to lacking hematite reaction and the consumption of protons by K-feldspar illitisation (▶ equation 4.17). The lower Fe^{2+} content results further in lacking siderite precipitation and the dissolution of the precursor mineral phase after ~6 days. Siderite dissolution produces bicarbonate which is in turn consumed by dolomite and ankerite precipitation (appendix B3-31A). The dolomite content increases further after ~300 years because of Mg-smectite and anhydrite dissolution and the release of Ca^{2+}, Mg^{2+} and bicarbonate content.

For the ***effective mineralogy*** data the effect of removing hematite is similar to the volumetric mineralogy. The main differences are the precipitation and equilibrated conditions of Mg-smectite after ~14.500 years and a final amount of 1.15 mol (appendix B3-32C). This mineral precipitation requires Mg^{2+} which is released from dolomite and ankerite dissolution. The remaining Ca^{2+} is further bonded in new formed anhydrite and the Fe^{2+} and bicarbonate precipitates as siderite (appendix B3-32A). This means that based on the initial mineral assemblage dolomite and ankerite (volumetric mineralogy data) or siderite (effective mineralogy data) are the final carbonate phases.

Effects of changing anhydrite, barite and galena content

For the ***volumetric mineralogy*** data the removal of galena from the initial data show similar results as described for the removal of hematite due to the relation of hematite reduction (▶ equation 6.4), galena dissolution (▶ equation 6.2) and the oxidation of HS^- to SO_4^{2-} (▶ equation 6.5). However minor amounts of hematite (~1%) dissolve and influence the precipitation/dissolution behaviour of siderite and ankerite due to the release of iron (appendix B3-33A). Hence dolomite and siderite precipitate again after ~10.000 years and ankerite dissolves in consequence to required protons and bicarbonate for dolomite and siderite. The removal of anhydrite from the initial mineral assemblage has a similar effect on the mineral reaction as galena. Galena dissolves and releases HS^- into the solution which is oxidised to SO_4^{2-} but no anhydrite precipitates as secondary mineral. Instead barite is formed (appendix B3-33B). Without anhydrite no Ca^{2+} is released and dolomite becomes undersaturated at the expense of ankerite which consumes Ca^{2+} and Mg^{2+} from anhydrite and/or dolomite. Fe^{2+} is procured by siderite dissolution. This redistribution of cations and bicarbonate from one carbonate phase to

another and especially the dissolution of siderite yield in an equilibrium stage between hematite and fluid. Hence no hematite dissolves even though HS^- is present due to galena dissolution and the presence of protons. The addition of 10 % anhydrite has the same effect as the removal, because the mineral stays in equilibrium with the fluid and negligible amounts of anhydrite dissolves only (appendix B3-35 and 37).

However the relation between hematite, Fe-carbonates and sulphates is highly sensitive as shown in the sensitivity analyses and only minor changes can cause different mineral reactions. A comparison of saturation indices of hematite (simulation without anhydrite/galena and plus 10 % anhydrite), shows that after ~10 years the saturation is near zero and minor changes of the rock-fluid system would cause hematite dissolution.

The ***effective mineralogy*** data show another effect of lacking galena. As described in the previous sections the relationship between the sulphates/sulphides and hematite yield in hematite dissolution and the reduction of Fe^{3+} to Fe^{2+} by HS^- released from galena. However in this simulation hematite still dissolves (appendix B3-34C) due to siderite precipitation and the associated dissolution of dolomite and ankerite which is in turn caused by Mg-smectite precipitation. Hence another species must be present which results in the reduction of iron. Therefore the simulation was run without any primary anhydrite, barite and galena which are not allowed to precipitate as secondary minerals during simulation. The results show that hematite still dissolves (appendix B3-39C) and that the amount of different S-species decreases (appendix B3-39H) at the time when hematite dissolution starts and Fe^{3+} is reduced to Fe^{2+}. Furthermore an increase of the SO_4^{2-} content is to note (appendix B3-39H). These observations indicate still a reduction of iron by S-species. However the amount of sulphur in the initial fluid suffices for reduction processes to Fe^{2+} which is further bonded in siderite. Note that the initial amount of hematite is more than twice the amount as for the volumetric mineralogy (▶ table 6.3) and that hematite is completely dissolved during simulation. Similar results show the simulations without anhydrite and plus additional amounts of 10 % anhydrite (appendix B3-36 and -38) due to the explanations as given for the volumetric mineralogy.

Effect of changing quartz content

The total quartz content (mono- and polycrystalline quartz, chert and authigenic quartz) ranges between 31.7 and 77.1 vol.-% for field A (appendix C3). The simulation of the test scenario was run with a relatively high quartz content for the volumetric mineralogy of >73.8 vol.-% which is slightly lower than for the maximum value because the same samples were chosen as for the determination of the effective mineralogy. Hence the total amount was reduced to 50 % and the initial amounts and mineral surface areas were calculated based on the lower quartz content. For the effective mineralogy the initial quartz content for the test scenario yields 25.1 % and was lowered to 12.0 % for sensitivity analysis.

For the ***volumetric mineralogy*** the lower quartz content has no effects on silica and short term carbonate and sulphate reactions (appendix B3-40A and B). Due to shifting of the mineral amounts to higher values, respectively more hematite is present in the initial mineral assemblage which dissolves completely contemporaneously to siderite precipitation (appendix B3-40A). In the sum more siderite (Δ=1.19) is formed for lower initial quartz content in comparison to the test scenario (Δ=0.56). For the ***effective mineralogy*** no effect for lowering the quartz content is noted which may be due to the already low amount (appendix B3-41).

Effects of changing K-feldspar content

The simulation was tested for the supply of 10 % K-feldspar and without K-feldspar. Additional K-feldspar has only effects on silica reactions, especially on the illitisation of K-feldspar (▶ equation 4.17). In comparison to the test scenario the fluid is saturated after ~30.000 years and ~60 % for the ***volumetric mineralogy*** and ~43 % for the ***effective mineralogy*** dissolve and is transformed to illite only (appendix B3-42 and 43). Hence the addition of K-feldspar has only minor effects on the mineral reactions during CO_2 storage. The removal of K-feldspar from the primary mineral assemblage results in lacking illite precipitation (appendix B3-44C). However the formation of Mg-smectite from kaolinite reaches no equilibrium after all kaolinite is consumed. The additional Mg-smectite formation is due to the dissolution of illite and the release of aluminium and silica into the solution. Contemporaneously the aqueous potassium concentration increases (appendix B3-44F). Carbonate precipitation produces protons (▶ equation 6.1) which are consumed by hematite dissolution (▶ equation 6.4). Hence the formation of Mg-smectite from kaolinite and illite dissolution seems to proceed under no consumption or release of protons because the pH is relatively constant during simulation time (appendix B3-44E).

Effect of changing kaolinite content

The effect of the kaolinite content is already analysed by the different test scenarios for the volumetric and effective mineralogy. There the initial amount yields 3.26 vol.-% and 58.2 %, respectively. For a more detailed description please regard to section 6.3.1.

6.4 Interpretation and discussion of geochemical modelling

Observation of mineral reactions on a short time scale can be reached from laboratory experiments. Information about long-term interactions between mineral phases with a fluid and CO_2 are available from natural analogues (Pham et al., 2011). However, differences in the outcome of mineral reactions from laboratory experiments and numerical modelling to field observations may be explained by the following factors (Gaus et al., 2008): (1) errors in kinetic and thermodynamic data for each mineral phase used in numerical simulations, (2) kinetic expressions may be too generalised to calculate properly and (3) incorrect assumptions like CO_2 charge and CO_2 pressure in natural analogues. Furthermore a generalisation of the rock composition, chemical composition of each mineral used in the numerical simulation, initial mineral specific surface area and the fluid composition may comprehend possible errors for a realistic model.

The decreasing pH at the beginning of the simulation is due to the dissociation of aqueous CO_2 into the fluid (▶ equation 1.1) and is reported by several authors for experimental and modelling CO_2-water-rock interactions (e.g. Kaszuba et al., 2003; Soong et al., 2004; Bateman et al., 2005; gaus et al., 2005; Giammar et al., 2005; Ketzer et al., 2009). Studies from Audigane et al. (2007) and Pham et al. (2011) showed that all pH evolution for the modelled systems are ending up at around pH 5, which may be due to buffering effects of carbonate reactions. This result is confirmed by this study since carbonate reactions are taking place over simulation time and the final pH is around 5 for both simulations (volumetric and effective mineralogy).

Carbonate reactions and CO_2 trapping was recognised in many natural systems (e.g. Baines and Worden, 2004; Gaus et al., 2004; Watson et al., 2004; Wardon, 2006; Pauwels et al., 2007),

numerical simulations (e.g. Gaus et al., 2005; Knauss et al., 2005; André et al., 2007; Cantucci et al., 2009), laboratory experiments (e.g. Ketzer et al., 2009; Pokrovsky et al. 2009) and field-scale test-sites (e.g. Assayag et al., 2009; Raistrick et al., 2009; Gislason et al., 2010). In this study a comparison between the initial amount, after 10 years of CO_2 storage and the final amount of dolomite, ankerite and siderite for the volumetric and effective mineralogy is listed in ▶ table 6.10. After 10 years negligible amounts of carbonates are dissolved for the volumetric data set. The short term dissolution of carbonate is shown by e.g. Ketzer et al. (2009) for sandstones containing ~5 vol.-% dolomite which was equilibrated with deionised water and by laboratory experiments in sandy sediments by Rochelle et al. (2002). On the other hand mineral trapping occurs within this period according to the effective mineralogy. For the long term reactions the opposite behaviour is the case: carbonate dissolution of dolomite and ankerite and carbonates precipitate for the other case due to the higher amounts of protons and bicarbonate. Bateman et al. (2005) recognised the redistribution of dissolved calcite in dolomite precipitates in quarzitic sandstone with initial amount of 3 wt.-% calcite. A comparison of volumetric and effective mineralogy data shows that short term reactions and especially the long term reactions are influenced by different initial mineral contents as they are listed in ▶ table 6.2 and the interaction of species and mineral reactions during the simulation. The short term carbonate reactions are basically the same, but start a few years later for the effective mineralogy data. This may be due to the lower initial carbonate content. The partial dissolution of anhydrite is due to the precipitation of carbonates and the required Ca^{2+}. The reaction starts later for the effective mineralogy which is also caused by the lower initial carbonate content. The changing bicarbonate (HCO_3^-) and CO_3^{2-} concentration within the solution (▶ figure 6.4) may indicate carbonate dissolution. Due to an increasing pH (▶ figure 6.2D and 6.3D) more CO_2 dissociates which results in the increasing concentration of HCO_3^- and CO_3^{2-}. However the precipitation of magnesite and dawsonite which is reported by other studies (e.g. Worden, 2006; Pauwel et al., 2007; Saldi et al., 2009) doesn't take place within the modelled system. The lacking dawsonite precipitation is confirmed by Gaus et al. (2004) for the Montmiral, Southeast Basin, France with a reservoir pressure of 360 bar and 100°C temperature. The reservoir water contains high NaCl-brines and the dissolution of K-feldspar may act as aluminium source. On the other hand dawsonite precipitated within the Meddokompos reservoir (Florina Basin, Greece) with a maximum pressure of 10 bar and a temperature of 43°C. The abundant Na-feldspar content and a high pH of 8.7 favour the formation of dawsonite. Hence the high NaCl content of the water, the high temperature and CO_2 partial pressure are probably the reason for the lacking dawsonite precipitation (Gaus et al., 2004; Pham et al., 2011).

The long term reactions are mainly influenced by the higher initial amount of kaolinite and the lower amount of K-feldspar and quartz for the effective mineralogy. The dissolution of K-feldspar results mainly in the precipitation of illite and the dissolution of kaolinite influence the precipitation of Mg-smectite. However Bjørlykke and Aagaard (1992) mentioned that the illitisation of K-feldspar is inhibited by the presence of smectite and kaolinite and that illite would precipitate from these minerals. This is not comprehensible for this model because K-feldspar and kaolinite are transformed to illite and Mg-smectite contemporaneously. Due to these reactions dolomite becomes undersaturated, dissolves and releases Ca^{2+} and especially Mg^{2+} which in consumed by Mg-smectite. In comparison, less aluminium and silica are available for clay mineral precipitation for the volumetric mineralogy. Hence dolomite stays in equilibrium and Mg-smectite precipitates but is dissolved completely due to the lacking Mg^{2+} content in the solution. According to both data sets hematite and galena are completely dissolved. Minor dissolution of K-feldspar is confirmed for the Sleipner area which is located in

the Norwegian part of the North Sea during CO_2 storage (Gunter et al., 2000; Gaus et al., 2004). The authors suggest that the reactivity of K-feldspar is limited by the absence of a sink for potassium. In this study illite (muscovite in the model) is formed on expense of K-feldspar and forces K-feldspar to dissolve consequently. For the Sleipner area kaolinite precipitates due to the dissolution of plagioclase and albite. Both feldspar minerals are lacking in the input data of this study and kaolinite becomes undersaturated and dissolves.

Table 6.10: The carbonate content at the initial stage, after 10 years of simulation and at the final stage as well as the differences (Δ) are listed for volumetric (VOL) and effective (EFF) mineralogy data.

VOL	initial	after 10 a	Δ	final	Δ
	mol/kgw	mol/kgw	mol/kgw	mol/kgw	mol/kgw
dolomite	0.54	0.37	- 0.17	0.44	- 0.10
ankerite	0.54	0.83	0.29	1.12	0.58
siderite	1.12	0.94	- 0.19	1.68	0.56
sum	2.19	2.13	- 0.06	3.24	1.05

EFF	initial	after 10 a	Δ	final	Δ
	mol/kgw	mol/kgw	mol/kgw	mol/kgw	mol/kgw
dolomite	0.28	0.12	0.16	0	- 0.28
ankerite	0.28	0.56	- 0.29	0	- 0.28
siderite	0.58	0.33	0.24	0.80	0.22
sum	1.13	1.01	0.12	0.80	- 0.33

For numerical modelling constant mineral reaction rates and specific surface areas are assumed which are independent of the affinity of the reaction (Pham et al., 2011). Therefore the transition-state-theory is used in this study which is based on rate laws (derived from dissolution rate experiments) from Aagaard and Helgeson (1982) and Lasaga (1984). These reaction rates allow minerals to precipitate as soon as the supersaturation of one mineral is reached. This means, that at even small oversaturations unrealistic large amounts of minerals such as dolomite and magnesite may precipitate (Gaus et al., 2010; Pham et al., 2011). These equations are used in e.g. studies from Audigane et al. (2007) for reactive transport modelling with TOUGHREACT. The code was developed by introducing reactive geochemical transport into the existing TOUGH 2 V2 which uses multi-phase fluid and heat flow (Xu and Pruess, 2001; Audigane et al., 2007). The model was conducted for 37°C and 100 bar for the Sleipner field and resulted in a decreasing pH and dissolution of carbonates at the beginning of the simulation. Silica reactions are dominated by (1) the formation of siderite, dolomite, kaolinite and chalcedony at expense of chlorite and calcite under the supply of CO_2, (2) the dissolution of albite and consequent precipitation of dawsonite and chalcedony and (3) the formation of K-feldspar and kaolinite from the reaction of muscovite with chalcedony (Audigane et al., 2007). In comparison, Pham et al. (2011) used the rate equations by Hellevang and Aagaard (2010) to show how sensitive carbonate reactions are on rate parameters such as the specific mineral surface area, the precipitation rate coefficient and the nucleation rates. The reactive mineral surface area is one of the most uncertainties of a model (Pham et al., 2011), since it is assumed to be constant during simulation time. Therefore the authors changed the density factor λ to

predict an entire surface area or a smooth surface area with few dislocations and hence a strongly reduced growth rate. The results show that the total amount of CO_2 stored in carbonate is 20 % lower than for the test scenario. Changing the nucleation rate of carbonates has only minor effects on the mineral reactions which are explained by Pham et al. (2011) by the similarity in nucleation rates at high carbonate supersaturation. Lower rate coefficients result in minor amounts of carbonate at the end of the simulation. However, the author showed that different rate constants are influencing the total amount and the type of carbonates (dolomite, ankerite, magnesite and dawsonite) formed during CO_2 storage.

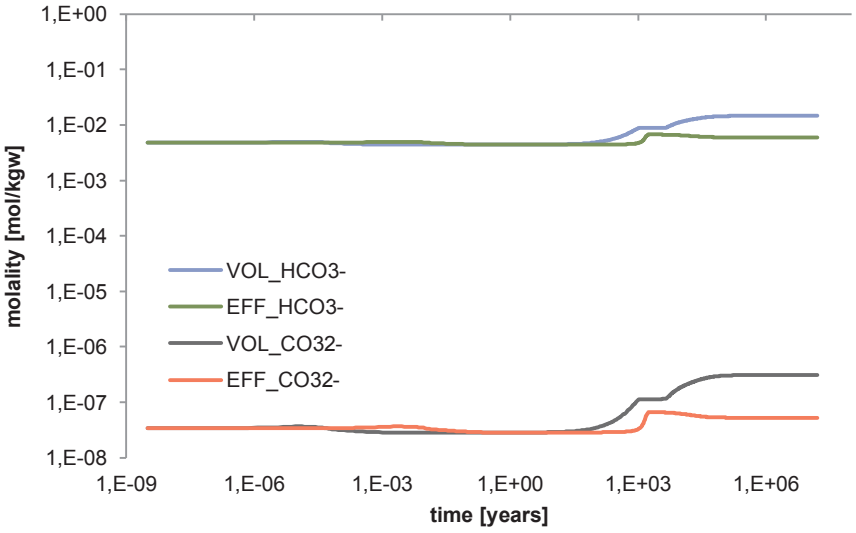

Figure 6.4: Change of HCO_3^- and CO_3^{2-} content for the volumetric (VOL) and effective data (EFF) over time.

7 Reactive transport modelling with coupled geochemical information

Geochemical modelling subdivides complex chemical systems in main water-rock reactions. But this tool is still a static 0-dimensional simulation and does not include any movement of a fluid and/or supercritical CO_2 within a reservoir structure. Therefore simulations were run with the Shell internal software MoReS to simulate mineral reactions in time and place for a simple 2-dimensional reservoir structure of field A.

7.1 Input data

The reservoir structure is represented by a 2D model with 50 gridblocks in the x-direction (total length 3000 m), 1 gridblock in the y-direction (length 1000 m) and 20 gridblocks in the z-direction with a total thickness of 120 m (▶ figure 7.1). The structure dips 1° in NNW to SSE direction. The gas-water contact is located at 3060 m depth.

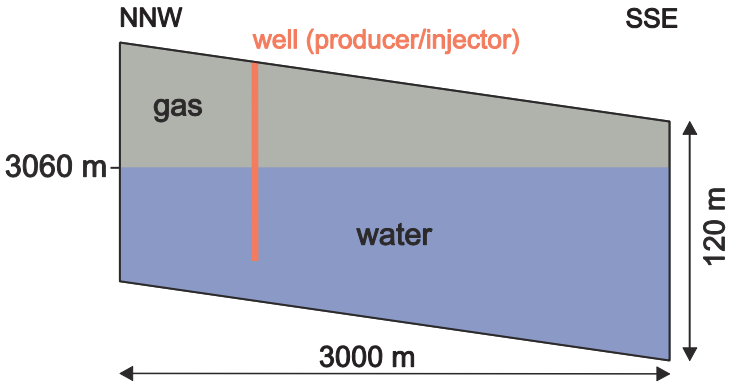

Figure 7.1: Sketch of the reservoir structure of field A which is used for reactive transport modelling in MoReS. The reservoir is located in approximately 3000 m depth and dips 1° in SSE direction.

Only part of the aquifer leg is modelled explicitly, which means that a (linear) analytical aquifer model is attached to the water leg (on the right hand side of the model in ▶ figure 7.1). This aquifer is assumed to have the same thickness as the reservoir and infinite length, with same rock and water properties (e.g. porosity, permeability, compressibility and viscosity) as in the explicitly modelled part of the water leg. The MoReS simulations were run for an equilibrated fluid composition as it is listed in ▶ table 6.2 for PHREEQCi input data. A two phase system (gas-water) without oil was defined for modelling. The gas phase used in the model is a simplified natural gas composition from field A provided by NAM (▶ table 7.2) and contains dominantly of methane and smaller amounts of nitrogen, carbon dioxide and C_{2+}. The geochemistry, which is provided by PHREEQCi, is coupled to the MoReS model using fugacities. For every gridblock and for every timestep MoReS calculates CO_2 fugacity from the internal EOS (equation of state) model, and then passes this to PHREEQCi. PHREEQCi then calculates the amount of CO_2 dissolving in the water and the water-brine reactions. A homogeneous porosity of 15 % and an anisotropic permeability (250 mD in x- and y-direction and 100 mD in z-direction) was chosen to simulate horizontal layering between sandstones and lower permeable sand-/siltstones.

These data represent the true values not completely because the porosity ranges from 1.00 to 26.7 % as they are listed in more detail in ▶ table 5.1. However for a first overview how the system would react during CO_2 injection a homogeneous porosity was chosen. In ▶ table 5.5 the horizontal permeability is listed and ranges between 0.01 mD and 9900 mD where 75 % are equal or smaller than ~180 mD. Less data (n=70) are available for vertical permeability for samples from field A. The minimum value yields 0.06 mD and the maximum 9739 mD with a mean permeability of 188 mD.

Table 7.1: A simplified natural gas composition from field A. Data were provided by NAM.

species	[%]
CH_4	90.6
C_2^+	5.16
N_2	3.79
CO_2	0.49

Apart from the reservoir and fluid properties information for the fluid saturation are required for the simulation. The properties which depend on the reservoir rock and the resident fluid are the relative permeability, the capillary pressure and the residual saturation. The specification for the residual saturation is needed because hysteresis is considered for the model. For the calculation of the relative permeability the Corey equations are used within MoReS (Manual MoReS, Shell, 2008) and are given for a 2-phase-system in ▶ equation 7.1 and 7.2.

$$k_{rw} = K_{rw}\left(\frac{S_w - S_{wc}}{1.0 - S_{wc} - S_{orw}}\right)^{n_w} \tag{7.1}$$

$$k_{rg} = K_{rg}\left(\frac{1.0 - S_w - S_{orw}}{1.0 - S_{wc} - S_{orw}}\right)^{n_g} \tag{7.2}$$

S_w is the water saturation and S_{wc} is the connate water saturation within the rock. The residual gas saturation with respect to water (S_{grw}) is zero during primary drainage.

Table 7.2: The input data for the Corey equations for calculating the relative permeability data within MoReS are listed for each argument for the primary drainage (PDR) and the imbibitions (IMB) (User Manual MoReS, Shell, 2011).

argument	explanation		PDR	IMB
1st argument	object ID of existing table that will be filled			
2nd argument	residual saturation of first phase, S_{r1}	S_{wc}	0.1	0.1
3rd argument	residual saturation of second phase, S_{r2}	S_{gc}	0.0	0.3
4th argument	endpoint relative permeability of first phase, K_{r1}, at a saturation of $1.0 - S_{r2}$	K_{rw}	1.0	0.5
5th argument	endpoint relative permeability of second phase, K_{r2}, at saturation S_{r1}	K_{rg}	1.0	1.0
6th argument	corey exponent of first phase	n_w	2.5	2.0
7th argument	corey exponent of second phase	n_g	2.0	2.0

K_{rw} is the value at a water saturation of S_{wc} and stands for the gas relative permeability for water at this endpoint. Whereas K_{rg} is the relative permeability for oil and is defined for a saturation of

1.0-S_{wc}. The Corey exponent for water is n_w and for gas n_g. By giving MoReS a number of input parameters (▶ table 7.2) for the Corey equation the program can generate the tables for the relative permeability internally. The first one is the primary drainage (PDR) table and represents the process whereby gas first infiltrates an originally water filled rock. The second table is the imbibition (IMB) table which gives data for how the fluids flow when water re-imbibes into a rock containing both gas and water. The capillary pressure (P_{cw}) is defined for different water saturation values (S_w). The input data for MoReS are listed in ▶ table 7.3. As sketched in ▶ figure 7.1 one well was chosen as producer and injector. The well was shut-in for two years before producing the natural gas for 15 years with a maximum production of $4.1*10^{05}$ m^3/day, followed by a second period of well closing for another two years. The MoReS-PHREEQC run was left to equilibrate for 2 years (prior to gas production) to check physical and chemical equilibrium. After this time, supercritical CO_2 was injected for 20 years with a final closer at the end of this period. The injection of 20 % of the pore volumes with CO_2 (537 m^3/year) is specified in the simulation input deck, but it may results in approximately less than 20 % due to gas (natural gas and CO_2) compression during injection. Two models were performed with an injection of CO_2 in the water leg (initial equilibrium and disequilibrium between rock and fluid) and another two models with injection of CO_2 into the gas field (initial equilibrium and disequilibrium between rock and fluid). The simulation time for each model is 10.000 years. Movies for mineral reactions were defined to run 150 years after injection start. The vertical movement of CO_2 is controlled by gravity and capillary pressure.

Table 7.3: Capillary pressure data (PSI) in dependence of the water saturation (S_w)

S_w	P_{cw}	S_w	P_{cw}
0.10	15.81	0.45	1.66
0.12	12.03	0.50	1.41
0.14	9.55	0.55	1.23
0.16	7.81	0.60	1.08
0.18	6.55	0.65	0.95
0.20	5.59	0.70	0.85
0.25	4.00	0.80	0.70
0.30	3.04	0.90	0.59
0.35	2.41	0.98	0.50
0.40	1.98	1.00	0.00

7.2 Injection into the water leg

Figure 7.2 shows changing reservoir pressure over time during the first 80 years of natural gas production and following CO_2 injection into the water leg (scenario with an initial equilibrium between rock and fluid). During production the reservoir pressure decreases from 311 to 148 bar with a short increasing period during the time of well shut-in after 17 years. With CO_2 injection the pressure is further increasing to a maximum of 367 bar. After injection stop the pressure stays constantly at around 308 bar. The expansion of CO_2 within the reservoir is shown in (▶ figure 7.3) for different time steps for the equilibrium model. At the beginning of injection the distribution of CO_2 is located at the top of the reservoir within the gas area. This rapid movement of CO_2 to the top of the reservoir structure may be caused by a relatively high vertical to horizontal permeability ratio (100/250). With increasing time the CO_2 moves downward until

the gas-water contact is reached in approximately 3060 depth. While reaching the water a breakdown between a dense, CO_2-rich phase and a less dense, CO_2 poor/free water phase results in buoyancy-driven downward migration and convection (e.g. Orr, 2005). The same results are reached for the disequilibrium model. Contemporaneously the pH changes according to CO_2 movement from initially 5.0 to 4.05 at the top of the reservoirs after CO_2 injection (▶ figure 7.4). However, for the disequilibrium model the pH decreases from initially 7.0 to 4.3 at the top of the reservoir in comparison to the surrounding area with a maximum of 7.7 at the time of 10 days after CO_2 injection (▶ figure 7.4).

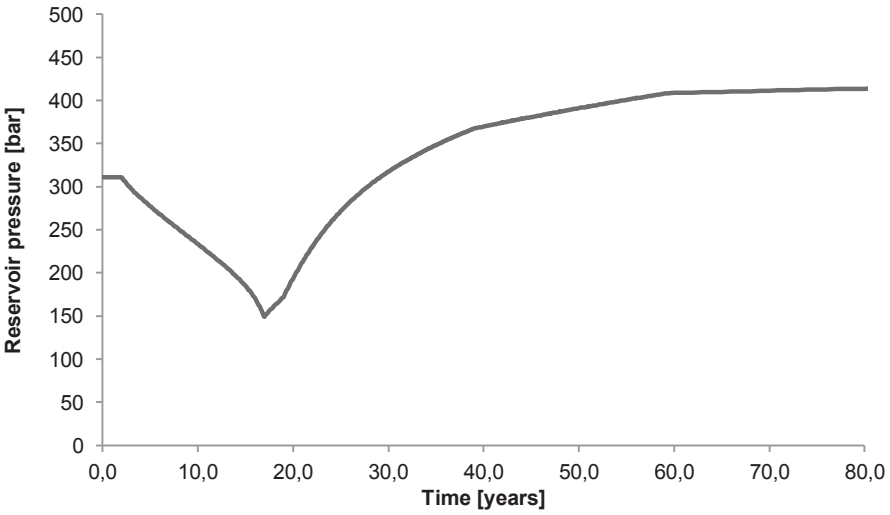

Figure 7.2: Changing reservoir pressure [bar] over the first 80 years of simulation time.

As shown in the PHREEQCi model short-term carbonate and sulphate reactions are lacking for the equilibrated fluid composition (compare section 6.2.2), but long-term silica are still present. However the MoReS simulation showed that minor carbonate reactions occur around the well within the first days and years of simulation time. At the top of the reservoir structure near the well and around the well the pH drops to around 4.0 and cause dolomite (▶ figure 7.5), ankerite and siderite to dissolve partly. Dolomite releases between $1.0*10^{-02}$ and $9.4*10^{-02}$ mol/m^3, ankerite between $1.5*10^{-02}$ and $5.8*10^{-02}$ mol/m^3 and siderite between $5.0*10^{-02}$ and $6.7*10^{-03}$ mol/m^3. Only slightly dissolution takes place further away from the well with increasing time. However, these amounts are negligible (smaller than $1*10^{-04}$). No sulphate (anhydrite and barite) and galena dissolution/precipitation are present. One most important reaction is the dissolution of hematite near the well with injection start and the expansion of the dissolution front to the flanks with increasing time and CO_2 movement (▶ figure 7.6). At the end of the simulation (after 200 years) 1.6 mol hematite are dissolved per cubic-meter in wide ranges within the reservoir structure. Quartz, K-feldspar and muscovite show no reactions. The reactivity of minerals which are far from equilibrium with the surrounding fluid is assumed to be higher than for the equilibrium model. However no other mineral reactions as they are listed for the equilibrium model are taking place during simulation time for the disequilibrium model. Hence a similar result was reached for the disequilibrium model in comparison to the equilibrium model for injection of CO_2 into the water leg.

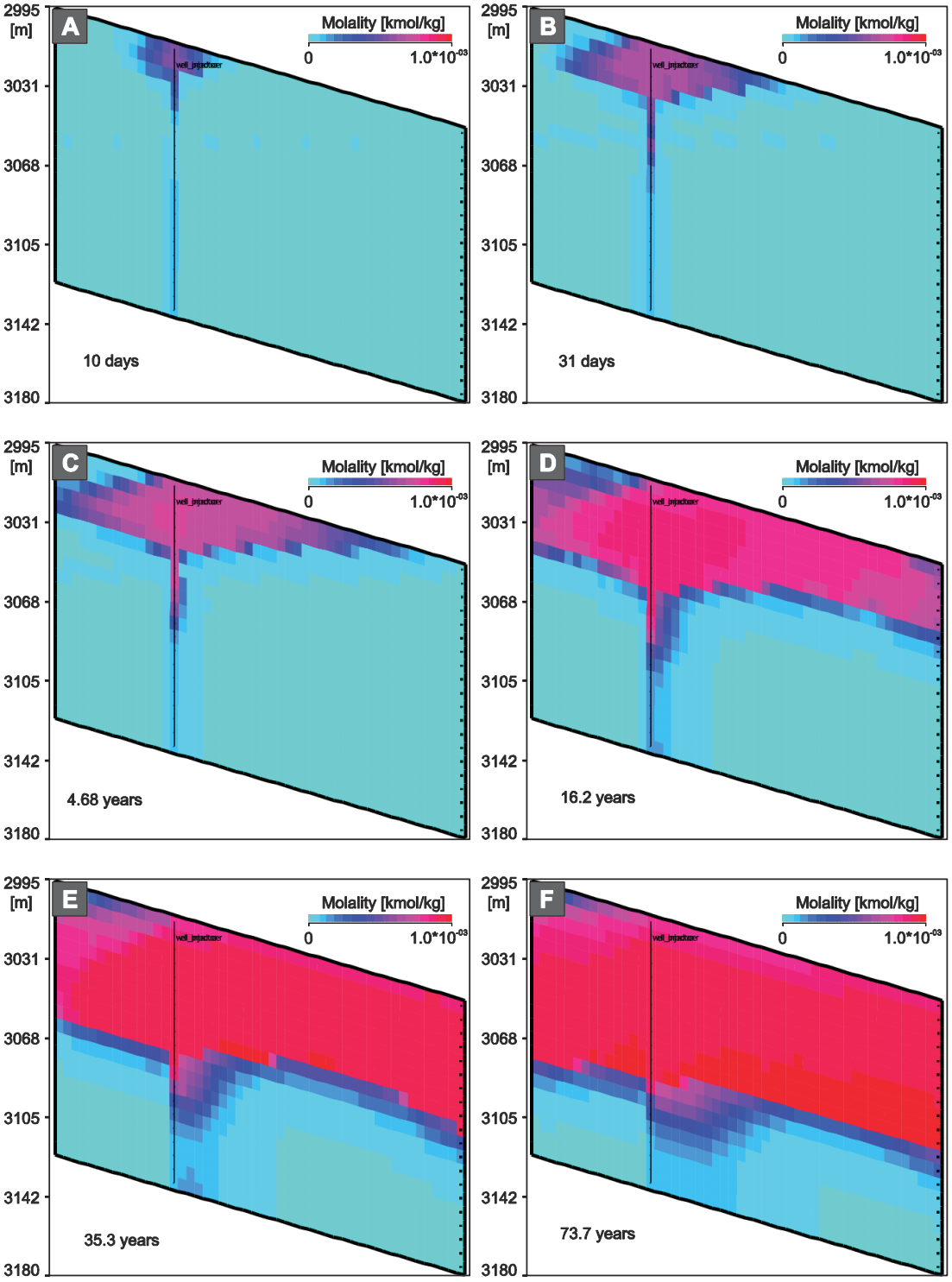

Figure 7.3: Mobility of aqueous CO_2 after injection into the water leg for a period of around 70 years. Note that CO_2 injection stopped after 20 years. Due to a low vertical permeability the CO_2 rises to the top of the reservoir and then propagating downwards until it reaches the gas-water contact. High density gas-water is further moving downwards into the water leg which may be explained to buoyancy migration and convection.

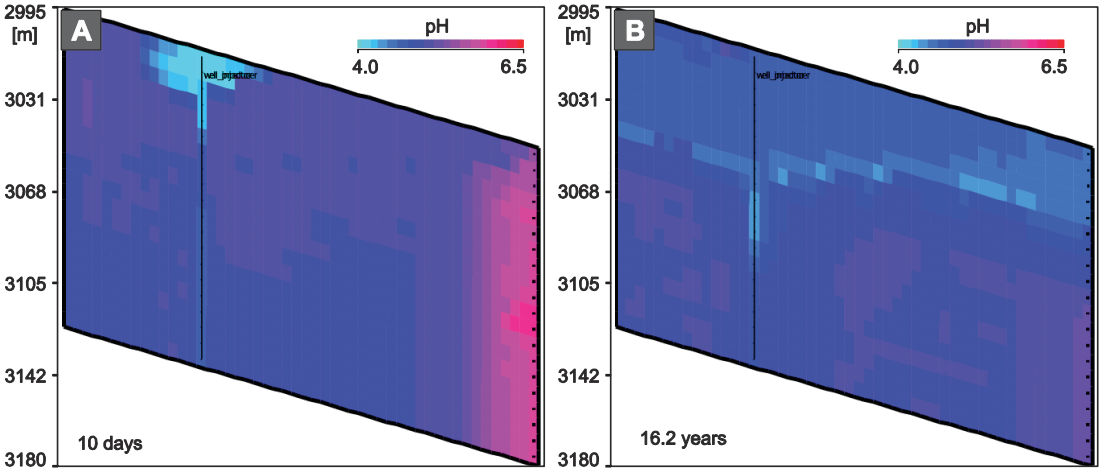

Figure 7.4: The dissociation of CO_2 within the formation water cause the pH to decrease to around 4.0 at the top of the reservoir (equilibrium model). With increasing time the pH stays constantly at around 5.0. The high pH at the right reservoir side in image A may be due to the boundary conditions used to represent the down dip aquifer.

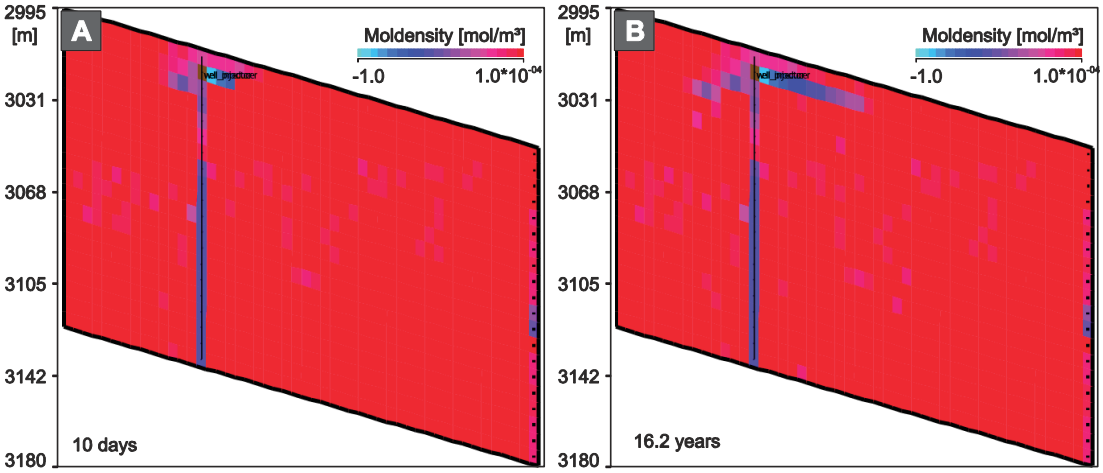

Figure 7.5: After starting CO_2 injection minor amounts of dolomite dissolves along the well and at the top of the reservoir (equilibrium model). After around 16 years the dissolution of dolomite stops.

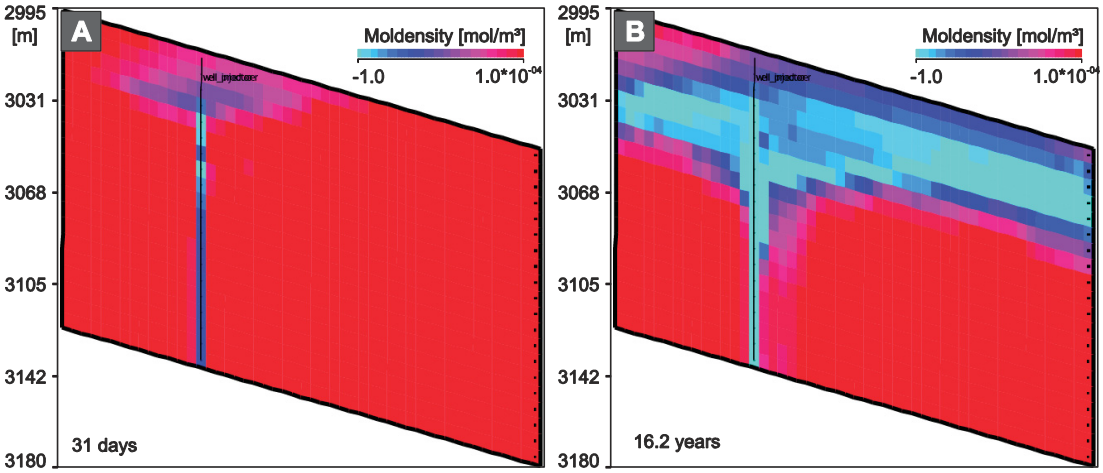

Figure 7.6: With CO_2 injection hematite dissolves along the well and at the top of the reservoir (equilibrium model). After around 16 years the large amounts of hematite are dissolved in the gas area.

7.3 Injection into the gas area

The injection of CO_2 into the reservoir was defined to take place in around 3045 m depth above the gas water contact. The movement of CO_2 is slightly different in comparison to the scenario for injection into the water leg. The CO_2 propagate from the top of the reservoir structure in direction to both flanks until the gas water contact is reached. Then a nearly horizontal CO_2 movement within in the water leg is to recognise (▶ figure 7.7). In close location around the well the pH drops down to around 4.0 as a consequence of CO_2 injection. With increasing time and CO_2 movement the pH increases in this area to around 4.6. In the surrounding area the pH yields initially 5.0 and is lowered also to around 4.6 due to CO_2 movement (▶ figure 7.8).

The relatively low pH immediately after injection near the well causes dolomite (▶ figure 7.9), ankerite and siderite to dissolve partly within the same range as for the "injection into the water" model. During the first 30 years a change in the hematite concentration is to note (▶ figure 7.10). The spatial dissolution behaviour is linked to the movement of CO_2 through the reservoir (▶ figure 7.7). No other silica (K-feldspar, quartz and muscovite), sulphate (anhydrite and barite) and galena reactions are taking place during simulation time for the equilibrium and disequilibrium model.

However, the different simulation for the place of injection (water or gas legs) and equilibrium stage between rock and fluid (equilibrium or disequilibrium) show similar results: Only minor dissolution of carbonates near the well within the first days and years, the dissolution of hematite during simulation time of 150 years and lacking sulphate, sulphide and silica reactions.

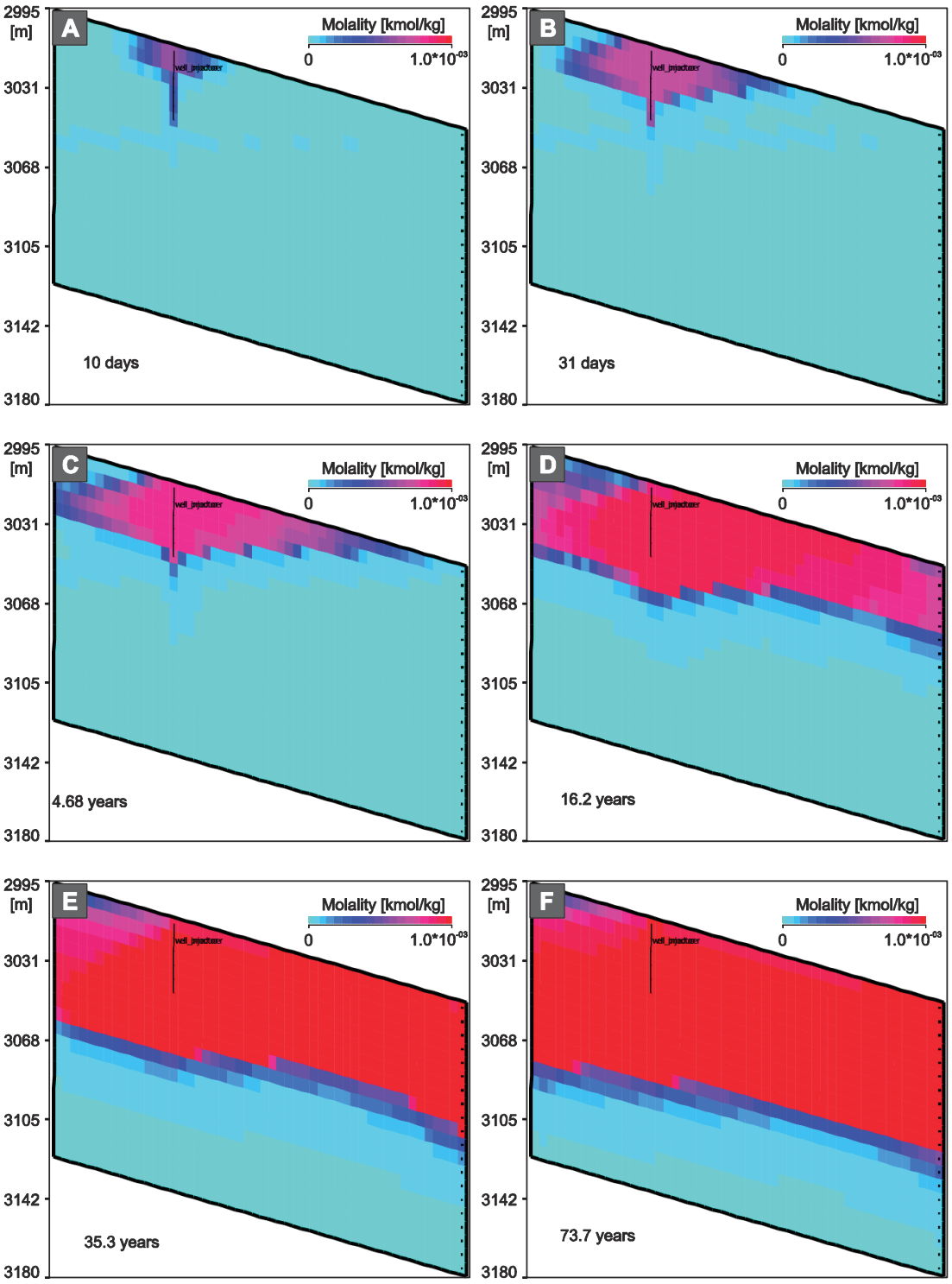

Figure 7.7: Mobility of aqueous CO_2 after injection into the gas area for a period of around 70 years. Note that CO_2 injection stopped after 20 years. The CO_2 is injected in around 3045 m depth and is then propagating downwards until it reaches the gas-water contact. High density gas-water which is nearly horizontal orientated is the migrating downwards.

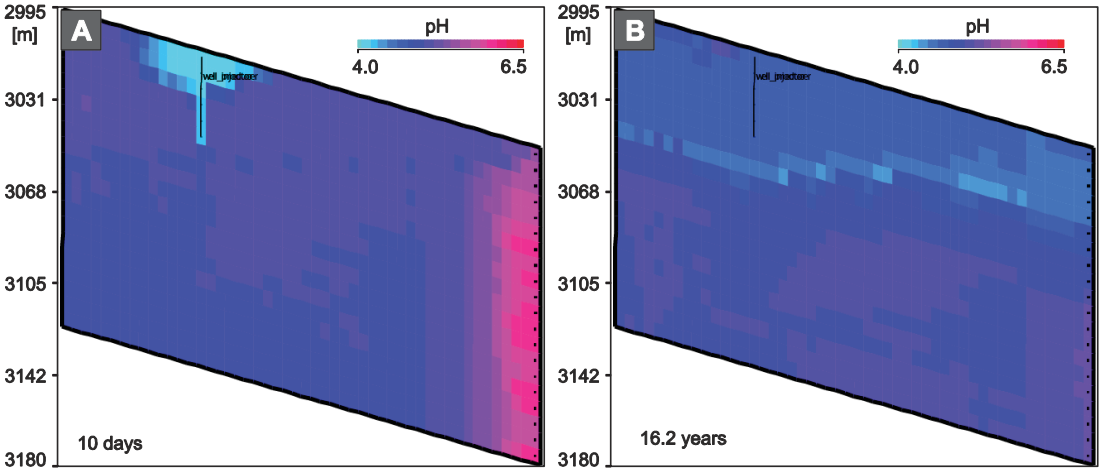

Figure 7.8: Due to the injection of CO_2 at around 3045 m depth the pH is lowered to around 4.0 near the well. With increasing time (step B) the pH stays constantly at around 4.6. The high pH at the right reservoir side in image A may be due to numerical simulation problems.

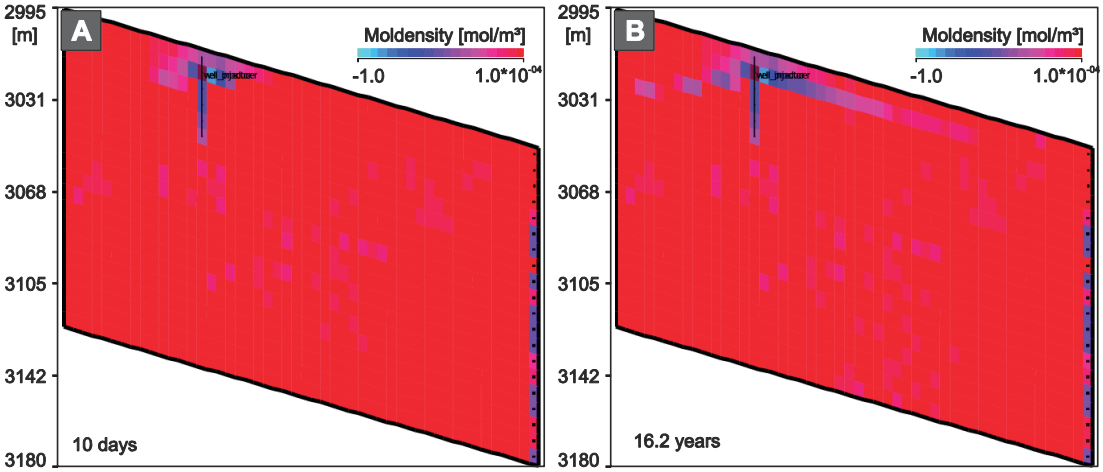

Figure 7.9: Immediately (10 days) after starting CO_2 injection minor amounts of dolomite dissolves along the well and at the top of the reservoir (equilibrium model). After around 16 years the dissolution of dolomite stops.

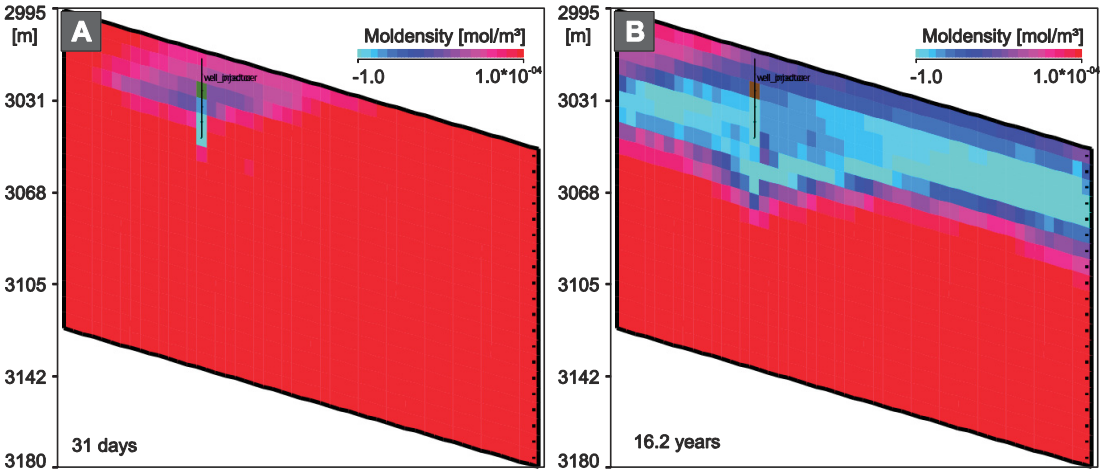

Figure 7.10: With CO_2 injection hematite dissolves along the well and at the top of the reservoir (equilibrium model). After around 16 years the large amounts of hematite are dissolved in the gas area above the gas-water contact.

7.4 Sensitivity analysis

For the MoReS simulation for an equilibrium stage between rock and fluid and the injection of CO_2 into the gas leg the sensitivity and the capacity was tested for a different sandstone porosity and permeability. The homogeneous sandstone porosity was set to 10 % and 20 %. The lower the porosity the more CO_2 is injected into the reservoir rock and the more is dissolved in the formation water and less residual CO_2 is present within the pore space. A change in the rock permeability to minus and plus 100 mD to the horizontal and vertical permeability has only minor influences on the behaviour of CO_2 and expansion through the reservoir rock. With a lower permeability model the migration of CO_2 is a few days slower than for higher permeability data.

7.5 Discussion of reactive transport modelling results

Limited mineral reactions occur within the first 150 years during simulation time. This circumstance may be caused by an equilibrate system with saturation indexes around zero. However batch experiments modelled with the software code PHREEQCi include a static model without any fluid or gas flow. Since no sulphate, sulphide and silica reactions and only minor carbonate reactions are taking place for the reactive transport model in MoReS an explanation may be an equilibrium stage which is caused by fluid flow in reservoir scale and by the low reactivity of the components. Hematite is reactive according to the MoReS model and dissolves consequently during simulation time which may be due to the sensitive relationship between hematite and the lower pH which is caused by CO_2 dissociation, also shown in the PHREEQCi model (compare chapter 6). However, within the first 150 years of simulation the results achieved from the MoReS simulation confirm the mineral reactions from the PHREEQCi model for dolomite and ankerite dissolution. Siderite precipitation and the starting long-term K-feldspar dissolution as it is recognised in the geochemical model could not be proven for the MoReS simulation. Furthermore the dissolution of hematite starts for the geochemical model after around 100 years but is recognised for the reactive transport model in the area around the well directly after CO_2 injection. Hence the mineral reactions taking place for the geochemical and the reactive transport model are comparable even though the mineral reactions are not taking place within one grid block, but near or further away from the injection well. This circumstance may be caused by a higher pressure around the injection well during injection and an increasing CO_2 partial pressure which causes greater amounts of CO_2 to dissolve in water and thus forces a greater equilibrium disturbance in this area.

The low reactivity of the minerals under the supply of CO_2 may be caused by previous CO_2-water-rock interaction as they are discussed in the section 4.5.3 about the influence of CO_2 on diagenetic mineral reactions. Residual amounts of CO_2 (< 1%) within the natural gas of field A indicates the presence of the gas before the injection of supercritical CO_2 during storage procedure.

8 Conclusions

Rotliegend sandstones from the Upper Slochteren Formation are characterised by a similar detrital mineral assemblage but show differences in composition of type, amount and distribution of authigenic cements. These differences have a major influence on the mineral (detrital and authigenic) accessibility in contact to open pores in a sandstone body. Therefore the comparison between volumetric sandstone analysis (bulk analysis) and the determination of the effective mineralogy (minerals in exposure to open pores) show significant differences in the percentage amount of potential reactive mineral phases. Geochemical mineral reactions in a water saturated system under the supply of CO_2 were modelled for both data sets with the software code PHREEQCi. These results were coupled with the software MoReS for reactive transport modelling.

Diagenesis

(1) No major differences are to note for the detrital inventory between the gas-bearing fields A, B and C. The dominant grain types are quartz, K-feldspar and felsic volcanic grains.

(2) Eodiagenetic and early mesodiagenetic processes are comparable between the sediments according to their spatial situation within the sedimentary basin. They include the formation of tangential illite and Fe-oxide, the precipitation of syntaxial quartz overgrowth, dolomite, anhydrite, barite and grain rimming kaolinite cements. Blocky carbonate and/or sulphate partly fill the pore space. Early framework stabilising cements like calcite, dolomite, anhydrite or halite as it is reported by other Rotliegend studies, were obviously present but no relicts appear to be preserve. Mesodiagenetic reactions are strongly related to changing fluid conditions circulating through the sandstone. Commonly samples from field A are less cemented in comparison to sandstones from field B and C.

(3) One important feature is the bleaching of red beds, especially of sandstones which are located near the basin margin, and the precipitation of Fe^{2+}-rich cements, like Fe-rich dolomite, ankerite and siderite which surround earlier dolomite cements in samples from field A. Solid bitumen is proven for porous, bleached sandstones from field A and B covering detrital grains and earlier authigenic minerals. Residual amounts of Fe-oxide are still present in red to grey-red coloured sandstones from field B and C. Partly an extensive post-bitumen precipitation of quartz occurs.

(4) The (partly) dissolution of unstable feldspar grains and the precipitation of fibrous and/or meshwork illite and vermicular kaolinite at the expense of the detrital grain is a common feature in all samples investigated in this study. Contemporaneously to early feldspar dissolution albite formation appears due to the exchange of potassium against sodium. A second period of feldspar dissolution occurs after bitumen migration. Feldspar dissolution is more intense further to the basin centre (field B and especially C) in comparison to the basin margin (field A). Leaching processes may be caused by acidic CO_2-rich fluids which may have been generated from underlying Carboniferous coals and/or are due to oxidation of hydrocarbons within the sandstone body.

(5) Vermicular kaolinite precipitated in open pores before hydrocarbon migration in all samples. An additional generation, which is partly larger in size and impregnated by bitumen, was formed after the event in sandstones attributed to field A. The most

important phenomena are single kaolinite plates, which are either arranged as grain rimming kaolinite on detrital grain surface areas, forming dense pore filling cements or appear as sheaf-like structures with transition forms to kaolinite "booklets". In samples from field B grain rimming kaolinite are scattered distributed in comparison to a dense arrangement on grain surface areas from field C. In sandstones located further to the basin centre the aggregation of two or more crystals forming elongated minerals, partly pore bridging, are common. Sheaf-like arranged kaolinite aggregations which seem to be due to widening of precursor kaolinite "booklets" are more frequent in samples from field C than for field B.

(6) The origin of early mesodiagenetic grain rimming kaolinite may be controlled by a previous precipitation of Mg-rich chlorite and the transformation to kaolinite in presence of calcite and under the supply of CO_2 and increasing temperature. Another opportunity is the direct precipitation out of an Al-rich fluid under the presence of ions and/or (organic) molecules which are blocking the hydroxyl groups on the crystals surface area and inhibit the formation of vermicular structures.

(7) Further evidences are found which may document the presence of CO_2 and linked acidic fluid conditions during burial diagenesis. For example the illititsation and kaolinitisation of detrital feldspar grains take place under the consumption of protons. The reduction of Fe^{3+} to Fe^{2+} during bleaching of red beds occurs under reducing acidic fluid conditions and may influence the carbonate precipitation/dissolution behaviour.

(8) Late mesodiagenetic cements are anhydrite and barite which occur independent to their spatial position within the basin. A further precipitate in sandstones from field A is galena (PbS). The transport of soluble and further precipitation of galena requires very acidic fluid conditions and the presence of sulphur species and lead which may be generated from detrital grains or precursor sulphates. However it is not clear if galena precipitation is controlled by diagenetic reactions or by drilling.

Spatial mineral arrangement

(9) No significant differences between the samples are to note for the porosity values and intergranular volume, but the horizontal permeability is decreasing from the southern basin margin to the northern area due to higher cement (esp. clay minerals like kaolinite) contents.

(10) Based on point counting data the volumetric composition of the sandstone is dominated by the mineralogy of detrital grains like quartz and K-feldspar.

(11) Anticipation between pore exposed (effective mineralogy) and total volumetric mineral content was clearly confirmed by petrographic and modelling approaches.

(12) Using pore lining image analysis on thin section images the effective can be identified. The analyses maintain the conclusions from petrographic investigations: Grain surface areas in samples from field A are less covered by authigenic minerals like illite cutan, Fe-oxide, quartz, carbonate and sulphate than in comparison to sandstones from field B and C where a partly intensive cementation by kaolinite, quartz and illite occurs. However these authigenic minerals are covering and blocking especially in sandstones from field B large amounts of grain surface areas and hence stay in direct contact to a pore fluid and/or CO_2 during storage procedures. The analysis maintained that especially in samples from field A solid bitumen covers high amounts of detrital and authigenic minerals.

(13) Due to the diagenetic evolution of the sandstones different authigenic minerals are surrounding earlier precipitates and may protect the enclosed mineral phase for potential water-rock-(CO_2) interactions. The main carbonate reaction partner in samples from field B and C is dolomite whereas in samples from field A dolomite is blocked by ankerite/siderite and partly by blocky anhydrite cement. Vermicular kaolinite is partly surrounded by carbonate, sulphates and quartz.

(14) Pore lining image analysis is not applicable for intensive cemented, highly compacted sandstones were the mineral surface area is covered by clay minerals (like in most samples from field C). Therefore correction factors were calculated which are based on theoretical calculations for e.g. meshwork illite or grain rimming kaolinite.

(15) The specific surface areas which were calculated for each mineral investigated in geochemical modelling are in a good agreement with literature data.

Geochemical modelling

(16) Kinetic modelling was performed for an equilibrium and disequilibrium stage between the initial fluid composition and the reservoir rock (field A) for the volumetric and effective mineralogical data set, respectively. An initial equilibrium inhibits short-term (including the first minutes to hundreds of years) carbonate and sulphate reactions. But long-term (including hundreds to thousands of years) silica, carbonate and sulphate reactions are comparable with the non equilibrated initial fluid composition.

(17) For the disequilibrium model the short-term reactions are comparable for both data sets (volumetric and effective). However for the effective mineralogy, where kaolinite and quartz are the main reactants, the carbonate and sulphate reactions start a few seconds later but the pattern is similar in comparison to the volumetric simulation. The main differences are present for the long-term reactions. Due to minor initial amounts of K-feldspar for the effective mineralogy data less of the mineral dissolves and provides potassium which is in turn consumed by muscovite (represents illite). Hence more aluminium is available for Mg-smectite precipitation. Since this mineral requires magnesium dolomite and ankerite are undersaturated and dissolve consequently. Furthermore Mg-smectite requires silica which results in the partial dissolution of quartz.

(18) The precipitation/dissolution behaviour of carbonates (dolomite/ankerite/siderite) which require Ca^{2+}, Mg^{2+} and Fe^{2+} is mainly controlled by the dissolution of hematite and the formation of Mg-smectite which is linked to the availability of magnesium and iron in the solution for both data sets.

(19) Mineral CO_2 trapping occurs due to the effective mineralogy data within the first ten years, but is absent for the volumetric mineralogy model. For long-term reactions the other way round is the case. This means that in dependence on the mineral assemblage and the consideration of the effective mineralogy different results for CO_2 trapping come to pass.

(20) Sensitivity analyses showed that changing the K-feldspar content has a major influence on the precipitation of muscovite and in consequence on the availability of aluminium and silica in the solution for Mg-smectite precipitation. Changing the quartz content to lower amounts has no effects. Higher carbonate contents slow down the reaction rates whereas removing ankerite and siderite from the initial mineral assemblage results in lacking short-term carbonate reactions.

(21) The mineral reaction rates are directly linked to the water saturation of the rock: The higher the content the faster are the ractions.

(22) Lower temperatures and lower CO_2 partial pressure are affecting the solubility of CO_2 within the fluid and cause the pH to decrease which results in a faster short- and long-term carbonate reaction. Since the illitisation of K-feldspar requires protons the reactions slow down and results in a precipitation of kaolinite due to lacking magnesium and linked Mg-smectite precipitation and an oversaturation with respect to aluminium.

Reactive transport modelling coupled with geochemical modelling results

(23) With the software code MoReS coupled with the geochemical results of PHREEQCi the mineral reactions in combination with reactive fluid transport was tested. On the one hand the rock stays in equilibrium with the surrounding fluid and on the other hand a disequilibrium stage was assumed. The simulation show for the CO_2 injection into the water leg and into the gas area minor carbonate reactions directly after CO_2 injection within the first days and years around the well and at the top of the reservoir. Hematite dissolves consequently due to a lower pH as a consequence of CO_2 injection. No other mineral reactions, neither short-term sulphate nor silica, are taking place within the first 150 years of simulation time.

(24) The low reactivity of the reservoir rock under the supply of CO_2 during storage procedure confirms the presence of CO_2 during diagenesis as the minerals seems to be acid-resistant.

List of references

Aagaard, P. and Helgeson, H.C., 1982, Thermodynamic and kinetic constraints on reaction rates among minerals and aqueous solutions: I. Theoretical considerations. *American Journal of Science*, 282, pp. 237-285.

Aagaard, P., Egeberg, P.K., Saigal, G.C., Morad, S. and Bjørlykke, K., 1990, Diagenetic Albitization of Detrital K-Feldspars in Jurassic, Lower Cretaceous and Tertiary Clastic Reservoir Rocks from Offshore Norway, 2. Formation Water Chemistry and Kinetic Considerations. *Journal of Sedimentary Petrology*, 60, pp. 575-581.

Abercrombie, H.J., Hutcheon, I.E., Bloch, J.D. and Decaritat, P., 1994, Silica Activity and the Smectite-Illite Reaction. *Geology*, 22, pp. 539-542.

Abramovitz, T., Thybo, H. and Grp, M.L.W., 1998, Seismic structure across the Caledonian Deformation Front along MONA LISA profile 1 in the southeastern North Sea. *Tectonophysics*, 288, pp. 153-176.

Abramovitz, T. and Thybo, H., 1999, Pre-Zechstein structures around the MONA LISA deep seismic lines in the southern Horn Graben area. *Bulletin of the Geological Society of Denmark*, 45, pp. 99-116.

Aharonov, E., Spiegelman, M. and Kelemen, P., 1997, Three-dimensional flow and reaction in porous media: Implications for the Earth's mantle and sedimentary basins. *Journal of Geophysical Research-Solid Earth*, 102, pp. 14821-14833.

Aichroth, B., Prodehl, C. and Thybo, H., 1992, Crustal Structure Along the Central Segment of the Egt from Seismic-Refraction Studies. *Tectonophysics*, 207, pp. 43-64.

Al-Hasani, S., 2004, *Internal Report NAM*, No. EP200405202958.

Al-Kharusi, A.S. and Blunt, M.J., 2007, Network extraction from sandstone and carbonate pore space images *Journal of Petroleum Science and Engineering*, 56, pp. 219-231.

Allis, R., Chidsey, T., Gwynn, W., Morgan, C., White, S., Adams, M. and Moore, J., 2001, Natural CO_2 reservoirs on the Colorado Plateau and Southern Rocky Mountains: candidates for CO_2 sequestration. In *Proceedings of the First National Conference on Carbon Sequestration* (Washington DC: Proceedings of the First National Conference on Carbon Sequestration), pp. 1-19.

Amirtharaj, E.S., Ioannidis, M.A., Parker, B. and Tsakiroglou, C.D., 2011, Statistical Synthesis of Imaging and Porosimetry Data for the Characterization of Microstructure and Transport Properties of Sandstones. *Transport in Porous Media*, 86, pp. 135-154.

Amthor, J.E. and Okkerman, J., 1998, Influence of early diagenesis on reservoir quality of Rotliegende sandstones, northern Netherlands. *American Association of Petroleum Geologists Bulletin*, 82, pp. 2246-2265.

André, L., Audigane, P., Azaroual, M. and Menjoz, A., 2007, Numerical modeling of fluid-rock chemical interactions at the supercritical CO_2-liquid interface during CO_2 injection into a carbonate reservoir, the Dogger aquifer (Paris Basin, France). *Energy Conversion and Management*, 48, pp. 1782-1797.

Assayag, N., Matter, J., Ader, M., Goldberg, D. and Agrinier, P., 2009, Water-rock interactions during a CO_2 injection field-test: Implications on host rock dissolution and alteration effects. *Chemical Geology*, 265, pp. 227-235.

Aste, T., Saadatfar, M. and Senden, T.J., 2005, Geometrical structure of disordered sphere packings. *Physical Review E*, 71, p. 15.

Audigane, P., Gaus, I., Czernichowski-Lauriol, I., Pruess, K. and Xu, T.F., 2007, Two-dimensional reactive transport modeling of CO2 injection in a saline Aquifer at the Sleipner site, North Sea. *American Journal of Science*, 307, pp. 974-1008.

Atkins, J.E. and McBride, E.F., 1992, Porosity and Packing of Holocene River, Dune, and Beach Sands. *American Association of Petroleum Geologists Bulletin*, 76, pp. 339-355.

Aylmore, L.A.G., Sillis, I.D. and Quirk, J.P., 1970, Surface area of homoionic illite and montmorillonite clay minerals as measured by the sorption of nitrogen and carbon dioxide. *Clays and Clay Minerals*, 18, pp. 91-96.

Bachmann, G.H. and Grosse, S., 1989, Struktur und Entstehung des Norddeutschen Beckens - geologisch und geophysikalische Interpretation einer verbesserten Bouguer -Schwerekarte. *Nds. Akad. Geowiss. Veröfftl.*, 2, pp. 23-47.

Bachmann, G.-H. and Hoffmann, N., 1997, Development of the Rotliegend Basin in Northern Germany. *Geologisches Jahrbuch*, D103, pp. 9-31.

Bachu, S., Gunter, W.D. and Perkins, E.H., 1994, Aquifer disposal of CO_2: hydrodynamic and mineral trapping. *Energy Conversion and Management*, 35, pp. 269-279.

Bachu, S. and Adams, J.J., 2003, Sequestration of CO_2 in geological media in response to climate change: capacity of deep saline aquifers to sequester CO_2 in solution. *Energy Conversion and Management*, 44, pp. 3151-3175.

Baines, S.J. and Worden, R.H., 2004, The long-term fate of CO_2 in the subsurface: natural analogues for CO_2 storage. *Geological Society of London Special Publications*, 233, pp. 59-85.

Baker, A.P. and Kastner, M., 1981, Constraints on the Formation of Sedimentary Dolomite. *Science*, 213, pp. 214-216.

Bakke, S. and Øren, P., 1997, 3-D Pore-Scale Modelling of Sandstones and Flow Simulations in the Pore Networks. *Society of Petroleum Engineers*, 2, pp. 136-149.

Balan, E., Saitta, A.M., Mauri, F. and Calas, G., 2001, First-principles modeling of the infrared spectrum of kaolinite. *American Mineralogist*, 86, pp. 1321-1330.

Baldschuhn, R., Frisch, U. and Kockel, F., 1996, Geotektonischer Atlas von NW-Deutschland / Tectonic Atlas of NW-German. (Hannover: BGR / Federal Institute for Geosciences and Natural Resources).

Baldschuhn, R., Binot, F., Fleig, S. and Kockel, F., 2001, Geotektonischer Atlas von Nordwest-Deutschland und dem deutschen Nordsee-Sektor - Strukturen, Strukturentwicklung, Paläogeographieg. *Geologisches Jahrbuch*, A153, pp. 1-88.

Barclay, S.A. and Worden, R.H., 2000, Geochemical modelling of diagenetic reactions in a sub-arkosic sandstone. *Clay Minerals*, 35, pp. 57-67.

Bartels, J., Clauser, C., Kühn, M., Pape, H. and Schneider, W., 2005, Reactive flow and permeability prediction - numerical simulation of complex hydrogeothermal problems. In *Petrophysical properties of cristalline rocks,* P.K. Harvey, P.A. Brewer and V.A. Pezard (Ed.), pp 133-151 (London: Geological Society Special Publications)

Bateman, K., Turner, G., Pearce, J.M., Noy, D.J., Birchall, D. and Rochelle, C.A., 2005, Large-scale column experiment: Study of CO_2, porewater, rock reactions and model test case. *Oil & Gas Science and Technology-Revue de l'Institut Français du Petrole*, 60, pp. 161-175.

Bath, A.H., Milodowski, A.E. and Spiro, B., 1987, Diagenesis of carbonate cements in Permo-Triassic sandstone in the Wessex and East Yorkshire - Lancashire basins, UK: a stable isotope study. In *Diagenesis of sedimentary sequences*, J.D. Marshall (Ed.), pp. 173-190 (London: Geological Society Special Publications).

Bayer, U., Scheck, M., Rabbel, W., Krawczyk, C.M., Gotze, H.J., Stiller, M., Beilecke, T., Marotta, A.M., Barrio-Alvers, L. and Kuder, J., 1999, An integrated study of the NE German Basin. *Tectonophysics*, 314, pp. 285-307.

Bayer, U., Grad, M., Pharaoh, T.C., Thybo, H., Guterch, A., Banka, D., Lamarche, J., Lassen, A., Lewerenz, B., Scheck, M. and Marotta, A.M., 2002, The southern margin of the East European Craton: new results from seismic sounding and potential fields between the North Sea and Poland. *Tectonophysics*, 360, pp. 301-314.

Beard, D.C. and Weyl, P.K., 1973, Influence of Texture on Porosity and Permeability of Unconsolidated Sand. *American Association of Petroleum Geologists Bulletin*, 57, pp. 349-369.

Ben Baccar, M., Fritz, B. and Made, B., 1993, Diagenetic Albitization of K-Feldspar and Plagioclase in Sandstone Reservoirs - Thermodynamic and Kinetic Modeling. *Journal of Sedimentary Petrology*, 63, pp. 1100-1109.

Benek, R., Kramer, W., McCann, T., Scheck, M., Negendank, J.F.W., Korich, D., Huebscher, H.D. and Bayer, U., 1996, Permo-carboniferous magmatism of the Northeast German Basin. *Tectonophysics*, 266, pp. 379-404.

Bentz, A., 1958, Relations between oil fields and sedimentary troughs in northwest German Basin. In *Habitat of Oil*, L.-G.-. Weeks (Ed.), pp. 1054-1066 (Tulsa).

Bernabe, Y., 1991, Pore Geometry and Pressure-Dependence of the Transport-Properties in Sandstones. *Geophysics*, 56, pp. 436-446.

Bernabe, Y., Brace, W.F. and Evans, B., 1982, Permeability, porosity and pore geometry of hot-pressed calcite. *Mechanics of materials*, 1, pp. 173-183.

Bernal, J.D., 1960, Geometry of the Structure of Monatomic Liquids. *Nature*, 185, pp. 68-70.

Bernal, J.D. and Mason, J., 1960, Co-Ordination of Randomly Packed Spheres. *Nature*, 188, pp. 910-911

Berner, R.A., 1980, *Early Diagenesis: A Theoretical Approach* (Princeton: Princeton Series in Geochemistry, Princeton University Press).

Berthelsen, A., 1992, From Precambrian to Variscian Europe. In *The European Geotraverse - A Continent Revealed*, D. Blundell, R. Freeman and S. Müller (Eds.), pp. 153-164 (Cambridge University Press).

Bertier, P., Swennen, R., Laenen, B., Lagrou, D. and Dreesen, R., 2006, Experimental identification of CO_2-water-rock interactions caused by sequestration of CO_2 in Westphalian and Buntsandstein sandstones of the Campine Basin (NE-Belgium). *Journal of Geochemical Exploration*, 89, pp. 10-14.

Bertier, P., Ferket, H., Swennen, R., Laenen, B., Dreesen, R. and van Tongeren, P., 2009, CO_2-water-rock interactions induced by CO_2-flooding of fluvial sandstones: An integrated study based on detailed reservoir characterisation, experimental work and numerical modelling. (CO2-WRI in fluvial sandstones), Presentation.

Best, G., Kockel, F. and Schöneich, H., 1983, Geological history of the southern Horn Graben. In *Petroleum geology of the southeastern North Sea and the adjacent onshore areas*, J.P.H. Kaasschieter and T.J.A. Reijers (Eds.), pp. 25-33 (Geologie en Mijnbouw).

Betz, D., Fuhrer, F., Greiner, G. and Plein, E., 1987, Evolution of the Lower Saxony Basin. *Tectonophysics*, 137, pp. 127-170.

Beyer, D., 2010, Petrographische Untersuchungen an CO_2-Speichergesteinen am Beispiel von Rotliegend-Sandsteinen in den nördlichen Niederlanden, Diploma Thesis, University of Jena, p. 128.

Bildstein, O., Worden, R.H. and Brosse, E., 2001, Assessment of anhydrite dissolution as the rate-limiting step during thermochemical sulfate reduction *Chemical Geology*, 176, pp. 173-189.

Bitzer, K., Travé, A. and Carmona, J.M., 2001, Fluid flow processes at basin scale. *Acta Geologicahispanica*, 36, pp. 1-20.

Bjørkum, P.A. and Gjelsvik, N., 1988, An Isochemical Model for Formation of Authigenic Kaolinite, K-Feldspar and Illite in Sediments. *Journal of Sedimentary Petrology*, 58, pp. 506-511.

Bjørlykke, K., 1983, Diagenetic rections in sandstones. In *Sediment Diagenesis*, A. Parker and B.W. Sellwood (Eds.), pp. 169-211(NATO ASI Series C).

Bjørlykke, K., 1984, Formation of secondary porosity. How important is it? In *Clastic diagenesis*, D.A. McDonald and R.C. Surdam (Eds.), pp. 277-286 (American Association of Petroleum Geologists).

Bjørlykke, K., 2010, Subsurface Water and Fluid Flow in Sedimentary Basins. In *Petroleum Geoscience: From Sedimentary Environments to Rock Physics*, K. Bjørlykke (Ed.) (Heidelberg, Dordrecht, London, New York: Springer).

Bjørlykke, K., Aagaard, P., Dypvik, H., Hastings, D.D. and Harper, A.S., 1986, Diagenesis and reservoir properties of Jurassic sandstones from the Haltenbanken area, offshore Mid Norway. In *Habitat of Hydrocarbons on the Norwegian Continental Shelf*, A.M. Spencer, E. Holter, C.J. Campell, P.H.H. Hanslien, E. Nelson, E. Nysæther and E.G. Ormaasen (Eds.) (London Graham and Trotman).

Bjørlykke, K., Mo, A. and Palm, E., 1988, Modeling of Thermal-Convection in Sedimentary Basins and Its Relevance to Diagenetic Reactions. *Marine and Petroleum Geology*, 5, pp. 338-351.

Bjørlykke, K., Ramm, M. and Saigal, G.C., 1989, Sandstone Diagenesis and Porosity Modification during Basin Evolution. *Geologische Rundschau*, 78, pp. 243-268.

Bjørlykke, K. and Aagaard, P., 1992, Clay minerals in North Sea Sandstones. In *Origin, Diagenesis and Petrophysics of Clay Minerals in Sandstones*, D.W. Houseknecht and E.D. Pittman (Eds.), pp. 65-80 (Tulsa: Special Publications of the Society of economic Paleontologie and Mineralogie).

Bjørlykke, K. and Egeberg, P.K., 1993, Quartz Cementation in Sedimentary Basins. *American Association of Petroleum Geologists Bulletin*, 77, pp. 1538-1548.

Blake, R.E. and Walter, L.M., 1996, Effects of organic acids on the dissolution of orthoclase at 80 degrees C and pH 6. *Chemical Geology*, 132, pp. 91-102.

Blake, R.E. and Walter, L.M., 1999, Kinetics of feldspar and quartz dissolution at 70-80°C and near-neutral pH: effects of organic acids and NaCl. *Geochimica Et Cosmochimica Acta*, 63, pp. 2043-2059.

Boles, J.R., 1982, Active Albitization of Plagioclase, Gulf-Coast Tertiary. *American Journal of Science*, 282, pp. 165-180.

Boles, J.R. and Franks, S.G., 1979, Clay Diagenesis in Wilcox Sandstones of Southwest Texas - Implications of Smectite Diagenesis on Sandstone Cementation. *Journal of Sedimentary Petrology*, 49, pp. 55-70.

Boles, J.R. and Ramseyer, K., 1987, Diagenetic Carbonate in Miocene Sandstone Reservoir, San-Joaquin Basin, California. *American Association of Petroleum Geologists Bulletin*, 71, pp. 1475-1487.

Bradley, J.S., 1980, Fluid and electrical formation conductivity factors calculated for a spherical-grain onion-skin model. *The log analysist*, 21, Abstract.

Brady, P.V., Cygan, R.T. and Nagy, K.L., 1996, Molecular controls on kaolinite surface charge. *Journal of Colloid and Interface Science*, 183, pp. 356-364.

Brantley, S.L. and Mellott, N.P., 2000, Surface area and porosity of primary silicate minerals. *American Mineralogist*, 85, pp. 1767-1783.

Breitkreuz, C. and Kennedy, A., 1999, Magmatic flare-up at the Carboniferous/Permian boundary in the NE German basin revealed by SHRIMP zircon ages. *Tectonophysics*, 302, pp. 307-326.

Brime, C. and Eberl, D.D., 2002, Growth mechanisms of low-grade illites based on shapes of crystal thickness distributions. *Schweizer Mineralogische und Petrologische Mitteilungen*, 82, pp. 203-209.

Brindley, G.W. and Brown, G., 1980, *Crystal structures of clay minerals and their X-ray identification* (London: Mineralogical Society Monograph).

Brink, H.-J., 1984, Die Salzstockverteilung in Nordwestdeutschland. *Geowissenschaften in unserer Zeit*, 2, pp. 160-166.

Brink, H.J., 2005, The evolution of the North German Basin and the metamorphism of the lower crust. *International Journal of Earth Sciences*, 94, pp. 1103-1116.

Broholm, M.M., Crouzet, C., Arvin, E. and Mouvet, C., 2000, Concurrent nitrate and Fe(III) reduction during anaerobic biodegradation of phenols in a sandstone aquifer. *Journal of Contaminant Hydrology*, 44, pp. 275-300.

Brower, K.R. and Morrow, N.R., 1985, Fluid flow in cracks as related to low-permeability gas sands. *Society of Petroleum Engineers Journal*, 25, pp. 191-201.

Brunauer, S., Emmett, P.H. and Teller, E., 1938, Adsorption of gases in multimolecular layers. *J. Am. Chem. Soc*, 60, pp. 309-331.

Bryant, S., Cade, C. and Mellor, D., 1993, Permeability Prediction from Geologic Models. *American Association of Petroleum Geologists Bulletin*, 77, pp. 1338-1350.

Bryant, S. and Pallatt, N., 1996, Predicting formation factor and resistivity index in simple sandstones. *Journal of Petroleum Science and Engineering*, 15, pp. 169-179.

Burley, S.D., 1984, Patterns of Diagenesis in the Sherwood Sandstone Group (Triassic), United-Kingdom. *Clay Minerals*, 19, pp. 403-440.

Burley, S.D. and Kantorowicz, J.D., 1986, Thin-Section and SEM Textural Criteria for the Recognition of Cement-Dissolution Porosity in Sandstones. *Sedimentology*, 33, pp. 587-604.

Burley, S.D., Mullis, J. and Matter, A., 1989, Timing Diagenesis in the Tartan Reservoir (Uk North-Sea) - Constraints from Combined Cathodoluminescence Microscopy and Fluid Inclusion Studies. *Marine and Petroleum Geology*, 6, pp. 98-120.

Cantucci, B., Montegrossi, G., Vaselli, O., Tassi, F., Quattrocchi, F. and Perkins, E.H., 2009, Geochemical modeling of CO_2 storage in deep reservoirs: The Weyburn Project (Canada) case study. *Chemical Geology*, 265, pp. 181-197.

Carothers, W.W. and Kharaka, Y.K., 1978, Aliphatic Acid Anions in Oil-Field Waters - Implications for Origin of Natural Gas. *American Association of Petroleum Geology Bulletin*, 62, pp. 2441-2453.

Cathles, L.M., Schoell, M. and Simon, R., 1986, CO_2 generation during steamflooding: A geologically based kinetic theory that includes carbon isotope effects and applicatio to high-temperature steamfloods. *SPE*, 16267.

Celia, M.A., Bachu, S., Nordbotten, J.M., Gasda, S.E. and Dahle, H.K., 2005, Quantitative estimation of CO_2 leakage from geological storage: Analytical models, numerical models and data needs. In *Proceedings of 7th International Conference on Greenhouse Gas Control Technologies* (Vancouver, Canada, pp. 663-672.

Chan, M.A., Parry, W.T. and Bowman, J.R., 2000, Diagenetic hematite and manganese oxides and fault-related fluid flow in Jurassic sandstones, southeastern Utah. *American Association of Petroleum Geologists Bulletin*, 84, pp. 1281-1310.

Chukhrov, F.V., 1973, Mineralogical and Geochemical Criteria in Genesis of Red Beds. *Chemical Geology*, 12, pp. 67-75.

Clauer, N., Rinckenbach, T., Weber, F., Sommer, F., Chaudhuri, S. and O'Neil, J.R., 1999, Diagenetic evolution of clay minerals in oil-bearing neogene sandstones and associated shales, Mahakam Delta Basin, Kalimantan, Indonesia. *American Association of Petroleum Geologists Bulletin*,, 83, pp. 62-87.

Clausen, O.R. and Pedersen, P.K., 1999, Late Triassic structural evolution of the southern margin of the Ringkobing-Fyn High, Denmark. *Marine and Petroleum Geology*, 16, pp. 653-665.

Clément, J.-C., Shrestha, J., Ehrenfeld, J.G. and Jaffé, P.R., 2005, Ammonium oxidation coupled to dissimilatory reduction of iron under anaerobic conditions in wetland soils. *Soil and Biology & Biochemistry*, 37, pp. 2323-2328.

Clifford, T.N., Rex, D.C., Green, R., Le Roex, A.P., Pienaar, H.S. and Buehmann, D., 1999, Chromian illite-ankerite-quartz parageneses from the Kintail district of southern Ross-shire, Scotland *Mineralogical Magazine*, 63, pp. 37-52.

Coelho, D., Thovert, J.F. and Adler, P.M., 1997, Geometrical and transport properties of random packings of spheres and aspherical particles. *Physical Review E*, 55, pp. 1959-1978.

Constantinides, G.N. and Payatakes, A.C., 1989, Effects of Precursor Wetting Films in Immiscible Displacement Through Porous Media. *Transport in Porous Media*, 38, pp. 291-317.

Crossey, L.J., Surdam, R. and Lahann, C., 1986, Application of organic/inorganic diagenesis to porosity prediction. In *Roles of lnorganic Matter in Sediment Diagenesis*, D.L. Gaulier (Ed.), pp. 147-155 (Society of Economical Paleontology and Mineralogy Special Publications).

Crowley, T.J., 2000, Causes of Climate Change Over the Past 1000 Years. *Science*, 289, pp. 270-277.

Cullers, R.L., Bock, B. and Guidotti, C., 1997, Elemental distributions and neodymium isotopic compositions of Silurian metasediments, western Maine, USA: Redistribution of the rare earth elements. *Geochimica Et Cosmochimica Acta*, 61, pp. 1847-1861.

Curtis, C.D., 1967, Diagenetic Iron Minerals in Some British Carboniferous Sediments. *Geochimica Et Cosmochimica Acta*, 31, pp. 2109-2123.

Curtis, C.D., 1978, Possible links between sandstone diagenesis and depth related geochemical reactions occuring in enclosing mudstones. *Journal of the Geological Society of London*, 135, pp. 107-117.

Curtis, C.D., 1983, Link between Aluminum Mobility and Destruction of Secondary Porosity. *American Association of Petroleum Geologists Bulletin*, 67, pp. 380-384.

Curtis, C.D. and Spears, D.A., 1971, Diagenetic Development of Kaolinite. *Clays and Clay Minerals*, 19, pp. 219-227.

Dadlez, R., Narkiewicz, M., Stephenson, R.A., Visser, M.T.M. and vanWees, J.D., 1995, Tectonic evolution of the Mid-Polish Trough: Modelling implications and significance for central European geology. *Tectonophysics*, 252, pp. 179-195.

Darby, D., Wilkinson, M., Fallick, A.E. and Haszeldine, R.S., 1997, Illite dates record deep fluid movements in petroleum basins. *Petroleum Geoscience*, 3, pp. 133-140.

de Jager, J., 2007, Geological development. In *Geology of the Nerherlands*, T.E. Wong, D.A.J. Batjes and J. de Jager (Eds.) (Royal Netherlands Academy of Arts and Sciences).

de Jager, J., Doyle, M.A., Grantham, P.J. and Mabillard, J.E., 1996, Hydrocarbon habitat of the West Netherlands Basin. In *Geology of gas and oil under the Netherlands*, H.E. Rondeel, D.A.J. Batjes and W.H. Nieuwenhuijs (Eds.), pp. 191-209 (Dordrecht: Royal Geological and Mining Society of the Netherlands (KNGMG)/Kluwer Academic Publishers).

de Reuver, F.J.M., 1998, *Internal Report NAM*, No. 199806000198.

Deer, W.A., Howie, R.A. and Zussman, J., 1992, *An introduction to the rock-forming minerals* (Harlow: Longman).

Deutrich, T., 1993, Illitbildung in Rotliegendsandsteinen des Norddeutschen Beckens. Dissertation, Johannes Gutenberg Universität Mainz. Dissertation.

Dickinson, W.R., 1985, Interpreting Provenance Relations from Detrital Modes of Sandstones. In *Provenance of Arenites*, G.G. Zuffa (Ed.), pp. 333-361 (Dordrecht: Reidel).

Dixon, S.A., Summers, D.M. and Surdam, R.C., 1989, Diagenesis and Preservation of Porosity in Norphlet Formation (Upper Jurassic), Southern Alabama. *American Association of Petroleum Geologists Bulletin*, 73, pp. 707-728.

Dogan, A.U., Dogan, M., Onal, M., Sarikaya, Y., Aburub, A. and Wurster, D.E., 2006, Baseline studies of the clay minerals society source clays: specific surface area by the Brunauer Emmett Teller (BET) Method. *Clays and Clay Minerals*, 54, pp. 62-66.

Doughty, C., Pruess, K., Benson, S.M., Hovorka, S.D., Knox, P.R. and Green, C.T., 2001, Capacity investigation of brine-bearing sands of the Frio Formation for geologic sequestration of CO_2. In *Proceedings of First National Conference on Carbon Sequestration* (Washington D.C.: United States Department of Energy, National Energy Technology Laboratory), p. 16.

Doyen, P.M., 1988, Permeability, conductivity and pore geometry of sandstones. *Journal of Geophysical Research*, 93, pp. 7729-7740.

Drever, J.I., 1997, *The geochemistry of natural waters* (Upper Saddle River: Prentice hall).

Drong, H.J., 1979, Diagenetische Veränderungen in den Rotliegend Sandsteinen im NW-Deutschen Becken. *Geologische Rundschau*, 68, pp. 1172-1183.

Drong, H.J., Plein, E., Sannemann, D., Schuepbach, M.A. and Zimdars, J., 1982, Der Schneverdingen-Sandstein des Rotliegenden - eine äolische Sedimentfüllung alter Grabenstrukturen. *Zeitschrift der Deutschen Geologischen Gesellschaft*, 133, pp. 699-725.

Drory, M.D. and Glaeser, A.M., 1985, The stability of pore cannels: experimental observations. *Journal of the American Ceramic Society*, 68, pp. 14-15.

Duan, Z.H. and Sun, R., 2003, An improved model calculating CO_2 solubility in pure water and aqueous NaCl solutions from 273 to 533 K and from 0 to 2000 bar. *Chemical Geology*, 193, pp. 257-271.

Dudek, T. and Srodoń, J., 2003, Thickness distribution of Illite Crystals in Shales. II: Origin of the Distribution and Mechnanism of Smectite Illitization in Shales. *Clays and Clay Minerals*, 51, pp. 529-542.

Duin, E.J.T., Doornenbal, J.C., Rijkers, R.H.B., Verbeek, J.W. and Wong, T.E., 2006, Subsurface structure of the Netherlands - results of recent onshore and offshore mapping. *Netherlands Journal of Geosciences - Geologie En Mijnbouw*, 85, pp. 245-276.

Dullien, F.A.L., 1979, Porous media: Fluid transport and pore structure. *Academic Press*, 396.

Ehrenberg, S.N., 1989, Assessing the Relative Importance of Compaction Processes and Cementation to Reduction of Porosity in Sandstones - Discussion - Compaction and Porosity Evolution of Pliocene Sandstones, Ventura-Basin, California - Discussion. *American Association of Petroleum Geologists Bulletin*, 73, pp. 1274-1276.

Ehrenberg, S.N., 1991, Kaolinized, Potassium-Leached Zones at the Contacts of the Garn Formation, Haltenbanken, Mid-Norwegian Continental-Shelf. *Marine and Petroleum Geology*, 8, pp. 250-269.

Ehrenberg, S.N., Skjevrak, I. and Gilje, A.E., 1995, Asphaltene-rich residues in sandstone reservoirs of Haltenbanken province, mid-Norwegian continental shelf. *Marine and Petroleum Geology*, 12, pp. 53-69.

Emmanuel, S., Ague, J.J. and Walderhaug, O., 2010, Interfacial energy effects and the evolution of pore size distributions during quartz precipitation in sandstone. *Geochimica Et Cosmochimica Acta*, 74, pp. 3539-3552.

Enick, R.M. and Klara, S.M., 2001, CO_2 solubility in water and brine under reservoir conditions. *Chemical Engineering Communications*, 90, pp. 23-33.

Ennis-King, J.P. and Paterson, L., 2003, Role of convective mixing in the long-term storage of carbon dioxide in deep saline formations. In *Society of Petroleum Engineers Annual Technical Conference and Exhibition* (Denver, Colorado).

Errat, D., Thomas, G.M. and Wall, G.R.T., 1999, The evolution of the Central North Sea Rift. In *Petroleum Geology of Northwest Europe*, A.J. Fleet and S.A.R. Boldy (Eds.) (Lodon: Geological Society).

Eskenazy, G.M., 1999, Aspects of the geochemistry of rare earth elements in coal: an experimental approach. *International Journal of Coal Geology*, 38, pp. 285-295.

Etheridge, D., Steele, L., Francy, R. and Langenfelds, R., 1998, Atmospheric methane between 1000 a.d. and present: Evidence of anthropogenic emissions and climatic variability. *Journal of Geophysical Research*, 103, pp. 709-731.

Evans, D., Graham, C., Armour, A. and Bathurst, P., 2003, *The Millennium Atlas: Petroleum Geology of the Central and Northern North Sea* (London).

Farmer, V.C., 1974, The layer silicates. In *The Infrared Spectra of Minerals*, V.C. Farmer (Ed.), pp. 331-364 (London: Mineralogical Society).

Finney, J.L., 1970, Random Packings and Structure of Simple Liquids .1. Geometry of Random Close Packing. *Proceedings of the Royal Society of London Series a-Mathematical and Physical Sciences*, 319, pp. 479-493.

Fischer, C. and Gaupp, R., 2005, Change of black shale organic material surface area during oxidative weathering: Implications for rock-water surface evolution. *Geochimica Et Cosmochimica Acta*, 69, pp. 1213-1224.

Folk, R.L., 1976, Reddening of Desert Sands - Simpson Desert, N T, Australia. *Journal of Sedimentary Petrology*, 46, pp. 604-615.

Frank, F., Zinkernagel, U. and Füchtbauer, H., 1992, Zur Liefergebietsfrage der Sandsteine des Nordwestdeutschen Oberkarbons. *DGMK-Forschungsbericht*, 384, pp. 1-167.

Franke, W., 1995, Geodynamic evolution. In *The Pre-Permian Geology of Central and Eastern Europe*, D. Dallmayer, W. Franke and K.W. Weber (Eds.), pp. 579-594 (Berlin: Springer).

Friedmann, S.J., 2006, The ICE framework for site selection and a description of potential due diligence requirements. In *International Symposium on site characterisation for CO_2 geological storage* (Berkeley), p. 28.

Friedrich, K., Fakirov, S. and Zhang, Z., 2005, *Polymer Composites: From Nano- to Macro-Scale* (Springer).

Frost, R.L., Fredericks, P.M. and Bartlett, J.R., 1993, Fourier-Transform Raman-Spectroscopy of Kandite Clays. *Spectrochimica Acta Part a-Molecular and Biomolecular Spectroscopy*, 49, pp. 667-674.

Füchtbauer, H., 1979, Die Sandsteindiagenese im Spiegel der neueren Literatur. *International Journal of Earth Sciences*, 68, pp. 1125-1151.

Füchtbauer, H. et al., 1988, *Sedimente und Sedimentgesteine* (Stuttgart: Schweizerbart).

Fukuda, J., Yokoyama, T. and Kirino, Y., 2009, Characterization of the states and diffusivity of intergranular water in a chalcedonic quartz by high-temperature in situ infrared spectroscopy. *Mineralogical Magazine*, 73, pp. 825-835.

Gaitzsch, B., Ellenberg, J., Lützner, H. and Benek, R., 1995, Flechtlinger Scholle. In *Norddeutsches Rotliegendbecken, Rotliegend-Monographie Teil II*, E. Plein (Ed.), pp. 84-96 (Courier Forschungs-institut Senckenberg).

Gale, J., 2004, Why do we need to consider geological storage of CO_2? In *Geological Storage of Carbon Dioxide*, S.J. Baines and R.H. Worden (Eds.), pp. 7-15 (London: Geological Society Special Publications).

Garcia, A.J.V., Morad, S., De Ros, L.F. and Al-Aasm, I.S., 1998, Paleogeographical, paleoclimatic and burial history controls on the diagenetic evolution of Lower Cretaceous Serraria sandstones in Sergipe-Alagoas Basin, NE Braz. In *Carbonate Cementation in Sandstones: Distribution Patterns and Geochemical Evolution*, S. Morad (Ed.), pp. 107-140 (Oxford: International Association of Sedimentologists, Special Publications).

Garden, I.R., Guscott, S.C., Burley, S.D., Foxford, K.A., Walsh, J.J. and Marshall, J., 2001, An exhumed palaeo-hydrocarbon migration fairway in a faulted carrier system, Entrada Sandstone of SE Utah, USA. *Geofluids*, 1, pp. 195-213.

Gardolinski, J.E., Carrera, L.C.M., Cantao, M.P. and Wypych, F., 2000, Layered polymer-kaolinite nanocomposites. *Journal of Materials Science*, 35, pp. 3113-3119.

Gast, R., 1988, Rifting im Rotliegenden Niedersachsens. *Die Geowissenschaften*, 4, pp. 115-122.

Gast, R., 1991, The perennial Rotliegend saline lake in NW Germany. *Geologisches Jahrbuch*, A119, pp. 25-59.

Gast, R., Pasternack, M., Piske, J. and Rasch, H.-J., 1998, Das Rotliegend im Nordostdeutschen Raum, Stratigraphie, Fazies und Diagenese. *Geologisches Jahrbuch*, A149, pp. 59-79.

Gaupp, R., 1996, Diagenesis types and their application in diagenesis mapping. *Zentralblatt für Geologie und Paläontologie*, 1994, pp. 1183-1199.

Gaupp, R., 2005, Model conclusions. In *Palaeo Oil- and Gasfields in the Rotliegend of the North German Basin: Effects upon Hydrocarbon Reservoir Quality*, R. Gaupp (Ed.), pp. 5.1-5.17 (Hamburg: DGMK - Forschungsbericht).

Gaupp, R., 2008, Diagenesis of Rotliegend Reservoirs. In *Core Workshop "The Permian Rotliegend in the Netherlands" (*SHELL NAM).

Gaupp, R., Matter, A., Platt, J., Ramseyer, K. and Walzebuck, J., 1993, Diagenesis and Fluid Evolution of Deeply Buried Permian (Rotliegende) Gas-Reservoirs, Northwest Germany. *American Association of Petroleum Geologists Bulletin*, 77, pp. 1111-1128.

Gaupp, R., Gast, R. and Forster, C., 2000, Late Permian Playa Lake Deposits of the Southern Permian Basin (Central Europe). In *Lake basins trough space and time*, E.H. Gierlowski-Kordesch and K.R. Kelts (Eds.), pp. 75-86 (Tulsa: AAPG Studies in Geology).

Gaupp, R. and Okkerman, J., 2011, Diagenesis and reservoir quality of Rotliegend sandstones in the northern Netherlands - A review. In *The Permian Rotliegend of the Netherlands*, J. Grötsch and R. Gaupp (Eds.), pp. 193-228 (Tulsa, Oklahoma: SEPM Special Publication).

Gaupp, R., Möller, P., Lüders, V., di Primio, R. and Littke, R., 2008, Fluids in sedimentary basins: an overview. In *Dynamics of complex sedimentary basins. The example of the Central European Basin System*, R. Littke, U. Bayer, D. Gajewski and S. Nelskamp (Eds.), pp. 347-365 (Berlin, Heidelberg: Springer).

Gaus, I., Le Guern, C., Pearce, J., Pauwels, H., Shepherd, T., Hatziyannis, G. and Metaxas, A., 2004, Comparison of long term geochemical interactions at two natural CO_2 analogues Montmiral (Southeast basin, France). In *Proceedings of the 7th International Conference on Greenhouse Gas Control Technologies*, E.S. Rubin, D.W. Keith and C.F. Gilboy (Eds.) (Cheltenham, UK: IEA Greenhous Gas Program).

Gaus, I., Audigane, P., Andre, L., Lions, J., Jacquemet, N., Durst, P. and Czernichowski-Lauriol, I., 2008, Geochemical and solute transport modelling for CO_2 storage, what to expect from it? *Greenhousse Gas Control*, 2, pp. 605-625.

Geluk, M., 2005, Stratigraphy and tectonics of Permo-Triassic basins in the Netherlands and surrounding areas. Dissertation, Utrecht, Netherlands.

Geluk, M., Dusar, M. and de Vos, W., 2007, Pre-Silesian. In *Geology of the Nerherlands*, S. Wong, D.A.J. Batjes and J. de Jager (Eds.) (Royal Netherlands Academy of Arts and Sciences).

Gemmer, L., Nielsen, S.B. and Bayer, U., 2003, Late Cretaceous-Cenozoic evolution of the North German Basin - results from 3-D geodynamic modelling. *Tectonophysics*, 373, pp. 39-54.

George, G.T. and Berry, J.K., 1993, A new lithostratigraphical and depositional model for the Upper Rotliegend of the UK Sector of the Southern North Sea. In *Characterization of Fluvial and Aeolian Reservoirs*, C.P. North and D.J. Prosser (Eds.), pp. 291-319 (Geological Society Special Publication).

Getahun, A., Reed, M.H. and Symonds, R., 1996, Mount St. Augustine volcano fumarole wall rock alteration: mineralogy, zoning, composition and numerical models of its formation process. *Journal of Volcanology and Geothermal Research*, 71, pp. 73-107.

Gherardi, F., Xu, T. and Pruess, K., 2007, Numerical modeling of self-limiting and self-enhancing caprock alteration by CO_2 storage in a depleted gas reservoir. *Chemical Geology*, 244, pp. 103-129.

Giammar, D.E., Bruant, R.G. and Peters, C.A., 2005, Forsterite dissolution and magnesite precipitation at conditions relevant for deep saline aquifer storage and sequestration of carbon dioxide. *Chemical Geology*, 217, pp. 257-276.

Giesting, P., Guggenheim, S., Koster, A. F. and Busch, A., submitted, Interaction of Carbon Dioxide with Na-exchanged Montmorillonite at Pressures to 640 Bars: Implications for CO_2 Sequestration. International Journal of Greenhouse Gas Control.

Giles, M.R., 1987, Mass-Transfer and Problems of Secondary Porosity Creation in Deeply Buried Hydrocarbon Reservoirs. *Marine and Petroleum Geology*, 4, pp. 188-204.

Giles, M.R., 1996, *Diagenesis - a quantitative perspective* (Dordrecht: Kluwer Academic Publishers).

Giles, M.R. and Marshall, J.D., 1986, Constraints on the Development of Secondary Porosity in the Subsurface - Reevaluation of Processes. *Marine and Petroleum Geology*, 3, pp. 243-255.

Giordano, T.H. and Kharaka, Y.K., 1994, Organic ligand distribution and speciation in sedimentary basin brines, diagenetic fluids and related ore solutions. *The Geological Society, Special Publications*, 78, pp. 175-202.

Gislason, S.R., Wolff-Boenisch, D., Stefansson, A., Oelkers, E.H., Gunnlaugsson, E., Sigurdardottir, H., Sigfusson, B., Broecker, W.S., Matter, J.M., Stute, M., Axelsson, G. and Fridriksson, T., 2010, Mineral sequestration of carbon dioxide in basalt: A pre-injection overview of the CarbFix project. *International Journal of Greenhouse Gas Control*, 4, pp. 537-545.

Glasmann, J.R., Clark, R.A., Larter, S., Briedis, N.A. and Lundegard, P.D., 1989, Diagenesis and Hydrocarbon Accumulation, Brent Sandstone (Jurassic), Bergen High Area, North-Sea. *American Association of Petroleum Geologists Bulletin*, 73, pp. 1341-1360.

Glennie, K.W., 1972, Permian Rotliegend of Nortwest Europe interpreted in light of modem sedimentation studies. *American Association of Petroleum Geologists Bulletin*, 56, pp. 1048-1071.

Glennie, K.W., 1983, Early Permian (Rotliegendes) Paleowinds of the North-Sea. *Sedimentary Geology*, 34, pp. 245-265.

Glennie, K.W., 1998, Lower Permian – Rotliegend. In *Petroleum Geology of the North Sea*, K.W. Glennie (Ed.), pp. 137-174 (Oxford: Blackwell Science).

Glennie, K.W., Mudd, G.C. and Nagtegaal, P.J.C., 1978, Depositional environment and diagenesis of Permian Rotliegend sandstones in Leman bank and Sole Pit areas of the UK southern North Sea. *Journal of the Geological Society of London*, 135, pp. 25-34.

Glennie, K.W. and Provan, D.M.J., 1990, Lower Permian Rotliegend reservoir of the Southern North Sea gas province. In *Classic Petroleum Provinces*, J. Brooks (Ed.), pp. 399-416 (London: Geological Society Special Publications).

Gluyas, J. and Leonard, A., 1995, Diagenesis of the Rotliegend Sandstone - the Answer Aint Blowin in the Wind. *Marine and Petroleum Geology*, 12, pp. 491-497.

Goodchild, M.W. and Whitaker, J.H.M., 1986, A Petrographic Study of the Rotliegendes Sandstone Reservoir (Lower Permian) in the Rough Gas-Field. *Clay Minerals*, 21, pp. 459-477.

Gralla, P., 1988, Das Oberrotliegende in NW-Deutschland - Lithostratigraphie und Faziesanalyse. *Geologisches Jahrbuch*, A106, pp. 3-59.

Grecula, 2002, *Internal Report NAM*, (no number).

Gregersen, S. and Voss, P., 2002, Summary of project TOR: delineation of a stepwise, sharp, deep lithosphere transition across Germany-Denmark-Sweden. *Tectonophysics*, 360, pp. 61-73.

Gregersen, S., Glendrup, M., Larsen, T.B., Voss, P. and Rasmussen, P., 2005, Seismology: neotectonics and structure of the Baltic Shield. *Geological Survey of Denmark and Greenland Bulletin*, 7, pp. 25-28.

Gunter, W.D., 2005, CO_2 Capture and Storage - What it has to offer. In *APEC Carbon Capture and Storage Workshop* (Seoul, Korea), p. 18.

Gunter, W.D., Perkins, E.H. and McCann, T.J., 1993, Aquifer disposal of CO_2-rich gases: reaction design for added capacity. *Energy Conversion and Management*, 34, pp. 941-948.

Gunter, W.D., Wiwehar, B. and Perkins, E.H., 1997, Aquifer disposal of CO_2-rich greenhouse gases: Extension of the time scale of experiment for CO_2-sequestering reactions by geochemical modelling. *Mineralogy and Petrology*, 59, pp. 121-140.

Gunter, W.D., Perkins, E.H. and Hutcheon, I., 2000, Aquifer disposal of acid gases: modelling of water-rock reactions for trapping of acid wastes. *Applied Geochemistry*, 15, pp. 1085-1095.

Gunter, W.D., Bachu, S. and Benson, S., 2004, The role of hydrogeological and geochemical trapping in sedimentary basins for secure geological storage of carbon dioxide. In *Geological Storage of Carbon Dioxide*, S.J. Baines and R.H. Worden (Eds.), pp. 129-145, (London: Geological Society Special Publication).

Hall, B.D. and White, N., 1994, Origin of Anomalous Tertiary Subsidence Adjacent to North-Atlantic Continental Margins. *Marine and Petroleum Geology*, 11, pp. 702-714.

Hamilton, P.J., Giles, M.R. and Ainsworth, P., 1992, K-Ar dating of illites in Brent Group reservoirs: a regional perspective. In *Geology of the Brent Group* A.C. Morton (Ed.), pp. 377-400 (London: Geological Society Special Publications).

Hancock, N.J. and Taylor, A.M., 1978, Clay mineral diagenesis and oil migration in the Middle Jurassic Brent Sand Formation. *Journal of Geological Socienty London*, 135, pp. 69-72.

Hartmann, B.H., Ramseyer, K. and Matter, A., 2000, Diagenesis and pore-water evolution in Permian sandstones, Gharif Formation, Sultanate of Oman. *Journal of Sedimentary Research*, 70, pp. 533-544.

Hartog, F.A. and Jonkers, G., 2001, Lead Deposits in Dutch Natural Gas Systems *SPE Production & Facilities*, 17, pp. 122-128.

Harvie, C.E. and Weare, J.H., 1980, The Prediction of Mineral Solubilities in Natural-Waters - the Na-K-Mg-Ca-Cl-SO_4-H_2O System from Zero to High-Concentration at 25-Degrees-C. *Geochimica Et Cosmochimica Acta*, 44, pp. 981-997.

Harvie, C.E., Moller, N. and Weare, J.H., 1984, The Prediction of Mineral Solubilities in Natural-Waters - the Na-K-Mg-Ca-H-Cl-SO_4-OH-HCO_3-CO_3-CO_2-H_2O System to High Ionic Strengths at 25-Degrees-C. *Geochimica Et Cosmochimica Acta*, 48, pp. 723-751.

Haszeldine, R., S., Quinn, O., England, G., Wilkinson, M., Shipton, Z., K., Evans, J., P., Heath, J., Crossey, L., Ballentine, C., J. and Graham, C., M., 2005, Natural Geochemical Analogues for Carbon Dioxide Storage in Deep Geological Porous Reservoirs, a United Kingdom Perspective. *Oil & Gas Science and Technology - Rev. IFP*, 60, pp. 33-49.

Hay, R.L., Guldman, S.G., Matthews, J.C., Lander, R.H., Duffin, M.E. and Kyser, T.K., 1991, Clay mineral diagenesis in core KM-3 of Searles Lake, California. *Clays and Clay Minerals*, 39, pp. 84-96.

Hedemann, H.-A. and Teichmüller, R., 1971, Die paläogeographische Entwicklung des Oberkarbons. *Fortschr. Geol. Rheinld. u. Westf.*, 19, pp. 129-142.

Helgeson, H.C., Murphy, W.M. and Aagaard, P., 1984, Thermodynamic and Kinetic Constraints on Reaction-Rates among Minerals and Aqueous-Solutions .2. Rate Constants, Effective Surface-Area, and the Hydrolysis of Feldspar. *Geochimica Et Cosmochimica Acta*, 48, pp. 2405-2432.

Hellevang, H. and Aagaard, P., 2010, Can carbonate precipitation rates be derived from dissolution rate data? *Geochimica Et Cosmochimica Acta*, 74, pp. A396-A396.

Higgs, K.E., Zwingmann, H., Reyes, A.G. and Funnell, R.H., 2007, Diagenesis, porosity evolution, and petroleum emplacement in tight gas reservoirs, Taranaki Basin, New Zealand. *Journal of Sedimentary Research*, 77, pp. 1003-1025.

Hillier, S., 1994, Pore-Lining Chlorites in Siliciclastic Reservoir Sandstones - Electron-Microprobe, Sem and Xrd Data, and Implications for Their Origin. *Clay Minerals*, 29, pp. 665-679.

Hitchon, B., 1996, *Aquifer Disposal of Carbon Dioxide, Hydrodynamic and Mineral Trapping - Proof of Concept* (Alberta, Canada: Geoscience Publishing Ltd).

Hoffmann, N., Pokorski, J., Lindert, W. and Bachmann, G.H., 1997, Rotliegend stratigraphy, palaeogeography and facies in the eastern part of the Central European Basin. In *Proc. XIII Int. Congr. on Carboniferous - Permian, 1995* (Krakow, Prace Panstwowego Instytut Geologicznego CLVII), pp. 75-86.

Holliday, D.W., 1970, Petrology of Secondary Gypsum Rocks - a Review. *Journal of Sedimentary Petrology*, 40, p. 734 ff.

Holloway, S., 1996, The Underground Disposal of Carbon Dioxide. Final Report of JOULE II Project No. CT92-0031. *British Geological Survey*, p. 355

Holtz, M. and Bryant, S.L., 2005, Effects of Pre Network Geometry on Permanent Storage of Sequestered CO_2. In *AAPG annual convention abstract* (Calgary, Canada).

Horsfield, B., Schenk, H.-J., Mills, N. and Welte, D.H., 1992, An investigation of the in-reservoir conversion of oil to gas: compositional and kinetic findings from closed-system programmedtemperature pyrolysis. *Organic Geochemistry*, 19, pp. 191-204.

Hoth, N., Schlömann, M., Kassahun, A., Glombitza, F. and Häfner, F., 2005, Recycling of sequestrated CO_2 by microbial - biogeochemical transformation in the deep subsurface (RECOBIO). In *Investigation, Utilization and Protection of the Underground*, L. Stroink (Ed.).

Houseknecht, D.W., 1987, Assessing the Relative Importance of Compaction Processes and Cementation to Reduction of Porosity in Sandstones. *American Association of Petroleum Geologists Bulletin*, 71, pp. 633-642.

Howell, J. and Mountney, N., 1997, *Climatic cyclicity and accommodation space in arid to semi-arid depositional systems: an example from the Rotliegend Group of the UK Southern North Sea* (Geological Society of London Special Publication).

Hower, J., Eslinger, E.V., Hower, M.E. and Perry, E.A., 1976, Mechanism of Burial Metamorphism of Argillaceous Sediment .1. Mineralogical and Chemical Evidence. *Geological Society of America Bulletin*, 87, pp. 725-737.

Hutcheon, I., 1983, Diagenesis .3. Aspects of the Diagenesis of Coarse-Grained Siliciclastic Rocks. *Geological Association of Canada*, 10, pp. 4-14.

Hutcheon, I., 1989, Application of chemical and isotopic analyses of fluids to problems in sandstone diagenesis. In *Short Course in Burial Diagenesis*, I. Hutcheon (Ed.), pp. 249-310 (Montreal: Mineralogical Association of Canada).

Hutcheon, I., Oldershaw, A. and Ghent, E.D., 1980, Diagenesis of Cretaceous Sandstones of the Kootenay Formation at Elk Valley (Southeastern British-Columbia) and Mt Allan (Southwestern Alberta). *Geochimica Et Cosmochimica Acta*, 44, pp. 1425-1435.

ICS, 2003, International Stratigraphic Chart. International Commission on Stratigraphy. Available online.

IEAGHG, 2001, Natural Releases of CO_2. p. 14 (International Energy Agency (IEA) Greenhouse Gas (GHG) R&D Programme).

Ioannidis, M.A. and Chatzis, I., 1993, Network modeling of pore structure and transport properties of porous media. *Chemical Engineering Science*, 48, pp. 951-972.

IPCC, 1995, Intergovermental Panel on Climate Change (IPCC) Special Report - The Science of Climate Change. Contribution of Working Group I to the Second Assessment Report of the Intergovernmental Panel on Climate Change., p. 588, (Cambridge: Cambridge University Press).

IPCC, 2005, Intergovermental Panel on Climate Change (IPCC) Special Report - Carbon Dioxide Capture and Storage - Summary for Policymakers and Technical Summary. p. 431 (Cambridge: Cambridge University Press).

James, W.C., Wilmar, G.C. and Davidson, B.G., 1986, Role of Quartz Type and Grain-Size in Silica Diagenesis, Nugget Sandstone, South-Central Wyoming. *Journal of Sedimentary Petrology*, 56, pp. 657-662.

Jaritz, W., 1973, Zur Entstehung der Salzstrukturen Nordwestdeutschlands. *Geologisches Jahrbuch*, A 10, pp. 3-77.

Jasmund, K. and Lagaly, G., 1993, *Tonminerale und Tone - Struktur, Eigenschaften, Anwendungen und Einsatz in Industrie und Umwelt* (Darmstadt: Steinkopff-Verlag).

Johansson, U., Holmgren, A., Forsling, W. and Frost, R., 1998, Isotopic exchange of kaolinite hydroxyl protons: a diffuse reflectance infrared Fourier transform spectroscopy study [dagger]. *Analyst*, 123, pp. 641-645.

John, N., 2010, Illite Morphotypes – Appearance and possible formation mechanisms in relation to pore-geometries and diagenesis. Diploma Thesis, University of Jena.

Johnson, H., Warrington, G. and Stoker, S.J., 1994, Permian and Triassic of the Southern North Sea. In *Lithostratigraphic nomenclature of the North Sea*, R.W. Knox and W.G. Cordey (Eds.) (Nottingham: British Geological Survey).

Johnson, R.E., Sciegienka, J., Carlos-Cuellar, S. and Grassian, V.H., 2005, Heterogeneous Uptake of Gaseous Nitric Acid on Dolomite ($CaMg(CO_3)_2$) and Calcite ($CaCO_3$) Particles: A Knudsen Cell Study Using Multiple, Single, and Fractional Particle Layers. *Journal of Physical Chemistry*, 109, pp. 6901-6911.

Jordan, H. and Kockel, F., 1991, Die Leinetal-Structur und ihr Umfeld - ein tektonisches Konzept für Südniedersachsen. *Geologisches Jahrbuch*, A 126, pp. 171-196.

Karaca, S., Gurses, M.E. and Ejder, M., 2006, Adsorptive removal of phosphate from aqueous solutions using raw and calcinated dolomite. *Journal of Hazardous Material*, 128, pp. 273-279.

Kashefi, K. and Lovley, D.R., 2003, Extending the Upper Temperature Limit for Life. *Science*, 307, p. 934.

Kashefi, K., Holmes, D.E., Lovley, D.R. and Tor, J.M., 2004, Potential importance of dissimilatory Fe(III)-reducing microorganisms in hot sedimentary environments - The Subseafloor Biosphere at Mid-Ocean Ridges. *Geophysical Monograph Series*, 144, pp. 199-211.

Kaszuba, J.P., Janecky, D.R. and Snow, M.G., 2003, Carbon dioxide reaction processes in a model brine aquifer at 200 degrees C and 200 bars: implications for geologic sequestration of carbon. *Applied Geochemistry*, 18, pp. 1065-1080.

Katzung, G., 1975, Tektonik, Klima und Sedimentation in der Mitteleuropäischen Saxon-Senke und in angrenzenden Gebieten. *Zeitschrift der Deutschen Geologischen Gesellschaft*, 3, pp. 1453-1472.

Ketzer, J.M., Carpentier, B., Y., L.G. and Le Thiez, P., 2005, Geological Sequestration of CO_2 in Mature Hydrocarbon Fields - Basin and Reservoir Numerical Modelling of the Forties Field, North Sea. *Oil & Gas Science and Technology - Rev. IFP*, 60, pp. 259-273.

Ketzer, J.M., Iglesias, R., Einloft, S., Dullius, J., Ligabue, R. and de Lima, V., 2009, Water-rock-CO_2 interactions in saline aquifers aimed for carbon dioxide storage: Experimental and numerical modeling studies of the Rio Bonito Formation (Permian), southern Brasil. *Applied Geochemistry*, 24, pp. 760-767.

Kharaka, Y.K., Hull, R.W. and Carrothers, W.W., 1985, Water-rock interaction in sedimentary basins. In *Relationship of organic matter and mineral diagenesis*, pp. 79-176 (Society of Economic Paleontologists and Mineralogists Short Course).

Kharaka, Y.K., Law, L.M., Carothers, W.W. and Goerlitz, D.F., 1986, Role of organic species dissolved in formation waters from sedimentary basins in mineral diagenesis. In *Roles of Organic Matter in Sediment Diagenesis*, D.L. Gautier (Ed.), pp. 111-222 (Tulsa: SEPM Special Publications).

Kharaka, Y.K., Cole, D., Gunter, W.D., Knauss, K. and Nance, S., 2005, Geologic - Frio Brine Field Project (1) - Geochemistry of water and gases in the Frio Brine Pilot Test: Baseline data and changes during and post CO_2 injection. In *Fourth Annual conference on Carbon Capture and Storage* (Alexandria, Virginia, USA), p. 29.

Kilgore, B. and Elmore, R.D., 1989, A study of the relationship between hydrocarbon migration and the precipitacion of authigenic magnetic minerals in the Triassic Chugwater Formation, southern Montana. *Geological Society of America Bulletin*, 101, pp. 1280-1288.

Kley, J. and Voigt, T., 2008, Late Cretaceous intraplate thrusting in central Europe: Effect of Africa-Iberia-Europe convergence, not Alpine collision. *Geology*, 36, pp. 839-842.

Knauss, K.G., Johnson, J.W. and Steefel, C.I., 2005, Evaluation of the impact of CO_2, co-contaminant gas, aqueous fluid and reservoir rock interactions on the geologic sequestration of CO_2. *Chemical Geology*, 217, pp. 339-350.

Krawczyk, C.M., Eilts, F., Lassen, A. and Thybo, H., 2002, Seismic evidence of Caledonian deformed crust and uppermost mantle structures in the northern part of the Trans-European Suture Zone, SW Baltic Sea. *Tectonophysics*, 360, pp. 215-244.

Krooss, B.M., Friberg, L., Gensterblum, Y., Hollenstein, J., Prinz, D. and Littke, R., 2005, Investigation of the pyrolytic liberation of molecular nitrogen from Palaeozoic sedimentary rocks. *International Journal of Earth Sciences*, 94, pp. 1023-1038.

Kumar, A., Noh, M.H., Sepehrnoori, K., Pope, G.A., Bryant, S.L. and Lake, L.W., 2005, Simulating CO_2 storage in deep saline aquifers, Carbon Dioxide Capture for Storage in Deep Geologic Formations - Results from the CO_2 Capture Project. In *Geologic Storage of Carbon Dioxide with Monitoring and Verification*, S.M. Benson (Ed.), pp. 977-998 (London).

Lagaly, G., 1999, Introduction: from clay mineral–polymer interactions to clay mineral–polymer nanocomposites. *Applied Clay Science*, 15, pp. 1-9.

Lagaly, G., 2001, Pesticide-clay interactions and formulations. *Applied Clay Science*, 18, pp. 205-209.

Lahav, N., 1990, Preparation of Stable Suspensions of Delaminated Kaolinite by Combined Dimethylsulfoxide-Ammonium Fluoride Treatment. *Clays and Clay Minerals*, 38, pp. 219-222.

Laksana, 2000, *Internal Report NAM*; No. LAN-00.249.

Land, L.S. and Milliken, K.L., 1981, Feldspar Diagenesis in the Frio Formation, Brazoria County, Texas Gulf-Coast. *Geology*, 9, pp. 314-318.

Langenaeker, V., 2000, The Campine Basin. Stratigraphy, structural geology, coalification and hydrocarbon potential for the Devonian to Jurassic. *Aardkundige Mededelingen*, 10, pp. 1-142.

Lanson, B., Beaufort, D., Berger, G., Baradat, J. and Lacharpagne, J.C., 1996, Illitization of diagenetic kaolinite-to-dickite conversion series: Late-stage diagenesis of the Lower Permian Rotliegend sandstone reservoir, offshore of the Netherlands. *Journal of Sedimentary Research*, 66, pp. 501-518.

Lanson, B., Beaufort, D., Berger, G., Bauer, A., Cassagnabere, A. and Meunier, A., 2002, Authigenic kaolin and illitic minerals during burial diagenesis of sandstones: a review. *Clay Minerals*, 37, pp. 1-22.

Larter, S., Wilhelms, A., Head, I., Koopmans, M., Aplin, A.C., Di Primio, R., Zwach, C., Erdmann, M. and Telnaes, N., 2003, The controls on the composition of biodegraded oils in the deep subsurface - part 1: biodegradation rates in petroleum reservoirs. *Organic Geochemistry*, 34, pp. 601-613.

Lasaga, A.C., 1981, Transition state theory. *Reviews in Mineralogy*, 8, pp. 135-169.

Lasaga, A.C., 1984, Chemical kinetics of water-rock interactions. *Journal of Geophysical Research*, 89, pp. 4009-4025.

Latief, F.D.E., Biswal, B., Fauzi, U. and Hilfer, R., 2010, Continuum reconstruction of the pore scale microstructure for Fontainebleau sandstone. *Physica*, A 389, pp. 1607-1618.

le Baron, P.C., Wang, Z. and Pinnavaia, T.J., 1999, Polymer-layered silicate nanocomposites: an overview. *Applied Clay Science*, 15, pp. 11-29.

le Guen, Y., 2001, *Internal Report NAM*, No. 200108100577.

Leder, F. and Park, W.C., 1986, Porosity Reduction in Sandstone by Quartz Overgrowth. *American Association of Petroleum Geologists Bulletin*, 70, pp. 1713-1728.

Ledesert, B., Berger, G., Meunier, A., Genter, A. and Bouchet, A., 1999, Diagenetic-type reactions related to hydrothermal alteration in the Soultz-sous-Forets Granite, France. *European Journal of Mineralogy*, 11, pp. 731-741.

Lee, M., Aronson, J.L. and Savin, S.M., 1989, Timing and conditions of Permian Rotliegende Sandstone Diagenesis, Southern North Sea: K/Ar and Oxygen Isotopic Data. *American Association of Petroleum Geology Bulletin*, 73, pp. 195-213.

Lee, M.-K. and Bethke, C.M., 1994, Groundwater flow, late cementation, and petroleum accumulation in the Permian Lyons Sandstone, Denver Basin. *American Association of Petroleum Geology Bulletin*, 78, pp. 217-237.

Legler, B., Gebhardt, U. and Schneider, J.W., 2005, Late Permian non-marine-marine transitional profiles in the central Southern Permian Basin, northern Germany. *International Journal of Earth Sciences*, 94, pp. 851-862.

Levandowski, D.W., Kaley, M.E., Silverman, S.R. and Smalley, R.G., 1973, Cementation in Lyons sandstone and its role in oil accumulation, Denver Basin, Colorado. *American Association of Petroleum Geologists Bulletin*, 57, pp. 2217-2244.

Leveille, G.P., Primmer, T.J., Dudley, G., Ellis, D. and Allinson, G.J., 1997, Diagenetic controls on reservoir quality in Permian Rotliegendes sandstones, Jupiter Fields area, southern North Sea. In *Petroleum geology of the Southern North Sea: Future and Potential*, K. Ziegler, P. Turner and S.R. Daines (Eds.), pp. 105-122 (Geological Society Special Publications, London).

Liewig, N., Clauer, N. and Sommer, F., 1987, Rb-Sr and K-Ar Dating of Clay Diagenesis in Jurasic Sandstone Oil Reservoir, North Sea. *American Association of Petroleum Geologists Bulletin*, 71, pp. 1467-1474.

Liewig, N. and Clauer, N., 2000, K-Ar dating of varied microtextural illite in Permian gas reservoirs, northern Germany. *Clay Minerals*, 35, pp. 271-281.

Littke, R., Brauckmann, J. and Schaefer, R.G., 1996, Solid bitumen in Rotliegend gas reservoirs in northern Germany: Implications for their thermal and filling history. *Zentralblatt für Geologie und Paläontologie*, 11, pp. 1275-1292.

Lokhorst, A., 1998, *The Northwest European Gasatlas* (Haarlem).

Longiaru, S., 1987, Visual comparators for estimating the degree of sorting from plane and thin section. *Journal of Sedimentary Petrology*, 57, pp. 791-794.

Lu, P., Fu, Q., Seyfried, W., Hereford, A. and Zhu, C., 2010, Navajo Sandstone–brine–CO_2 interaction: implications for geological carbon sequestration. *Environmental Earth Sciences*, pp. 1-18.

Lüttge, A. and Arvidson, R.S., 2008, The Mineral-Water Interface. In *Kinetics of Water-Rock-Interaction*, S.L. Brantley, D.K. James and A.F. White (Eds.) (Springer).

Lynch, F.L., Mack, L.E. and Land, L.S., 1997, Burial diagenesis of illite/smectite in shales and the origins of authigenic quartz and secondary porosity in sandstones. *Geochimica Et Cosmochimica Acta*, 61, pp. 1995-2006.

Ma, C. and Eggleton, R.A., 1999, Cation exchange capacity of kaolinite. *Clays and Clay Minerals*, 47, pp. 174-180.

Machel, H.G., 2001, Bacterial and thermochemical sulfate reduction in diagenetic settings - old and new insights. *Sedimentary Geology*, 140, pp. 143-175.

Machel, H., G., 2005, Geological and Hydrogeological Evaluation of the Nisku Q-Pool in Alberta, Canada, for H2S and/or CO_2 Storage. *Oil & Gas Science and Technology - Rev. IFP*, 60, pp. 51-65.

Machel, H.G., Krouse, H.R. and Sassen, R., 1995, Products and Distinguishing Criteria of Bacterial and Thermochemical Sulfate Reduction. *Applied Geochemistry*, 10, pp. 373-389.

Macht, F., Totsche, K.U., Eusterhues, K. and Pronk, G., 2010, Topography and surface properties of clay minerals analyzed by atomic force microscopy. In *19th World Congress of Soil Science, Soil Solutions for a Changing World* (Brisbane, Australia).

Marx, J., HUebscher, H.-D., Hoth, K., Korich, D. and Kramer, W., 1995, Vulkanostratigraphie und Geochemie der Eruptivkomplexe. In *Norddeutsches Rotliegendbecken, Rotliegend-Monographie Teil II*, E. Plein (Ed.), pp. 54-83 (Frankfurt am Main: Courier Forschungsinstitut Senckenberg).

Matlack, K.S., Houseknecht, D.W. and Applin, K.R., 1989, Emplacement of Clay into Sand by Infiltration. *Journal of Sedimentary Petrology*, 59, pp. 77-87.

May, F., 2005, Alteration of wall rocks by CO_2-rich water ascending in fault zones: Natural analogues for reactions induced by CO_2 migrating along faults in siliciclastic reservoir and cap rocks. *Oil & Gas Science and Technology-Revue de l'Institut Francais du Petrole*, 60, pp. 19-32.

Maystrenko, Y., Bayer, U. and Scheck-Wenderoth, M., 2006, 3-D reconstruction of salt movements within the deepest post-Permian structure of the Central European Basin System - the Glückstadt Graben. *Netherlands Journal of Geosciences - Geologie en Mijnbouw*, 85, pp. 181-196.

McAulay, G.E., Burley, S.D. and Johnes, L.H., 1993, Silicate mineral authigenesis in the Hutton and NW Hutton fields: implications for sub-surface porosity development. In *Petroleum Geology of Northwest Europe*, J.R. Parker (Ed.), pp. 1377-1393 (The Geological Society London).

McBride, E.F., 1963, A classification of common sandstones. *Journal of Sedimentary Petrology*, 33, pp. 664-669.

McBride, E.F., 1989, Quartz cement in sandstones. *Journal of Sedimentary Petrology*, 26, pp. 69-112.

McCollom, T.M. and Seewald, J.S., 2003, Experimental study of the hydrothermal reactivity of organic acids and acid anions: II. Acetic acid, acetate, and valeric acid. *Geochimica Et Cosmochimica Acta*, 67, pp. 3645-3664.

McKinley, J.M., Worden, R.H. and Ruffell, A.H., 2003, Smectite in sandstones: a review of the controls on occurence and behaviour during diagenesis. In *Clay Mineral Cements in Sandstones*, R.H. Worden and S. Morad (Eds.), pp. 109-128 (Special Publication of the International Association of Sedimentologists).

McNeil, M.B. and Mohr, D.W., 1993, Formation of copper-iron sulfide minerals during corrosion of artifacts and possible implications for pseudogilding. *Geoarchaeology*, 8, pp. 23-33.

McNeil, M.B. and Little, B.J., 1999, The use of mineralogical data in interpretation of long-term mircobiological corrosion processes: sulfiding reactions. *Journal of the American Institute for Conservation*, 38, pp. 186-199.

McPherson, B.J.O.L. and Cole, B.S., 2000, Multiphase CO_2 flow, transport and sequestration in the Powder River basin, Wyoming. *Journal of Geochemical Exploration*, 96-70, pp. 65-70.

Menning, M., 1995, A numerical time scale for the Permian and Triassic periods: an integrated time analys. In *The Permian of northern Pangea*, P.A. Scholle, T. Peryt and D.S. Ulmer-Scholle (Eds.), pp. 77-97 (Berlin: Springer Verlag).

Metcalfe, R., Rochelle, C., Savage, D. and Higgo, J.W., 1994, Fluid-rock interactions during continental redbed diagenesis: implications for theoretical models of mineralization in sedimentary basins. In *Origin, Migration and Evolution of Fluids in Sedimentary Basins*, J. Parnell (Ed.), pp. 301-324 (Geological Society, Special Publications).

Meunier, A., Velde, B. and Zalba, P., 2004, Illite K-Ar dating and crystal growth processes in diagenetic environments: a critical review. *Terra Nova*, 16, pp. 296-304.

Milliken, K.L., Mack, L.E. and Land, L.S., 1994, Elemental Mobility in Sandstones during Burial - Whole-Rock Chemical and Isotopic Data, Frio Formation, South Texas. *Journal of Sedimentary Research Section a-Sedimentary Petrology and Processes*, 64, pp. 788-796.

Mohr, M., Kukla, P.A., Urai, J.L. and Bresser, G., 2005, Multiphase salt tectonic evolution in NW Germany: seismic interpretation and retro-deformation. *International Journal of Earth Sciences / Geologische Rundschau*, 94, pp. 917-940.

Molenaar, N., 1986, The Interrelation between Clay Infiltration, Quartz Cementation, and Compaction in Lower Givetian Terrestrial Sandstones, Northern Ardennes, Belgium. *Journal of Sedimentary Petrology*, 56, pp. 359-369.

Möller, J.J. and Rasmussen, E.S., 2003, Middle Jurassic – Early Cretaceous rifting of the Danish Central Graben. In *The Jurassic of Denmark and Greenland*, J.R. Ineson and F. Surlyk (Eds.), pp. 247-264 (Geological Survey of Denmark and Greenland Bulletin).

Morad, S., 1986, Albitization of K-Feldspar Grains in Proterozoic Arkoses and Greywackes from Southern Sweden. *Neues Jahrbuch Fur Mineralogie-Monatshefte*, pp. 145-156.

Morad, S., Bergan, M., Knarud, R. and Nystuen, J.P., 1990, Albitization of Detrital Plagioclase in Triassic Reservoir Sandstones from the Snorre Field, Norwegian North-Sea. *Journal of Sedimentary Petrology*, 60, pp. 411-425.

Morad, S., Ketzer, J.M. and De Ros, L.F., 2000, Spatial and temporal distribution of diagenetic alterations in siliciclastic rocks: implications for mass transfer in sedimentary basins. *Sedimentology*, 47, pp. 95-120.

Mortimer, C.E., 2001, *Das Basiswissen der Chemie* (Stuttgart, New York: Georg Thieme).

Moulton, G.F., 1922, Some features of redbed bleaching. *American Association of Petroleum Geologists Bulletin*, 10, pp. 304-311.

Muchez, P., Viaene, W. and Dusar, M., 1992, Diagenetic Control on Secondary Porosity in Flood-Plain Deposits - an Example of the Lower Triassic of Northeastern Belgium. *Sedimentary Geology*, 78, pp. 285-298.

Nabawy, B.S., Geraud, Y., Rochette, P. and Bur, N., 2009, Pore-throat characterization in highly porous and permeable sandstones. *American Association of Petroleum Geologists Bulletin*, 93, pp. 719-739.

Nairn, A.E.M. and Smithwick, M.E., 1976, Permian paleogeography and climatology. In *The Continental Permian in Central, West, and South Europe*, H. Falke (Ed.), pp. 283-312 (Dordrecht (Reidel).

Nicholls, C.A., Bedrock, M., Delbos, E.M. and Gelderloos, J., 1987, *Internal Report NAM*, No. ELN-01.046.

Nielsen, S.B., 2002, A post mid-Cretaceous North Sea model. *Bulletin of the Geological Society of Denmark*, 49, pp. 187-204.

NITG, 1998, Atlas of the subsurface of the Netherlands, Explanation to Map Sheet Almelo–Winterswijk (1:250.000). p. 134 (Harlem: Netherlands Institute for Applied Geoscience TNO - National Geological Survey).

Nordbotten, J.M., Celia, M.A. and Bachu, S., 2005, Injection and Storage of CO_2 in Deep Saline Aquifers: Analytical Solution for CO_2 Plume Evolution During Injection *Transport in Porous Media*, 58, pp. 339-360.

Oakman, C.D. and Partington, M.A., 1998, Cretaceous. In *Petroleum geology of the North Sea, basic concepts and recent advances*, K.W. Glennie (Ed.), pp. 294-349 (London: Blackwell Science Limited).

Obdam, A., van der Meer, L.G.H., May, F., Kervevan, C., Bech, N. and Wildenborg, A., 2003, Effective CO_2 storage capacity in aquifers, gas fields, oil fields and coal fields. Proceedings of the 6th International Conference on Greenhouse Gas Control Technologies (GHGT-6). J. Gale and Y. Kaya (Eds.) (Kyoto, Japan), pp. 339-344.

Oelkers, E.H., 2001, A general kinetic description of multi-oxide silicate mineral and glass dissolution. *Geochimica Et Cosmochimica Acta*, 65, pp. 3703-3719.

Oldenburg, C.M., Pruess, K. and Benson, S.M., 2001, Process Modeling of CO_2 Injection into Natural Gas Reservoirs for Carbon Sequestration and Enhanced Gas Recovery. *Energy & Fuels*, 15, pp. 293-298.

Olgaard, D.L. and Fitz Gerald, J.D., 1986, Interface healing in synthetic marbles: a SEM/TEM study. *Transactions of the American Geophysical Union*, 69, p. 1446.

Oosthuyzen, E.J., 1980, An elementary introduction to image analysis - a new field of interest at the international institute for metallurgy. (Randberg, South Africa).

Orr, L., 2005, Predicting Flow Behavior for Geologic Storage of CO2. Presentation at the Global Climate and Energy Project (GCEP) International Workshop Tsinghua University, Beijing, August 23, 2005. 22pp.

Osmanlioglu, A.E., 2002, Immobilization of radioactive waste by cementation with purified kaolin clay. *Waste Management*, 22, pp. 481-483.

Pagel, M., 1975, Determination of Physicochemical Conditions of Diagenetic Silicification of Athabasca Sandstones (Canada) by Fluid Inclusions. *Comptes Rendus Hebdomadaires Des Seances De l' Academie des Sciences Serie D*, 280, pp. 2301-2304.

Palandri, J.L. and Kharaka, Y.K., 2004, A compilation of rate parameters of warer-mineral interaction kinetics for application to geochemical modeling. In *open file report 2004-1068*, U.S.G. Survey (Ed.), p. 70 (Menlo Park, California, USA).

Palandri, J.L. and Kharaka, Y.K., 2005, Ferric iron-bearing sediments as a mineral trap for CO_2 sequestration: Iron reduction using sulfur-bearing waste gas. *Chemical Geology*, 217, pp. 351-364.

Parkhurst, D.L. and Appelo, C.A.J., 1999, User's Guide to PHREEQC (VERSION 2) - a computer program for speciation, batch-reaction, one-dimensional transport, and inverse geochemical calculations. *Water-Resources Investigations Report 99-4259*, p. 326.

Parks, G.A., 1984, Surface and interfacial free energies of quartz. *Journal of Geophysical Research*, 89, pp. 3997-4008.

Parnell, J., Carey, P.F. and Bottrell, S.H., 1994, The occurrence of authigenic minerals in solid bitumens *Journal of Sedimentary Research*, 64, pp. 95-100.

Parry, W.T., Chan, M.A. and Beitler, B., 2004, Chemical bleaching indicates episodes of fluid flow in deformation bands in sandstone. *American Association of Petroleum Geology Bulletin*, 88, pp. 175-191.

Paterson, L., 1996, *Internal Report NAM*. (no number).

Pauwels, H., Gaus, I., Lenindre, Y., Pearce, J. and Czernichowskilauriol, I., 2007, Chemistry of fluids from a natural analogue for a geological CO_2 storage site (Montmiral, France): Lessons for CO_2–water–rock interaction assessment and monitoring. *Applied Geochemistry*, 22, pp. 2817-2833.

Peng, D.Y. and Robinson, D.B., 1976, A new two-constant equation of state. *Ind. Eng. Chem. Fundam.*, 15, pp. 59-64.

Perry, E. and Hower, J., 1970, Burial Diagenesis in Gulf Coast Pelitic Sediments. *Clays and Clay Minerals*, 18, pp. 165-177.

Peters, C.A., 2009, Accessibilities of reactive minerals in consolidated sedimentary rock: An imaging study of three sandstones. *Chemical Geology*, 265, pp. 198-208.

Petschick, R., 2002, Röntgendiffraktometrie in der Sedimentologie. *Schriftenr. dt. geol. Ges.*, 18, pp. 99-118.

Pettijohn, F.J., Potter, P.E. and Siever, R., 1987, *Sand and Sandstone* (Berlin, Heidelberg, New York).

Pham, V.T.H., Lu, P., Aagaard, P., Zhu, C. and Hellevang, H., 2011, On the potential of CO_2-water-rock interactions for CO_2 storage using a modified kinetic model. *International Journal of Greenhouse Gas Control*, 5, pp. 1002-1015.

Pharaoh, T.C., 1999, Palaeozoic terranes and their lithospheric boundaries within the Trans-European Suture Zone (TESZ): a review. *Tectonophysics*, 314, pp. 17-41.

Pharaoh, T., England, R. and Lee, M., 1995, The Concealed Caledonide Basement of Eastern England and the Southern North-Sea - a Review. *Studia Geophysica Et Geodaetica*, 39, pp. 330-346.

Pilotti, M., 2000, Reconstruction of clastic porous media. *Transport in Porous Media*, 41, pp. 359-364.

Pitzer, K.S., 1979, Theory - Ion interaction approach. In *Activity Coefficients in Electrolyte Solutions*, R.M. Pytkowicz (Ed.), pp. 157-208 (Florida: CRC Press).

Platt, J., 1991, The diagenesis of Early Permian Rotliegend deposits from northwest Germany. Dissertation, University of Bern.

Platt, J.D., 1993, Controls on Clay Mineral Distribution and Chemistry in the Early Permian Rotliegend of Germany. *Clay Minerals*, 28, pp. 393-416.

Platt, J.D., 1994, Geochemical Evolution of Pore Waters in the Rotliegend (Early Permian) of Northern Germany. *Marine and Petroleum Geology*, 11, pp. 66-78.

Plein, E., 1978, Rotliegend-Ablagerungen im Norddeutschen Becken. *Zeitschrift der Deutschen Geologischen Gesellschaft*, 129, pp. 71-97.

Plein, E., 1990, The Southern Permian basin and its paleogeography. In *Sediments and Environmental Geochemistry*, D. Heling, P. Rothe, U. Förstner and P. Stoffers (Eds.).

Plein, E., 1993, Bemerkungen zum Ablauf der paläogeographischen Entwicklung im Stefan und Rotliegend des Norddeutschen Beckens. *Geologisches Jahrbuch*, A131, pp. 99-116.

Plein, E., 1995, *Norddeutsches Rotliegendbecken; Rotliegend-Monographie Teil II. Stratigraphie von Deutschland I.* (Senckenberg 183 (Frankfurt): Courier Forschungsinstitut).

Plummer, L.N., Parkhurst, D.L., Fleming, G.W. and Dunkle, S.A., 1988, A computer program incorporating Pitzer's equations for calculation of geochemical reactions in brines. *U.S. Geological SurveyWater-Resources Investigations*, 88, p. 310.

Pokrovsky, O.S., Golubev, S.V., Schott, J. and Castillo, A., 2009, Calcite, dolomite and magnesite dissolution kinetics in aqueous solutions at acid to circumneutral pH, 25 to 150 degrees C and 1 to 55 atm pCO_2: New constraints on CO_2 sequestration in sedimentary basins. *Chemical Geology*, 265, pp. 20-32.

Porter, G.A. and James, W.C., 1986, Influence of pressure, salinity, temperature and grain size on silica diagenesis in quartzose sandstones. *Chemical Geology*, 57, pp. 359-369.

Pouchou, J.-L. and Pichoir, F., 1991, Quantitative analysis of homogeneous or stratified microvolumes applying the model "PAP". In *Electron Probe Quantification*, K.F. Heinrich and D.E. Newbury (Eds.), pp. 31-75.

Praagman, N. and Snijder, J.H., 1988, *Internal Report NAM*, No. 15.112.

Pröpper, 1987, *Internal Report NAM,* No. 14.401.

Pruess, K., 2006, On leakage from geologic storage reservoirs of CO_2. In *International Symposium on site characterisation for CO_2 geological storage (CO2SC 2006)* (Berkeley, California), p. 23.

Pryor, W.A., 1973, Permeability-Porosity Patterns and Variations in Some Holocene Sand Bodies. *American Association of Petroleum Geologists Bulletin*, 57, pp. 162-189.

Putnis, A., Prieto, M. and Fernandezdiaz, L., 1995, Fluid Supersaturation and Crystallization in Porous-Media. *Geological Magazine*, 132, pp. 1-13.

Putnis, A. and Mauthe, G., 2001, The effect of pore size on cementation in porous rocks. *Geofluids*, 1, pp. 37-41.

Pye, K. and Krinsley, D.H., 1986, Diagenetic Carbonate and Evaporite Minerals in Rotliegend Aeolian Sandstones of the Southern North-Sea - Their Nature and Relationship to Secondary Porosity Development. *Clay Minerals*, 21, pp. 443-457.

Raistrick, M., Hutcheon, I., Shevalier, M., Nightinagle, M., Johnson, G., Taylor, S., Mayer, B., Durocher, K., Perkins, E. and Gunter, B., 2009, Carbon dioxide-water-silicate mineral reactions enhance CO_2 storage; evidence from produced fluid measurements and geochemical modeling at the IEA Weyburn-Midale Project. *Energy Procedia*, 1, pp. 3149-3155.

Reed, A.H., 1996, Quantification of marine sediment properties from planar and volumetric pore geometries. Louisiana State University and Agricultural and Mechanical College.

Reijers, T.J.A., H.F., M., Pestman, P.J. and Kouwe, W.F.P., 1993, *Lithofacies and their interpretation: a guide to standardised description of sedimentary deposits* (Haarlem: Mededelingen Rijks Geologische Dienst).

Renard, F. and Ortoleva, P., 1997, Water films at grain-grain contacts: Debye-Hückel, osmotic model of stress, salinity, and minerlogy dependence. *Geochimica Et Cosmochimica Acta*, 61, pp. 1963-1970.

RGD, 1991, *Geological Atlas of the subsurface of The Netherlands, Explanation to map sheet II Ameland-Leeuwarden (1:250,000)* (Harlem: Rijks Geologische Dienst).

Rieke, H., 2001, Sedimentologie, Faziesarchitektur und Faziesentwicklung des kontinentalen Rotliegenden im Norddeutschen Becken (NEDB). Potsdam.

Rieken, R., 1988, Lösungs-Zusammensetzung und Migrationsprozesse von Paläo-Fluidsystemen in Sedimentgesteinen des Norddeutschen Beckens. Dissertation, University of Göttingen.

Roberts, J.N. and Schwartz, L.M., 1985, Grain Consolidation and Electrical-Conductivity in Porous-Media. *Physical Review B*, 31, pp. 5990-5997.

Rochelle, C., Bateman, K. and Pierce, J.M., 2002, Geochemical interactions between supercritical CO_2 and the Utsira Formation: an experimental study. *British Geological Survey Report CR/02/060*.

Rochelle, C., Czernichowski-Lauriol, I. and Milodowski, A.E., 2004, The impact of chemical reactions on CO_2 storage in geological formations: a brief overview. In *Geological Storage of Carbon Dioxide*, S.J. Baines and R.H. Worden (Eds.), pp. 87-106 (London: Geological Society Special Publications).

Root, R.S., Gibson-Poole, C.M., Lang, S.C., Streit, J.E. and Underschultz, J., 2004, Opportunities for geological storage of carbon dioxide in the offshore Gippsland Basin, SE Australia: an example from the Upper Latrobe Group. In *Eastern Australasian Basin Symposium II*, P.J. Boult and D.R. Lang (Eds.) (Adelaide, South Australia: Petrol. Exploration Soc. of Australia, Special Publication).

Rutter, E.H., 1976, The kinetics of rock deformation by pressure solution. *Philosophical Transactions of the Royal Society of London*, 283, pp. 203-209.

Saigal, G.C. and Bjørlykke, K., 1987, Carbonate cements in clastic reservoir rocks from offshore Norway - relationship between isotopic composition, textural development and burial depth. In *Diagenesis of sedimentary sequences*, J.D. Marshall (Ed.), pp. 313-324 (London: Geological Society of London Special Publication).

Saigal, G.C., Morad, S., Bjørlykke, K., Egeberg, P.K. and Aagaard, P., 1988, Diagenetic Albitization of Detrital K-Feldspar in Jurassic, Lower Cretaceous, and Tertiary Clastic Reservoir Rocks from Offshore Norway .1. Textures and Origin. *Journal of Sedimentary Petrology*, 58, pp. 1003-1013.

Saldi, G.D., Jordan, G., Schott, J. and Oelkers, E.H., 2009, Magnesite growth rates as a function of temperature and saturation state. *Geochimica Et Cosmochimica Acta*, 73, pp. 5646-5657.

Saltelli, A., Ratto, M., Andres, T., Campolongo, F., Cariboni, J., Gatelli, D., Saisana, M. and Tarantola, S., 2008, *Global Sensitivity Analysis* (John Wiley and Sons).

Salvi, S., Quattrocchi, F., Angelone, M., Brunori, C.A., Billi, A., Buongiorno, F., Doumaz, F., Funiciello, R., Guerra, M., Lombardi, S., Mele, G., Pizzino, F. and Salvini, F., 2000, A multidisciplinary approach to earthquake research: implementation of a Geochemical Geographic Information System for the Gargano site, Southern Italy. *Natural Hazard*, 20, pp. 255-278.

Sanjuan, B., Girard, J.-P., Lanini, S., Bourguignon, A. and Brosse, E., 2003, Geochemical modelling of diagenetic illite and quartz cement formation in Bent sandstone reservoirs: example of the Hild Field, Norwegian North Sea. In *Clay Mineral Cements in Sandstones*, R.H. Worden and S. Morad (Eds.), pp. 425-452 (Special Publication of the International Association of Sedimentologists).

Scheck, M. and Bayer, U., 1999, Rolle des Zechstein -Salzes für die mesozoische Entwicklung des Nordostdeutschen Beckens. *Terra Nova*, 3, pp. 38-40.

Scheck, M., Bayer, U. and Lewerenz, B., 2003, Salt movements in the Northeast German Basin and its relation to major post-Permian tectonic phases - results from 3D structural modelling, backstripping and reflection seismic data. *Tectonophysics*, 361, pp. 277-299.

Scheck-Wenderoth, M. and Lamarche, J., 2005, Crustal memory and basin evolution in the Central European Basin System - new insights from a 3D structural model. *Tectonophysics*, 397, pp. 143-165.

Schenk, H.-J., di Primio, R. and Horsfield, B., 1997, The conversion of oil into gas in petroleum reservoirs. Part 1: Comparative kinetic investigation of gas generation from crude oils of lacustrine, marine and fluviodeltaic origin by programmed-temperature closed-system pyrolysis. *Organic Geochemistry*, 26, pp. 467-481.

Schikorr, G., 1933, Über Eisen(III).hydroxyd und ferromeagnetisches eisen(III)-hydroxyd. *Zeitschrift für Anorganische und Allgemeine Chemie*, 212, pp. 33-39.

Schneider, J.W. and Gebhardt, U., 1993, Litho- und Biofaziesmuster in intra- und extramontanen Senken des Rotliegend (Perm, Nord- und Ostdeutschland). *Geologisches Jahrbuch*, A 131, pp. 57-98.

Schöner, R., 2006, Comparison of Rotliegend sandstone diagenesis from the northern and southern margin of the Nort German Basin, and implication for the importance of organic maturation and migration. Dissertation, University Jena.

Schöner, R. and Gaupp, R., 2005, Contrasting red bed diagenesis: the southern and northern margin of the Central European Basin. *International Journal of Earth Sciences*, 94, pp. 897-916.

Schrijver, K., Williams-Jones, A.E., Bertrand, R. and Chagnon, A., 1996, Genesis and controls of hydrothermal dolomitization in sandstones of the Appalachian thrust belt, Québec, Canada: Implications for associated galena-barite mineralization. *Chemical Geology*, 129, pp. 257-279.

Schumacher, D., 1996, Hydrocarbon-Induced Alteration of Soils and Sediments. *American Association of Petroleum Geologists Memoir*, 66, pp. 71-89.

Schwartz, L.M. and Banavar, J.R., 1989, Transport properties of disordered continuum systems. *Physical Review B*, 39, pp. 11965-11970.

Sclater, J.G. and Christie, P.A., 1980, Continental streching: an explanation of the post-mid-Cretaceous subsidence of the central North Sea basin. *Journal of Geophysical Research*, 85, pp. 3711-3739.

Scotese, C.R. and McKerrow, W.S., 1990, Revised world map and introduction. In *Paleozoic Paleogeography and Biogeography*, W.S. McKerrow and C.R. Scotese (Eds.), pp. 1-21 (Geological Society of London Memoirs).

Scott, G.D., 1960, Packing of Equal Spheres. *Nature*, 188, pp. 908-909.

Scott, G.D. and Kilgour, D.M., 1969, Density of Random Close Packing of Spheres. *Journal of Physics D-Applied Physics*, 2, pp. 863-866.

Seewald, J.S., 2001, Aqueous geochemistry of low molecular weight hydrocarbons at elevated temperatures and pressures: Constraints from mineral buffered laboratory experiments. *Geochimica Et Cosmochimica Acta*, 65, pp. 1641-1664.

Seewald, J.S., 2003, Organic-inorganic interactions in petroleum-producing sedimentary basins. *Nature*, 426, pp. 327-333.

Segal, D.B., Ruth, M.D., Merin, I.S., Watanabe, H., Soda, K., Takano, O. and Sano, M., 1985, Remote Detection of Anomalous Mineralogy Associated with Hydrocarbon Production, Lisbon Valley, Utah. *American Association of Petroleum Geologists Bulletin*, 69, pp. 305-306.

Shebl, M.A. and Surdam, R.C., 1996, Redox reactions in hydrocarbon elastic reservoirs: Experimental validation of this mechanism for porosity enhancement. *Chemical Geology*, 132, pp. 103-117.

Shomali, Z.H., Roberts, R.G., Pedersen, L.B. and Grp, T.W., 2006, Lithospheric structure of the Tornquist Zone resolved by nonlinear P and S teleseismic tomography along the TOR array. *Tectonophysics*, 416, pp. 133-149.

Singh, B. and Mackinnon, I.D.R., 1996, Experimental transformation of kaolinite to halloysite. *Clays and Clay Minerals*, 44, pp. 825-834.

Sissingh, W., 2004, Paleozoic and Mesozoic igneous activity in the Netherlands: a tectonomagmatic review. *Netherlands Journal of Geosciences/Geologie en Mijnbouw*, 83, pp. 113-135.

Smith, L.B., Eberli, G.P., Masaferro, J.J. and Al-Dhahab, S., 2003, Discrimination of effective from ineffective porosity in heterogeneous Cretaceous carbonates, Al Ghubar field, Oman. *American Association of Petroleum Geologists Bulletin*, 87, pp. 1509-1529.

Soong, Y., Goodman, A.L., McCarthy-Jones, J.R. and Baltrus, J.P., 2004, Experimental and simulation studies on mineral trapping of CO_2 with brine. *Energy Conversion and Management*, 45, pp. 1845-1859.

Spiers, C.J. and Brzesowsky, R.H., 1993, Densification behaviour of wet granular salt: Theory versus experiment. (Seven Symposium of Salt), pp. 83-91.

Stäuble, A.J. and Milius, G., 1970, Geology of Groningen gas field, Netherland. In *Geology of giant petroleum fields*, M.T. Halbouty (Ed.), pp. 359-369 (Tulsa: American Association of Petroleum Geologists Memoir).

Stemmerik, I., Ineson, J.R. and Mitchell, J.G., 2000, Stratigraphy of the Rotliegend Group in the Danish part of the Northern Permian Basin, North Sea. *Journal of the Geological Society*, 157, pp. 1127-1136.

Strong, G.E. and Milodowski, A.E., 1987, Aspects of the diagenesis of the Sherwood Sandstone of the Wessex Basin and their influence on reservoir characteristics. In *Diagenesis of sedimentary sequences*, J. Marshall (Ed.), pp. 325-337 (London: Geological Society Special Publication).

Sullivan, M.D., Haszeldine, R.S., Boyce, A.J., Rogers, G. and Fallick, A.E., 1994, Late anhydrite cements mark basin inversion: isotopic and formation water evidence, Rotliegend Sandstone, North Sea. *Marine and Petroleum Geology*, 11, pp. 46-54.

Surdam, R.C., Boese, S.W. and Crossey, R.C., 1984, The geochemistry of secondary porosity. In *Clastic diagenesis*, D.A. McDonald and R.C. Surdam (Eds.), pp. 127-149 (Tulsa: AAPG memoirs).

Surdam, R.C. and Crossey, L.J., 1985, Mechanisms of organic/inorganic interactions in sandstone/shale sequences. *SEPM short course*, 17, pp. 177-272.

Surdam, R.C., Crossey, L.J., Hagen, E.S. and Heasler, H.P., 1989, Organic-Inorganic Interactions and Sandstone Diagenesis. *Aapg Bulletin-American Association of Petroleum Geologists*, 73, pp. 1-23.

Surdam, R.C., Jiao, Z.S. and Macgowan, D.B., 1993, Redox Reactions Involving Hydrocarbons and Mineral Oxidants - a Mechanism for Significant Porosity Enhancement in Sandstones. *American Association of Petroleum Geologists Bulletin*, 77, pp. 1509-1518.

Symonds, R.B., Gerlach, T.M. and Reed, M.H., 2001, Magmatic gas scrubbing: implications for volcano monitoring. *Journal of Volcanology and Geothermal Research*, 108, pp. 303-341.

Takeno, N., 2005, *Atlas of Eh-pH diagrams - Intercomparison of thermodynamic databases* (Geological Survey of Japan Open File Report No.419).

Tanner, B. and Meissner, R., 1996, Caledonian deformation upon southwest Baltica and its tectonic implications: Alternatives and consequences. *Tectonics*, 15, pp. 803-812.

Tans, P.P. and Keeling, R., 2011, www.esrl.noaa.gov/gmd/ccgg/trends/. Available online.

Tarasevich, Y.I. and Klimova, G.M., 2001, Complex-forming adsorbents based on kaolinite, aluminium oxide and polyphosphates for the extraction and concentration of heavy metal ions from water solutions. *Applied Clay Science*, 19, pp. 95-101.

Tesmer, M., Möller, P., Wieland, S., Jahnke, C., Voigt, H. and Pekdeger, A., 2007, Deep reaching fluid flow in the North-East German Basin. Origin and processes of groundwater salinization. *Journal of Hydrogeology*, 15, pp. 1291-1306.

Thompson, A.H., Katz, A.J. and Krohn, C.E., 1987, The microgeometry and transport properties of sedimentary rock. *Advances in Physics*, 36, pp. 625-694.

Thyne, G., 2001, A model for diagenetic mass transfer between adjacent sandstone and shale. *Marine and Petroleum Geology*, 18, pp. 743-755.

Tröger, W.E., 1967, *Optische Bestimmung der gesteinsbildenden Minerale - Teil 2* (Stuttgart: Schweizbart'sche Verlagsbuchhandlung).

Truesdell, A.H. and Jones, B.F., 1974, WATEQ, a computer program for calculating chemical equilibria of natural waters. *U.S. Geological Survey*, 2, pp. 233-274.

Trusheim, 1957, Über Halokinese und ihre Bedeutung für die strukturelle Entwicklung Norddeutschlands. *Zeitschrift der Deutschen Geologischen Gesellschaft*, 109, pp. 111-157.

Tucker, M.E., 1991, *Sedimentary Petrology. An Introduction to the Origin of Sedimentary Rocks* (Oxford, London, Edinburgh, Boston, Melbourne, Paris, Berlin, Vienna: Blackwell Scientific).

UCE, 2006, Utrecht Centre for Energy research (UCE) - CO2NET Lectures on Carbon Capture and Storage.

Uri, L., Dysthe, D.K. and Feder, J., 2004, Complex behaviour and structure of ductile granular material. *Geophysical Research Abstracts*, 6.

Vai, G.B., 2003, Development of the palaeogeography of Pangaea from Late Carboniferous to Early Permian. *Palaeogeography Palaeoclimatology Palaeoecology*, 196, pp. 125-155.

van Buggenum, J.M. and den Hartog Jager, D.G., 2007, Silesian. In *Geology of the Netherlands*, T.E. Wong, D.A.J. Batjes and J. de Jager (Eds.) (Royal Netherlands Academy of Arts and Sciences).

van der Marel, H.W. and Beutelspacher, H., 1976, *Atlas of infrared spectroscopy of clay minerals and their admixtures* (Amsterdam, The Netherlands: Elsevire).

van Houten, F.B., 1968, Iron Oxides in Red Beds. *Geological Society of America Bulletin*, 79, pp. 399-416.

van Keer, I., Muchez, P. and Viaene, W., 1998, Clay mineralogical variations and evolutions in sandstone sequences near a coal seam and shales in the Westphalian of the Campine Basin (NE Belgium). *Clay Minerals*, 33, pp. 159-169.

van Sande, J.M.M., Eggenkamp, I.M.M., Meij, R.E. and Sutherland, J.M., 2001, *Internal Report NAM*; No. ELN-01.046.

van Wees, J.-D., Stephenson, R.A., Ziegler, P.A., Bayer, U., McCann, T., Dadlez, R., Gaupp, R., Narkiewicz, M., Bitzer, F. and Scheck, M., 2000, On the origin of the Southern Permian Basin, Central Europe. *Marine and Petroleum Geology*, 17, pp. 43-59.

van Wijhe, D.H., 1987, Structural evolution of inverted basins in the Dutch offshore. *Tectonophysics*, 137, pp. 171-219.

van Wijhe, D.H. and Bless, M.J.M., 1974, The Westphalian of the Netherlands with special reference to miospore assemblages. *Geologie en Mijnbouw*, 53, pp. 295-328.

van Wijhe, D.H., Lutz, M. and Kaasschieter, J.P.H., 1980, The Rotliegend in The Netherlands and its gas accumulations. *Geologie en Mijnbouw*, 59, pp. 3-24.

Veenhof, E.N., 1996, Geological aspects of the Annerveen gas field, the Netherlands. In *Geology of gas and oil under the Netherlands*, Rondeel. et al. (Ed.), pp. 79-92.

Visscher, W.M. and Bolsterl, M., 1972, Random Packing of Equal and Unequal Spheres in 2 and 3 Dimensions. *Nature*, 239, pp. 504-507.

Walderhaug, O., 1990, A Fluid Inclusion Study of Quartz-Cemented Sandstones from Offshore Mid-Norway - Possible Evidence for Continued Quartz Cementation during Oil Emplacement. *Journal of Sedimentary Petrology*, 60, pp. 203-210.

Walker, T.R., 1967, Formation of Red Beds in Modern and Ancient Deserts. *Geological Society of America Bulletin*, 78, pp. 353-368.

Walker, T.R., 1976, Diagenetic origin of continental red beds. In *The continental Permian in Central, West and South Europe*, H. Falke (Ed.), pp. 240-282 (Dordrecht: Reidel).

Walker, T.R., 1984, Diagenetic Albitization of Potassium-Feldspar in Arkosic Sandstones. *Journal of Sedimentary Petrology*, 54, pp. 3-16.

Walker, T.R., Waugh, B. and Grone, A.J., 1978, Diagenesis in 1st-Cycle Desert Alluvium of Cenozoic Age, Southwestern United-States and Northwestern Mexico. *Geological Society of America Bulletin*, 89, pp. 19-32.

Warren, E.A. and Smalley, P.C., 1994, *North Sea Formation Waters Atlas* (London: The Geological Society of London).

Watson, M.N., Zwingmann, N., Lemon, N.M. and Tingate, P.R., 2003, Onshore Otway basin carbon dioxide accumulations: CO_2-induced diagenesis in natural analogues for underground storage of greenhouse gas. *APPEA*, pp. 637-652.

Watson, M.N., Boreham, C.J. and Tingate, P.R., 2004, Carbon dioxide and carbonate cements in the Otway Basin: Implications for geological storage of carbon dioxide. *APPEA Journal*, 44, pp. 703-720.

Waugh, B., 1970, Formation of Quartz Overgrowths in Penrith Sandstone (Lower Permian) of Northwest England as Revealed by Scanning Electron Microscopy. *Sedimentology*, 14, pp. 309-320.

Weaver, C.E., 1958, The Effects and Geologic Significance of Potassium Fixation by Expandable Clay Minerals Derived from Muscovite, Biotite, Chlorite, and Volcanic Material. *American Mineralogist*, 43, pp. 839-861.

Weiss, A. and Russow, J., 1963, Über die Lage der austauchbaren Kationen bei Kaolinit. *Proceedings of the International Clay Conference*, 1, pp. 203-213.

Wilkinson, M. and Haszeldine, R.S., 1996, Aluminium loss during sandstone diagenesis. *Journal of the geological Society London*, 153, pp. 657-660.

Wilkinson, M. and Haszeldine, R.S., 2002, Fibrous illite in oilfield sandstones - a nucleation kinetic theory of growth. *Terra Nova*, 14, pp. 56-60.

Wilkinson, M., Haszeldine, R.S. and Milliken, K.L., 2003, Cross-formational flux of aluminium and potassium in Gulf Coast (USA) sediments. In *Clay Mineral Cements in Sandstones*, R.H. Worden and S. Morad (Eds.), pp. 147-160 (Special Publication of the International Association of Sedimentologists).

Williams, L.A., Parks, G.A. and Crerar, D.A., 1985, Silica Diagenesis .1. Solubility Controls. *Journal of Sedimentary Petrology*, 55, pp. 301-311.

Wilson, M.D., 1992, Inherited grain-rimming clays in sandstones from eolian and shelf environments: Their origin and control on reservoir properties. In *Origin, diagenesis and petrophysics of clay minerals in sandstones*, D.W. Houseknecht and E.D. Pittman (Eds.), pp. 209-225 (Tulsa: SEPM - Special Publication).

Wilson, M.D. and Pittman, E.D., 1977, Authigenic clay in sandstones: recognition and influence on reservoir prpoerties and paleaoenvironment analysis. *Journal of Sedimentary Petrolegy*, 47, pp. 3-31.

Wilson, M.D. and Stanton, P.T., 1994, Diagenetic mechanisms of porosity and permeability reduction and enhancement in Reservoir quality assesment and prediction in clastic rocks. *SEPM short course*, 30, pp. 59-117.

Worden, R.H., 2006, Dawsonite cement in the Triassic Lam Formation, Shabwa Basin, Yemen: A natural analogue for a potential mineral product of subsurface CO_2 storage for greenhouse gas reduction. *Marine and Petroleum Geology*, 23, pp. 61-77.

Worden, R.H. and Smalley, P.C., 1996, H2S-producing reactions in deep carbonate gas reservoirs: Khuff Formation, Abu Dhabi. *Chemical Geology*, 133, pp. 157-171.

Worden, R.H. and Barclay, S.A., 2000, Internally-sourced quartz cement due to externally-derived CO_2 in sub-arkosic sandstones, North Sea. *Journal of Geochemical Exploration*, 69-70, pp. 645-649.

Worden, R.H. and Morad, S., 2000, Quartz cementation in oil field sandstones: a review of the key controversies. In *Quartz cementation in sandstones*, R.H. Worden and S. Morad (Eds.), pp. 1-21 (International Association of Sedimentologists Special Publications).

Worden, R.H. and Morad, S., 2003, Clay minerals in sandstones: controls on formation, distribution and evolution. In *Clay Mineral Cements in Sandstones*, R.H. Worden and S. Morad (Eds.), pp. 3-42 (Special Publication of the International Association of Sedimentologists).

Wright, V.P., 1992, Paleosol recognition: A guide to early diagenesis in terrestrial setting. In *Diagenesis III: Developments in Sedimentology*, K.H. Wolf (Ed.), pp. 591-619.

Xu, T.F. and Pruess, K., 2001, Modeling multiphase non-isothermal fluid flow and reactive geochemical transport in variably saturated fractured rocks: 1. Methodology. *American Journal of Science*, 301, pp. 16-33.

Xu, T., Kharaka, Y.K., Doughty, C., Freifeld, B.M. and Daley, T.M., 2010, Reactive transport modeling to study changes in water chemistry induced by CO_2 injection at the Frio-I Brine Pilot. *Chemical Geology*, 271, pp. 153-164.

Yang, C.S. and Baumfalk, Y.A., 1994, Milankovitch cyclicity in the Upper Rotliegend Group of The Netherlands. *Special Publications International Association of Sediment*, 19, pp. 47-61.

Yegorova, T., Bayer, U., Thybo, H., Maystrenko, Y., Scheck-Wenderoth, M. and Lyngsie, S.B., 2007, Gravity signals from the lithosphere in the Central European Basin System. *Tectonophysics*, 429, pp. 133-163.

Zerai, B., Saylor, B.Z. and Matisoff, G., 2006, Computer simulation of CO_2 trapped through mineral precipitation in the Rose Run Sandstone, Ohio. *Applied Geochemistry*, 21, pp. 223-240.

Zhou, Z.H. and Gunter, W.D., 1992, The Nature of the Surface-Charge of Kaolinite. *Clays and Clay Minerals*, 40, pp. 365-368.

Ziegler, P.A., 1990, *Geological Atlas of Western and Central Europe* (Amsterdam: Shell Intern. Petrol. Maatschappij B.V.,).

Ziegler, K., 2006, Clay minerals of the Permian Rotliegend Group in the North Sea and adjacent areas. *Clay Minerals*, 41, pp. 355-393.

Ziegler, K., Sellwood, B.W. and Fallick, A.E., 1994, Radiogenic and Stable-Isotope Evidence for Age and Origin of Authigenic Illites in the Rotliegend, Southern North-Sea. *Clay Minerals*, 29, pp. 555-565.

Zwingmann, H., Clauer, N. and Gaupp, R., 1999, Structure-related geochemical (REE) and isotopic (K-Ar, Rb-Sr, delta O-18) characteristics of clay minerals from Rotliegend sandstone reservoirs (Permian, northern Germany). *Geochimica Et Cosmochimica Acta*, 63, pp. 2805-2823.

Appendix

Content of appendix

Appendix A

A1 Core images and sedimentological well descriptions
- 01 Core images well Aw02
- 02 Core images well Aw03 and Aw04
- 03 Core images well Aw05
- 04 Core images well Bw01
- 05 Core images well Bw02
- 06 Core images well Bw03
- 07 Core images well Cw02 and Cw03
- 08 Core images well Cw04
- 09 Sedimentological description of wells from field A
- 10 Sedimentological description of wells from field B
- 11 Sedimentological description of wells from field C

A2 Thin section images
- 01 Authigenic and detrital minerals
- 02 Authigenic and detrital minerals
- 03 Authigenic and detrital minerals
- 04 Authigenic and detrital minerals
- 05 Authigenic and detrital minerals

A3 Secondary electron images
- 01 Authigenic and detrital minerals
- 02 Authigenic and detrital minerals
- 03 Authigenic and detrital minerals
- 04 Authigenic and detrital minerals

A4 Cross sections of wells
- 01 Cross section of field A for porosity and gamma ray logs
- 02 Cross section of field B for porosity and gamma ray logs
- 03 Cross section of field C for porosity and gamma ray logs
- 04 Cross section of field A for porosity and water saturation
- 05 Cross section of field B for porosity and water saturation
- 06 Cross section of field C for porosity and water saturation

Appendix A1-01: Core images of well Aw02 with porosity [%] and horizontal permeability [mD] data. Samples which are taken for the study are marked as grey circles.

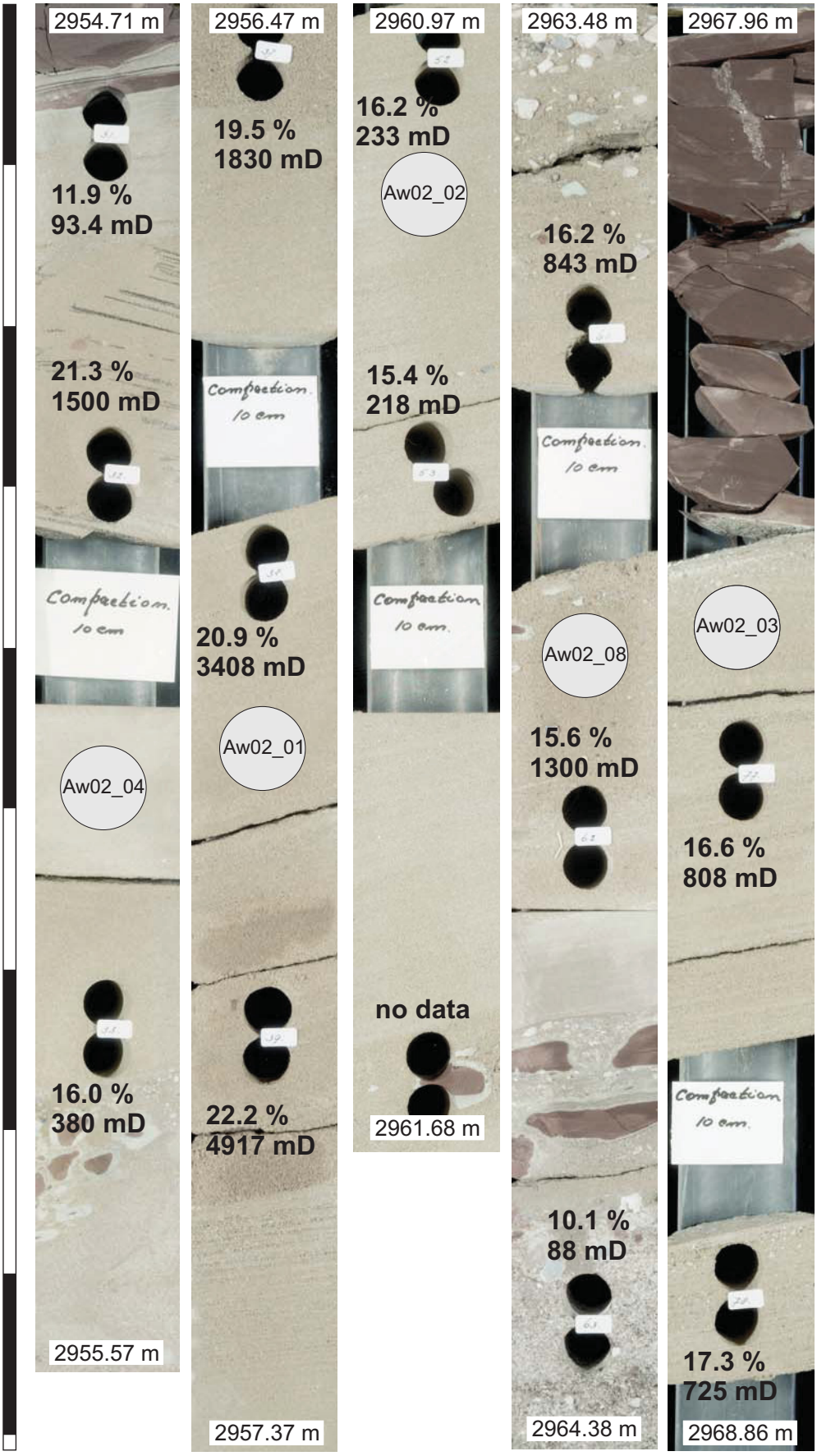

Appendix A1-01: Continuation

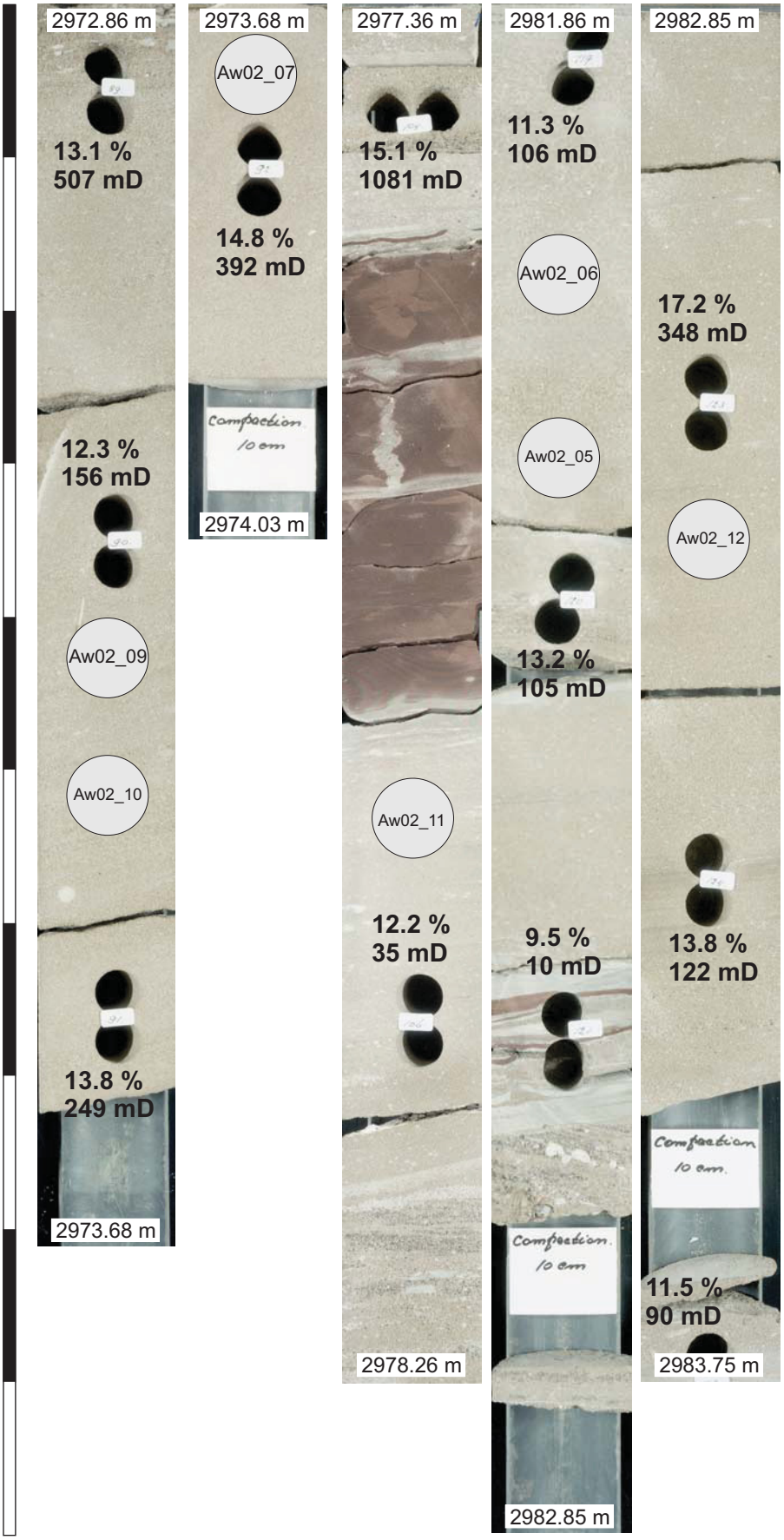

Appendix A1-02: Core images of wells Aw03 (left) and Aw04 (right) with porosity [%] and horizontal permeability [mD] data. Samples which are taken for the study are marked as grey circles.

Appendix A1-03: Core images of well Aw05 with porosity [%] and permeability [mD] data. Samples which are taken for the study are marked as grey circles.

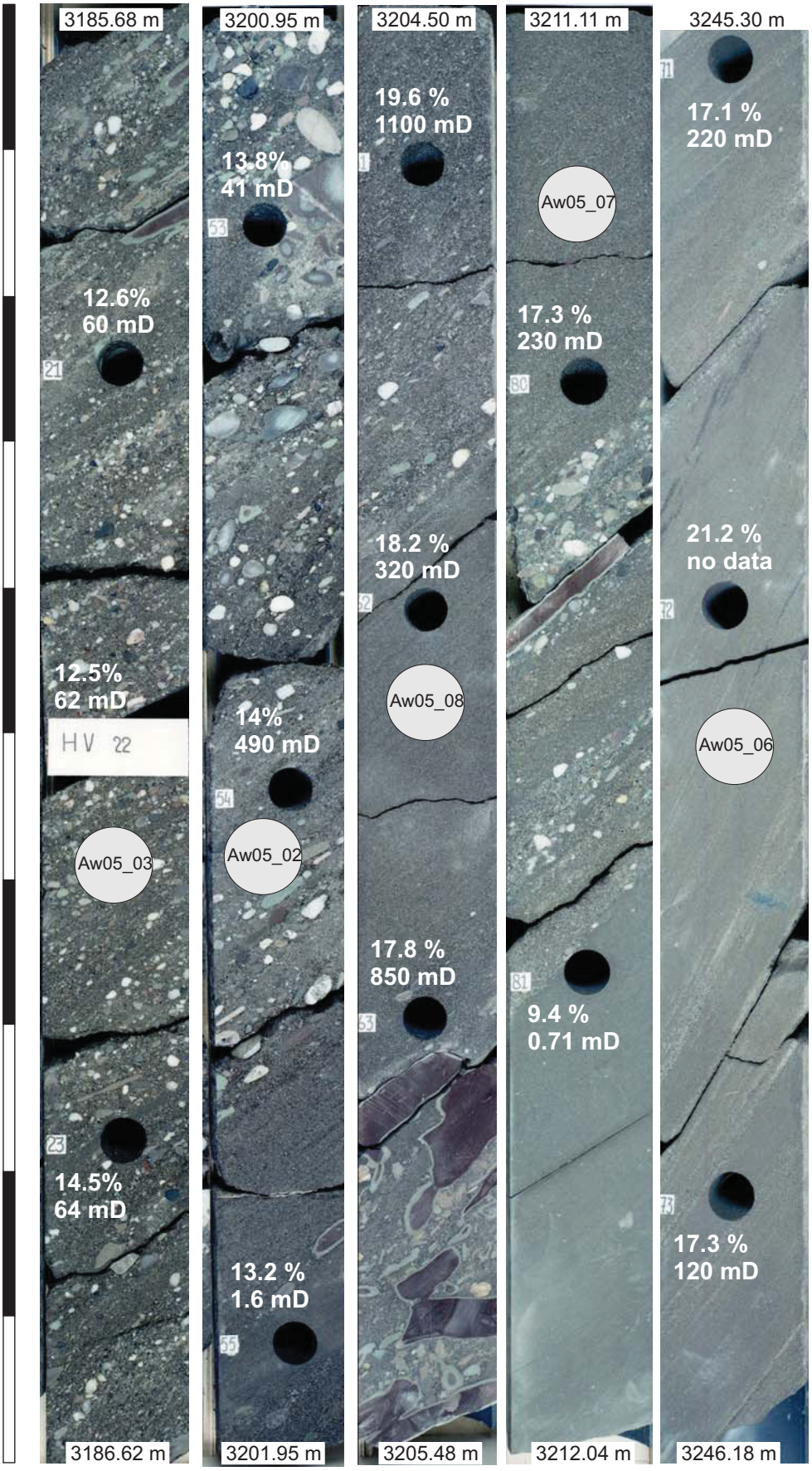

Appendix A1-03: Left: Continuation from well Aw05. Right: Core image from well Aw04. Samples which are taken for analysis are marked as grey circles.

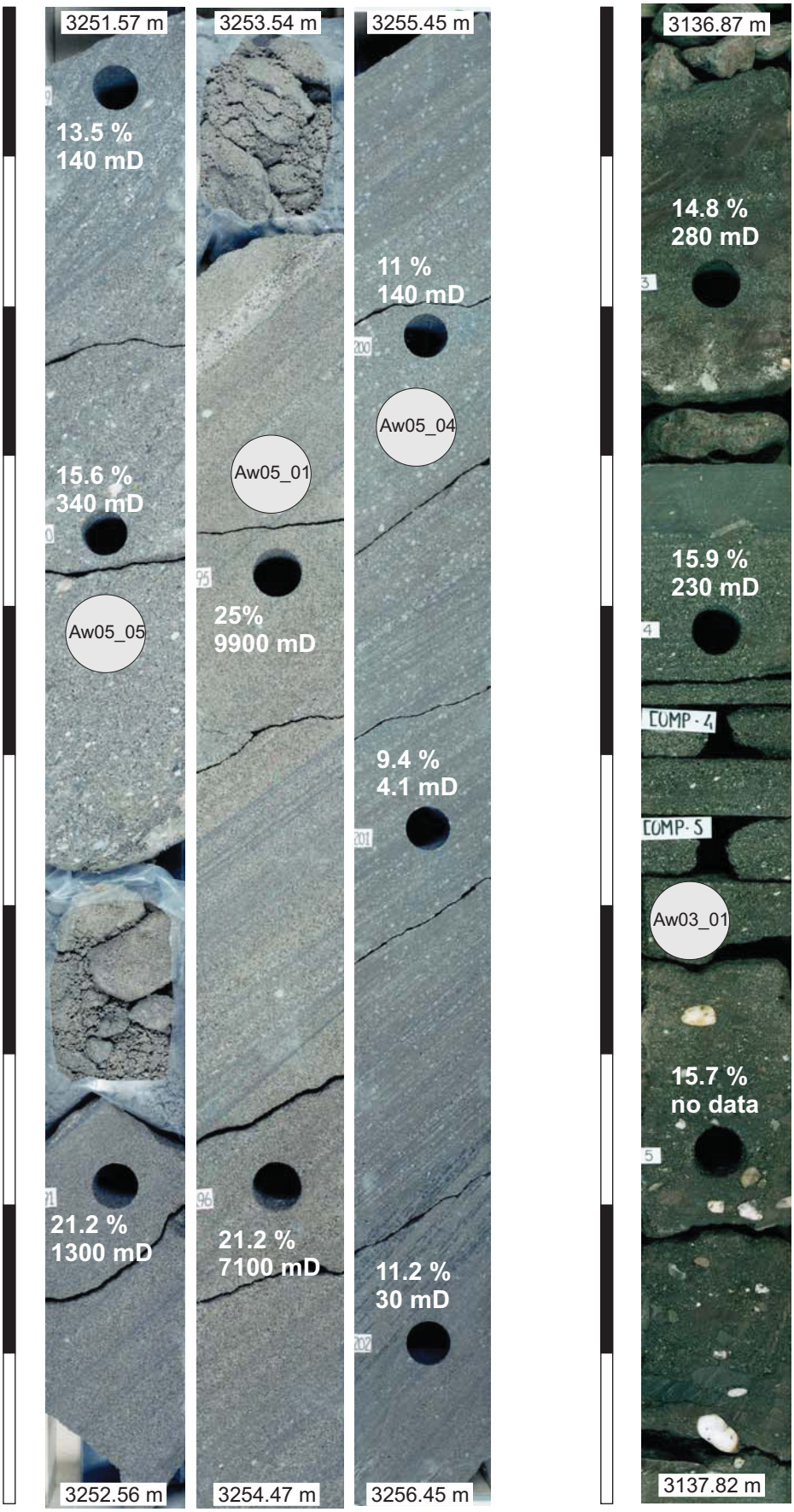

Appendix A1-04: Core images of well Bw01 with porosity [%] and horizontal permeability [mD] data. Samples which are taken for the study are marked as grey circle (plug)/rectangles.

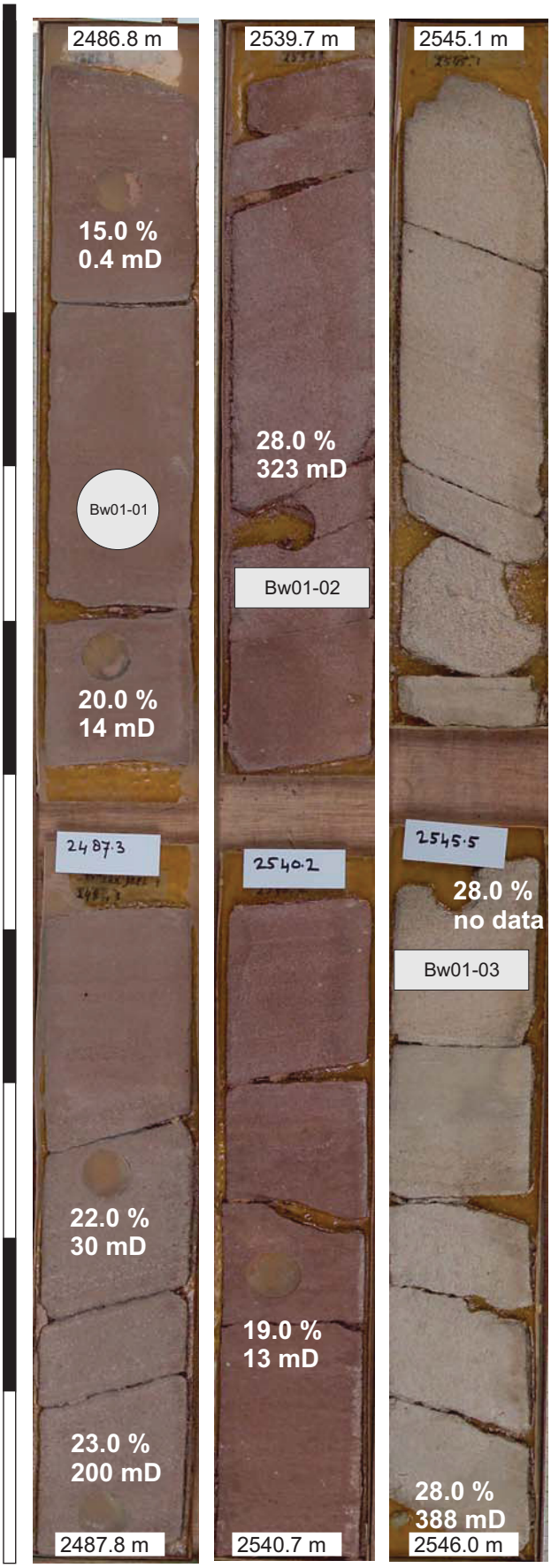

Appendix A1-05: Core images of well Bw02 with porosity [%] and horizontal permeability [mD] data. Samples which are taken for the study are marked as grey circles.

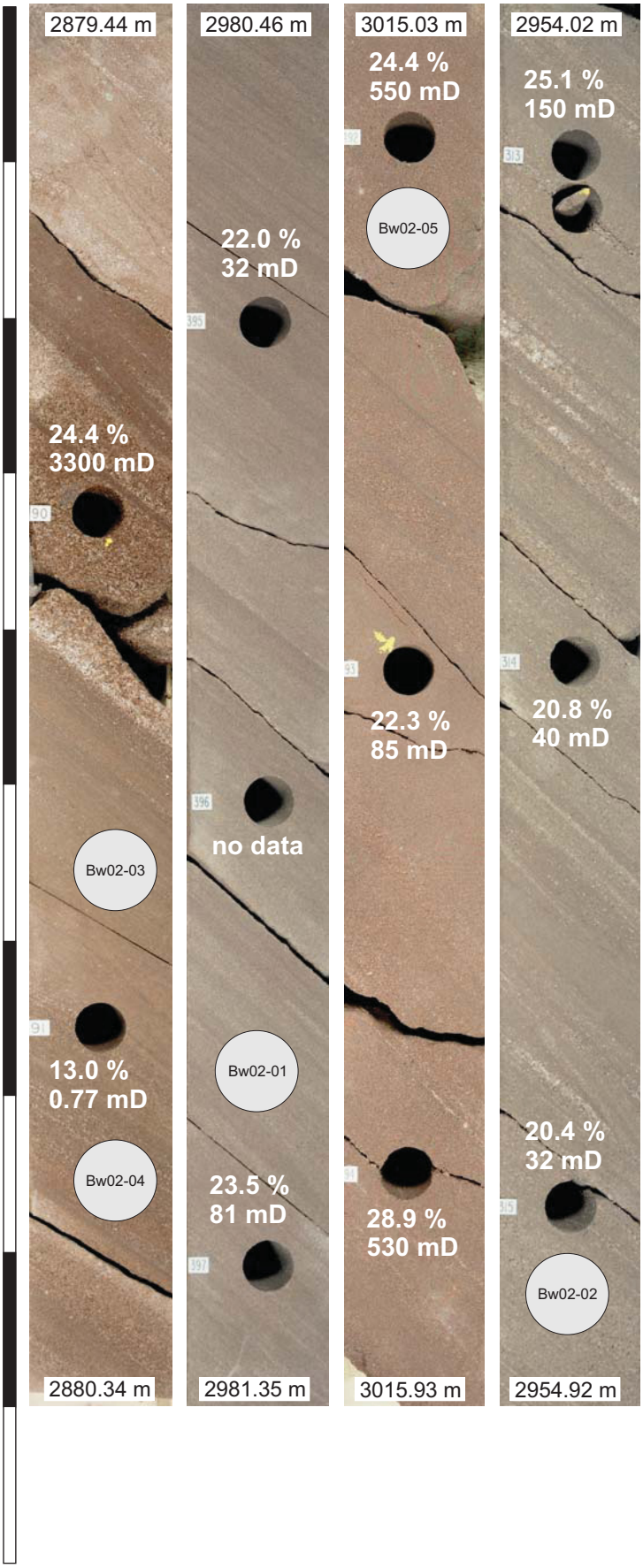

Appendix A1-06: Core images of well Bw03 with porosity [%] and horizontal permeability [mD] data. Samples which are taken for analysis are marked as grey circles.

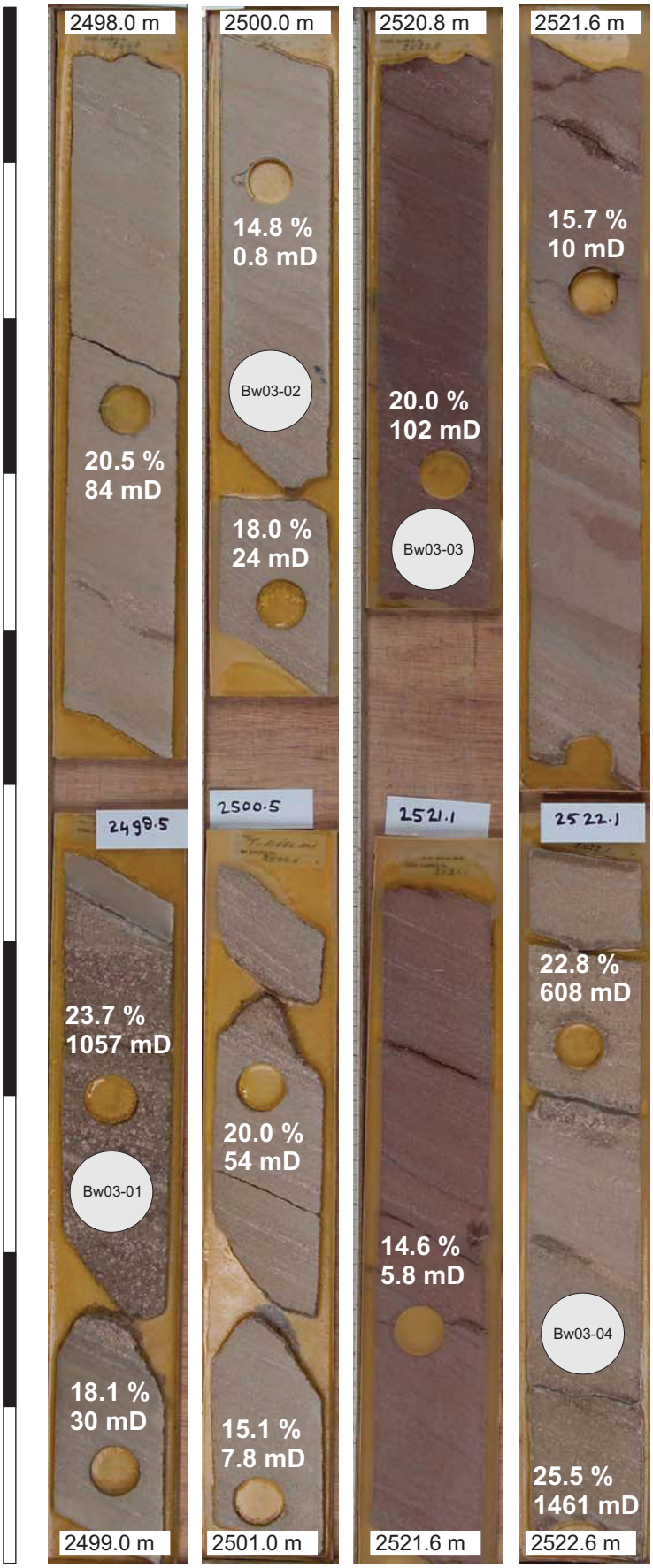

Appendix A1-07: Left: Core imagesof well Cw02. Right: Core images of well Cw03 with porosity [%] and horizontal permeability [mD] data. Samples which are taken for analysis are marked as grey circles.

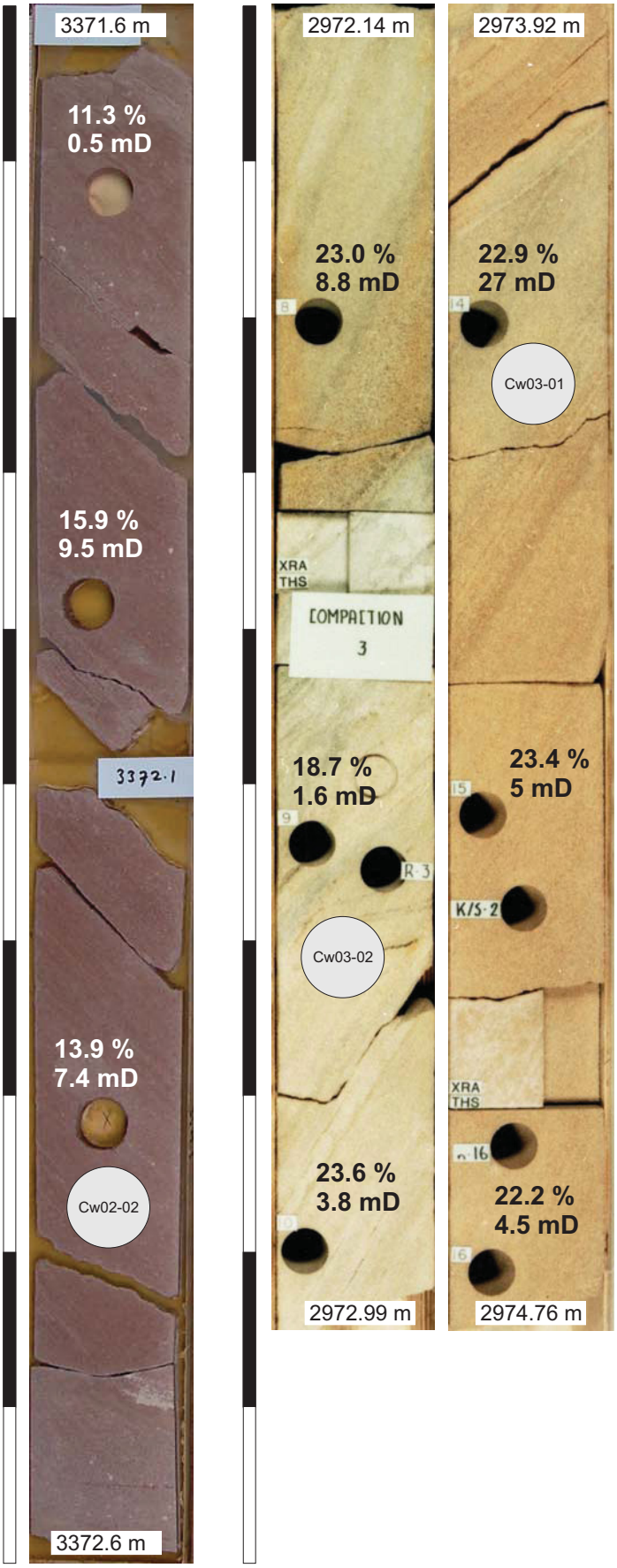

Appendix A1-08: Core images of well Cw04 with porosity [%] and horizontal permeability [mD] data. Samples which are taken for the study are marked as grey circles (plugs)/rectangles.

Appendix A1-09: Sedimentological description of wells from field A which are investigated in this study. For determination gamma ray logs and core images provided by NAM were evaluated.

Well Aw02

The cored basis of well Aw02 consists of grey to grey-brown coloured conglomerates and pebbles (~5 m) which indicate the base of a fining-upward cycle with a total thickness of ~10 m. Medium grained sandstones with horizontal lamination are interstratified (~0.80 m). The conglomerates are moderately sorted and clast-supported with a sandy matrix. The grains are well rounded with a high to low sphericity. The pebbly sandstones are poorly sorted and show a higher matrix content which leads to a mud-supported texture. Abundant clast types are mud-, silt- and fine grained sandstones, low metamorphic and volcanic rock fragments. There are only minor clast imbrications. The basis of the conglomerate sequence is not cored. The rocks are overlaid by fine to medium grained sandstones with interstratified silty mudstone layers. The sediments show horizontal lamination on a millimetre to centimetre scale with subtle to noticeable grain size differences between the laminae. In some parts of the sandstone dark grey laminae are present and may be interpreted as bitumen impregnations. They may be linked to coarser grained units. Minor low-angle cross-stratification (5-15°) is present in centimetre thick sandstone layers. Fining-upward units of secondary order (~10 cm thickness) occur in some horizons and are mostly overlain by silty mudstones. Minor amounts of laminated pebbles are present. Cementation (anhydrite) is either parallel to bedding or mottled. The silty mudstone layers are 0.05 to 0.80 m thick and are red to subordinated green coloured. Horizontal lamination is due to grain size differences between mudstone and siltstone. Desiccation cracks are ancillary present. The green colour of bleached mudstone occurs mostly parallel to bedding. The top of a silty mudstone layer is covered by a ~3 m thick conglomerate and pebbly sandstone. The conglomerate unit show an erosive base with reworked mudstone material. Conglomerates as well as the pebbly sandstones are poorly to moderately sorted and the pebbles are rounded to well rounded with a low to high sphericity. The depositions are mud-supported with a sandy matrix. Millimetres to centimetre thick silt-layers are interstratified. The top of the cored interval consists of fine to medium grained sandstone and silty mudstone which have similar properties like the underlying sequence. The difference is given in a higher amount of low-angle cross-stratificated (5-15°) horizons. These depositions are covered by a ~6 m thick moderately sorted, well rounded, clast-supported conglomerate. Bedding is indicated by elongated pebbles. The total thickness of the cored interval yields 40.75 m. The top of the Rotliegend deposits is located at 2892 m depth.

Well Aw03

Only ~13 m of the Aw03 well is cored. At the basis medium to coarse grained sandstones were deposited. They show horizontal lamination to a low-angle cross-stratification (5-15°) and mottled anhydrite cementation. Between 3148.18 to 3146.60 and 3145.00 to 3141.63 no core material is available. Above an expeditiously change (centimetre to decimetre scale) between mudstones, silty mudstones, fine to medium grained sandstones and pebbly sandstones are present. The coarse grained sediments contain large amounts of mudstone extraclasts. Structureless to horizontal lamination is common, whereas a low-angle cross-stratification (5-15°) is a subordinate feature.

Appendix A1-09: Continuation

Well Aw04

In well Aw04 the cored base (~5 m) consists of grey coloured very fine to medium grained sandstones. The sandstones are bimodal well sorted. On a centimetre to metre scale different sedimentary structures are changing from parallel horizontal lamination to low- and high-angle cross-stratification (5-30°) and structure less/massive horizons with a partly bimodal grain size distribution. Mudstones and clay matrix within the sandstones are absent. Mottled anhydrite cementation is present in some horizons. The sandstones are overlaid by a ~2 m thick structureless pebbly sandstone unit. The pebbles are poorly sorted and (well) rounded. A fining-upward cycle is recognised to the overlaid sediments where the top is a silty mudstone layer with a sand filled desiccation crack. The upper unit (~13 m) consists of fine to medium grained sandstones with mainly horizontal lamination. Some horizons are cross stratified with a low or high angle (5-30°). Mottled anhydrite and/or dolomite cementation is present. On the upper ~5 m fine and coarse grained sediments were expeditiously changing on decimetre scale. Pebbly sandstones often contain mudstone extraclasts. The top of the cored interval is characterised by fine grained structureless and low- to high-angle cross-stratified (5-30°) sandstones. Some horizons are horizontal laminated with a bimodal grain size distribution.

The permeability ranges between 0.1 and 1974 mD with an average of 310 mD. The high permeabilities (>100 mD) are linked to fine- and medium grained sandstones. The mean porosity yield 17 %, where the minimum porosity is about 9% and the maximum 27% of the total rock volume. The mean grain density is 2.68 g/cm^3. The top Rotliegend level is located at a depth of ~2850 m (at well Aw04) (appendix).

Interpretation for well Aw02, Aw03 and Aw04

The conglomerates and pebbly sandstones are characterised by (well)-rounded pebbles, mud- to clast-supported texture and a partly high grain sphericity. This indicates a moderate to high energetic environment which may be represented by a braided fluvial system (*gravelly braided river*). Furthermore laminated fine to medium grained sandstones with subordinated low-angle cross-bedding with a clearly defined channel floor suggest channel fill depositions (*sandy braided river*). Overall fining-upward trends with units about ~10 m thickness reflect the change between gravelly and sandy stream sediments. Thin silty mudstone beds were deposited as overbank fines in a low energetic environment (Penney, 1986; Nicholls et al., 1987; de Reuver, 1998). Fine to coarse grained sediments (e.g. well Aw03) are deposited under changing energetic conditions in a braided river environment. Mudstone clasts in the upper part of the cored interval suggest a short transport way. The good sorted, very fine to fine grained sediments and the absence of clay material indicate deposition in a dominated aeolian environment (e.g. well Aw04). Lamination with bimodal grain size distribution is characteristic for dry aeolian sandflats, whereas dune slip faces show a high-angle cross-stratification. Structureless to low-angle cross-stratificated sheetflood depositions are interstratified. The fine to coarse grained and pebbly sandstone horizons (middle core interval) with horizontal lamination and subordinated low- to high-angle cross-stratification (5-30°) indicate channel fill depositions of a braided river environment (de Reuver, 1998).

Appendix A1-09: Continuation

Well Aw05

The basal succession of well Aw05 is composed of conglomerates and medium- to fine grained sandstone with minor interstratified mudstone layers. The coarser grained sediments are grey to grey-brown coloured, whereas mudstone layers and clasts are red and green. The total thickness of the conglomerates yields ~20 m. For some sections the term breccia is more adequate. The sediments are mud- to clast-supported and contain varying portions of silt or sand matrix. The clasts are subangular to well rounded with a low to high sphericity. A poor sorting with pebble sizes usually between 5 mm and 5 cm is to mention. Bedding is often indicated by imbricated elongate clasts. The interbedded sandstones show a low-angle cross-stratification (5-15°) on a millimetre to centimetre scale with subtle to noticeable grain size differences between the laminae. Mottled and horizontal anhydrite cementation which is parallel to bedding is present in some horizons. The conglomerates are overlaid by fine to medium grained sandstones with minor amounts of thin (~1 to 3 m thickness) interstratified conglomerates and pebbly sandstones. Low-angle cross-stratification (5-15°) is present in the sandstone sequences. Some horizons with decimetre in size show a high-angle cross-stratification (15-30°). Subordinated curved non-parallel lamination in the sandstones sequences is present. The bedding is due to differences in grain size on a millimetre to centimetre scale. The boundaries between the different successions are normally sharp. Furthermore colour differences may effect a lamination and may be explained as bitumen impregnation in coarser grained laminae. From basis to top of the cored interval the amount of centimetre large clay fragments increase. Often they are red coloured with a green rim. Mudstone layers are not present. In some horizons (maximum thickness 1.0 m) a fining-upward cycle is to recognise. At the top of the cored interval thicker silty and/or sandy mudstone layers with thicknesses between 1.0 and 3.5 m are present. Furthermore the sequence is indicated by variable grain sizes from silty mudstones to conglomerates and an expeditiously change between the units, respectively. The finer grained units are laminated or show a disturbed or wavy structure. The youngest depositions are massiv. Desiccation cracks are present in some horizons. The silt and sand laminae as well as the rim of the mudstone depositions are bleached (grey and green coloured). The permeability ranges between 0.1 and 9900 mD (appendix C4), whereas the highest values are reached in fine to medium grained sandstones. Mean porosity is 12 % with a minimum of <5 % and maximum of 25 %. In comparison to the mean gas-water contact of the field A (3060 m) is located at 3181.5 m depth. This phenomenon is due to the conglomerate successions at the southern basin margin. The top Rotliegend is located at 2973 m depth.

<u>Interpretation well Aw05</u>

Poor sorting and high matrix content of the conglomerates in combination with abraded clay fragments indicate that the sediments were deposited under high energetic conditions. The paleogeographic position of the sediments is close to the basin margin where gravity-flow processes have taken place. The coarse grained sediments (pebbly sandstones and conglomerates) may be deposited within an alluvial fan, whereas the fine- to medium grained

sandstones and mudstones are depositions of a braided river environment (*gravelly and sandy braided river*). Bed thicknesses and grain size differences reflect variation in flow energy and transitions between alluvial fan and braided river depositions. In a low energetic environment mudstones were deposited as overbank fines (de Reuver, 1998).

Appendix A1-10: Sedimentological description of wells from field B which are investigated in this study. For determination gamma ray logs and core images provided by NAM were evaluated.

Well Bw01

The basal succession consists of horizontal laminated, brown-red coloured mudstones and silty to fine grained sandstones (~25 m thickness). The sandstones show partly a low-angle cross-stratification (5-15°) and wavy to disturbed structures. Bleached sandstones and mudstones horizons are intercalated (0.10 to 1.80 m thickness). Desiccation cracks are partly present. Above the succession red coloured (partly light-grey), fine to medium grained sandstones with horizontal lamination and non-stratified homogeneous structures were deposited. The mm- to cm-thick lamination is due to grain size differences. The succession is at least ~75 m thick and is overlaid by red-brown mudstones with intercalated sandstone horizons (~25 m).

Well Bw02

A detailed well description was further compiled by Nicholls (1987) and these information are included in the following description. The basal succession of at least ~30 m thickness consists of red-brown coloured fine to medium grained stratified sandstones and very fine grained wavy and adhesion rippled sandstone facies. Some well cross-bedded sandstone layers were intercalated. Furthermore discrete mudstone beds (mostly less than 0.2 m thick but one horizon shows 1.9 m thickness) with desiccation cracks are present. The succession is overlaid by wavy and adhesion rippled very fine grained sandstones which pass transitionally into muddy siltstone/sandstone facies (~23 m thick). Fluidisation in the sandstone facies is a common feature. The muddy siltstone/sandstone depositions show locally wavy to disturbed structures and ripple lamination. In the upper part a ~80 m thick wavy and adhesion rippled sandstones were deposited. The sandstones are red-brown to yellow-brown coloured and mostly fine to medium grained. Locally well cross-bedded sandstones (low angle: 5-15°) and muddy siltstones/sandstones are intercalated. The depositions of the following sediments have similar structures as the underlying sandstones and siltstones deposits. The main differences are intercalated mudstone horizons which not extend more than 0.4 m thickness. Locally desiccation cracks and curled clay flakes are present. In addition the stratified sandstones are horizontally bedded and the sorting is only moderate. In comparison, the lower sandstones are mostly good sorted. The lamination is due to grain size differences between fine and coarse grained sand. A fining upward interval from red coloured muddy siltstone/sandstone facies at the bottom to mudstone depositions at the top is located above (~3 m thick). Siltstone and sandstone intercalations show irregular wavy to disturbed structures. The contact between the mudstone and the overlaying sandstones is sharp. An interval of ~7 m thickness consists of wavy and adhesion rippled and fine to medium grained stratified sandstones. The stratified sediments show horizontal lamination on a millimetre to centimetre scale with subtle to noticeable grain size differences between the laminae. At least 35 m thick mudstones and muddy siltstones/sandstones were deposited above the sandstone unit. Disturbed structures and irregular bedding is common. Locally thin (<0.3 m thick) stratified and non-stratified sandstones are interbedded. Grey to white coloured sandstones and green/red-brown mudstones appear in a ~4 m thick unit. The sandstones show horizontal lamination as well as low-angle cross-stratification (5-15°). The top of the cored interval are a ~28 m thick red-brown coloured

mudstone and muddy siltstone/sandstone deposits. Admixed sand and silt occurs in disturbed structures and irregular wavy bedding. Mottled anhydrite cementation is locally present.

Well Bw03

The cored basis of well Bw03 consists of red to red-brown coloured mudstones and siltstones (~15 m) which indicate the base of a coarsening-upward cycle with a total thickness of ~25 m. The interval above the coarsest sediments is not cored. The mudstones with intercalated siltstones (mm- to cm-thickness) show a wavy lamination and adhesions ripples. Some coarse grained sandstone horizons are intercalated with centimetre thicknesses. Above the succession fine grained sandstones with a low-angle cross-stratification (5-15°) are deposited. The bedding, on a millimetre to centimetre scale, is due to a noticeable grain size differences between the laminae. Were silty sandstone layers are intercalated wavy lamination is present in some parts. About the overlaying sediments (~44 m) no data are available. At the basis of the second cored interval (~40 m) stratification of medium and coarse grained sediments with intercalated clay layers were deposited. The sediments are light red, red or brown coloured. They show a homogeneous structure with unclear horizontal lamination. Some horizons are cross-stratified with a low angle (5-15°). Were the mudstone/silt content is higher, wavy lamination is present. A fining-upward cycle with a thickness of ~5 m is present in the middle of the succession.

<u>Interpretation for well Bw01, Bw02 and Bw03</u>

The field is located near the lake margin and is mainly influenced by (shallow) desert lake and lower desert plain environments. Wavy to adhesion rippled sandstones are interpreted to be deposited in damp interdune areas. The transition to muddy siltstone/sandstone indicates the change to a subaqueous environment such as at the lake margin or in emphemeral pools. Desiccation cracks and curled clay flakes within the thin mudstone horizons indicate a shallow pond or pool deposition. Well cross-bedded sandstones are deposited at the margin of a dune or as small scale aeolian dune. The stratified sandstone facies are depositions of dry aeolian interdune areas. Note that the same facies type is deposited by fluvial processes (as sheet floods or braided river depositions) in the area of field A.

Appendix A1-11: Sedimentological description of wells from field B which are investigated in this study. For determination gamma ray logs and core images provided by NAM were evaluated.

Well Cw02

In total, ~94 m of well Cw02 are cored. Fine to medium grained red coloured sandstones and silty mudstones are the dominant deposits. The sandstones are characterized by a low-angle (5-15°) to high-angle (15-25°) cross stratification in mm-scale. In some horizons this cross stratification steps back and a structure-less sandstone is present. Partly, coarser grained sandstone laminae (mm- to cm-scale) are intercalated. The thicknesses vary between less than 10 cm up to maximum 4.10 m.

Well Cw03

Available data for well Cw03 are a cored interval between 2970 m and 2989 m depth. The sequence consists of light brown to brown coloured medium grained sandstones with a high-angle (15-25°) cross stratification in intercalation with silty mudstones which show a wavy lamination to low-angle (5-15°) cross stratification. The lamination is due to grain size differences. The sandstone thickness varies between 0.20 and 3.20 m and the silty mudstones between 0.10 and 4.60 m. In a light brown coloured sandstone horizon in 2972.50 to 2975.70 m depth dark coloured laminas parallel to the sandstone stratification may indicate bitumen impregnations. The cored section is cut by a structureless light brown coloured fine grained sandstone with 0.50 m thickness.

Well Cw04

The total cored interval of well Cw04 yield ~30 m. The basis (~7 m) consists of sandy claystones, siltstones and mudstones which show a horizontal to wavy lamination (due to the total silt content). A red-brown coloured fine grained sandstone horizon (~1.20 m) with horizontal to low-angle cross-stratification is intercalated. Within this section a coarsening upward, followed by a fining upward and again a development to fine grained sandstones is present. The overlaying ~23 m are dominated by a change (on a dm- to m-scale) of different grain sizes and facies types.

<u>Interpretation for well Cw02, Cw03 and Cw04</u>

The field C is located near the lake margin and is mainly influenced by (shallow) desert lake and lower desert plain environments. Medium grained cross stratified sandstone are interpreted as dune deposits. Whereas adhesion rippled sandstones indicate a damp interdune environment. The transition to muddy siltstone/sandstone indicates the change to a subaqueous environment such as at the lake margin or in emphemeral pools. Silty mudstones with wavy lamination wet sandflats which are mainly influenced by groundwater fluctuation.

Appendix A2-01

A Detrital K-feldspar in contact to dolomite crystals crowing corrosively against the grain. Sample: Aw02-06
B Same images as in A under crossed polarized light. Sample: Aw02-06
C Detrital microcline grain under crossed polarized light. Sample: Cw04_2734.9
D Mafic volcanic grain (Lv_{maf}). Sample: Aw05-03
E Layered sedimentary grain (Ls_{psam}). Sample: Aw05-03
F Polycrystalline quartz grain (Qp). Sample: Aw02-03
G Backscatter electron image of a felsic volcanic grain build up by quartz and K-feldspar. Sample: Aw02-06
H Green coloured helminth-chlorite in a chalcedony grain. Sample: Aw03-01

Appendix A2-02

A Different dissolution stages of K-feldspar grains to the point of total dissolution and the formation of on "oversized pore". Sample: Cw04-05
B Illitisation of a detrital K-feldspar grain under crossed polarized light. Sample: Cw04-05
C Green coloured illite/smectite as alteration product in a partly dissolved volcanic rock fragment. Sample: Aw05-07
D Green coloured illite/smectite as alteration product in a partly dissolved volcanic rock fragment. Grain rimming early diagenetic kaolinite cement. Sample: Bw01-02
E Kaolinite “booklets” as alteration product of K-feldspar or volcanic rock fragment. Note the residual Fe-oxide coating around the former grain. Sample: Bw03-01
F Dolomitisation of a volcanic rock fragment and partly dissolved K-feldspar grain. Sample: Aw02-03
G Green coloured illite/smectite as alteration product of volcanic rock fragments. Aggregation of kaolinite “booklets” forming a larger “booklet”-structure. Sample: Aw02-03

Appendix A2-03

A Thick Fe-oxide coatings on detrital grains with grain rimming kaolinite growing perpendicular into the pore space. A mesodiagenetic pore filling, blocky quartz covers kaolinite. Sample: Cw02-01
B Grain rimming kaolinite growing perpendicular into the pore space. Note the different kaolinite sizes and the partly sheaf like arrangement. Sample: Cw02-01
C Elongated kaolinite growing perpendicular to the grain surface are and single kaolinite crystals within the inter- and intragranular pore space. Sample: Cw02-01
D Pore-bridging grain rimming kaolinite. Sample: Cw04-05
E Grain rimming kaolinite growing after an early diagenetic syntaxial quartz overgrowth. Sample: Cw04-05
F Grain rimming kaolinite and pore filling kaolinite forming a dense cluster in an elongated pore throat. Sample: Bw01-02
G Kaolinite “booklets” and elongated, sheaf-like kaolinite in direct neighborhood. Note the transition forms between these two kaolinite types. Sample: Bw02-01
H Kaolinite “booklets” are often arraigned as aggregations. Sample: Aw02-12

Appendix A2-04

A Pore filling anhydrite cement surrounding a single dolomite crystal. Sample: Aw03-01
B Intensive anhydrite cementation. Sample: Cw04-2728.3

C Intergranular anhydrite precipitated after an early diagenetic syntaxial quartz overgrowth and is followed by intragranualr anhydrite precipitation. Sample: Cw02-01
D Intensive carbonate cementation replaces detrital grains which results in a relatively high intergranular volume. Sample: Aw01-2924.5
E Blocky carbonate cements growing corrosively against K-feldspar. Sample: Aw05-03
F Blocky carbonate is surrounded by a dark coloured rim (bitumen?, Fe-oxide?). Sample: Aw02-03
G Precipitation of galena (PbS) on detrital grains. Sample: Aw02-03
H Single carbonate rhombohedra within the intergranular pore space. Sample: Aw04-01

Appendix A2-05

A Solid bitumen with shrinking cracks around detrital grains. Sample: Aw05-07
B Bitumen coatings around a partly dissolved K-feldspar grain. Sample: Aw05-03
C Bitumen coatings covering authigenic kaolinite "booklets" and detrital grains. Sample: Aw05-03
D Less cemented porous sandstone with a good pore connectivity. Sample: Aw02-08
E Backscatter electron images of a porous sandstone with quartz grains and a volcanic rock fragment. Note that the space between grain-grain contacts is free of authigenic minerals and may act as pathways for e.g. fluid migration. Sample: Aw02-03
F Kaolinite "booklets" with and without bitumen coating and different crystal sizes in direct neighborhood. Sample: Aw05-07
G Thin illite coatings around detrital grains (light coloured rims) under crossed polarized light. Sample: Aw02-08
H Poorly sorted sandstone from the southern basin margin. Sample: Aw05-03

Appendix A2-01: Thin section images of minerals. For abbreviations compare "List of abbreviations".

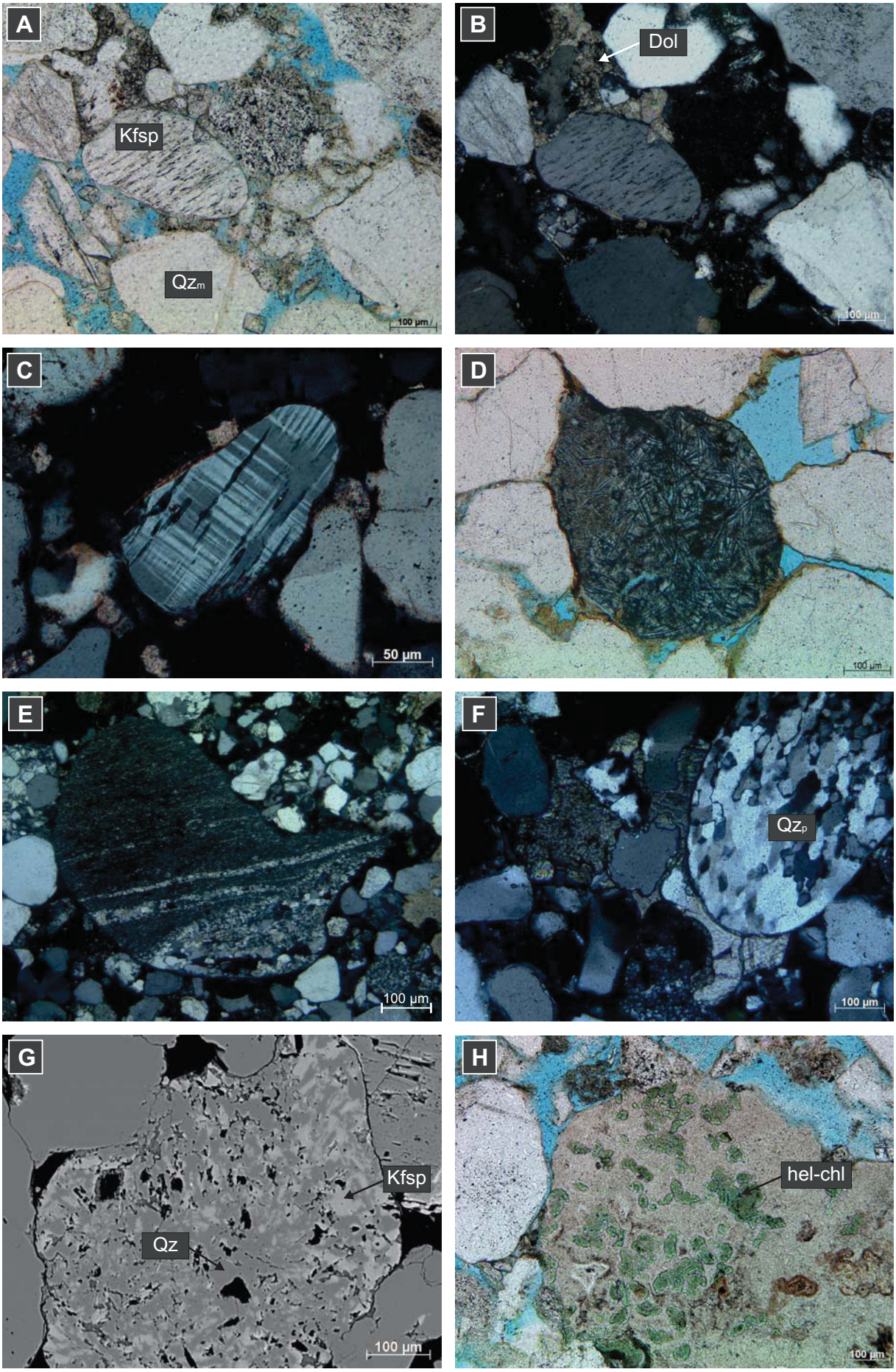

Appendix A2-02; Thin section images of minerals. For abbreviations compare "List of abbreviations".

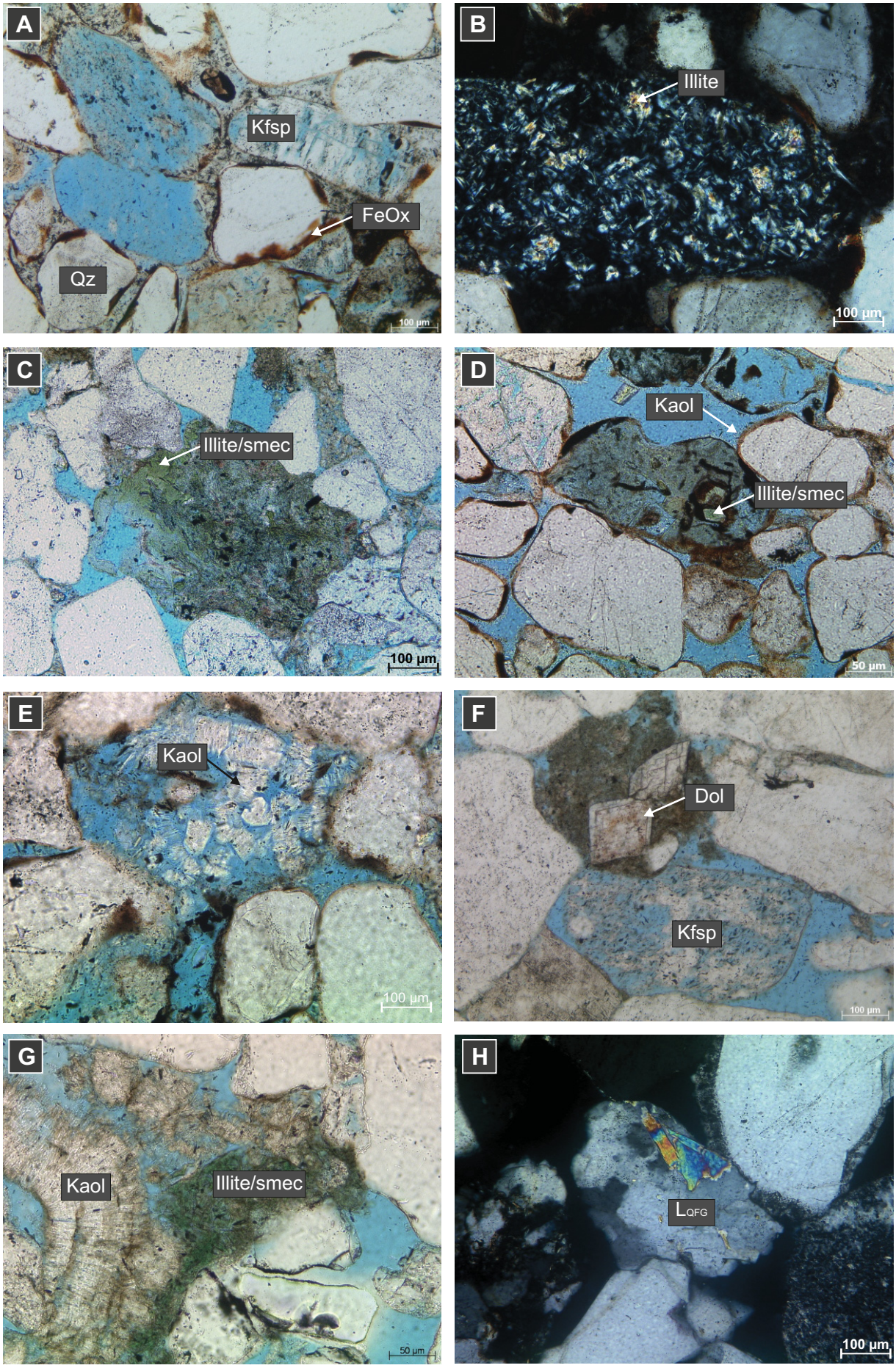

Appendix A2-03; Thin section images of minerals. For abbreviations compare "List of abbreviations".

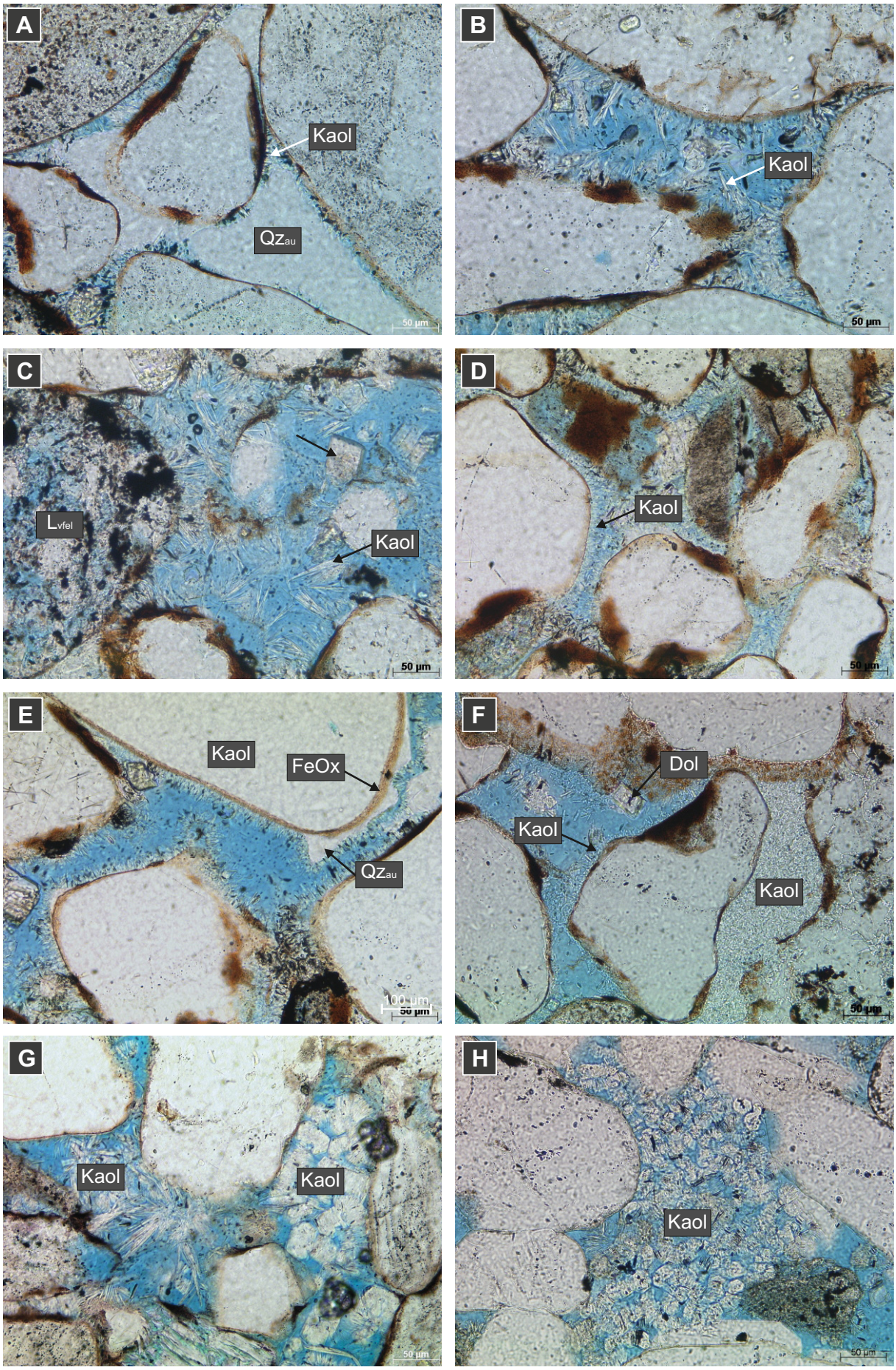

Appendix A2-04; Thin section images of minerals. For abbreviations compare "List of abbreviations".

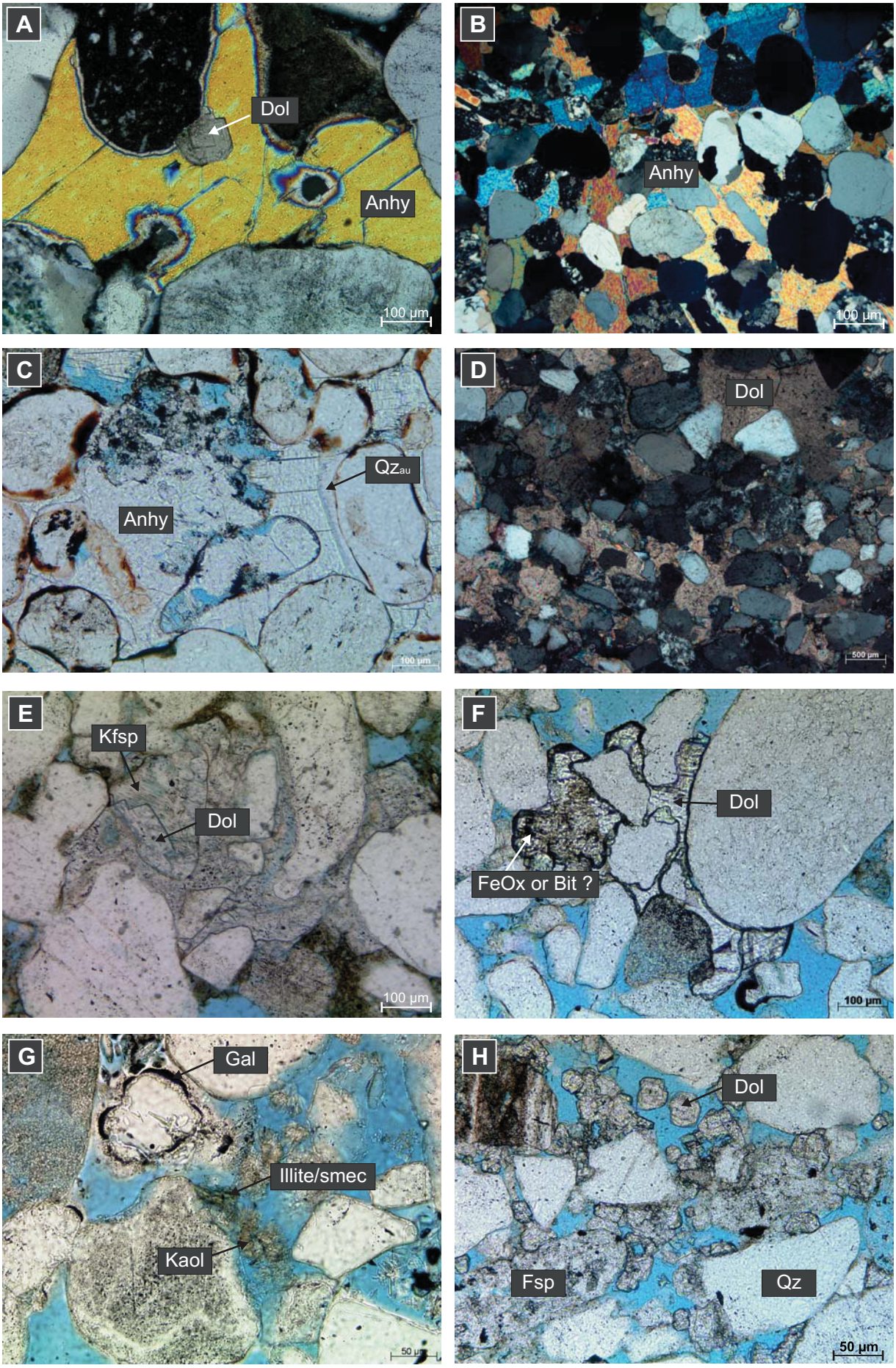

Appendix A2-05; Thin section images of minerals. For abbreviations compare "List of abbreviations".

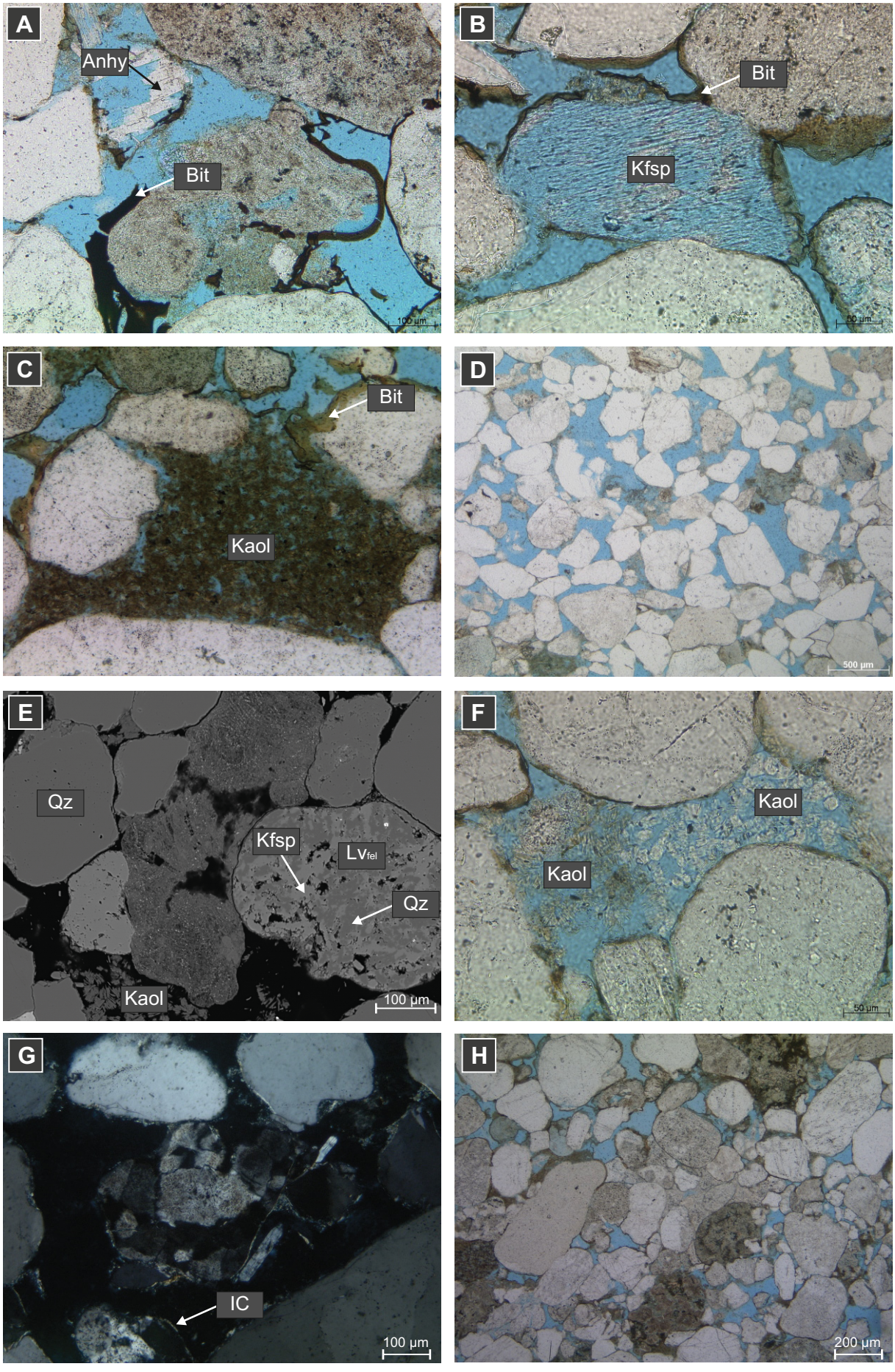

Appendix A3 – Secondary electron images

Appendix A3-01

A Arrangement of kaolonite "booklets" in a pore throat surrounded by detrital quartz grains with irrgeluar distributed voids on the surface area. Sample: Aw02-12
B Dense structure of kaolinite crystals with different thicknesses and sizes growing perpendicular on a grain surface area. Sample: Cw04-05
C Single kaolinite crystals growing on the surface area of a detrital grain are partly covered by fibrous illite. Sample: Bw01-01
D Grain surface area with grain rimming kaolinite and cubic dolomite. Sample: Bw01-01
E Grain rimming kaolinite forming elongated minerals by the aggregation of several crystals. Sample: Cw03-02
F Magnification of image E. Sample: Cw03-02
G Pore bridging kaolinite growing perpendicular from on detrital grains into the pore space. Sample: Cw03-02
H Coexisting kaolinite and idiomorph quartz crystals. Sample: Aw03-01

Appendix A3-02

A Two quartz generations with early microcrystalline quartz and a later, partly idiomorph formed quartz overgrowth which coexist with kaolinite. Sample: Aw03-01
B Rough surface area of detrital quartz grains with carbonate cement in between. The carbonate (dolomite) shows an irregular surface area in form of small steps. Sample: Aw03-01
C Early diagenetic meshwork illite is followed by kaolinite and barite precipitation. Sample: Aw03-01
D Meshwork illite forming a honeycomb structure. Sample: Aw03-01
E Partly dissolved K-feldspar grain. Sample: Cw04-05
F Illitisation of a K-feldspar grain. Sample: Cw02-01
G Backscatter electron image of disperse distributed Fe-oxide intercalated in a clay cutan. Sample: Cw04-05
H Small calcite crystals growing on kaolinite. Sample: Bw01-02

Appendix A3-03

A Kaolinite crystals arraigned as "booklets". Sample: Aw03-01
B Lath-like anhydrite with small Fe-oxide aggregates on the surface area. Sample: Aw03-01
C Fibrous illite intergrown with quartz. Sample: Cw02-01
D Dense kaolinite structures and dolomite crystals. Sample: Cw02-01
E Fibrous, hairy illite. Sample: Cw-03-02
F Kaolinite with small Fe-oxide and illite growing on the crystal surface area. Sample: Bw01-02
G Irregular dolomite surface area with growing structures. Samples: Bw01-02
H Elongated kaolinite with a sheaf-like arrangement. Sample: Cw02-01

Appendix A3-04

A Anhydrite with halite. Sample: Aw03-01
B Kaolinite "booklet" with different crystal thicknesses and space between them. Sample: Cw02-01
C Authigenic dolomite arraigned between detrital grains. Sample: Aw03-01

D Irregular dolomite surface area in form of steps. Sample: Aw03-01
E Calcite in coexistence with kaolinite. Sample: Bw01-01
F Fibrous illite (?). Sample: Bw01-01
G Overview about the grain arrangement in sample Aw04-01
H Surface area of a detrital grain covered by tangential illite cutan (IC). Image from D. Bayer, 2010, unpublished. Sample: Aw05-03.

Appendix A3-01; Secondary electron images of minerals. For abbr. compare "List of abbreviations".

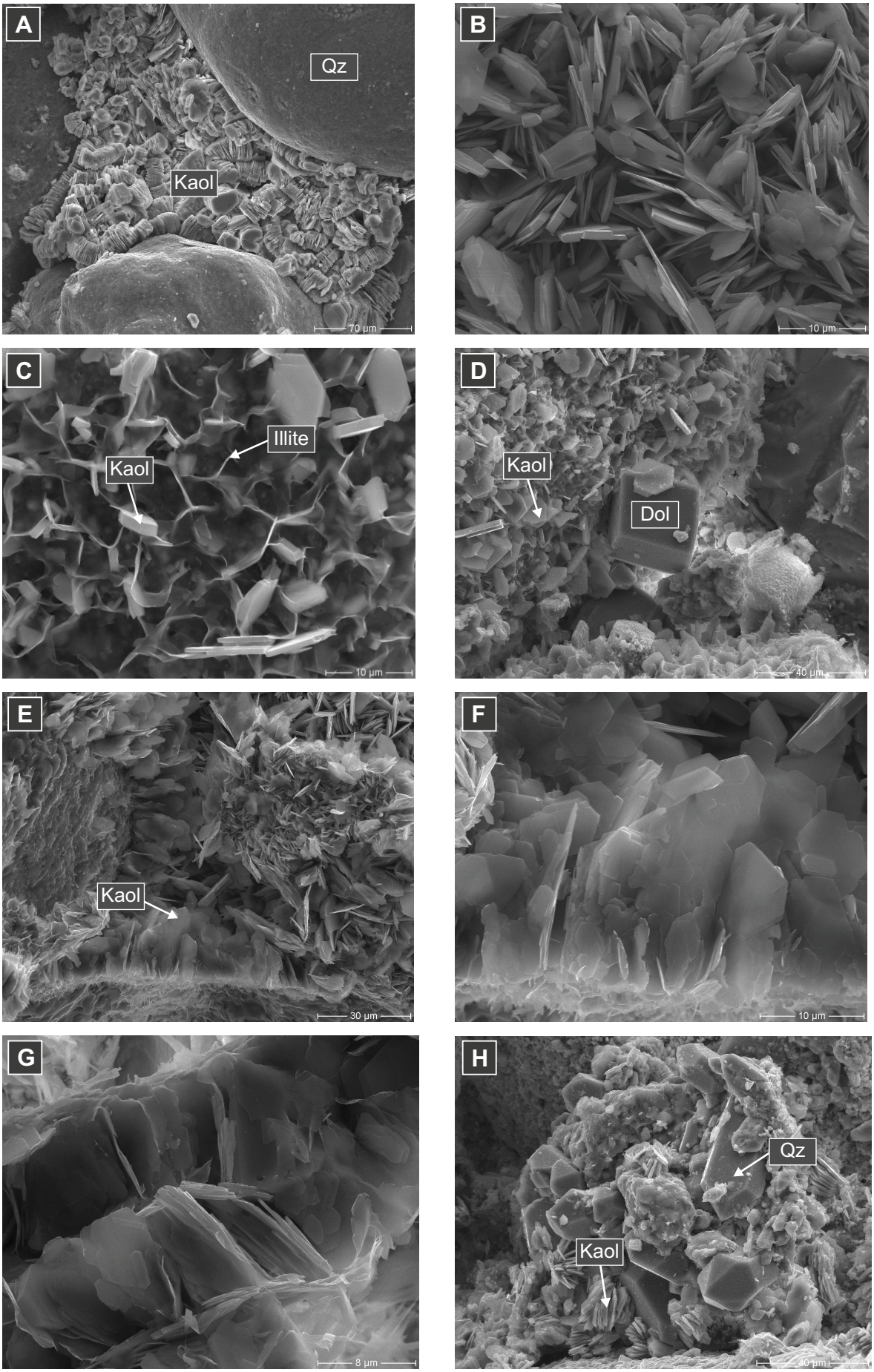

Appendix A3-02; Secondary electron images of minerals. For abbr. compare "List of abbreviations".

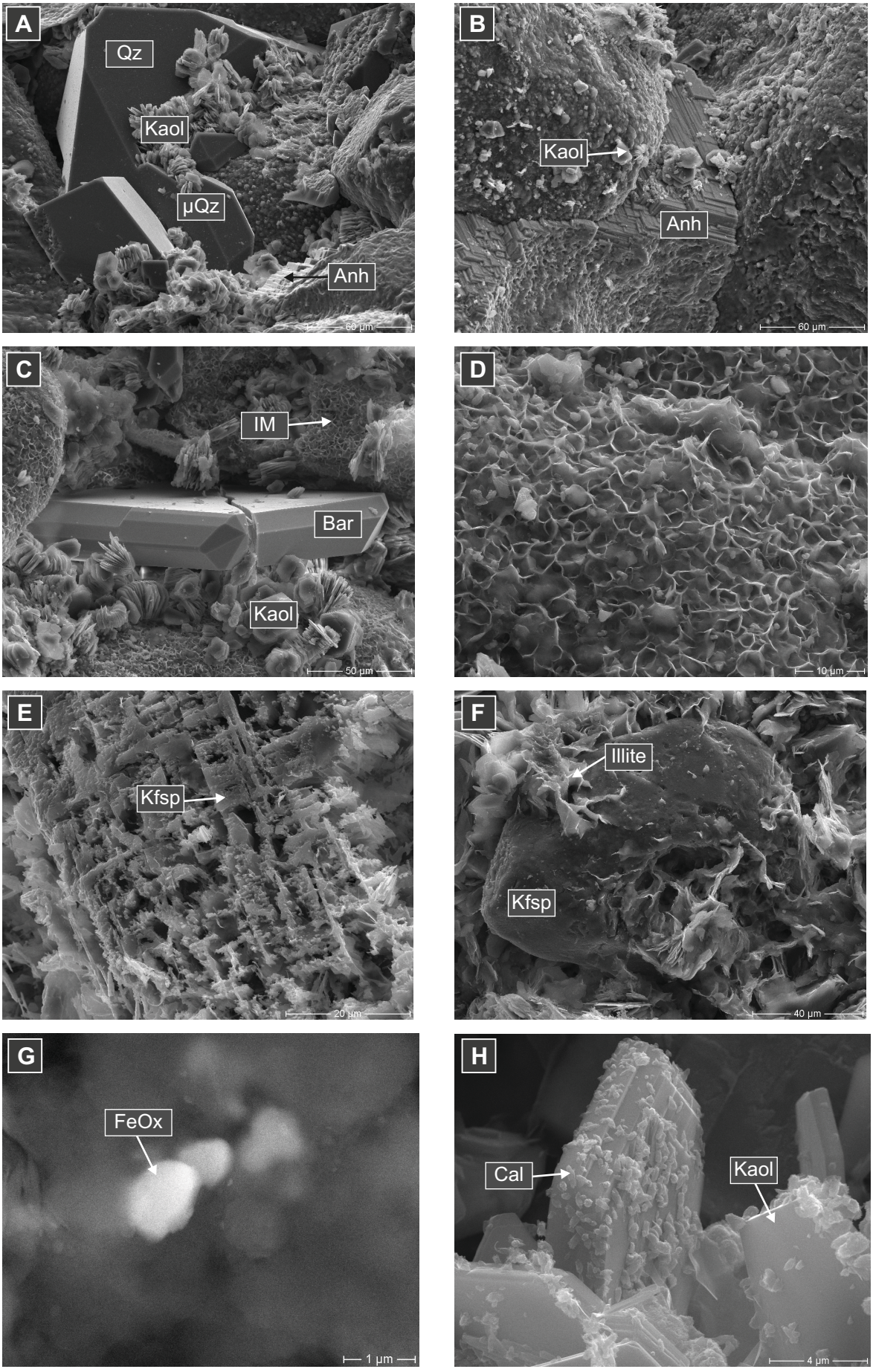

Appendix A3-03; Secondary electron images of minerals. For abbr. compare "List of abbreviations".

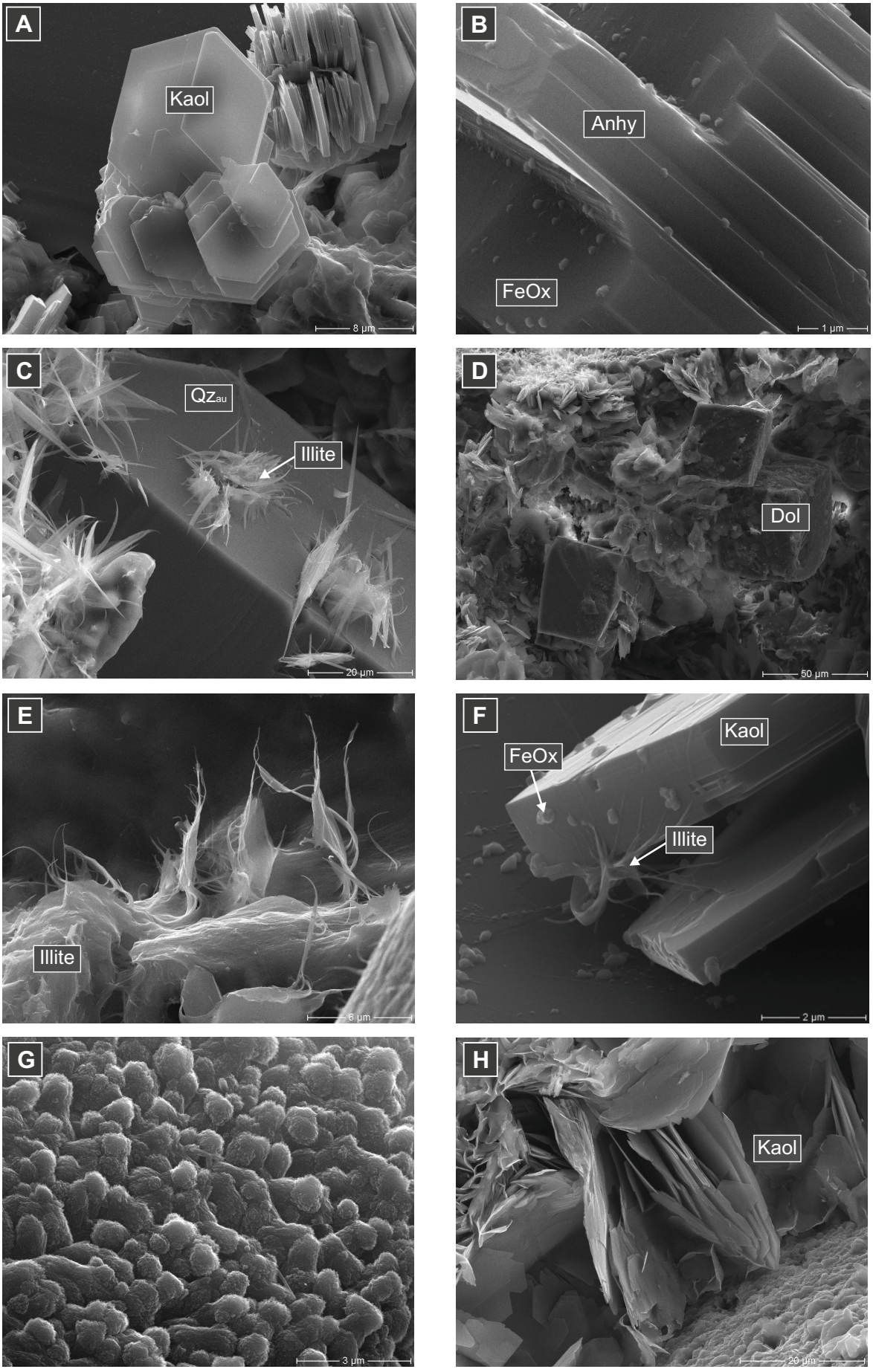

Appendix A3-04; Secondary electron images of minerals. For abbr. compare "List of abbreviations".

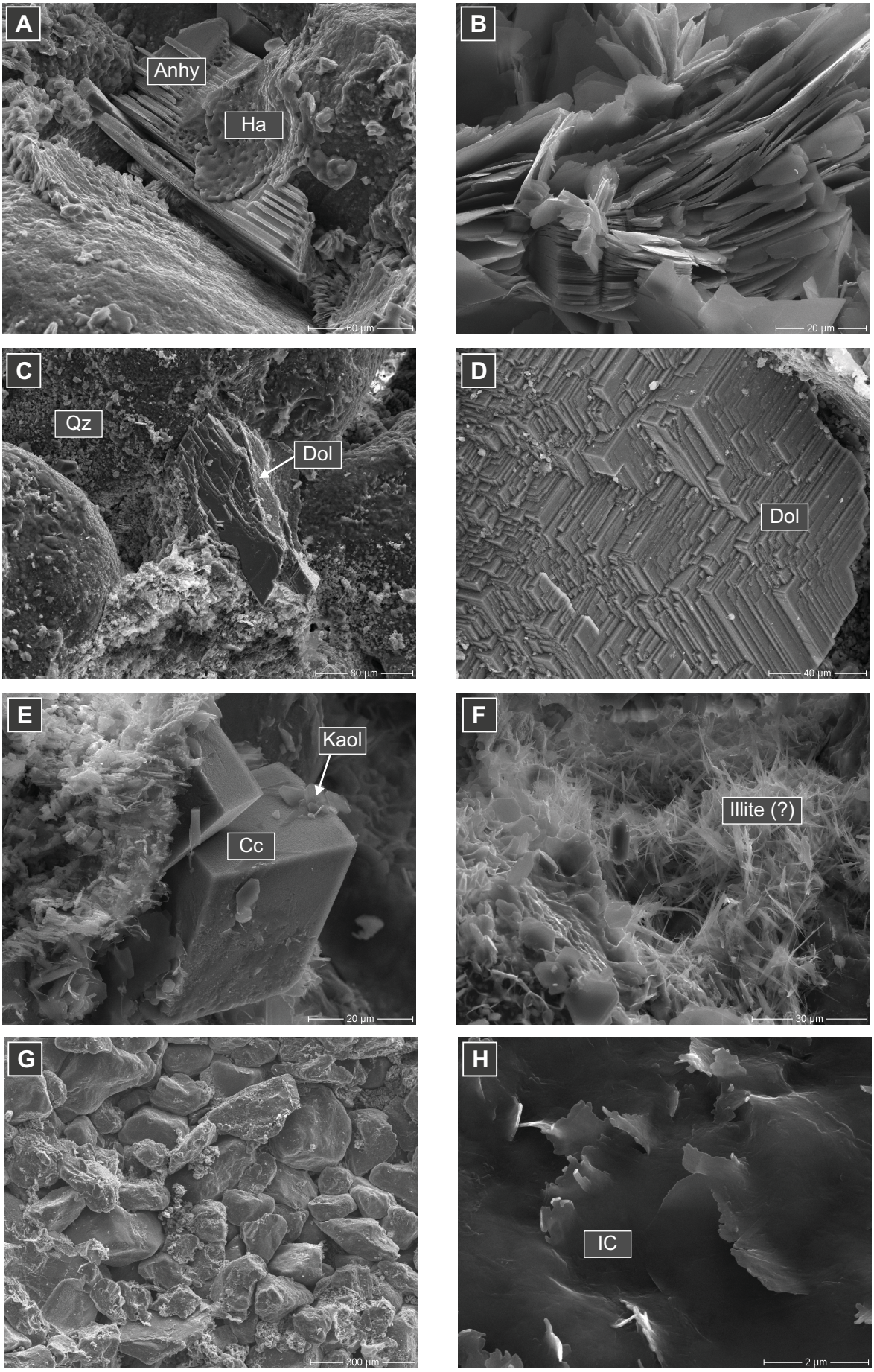

Appendix A4-01: Cross section of field A for wells Aw02, Aw03, Aw04 and Aw05 created with PETREL. A gamma ray ≤ 50 counts per seconds (cps) is defined as shale, ≥50 – <100 cps as fine grained sandstone and ≥ 100 cps as sandstone. The top ot the Upper Slochteren Formation (ROSL_T) is used as reference horizon. GR = Gamma ray [cps]. Por = Porosity [%].

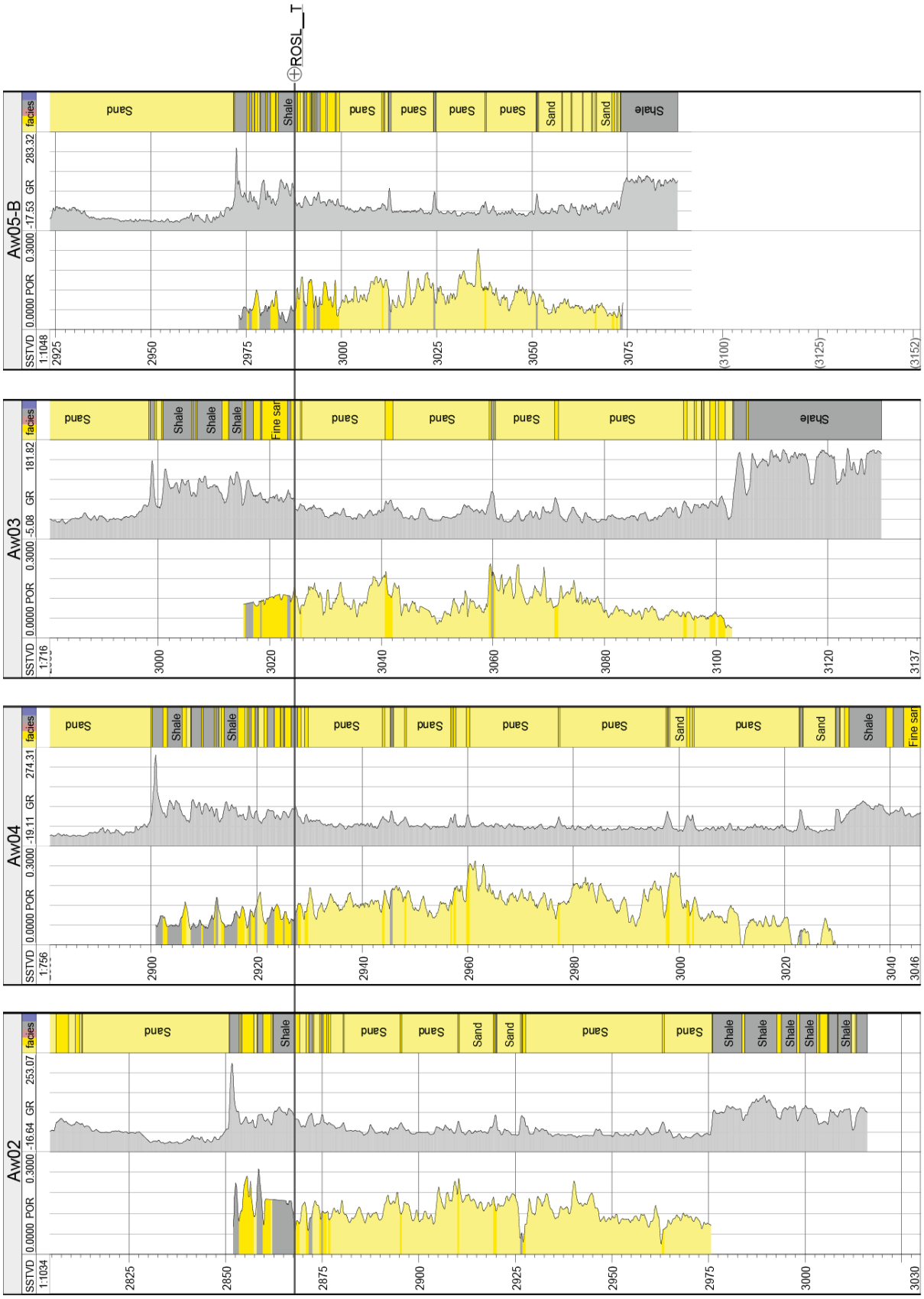

Appendix A4-02: Cross section of field B for wells Bw01, Bw02 and Bw03 created with PETREL. A gamma ray ≤ 50 counts per seconds (cps) is defined as shale, ≥50 – <100 cps as fine grained sandstone and ≥ 100 cps as sandstone. The top of the Upper Slochteren Formation (ROSL_T) is used as reference horizon. No gamma ray data are available for well Bw02. GR = Gamma ray [cps]. Por = Porosity [%].

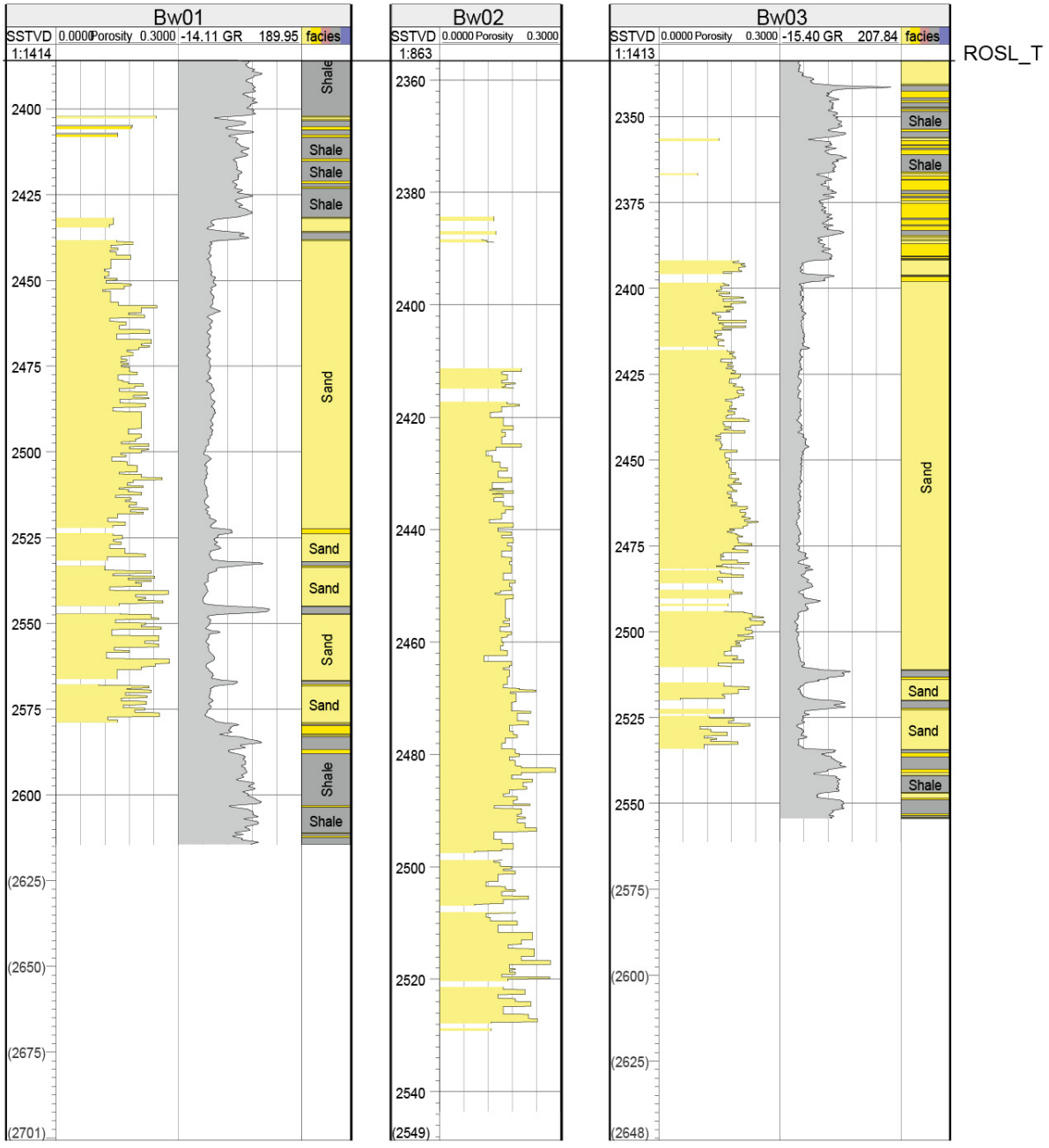

Appendix A4-03: Cross section of field C for wells Cw02, Cw03 and Cw04 created with PETREL. A gamma ray ≤ 50 counts per seconds (cps) is defined as shale, ≥50 – <100 cps as fine grained sandstone and ≥ 100 cps as sandstone. The top of the Upper Slochteren Formation (ROSLU) is used as reference horizon. GR = Gamma ray [cps]; POR = Porosity [%].

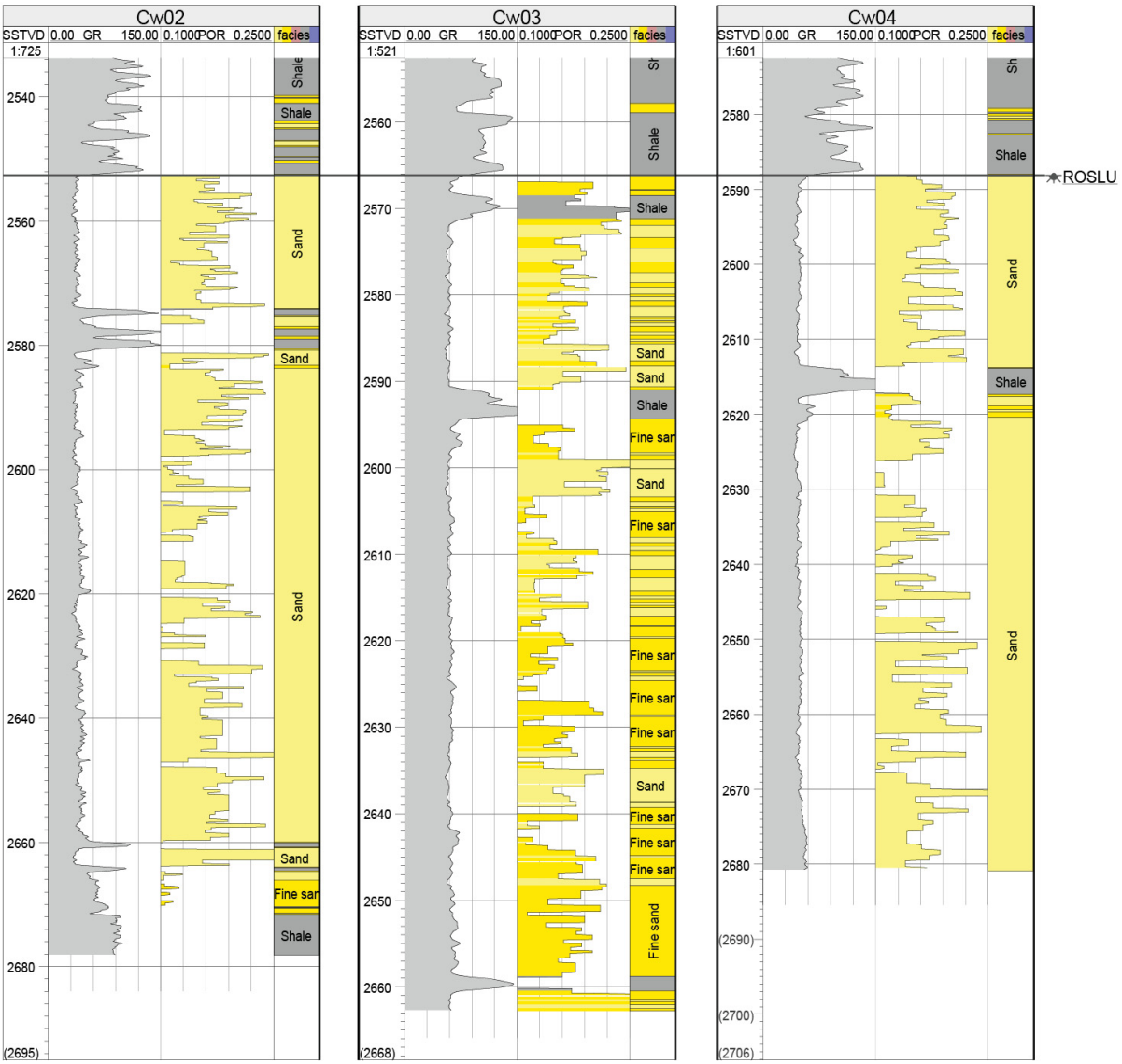

Appendix A4-04: Cross section of field A for wells Aw13, Aw14, Aw02 and Aw04 from northwest to southeast created with PETREL. The Upper Slochteren Formation (ROSL_T) is used as reference horizon. Sw = Water saturation [%]. POR = Porosity [%].

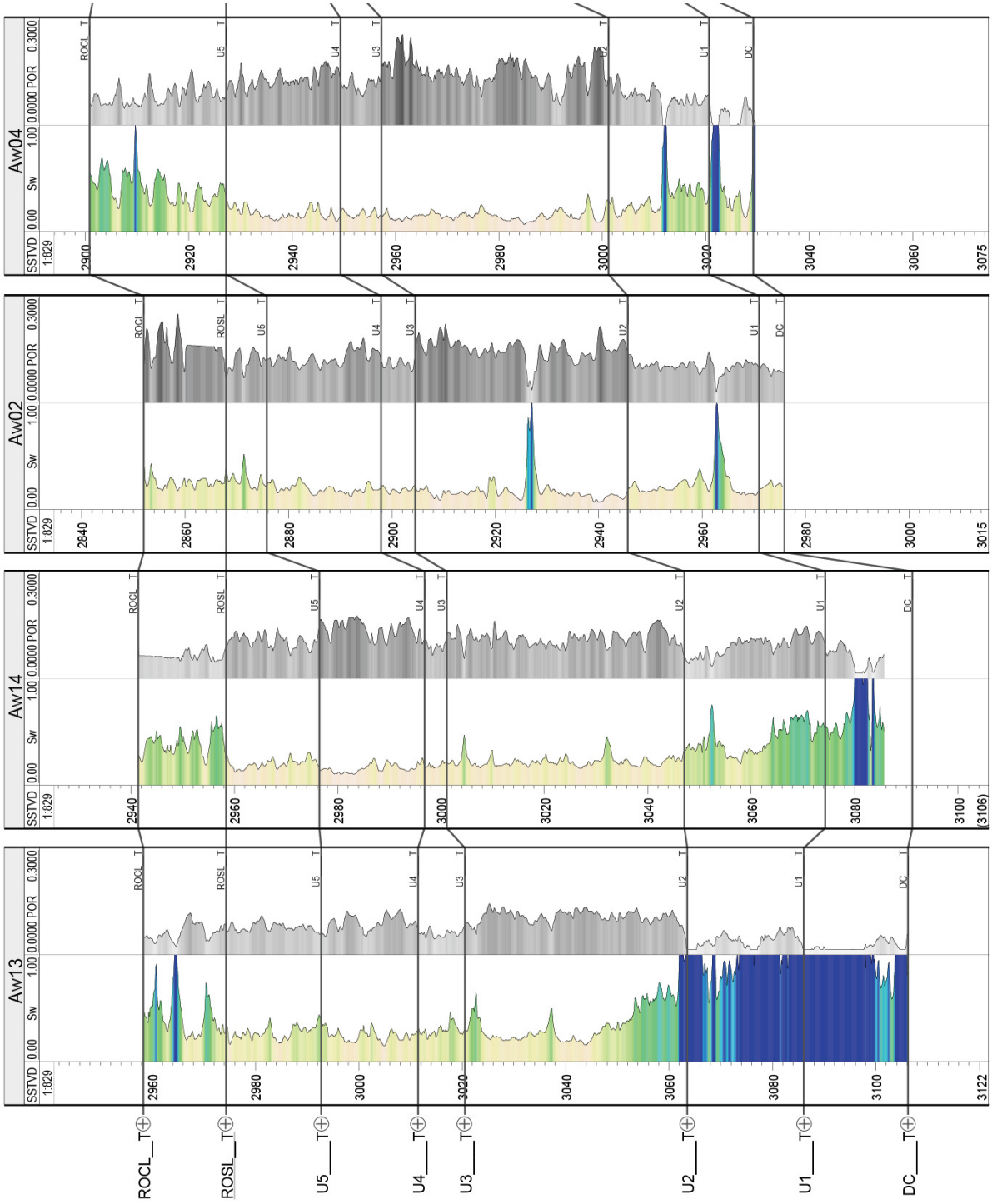

Appendix A4-04: Continuation

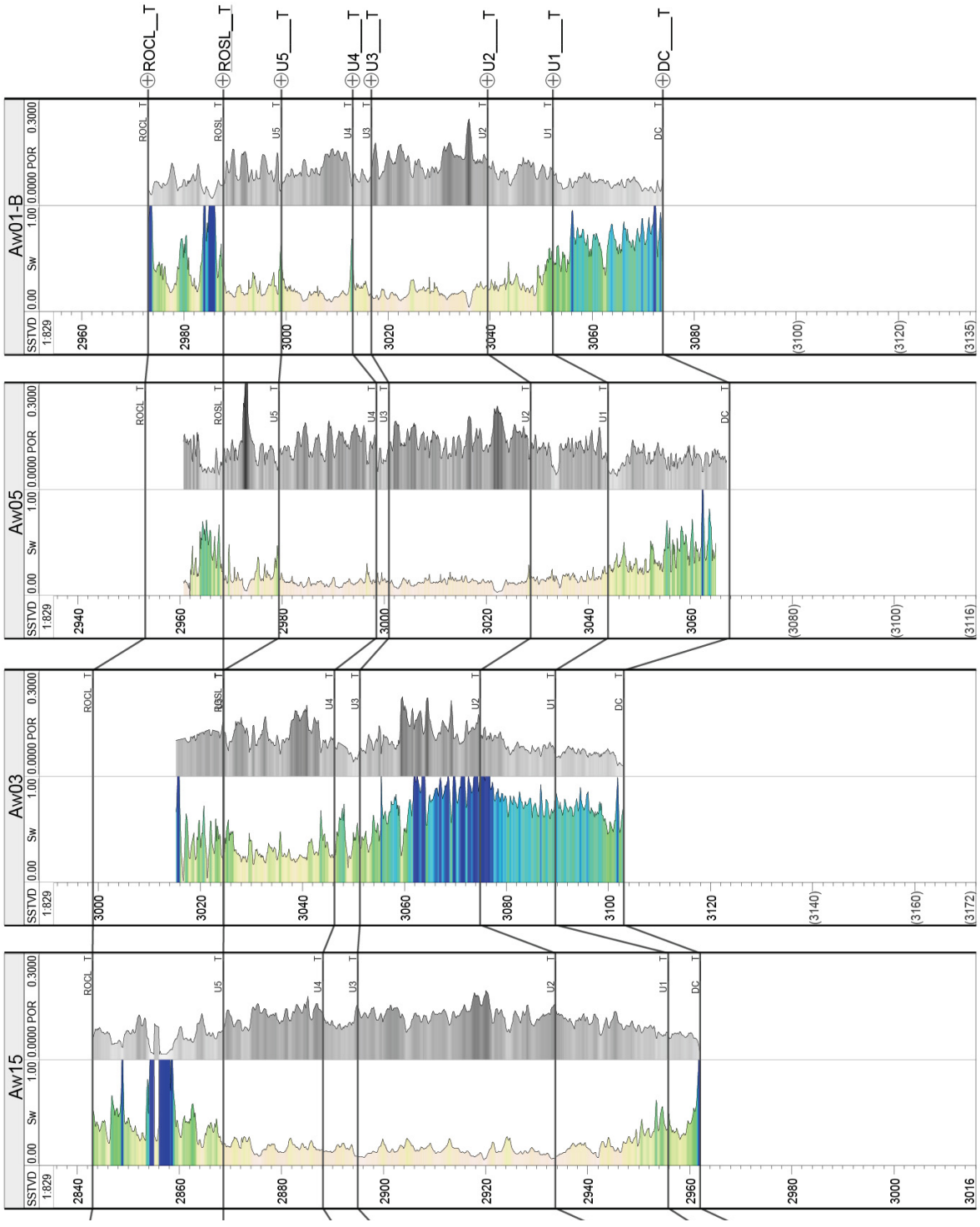

Appendix A4-05: Cross section of field B for wells Bw01, Bw07, Bw04 and Bw08 created with PETREL. The top of the Upper Slochteren Formation (ROSL_T) is used as reference horizon. Sw = Water saturation [%]. Por = Porosity [%].

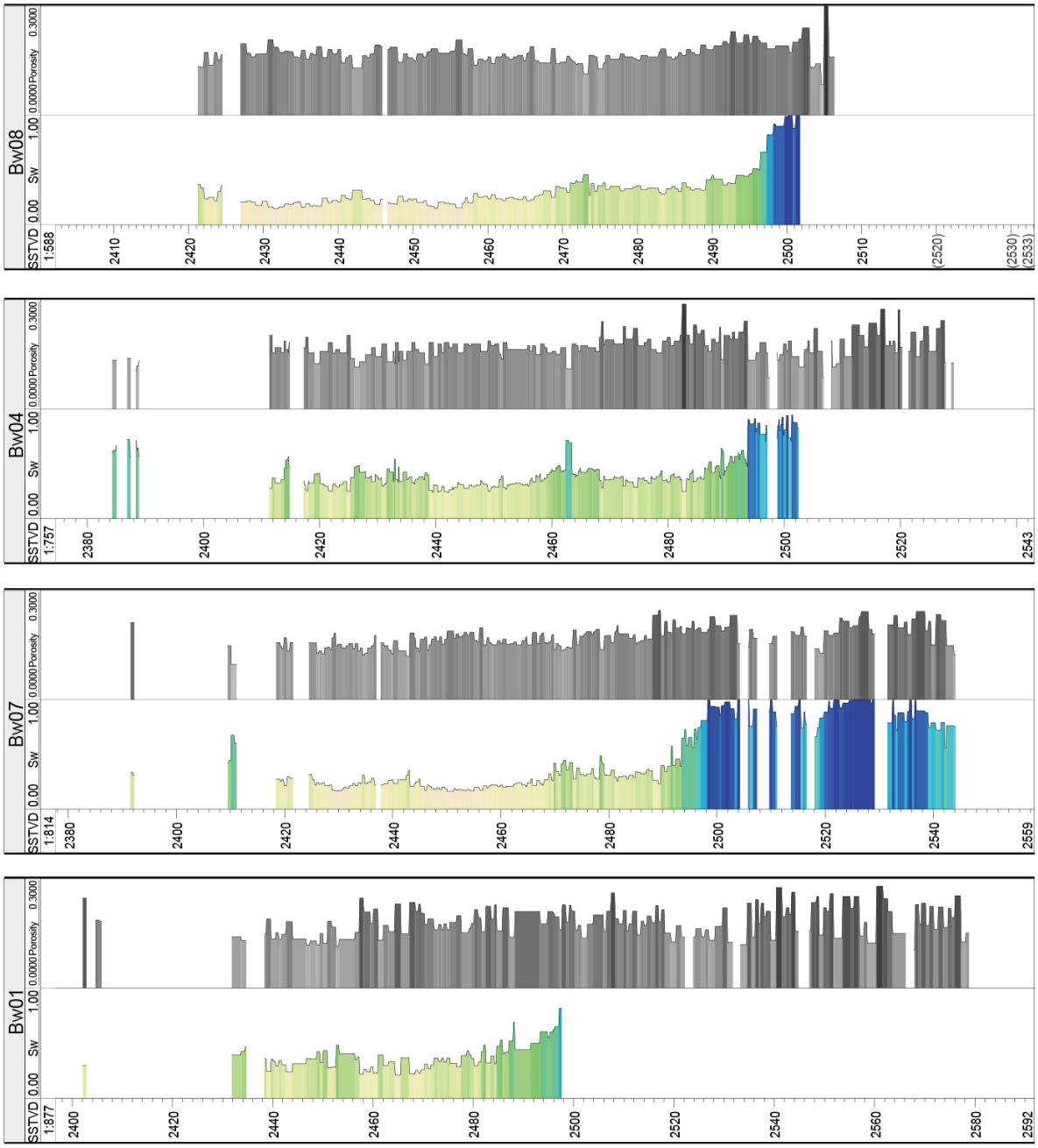

Appendix A4-06: Cross section of field C for wells Cw02, Cw03 and Cw04 created with PETREL. The top of the Upper Slochteren Formation (ROSLU) is used as reference horizon. Sw = Water saturation [%]. Por = Porosity [%].

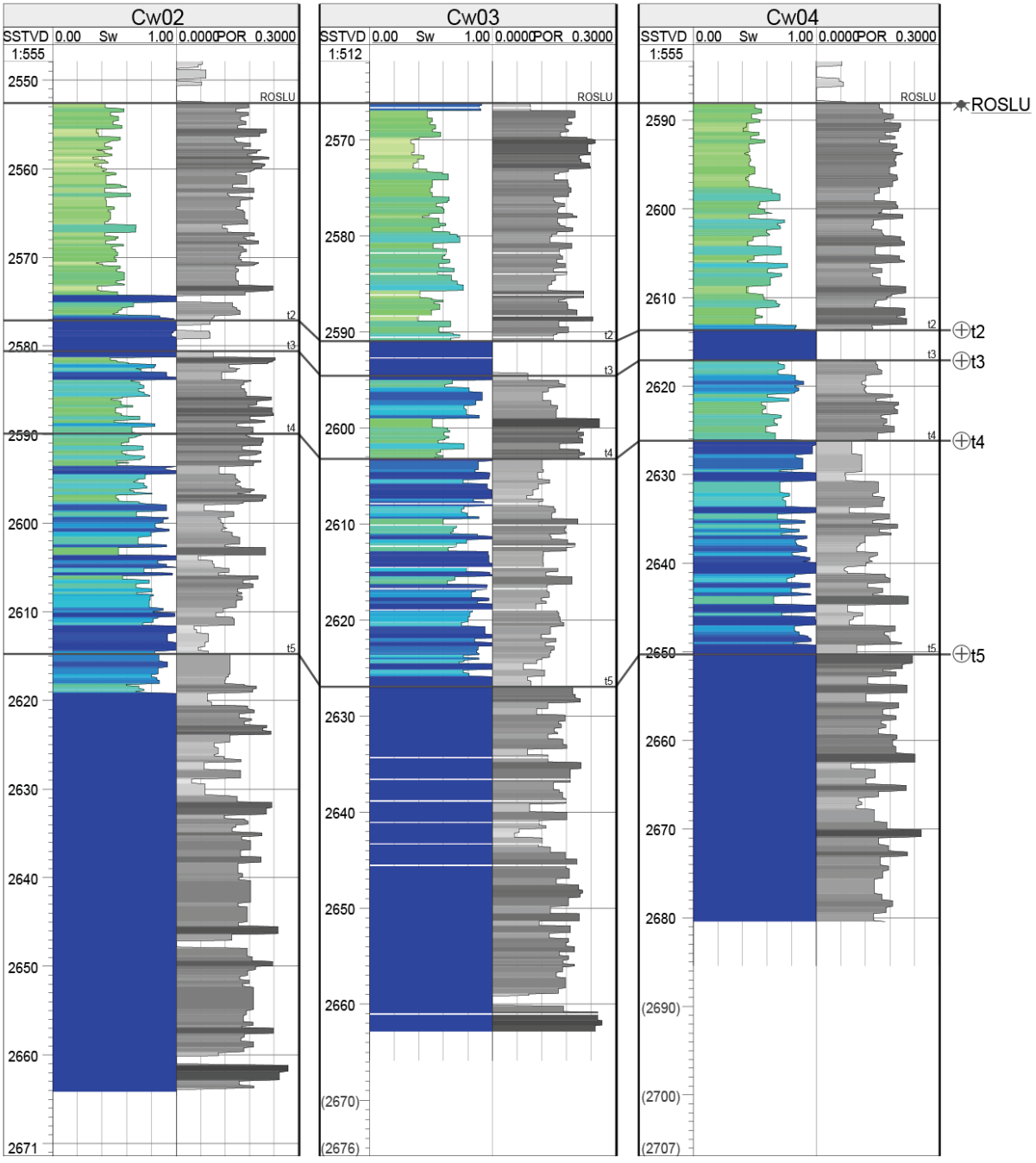

Appendix B

B1 Example for X-Ray diffraction pattern of sample Cw02-01

B2 Infrared spectroscopy for kaolinite determination

B3 Results of PHREEQCi Modelling
- 01 Volumetric mineralogy data set
- 02 Effective mineralogy data set
- 03 to 40 Sensitivity analyses

Appendix B1-01: X-Ray diffraction diagram of the < 2µm fraction, sample Cw02-01.

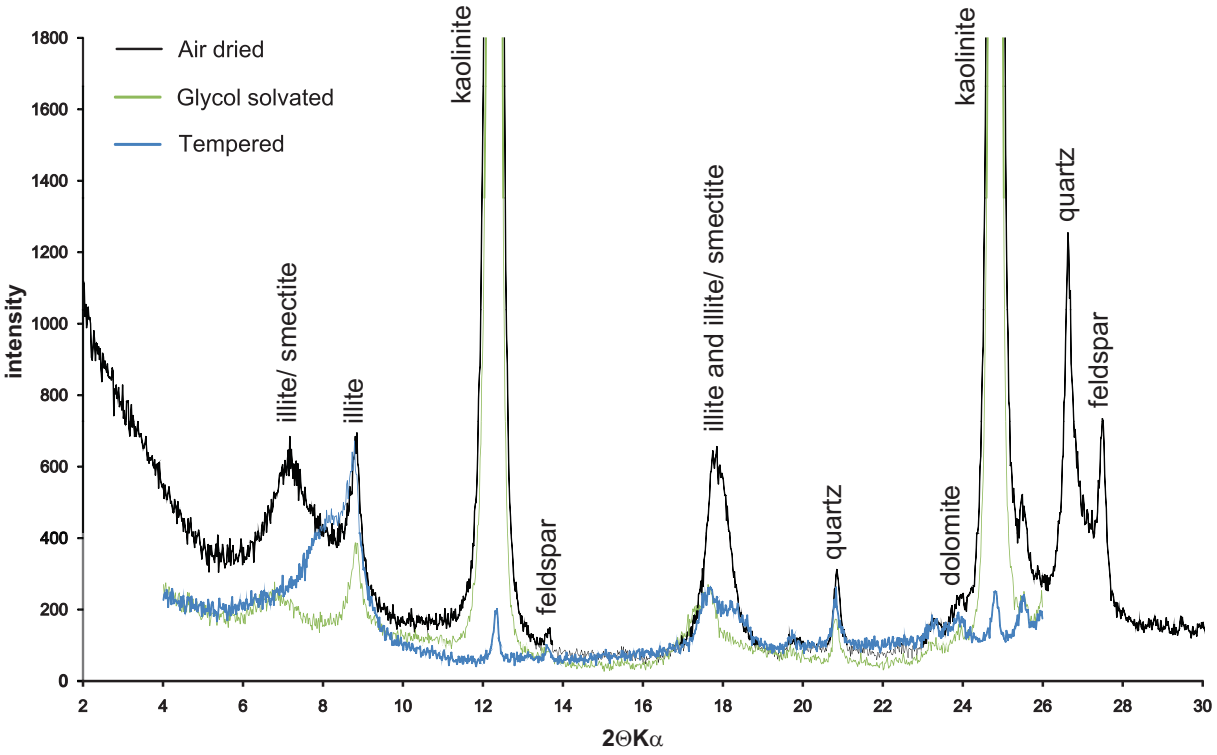

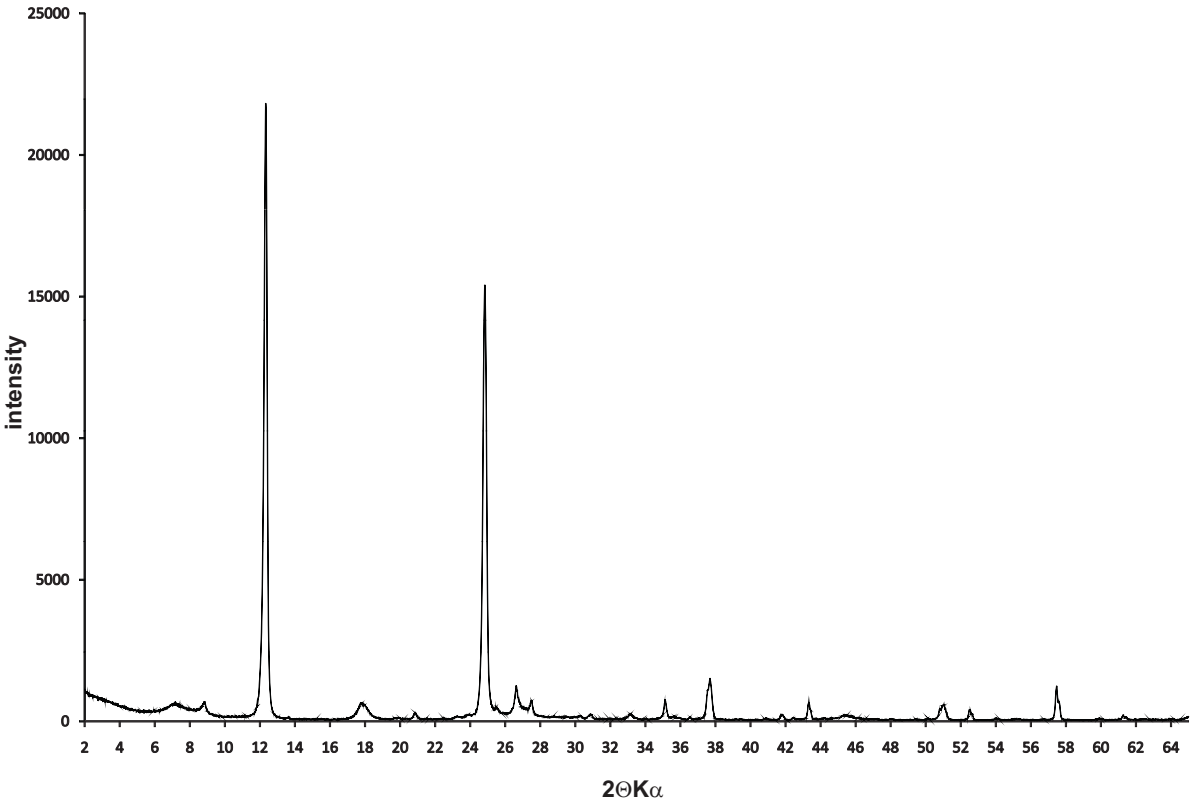

Appendix B2: Results of local IR-Spectroscopy for thin section Bw01-02-01. Image A shows the optical microscopic image with kaolinite in the pore space. Intensity at wavelength of B: 800 cm^{-1};C: 1400 cm^{-1} and D: 3700 cm^{-1}. Image D indicates the presence of kaolinite (red to orange colour).

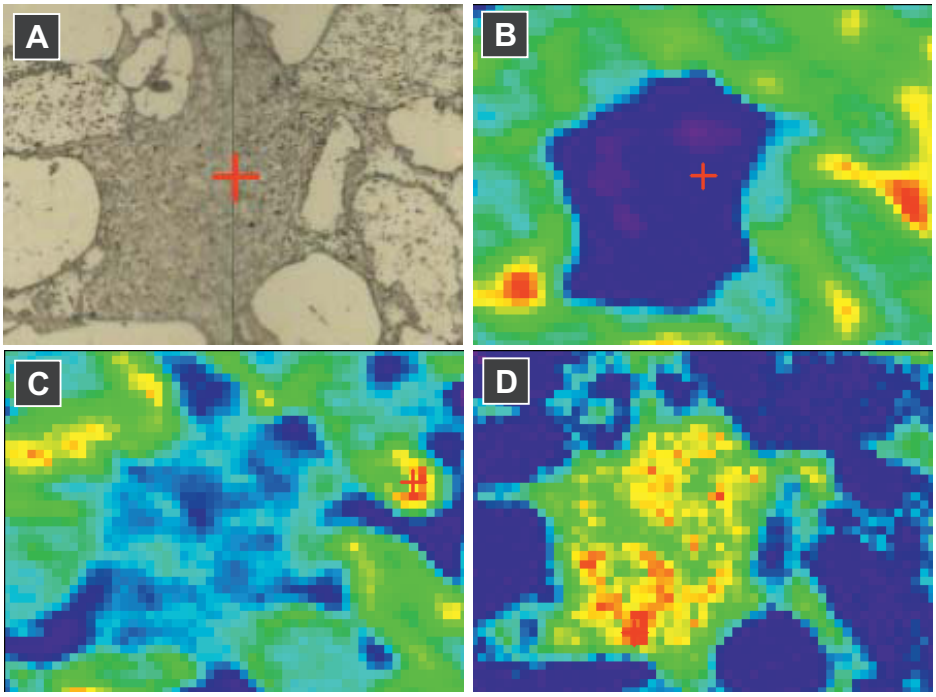

Appendix B3 – PHREEQCi modelling results

Test scenarios

1 Volumetric mineralogy data (VOL)
2 Effective mineralogy data (EFF)

Sensitivity analysis (please regard to the enclosed CD-ROM)

3	VOL	Model runs without CO_2
4	EFF	Model runs without CO_2
5	VOL	Initial equilibrium between rock and fluid
6	EFF	Initial equilibrium between rock and fluid
7	VOL	Changing initial fluid composition to lower salinity
8	EFF	Changing initial fluid composition to lower salinity
9	VOL	Changing temperature to 20°C
10	VOL	Changing temperature to 50°C
11	EFF	Changing temperature to 20°C
12	EFF	Changing temperature to 50°C
13	VOL	Changing pressure to 10 bar
14	VOL	Changing pressure to 50 bar
15	VOL	Changing pressure to 300 bar
16	EFF	Changing pressure to 10 bar
17	EFF	Changing pressure to 50 bar
18	EFF	Changing pressure to 300 bar
19	VOL	Changing the water-rock-ratio to 5% water saturation
20	VOL	Changing the water-rock-ratio to 50% water saturation
21	VOL	Changing the water-rock-ratio to 75% water saturation
22	VOL	Changing the water-rock-ratio to 100% water saturation
23	EFF	Changing the water-rock-ratio to 5% water saturation
24	EFF	Changing the water-rock-ratio to 50% water saturation
25	EFF	Changing the water-rock-ratio to 75% water saturation
26	EFF	Changing the water-rock-ratio to 100% water saturation
27	VOL	Changing the carbonate content to 10% Dolomite, 10% Ankerite and 10% Siderite
28	EFF	Changing the carbonate content to 10% Dolomite, 10% Ankerite and 10% Siderite
29	VOL	Changing the carbonate content to 30% Dolomite, 0% Ankerite and 0% Siderite
30	EFF	Changing the carbonate content to 30% Dolomite, 0% Ankerite and 0% Siderite
31	VOL	Removing hematite from the initial mineral assemblage
32	EFF	Removing hematite from the initial mineral assemblage
33	VOL	Removing galena from the initial mineral assemblage
34	EFF	Removing galena from the initial mineral assemblage
35	VOL	Adding 10% anhydrite to the initial mineral assemblage
36	EFF	Adding 10% anhydrite to the initial mineral assemblage
37	VOL	Removing anhydrite and barite from the initial mineral assemblage
38	EFF	Removing anhydrite and barite from the initial mineral assemblage
39	EFF	Removing anhydrite, barite and galena from the initial mineral assemblage
40	VOL	Removing 50% quartz from the initial mineral assemblage
41	EFF	Removing 50% quartz from the initial mineral assemblage
42	VOL	Adding 10% K-feldspar to the initial mineral assemblage
43	EFF	Adding 10% K-feldspar to the initial mineral assemblage
44	VOL	Removing K-feldspar from the initial mineral assemblage

Appendix C

C1 Sample list
- 01 Grain size and rock colour
- 02 Applied methods

C2 Petrographic analyses

C3 Porosity and permeability data

C4 Electron microprobe analyses
- 01 Silica minerals
- 02 Carbonate minerals

C5 Total digestions of sandstone samples

C6 Pore lining image analysis

C7 BET surface area

C8 Natural gas composition from field A

Appendix C1-01: Samples investigated in this study from field A, B and C. Grain size and the rock colour after the "Rock Color Chart of the Geological Society of America" are listed.

Field A

well	sample	depth [m]	core	gr. size [mm]	colour
Aw02	1	2956.90	3	0.25-0.35	light olive gray (5 Y 6/1)
Aw02	2	2961.00	3	0.177-0.35	light olive gray (5 Y 6/1)
Aw02	3	2968.31	3	0.5-0.71	light olive gray (5 Y 6/1)
Aw02	4	2955.20	3	0.177-0.25	olive gray (5 Y 4/1)
Aw02	5	2982.17	5	0.71-1.0	light olive gray (5 Y 6/1)
Aw02	6	2982.02	5	0.35-0.50	olive gray (5 Y 4/1)
Aw02	7	2974.02	5	0.35-0.5	pale yellowish brown (10 YR 4/2)
Aw02	8	2963.91	3	0.35-0.50	light olive gray (5 Y 6/1) to pale yell. brown (10 YR 6/2)
Aw02	9	2973.31	4	0.5-0.71	light olive gray (5 Y 6/1)
Aw02	10	2973.41	4	0.25-0.35	pale yell. brown (10 YR 4/2) to light olive gray (5 Y 6/1)
Aw02	11	2977.90	5	0.177-0.25	pinkish gray (5 YR 8/1) to yell. gray (5 Y 8/1)
Aw02	12	2983.25	5	0.35-0.5	light olive gray (5 Y 6/1)
Aw03	1	3137.46	2	0.35-2.0	olive gray (5 Y 4/1) (varying colour of rock fragments)
Aw04	1	2973.47	1	0.177-0.25	pale yellowish brown (10 YR 6/2)
Aw04	2	2974.32	1	0.177-0.25	pale yellowish brown (10 YR 6/2)
Aw04	3	2993.95	2	0.35-0.5	pale yellowish brown (10 YR 4/2)
Aw04	4	2996.10	2	0.35-0.50	light olive gray (5 Y 6/1)
Aw05	1	3253.86	9	0.35-0.5	olive gray (5 Y 4/1)
Aw05	2	3201.50	4	0.35-2.0	olive gray (5 Y 4/1) (varying colour of rock fragments)
Aw05	3	3186.25	2	0.25-2.0	olive gray (5 Y 4/1) (varying colour of rock fragments)
Aw05	4	3255.76	9	0.25-0.35	light olive gray (5 Y 6/1)
Aw05	5	3251.99	9	0.35-2.0	olive gray (5 Y 4/1) (varying colour of rock fragments)
Aw05	6	3245.80	8	0.177-0.25	light olive gray (5 Y 6/1)
Aw05	7	3211.30	5	0.35-0.71	olive gray (5 Y 4/1)
Aw05	8	3204.98	5	0.25-0.35	light olive gray (5 Y 6/1)

Field B

well	sample	depth [m]	core	gr. size [mm]	colour
Bw01	2	2540.05	3	0.25-0.35	pale reddish brown (10 R 5/4)
Bw01	3	2487.00	1	0.35-0.5	pale red to pale reddish brown (10R 7/4 to 10 R 5/4)
Bw02	1	2981.16	12	0.25-0.35	pale red (5 R 6/2)
Bw02	2	2954.88	10	0.5-0.71	pale yellowish brown (10 YR 6/2)
Bw02	3	2880.00	6	0.177-0.5	grayish orange pink (5 YR 7/2) to pale brown (5 YR 5/2)
Bw02	4	2880.19	6	0.25-5.0	pale brown (5 YR 5/2)
Bw02	5	3015.17	14	0.35-0.5	pale red. brown (10 R 5/4) to mod. red. brown (10 R 4/6)
Bw03	1	2498.70	5	0.71-1.0	very pale oran. (10 YR 8/2) to pale yell. brown (10YR 6/2)
Bw03	2	2500.25	1	0.25-0.35	very pale oran. (10 YR 8/2) to pale yell. brown (10YR 6/2)
Bw03	3	2521.02	2	0.177-0.35	pale red (5 R 6/2)
Bw03	4	2522.45	2	0.25-0.65	pale yellowish brown (10 YR 6/2)

Appendix C1-01: Continuation

Field C

well	sample	depth [m]	core	gr. size [mm]	colour
Cw01	1	2600.80	6	0.2-0.35	pale red (5 R 6/2)
Cw01	2	2754.75	13	0.25-0.35	very pale orange (10 YR 8/2)
Cw02	1	3293.88	2	0.5-0.71	pale red (5 R 6/2)
Cw02	2	3372.40	4	0.25-0.35	pale red (5 R 6/2)
Cw03	1	2974.17	1	0.35-0.5	very pale orange (10 YR 8/2) to gr. orange (10 YR 7/4)
Cw03	2	2972.68	1	0.177-0.25	very pale orange (10 YR 8/2) to gr. orange (10 YR 7/4)
Cw04	1	2711.35	1	0.177-0.5	pale red (10 R 6/2) to grayish red (5 R 4/2)
Cw04	2	2711.30	1	0.25-0.35	pale brown (5 YR 5/2)
Cw04	3	2712.30	1	0.125-0.25	grayish orange pink (5 YR 7/2)
Cw04	4	2715.53	1	0.125-0.25	grayish orange pink (5 YR 7/2)
Cw04	5	2714.80	1	0.35-0.5	pale red (5 R 6/2)

Appendix C1-02: Applied methods for the samples investigated in this study. TS = Thin section analysis (covered or polished); EMS = Electron microscope analysis; BET = Surface area measurement; HR-SEM = High resolution secondary electron microscopy; IR-S = Infrared-spectroscopy; XRD = X-Ray diffractometry; ICP = ICP-MS and -OES analysis; IA = Pore lining image analysis; M = not enough material for XRD analysis.

Field A

well	sample	TS	EMS	BET	HR-SEM	IR-S	XRD	ICP	IA
Aw02	1	x		x			M	x	x
Aw02	2	x		x			M	x	x
Aw02	3	x	x	x			M	x	
Aw02	4			x			M		x
Aw02	5								
Aw02	6			x			M		x
Aw02	7								
Aw02	8	x		x			M		
Aw02	9								
Aw02	10								
Aw02	11								
Aw02	12	x		x	x		M	x	x
Aw03	1	x	x	x	x		x	x	
Aw04	1			x			M		
Aw04	2	x	x	x			M	x	x
Aw04	3			x			M		
Aw04	4	x	x	x			M	x	x
Aw05	1	x		x			M	x	x
Aw05	2								
Aw05	3	x		x			M	x	x
Aw05	4	x		x			x	x	x
Aw05	5								
Aw05	6	x	x						
Aw05	7	x		x			x	x	
Aw05	8	x	x						

Appendix C1-02: Continuation

Field B

well	sample	TS	EMS	BET	REM	IR-S	XRD	ICP	IA
Bw01	1	x		x			x	x	x
Bw01	2	x	x	x	x	x	x	x	
Bw01	3								
Bw02	1	x		x			x	x	x
Bw02	2			x			M		x
Bw02	3			x	x		M		x
Bw02	4								
Bw02	5	x	x	x			x	x	x
Bw03	1								
Bw03	2								
Bw03	3								
Bw03	4								

Field C

well	sample	TS	EMS	BET	REM	IR-S	XRD	ICP	IA
Cw01	1								
Cw01	2								
Cw02	1	x	x	x	x		x	x	
Cw02	2								
Cw03	1	x		x			x	x	
Cw03	2	x		x	x		M		
Cw04	1	x		x			x	x	
Cw04	2	x							
Cw04	3					x	x		
Cw04	4						x		
Cw04	5	x		x	x		x	x	

Appendix C2: Petrographic data derived from thin section analysis and point counting of 300 points per thin section. For abbr. compare "List of abbreviations.

Field	**A**	**A**	**A**	**A**	**A**	**A**	**A**
well	**Aw01**	**Aw01**	**Aw01**	**Aw01**	**Aw01**	**Aw01**	**Aw01**
sample	Aw01-01	Aw01-02	Aw01-03	Aw01-04	Aw01-05	Aw01-06	Aw01-07
depth [m]	2924.52	2932.78	2936.30	2943.05	2944.11	2976.3	2996.55
Qz_m	33,0	38,3	30,3	33,0	33,0	43,7	39,7
Qz_p	3,7	12,7	10,0	10,0	6,3	7,7	10,3
Qc	<1.0	4,0	1,0	4,0	3,0	4,0	2,0
Kfsp	13,0	9,0	10,0	8,3	9,6	9,0	11,0
Plag	1,5	<1.0	<1.0	<1.0	<1.0	1,3	<1.0
Lv_{fel}	1,0	1,0	1,0	1,0	1,0	2,0	2,0
Lv_{maf}	1,0	1,0	0,0	<1.0	0,0	1,0	1,0
Lm_{pel}	<1.0	1,0	1,0	10,0	2,0	<1.0	<1.0
L_{QFG}	1,7	5,0	6,0	4,0	8,0	6,0	2,0
Ls_{psam}	0,0	1,0	0,0	0,0	<1.0	<1.0	<1.0
Ls_{pel}	<1.0	0,0	0,0	0,0	0,0	0,0	0,0
Lil	0,0	0,0	1,3	0,0	<1.0	0,0	0,0
Lc	0,0	0,0	0,0	0,0	0,0	0,0	0,0
Muscovite	0,0	<1.0	<1.0	<1.0	0,0	<1.0	0,0
Fe-oxide	4,5	5,7	14,6	4,3	3,7	6,7	5,3
Qz_{au}	0,0	2,0	3,3	4,7	3,0	6,7	6,0
$Kfsp_{au}$	0,0	0,0	0,0	0,0	0,0	0,0	0,0
Carbonate	38,0	3,0	14,0	10,3	4,3	3,0	7,0
Anhydrite	0,0	0,0	0,0	0,0	0,0	<1.0	2,3
Barite	?	?	?	?	?	?	?
Kaol "booklets"	0,0	<1.0	0,0	0,0	1,7	0,0	2,0
Radial kaol	0,0	0,0	0,0	0,0	0,0	0,0	0,0
IC	1,3	4,7	1,3	1,0	3,3	1,0	0,0
Bitumen	0,0	0,0	0,0	0,0	<1.0	0,0	0,0
Por_{inter}	1,0	11,0	6,0	8,7	19,3	6,0	6,0
Por_{intra}	<1.0	0,0	0,0	<1.0	1,3	1,3	3,3
Fsp leaching	+	+	+	+	++	+	+
Illitisation	-	-	-	-	-	-	-
Kaolinitisation	-	-	-	-	+	-	-
Σ (all)	99,7	99,4	99,8	99,3	99,5	99,4	99,9
Σ (authigenic min.)	43,8	15,4	33,2	20,3	16,0	17,4	22,6
Σ (detrital grains)	54,9	73,0	60,6	70,3	62,9	74,7	68,0
Σ (pore space)	1,0	11,0	6,0	8,7	20,6	7,3	9,3
IGV [%]	44,8	26,4	39,2	29,0	35,3	23,4	28,6
sorting	0,50	0,71	0,35	2,00	0,35	0,35	0,50
roundness	2-4	2-4	2-4	2-4	2-4	3-5	2-5
sphericity	low	low	low	low	low	low	low
grain contacts	1>2>rest	1>2>rest	1>2>rest	1>2>0	1>0>2	2>3>1	2>1>rest
grain size [µm]	71	216	108	218	229	203	258
facies	sheetfl.	channel	channel	channel	dune core	*no data*	dune base
facies_assumed	fluviatile	fluviatile	fluviatile	fluviatile	dune	dune	fluviatile

Appendix C2: Continuation

Field	**A**	**A**	**A**	**A**	**A**	**A**	**A**
well	**Aw02**	**Aw02**	**Aw02**	**Aw02**	**Aw02**	**Aw02**	**Aw02**
sample	Aw02-01	Aw02-02	Aw02-03	Aw02-04	Aw02-06	Aw02-08	Aw02-12
depth [m]	2956,90	2961,00	2968,31	2955,20	2982,02	2963,91	2983,25
Qz_m	38,0	40,7	40,0	39,0	40,7	39,3	43,7
Qz_p	16,0	16,7	16,7	10,7	15,0	21,7	15,3
Qc	2,0	3,0	2,0	1,0	1,0	3,0	2,0
Kfsp	7,7	6,7	8,3	8,3	7,3	6,0	8,7
Plag	<1.0	<1.0	0,0	1,0	<1.0	<1.0	<1.0
Lv_{fel}	1,7	3,0	1,3	2,0	2,0	2,3	1,0
Lv_{maf}	2,0	2,3	1,7	2,3	3,7	1,7	1,7
Lm_{pel}	<1.0	<1.0	1,0	0,0	0,0	<1.0	1,0
L_{QFG}	2,7	2,0	0,0	8,0	4,7	1,0	<1.0
Ls_{psam}	0,0	0,0	0,0	0,0	0,0	0,0	0,0
Ls_{pel}	0,0	0,0	0,0	<1.0	0,0	0,0	0,0
Lil	<1.0	0,0	0,0	0,0	0,0	0,0	0,0
Lc	0,0	0,0	0,0	0,0	0,0	0,0	0,0
Muscovite	0,0	0,0	<1.0	<1.0	<1.0	0,0	0,0
Fe-oxide	6,3	2,7	4,7	<1.0	<1.0	2,7	5,3
Qz_{au}	0,0	2,7	<1.0	<1.0	4,3	0,0	0,0
$Kfsp_{au}$	0,0	0,0	0,0	0,0	0,0	0,0	0,0
Carbonate	4,7	4,0	9,0	8,0	8,7	3,7	4,0
Anhydrite	0,0	0,0	0,0	0,0	2,3	<1.0	<1.0
Barite	?	?	<1.0	?	?	?	?
Kaol "booklets"	<1.0	1,0	<1.0	2,0	2,0	<1.0	3,3
Radial kaol	0,0	0,0	0,0	0,0	0,0	0,0	0,0
IC	0,0	2,0	0,0	<1.0	<1.0	1,7	<1.0
Bitumen	<1.0	<1.0	1,0	0,0	0,0	0,0	0,0
Por_{inter}	17,7	12,0	12,7	15,0	7,3	16,7	11,7
Por_{intra}	1,0	1,0	1,0	2,0	<1.0	<1.0	2,0
Fsp leaching	+	+	++	++	++	+	++
Illitisation	+	+	+	+	+	+	+
Kaolinitisation	-	-	-	-	-	-	-
Σ (all)	99,8	99,8	99,4	99,3	99,0	99,8	99,7
Σ (authigenic min.)	11,0	12,4	14,7	10,0	17,3	8,1	12,6
Σ (detrital grains)	70,1	74,4	71,0	72,3	74,4	75,0	73,4
Σ (pore space)	18,7	13,0	13,7	17,0	7,3	16,7	13,7
IGV [%]	28,7	24,4	27,4	25,0	24,6	24,8	24,3
sorting	1,00	1,00	1,00	0,50	0,71	0,50	0,50
roundness	3-5	3-5	3-4	3-5	3-5	3-5	4-5
sphericity	low	low	high	low	high	low	high
grain contacts	1>2>rest	2>1>rest	1>0>2	1>2>3	1>2>0	1>0>2	1>2>rest
grain size [µm]	178	174	192	117	194	320	225
facies	*no data*	*no data*	*no data*	*no data*	*no data*	*no data*	*no data*
facies_assumed	fluviatile	fluviatile	fluviatile	fluviatile	fluviatile	fluviatile	fluviatile

Appendix C2: Continuation

Field	**A**	**A**	**A**	**A**	**A**	**A**	**A**
well	**Aw03**	**Aw04**	**Aw04**	**Aw05**	**Aw05**	**Aw05**	**Aw05**
sample	Aw03-01	Aw04-02	Aw04-04	Aw05-01	Aw05-03	Aw05-04	Aw05-07
depth [m]	3137,46	2974,32	2996,10	3253,86	3186,25	3255,76	3211,30
Qz_m	38,7	36,0	41,0	38,7	28,0	44,7	31,7
Qz_p	21,3	13,3	15,0	18,3	21,0	12,0	17,0
Qc	1,7	2,0	2,0	0,0	1,0	1,0	1,0
Kfsp	9,0	7,3	7,3	2,7	7,3	6,3	5,7
Plag	<1.0	<1.0	<1.0	0,0	<1.0	<1.0	<1.0
Lv_{fel}	3,3	5,7	4,7	6,3	15,3	5,7	16,7
Lv_{maf}	<1.0	0,0	<1.0	0,0	1,7	0,0	1,0
Lm_{pel}	0,0	<1.0	1,0	0,0	0,0	<1.0	0,0
L_{QFG}	0,0	<1.0	0,0	2,3	0,0	4,3	0,0
Ls_{psam}	<1.0	0,0	0,0	0,0	1,0	0,0	0,0
Ls_{pel}	0,0	0,0	0,0	0,0	<1.0	0,0	0,0
Lil	0,0	0,0	0,0	0,0	0,0	<1.0	0,0
Lc	0,0	0,0	0,0	0,0	0,0	0,0	0,0
Muscovite	0,0	<1.0	0,0	0,0	0,0	<1.0	<1.0
Fe-oxide	0,0	4,3	5,0	0,0	<1.0	1,0	0,0
Qz_{au}	0,0	0,0	0,0	1,7	1,7	2,0	1,0
$Kfsp_{au}$	0,0	0,0	0,0	0,0	0,0	0,0	0,0
Carbonate	9,0	5,3	3,0	1,0	4,3	12,7	2,0
Anhydrite	<1.0	0,0	1,3	<1.0	1,0	4,7	0,0
Barite	?	?	?	?	?	?	?
Kaol "booklets"	<1.0	<1.0	1,0	1,7	3,3	<1.0	2,7
Radial kaol	0,0	0,0	0,0	0,0	0,0	0,0	0,0
IC	0,0	0,0	<1.0	0,0	1,7	1,3	1,0
Bitumen	5,0	1,7	0,0	0,0	3,0	0,0	5,3
Por_{inter}	11,0	23,0	17,3	26,7	7,7	4,0	12,0
Por_{intra}	<1.0	1,3	1,0	-	1,7	<1.0	2,7
Fsp leaching	+	++	++	+	++	+	++
Illitisation	+	+	+	-	-	-	+
Kaolinitisation	-	-	-	-	-	-	-
Σ (all)	99,0	99,9	99,7	99,4	99,7	99,7	99,8
Σ (authigenic min.)	14,0	11,3	10,3	4,4	15,0	21,7	12,0
Σ (detrital grains)	73,0	63,3	72,0	68,3	75,3	73,0	73,1
Σ (pore space)	11,0	24,3	18,3	26,7	9,4	4,0	14,7
IGV [%]	25,0	30,0	22,7	31,1	22,7	24,7	24,0
sorting	1,00	0,35	0,71	0,35	2,00	0,71	0,71
roundness	3-5	2-4	3-5	3-5	2-5	3-4	3-5
sphericity	high	high	low	high	low tohigh	low	low to high
grain contacts	1>2>rest	1>2>0	1>2>0	0>1>2	2>3>1	2>1>3	2>1>3
grain size [µm]	377	117	249	422	650	263	580
facies	*no data*	sheetfl.	dry sf	*no data*	*no data*	*no data*	*no data*
facies_assumed	fluviatile	fluviatile	dry sf	fluviatile	?	fluviatile	?

Appendix C2: Continuation

Field	**B**	**B**	**B**	**B**	**B**	**B**	**B**
well	**Bw01**	**Bw01**	**Bw01**	**Bw01**	**Bw01**	**Bw01**	**Bw01**
sample	Bw01-01	Bw01-02	Bw01-03	Bw01-04	Bw01-05	Bw01-06	Bw01-07
depth [m]	2545,60	2540,05	2539,70	2541,70	2543,70	2545,30	2546,60
Qz_m	35,0	29,7	33,7	28,0	37,7	38,7	38,7
Qz_p	11,3	9,0	15,7	31,7	14,0	21,3	17,3
Qc	0,0	1,0	3,0	3,0	1,0	1,7	4,0
Kfsp	7,0	5,3	1,7	<1.0	8,3	3,0	7,7
Plag	<1.0	0,0	<1.0	0,0	0,0	<1.0	0,0
Lv_{fel}	12,0	12,0	2,3	<1.0	3,3	3,7	1,3
Lv_{maf}	0,0	<1.0	0,0	<1.0	0,0	<1.0	0,0
Lm_{pel}	0,0	0,0	1,0	0,0	<1.0	<1.0	<1.0
L_{QFG}	0,0	0,0	4,7	2,3	2,3	2,3	1,3
Ls_{psam}	0,0	0,0	0,0	<1.0	<1.0	<1.0	0,0
Ls_{pel}	0,0	0,0	0,0	0,0	0,0	0,0	0,0
Lil	0,0	0,0	0,0	0,0	0,0	0,0	0,0
Lc	0,0	0,0	0,0	0,0	0,0	0,0	0,0
Muscovite	<1.0	0,0	<1.0	0,0	<1.0	0,0	0,0
Fe-oxide	<1.0	13,7	15,3	8,7	13,0	0,0	0,0
Qz_{au}	<1.0	0,0	<1.0	1,3	1,3	0,0	<1.0
$Kfsp_{au}$	0,0	0,0	0,0	0,0	0,0	0,0	0,0
Carbonate	2,0	4,7	8,3	9,0	11,3	12,0	2,0
Anhydrite	0,0	0,0	0,0	0,0	0,0	0,0	<1.0
Barite	?	<1.0	?	?	?	?	?
Kaol "booklets"	3,8	6,6	6,0	5,0	2,3	1,3	6,6
Radial kaol	0,0	0,0	0,0	0,0	0,0	<1.0	0,0
IC	1,3	<1.0	0,0	0,0	0,0	0,0	1,0
Bitumen	<1.0	0,0	0,0	0,0	<1.0	0,0	0,0
Por_{inter}	22,2	10,3	7,9	9,3	5,4	13,7	16,3
Por_{intra}	5,0	6,7	<1.0	1,0	<1.0	1,3	3,0
Fsp leaching	+++	++	+	-	+	+	+
Illitisation	+	++	-	-	-	+	+
Kaolinitisation	-	-	-	-	-	-	++
Σ (all)	99,6	99,0	99,6	99,3	99,9	99,0	99,2
Σ (authigenic min.)	7,1	25,0	29,6	24,0	27,9	13,3	9,6
Σ (detrital grains)	65,3	57,0	62,1	65,0	66,6	70,7	70,3
Σ (pore space)	27,2	17,0	7,9	10,3	5,4	15,0	19,3
IGV [%]	29,3	35,3	37,5	33,3	33,3	27,0	25,9
sorting	1,00	0,50	1,00	2,00	0,50	2,00	1,00
roundness	1-4	3-5	1-3	3-5	3-5	3-5	2-4
sphericity	low to high	low	low	low to high	low to high	low to high	low to high
grain contacts	1>2>rest	1>2>rest	2>1>rest	1>0>2	1>2>3	1>2>rest	2>1>0
grain size [µm]	195	265	218	480	178	418	293
facies	*no data*	*no data*	*no data*	*no data*	*no data*	*no data*	*no data*
facies_assumed	fluviatile	dune	fluviatile	fluviatile	fluviatile	dune	dune

Appendix C2: Continuation

Field	**B**	**B**	**B**	**B**	**B**	**B**	**B**
well	**Bw01**	**Bw01**	**Bw01**	**Bw01**	**Bw01**	**Bw01**	**Bw01**
sample	Bw01-08	Bw01-09	Bw01-10	Bw01-11	Bw01-12	Bw01-13	Bw01-14
depth [m]	2549,30	2551,20	2552,30	2553,20	2556,00	2557,90	2559,90
Qz_m	43,7	39,3	45,0	36,3	41,0	39,7	37,0
Qz_p	12,3	15,3	13,7	12,0	13,7	13,7	14,7
Qc	1,0	1,7	2,3	1,3	1,0	2,0	1,3
Kfsp	5,7	3,3	5,3	4,3	4,0	2,0	4,0
Plag	0,0	<1.0	0,0	0,0	<1.0	<1.0	0,0
Lv_{fel}	2,7	2,3	2,3	4,0	4,0	2,7	3,7
Lv_{maf}	0,0	<1.0	<1.0	0,0	0,0	0,0	0,0
Lm_{pel}	0,0	<1.0	<1.0	<1.0	1,0	1,0	1,0
L_{QFG}	<1.0	1,7	3,7	3,0	1,7	2,3	3,3
Ls_{psam}	0,0	<1.0	<1.0	0,0	0,0	0,0	<1.0
Ls_{pel}	0,0	0,0	0,0	0,0	0,0	0,0	0,0
Lil	0,0	0,0	<1.0	0,0	0,0	1,0	1,7
Lc	0,0	0,0	0,0	0,0	0,0	0,0	0,0
Muscovite	<1.0	0,0	0,0	0,0	0,0	0,0	0,0
Fe-oxide	0,0	8,7	2,0	7,7	4,3	2,0	1,0
Qz_{au}	<1.0	1,7	<1.0	<1.0	<1.0	<1.0	<1.0
$Kfsp_{au}$	0,0	0,0	0,0	0,0	0,0	0,0	0,0
Carbonate	19,0	1,0	3,0	1,7	0,0	<1.0	0,0
Anhydrite	0,0	0,0	0,0	0,0	5,3	<1.0	2,7
Barite	?	?	?	?	?	?	?
Kaol "booklets"	2,7	7,7	3,0	7,7	8,0	10,2	7,8
Radial kaol	0,0	1,0	0,0	<1.0	0,0	<1.0	<1.0
IC	1,0	<1.0	7,3	1,0	3,3	1,3	6,0
Bitumen	0,0	0,0	0,0	0,0	0,0	0,0	0,0
Por_{inter}	8,0	12,0	8,0	16,7	8,3	18,8	12,3
Por_{intra}	3,7	3,3	3,7	4,0	4,3	2,3	2,7
Fsp leaching	+	+	+	+	+	++	+
Illitisation	+	+	+	+	+	++	+
Kaolinitisation	+	-	-	-	+	+	-
Σ (all)	99,8	99,0	99,3	99,7	99,9	99,0	99,2
Σ (authigenic min.)	22,7	20,1	15,3	18,1	20,9	13,5	17,5
Σ (detrital grains)	65,4	63,6	72,3	60,9	66,4	64,4	66,7
Σ (pore space)	11,7	15,3	11,7	20,7	12,6	21,1	15,0
IGV [%]	30,7	32,1	23,3	34,8	29,2	32,3	29,8
sorting	2,00	0,50	1,00	0,71	0,35	0,35	0,35
roundness	1-3	2-4	3-5	3-5	3-5	3-5	3-6
sphericity	low	low	low	low to high	low to high	low to high	low to high
grain contacts	2>1>3	2>1>3	2>1>3	1>2>0	1>0>2	1>0>2	1>2>3
grain size [µm]	142	241	289	254	310	271	344
facies	*no data*	*no data*	*no data*	*no data*	*no data*	*no data*	*no data*
facies_assumed	dry sf	dry sf	fluviatile	dune	dune	dune	dune

Appendix C2: Continuation

Field	**B**	**B**	**B**	**B**	**B**	**B**	**B**
well	**Bw01**	**Bw01**	**Bw01**	**Bw01**	**Bw01**	**Bw02**	**Bw02**
sample	Bw01-15	Bw01-16	Bw01-17	Bw01-18	Bw01-19	Bw02-01	Bw02-02
depth [m]	2563,90	2565,60	2566,90	2568,70	2574,90	2981,16	2954,88
Qz_m	42,3	36,0	38,0	38,3	40,0	43,0	39,3
Qz_p	8,0	14,7	10,0	9,3	12,3	7,0	16,3
Qc	1,7	2,0	1,3	2,3	<1.0	0,0	<1.0
Kfsp	4,7	6,0	6,0	7,3	10,0	7,3	3,3
Plag	0,0	0,0	0,0	0,0	0,0	0,0	0,0
Lv_{fel}	1,7	1,3	2,6	3,7	7,3	5,3	8,3
Lv_{maf}	0,0	<1.0	0,0	0,0	0,0	0,0	<1.0
Lm_{pel}	1,0	<1.0	1,0	<1.0	<1.0	0,0	0,0
L_{QFG}	3,3	2,3	3,3	3,0	2,0	3,0	3,7
Ls_{psam}	<1.0	0,0	0,0	<1.0	0,0	0,0	0,0
Ls_{pel}	0,0	0,0	0,0	0,0	0,0	0,0	0,0
Lil	1,3	<1.0	<1.0	0,0	0,0	0,0	0,0
Lc	0,0	0,0	0,0	0,0	0,0	0,0	0,0
Muscovite	<1.0	0,0	0,0	<1.0	1,0	0,0	<1.0
Fe-oxide	10,0	9,3	18,0	10,3	9,3	5,7	<1.0
Qz_{au}	<1.0	0,0	<1.0	<1.0	<1.0	0,0	<1.0
$Kfsp_{au}$	0,0	0,0	0,0	<1.0	0,0	0,0	0,0
Carbonate	7,0	4,0	4,7	18,3	2,3	4,7	3,6
Anhydrite	0,0	<1.0	0,0	<1.0	<1.0	0,0	0,0
Barite	?	?	?	?	?	?	?
Kaol "booklets"	5,3	9,0	5,3	1,0	3,0	7,6	5,7
Radial kaol	0,0	0,0	<1.0	0,0	0,0	0,0	0,0
IC	2,0	0,0	0,0	0,0	0,0	0,0	0,0
Bitumen	0,0	0,0	0,0	0,0	0,0	0,0	0,0
Por_{inter}	9,0	11,5	6,7	5,7	10,3	14,7	16,9
Por_{intra}	2,7	3,3	2,7	0,0	2,3	1,7	2,3
Fsp leaching	+	-	+	+	+	++	++
Illitisation	+	+	+	+	+	+	+
Kaolinitisation	-	-	-	-	-	++	+
Σ (all)	100,0	99,4	99,6	99,2	99,8	100,0	99,4
Σ (authigenic min.)	24,3	22,3	28,0	29,6	14,6	18,0	9,3
Σ (detrital grains)	64,0	62,3	62,2	63,9	72,6	65,6	70,9
Σ (pore space)	11,7	14,8	9,4	5,7	12,6	16,4	19,2
IGV [%]	33,3	33,8	34,7	35,3	24,9	32,7	26,2
sorting	0,71	0,35	0,71	0,71	0,71	0,35	1,00
roundness	2-4	3-5	2-4	2-4	2-4	3-5	3-5
sphericity	low to high	low to high	low to high	low	low	low	low
grain contacts	2>3>1	1>2>3	1>2>rest	1>3>2	2>3>1	1>2>0	1>2>3
grain size [µm]	124	301	210	102	195	171	108
facies	*no data*	*no data*	*no data*	*no data*	*no data*	*no data*	*no data*
facies_assumed	fluviatile	dry sf	dune	wet sf	wet sf	dry sf	fluviatile

Appendix C2: Continuation

Field	**B**	**B**	**C**	**C**	**C**	**C**	**C**
well	**Bw02**	**Bw02**	**Cw02**	**Cw03-03**	**Cw03-03**	**Cw03-03**	**Cw03-03**
sample	Bw02-03	Bw02-05	Cw02-01	Cw03-01	Cw03-03	Cw03-04	Cw03-05
depth [m]	2880,00	3015,17	3293,88	2974,17	2971,00	2973,00	2984,00
Qz_m	46,3	39,3	31,7	43,3	42,0	40,0	40,0
Qz_p	5,3	14,3	11,3	8,0	7,3	11,7	10,3
Qc	0,0	0,0	0,0	0,0	6,0	3,7	2,0
Kfsp	7,7	4,7	3,3	4,3	6,0	7,0	4,3
Plag	0,0	<1.0	0,0	0,0	<1.0	<1.0	<1.0
Lv_{fel}	9,3	6,3	16,0	7,3	7,0	4,7	5,0
Lv_{maf}	0,0	<1.0	0,0	0,0	0,0	0,0	0,0
Lm_{pel}	0,0	0,0	0,0	0,0	0,0	1,3	0,0
L_{QFG}	7,7	0,0	1,7	2,3	2,0	2,3	1,3
Ls_{psam}	0,0	0,0	0,0	0,0	0,0	0,0	0,0
Ls_{pel}	0,0	0,0	0,0	0,0	0,0	0,0	0,0
Lil	0,0	0,0	0,0	0,0	0,0	0,0	0,0
Lc	0,0	0,0	0,0	0,0	0,0	0,0	0,0
Muscovite	<1.0	0,0	0,0	0,0	0,0	0,0	0,0
Fe-oxide	2,0	11,0	5,7	1,3	2,0	4,0	11,0
Qz_{au}	<1.0	<1.0	2,0	1,3	4,3	2,3	<1.0
$Kfsp_{au}$	0,0	0,0	0,0	0,0	0,0	0,0	0,0
Carbonate	3,3	1,3	<1.0	1,7	0,0	5,0	8,3
Anhydrite	<1.0	0,0	3,0	1,0	<1.0	0,0	0,0
Barite	?	?	?	?	?	?	?
Kaol "booklets"	10,3	5,3	9,2	7,8	2,8	4,6	10,2
Radial kaol	0,0	0,0	0,0	0,0	0,0	0,0	<1.0
IC	0,0	0,0	0,0	2,0	4,0	4,0	0,0
Bitumen	0,0	<1.0	0,0	0,0	0,0	0,0	0,0
Por_{inter}	7,7	13,1	10,4	15,0	12,6	6,7	7,5
Por_{intra}	<1.0	4,3	5,7	4,0	3,3	2,3	0,0
Fsp leaching	+	+++	+++	++	+++	+++	++
Illitisation	+	-	+	+	++	++	+
Kaolinitisation	-	-	-	-	-	+	-
Σ (all)	99,6	99,6	100,0	99,3	99,3	99,6	99,9
Σ (authigenic min.)	15,6	17,6	19,9	15,1	13,1	19,9	29,5
Σ (detrital grains)	76,3	64,6	64,0	65,2	70,3	70,7	62,9
Σ (pore space)	7,7	17,4	16,1	19,0	15,9	9,0	7,5
IGV [%]	23,3	30,7	30,3	30,1	25,7	26,6	37,0
sorting	1,00	0,71	0,71	0,35	0,00	0,71	1,00
roundness	3-5	3-5	4-5	3-5	3-5	3-5	2-5
sphericity	low	low	low	low	low	high	low
grain contacts	2>1>0	1>2>3	1>2>rest	2>1>3	1>0>2	1>0>2	2>1>3
grain size [µm]	153	230	352	207	221	208	163
facies	*no data*	*no data*	*no data*	dune core	dune core	dune core	wet sf
facies_assumed	fluviatile	?	dune	dune	dune	dune	wet sf

Appendix C2: Continuation

Field	**C**	**C**	**C**	**C**	**C**	**C**	**C**
well	**Cw04**	**Cw04**	**Cw04**	**Cw04**	**Cw04**	**Cw04**	**Cw04**
sample	Cw04-01	Cw04-02	Cw04-05	Cw04-06	Cw04-07	Cw04-08	Cw04-09
depth [m]	2711,35	2711,30	2714,80	2710,90	2711,20	2713,30	2714,50
Qz_m	37,0	38,0	34,7	32,3	38,0	34,7	38,0
Qz_p	6,3	8,0	8,3	14,0	9,0	14,7	14,7
Qc	<1.0	<1.0	<1.0	2,0	4,0	2,0	2,0
Kfsp	4,0	3,7	6,3	6,0	6,0	6,0	6,3
Plag	0,0	0,0	0,0	1,0	<1.0	0,0	<1.0
Lv_{fel}	9,0	12,3	6,3	4,0	5,0	5,0	8,3
Lv_{maf}	0,0	0,0	0,0	<1.0	<1.0	1,0	<1.0
Lm_{pel}	0,0	0,0	0,0	0,0	2,7	1,0	1,0
L_{QFG}	0,0	0,0	2,0	1,0	0,0	2,0	4,0
Ls_{psam}	0,0	0,0	0,0	0,0	0,0	0,0	0,0
Ls_{pel}	0,0	0,0	0,0	0,0	0,0	0,0	0,0
Lil	0,0	1,0	0,0	0,0	0,0	1,0	0,0
Lc	0,0	0,0	0,0	0,0	0,0	0,0	0,0
Muscovite	0,0	<1.0	<1.0	0,0	0,0	0,0	0,0
Fe-oxide	9,0	9,0	14,0	2,0	1,0	6,0	5,3
Qz_{au}	0,0	<1.0	0,0	11,7	7,3	1,0	2,0
$Kfsp_{au}$	0,0	0,0	0,0	0,0	0,0	0,0	0,0
Carbonate	23,0	16,0	2,0	3,0	5,7	10,3	<1.0
Anhydrite	1,0	<1.0	0,0	4,3	4,3	<1.0	0,0
Barite	?	?	?	?	?	?	?
Kaol "booklets"	<1.0	1,8	9,4	<1.0	2,4	2,8	2,4
Radial kaol	0,0	0,0	<1.0	0,0	0,0	0,0	0,0
IC	0,0	0,0	0,0	4,0	2,0	2,0	6,0
Bitumen	0,0	0,0	0,0	0,0	0,0	0,0	0,0
Por_{inter}	4,5	5,8	12,8	11,3	11,0	6,4	5,3
Por_{intra}	6,0	3,7	4,0	3,3	1,0	3,7	4,3
Fsp leaching	++	++	++	++	+	++	+
Illitisation	+	+	++	+	-	-	+
Kaolinitisation	-	-	-	-	-	-	-
Σ (all)	99,8	99,3	99,8	99,9	99,4	99,6	99,6
Σ (authigenic min.)	33,0	26,8	25,4	25,0	22,7	22,1	15,7
Σ (detrital grains)	56,3	63,0	57,6	60,3	64,7	67,4	74,3
Σ (pore space)	10,5	9,5	16,8	14,6	12,0	10,1	9,6
IGV [%]	37,5	32,6	38,2	36,3	33,7	28,5	21,0
sorting	0,50	1,00	0,50	1,00	1,00	0,71	0,71
roundness	2-4	2-5	4-6	2-4	2-5	2-4	3-5
sphericity	low	low	low	low	low	low	low
grain contacts	1>2>rest	2>1>rest	2>1>0	1>2>0	1>3>2	2>1>rest	2>3>1
grain size [µm]	138	196	243	218	215	186	233
facies	dry sf	dry sf	*no data*	damp sf	dry sf	dune core	dune base
facies_assumed	dry sf	dry sf	dry sf	damp sf	dry sf	dune	dune

Appendix C2: Continuation

Field	**C**	**C**	**C**	**C**	**C**	**C**	**C**
well	**Cw04**	**Cw04**	**Cw04**	**Cw04**	**Cw04**	**Cw04**	**Cw04**
sample	Cw04-10	Cw04-11	Cw04-12	Cw04-13	Cw04-14	Cw04-15	Cw04-16
depth [m]	2715,40	2716,30	2717,50	2718,10	2719,30	2721,70	2723,20
Qz_m	32,7	36,0	40,7	36,0	35,0	38,0	37,3
Qz_p	15,3	15,3	9,7	11,3	14,7	11,7	13,7
Qc	4,3	5,0	3,0	3,0	2,7	2,0	3,0
Kfsp	8,0	7,3	6,3	6,3	6,3	6,0	7,3
Plag	<1.0	1,0	<1.0	<1.0	0,0	<1.0	0,0
Lv_{fel}	6,3	3,7	4,7	3,7	3,3	5,0	3,7
Lv_{maf}	<1.0	0,0	0,0	0,0	0,0	0,0	0,0
Lm_{pel}	1,0	<1.0	<1.0	1,0	1,3	1,0	1,3
L_{QFG}	1,0	3,0	4,3	2,3	2,7	2,3	1,3
Ls_{psam}	0,0	0,0	0,0	0,0	0,0	0,0	0,0
Ls_{pel}	0,0	0,0	0,0	0,0	0,0	0,0	0,0
Lil	0,0	0,0	0,0	0,0	0,0	0,0	0,0
Lc	0,0	0,0	0,0	0,0	0,0	0,0	0,0
Muscovite	0,0	0,0	0,0	0,0	0,0	0,0	0,0
Fe-oxide	1,7	<1.0	6,7	8,7	4,3	5,7	<1.0
Qz_{au}	1,3	3,0	3,0	5,7	11,7	1,7	3,7
$Kfsp_{au}$	0,0	0,0	0,0	0,0	0,0	0,0	0,0
Carbonate	16,3	7,7	<1.0	10,0	4,3	9,3	1,3
Anhydrite	0,0	1,0	<1.0	0,0	0,0	1,7	3,7
Barite	?	?	?	?	?	?	?
Kaol "booklets"	<1.0	1,4	8,4	2,4	4,0	4,0	7,8
Radial kaol	0,0	0,0	0,0	0,0	<1.0	0,0	0,0
IC	4,7	1,0	2,0	<1.0	1,0	5,0	5,0
Bitumen	0,0	2,0	0,0	0,0	0,0	0,0	0,0
Por_{inter}	3,0	9,6	10,3	4,7	3,3	3,7	8,2
Por_{intra}	4,3	2,7	<1.0	4,7	4,7	2,3	2,7
Fsp leaching	+	++	+	+	++	++	++
Illitisation	+	++	+	++	+	++	+
Kaolinitisation	-	-	-	-	-	-	-
Σ (all)	99,9	99,7	99,1	99,8	99,3	99,4	100,0
Σ (authigenic min.)	24,0	16,1	20,1	26,8	25,3	27,4	21,5
Σ (detrital grains)	68,6	71,3	68,7	63,6	66,0	66,0	67,6
Σ (pore space)	7,3	12,3	10,3	9,4	8,0	6,0	10,9
IGV [%]	27,0	25,7	30,4	31,5	28,6	31,1	29,7
sorting	1,00	0,35	0,71	0,35	0,50	0,35	0,35
roundness	2-5	3-5	3-5	3-5	3-5	3-5	3-5
sphericity	low	high	low	low	low	low	low
grain contacts	2>1>rest	2>1>rest	1>2>rest	1>2>rest	1>2>rest	1>2>rest	1>2>rest
grain size [µm]	202	294	157	259	332	258	243
facies	dune core	dune core	dune base	dry sf	dune core	dune core	dune core
facies_assumed	dune	dune	dune	dry sf	dune	dune	dune

Appendix C2: Continuation

Field	**C**	**C**	**C**	**C**	**C**	**C**	**C**
well	**Cw04**	**Cw04**	**Cw04**	**Cw04**	**Cw04**	**Cw04**	**Cw04**
sample	Cw04-17	Cw04-18	Cw04-19	Cw04-20	Cw04-21	Cw04-22	Cw04-23
depth [m]	2724,70	2725,60	2728,00	2728.3	2731,60	2734,90	2736,10
Qz_m	39,0	30,7	31,0	29,3	34,7	35,3	36,0
Qz_p	9,7	14,7	9,0	16,0	10,3	6,0	9,3
Qc	1,7	1,0	2,0	1,0	1,0	1,3	1,0
Kfsp	3,3	4,0	6,7	3,0	4,3	6,3	8,0
Plag	0,0	0,0	1,0	<1.0	0,0	<1.0	<1.0
Lv_{fel}	4,3	1,7	5,7	8,0	3,7	3,0	1,3
Lv_{maf}	1,0	<1.0	1,0	0,0	0,0	0,0	0,0
Lm_{pel}	1,7	1,3	<1.0	1,0	1,3	1,0	2,0
L_{QFG}	1,3	2,7	1,7	3,0	<1.0	0,0	<1.0
Ls_{psam}	0,0	0,0	0,0	1,0	0,0	0,0	0,0
Ls_{pel}	0,0	0,0	0,0	0,0	0,0	0,0	0,0
Lil	0,0	0,0	0,0	0,0	0,0	0,0	0,0
Lc	0,0	0,0	0,0	0,0	0,0	0,0	0,0
Muscovite	0,0	0,0	0,0	0,0	0,0	0,0	<1.0
Fe-oxide	17,7	16,7	15,0	2,3	17,3	15,3	13,3
Qz_{au}	0,0	<1.0	2,3	8,0	4,7	1,7	2,7
$Kfsp_{au}$	0,0	0,0	0,0	0,0	0,0	0,0	0,0
Carbonate	2,0	<1.0	7,3	<1.0	<1.0	7,0	15,3
Anhydrite	0,0	<1.0	<1.0	23,0	1,0	1,7	1,7
Barite	?	?	?	?	?	?	?
Kaol "booklets"	7,0	9,3	7,0	2,7	8,0	8,6	3,2
Radial kaol	0,0	0,0	0,0	0,0	0,0	0,0	0,0
IC	3,0	2,0	<1.0	1,7	0,0	0,0	0,0
Bitumen	0,0	0,0	0,0	0,0	0,0	0,0	0,0
Por_{inter}	4,0	11,2	6,0	<1.0	8,3	7,7	3,4
Por_{intra}	4,3	4,3	4,3	<1.0	4,7	4,7	2,7
Fsp leaching	++	+++	++	+	+++	+++	++
Illitisation	+	++	++	++	+	+	+
Kaolinitisation	+	+	+	-	-	-	-
Σ (all)	100,0	99,6	100,0	100,0	99,3	99,6	99,9
Σ (authigenic min.)	29,7	28,0	31,6	37,7	31,0	34,3	36,2
Σ (detrital grains)	62,0	56,1	58,1	62,3	55,3	52,9	57,6
Σ (pore space)	8,3	15,5	10,3	0,0	13,0	12,4	6,1
IGV [%]	33,7	39,2	37,6	37,7	39,3	42,0	39,6
sorting	0,50	0,50	0,35	0,35	0,50	0,35	1,50
roundness	3-5	3-5	2-4	4-6	2-4	3-4	2-4
sphericity	low	low	low	high	low	low	low
grain contacts	1>2>rest	1>2>rest	1>2>rest	1>0>2	1>2>rest	1>2>rest	1>2>rest
grain size [µm]	244	224	228	184	169	212	162
facies	wet sf	dune base	dry sf	dune core	dune core	dune core	dry sf
facies_assumed	dry sf	dune	dry sf	dune	dune	dune	dry sf

Appendix C2: Continuation

Field	**C**
well	**Cw04**
sample	Cw04-24
depth [m]	2740,30
Qz_m	45,0
Qz_p	10,0
Qc	1,0
Kfsp	6,3
Plag	<1.0
Lv_{fel}	3,0
Lv_{maf}	0,0
Lm_{pel}	2,0
L_{QFG}	1,0
Ls_{psam}	0,0
Ls_{pel}	0,0
Lil	4,0
Lc	0,0
Muscovite	<1.0
Fe-oxide	4,3
Qz_{au}	<1.0
$Kfsp_{au}$	0,0
Carbonate	14,7
Anhydrite	1,3
Barite	?
Kaol "booklets"	4,0
Radial kaol	0,0
IC	0,0
Bitumen	0,0
Por_{inter}	3,1
Por_{intra}	<1.0
Fsp leaching	+
Illitisation	+
Kaolinitisation	-
Σ (all)	99,7
Σ (authigenic min.)	24,3
Σ (detrital grains)	72,3
Σ (pore space)	3,1
IGV [%]	27,4
sorting	0,71
roundness	2-4
sphericity	high
grain contacts	2>3>1
grain size [µm]	146
facies	wet sf
facies_assumed	wet sf

Appendix C3: Approximate porosity and horizontal permeability data of selected samples. The data are derived from plug measurements by NAM of adjacent samples. Please regard to the core images in appendix A1.

sample	depth [m]	porosity [%]	permeability [mD]
Aw02-01	2956.90	20.0	3408
Aw02-02	2961.00	16.0	233
Aw02-03	2968.31	17.0	808
Aw02-04	2955.20	21.0	1500
Aw02-05	2982.17	13.0	105
Aw02-06	2982.02	11.0	106
Aw02-07	2974.02	12.0	250
Aw02-08	2963.91	16.0	1300
Aw02-09	2973.31	12.0	156
Aw02-10	2973.41	12.0	156
Aw02-11	2977.90	12.0	35
Aw02-12	2983.25	17.0	348
Aw04-01	2973.47	26.0	1964
Aw04-02	2974.32	23.0	630
Aw04-03	2993.95	18.0	225
Aw04-04	2996.10	19.0	225
Aw05-01	3253.86	25.0	9900
Aw05-02	3201.50	14.0	490
Aw05-03	3186.25	12.5	62
Aw05-04	3255.76	11.0	140
Aw05-05	3251.99	16.0	340
Aw05-06	3245.80	21.0	220
Aw05-07	3211.30	17.0	230
Aw05-08	3204.98	18.0	320
Aw04-03	3137.46	16.0	230
Bw01-01	2545.60	28.0	388
Bw01-02	2540.05	28.0	323
Bw01-03	2487.00	20.0	14
Bw02-01	2981.16	23.0	81
Bw02-02	2954.88	20.0	32
Bw02-03	2880.00	13.0	0.77
Bw02-04	2880.19	13.0	0.77
Bw02-05	3015.17	24.4	550
Bw03-01	2498.70	23.0	1057
Bw03-02	2500.25	18.0	24
Bw03-03	2521.02	20.0	102
Bw03-04	2522.45	25.0	1461
Cw01-01	2600.80	13.0	0.5
Cw01-02	2754.75	17.0	2.7
Cw02-01	3293.88	14.5	2.1
Cw02-02	3372.40	13.9	7.4
Cw03-01	2974.17	23.0	27
Cw03-02	2972.68	19.0	1.6
Cw04-01	2711.35	15.0	45
Cw04-02	2711.30	15.0	45
Cw04-05	2714.80	17.0	2.8
Cw04-03	2712.30	sand	-
Cw04-04	2715.53	sand	-

Appendix C4-01: Electron microprobe analyses of silica minerals in Upper Rotliegend samples.

		O	Na	Mg	Al	Si	K	Ca	Ti	Mn	Fe	sum
mineral	**sample**	[wt.-%]	[wt.-%]	[wt.-%]	[wt.-%]	[wt.-%]	[wt.-%]	[wt.-%]	[wt.-%]	[wt.-%]	[wt.-%]	[wt.-%]
albite	Aw04-04_50	48.6	7.32	0.00	10.3	32.2	0.07	0.05	0.34	0.02	0.02	99.0
albite	Aw04-04_59	43.5	5.15	0.01	8.90	29.4	0.84	0.24	0.00	0.00	0.03	88.1
albite	Aw04-02_66	43.8	6.73	0.02	8.83	29.5	0.19	0.01	0.00	0.00	0.06	89.1
Ill/smec	Aw02-03_02	36.2	0.22	1.82	9.45	20.5	5.97	0.10	0.10	0.02	6.28	80.7
Ill/smec	Aw02-03_05	39.7	0.19	1.45	11.8	22.6	6.10	0.11	0.08	0.01	3.71	85.7
Ill/smec	Aw02-03_06	37.4	0.20	1.79	8.89	21.9	6.31	0.08	0.21	0.02	6.22	83.1
Ill/smec	Aw02-03_07	37.4	0.24	1.90	9.06	21.8	6.55	0.12	0.19	0.01	5.79	83.1
Ill/smec	Aw02-03_16	40.4	0.15	2.35	8.48	24.2	5.76	0.13	0.02	0.02	8.28	89.8
Ill/smec	Aw02-03_17	40.1	0.14	2.13	7.98	24.1	6.00	0.10	0.02	0.04	9.69	90.4
Ill/smec	Aw02-03_18	39.0	0.17	2.08	8.96	22.9	5.84	0.14	0.03	0.04	7.66	86.8
Ill/smec	Aw03-01_01	39.1	0.10	1.54	7.91	23.3	6.37	0.24	0.00	0.02	10.8	89.3
Ill/smec	Aw03-01_02	41.1	0.09	1.39	12.2	23.3	6.49	0.65	0.00	0.00	4.02	89.3
Ill/smec	Aw03-01_03	41.9	0.08	1.43	12.3	23.8	6.76	0.26	0.00	0.01	4.64	91.3
Ill/smec	Aw03-01_05	40.6	0.06	1.13	13.1	22.7	6.81	0.14	0.00	0.00	2.75	87.3
Ill/smec	Aw03-01_06	41.6	0.05	1.75	11.0	24.1	6.75	0.31	0.00	0.00	6.05	91.6
Ill/smec	Aw03-01_07	43.0	0.09	1.85	11.6	24.7	6.71	0.50	0.00	0.00	5.98	94.4
Ill/smec	Aw03-01_08	41.0	0.06	1.57	11.6	23.3	6.58	0.28	0.00	0.01	5.39	89.8
Ill/smec	Aw03-01_12	41.3	0.08	1.02	15.1	22.3	6.23	0.11	0.00	0.02	1.63	87.8
Ill/smec	Aw03-01_14	42.4	0.02	0.05	20.2	21.4	0.04	0.04	0.00	0.01	0.08	84.3
Ill/smec	Aw03-01_22	41.9	0.11	1.59	11.0	24.5	6.86	0.10	0.00	0.00	5.88	92.0
Ill/smec	Aw03-01_23	38.5	0.33	8.13	7.33	20.0	7.70	0.03	0.00	0.04	7.53	89.5
Ill/smec	Aw03-01_24	37.3	0.10	1.74	8.68	21.8	6.35	0.16	0.00	0.02	7.39	83.5
Ill/smec	Aw03-01_28	35.7	0.08	1.66	9.20	21.0	7.11	0.23	0.00	0.03	3.26	78.2
Ill/smec	Aw03-01_29	36.8	0.13	1.75	10.0	20.2	6.04	2.15	0.00	0.03	5.50	82.7
Ill/smec	Aw03-01_30	36.7	0.08	1.92	9.04	21.3	6.40	0.19	0.00	0.03	5.97	81.6
Ill/smec	Aw03-01_35	52.7	0.00	0.00	0.42	45.8	0.16	0.08	0.00	0.00	0.15	99.3
Ill/smec	Aw03-01_37	41.6	0.14	1.75	10.2	25.3	6.57	0.19	0.00	0.04	3.71	89.4
Ill/smec	Aw03-01_38	41.3	0.15	2.22	9.67	25.0	6.63	0.29	0.00	0.01	4.37	89.7
Ill/smec	Aw03-01_39	43.2	0.11	1.85	11.4	25.7	6.69	0.19	0.00	0.03	3.85	93.0
Ill/smec	Aw03-01_40	40.0	0.17	1.39	11.0	23.4	7.14	0.19	0.00	0.04	3.65	86.9
Ill/smec	Aw03-01_42	42.0	0.13	2.28	10.9	25.0	6.25	0.28	0.00	0.01	3.19	90.1
Ill/smec	Aw03-01_45	43.2	0.06	1.19	14.2	24.1	8.20	0.02	0.00	0.00	2.26	93.3
Ill/smec	Aw03-01_46	36.7	0.12	0.49	9.06	22.8	9.41	0.16	0.00	0.00	1.30	80.1
Ill/smec	Aw03-01-47	37.3	0.04	1.00	12.9	20.3	6.19	0.15	0.00	0.02	2.23	80.2
Ill/smec	Aw03-01-48	36.0	0.05	1.29	10.8	20.4	5.96	0.17	0.00	0.01	3.55	78.2
Ill/smec	Aw03-01-49	34.7	0.03	1.17	10.9	19.4	5.33	0.12	0.00	0.01	3.52	75.2
Ill/smec	Bw01-01_75	38.1	0.36	0.93	12.7	20.4	6.35	0.02	0.09	0.00	5.34	84.3
Ill/smec	Bw01-01_76	35.7	0.33	0.95	11.7	19.1	5.99	0.03	0.03	0.01	5.43	79.2
Ill/smec	Bw01-01_78	43.3	0.27	0.93	14.3	24.6	6.09	0.26	0.04	0.01	1.49	91.4
Ill/smec	Bw01-01_79	44.1	0.24	1.08	15.1	24.7	6.48	0.09	0.02	0.00	1.36	93.2
Ill/smec	Bw01-01_80	41.2	0.23	1.06	13.1	23.4	6.14	1.12	0.03	0.02	1.43	87.7
Ill/smec	Bw01-01_81	40.0	0.26	0.63	9.95	25.5	4.97	0.43	0.04	0.02	1.23	83.1
Ill/smec	Bw01-01_82	36.9	0.22	0.74	13.6	20.2	4.67	0.06	0.01	0.00	1.18	77.6
Ill/smec	Bw01-01_83	37.7	0.33	0.85	13.5	20.5	6.09	0.02	0.04	0.01	1.29	80.4
Ill/smec	Bw01-01_84	36.3	0.49	0.86	12.3	19.2	5.81	2.62	0.03	0.00	1.86	79.5
Ill/smec	Bw01-01_91	39.9	0.16	1.70	9.86	23.0	7.94	0.14	0.06	0.06	7.04	89.9
Ill/smec	Bw01-01_92	39.9	0.18	1.30	11.8	22.3	7.59	0.04	0.06	0.03	5.30	88.5
Ill/smec	Bw01-01_93	39.0	0.21	1.31	11.4	22.1	6.27	0.02	0.05	0.00	5.06	85.5
Ill/smec	Bw01-01_94	37.0	0.26	1.35	9.70	21.0	6.99	0.02	0.76	0.01	5.36	82.5
Ill/smec	Aw04-04_42	38.2	0.37	2.12	5.8	23.6	6.57	0.09	0.07	0.02	11.0	87.9

Appendix C4-01: Continutation

		O	Na	Mg	Al	Si	K	Ca	Ti	Mn	Fe	sum
mineral	**sample**	[wt.-%]	[wt.-%]	[wt.-%]	[wt.-%]	[wt.-%]	[wt.-%]	[wt.-%]	[wt.-%]	[wt.-%]	[wt.-%]	[wt.-%]
ill/smec	Aw04-04_43	39.8	0.02	1.35	12.2	22.5	6.15	0.20	0.02	0.01	3.65	85.9
ill/smec	Aw04-04_60	38.5	0.29	2.15	10.6	22.8	5.31	0.07	0.03	0.00	1.47	81.2
ill/smec	Aw04-04_61	38.8	0.09	2.06	11.4	22.7	4.70	0.12	0.03	0.00	1.38	81.3
ill/smec	Aw04-04_62	38.5	0.21	1.98	11.0	22.6	5.31	0.25	0.03	0.01	1.25	81.1
ill/smec	Aw04-04_63	39.8	0.21	2.00	10.7	23.7	5.50	0.24	0.04	0.03	2.03	84.2
ill/smec	Aw04-04_64	39.7	0.36	2.03	11.7	22.8	5.94	0.49	0.05	0.01	1.59	84.6
ill/smec	Bw01-01_85	38.4	0.32	1.04	11.3	20.0	6.72	0.00	2.99	0.02	4.86	85.6
ill/smec	Bw01-01_86	37.5	0.30	1.12	11.5	20.5	7.11	0.00	0.34	0.00	4.90	83.3
ill/smec	Bw01-01_87	40.4	0.26	1.53	10.7	22.9	7.09	0.00	0.20	0.04	7.35	90.5
ill/smec	Bw01-01_88	38.0	0.37	1.16	11.2	20.9	6.83	0.57	0.30	0.00	5.43	84.7
ill/smec	Bw01-01_89	40.3	0.26	1.07	12.0	22.2	7.64	0.06	0.41	0.01	5.97	89.9
ill/smec	Bw01-01_90	38.5	0.28	0.91	11.6	20.3	6.45	0.05	3.21	0.02	3.17	84.5
IC	Cw02-01_30	36.4	0.13	1.18	9.31	22.2	4.18	0.21	0.00	0.00	3.50	77.1
IC	Cw02-01_32	32.0	0.06	0.80	9.31	18.1	3.38	0.63	0.00	0.02	5.36	69.7
IC	Cw02-01_33	29.5	0.08	0.67	7.40	17.3	3.26	0.49	0.00	0.03	6.48	65.2
IC	Bw02-05_64	31.0	0.05	0.82	9.35	15.1	4.00	0.31	0.00	0.00	13.9	74.5
IC	Bw02-05_65	35.3	0.08	0.89	11.2	19.7	5.51	0.34	0.00	0.01	3.71	76.7
IC	Bw02-05_73	33.2	0.09	0.97	10.7	18.1	5.25	0.97	0.00	0.01	3.35	72.7
IC	Bw02-05_74	33.5	0.09	0.82	11.2	18.0	5.19	0.15	0.00	0.03	4.92	73.9
IC	Aw04-04_35	39.4	0.19	0.82	11.9	22.5	5.49	1.40	0.68	0.03	1.43	83.8
IC	Aw04-02_68	37.6	0.37	1.39	10.7	21.0	6.23	2.80	0.07	0.00	2.32	82.6
IC	Aw04-02_69	38.8	0.37	1.53	11.6	21.8	6.06	1.59	0.03	0.02	2.24	84.1
IC	Aw04-02_70	41.0	0.27	1.28	14.0	22.5	6.24	0.02	0.36	0.02	1.35	87.1
hel-chl	Aw03-01_15	39.4	0.20	2.59	9.58	21.9	6.22	0.25	0.00	0.05	9.59	89.8
hel-chl	Aw03-01_16	40.9	0.14	2.94	9.32	23.1	6.01	0.06	0.00	0.03	10.8	93.2
hel-chl	Aw03-01_17	39.9	0.21	2.58	8.95	22.6	6.44	0.09	0.00	0.04	10.4	91.2
hel-chl	Aw03-01_18	39.6	0.22	2.78	9.09	22.1	6.39	0.06	0.00	0.03	10.5	90.7
hel-chl	Aw03-01_19	39.4	0.17	2.70	9.10	22.0	6.27	0.19	0.00	0.02	10.7	90.5
hel-chl	Aw03-01_53	39.8	0.15	2.40	6.10	24.8	6.58	0.14	0.00	0.00	11.0	90.9
hel-chl	Aw03-01_55	35.6	0.17	2.29	4.87	22.3	5.74	0.09	0.00	0.04	10.7	81.8
hel-chl	Aw03-01_56	34.5	0.16	2.27	4.78	21.7	5.13	0.17	0.00	0.04	9.75	78.5
hel-chl	Aw03-01_57	34.8	0.12	2.13	5.63	21.5	5.55	0.12	0.00	0.02	9.41	79.3
hel-chl	Aw03-01_58	35.8	0.12	2.31	5.60	22.3	5.56	0.11	0.00	0.03	9.34	81.2
hel-chl	Aw03-01_59	36.1	0.09	2.31	5.90	22.3	5.92	0.08	0.00	0.02	9.33	82.0
hel-chl	Aw03-01_60	35.4	0.10	2.36	5.61	21.8	5.97	0.07	0.00	0.00	9.70	81.0
hel-chl	Aw03-01_61	37.1	0.11	2.49	6.02	22.7	6.05	0.09	0.00	0.03	10.1	84.6
hel-chl	Aw03-01_62	35.3	0.15	2.30	5.30	21.9	5.70	0.16	0.00	0.02	9.89	80.7
hel-chl	Aw03-01_63	40.7	0.21	2.69	6.88	24.8	6.81	0.11	0.00	0.03	10.6	92.9
hel-chl	Aw03-01_64	36.9	0.12	2.50	5.70	22.7	6.13	0.07	0.00	0.03	10.2	84.4
hel-chl	Aw03-01_65	41.5	0.16	2.73	6.48	25.6	6.66	0.12	0.00	0.03	11.5	94.9
hel-chl	Aw03-01_66	41.2	0.11	2.83	6.30	25.5	6.66	0.12	0.00	0.00	11.2	94.0
hel-chl	Aw03-01_67	40.9	0.07	2.49	7.19	24.9	6.76	0.15	0.00	0.07	10.7	93.1
hel-chl	Aw03-01_68	39.5	0.08	2.60	6.10	24.5	6.27	0.18	0.00	0.02	10.76	90.0
hel-chl	Aw03-01_69	47.1	6.97	0.00	9.19	32.0	0.05	0.01	0.00	0.00	0.04	95.4
kaolinite	Cw02-01_11	43.3	0.01	0.03	20.58	21.9	0.01	0.06	0.00	0.01	0.07	85.9
kaolinite	Cw02-01_12	42.4	0.02	0.00	19.71	21.8	0.03	0.03	0.00	0.00	0.10	84.1
kaolinite	Cw02-01_14	41.5	0.03	0.05	19.51	21.1	0.04	0.10	0.00	0.03	0.10	82.4
kaolinite	Cw02-01_15	43.1	0.04	0.05	20.15	22.0	0.02	0.10	0.00	0.03	0.09	85.6

Appendix C4-01: Continutation

		O	Na	Mg	Al	Si	K	Ca	Ti	Mn	Fe	sum
mineral	**sample**	[wt.-%]	[wt.-%]	[wt.-%]	[wt.-%]	[wt.-%]	[wt.-%]	[wt.-%]	[wt.-%]	[wt.-%]	[wt.-%]	[wt.-%]
kaolinite	Cw02-01_16	42.6	0.03	0.12	19.65	21.9	0.04	0.23	0.00	0.00	0.16	84.7
kaolinite	Cw02-01_17	43.2	0.03	0.04	20.22	22.1	0.04	0.09	0.00	0.00	0.11	85.8
kaolinite	Cw02-01_18	42.8	0.01	0.05	20.24	21.7	0.03	0.10	0.00	0.00	0.12	85.1
kaolinite	Cw02-01_02	44.1	0.02	0.05	20.81	22.4	0.03	0.11	0.00	0.01	0.11	87.6
kaolinite	Cw02-01_20	43.7	0.04	0.02	20.39	22.4	0.03	0.03	0.00	0.00	0.05	86.7
kaolinite	Cw02-01_21	42.9	0.01	0.04	20.22	21.8	0.03	0.08	0.00	0.00	0.04	85.2
kaolinite	Cw02-01_22	44.0	0.02	0.03	20.54	22.5	0.02	0.05	0.00	0.01	0.10	87.2
kaolinite	Cw02-01_23	43.3	0.02	0.04	19.81	22.5	0.02	0.13	0.00	0.00	0.10	85.9
kaolinite	Cw02-01_24	43.9	0.01	0.01	20.51	22.4	0.01	0.07	0.00	0.01	0.09	87.0
kaolinite	Cw02-01_25	44.4	0.00	0.03	20.73	22.7	0.02	0.05	0.00	0.03	0.09	88.0
kaolinite	Cw02-01_28	44.2	0.02	0.07	20.55	22.6	0.06	0.05	0.00	0.02	0.04	87.6
kaolinite	Cw02-01_29	43.6	0.03	0.03	20.49	22.2	0.05	0.05	0.00	0.00	0.10	86.6
kaolinite	Cw02-01_03	43.0	0.04	0.01	20.32	21.8	0.01	0.06	0.00	0.03	0.07	85.3
kaolinite	Cw02-01_34	43.1	0.03	0.02	19.55	22.5	0.05	0.10	0.00	0.00	0.06	85.4
kaolinite	Cw02-01_35	43.2	0.01	0.06	20.22	22.0	0.02	0.13	0.00	0.00	0.07	85.8
kaolinite	Cw02-01_37	43.6	0.02	0.05	20.12	22.5	0.05	0.07	0.00	0.00	0.07	86.5
kaolinite	Cw02-01_40	44.7	0.02	0.04	20.61	23.1	0.03	0.08	0.00	0.01	0.14	88.8
kaolinite	Cw02-01_41	43.7	0.02	0.05	20.41	22.4	0.03	0.11	0.00	0.01	0.12	86.8
kaolinite	Cw02-01_42	45.0	0.01	0.03	20.98	23.0	0.05	0.11	0.00	0.00	0.07	89.3
kaolinite	Cw02-01_43	44.4	0.01	0.05	20.28	23.1	0.04	0.08	0.00	0.00	0.09	88.0
kaolinite	Cw02-01_44	42.6	0.01	0.03	19.13	22.4	0.02	0.06	0.00	0.00	0.07	84.2
kaolinite	Cw02-01_47	44.1	0.04	0.04	20.48	22.7	0.06	0.05	0.00	0.00	0.12	87.6
kaolinite	Cw02-01_48	44.1	0.01	0.02	20.24	22.8	0.04	0.10	0.00	0.01	0.07	87.4
kaolinite	Cw02-01_49	44.2	0.01	0.00	20.67	22.6	0.04	0.14	0.00	0.00	0.13	87.8
kaolinite	Cw02-01_05	43.3	0.02	0.01	20.15	22.2	0.05	0.10	0.00	0.03	0.12	86.0
kaolinite	Cw02-01_50	44.0	0.03	0.03	20.76	22.3	0.02	0.06	0.00	0.01	0.08	87.4
kaolinite	Cw02-01_51	43.0	0.07	0.00	20.30	21.8	0.09	0.05	0.00	0.00	0.09	85.4
kaolinite	Cw02-01_06	41.0	0.04	0.04	19.20	20.9	0.03	0.09	0.00	0.00	0.07	81.4
kaolinite	Cw02-01_07	41.5	0.03	0.03	19.40	21.2	0.01	0.11	0.00	0.00	0.11	82.4
kaolinite	Cw02-01_08	27.1	0.05	0.12	11.18	14.8	0.24	0.17	0.00	0.00	0.12	53.7
kaolinite	Bw01-01_70	40.8	0.00	0.02	18.57	21.3	0.03	0.01	0.00	0.00	0.04	80.8
kaolinite	Bw01-01_77	41.9	0.02	0.02	19.11	21.8	0.05	0.03	0.00	0.01	0.01	83.0
kaolinite	Bw02-05_55	33.9	0.11	1.30	12.60	18.0	3.90	0.08	0.00	0.01	1.54	71.4
kaolinite	Bw02-05_56	41.7	0.04	0.08	19.67	21.1	0.05	0.05	0.00	0.00	0.05	82.8
kaolinite	Bw02-05_66	42.1	0.05	0.17	19.19	21.8	0.13	0.01	0.00	0.00	0.08	83.5
kaolinite	Bw02-05_67	43.3	0.04	0.10	19.99	22.3	0.05	0.04	0.00	0.00	0.01	85.9
kaolinite	Aw04-04_56	41.3	0.02	0.04	18.97	21.3	0.13	0.04	0.00	0.00	0.08	81.9
kaolinite	Aw04-04_57	31.5	0.04	0.04	13.64	16.8	0.39	0.03	0.03	0.00	0.12	62.6
kaolinite	Aw04-04_58	38.7	0.02	0.01	18.75	19.3	0.03	0.04	0.02	0.02	0.00	76.9
Kfsp	Aw03-01_34	40.5	0.12	0.03	7.90	27.1	12.68	0.02	0.00	0.00	0.08	88.4
Kfsp	Aw03-01_31	38.5	0.23	0.15	8.09	25.3	10.7	0.14	0.00	0.00	0.23	83.4
Kfsp	Aw02-03_09	45.1	0.63	0.02	9.90	29.2	13.1	0.03	0.01	0.00	0.07	98.1
Kfsp	Aw03-01_41	39.6	0.22	0.04	7.84	26.5	11.4	0.00	0.00	0.00	0.09	85.7
Kfsp	Aw03-01_43	34.9	0.11	0.35	8.30	22.0	9.65	0.11	0.00	0.00	0.72	76.1
Kfsp	Aw03-01_44	36.3	0.10	0.17	7.59	23.8	10.8	0.04	0.00	0.00	0.38	79.2
Kfsp	Cw02-01_01	46.3	0.64	0.00	9.96	30.3	13.1	0.00	0.00	0.03	0.00	100
Kfsp	Cw02-01_36	45.7	0.85	0.02	9.85	29.8	12.8	0.06	0.00	0.01	0.00	99.1
Kfsp	Cw02-1_9	51.6	0.03	0.13	4.63	41.1	2.25	0.03	0.00	0.00	0.39	100

Appendix C4-01: Continutation

		O	Na	Mg	Al	Si	K	Ca	Ti	Mn	Fe	sum
mineral	**sample**	[wt.-%]	[wt.-%]	[wt.-%]	[wt.-%]	[wt.-%]	[wt.-%]	[wt.-%]	[wt.-%]	[wt.-%]	[wt.-%]	[wt.-%]
Kfsp	Bw02-05_68	47.7	0.66	0.00	9.89	31.6	13.2	0.03	0.00	0.00	0.01	103
Kfsp	Aw04-04_49	47.4	0.12	0.10	10.9	31.6	7.45	0.04	0.01	0.02	0.20	97.8
Kfsp	Aw04-02_67	44.4	0.28	0.01	9.65	28.9	13.3	0.01	0.00	0.02	0.03	96.6
matrix	Aw02-03_19	38.8	0.07	2.10	5.29	24.3	7.54	0.03	0.02	0.02	12.1	90.3
matrix	Aw02-03_20	36.9	0.05	2.22	4.51	23.1	7.40	0.04	0.01	0.01	12.5	86.7
matrix	Aw02-03_21	40.1	0.05	2.54	4.29	25.6	8.15	0.07	0.00	0.00	13.3	94.0
matrix	Aw02-03_22	39.1	0.11	2.35	4.97	24.6	7.67	0.04	0.00	0.01	12.1	90.9
matrix	Aw02-03_23	38.8	0.10	2.21	3.84	24.6	7.52	0.04	0.02	0.02	14.7	91.8
matrix	Aw02-03_24	35.7	0.06	2.12	4.60	22.2	6.69	0.05	0.00	0.00	12.3	83.8
matrix	Aw02-03_25	38.5	0.05	1.86	4.19	24.2	7.36	0.04	0.05	0.05	15.3	91.6
matrix	Aw02-03_26	38.3	0.05	2.26	2.89	24.8	7.43	0.03	0.00	0.00	15.6	91.3
matrix	Aw02-03_27	39.1	0.06	2.51	3.35	25.2	7.91	0.02	0.01	0.02	14.3	92.6
matrix	Aw02-03_28	39.4	0.04	2.44	3.41	25.3	7.99	0.08	0.02	0.01	14.8	93.5
matrix	Aw02-03_29	39.7	0.07	2.26	4.51	25.1	7.47	0.08	0.00	0.00	13.9	93.1
matrix	Aw02-03_30	39.7	0.06	2.41	4.13	25.4	7.48	0.06	0.00	0.03	13.9	93.1
matrix	Aw02-03_31	39.6	0.09	2.25	4.42	25.2	7.22	0.04	0.01	0.01	13.8	92.6
matrix	Aw02-03_32	38.1	0.08	1.98	3.51	24.2	7.18	0.04	0.00	0.02	16.0	91.1
matrix	Aw02-03_08	42.0	0.40	0.02	9.01	27.4	12.3	0.01	0.03	0.02	0.03	91.2
matrix	Aw02-03_11	39.6	0.12	1.89	9.47	23.4	5.86	0.06	0.13	0.00	6.97	87.5
matrix	Aw02-03_12	40.6	0.31	2.29	8.16	24.4	6.19	0.06	0.06	0.00	9.15	91.3
matrix	Aw02-03_13	41.2	0.30	2.22	8.74	24.5	6.17	0.08	0.05	0.03	9.09	92.3
matrix	Aw02-03_15	40.0	0.09	1.95	10.22	23.0	6.15	0.09	0.02	0.02	7.00	88.5
quartz	Aw02-03_01	51.3	0.10	0.03	1.06	43.6	1.14	0.07	0.10	0.00	1.09	98.5
quartz	Aw03-01_26	38.5	0.16	1.76	9.15	22.5	6.14	0.23	0.00	0.02	7.45	85.8
quartz	Aw03-01_27	51.5	0.08	0.03	1.16	44.0	1.53	0.07	0.00	0.00	0.13	98.5
quartz	Aw03-01_33	50.8	0.09	0.02	0.96	43.4	1.05	0.07	0.00	0.02	0.65	97.1
Ti-Fe	Aw02-03_04	38.3	0.09	0.10	1.54	2.48	0.71	0.05	50.4	0.04	0.40	94.1
Ti-Fe	Bw01-01_72	38.9	0.05	0.01	0.03	0.05	0.07	0.05	55.1	0.02	4.44	98.7
Ti-Fe	Bw01-01_73	30.4	0.00	0.01	0.14	0.23	0.08	0.04	2.02	0.00	66.6	99.5
Ti-Fe	Bw01-01_74	30.2	0.00	0.02	0.15	0.28	0.10	0.23	2.80	0.04	64.5	98.2
Ti-Fe	Aw02-03_10	38.6	0.12	0.08	0.49	0.77	0.29	0.06	55.3	0.06	0.54	96.3
Ti-Fe	Aw02-03_14	38.0	0.02	0.00	0.13	0.29	0.21	0.07	55.9	0.03	0.42	95.1
Ti-Fe	Aw04-04_45	38.8	0.03	0.00	0.10	0.59	0.05	0.14	56.4	0.02	0.80	96.9
Ti-Fe	Aw04-04_51	37.9	0.04	0.00	0.03	0.16	0.02	0.08	56.2	0.00	0.25	94.7

Appendix C4-02: Electron microprobe analyses of carbonate minerals in Upper Rotliegend samples.

mineral	sample	$MgCO_3$ [mol%]	$CaCO_3$ [mol%]	$MnCO_3$ [mol%]	$FeCO_3$ [mol%]
ankerite	Cw02-01	38.7	50.6	0.15	10.6
ankerite	Cw02-01	40.1	49.5	0.16	10.3
ankerite	Bw02-05	25.3	52.3	0.52	21.9
ankerite	Bw02-05	22.3	52.3	0.26	25.2
ankerite	Bw02-05	24.3	53.2	0.63	21.8
ankerite	Bw02-05	25.7	52.5	0.29	21.6
ankerite	Bw02-05	25.0	52.7	0.61	21.7
ankerite	Bw02-05	36.2	52.8	0.48	10.5
ankerite	Aw04-04	25.1	51.4	0.99	22.6
ankerite	Aw04-04	22.9	52.8	1.04	23.3
ankerite	Aw04-04	20.4	53.4	1.59	24.6
dolomite	Cw02-01	46.0	48.4	0.12	5.45
dolomite	Cw02-01	51.7	47.5	0.70	0.17
dolomite	Cw02-01	51.0	48.2	0.62	0.12
dolomite	Cw02-01	50.5	48.8	0.53	0.17
dolomite	Bw02-05	52.7	46.7	0.48	0.16
dolomite	Bw02-05	51.4	48.1	0.40	0.16
dolomite	Bw02-05	51.2	48.3	0.31	0.23
dolomite	Bw02-05	52.1	47.4	0.16	0.29
dolomite	Bw02-05	44.9	50.2	0.52	4.34
dolomite	Bw02-05	50.0	49.5	0.34	0.25
dolomite	Bw02-05	48.3	50.1	0.32	1.19
dolomite	Aw02-03	48.2	50.1	1.57	0.08
dolomite	Aw04-04	48.1	50.7	1.11	0.12
dolomite	Aw04-04	47.9	51.0	0.96	0.16
dolomite	Aw04-04	48.6	50.4	0.92	0.09
dolomite	Aw04-04	48.4	50.5	0.87	0.18
dolomite	Aw04-04	48.4	50.5	1.07	0.05
dolomite	Aw04-04	48.1	51.0	0.84	0.06
dolomite	Aw04-04	48.1	50.8	0.79	0.27
dolomite	Aw04-04	48.4	50.5	0.89	0.23
siderite	Aw02-03	50.1	2.65	0.82	46.4
siderite	Aw02-03	46.4	1.92	0.82	50.8
siderite	Aw02-03	43.3	0.79	0.90	55.0
siderite	Aw02-03	48.1	2.98	0.71	48.2
siderite	Aw02-03	10.5	7.57	0.28	81.6
siderite	Aw02-03	19.6	5.73	0.25	74.4
siderite	Aw02-03	34.7	3.40	0.77	61.1
siderite	Aw04-04	11.2	6.40	0.13	82.2
siderite	Aw04-04	18.5	5.39	0.15	75.9
siderite	Aw04-04	11.1	6.79	0.13	82.0
siderite	Aw04-04	15.3	6.71	0.14	77.9
siderite	Aw04-04	13.4	6.42	0.12	80.0
siderite	Aw04-04	13.4	5.67	0.05	80.9

Appendix C5: Total digestions of sandstones measured by ICP-OES and -MS. SD = Standard deviation.

Sample	Al µg/g	SD Al µg/g	Ba µg/g	Ba SD µg/g	Ca µg/g	SD Ca µg/g	Fe µg/g	SD Fe µg/g	K µg/g	SD K µg/g	Mg µg/g	SD Mg µg/g
Aw02-01	25981	96.0	1175	5.00	6707	19.0	5654	38.0	13731	135	4657	0.60
Aw02-02	27444	126	650	0.10	3758	20.0	8742	57.0	13196	46.0	3198	14.0
Aw02-03	22973	92.0	997	12.0	4115	0.40	16175	111	12196	74.0	5900	13.0
Aw02-08	17314	40.0	1243	12.0	8682	20.0	9448	40.0	10108	20.0	6824	20.0
Aw02-12	23500	10.0	626	7.00	8098	1.00	6018	20.0	11208	61.0	3454	4.00
Aw03-01	16604	83.0	267	1.00	7310	42.0	11097	42.0	8292	42.0	4715	0.10
Aw04-02	27250	82.0	893	3.00	9690	18.0	8552	41.0	12242	2.00	6582	0.60
Aw04-04	18100	78.0	638	0.20	11274	78.0	6783	39.0	7760	78.0	3595	20.0
Aw05-01	6970	4.0	245	1.00	3670	18.0	3521	0.40	3486	40.0	1927	16.0
Aw05-03	24524	14.0	583	8.00	11821	99.0	6746	40.0	12798	60.0	7257	4.00
Aw05-04	21073	26.0	245	1.00	26285	16.0	10643	62.0	9454	42.0	9382	9.00
Aw05-07	27149	17.0	827	1.00	2496	16.0	7470	9.00	14658	87.0	2707	17.0
Bw01-01	23033	76.0	1034	7.00	6489	17.0	2559	19.0	7181	38.0	3205	1.00
Bw01-02	27931	150	4312	45.0	5585	27.0	5920	21.0	8604	68.0	1959	11.0
Bw02-01	26728	80.0	6579	0.00	6014	56.0	5991	44.0	5514	64.0	2892	26.0
Bw02-02	24768	36.0	600	3.00	8079	72.0	5481	4.00	5043	18.0	2184	7.00
Bw02-03	39573	140	368	3.00	4182	20.0	5223	20.0	5542	40.0	2571	20.0
Bw02-05	16095	38.0	5461	26.0	8788	4.00	5913	15.0	3709	2.0	3868	4.00
Cw02-01	28977	207	304	3.00	13257	38.0	6386	28.0	7284	87.0	2549	4.00
Cw03-01	33850	2.0	458	0.20	4129	20.0	3486	8.00	9103	6.00	4031	18.0
Cw04-01	35481	157	371	0.20	17231	174	11908	70.0	11194	139	10166	2.00
Cw04-05	35956	130	387	3.00	5029	1.00	8482	19.0	11265	6.00	5151	19.0

Sample	Mn µg/g	SD Mn µg/g	Na µg/g	SD Na µg/g	Ni µg/g	Ni SD µg/g	P µg/g	SD P µg/g	Sr µg/g	Sr SD µg/g	Ti µg/g	SD Ti µg/g
Aw02-01	260	3.00	5633	2.00	5.90	0.10	212	19.0	121	1.00	804	4.00
Aw02-02	183	1.00	4940	37.0	7.80	0.05	204	8.00	88	0.70	809	3.00
Aw02-03	384	6.00	4716	37.0	28.1	0.40	221	37.0	102	1.00	792	4.00
Aw02-08	256	3.00	2824	8.00	9.40	0.20	165	0.80	95.7	0.20	529	1.00
Aw02-12	265	4.00	4231	0.40	5.10	0.01	198	2.00	92.9	0.60	557	4.00
Aw03-01	366	2.00	2421	10.0	9.40	0.08	191	15.0	66.8	0.20	875	2.00
Aw04-02	376	5.00	7856	61.0	9.30	0.40	245	20.0	107	0.80	1080	2.00
Aw04-04	214	3.00	7897	39.0	5.30	0.10	160	14.0	114	0.80	686	2.00
Aw05-01	144	0.40	783	10.0	2.72	0.01	80.0	14.0	46.4	0.60	266	1.00
Aw05-03	565	11.0	4075	12.0	5.76	0.00	226	4.00	70	0.60	1213	1.00
Aw05-04	847	0.30	3107	6.00	8.50	0.10	196	6.00	131	0.05	989	0.90
Aw05-07	162	3.00	5851	0.30	7.70	0.30	287	14.0	89	0.30	832	0.30
Bw01-01	112	0.80	6927	19.0	6.00	0.20	210	38.0	286	2.00	684	2.00
Bw01-02	75.0	0.50	6634	87.0	6.40	0.40	255	8.0	457	0.60	607	4.00
Bw02-01	185	2.00	1379	15.0	3.80	0.10	204	5.00	376	0.70	802	9.00
Bw02-02	184	0.10	2368	11.0	3.14	0.00	215	18.0	122	2.00	798	0.70
Bw02-03	168	5.00	1423	8.00	6.20	0.20	377	0.60	405	0.60	970	0.20
Bw02-05	170	0.60	3091	13.0	2.96	0.08	122	13.0	517	0.08	490	4.00
Cw02-01	50.7	0.30	2130	33.0	5.80	0.40	179	5.00	218	1.00	526	0.90
Cw03-01	33.7	0.40	1904	1.00	8.50	0.20	204	10.0	264	2.00	589	0.80
Cw04-01	215	2.00	2002	35.0	13.6	0.30	291	16.0	348	5.00	1327	3.00
Cw04-05	75.1	0.00	2383	6.00	8.80	0.10	242	19.0	279	6.00	796	2.00

Appendix C5: Continuation

Sample	Zn µg/g	Zn SD µg/g	Li µg/g	Li SD µg/g	Sc µg/g	Sc SD µg/g	V µg/g	V SD µg/g	Cr µg/g	Cr SD µg/g	Co µg/g	Co SD µg/g
Aw02-01	13.6	0.60	18.3	0.04	2.23	0.02	12.5	0.20	8.60	0.10	4.58	0.08
Aw02-02	19.2	0.10	24.5	0.20	2.61	0.07	12.6	0.01	10.5	0.04	5.73	0.04
Aw02-03	61.0	1.00	16.6	0.20	1.99	0.04	13.6	0.04	6.90	0.10	13.1	0.20
Aw02-08	20.7	0.20	16.2	0.10	1.75	0.02	8.50	0.10	3.37	0.08	6.39	2E-03
Aw02-12	11.5	0.08	17.9	0.20	1.60	0.04	8.60	0.20	3.32	2E-03	8.80	0.10
Aw03-01	19.3	0.04	17.0	0.20	2.52	4E-03	12.6	0.06	12.0	0.20	6.80	0.10
Aw04-02	11.8	0.01	21.3	0.40	2.60	0.04	17.2	0.40	11.0	0.01	5.70	0.10
Aw04-04	7.90	0.20	18.6	0.10	1.76	0.04	11.4	0.02	17.0	0.20	3.40	0.06
Aw05-01	6.33	0.06	12.3	0.01	1.03	4E-03	4.70	0.10	0.94	2E-03	2.27	0.02
Aw05-03	6.70	0.20	20.3	0.20	3.47	0.06	15.9	0.10	11.3	0.20	4.00	0.10
Aw05-04	15.0	0.40	26.2	0.20	2.67	0.00	17.6	0.40	23.9	0.02	5.27	0.05
Aw05-07	7.70	0.10	21.8	0.20	2.39	0.03	14.9	0.07	5.70	0.20	5.56	0.09
Bw01-01	7.20	0.40	47.8	0.08	1.74	0.04	10.1	0.20	7.23	0.02	7.49	0.08
Bw01-02	12.7	0.10	62.0	0.40	1.81	4E-03	9.48	0.06	6.70	0.20	9.40	0.20
Bw02-01	9.7	0.02	62.5	0.00	2.26	0.04	12.2	0.40	3.53	0.04	7.30	0.10
Bw02-02	5.40	0.02	56.5	0.70	1.90	0.02	10.6	0.01	10.3	0.20	1.27	0.04
Bw02-03	8.37	6E-03	81.3	0.80	2.13	0.06	14.7	0.20	4.45	0.02	1.95	0.04
Bw02-05	12.7	0.40	32.2	0.40	1.42	8E-04	8.10	0.20	3.67	0.04	1.96	0.02
Cw02-01	10.7	0.02	63.6	0.50	1.75	0.05	11.0	0.02	2.26	0.05	3.22	0.01
Cw03-01	10.3	0.40	52.3	0.40	1.37	0.04	9.42	8E-03	4.70	0.10	2.83	1E-03
Cw04-01	16.3	0.50	46.0	0.20	2.91	0.02	21.8	0.00	8.68	0.07	8.10	0.10
Cw04-05	12.4	0.20	43.9	0.40	1.88	0.04	14.1	0.20	2.37	0.02	4.15	0.02

Sample	Cu µg/g	Cu SD µg/g	As µg/g	As SD µg/g	Y µg/g	Y SD µg/g	Cd µg/g	Cd SD µg/g	Cs µg/g	Cs SD µg/g	La µg/g	La SD µg/g
Aw02-01	7.70	0.10	2.40	0.20	6.15	0.04	0.06	0.01	1.69	0.01	6.84	2E-03
Aw02-02	6.83	0.04	2.57	0.05	5.81	0.04	0.04	0.00	1.80	0.00	7.77	0.07
Aw02-03	10.0	0.10	3.50	0.20	6.02	0.09	< 0,06	-	1.48	1E-04	5.29	0.06
Aw02-08	7.95	2E-03	1.60	0.20	4.86	0.08	< 0,06	-	1.22	0.04	5.54	0.04
Aw02-12	25.0	0.10	1.30	0.10	7.62	4E-03	< 0,06	-	1.28	0.02	5.87	0.01
Aw03-01	8.30	0.00	1.40	0.20	5.99	0.08	0.07	0.01	1.31	4E-03	6.44	0.02
Aw04-02	4.51	0.04	2.70	0.20	6.28	0.04	< 0,06	-	1.70	0.04	8.82	0.04
Aw04-04	1.39	0.02	1.80	0.20	4.71	0.06	0.10	0.02	1.09	0.02	6.61	0.06
Aw05-01	15.0	0.20	1.10	0.10	3.20	0.01	< 0,06	-	0.52	6E-03	3.94	0.04
Aw05-03	4.80	0.10	2.40	0.04	7.70	0.10	0.10	0.01	2.23	1E-03	6.03	0.08
Aw05-04	3.73	0.00	1.80	0.20	9.05	0.09	0.09	0.02	1.51	0.02	8.03	4E-03
Aw05-07	7.76	0.05	1.70	0.20	5.40	0.05	< 0,06	-	2.02	2E-03	4.80	0.05
Bw01-01	20.4	0.10	1.90	0.20	5.19	0.02	< 0,06	-	1.81	0.01	6.21	0.04
Bw01-02	31.7	0.04	2.60	0.40	5.27	7E-03	0.04	0.00	2.71	1E-03	6.68	0.02
Bw02-01	21.8	0.01	2.30	0.02	5.95	0.00	0.06	0.01	2.07	2E-03	7.51	0.04
Bw02-02	1.13	0.07	1.90	0.20	6.90	0.04	< 0,06	-	1.85	0.01	6.10	4E-03
Bw02-03	5.70	0.10	4.25	0.01	6.78	0.06	< 0,06	-	2.78	0.01	10.9	0.10
Bw02-05	2.00	0.10	2.66	0.02	4.32	0.02	< 0,06	-	1.09	0.02	4.31	0.06
Cw02-01	6.99	5E-03	2.30	0.40	9.23	0.07	0.09	0.02	1.74	0.01	6.50	0.05
Cw03-01	6.31	0.04	5.70	0.40	5.86	0.06	< 0,06	-	1.33	0.02	7.72	0.06
Cw04-01	13.8	0.09	5.20	0.50	9.92	0.02	0.09	0.00	2.28	0.03	14.3	1E-03
Cw04-05	10.3	0.20	3.80	0.10	7.05	0.06	< 0,06	-	2.06	0.01	8.71	0.09

Appendix C5: Continuation

Sample	Ce µg/g	Ce SD µg/g	Pr µg/g	Pr SD µg/g	Nd µg/g	Nd SD µg/g	Sm µg/g	Sm SD µg/g	Eu µg/g	Eu SD µg/g	Tb µg/g	Tb SD µg/g
Aw02-01	14.1	0.08	1.71	0.01	6.78	0.00	1.48	0.02	0.37	6E-03	0.20	4E-03
Aw02-02	15.5	2E-03	1.89	0.02	7.50	0.10	1.53	7E-03	0.37	5E-03	0.19	0.00
Aw02-03	10.6	4E-03	1.28	4E-04	5.21	0.04	1.23	0.02	0.32	4E-03	0.20	1E-03
Aw02-08	11.0	0.02	1.35	8E-03	5.46	0.06	1.16	0.04	0.25	2E-03	0.16	4E-04
Aw02-12	11.0	0.08	1.39	1E-03	5.48	1E-03	1.23	0.04	0.35	6E-03	0.23	4E-03
Aw03-01	13.4	0.10	1.62	4E-03	6.58	2E-03	1.41	0.04	0.31	4E-03	0.19	1E-03
Aw04-02	17.8	0.08	2.17	1E-03	8.74	4E-03	1.84	0.02	0.44	0.01	0.22	4E-03
Aw04-04	13.5	0.02	1.62	0.04	6.53	0.08	1.31	0.04	0.29	0.01	0.16	2E-03
Aw05-01	8.31	0.06	0.99	8E-04	3.90	0.01	0.78	0.04	0.15	2E-03	0.10	6E-04
Aw05-03	11.9	0.10	1.54	0.02	6.24	1E-03	1.41	0.02	0.31	4E-03	0.23	8E-03
Aw05-04	16.7	0.10	2.07	0.02	8.40	0.20	1.73	4E-03	0.42	5E-03	0.26	2E-03
Aw05-07	9.62	7E-03	1.20	1E-03	4.91	0.07	1.19	0.02	0.32	1E-04	0.18	5E-03
Bw01-01	12.0	0.08	1.51	8E-03	5.94	0.06	1.29	0.01	0.29	2E-04	0.17	4E-04
Bw01-02	12.5	0.09	1.63	9E-03	6.68	2E-03	1.45	9E-03	0.27	6E-03	0.18	4E-03
Bw02-01	15.0	0.05	1.86	0.02	7.44	0.04	1.46	0.04	0.27	0.01	0.20	2E-03
Bw02-02	12.3	0.09	1.55	5E-03	6.29	0.02	1.38	0.02	0.35	0.01	0.22	2E-04
Bw02-03	21.3	0.20	2.71	0.02	10.8	0.20	2.23	0.02	0.51	0.01	0.24	2E-03
Bw02-05	8.38	2E-03	1.02	0.02	4.12	0.04	0.93	0.04	0.15	0.01	0.15	4E-03
Cw02-01	12.6	1E-03	1.54	0.01	6.05	4E-03	1.34	0.04	0.31	1E-04	0.26	5E-03
Cw03-01	14.6	0.10	1.80	0.02	7.01	0.06	1.57	0.02	0.41	1E-03	0.20	2E-03
Cw04-01	29.2	0.02	3.57	0.03	13.6	0.05	2.68	0.03	0.62	0.01	0.35	2E-03
Cw04-05	16.7	0.10	2.05	0.02	7.87	0.04	1.74	4E-03	0.41	6E-03	0.24	4E-03

Sample	Gd µg/g	Gd SD µg/g	Dy µg/g	Dy SD µg/g	Ho µg/g	Ho SD µg/g	Er µg/g	Er SD µg/g	Tm µg/g	Tm SD µg/g	Yb µg/g	Yb SD µg/g
Aw02-01	1.38	0.02	1.28	8E-03	0.24	1E-03	0.70	0.02	0.10	1E-03	0.68	0.01
Aw02-02	1.32	0.04	1.15	0.04	0.22	4E-03	0.63	1E-03	0.09	7E-04	0.63	5E-03
Aw02-03	1.29	0.04	1.20	7E-03	0.23	2E-03	0.67	0.00	0.10	4E-03	0.65	0.01
Aw02-08	1.08	0.04	0.97	0.02	0.19	2E-03	0.53	4E-03	0.08	1E-04	0.52	6E-03
Aw02-12	1.40	0.01	1.42	0.02	0.29	2E-03	0.82	0.01	0.11	2E-03	0.73	8E-03
Aw03-01	1.27	6E-03	1.18	0.02	0.24	4E-03	0.69	0.01	0.10	6E-04	0.68	8E-03
Aw04-02	1.60	0.04	1.31	0.02	0.25	1E-04	0.70	0.01	0.10	2E-03	0.66	0.02
Aw04-04	1.11	0.04	0.97	8E-04	0.19	1E-04	0.55	0.01	0.08	1E-04	0.55	8E-03
Aw05-01	0.68	2E-04	0.62	0.02	0.12	2E-03	0.37	4E-03	0.06	2E-03	0.42	0.00
Aw05-03	1.53	0.04	1.45	0.04	0.29	6E-03	0.86	6E-03	0.12	1E-03	0.87	0.02
Aw05-04	1.61	7E-03	1.70	0.02	0.33	5E-03	0.98	0.01	0.14	0.00	0.92	0.01
Aw05-07	1.24	0.01	1.08	0.01	0.22	3E-03	0.61	0.01	0.09	2E-04	0.59	7E-03
Bw01-01	1.20	0.02	1.05	0.01	0.20	4E-03	0.59	0.01	0.08	2E-03	0.56	0.01
Bw01-02	1.26	0.02	1.05	0.01	0.21	7E-03	0.60	1E-03	0.08	2E-03	0.59	6E-04
Bw02-01	1.30	0.04	1.20	4E-03	0.23	4E-03	0.68	7E-03	0.10	2E-03	0.65	5E-03
Bw02-02	1.43	0.01	1.37	9E-04	0.26	4E-03	0.76	7E-03	0.10	1E-04	0.69	4E-03
Bw02-03	1.69	0.04	1.41	4E-03	0.27	2E-03	0.81	0.02	0.12	2E-04	0.83	6E-04
Bw02-05	0.97	4E-03	0.87	0.01	0.17	4E-03	0.49	0.01	0.07	2E-03	0.48	4E-03
Cw02-01	1.52	0.02	1.73	0.01	0.33	4E-03	0.95	0.02	0.12	2E-03	0.86	7E-04
Cw03-01	1.45	6E-03	1.16	1E-03	0.23	4E-03	0.67	2E-04	0.10	4E-03	0.67	0.02
Cw04-01	2.40	0.03	2.03	1E-03	0.39	3E-04	1.11	0.02	0.16	3E-03	1.06	3E-03
Cw04-05	1.58	0.02	1.42	0.02	0.27	7E-03	0.79	0.02	0.11	1E-03	0.77	7E-03

Appendix C5: Continuation

Sample	Lu µg/g	Lu SD µg/g	Pb µg/g	Pb SD µg/g	Th µg/g	Th SD µg/g	U µg/g	U SD µg/g
Aw02-01	0.10	2E-03	6.25	0.02	2.67	0.02	0.97	0.01
Aw02-02	0.09	1E-04	5.45	0.04	2.63	9E-03	0.84	5E-03
Aw02-03	0.10	2E-03	6.41	0.06	2.41	0.04	1.06	2E-03
Aw02-08	0.07	2E-03	4.71	2E-03	2.18	0.02	0.67	8E-03
Aw02-12	0.11	8E-04	4.89	0.06	2.45	4E-03	0.79	0.01
Aw03-01	0.10	2E-03	3.97	0.02	2.37	0.01	0.81	8E-04
Aw04-02	0.10	2E-03	5.05	0.08	2.74	0.02	0.93	6E-03
Aw04-04	0.09	1E-03	3.44	0.02	2.37	0.02	0.86	0.02
Aw05-01	0.06	1E-04	2.15	8E-03	1.87	0.01	0.65	8E-04
Aw05-03	0.13	1E-04	4.70	0.02	3.31	0.04	1.30	0.01
Aw05-04	0.14	0.00	4.31	0.04	2.63	0.04	0.96	7E-04
Aw05-07	0.09	2E-03	6.34	0.03	2.94	0.02	0.92	0.01
Bw01-01	0.08	2E-03	6.26	0.04	2.60	0.02	0.65	4E-04
Bw01-02	0.09	1E-03	9.57	0.06	2.73	0.02	0.60	0.006
Bw02-01	0.10	4E-03	4.72	2E-03	2.57	1E-03	0.74	4E-03
Bw02-02	0.10	4E-03	3.58	0.02	2.54	0.01	0.62	0.01
Bw02-03	0.12	2E-03	9.60	0.10	3.75	0.04	0.74	8E-03
Bw02-05	0.07	4E-03	3.91	0.02	1.90	2E-03	0.52	6E-03
Cw02-01	0.12	2E-03	5.78	0.01	4.05	0.00	1.01	0.01
Cw03-01	0.10	2E-03	23.1	0.20	2.98	0.02	0.67	8E-03
Cw04-01	0.15	2E-03	9.66	0.09	4.32	0.01	1.06	0.02
Cw04-05	0.11	1E-03	8.71	0.06	3.89	0.02	0.84	2E-04

Appendix C6: Pore lining image analysis for determination of minerals in exposure to open pores [%]. Authigenic minerals covering detrital grains are listed in combination with the grain type (e.g. Qz_m + cut). For abbreviation compare "List of abbreviations".

mineral phase	Aw02-02	Aw02-04	Aw02-06	Aw02-08	Aw02-12	Aw04-02	Aw04-04	Aw05-01
Qz_m	26.4	12.1	28.1	11.7	26.3	58.2	48.3	22.4
Qz_m*ill/smec	0.29	0.00	0.00	0.00	0.00	0.00	0.00	0.00
Qz_m + cut	21.3	34.9	16.1	21.2	16.8	0.13	0.41	0.00
Qz_m + FeOx	0.83	0.32	0.00	0.00	0.00	1.54	1.54	1.30
Qz_m + gal	0.34	0.00	0.00	0.00	0.00	0.00	0.00	0.00
Qz_m + bit	0.00	0.00	0.00	0.00	0.00	0.00	0.52	23.1
Qz_m + kaol	0.00	0.00	0.00	0.00	0.00	0.00	0.00	0.00
Qz_m + FeOx + kaol	0.00	0.00	0.00	0.00	0.00	0.00	0.00	0.00
Qz_m + FeOx + bit	0.00	0.00	0.00	0.00	0.00	0.00	0.00	0.00
Qz_p	2.09	0.00	0.79	0.72	1.59	0.88	2.03	0.77
Qz_p + cut	0.37	4.87	4.59	9.90	7.43	0.00	0.00	0.00
Qz_p + Feox	0.24	0.00	0.00	0.00	0.00	0.00	0.00	0.54
Qz_p + kao	0.51	0.00	0.00	0.00	0.00	0.00	0.00	0.00
Qc + cut	0.00	0.00	0.70	0.76	0.00	0.00	0.00	0.00
Qz_p + bit	0.00	0.00	0.00	0.00	0.00	0.00	0.00	2.43
Kfsp	9.78	9.93	6.40	10.2	3.41	14.5	8.64	10.1
Kfsp*ill	1.08	3.45	0.35	0.07	0.29	0.00	0.24	0.00
Kfsp*kaol	0.10	0.00	0.00	0.00	0.00	0.00	0.00	0.00
Kfsp + cut	2.25	2.27	0.67	3.32	0.65	0.00	0.00	0.00
Kfsp + FeOx	0.28	0.00	0.00	0.00	0.00	0.00	0.00	0.00
Kfsp + bit	0.00	0.00	0.00	0.00	0.00	0.00	0.00	3.95
Kfsp + kaol	0.00	0.00	0.00	0.00	0.00	0.00	0.00	0.00
Kfsp + FeOx + kaol	0.00	0.00	0.00	0.00	0.00	0.00	0.00	0.00
Plag	0.00	0.00	0.00	0.00	0.00	0.00	0.00	0.00
Lv_{fel}	11.0	4.62	3.06	3.35	8.74	9.02	7.24	1.21
Lv_{fel}*ill	0.79	8.15	0.33	1.60	2.86	1.39	0.79	0.72
Lv_{fel}*dol	0.00	0.00	0.44	0.00	0.00	0.00	0.00	0.00
Lv_{fel}*kao	0.00	0.00	0.28	0.00	0.00	0.00	0.00	0.00
Lv_{fel} + cut	2.70	4.52	1.03	2.96	0.00	0.00	0.00	0.00
Lv_{fel}*ill + FeOx	0.00	0.00	0.00	0.26	0.00	0.00	0.00	0.00
Lv_{fel}*ill + cut	0.00	0.15	0.00	1.21	0.00	0.00	0.00	0.00
Lv_{fel} + bit	0.00	0.00	0.00	0.00	0.00	0.00	0.00	0.00
Lv_{fel} + FeOx	0.00	0.00	0.00	0.00	0.00	0.07	0.00	0.00
Lv_{fel} + FeOx + kaol	0.00	0.00	0.00	0.00	0.00	0.00	0.00	0.00
Lv_{fel} + kaol	0.00	0.00	0.00	0.00	0.00	0.00	0.00	0.00
Lv_{maf}	1.78	1.59	0.00	0.00	0.00	0.38	0.00	0.00
Lv_{maf} + cut	0.00	0.24	0.00	0.00	0.00	0.00	0.00	0.00
Lv_{maf}*ill/smec	0.00	0.00	0.60	0.00	0.00	0.00	0.00	0.00
Lm_{pel}	0.00	2.05	0.00	0.00	0.00	0.00	0.00	0.00
L_{QFG}	1.79	0.18	0.00	0.63	0.00	0.00	0.00	0.00
L_{QFG} + cut	0.46	0.00	0.66	0.26	0.00	0.00	0.00	0.00
Ls_{psam}	0.00	0.22	0.00	0.00	0.00	0.00	0.00	0.00
Ls_{pel}	0.23	0.00	0.00	0.00	0.00	0.00	0.00	0.00
Lc	0.00	0.31	0.00	0.00	0.00	0.00	0.00	0.00
Mica	0.14	0.02	0.00	0.00	0.00	0.00	0.00	0.13
FeOx	0.65	0.00	0.34	0.74	0.09	1.45	0.51	0.19
FeOx + bit	0.07	0.00	0.00	0.00	0.00	0.00	0.00	0.00

Appendix C6: Continuation

mineral phase	Aw02-02	Aw02-04	Aw02-06	Aw02-08	Aw02-12	Aw04-02	Aw04-04	Aw05-01
cut	0.03	2.53	0.19	1.26	0.05	0.00	0.00	0.00
Qz	0.00	0.00	0.00	0.00	0.00	0.78	1.30	0.00
dol	2.61	0.00	13.65	4.38	9.41	2.63	8.14	5.73
anhy	0.29	0.00	1.03	0.00	0.00	0.00	0.76	1.27
bar	0.00	0.29	0.00	0.00	0.00	0.00	0.00	0.00
gal	0.23	1.82	0.41	0.03	1.77	0.00	0.00	0.00
kaol	4.27	1.85	14.3	5.17	15.5	5.03	6.65	11.9
kaol + bit	6.43	0.00	5.90	17.6	5.02	2.62	9.86	14.1
IM	0.00	0.45	0.00	0.00	0.00	0.00	0.00	0.00
Bit	0.00	0.00	0.00	0.00	0.00	0.00	0.00	0.00
*ill	0.74	0.08	0.00	0.00	0.00	1.03	2.5	0.30
*ill/smec	0.00	0.00	0.00	0.08	0.18	0.00	0.00	0.00
*ill/smec + FeOx	0.00	0.00	0.00	2.54	0.00	0.00	0.00	0.00
*kao	0.00	3.02	0.00	0.00	0.00	0.00	0.00	0.00
opaque	0.00	0.00	0.00	0.00	0.00	0.39	0.56	0.00
sum	100	100	100	100	100	100	100	100

mineral phase	Aw05-03	Aw05-04	Bw01-01	Bw02-01	Bw02-02	Bw02-03	Bw02-05
Qz_m	6.10	32.4	28.0	10.3	1.03	12.7	0.43
Qz_m*ill/smec	0.00	0.00	0.00	0.00	0.00	0.00	0.00
Qz_m + cut	0.00	0.28	1.50	0.00	0.00	0.00	0.00
Qz_m + FeOx	0.00	9.62	0.08	14.4	3.75	14.91	40.5
Qz_m + gal	0.00	0.00	0.23	0.00	0.00	0.00	0.00
Qz_m + bit	36.6	1.56	0.50	0.29	0.00	2.86	0.00
Qz_m + kaol	0.00	0.00	2.30	7.20	0.00	1.14	0.00
Qz_m + FeOx + kaol	0.00	0.00	0.00	9.88	44.0	0.00	0.31
Qz_m + FeOx + bit	0.00	0.00	0.00	0.00	0.00	1.09	0.00
Qz_p	0.00	0.54	1.78	0.00	0.00	0.05	0.07
Qz_p + cut	0.00	0.00	0.55	0.00	0.00	0.00	0.00
Qz_p + Feox	0.00	0.00	0.00	0.00	0.84	0.00	0.93
Qz_p + kao	0.00	0.00	0.00	0.00	0.00	0.00	0.00
Qc + cut	0.00	0.00	0.00	0.00	0.00	0.00	0.00
Qz_p + bit	0.00	0.00	0.00	0.00	0.00	0.48	0.00
Kfsp	4.35	14.0	14.1	9.64	3.23	6.94	2.35
Kfsp*ill	0.00	0.00	1.59	0.00	1.07	1.38	0.22
Kfsp*kaol	0.00	0.00	0.00	0.00	0.00	0.00	0.00
Kfsp + cut	0.00	0.00	0.00	0.00	0.00	0.00	0.00
Kfsp + FeOx	0.00	0.12	0.00	0.04	0.00	0.29	0.00
Kfsp + bit	12.5	0.00	0.00	0.00	0.00	0.00	0.00
Kfsp + kaol	0.00	0.00	0.28	0.22	0.43	0.00	0.00
Kfsp + FeOx + kaol	0.00	0.00	0.00	0.53	0.00	0.50	0.00
Plag	0.00	0.00	0.00	0.00	0.00	0.00	0.00
Lv_{fel}	0.59	10.3	0.00	1.12	0.90	1.29	0.90
Lv_{fel}*ill	0.00	0.00	1.18	0.14	0.86	3.15	0.00
Lv_{fel}*dol	0.00	0.00	0.00	0.00	0.00	0.00	0.00
Lv_{fel}*kao	0.00	0.00	0.00	0.00	0.00	0.00	0.00

Appendix C6: Continuation

mineral phase	Aw05-03	Aw05-04	Bw01-01	Bw02-01	Bw02-02	Bw02-03	Bw02-05
Lv_{fel} + cut	0.00	0.00	0.00	0.00	0.00	0.00	0.00
Lv_{fel}*ill + FeOx	0.00	0.00	0.00	0.59	0.00	0.00	0.05
Lv_{fel}*ill + cut	0.00	0.00	0.00	0.00	0.00	0.00	0.00
Lv_{fel} + bit	6.77	0.00	0.00	0.00	0.00	0.00	0.00
Lv_{fel} + FeOx	0.00	0.52	0.00	0.87	0.50	1.20	2.32
Lv_{fel} + FeOx + kaol	0.00	0.00	0.00	0.38	0.56	0.48	0.00
Lv_{fel} + kaol	0.00	0.00	0.00	0.00	2.54	0.00	0.00
Lv_{maf}	0.00	0.00	0.00	0.00	0.00	0.00	0.00
Lv_{maf} + cut	0.00	0.00	0.00	0.00	0.00	0.00	0.00
Lv_{maf}*ill/smec	0.00	0.00	0.00	0.00	0.00	0.00	0.00
Lm_{pel}	0.00	0.00	0.00	0.00	0.00	0.00	0.00
L_{QFG}	0.00	0.23	0.00	0.00	0.00	0.12	0.00
L_{QFG} + cut	0.00	0.00	0.00	0.00	0.00	0.00	0.00
Ls_{psam}	0.00	0.00	0.00	0.00	0.00	0.00	0.00
Ls_{pel}	0.00	0.00	0.00	0.00	0.00	0.00	0.00
Lc	0.00	0.00	0.00	0.00	0.00	0.00	0.00
Mica	0.00	0.00	0.00	0.02	0.00	0.00	0.00
FeOx	0.00	0.12	0.19	4.70	0.00	3.36	5.73
FeOx + bit	0.00	0.00	0.00	0.00	0.00	0.00	0.00
cut	0.00	0.00	0.00	0.00	0.00	0.00	0.00
qz	4.38	4.57	0.00	1.78	3.56	6.39	2.59
dol	1.03	4.30	4.88	6.57	9.00	5.80	9.46
anhy	0.99	2.32	0.00	0.00	0.00	0.00	2.87
bar	0.00	0.00	0.00	0.00	0.00	0.00	0.00
gal	0.00	0.00	0.03	0.00	0.00	0.00	0.00
kaol	0.00	0.00	37.6	26.0	19.6	28.5	28.8
kaol + bit	17.5	18.2	0.00	0.00	0.00	0.00	0.00
IM	0.00	0.00	0.00	0.00	0.00	0.00	0.00
bit	0.00	0.00	0.00	0.00	0.00	0.00	0.00
*ill	0.00	0.00	0.85	0.78	2.76	1.15	0.00
*ill/smec	0.00	0.00	0.00	0.00	0.00	0.00	0.00
*ill/smec + FeOx	0.00	0.00	0.00	0.00	0.00	0.00	0.00
*kao	0.00	0.00	0.00	0.00	0.00	0.00	0.00
opaque	9.07	1.06	4.40	4.49	5.40	6.17	2.47
sum	100	100	100	100	100	100	100

Appendix C7: Total surface area determination using BET-analysis after Brunauer et al. (1938) with N_2 as adsorption gas.

	SSA	2σ	total SSA
	[m^2/g]	[m^2/g]	[m^2]
Aw02-01	1.75	6.0E-02	7.44
Aw02-02	1.85	1.7E-02	6.93
Aw02-03	1.37	5.0E-03	5.98
Aw02-08	1.03	1.0E-02	3.32
Aw02-12	1.40	1.7E-02	4.29
Aw03-01	1.34	3.0E-03	5.37
Aw04-02	1.55	8.0E-03	5.82
Aw04-04	1.06	2.0E-03	7.06
Aw05-01	0.20	2.6E-03	1.59
Aw05-03	1.79	6.0E-03	7.80
Aw05-04	0.93	1.0E-02	3.67
Aw05-07	1.21	6.0E-03	5.43
Bw01-01	1.39	1.1E-02	5.05
Bw01-02	2.04	4.0E-03	9.22
Bw02-01	1.68	1.2E-02	8.47
Bw02-02	1.63	1.0E-02	11.4
Bw02-03	2.09	7.0E-03	8.98
Bw02-05	1.08	1.3E-02	3.88
Cw02-01	0.99	8.1E-03	3.56
Cw03-01	1.37	1.7E-02	4.43
Cw03-02	1.87	2.3E-02	12.1
Cw04-01	1.73	3.0E-03	8.90
Cw04-05	1.43	1.9E-02	5.98
Aw02-04	1.61	8.0E-03	7.34
Aw02-06	1.00	2.3E-02	5.08
Aw04-01	0.91	1.2E-02	3.83
Aw04-03	0.75	2.4E-03	3.72
Al_2O_3 standard	79.4	1.7E-01	-
Target value	79.8	4.0E-01	-

Appendix C8: Composition of natural gas from field A. Results are listed in mol%.

Well	**Aw01**	**Aw01**	**Aw11**	**Aw11**
Date	05/02/85	02/04/85	28/11/70	27/11/70
depth [m]	-	-	3027.0-3040.8	3027.0-3040.8
methane (C1)	90.5	90.5	90.9	90.8
ethane (C2)	3.57	3.51	3.80	4.00
+ ethane (C2+)	-	-	0.30	0.30
propane (C3)	0.75	0.77	-	-
iso-Butane (I-C4)	0.12	0.13	-	-
normal-Butane (N-C4)	0.15	0.16	-	-
iso-Pentane (I-C5)	0.05	0.05	-	-
normal-Pentane (N-C5)	0.04	0.05	-	-
+ hexane (C6+)	0.09	0.10	-	-
cyclo C6 (C6H12)	-	-	-	-
CO_2	0.69	0.68	0.70	0.60
N_2	4.00	4.07	4.20	4.30
H_2S	<0.01	<0.01	-	-